Pham, Xuan Phuc (2008) *Green water and loading on high speed containerships.* PhD thesis.

http://theses.gla.ac.uk/249/

Copyright and moral rights for this thesis are retained by the author

A copy can be downloaded for personal non-commercial research or study, without prior permission or charge

This thesis cannot be reproduced or quoted extensively from without first obtaining permission in writing from the Author

The content must not be changed in any way or sold commercially in any format or medium without the formal permission of the Author

When referring to this work, full bibliographic details including the author, title, awarding institution and date of the thesis must be given

Glasgow Theses Service
http://theses.gla.ac.uk/
theses@gla.ac.uk

Green Water and Loading on High Speed Containerships

By

Xuan Phuc Pham

B.Eng.

A Thesis Submitted to the University of Glasgow in Fulfilment of the Degree of Doctor of Philosophy

Department of Naval Architecture and Marine Engineering

University of Glasgow

December 2007

To my dearest parents Thi Thu Nguyen and Van Xuan Pham,
to my darling wife Huong Thuy Tran,
to my much loved sisters and their children,
this thesis is dedicated.

DECLARATION

Except where reference is made to the work of others,
this thesis is believed to be original.

Acknowledgements

This thesis has taken seven years of continual research to complete with immense amount of patience and support from the following people I wish to pay my deepest gratitude to.

Firstly, I would like to express my limitless thank to my supervisor, Dr. Kamlesh Varyani. More than a supervisor, like a father he has guided me through the research with his extensive knowledge, experience and ever optimism. Without him, this thesis could never have been accomplished.

Special thanks are sent to Professor Nigel Barltrop, for his availability and willingness to share his immense knowledge and practical experience that always inspired me to do things better than it had been.

Sincere thanks must go to the technical staff, Charlie Keay, David Sinclair, Bill McGuffy, Jack Sharkey, Frank Sweeney, Bill Wright, Grant Dunning and Donald Nicholson, for their tireless assistance in carrying out the tests for this research and above all their invaluable friendship that helped me feel more like home.

A warm thank to Thelma Will who has been taking care of me as a mother. Her bright smile will be remembered in my life since it has enlightened me and made me feel more optimistic in numerous occasions.

Great thanks to my flatmate Jie Xia for her invaluable help in cooking and extra-ordinary tolerance in putting up with many of my unreasonable frustrations during the time of writing up this thesis.

Deep appreciation is also sent to Yanzhuo Xue, Nana Yang, Liang Shen, Xu Li and Quixin Gao for their great friendship and tremendous help during my joyful time in the Department and in Pinkston Drive.

I would also like to thank my office mates for their friendship and willingness to help whenever I asked for.

Finally, I would like to thank my parents and my dearest wife Huong Thuy Tran, who have given me limitless encouragement and understanding over the years. This thesis is dedicated to them.

Summary

Green water problem and its loading effects on high speed containerships was investigated with the purpose of developing a modelling framework that can practically guide naval architects to a better understanding of this problem and improvements in design.

The research began by reviewing extensive publications relevant to the understanding of green water, limitations in the ways the problem had been addressed and establishing a methodology that could effectively unlock the physics and efficiently solve the problem.

As a first step, a summarised background to how green water started, developed and finally took place was presented. An experimental programme was then implemented in order to observe the occurrence and to explore the physics behind these events.

From the outcome of the experiments, it was obvious that green water modelling could be developed and solved by Computational Fluid Dynamics (CFD) technique through Volume of Fluid (VoF) method. To provide a starting point for this research, theoretical background of CFD was briefly introduced. Furthermore, in order to validate this approach, two benchmark tests were implemented and compared with published experimental data. It showed that in both cases, the simulation could accurately reproduce the results obtained from experiments.

Following this analysis, research continued to expand the CFD simulation to modelling of green water. Due to the complex and random nature of green water, development of the simulation framework was semi-empirical and based partly on experimental data. A pure theoretical approach could have been adopted.

However, taking into consideration current limitations in ship motion prediction theories and sensitivity of green water to elemental factors, it was justified that semi-empirical approach was appropriate.

The simulation was conducted and the output results were compared with experimental results for a variety of test conditions that involved ship velocity, wave height and period. Good agreement between simulation and experiment was obtained. For all loading cases, experimental results were reproduced fairly well. This suggested that the modelling framework was adequate for all practical purposes.

Investigation was also conducted on a series of rectangular breakwaters that were fitted on the forecastle deck. Changes in water behaviour and loading following changes in the breakwater were well reflected. This implied that instead of a rectangular breakwater, the simulation model could also be applied to other types of breakwaters.

The results suggested that the simulation methodology has many practical applications. Within naval architecture, it can be used to perform parametric studies in order to select an optimal design of breakwater for a ship. In other sectors such as coastal engineering, the methodology can be adopted to investigate the interaction between water surge and a seawall or offshore breakwater.

In conclusion, it was found that the developed modelling framework shows potential for simple modelling of green water in which the behaviour of the water and its loading effects could be well reflected. It was further concluded that, provided appropriate principles are applied, the methodology has potential for other engineering applications. While it is acknowledged that current model may be limited by its semi-empirical basis and issues associated with computational requirements, it is noted that considerable possibilities for future research and development remains to be explored.

Table of Contents

List of Figures

List of Tables

Nomenclature

Roman

a	acceleration vector
$a_{gravity}$	acceleration due to gravity and pitch angle
a_x	acceleration in x-direction
A_i	sectional area of strip
A_p	area of each perforation
b	half beam at knuckle or deck edge
B	breadth of ship
B_{local}	local breadth of ship
$B_{takeoff}$	breadth of ship at the position water particle takes off the deck edge
Cb	block coefficient of ship
d	draught of ship
D	depth of ship
D_p	diameter of perforation
e	internal energy of fluid element
f_x	body force in x-direction
f_y	body force in y-direction
f_z	body force in z-direction
f	body force vector
F	force vector
F_{impact}	impact force
FB	freeboard
FB_{extra}	equivalent added freeboard due to introduced knuckles in ship bow
FBE	freeboard exceedance
Fn	Froude's number
F_{peak}	peak force

g	gravity constant ($9.81 m/s^2$)
GM	distance between meta centre and transverse centre of gravity
h	height of knuckle or deck edge above keel
h_0	initial water depth in reservoir prior to dam break
h_{lc}	height of load-cell unit
$H(x,t)$	height of water downstream after the dam breaks, dependent on time and longitudinal distance downstream
H_0	initial water height behind the dam
H_e	encountered wave height
H_{gw}	green water height on deck
H_{gen}	generated wave height
H_{max}	maximum green water height
H_{stem_head}	water height at stem head of ship
H_{wanted}	required wave height
Kxx	radius of gyration around x axis
Kyy	radius of gyration around y axis
Lpp	length between perpendiculars
M	mass
p	pressure
P	pressure
P_d	dynamic pressure from falling block of water from wave prior to collapse on deck
P_{deck}	deck pressure
P_i	dynamic pressure from upward vertical velocity of the deck
P_s	hydrostatic pressure
P_t	total pressure
Q	discharge rate of water jet
r	notional relative motion
r_c	corrected relative motion
$\dot{r}_c$	first derivative of corrected relative motion
r_0	amplitude of notional relative motion

r_S	relative wave motion including swell-ups
R	range of flight of water particle
Rn	Reynold number
s	absolute vertical displacement
$\dot{s}$	absolute vertical velocity
$\ddot{s}$	absolute vertical acceleration
s_0	amplitude of absolute vertical displacement
t	time
T_F	time of flight of water particle
u	velocity in x-direction
u_0	horizontal component of orbital velocity at surface
u_t	total relative velocity
U	ship velocity
U_{front}	velocity of front water
U_{gw}	velocity of green water flow
U_R	horizontal component of total velocity of water particle
v	velocity in y-direction
v_{deck}	vertical velocity of deck
v_{gw}	velocity of green water flow
V	velocity of fluid element
w	velocity in z direction
x	distance in x-direction or x coordinate
x_I	longitudinal distance at which water particle lands on deck
$x_{takeoff}$	longitudinal distance at which water particle takes off the deck edge
y	y coordinate
y_I	transverse distance from ship centreline of the position where water particle lands on deck
z	z coordinate
z_φ	depth of effective centroid between centroids of sectional areas of a strip

Greek

α_e	maximum encountered wave slope
β	factor related to the location of the structure along the ship, highest at the bow (for breakwater design)
δ	flare angle at deck edge
Δ	ship displacement
Δt	time difference
ε	bearing of trajectory relative to axis of ship
γ	grid refinement factor
κ	grid size
η_3	heave displacement
$\dot{\eta}_3$	first derivative of heave
$\ddot{\eta}_3$	second derivative of heave
η_5	pitch angle in radians
$\dot{\eta}_5$	first derivative of pitch
$\ddot{\eta}_5$	second derivative of pitch
λ	wavelength
λ_e	encountered wave length
φ_I	source strength
θ	taper angle at deck edge
ρ	water density (1025kg/m^3 for sea water and 1000kg/m^3 for fresh water)
τ_{ij}	stress in j-direction exerted on a plane perpendicular to i-axis
ω	wave frequency in rad/s
ω_e	encounter wave frequency in rad/s
Ψ_1	integral by Shearer (1950)
Ψ_2	integral by Shearer (1950)
υ	kinematic fluid viscosity
ζ	incident wave elevation

ζ_{bw} bow wave elevation

ζ_c corrected wave elevation

$\dot{\zeta}_c$ first derivative of corrected wave elevation

ζ_{0f} far-field radiated wave

ζ_s surface elevation at the side of the ship

ζ_{nw} non-wave or local disturbance (for bow wave calculation)

ζ_{sux} dynamic swell-up elevation in x direction

ζ_{suy} dynamic swell-up elevation in y direction

ζ_w wave disturbance due to the source (for bow wave calculation)

Symbol

ℓ distance from FP at which minimum θ occurs

$\Re$ repeatability index

Acronyms

2D	Two dimension
3D	Three dimension
AP	Aft Perpendicular
CFD	Computational Fluid Dynamics
CPU	Central Processing Unit
FP	Forward Perpendicular
FPSO	Floating Production, Storage and Offloading unit
FVM	Finite Volume Method
GRP	Glass Reinforced Plastic
ITTC	International Towing Tank Conference
LC	Load Cell
LCG	Longitudinal Centre of Gravity
LVDT	Linear Variable Differential Transformer
PC	Personal Computer
PISO	Pressure-Implicit with Splitting of Operators
PRESTO	PREssure STaggering Option
QUICK	Quadratic Upwind Interpolation of Convective Kinematics
RAO	Response Amplitude Operator
RANSE	Reynold-Averaged Navier-Stokes Equations
SIMPLE	Semi-Implicit Method for Pressure-Linked Equations
SIMPLEC	SIMPLE-Consistent
SUC	Swell-Up Coefficient
VCR	Video Cassette Recorder
VOF	Volume of Fluid
WP	Wave Probe

Chapter 1:
Introduction

1.1 Introduction

1.1.1 Problems of water shipment onto ship decks

Ships travelling in open sea expose themselves to numerous environmental factors such as wind, waves and current. When badly combined, these factors can result in very unfriendly motions of the ships that consequently lead to a number of issues for naval architects to deal with.

Amongst the most concerned issues is the shipment of water on to the ship deck. It happens when the relative motions between the ship deck and the local water surface become so excessive that water can overcome the deck edge and, following its momentum, intrudes deck area. In small quantities, this water takes the form of spray and causes little harm other than wetting the deck. In large quantities, however, the water is shipped in flows and can be very destructive. In order to distinguish the two forms, the latter is widely referred to as ‘green water’. ‘Green’ water is termed simply because seawater is rather green than blue (Buchner, 2002).

Apart from causing inconveniences in wetting the deck, the reason that green water has been seriously considered is because it greatly affects safety and operability of ships in both naval and merchant services. Whilst spray can disturb the manning on deck and affect visibility to forecastle deck, green water can seriously endanger crew’s lives and challenge the structural integrity of deck machineries, equipment and structures.

When serious green water takes place, ships may be forced to reduce their speed or to change heading so that potential threats can be minimised. The operability of the ships is also restrained to a great deal in such situations. For some ship categories such as naval ships, this causes great concern since such remedies against deck wetness are not regarded as regulation (Bales, 1978, 1979a, 1979b). Therefore, an effective design of ship hull is still desirable. For merchant ships, involuntary speed loss and change of heading exert immense pressure on the shipping schedule and failure will result in considerable loss of income.

1.1.2 Green water problems to containerships

Containerships are the fastest growing type in the commercial shipping history. Designing a big, economic and faster containership has been the major trend during the last four decades. The loading capacity of containerships has increased from a few hundred containers for the first full containership to more than 8000TEU for the most modern ships now in operation. This evolution was a cutting edge technology and a lot of research and development work is required in order to push the limits. Containerships with higher container capacities have to operate at higher speeds than those ships with lower capacity, because they need more harbour time. In doing so, the containerships should be capable of fighting the bad seas in order to protect the containers.

Tight schedule, high operational speed and large amount of uncovered deck cargo have made green water a genuine concern for containerships. When happens, besides endangering manning on deck, green water carrying high kinetic energy can cause serious damage to structures, cargo, and equipment. Most vulnerable of all is the forecastle deck upfront. Secondly, containers, not covered by any means on deck, are highly at risk to green water. All of these issues must be considered and dealt with at the design stage of containerships.

Massive damage can be predicted when ferocious green water occurs and this inflicts on many parties. For ship owners, together with the visible costly affairs of structural damage and loss of containers are substantial costs of recovering the ruined container stacks, ship repair, downtime and upset sailing schedule. To other parties, there are thousands of drifting containers, barely afloat in the water. Close to the shipping lanes, these floating containers are real danger, especially to small ships. If containing toxic chemicals, they are hazardous to local water and seriously affect the fishing industries and beach economies.

In terms of design, class rules and regulations have shown limitations in dealing with green water and its loading. Accidents have taken place, quoting green water and limitations in design standards being the culprits. With the new generation of ultra large, deep sea containerships being developed, design limits are once again pushed beyond experiences. Under the pressure of competition between ship owners, shipyards and ship classification societies, solutions to green water incidents are, more than ever, becoming urgently needed. This inspires further research into the issues of green water loading.

1.1.3 Research concepts and design practices to cope with green water problem

Either based on common sense or true engineering work, history of naval architecture has seen many concepts and design practices put into use in order to minimise the problem of green water. Bulwark has been a natural design option in raising the freeboard of ships and this helps to reduce the risk of green water. However, in the bow bulwark design of some ships, a case example showed that an amount of approximately 1000 tonnes of sea water was lifted out of the ocean by the ship's forecastle and forward foredeck when rising up from a severe pitch into a head sea, thereby depressing the deck plating and twisting the bed plates of several items of mooring machinery (Olsen, 2005). The additional bulwark also means additional reinforcement structures. And despite being reinforced, large bulwark may still not be strong enough to cope with the impact load caused when the ship pitches into the incident waves.

Increasing bow flare has been thought as an adaptive design to naturally shed water away as the ship pitches into the water, and hence, helps to lessen green water risk (Swaan & Vossers, 1961). The design also helps to increase the cargo deck area at the bow, and therefore, is highly encouraged by ship owners. However, Lloyd and Hammond (1982) and Lloyd et al. (1985) found that such design could backfire as it may increase the risks of green water and slamming.

Other novel modifications to the ship bow are bow knuckle and overhang extensions. They were also investigated and tested by various researchers, e.g. Newton (1960), Lloyd (1983, 1984), and Johnson (1996). However, the findings remained inconclusive and relatively tentative. Mizouguchi (1988) carried out both experimental and numerical investigation into the behaviour of green water with different deck areas and shapes. Even though it was reported that the deck water height and velocity were strongly affected by these parameters, more

extensive numerical work was suggested before practical conclusions could be achieved.

Onto the practical design, many naval architects decided to avoid green water risk by positioning the accommodation and navigation superstructure forward of the container stow and thereby presenting green water to the command location of the ship rather than to the cargo. However, there have been poor feedbacks from shipmasters as they experienced difficult navigation in aggressive sea conditions, and channel/berth manoeuvring of the ship.

Subsequent designs into the 1980's, and onwards did see ships fitted with breakwaters forward, two thirds or three quarters length from forward accommodation. This idea could be adopted from the way breakwaters were used in coastal engineering The inclusion of a forward cargo protecting breakwater, generally acting as a wall against green water flooding over the forecastle deck when the ship was pitching into a sea, became a common structural feature. Design of breakwater has come in great variety. Popular in use are V-shape breakwater and vane-type breakwater as discussed by Pham & Varyani (2004, 2006a). Recent practical designs have seen employment of simpler breakwater like a rectangular wall positioned across the forecastle deck (double skin breakwater). This breakwater is likely to face much greater green water loading than other designs. However, it requires minimal space and helps to maximise the deck area. This definitely becomes ship owners' favourite since it is cost effective. As a result, this breakwater is getting more and more popular with containerships.

On some ships, perforations are introduced in the breakwater to create the passages for part of green water to pass through. The breakwater becomes permeable and this certainly lightens green water impact. Part of the kinetic energy carried by green water is taken away by the water jets coming off the back of the breakwater. This literally means the protected structure will have to share part of the loading that would have been taken by the breakwater. By varying the

permeability, optimal loading trade-off between breakwater and protected structures can be achieved.

The early 1990's saw new designs of containerships produced with shelter whaleback cover for the forecastle deck. The coincidence of this design, with similar features in fishing craft, was not entirely new but did add to the "Ship of the Future" concept. To add shelter over the forecastle head, thereby protecting both the forward deck machinery and shedding water when the ship is in a short swell and heavy sea condition, does increase confidence when achieving the tight time schedules of the feeder ship. The mariner is likely to have some misgivings relating to the forecastle whaleback shelters. Questions may arise regarding entrapment of crew under the shelter in heavy sea conditions. The aft sloping shape of such shelters may accelerate water flow against container stows extending above the after edge of the shelter and cause damage. The positioning of mooring rope apertures or Panama leads through the bulwark of the shelter would need to suit the operational requirements of the ship.

To summarise the above, many practical concepts obtained from research and design practices have lead the way to effectively cope with green water. This is not comprehensive but there is continual effort to improve designs in order to tackle the problem of green water.

1.1.4 Evaluation of green water problem

Thanks to extra-ordinary progresses in mathematics and their subsequent applications into engineering, the knowledge of ship behaviour in waves has recently become a true science. With it, the evaluation of green water becomes more quantitative.

Building on the underlying works in ship hydrodynamics by Ursell (1949a, 1949b, 1953), Korvin-Kroukovsky (1955, 1957) and Tasai (1959, 1960, 1961a, 1961b), ship motion theories were quickly developed and started to set up the foundation for solving the problem of green water. The first numerical model for evaluating green water was established by Ochi (1964) when probabilistic measures were applied to estimate the occurrence of green water in irregular seas. Later, it was expanded by Price and Bishop (1974) and still proves to be a solid methodology to investigate green water issue as the works by Guedes Soares and Ramos (1997), Buchner (2002) and Guedes Soares and Pascoal (2005).

Time-based numerical evaluation was also pursued by other researchers and very encouraging achievements have been made by Mizouguchi (1988) and Crossland and Johnson (1998). By setting a series of practical threshold conditions, the occurrence of deck wetting event and its scale could be evaluated in time. A combined approach was also used by Oliver (1981) in which green water events were estimated by probabilistic method and time streaming was used to predict the durations of threshold crossing and hence volume of water shipped on board.

Recent advances in computation capability whilst remaining at affordable costs have lead to the widespread application of CFD into analysis of green water loading following a green water event (not prediction of the occurrence of green water event itself). Example works include Buchner (2002), Nielsen and Mayer (2003), Stansberg et al. (2003), Kleefsman et al. (2005), and Yamasaki et al. (2005). Transient behaviour of water surface associated with the immersion of

different bow configuration can be evaluated by solving the simplified Navier-Stokes equations. By doing so, not only the loading of deck structures can be calculated when green water takes place, effects of bow shapes are also taken into consideration. Even though still limited by the computational requirements, the method has led the way to a comprehensive analysis of green water loading.

1.2 Research motivation

Great challenges in the investigation of green water to containerships together with inspired interest in exploring the application of CFD in ship hydrodynamics is the prime motivation of this research. Most of the CFD analyses so far have been carried out for stationary ships such as FPSO's. This was justifiable because of the nature of their services. Containerships, on the other hand, rely on their speed to keep up with tight schedule. CFD simulation should, therefore, include the velocity of the ship within the framework of the mathematical model.

With the Simulation-Based Design (SBD) getting more effective in practice, the need for extending CFD analysis into the design process is ever growing. Breakwaters and other novel design concepts can be modelled and results compared within a parametric investigation. Optimisation can therefore be performed to develop the guidelines for construction of such structures rather than relying on classification rules which, according to Varyani et al. (2006), have shown a lot of limitations.

Finally, despite having achieved great successes in many engineering sectors, CFD is a new analysis technique and it needs extensive validation. Parallel experiment is therefore essential for launching a systematic approach to seek a reliable solution to the targeted problem. So far, experimental data in the area of green water and especially the use of breakwaters have been very scarce. Validation is, consequently, lacking and this creates another incentive to carrying this research.

1.3 Project aims and objectives

The ultimate goal of this research is to develop a versatile, flexible and reliable modelling framework which can well simulate green water behaviour and accurately estimate the loading. In order to achieve this, intermediate aims were set and they are as follows:

1. To obtain a comprehensive knowledge of green water and its related issues through review of critical researches in the field.
2. To acquire a fundamental mathematical model that can well explain the stages in the development of green water.
3. To observe green water and to analyse the characteristics of green water flow as it happens so that a physical understanding of the problem can be obtained.
4. To derive a hydraulic model to represent green water flow based on the characteristics identified above.
5. To select a suitable modelling environment for simulating the hydraulic model used for green water.
6. To simulate the model and systematically validate the output results with experimental results.
7. To evaluate the general performance of the modelling framework and its application.
8. To review the modelling framework and identify the limitations that could restrict the accuracy and versatility in prediction. Based on the above, future works are suggested.

1.4 Outline of thesis

This thesis consists of ten Chapters through which the development of the research work carried out for this project is presented. The contents of the Chapters are summarised as below.

Chapter 1 gives a brief explanation to what green water is and the possible problems. Common practices that naval architects have adopted to reduce green water effects are then listed together with a summarised review of evaluation of green water. Finally, the motivation to this research is explained along with aims and objectives so that a suitable approach is planned and executed.

In Chapter 2, the histories of research of green water problem are reviewed in detail. Apart from highlighting the achievements from these researches in dealing with green water, the review also discusses the limitations and what can be expanded. The outcome then assists in establishing an effective approach and methodology for fulfilling the aims and objectives set in Chapter 1.

Chapter 3 aims to provide a simplified mathematical background on how green water can take place when ships travel in waves. For illustration, strip theory was used to demonstrate the stages through which water gets shipped onto the ship deck.

The experiments are essential to investigate the physics of green water and Chapter 4 is dedicated to outlining the setup of green water tests and the conditions in which the tests were carried out. It also briefly explains how the experimental data are analysed in order to understand the physics of green water.

Chapter 5 presents the test data and discusses the characteristics of green water as it happens in reality. Key parameters that influence the behaviour of green water are then identified. From these, a hydraulic model that is friendly to CFD

modelling and at the same time can also reproduce green water characteristics is configured.

Chapter 6 explains the mathematical model on which CFD is constructed and why it is suitable for dealing with hydrodynamic problems. In order to provide evidences that CFD is capable of handling complex problem such as green water, two benchmark problems that are relevant and similar in nature to green water are modelled and tested. Validation of the results is carried out to justify the adequacy of CFD technique when it is applied to simulate green water on deck.

In Chapter 7, the CFD setup of green water modelling framework is described in detail.

Chapter 8 focuses on validating the simulation results with the corresponding experimental results. Results from simulations with and without breakwaters are compared with the model test results. Discussion is concentrated on the agreement between the two sets of data and on the adequacy of the developed modelling framework. A summary of the overall performance of green water modelling framework is then presented.

Chapter 9 reviews all the stages of the methodology used in this project, aiming to identify the limitations that can be improved for future research. Suggestions are also promptly made on how these limitations can be addressed. It then moves on to discuss the modelling framework for engineering applications. Illustrative simulations are also presented accordingly.

In the final Chapter, a statement is given of the findings and conclusions reached after examination of the results of the studies presented in the preceding Chapters. This is accompanied by suggestions for the desired progression of this work, beyond what has been achieved in the course of these studies.

1.5 Research approach

Following the aims set out in Section 1.3, a systematic approach for this research was engineered so that it could steadily and efficiently lead to achievement of the goals of the project.

To start with, a rigorous review of previous researches was undertaken so that a fundamental background of green water could be achieved. At the same time, relevant ideas and concepts on how to solve similar problems to the quests for this research were also collected and analysed.

Even though the project set out to focus on the simulation of green water once it has happened, a mathematical background to the stages through which green water comes into being is also highly important and relevant. The information gathered from these stages can certainly be used as input for the simulation. Therefore, a brief demonstrative background of how green water developed was explained using the simple strip theory although this could also be applied with other ship motion theories.

To get the real physics of green water when full-scale trials are not available, experiments are the closest way. Based on ideas collected from other researches and piloting experimental programme, green water experiments were designed and set up in the way that key characteristics of green water behaviour are captured. Not only being used for exploring the physics of green water, experimental data were also recorded for validation at later stage.

The project then moved to analysing the test data in order to seek the generic characteristics which could link green water to some simple hydraulic model. A new hydraulic model that was most suitable for green water observed in this project was then established.

For a modelling framework to work well, a suitable modelling environment is essential. Out of many available environments available in the hydrodynamics arena, CFD has proved to be the most powerful and the most comprehensively tested. This simulation technique was therefore chosen to implement the hydraulic model that had been developed. For validation, two benchmark tests of similar hydrodynamic characteristics to green water problem were carried out. The outcome of the benchmark tests would consolidate whether or not CFD would be capable of simulating green water.

Using part of the test data for laying out the foundation, simulations were launched for systematically varied conditions of waves and ship velocity. Generic breakwaters were also modelled on forecastle deck and simulation was accomplished. The project then validated the output results using the experimental data collected earlier.

Based on the validation outcome, the simulation model would be assessed on whether it was practically good to represent green water in the interaction with deck structures. Comments would also be made on whether modification to ship bow or the use of breakwater was a more effective way to deal with green water.

Finally, the project looked into the overall performance of the modelling framework, its limitation and the range of its possible applications in engineering.

Chapter 2:
Review of Research in Green Water Problem

2.1 Introduction

This Chapter presents a historical overview of work carried out by various researchers or research groups, to investigate the nature of green water, its physical definition and possible numerical methods to model the problem. Discussion will be made of the techniques and findings of these investigations and its relevance.

2.2 General physics of green water

Green water or deck wetting must have started to become of prime concern in boat/ship building thousands of years ago. Pictures of medieval ships (Figure 2.2.1) already saw ships having highly elevated bulwarks at both ends to reduce the risk of water getting shipped on board. Following the progression in sciences over the time, the assessment of deck wetting phenomenon has gradually moved out of the qualitative zone into a real science. In modern era when research in every field flourishes thanks to advances in mathematics and computation, investigation into this subject has become more intensive than ever seen.

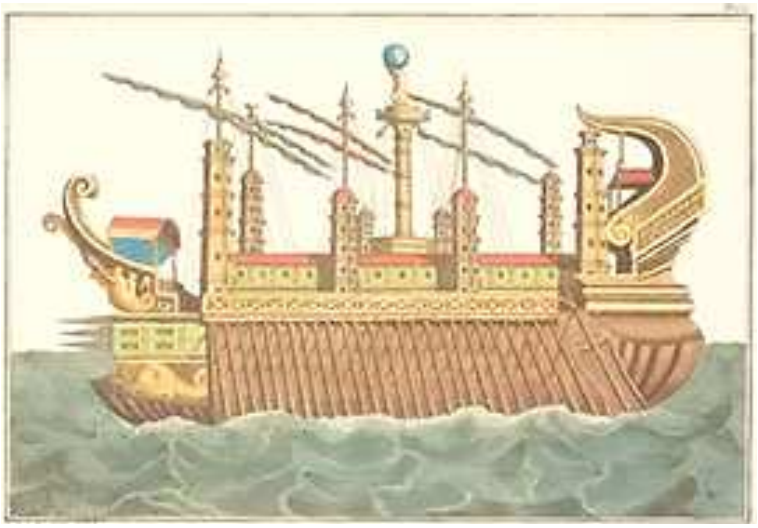

Figure 2.2.1 Medieval ship with elevated bulwarks at bow and stern. (http://www.AllPosters.com [accessed 22 November 2007])

In general, green water is one effect of ship motions when the ship travels in waves. Putting aside historical review of the wave theories, calculation of ship motions started a number of years ago and still remains a challenge to researchers for improvements. With a complicated hull shape and normally operating in larger waves than assumed in every theory, ship creates a lot of non-linear issues that make the estimation of ship motions difficult.

In order to reduce the number of non-linearities, most ship motion theories assume waves of small amplitudes so that motion equations can be simplified.

It is noted that the precision of solving motion equations relies considerably on the calculation of the added mass and damping force of the ship hull when it oscillates in water. Starting with a model of a circular cylinder, Ursell (1949a, 1949b, 1953) provided a method based on source distribution to exactly calculate these values. Building on this success, Korvin-Kroukovsky (1955, 1957) and Tasai (1959, 1960, 1961b) applied the Lewis and Theodorsen transformation and conformal mapping technique to introduce the methods for calculating sectional added mass

and damping coefficients for 2D ship shape sections. These pioneering works set the solid foundation for the later on known as strip theory that was comprehensively presented in Salvesen et al. (1970). The theory predicts relatively well the response of the ship provided appropriate principles are satisfied, e.g. small wave amplitudes and slender body ship. However, in situation when shipping of water on deck is likely to occur, the wave field is usually severe and falls outside the range specified by strip theory. Many non-linearities then arise and start to affect the resultant response of the ship significantly.

Attempts to address these non-linearities have been continual. For example, Fonseca & Guedes Soares (1998) assumed that the main component of the non-linearity of loads associated with vertical motion was involved with hydrostatic and Froude-Krylov forces. They, therefore, incorporated only the non-linearity associated with hydrostatic loads and Froude-Krylov forces into strip method for vertical motion prediction. The force acting on the instantaneous hull wetted surface was computed in time domain. Therefore, larger amplitude vertical motions of ship could be predicted with better accuracy.

Solutions based on source distribution for 3D ship hulls were also available in the works of Haskind (1947, 1953), and Newman (1957, 1959, 1978). However, at the very beginning, the 3D solutions did not show any clear-cut advantages over the 2D strip methods in ship motion calculations and validation with experiment. In fact, with larger number of equations to be solved at every time step, the computational requirement for the 3D method was much higher. Therefore, 2D strip method was more popular in applications.

Later, both methods were improved by many researches. More and more non-linear factors in motion equations such as loads due to green water on deck (Dillingham, 1981) can be included and the results are getting ever closer to the actual values. Nowadays, thanks to the availability of powerful computational resources at affordable costs, analysis of ship motions can include 3D effects and

more non-linearities in calculation. Nonetheless, there is still a gap to bridge between the numerical solutions and experimental results especially in steeper waves or waves of large amplitude.

Once ship motions are calculated and incident waves are known, relative motions between any point on the ship and the water surface can be approximated. Excluding other disturbances, Crossland and Johnson (1998) termed this the notional relative motions. However, due to the form effects, ship translating in water does disturb the water surface and create what is normally referred to as bow wave. For a slender ship, Shearer (1950) provided a theoretical method to calculate this bow wave assuming the ship hull could be represented by a line of sources located at the centreline. For slender hull forms running at velocity less than Froude number of 0.5, the method predicted the bow wave relatively well. At higher velocity, underestimation became more distinct. However, Fn = 0.5 is already well beyond the velocity range of containership. Ogilvie (1972) also used slender body theory to calculate the bow wave generated by a fine ship bow. His validation with experimental data was fine. Waniewski et al. (2002) measured the bow wave generated by an angled plate in a flume and compared the results with both experimental data and numerical results by Ogilvie (1972). The agreement was not quite satisfactory. Waniewski et al. (2002) then concluded that the bow wave flow was highly non-linear and there appeared to be no satisfactory analytical solution to this flow indeed.

When heaving and pitching in water, a ship also creates radiated waves. The calculation of the amplitude of these waves could be found in Tasai (1961a), which was later extended and adapted to computation by Gallagher and Rainey (1992).

Together with trim and sinkage, these disturbances are the main sources of intensifying the relative motions between ship and water surface.

Tasaki (1963) introduced the term ‘static swell-up’, which was composed of bow wave, trim and sinkage of the ship body when running in still water at constant velocity. He also described the ‘dynamic swell-up’ of water surface due to the relative vertical velocity of the bow and waves. An empirical formula to evaluate the height of the dynamic swell-up was also developed based upon his tank test results.

Bales (1979), on the other hand, divided the components of relative motions into three groups. The first group termed kinematic effect included heave, pitch and undisturbed incident wave. The second group, dynamic swell up, were the disturbances due to hull oscillation. Finally, the third group was the distortion of incident wave due to the presence of the hull in wave field. These factors were analysed individually and the resultant motion could be found, giving the corrected or actual relative motion.

Blok and Huisman (1983) combined heave, pitch and incident wave components together and named the resultant ‘undisturbed relative motion’. The swell-up coefficient was then approximated as a function of this relative motion and bow wave disturbance. This was then added to the undisturbed relative motion to get the corrected relative motions for further analysis.

Crossland and Johnson (1998) adopted the solutions for bow wave by Shearer (1950), solutions for radiated wave by Tasai (1961a) and modified by Gallagher and Rainey (1992) to add to the notional relative motions. The resultant was referred to as corrected relative motion and it was used in their investigation of the occurrence of green water event.

It is evident that the shipping of green water is a premier function of relative motion between waves and ship bow. In every research in green water, one way or another, the event of green water is decided based on the comparison between this relative motion and the available freeboard (in still water). From this point, there

are two approaches known to estimate the frequency of green water taking places. The first approach is statistical and the other based on time-domain.

Ochi (1964) has been widely acknowledged as the researcher who set the foundation for statistical assessment of green water shipping (or often referred to as probabilistic method). In his work, Ochi (1964) carried out model tests with a thirteen-foot Mariner model cargo ship in irregular seas. The relative motion, even when severe, was found closely following the Rayleigh distribution. The probability of deck wetness was therefore a function of freeboard and the variance of relative motion:

$$\text{Probability of deck wetness} = e^{-FB^2/Rr} \tag{2.2.1}$$

where

FB = freeboard at ship bow
Rr = variance of relative motion between wave and ship bow

In the same year, Goodrich (1964) used probabilistic technique to specifically evaluate the influence of the freeboard on wetness. Using the experimental data by Vosser et al. (1960) for analysis, Goodrich (1964) assumed that the short term distribution of the variation of relative vertical motion of the bow had a Rayleigh distribution. The probability of exceeding a specific value of freeboard would then be calculated as in equation (2.2.1). However, Goodrich (1964) claimed that in order to obtain the long-term distribution of relative bow motion, a weighting factor for weather distribution must be included. Equation (2.2.1), therefore, became:

$$\text{Probability of deck wetness} = \sum_j e^{-FB^2/Rr} \times P_j \tag{2.2.2}$$

where P_j is the weighting factor for the general weather probability distribution.

Tasai (1969) also used equation (2.2.1) to calculate the frequency of deck wetness and compared with his model test data using two tankers of full form. The agreement was relatively good and he emphasised the importance of including dynamic swell-up in the calculation of relative motions for obtaining a good prediction.

Further validation of the method was carried out by Hong et al. (1993) with a containership model S-175 tested in irregular waves. It was found that there was a good agreement at test velocity corresponding to Fn = 0.275 but poor at Fn = 0.15. Freeboard at the stem head should be used in Equation (2.2.1) and it should take into account the trim and diffracted waves.

This method was later expanded in greater detail by Price and Bishop (1974) and remains a very useful tool in the analysis of green water in irregular waves as stated by Buchner (2002) and Guedes Soares and Pascoal, (2005). From his experimental data with FPSO models, Buchner (2002) assumed a quadratic relation between the linear relative motion and the non-linear relative motion and modified the Rayleigh distribution. The prediction of the probability of green water was then well improved for large waves. Guedes Soares and Pascoal (2005) tested various probability distribution models using the experimental data on a FPSO for wave excitation, ship motions and relative motions. They concluded that the statistics of wave and heave and pitch indicated that FPSO motions were essentially linear. The distribution of crest height might deviate from the Gaussian model but the probability of green water could still be estimated by this distribution model for large peak periods. When green water took place, they found that the maxima of the water height above deck were well modelled by a Weibull distribution with exponent between 1.3 and 1.4.

A clear advantage of statistical approach is its capability of produce quick results. It is also easily coded in ship motions program and requires very little computational effort.

However, there have been debates around statistical approach on the fact that the method assumes every time when the freeboard of ship is exceeded, deck wetting occurs. Sea masters and various other researchers have argued that the translation from a freeboard exceedance into a deck wetness event very much depends on factors including the sea conditions, ship velocity and the above water bow form. As in many times, water was observed to exceed the main deck but no water was shipped in (Maruo and Song (1994) and Wu et al. (2000)).

Time domain assessment of green water has therefore become an interest to other researchers. Time domain simulation, as its name suggests, looks at the status of the ship and water surface at the very instant of time and judges whether or not the deck is wetted. Since the calculations are implemented at every time step and so is the check, time domain approach demands more computational efforts.

Lloyd and Hammond (1982), Lloyd (1983,1984) and Lloyd et al. (1985) carried out systematic green water tests using narrow beam frigate models with varied bow shapes. Based on the outcome of the tests, a time-domain method was developed to predict the occurrence of deck wetting. The method used strip theory as a foundation and only looked at motions of the ships in vertical plane to estimate the relative motions between ship deck and water surface. The code was later improved and reported by Crossland and Johnson (1998). The simulation results were also validated with their experiments on three generic frigate models.

Cozijn (1995) and Buchner and Cozijn (1997) used boundary integral and panel methods to simulate in time domain the shipment of water on board FPSOs in head seas without forward velocity. The water surface and ship body were defined by nodes and these nodes were updated at every time step. If any nodes that

represented the water surface moved into the ship deck area, green water was understood to take place. However, by defining the water surface by multiple nodes, the method suffered difficulties in achieving convergence when the water reached the sharp deck edge. In general, Buchner (2002) concluded that the method made it difficult to deal with complex free surface flow close to discontinuities in the boundaries.

Similar method was used by Greco et al. (2000a,b,c, 2001) and Faltinsen et al. (2002), and in order to prevent the problems of water reaching the sharp deck edge, they forced the water to leave the bow in tangential direction. Then when the freeboard was exceeded, the fluid velocity relative to the ship would determine if the water would flow into the deck. Simulation of green water shipped onto the deck in the form of a plunging breaker and impact with deck structure was also performed.

This method was also applied by Schonberg and Rainey (2002).

Recent trend in ship hydrodynamics has seen the simulation of green water implemented using CFD and Volume of Fluid (VOF) technique. 3D simulation in regular waves with truncated ship bow has been carried out in the works of Huijsmans and van Groesen (2004), Kleefsman et al. (2005), Yamasaki et al. (2005) and Zhang et al. (2005). Due to the substantial requirement of computation, the ship bodies in these simulations were either fixed or forced to heave and pitch with pre-determined motions. However, with numerous of non-linearities being included, the method appears to be highly promising especially when computation is getting more and more powerful on day-to-day basis.

2.3 Simulation of green water on deck and its loading

Besides the investigation into how and when green water takes place, a lot of researches have been dedicated to evaluate the characteristics of green water flow as it enters the deck and the subsequent loading effects on deck structures.

2.3.1 Green water flow on deck

In the evaluation of green water to a floating platform, Oliver (1981) assumed that green water on deck was simply the volume sliced off the wave when it exceeded the platform. The initial shape of green water was therefore sinusoidal with the height equal to the freeboard exceedance. In this way, the volume of the water on deck could be estimated based on the sinusoidal surface that encapsulated the water mass. In order to account for the turbulent character of green water, a dispersion factor could be used to get the estimation closer to the real value. Hamoudi (1995) and Hamoudi and Varyani (1994, 1997,1998) used this technique to estimate the volume of green water shipped on board a containership. They also carried out model tests in which a catch tank was set up to contain and measure green water volume in each shipment. The dispersion factor was then calculated based on the ratio between water captured and theoretical volume.

Mizouguchi (1988), on the other hand, treated green water flow propagating on deck as shallow water, with initial conditions similar to a dam-break model. To support this, he carried out experiments with a containership model and measured green water heights at 40 points on the forecastle deck. To transform the results into numerical simulation for parametric studies, Mizouguchi (1988) assumed that the water height of the dam was equal to the relative height between the deck and the surrounding waves. The simulation results were well correlated with experimental results and also helped to understand the change in green water flow with changes in deck area and shape.

Luit et al. (2002) assumed that green water on deck behaved like a shallow water problem but focused more on the effects of green water on the motions and bending moment. With these effects integrated in their Large Amplitude Motion Program (LAMP), good estimation of both ship motions and midship bending moment was produced. Validation with experimental data using a large containership model was also carried out showing good correlation.

Buchner (1995a, 1995b, 1996) analysed the experimental data with FPSO models and concluded that dam-break model was suitable for simulating green water flow onto deck. However, by monitoring the shape of green water flow on deck, he figured out that the initial water height behind the dam should be equal to 9/4 times the freeboard exceedance at the bow stem head (see Section 7.2.1). Simulation was then carried out using CFD with VOF technique and showed good correlation with experimental data.

Ogawa et al. (1998, 2000) carried out experiments using a tanker model travelling at various velocities, i.e. Fn = 0.025 to 0.14. From camera monitoring, they reported that due to the dynamics associated with the forward velocity, green water flow did not strictly behave like a dam-break problem. They proposed to use model of flooded waves instead and their comparison with experimental data was good.

After the heuristic investigation into green water using CFD (Pham et al. 2003a), Varyani et al. (2004) measured the average green water velocity on deck and adopted the combination of dam-break and water jet models to simulate green water on deck. Their comparison with the test data of S-175 containership model was good. Like Ogawa et al. (1998), they also found that for ship with forward velocity, the model of dam-break underestimated green water loading by a great deal.

Nielsen and Mayer (2004) employed a finite volume method and described the free surface geometry using an interface capturing scheme similar to the VOF methodology of Hirt and Nichols (1981). They simulated green water shipping onto both fixed and moving ship (in vertical plane) in 2D and 3D. The simulation results were later compared with experimental data by Greco (2001) and Buchner (1995), showing "…*a favourable agreement*…" (Nielsen, 2003). In the case when vertical ship motions were incorporated, heave and pitch motions were introduced via transfer functions. One of the important conclusions they drew from this was that the results from 2D and 3D simulation were very similar, which indicated that 3D effects were not dominant.

In the process of reviewing a software, Stansberg et al. (2004) compared the experimental results from a green water test using an stationary FPSO model with CFD simulation results and found that CFD based on VOF technique could predict the water propagation on deck and the impact load on a vertical surface very well.

With the capability of CFD technique to handle a lot of non-linearities involved in the interaction between water and solid structures, the synchronism of green water occurrence, the shipment of water onto deck and the behaviour of green water on deck has been made possible in CFD simulation. Successfully simulating the waves and a moving ship body, the works by Kleefsman et al. (2005) and Yamasaki et al. (2005) have shown the full sequence of interaction between incident waves and ship body. All the phases of green water problem were reflected and they were correlated well with the experiment (Yamasaki et al., 2005). However, there are still many challenges in this stream of research. Firstly, no forward velocity was simulated. Secondly, the ship motions were still pre-determined by separate modelling and then introduced into CFD simulation via transfer functions. Finally, only truncated body of ship could be modelled due to substantial computation required. Hence, until all these issues can be addressed, a

simplified model to simulate green water on deck is still necessary in evaluating green water and its loading effects on deck.

2.3.2 Green water loading effects

The evaluation of green water loading effects is seen as the most important objective in the research on green water. In head seas, green water loads are normally categorised as longitudinal and vertical. Longitudinal green water load accounts for damages to deck structures, cargo and deck machinery. Vertical green water load is usually of primary concern to deck plating.

Ochi (1964) related the vertical deck pressure to static pressure caused by water shipped on board although later researches showed that the dynamics of this water and the ship could contribute significantly to the total pressure on deck.

Oliver (1981) gave a more detailed guidelines on calculating both the deck pressure and the pressure on a vertical surface. For deck pressure, he identified three components that added up to the total pressure:

$$P_t = P_S + P_d + P_i \tag{2.3.1}$$

where

P_s = hydrostatic pressure of any water on deck at the time of impact

P_d = dynamic pressure from falling block of water from wave prior to collapse on deck

P_i = dynamic pressure from upward vertical velocity of the deck

The pressure on a vertical surface according to Oliver (1981) comprised of two parts, i.e. static and dynamic. The static pressure is calculated based on the water head in front of the surface and the dynamic pressure is proportional to the square of the total relative velocity u_t between the structure and the water:

$$P_s = \frac{1}{2}\rho u_t^2 \tag{2.3.2}$$

Oliver (1981) also noted that depending on the situation, green water could be highly disturbed and turbulent rather than a solid block of water. Therefore, a turbulence coefficient could be sensibly included in the formula for dynamic pressure. These guidelines only provided some theoretical background to estimating green water loading and no validation was carried out.

Mizouguchi (1988) analysed the experimental data he carried out and claimed that the impact pressure on a vertical surface could be estimated well by the empirical equation proposed by Suhara et al. (1973):

$$P_d = 1.4\rho u^2 \tag{2.3.3}$$

Buchner (2002) stated that equation (2.3.3) was conservative in estimating the mean impact pressure on a panel. It could give a good approximation of high local impact pressure but from a design point of view, it was overestimating the design pressure. In terms of deck pressure, Buchner (1995a, 1995b, 1996, 2002) listed three components:

- Static pressure due to the water head on deck
- Dynamic pressure due to the acceleration of the deck
- Rate of change of the water height on deck

in which the last component was very important and could explain the sharp peak impact load as noticed in experiments. This formula was later validated by experimental data of Ogawa et al. (1998) and Varyani et al. (2004), giving good correlation. Even though the formula still relies on experimental inputs, it gives a good understanding of the physics behind the deck pressure caused by green water.

2.4 Experimental studies in green water

Besides extensive analytical evaluation of green water, there have been also numerous experimental investigations into this problem.

It is unquestionable that there is a strong influence of above water bow form on the frequency as well as the severity of green water. Sea trials have reported that there are ships of similar principal particulars and types but some shows a far better performance against green water than the others. The reason appears to be with the bow features and this subsequently led to a series of dedicated research into the effects of these features, e.g. freeboard, flare angle, bow knuckle and length of overhang.

Edward and Todd (1938) tested three model drifters with different freeboards and bow flares. Having analysed the results, they confirmed the effectiveness of increased freeboard in keeping the deck dry. A fine-form ship with a bow flare also appeared to produce some advantages in preventing green water to get shipped on board.

The first extensive series of experiments with generically varied bow shapes was carried out by Newton (1960). Using a parent hull of a frigate, he increased the freeboard by adding bulwarks of different heights and then added knuckles to the lines plan from station 2 to 4. In total, five models were tested. No loading was measured and only qualitative assessment of deck wetness was executed. Newton (1960) focused on zoning the degrees of wetness which he claimed could be done by plotting wetness contours based on geometric and dynamic characteristics of the ship together with the waves encountered. Regarding the effects of bow features, Newton (1960) stated that increasing flare angle by an added knuckle was having the same effects as increasing freeboard if not more advantageous. The increased flare angle helped shedding the water away at early stage by virtue

of the depth of the knuckle. A formula to assess the effect of a knuckle in terms of freeboard was introduced as follow:

$$FB_{extra} = \frac{\ell}{b} \times \frac{h}{D} \sin\theta \qquad (2.4.1)$$

where

θ = minimum slope of section at knuckle or deck edge

ℓ = distance from FP at which this minimum θ occurs

b = half beam at knuckle or deck edge at this section

h = height of knuckle or deck edge above keel at this section

D = depth of ship at this section

FB_{extra} was then added to the physical freeboard to find the effective freeboard for the ship.

More extensive test series with six ship models was carried out by Swaan and Vosser (1961). The ships had similar principal dimensions and displacement but differed in section shape in the fore-body and in prismatic coefficient. Only ship motions and midship bending moments were measured. It was noticed that U-shaped (referring the shape of the lines plan) ships appeared to be better in dealing with wetness. They also concluded that the extreme bow flare could reduce deck wetness to the forecastle despite the potential increase in slamming risk.

With the interest in investigating how green water flowed onto the main deck from the ship side, Goda et al. (1978) conducted a 2D model test using a cargo ship hull. The water flow was assimilated to a 2D dam-break problem based on which the volume as well as the deck pressure could be estimated.

Lloyd and Hammond (1982), Lloyd (1983, 1984) and Lloyd et al. (1985) carried out comprehensive testing of a generically designed family of nine above water

bow forms based on the parent hull of a narrow beam LEANDER frigate. All the bow features including freeboard, bow flare, and bow overhang were varied systematically for testing. Lloyd et al. (1985) concluded that the motions were essentially independent of above water bow form despite the evidence that swell-up might be affected by this. As far as green water was concerned, increased freeboard unquestionably reduced green water. Small overhang (distance from stem head to forward perpendicular) was found to cause greater relative motions and hence, more deck wetness events. Similar results were obtained for the case of excessive flare angle. A very fine raked bow with very little flare appeared to possess the best performance in all respects.

Green water loading was also measured via a pressure sensitive array mounted on deck. With respect to experimental techniques, Lloyd (1983) pointed out several drawbacks of using catch-tank approach to quantify the shipped water on board. According to him, the weight of water flowing through the duct would tend to sink and trim the model bow down and thereby reduce the freeboard. As a result, the wetness frequency would tend to be increased. Furthermore, there was a possibility that the motion of the residual water in the catch tank may adversely influence the pitch motions of the model, leading to the deviation from true ship behaviour in waves.

O'Dea and Walden (1984) used a frigate model with four interchangeable bows to investigate the effects of the bow flare and knuckle on green water performance. Contradicting to Newton (1960) and Lloyd et al. (1985), their experimental data showed that the increased bow flare did improve the deck wetness situation. Knuckles, however, did not show any conclusive advantages or disadvantages whatsoever.

Takagi and Niimi (1990) studied the bow deck wetness by expanding Wagner's theory on wedge entry assumption and applying self-similar flow. They treated the bow like a tetrahedron or hexahedron, by which the bow shape features could be

modified by symmetrically adjusting the intermediate knuckle at the sides. Theories were developed and validated against experimental data with wedge shape model. Similar to O'Dea and Walden (1984), the results showed that bow flares improved the ability to fend off green water. Specially, if increasing the bow flare by a high knuckle, the reduction in deck wetness was more effective.

Buchner (2002) investigated the effects of bow flare of a FPSO model on green water and reported the observation of the changes in relative motions. Generally, the bow flare pushed water away when the ship pitched into the water. As a result, ripple was created progressing away on top of the surrounding water profile. As the flare increased, the magnitude of the ripple also increased and became more visible especially in the curve of relative motion around the bow. However, as soon as the surrounding water exceeded the deck, the effect of flare disappeared.

Regarding experiments with travelling containership models, highlighted works include studies by Hamoudi and Varyani (1994), Varyani et al. (2004) and Fonseca and Guedes Soares (2005) in which green water loads on deck were recorded to validate the CFD simulation results.

Away from the effects of above water bow shape, other experiments were also carried out to observe the behaviour of green water once it has been shipped on board. Cox and Ortega (2002) carried out an experiment to quantify a transient wave overtopping a horizontal deck fixed above the free surface. Their data showed that the structure increased the free surface above the leading edge of the deck by 20 percent. The velocity profile at the leading edge was, however, relatively uniform. Moreover, the maximum horizontal velocity was similar to the maximum water particle velocity at the crest. Under the deck, however, the water was accelerated to 2.5 times the corresponding velocity without the deck. After collapsing on deck the shipped water developed into a bore of a velocity of 2.4 times the maximum water particle velocity.

Recently, Ryu and Chang (2005) used Particle Image Velocimetry (PIV) technique combined with shadowgraphy to capture the velocity field of the interaction between a plunging wave and a 2D structure. From what they observed, it was found that the maximum fluid particle velocity in front of the structure during the impact was approximately 1.5 times the phase velocity of the wave. The maximum horizontal velocity above the deck was less than the phase velocity. By comparing this with the velocity of the water particles in the flow created by a dam-break model:

$$u = \frac{2}{3}\left(\frac{x}{t} + \sqrt{g.h_0}\right) \tag{2.4.2}$$

where

h_0 = initial water depth in the reservoir prior to dam-break

x = distance away from the dam

t = time

g = gravity

Ryu and Chang (2005) concluded that dam-break model did not work well in predicting green water velocity.

PIV technique was also applied by Tanizawa et al. (2004) in their attempt to evaluate the behaviour of green water on deck using experimental approach. From their observation, it was reported that depending on the wave length, the interaction between ship bow and waves could result in reflected water by the bow and the major shipment of water onto the deck. One of the important conclusions was that the air entrapment during the impact could account for the fluctuation in the impact pressure curves they recorded.

2.5 Breakwater and its design in reducing green water loads

2.5.1 Research on breakwaters

Despite being popular in use on ships, it is a surprise that very little research has been done on breakwater and its ability to reduce green water loads.

Buchner (1996, 2002) discussed some qualitative evaluation of the efficiency of protecting breakwaters on deck. Two types of breakwater were compared, the first was traditional V-shape breakwater and the second was vane-type breakwater. The latter was reported to effectively reduce water that piles up in front of the breakwater. As a result, less solid water could reach protected structures and also less green water load was sustained by the breakwater itself. However, no data or more comprehensive results were published.

The only comprehensive studies in performance of generically designed breakwaters were carried out by Pham and Varyani (2004, 2005, 2006a, 2006b) and Varyani et al. (2005, 2006, 2007). Using CFD, breakwaters of various designs were investigated by simulation. The loads on breakwaters and on protected structures were compared to find out the advantages and disadvantages of each type of breakwater. Validation with experimental data was, however, not accomplished.

2.5.2 Guidelines on design of breakwaters

Besides limited research on breakwaters, guidelines for their design are also very short-supplied and obscure, if available (Varyani et al., 2006). None of the four major classification rules for ships, i.e. Det Norske Veritas (2002), Lloyd's Register (2005), American Bureau of Shipping (2006) and Bureau Veritas (2005), refer in detail to breakwater design. Rather, design pressures and loads on such structures are derived from the equations for the pressure on the forward faces of

superstructures and deckhouses. These loads typically vary with height above the forecastle deck, characterised by the tier (level) in the superstructure. Lloyd's Register rules (2005) give the following equation for the head of water to consider:

$$h = \alpha \delta (\beta\lambda - \gamma) \qquad (2.5.1)$$

where:

α = coefficient for the tier, greatest for the lowest tier, which is appropriate for breakwaters

δ = coefficient which depends on the breadth of the obstruction (breakwater) relative to the hull breadth

β = factor related to the location of the structure along the ship, highest at the bow

λ = relative motion of the water surface to the ship in expected extreme weather, dependent on ship size

γ = height of the object above waterline

The term in parentheses is effectively the potential head of water over the object being loaded. For objects not likely to be directly immersed, a minimum pressure also applies to allow for water moving on the deck and for spray.

Similar formulations are available from other classification societies. It is noted that the above equations contain no reference to the shape of the obstruction, and so are not directly appropriate to anything but vertical faced breakwaters arranged across the beam of the structure. Application to V shape, vane and perforated breakwaters is therefore limited.

It is also noted that the above equations produce pressures that typically reduce with distance aft, so that the requirements of green water protection along the sides of a ship reduce. However, experience of operation of FPSOs has resulted in

vane type breakwaters being retro-fitted along the ship sides. Buchner and van Ballegoyen (1997), Buchner (2002) noted that there can be an increase in freeboard exceedence near and aft of midships, attributed to the amplification of high frequency wave components.

The classification rules give pressures acting on various types of decks, but with the exception of specific ships such as fishing trawlers, these pressures are not consistent with the special case of whaleback decks. Additionally, the effect of a breakwater or other major deck obstruction is to restrict flow and thus to increase pressures on the deck plating immediately forward of the obstruction. Such increase in pressure may be considered by taking deck pressures to be no less than the corresponding first tier deckhouse pressure.

For reasons noted above, there is considerable uncertainty over the use of standard classification society rules for the type of breakwater design. However, the classification rules do allow design by direct calculation, and this approach, coupled with design pressures produced by CFD methods such as from current research, is a valuable tool in the efficient design of breakwater structures.

2.5.3 Breakwater or above water ship bow modification to deal with green water problem

None of any research known so far has raised the question of which option is more effective to deal with green water issue: use of breakwaters or modifying the above water ship bow. Whilst the latter is to prevent or mitigate the shipment of green water on deck in the first place, the former provides an obstruction to green water when it happens.

As discussed in Section 2.4, despite a number of experimental works, there has not been any consistent conclusion on how (above water) bow features can change the performance of the ship against green water. Depending on ship types tested

and conditions in which the experiments were carried out, the outcome appeared to be relatively tentative and could be very different. Furthermore, inclusion of these bow features may also incur additional costs of construction.

Breakwaters of any design provide immediate protection to deck cargo or deck structures. Even though it does not prevent green water from happening, it creates an obstruction to green water flow and thereby reduces the amount of solid water that can reach and damage deck cargo and deck structures. The gain from having a breakwater, however, also comes at a cost. By obstructing green water at early stage, breakwaters takes on substantial loading that would have been faced by vertical structures. From a construction point of view, such substantial loading often has a direct load path back into the main hull structure. In the case of a breakwater, the provision of adequate load path can be complicated by following issues (Varyani et al. 2006):

- Breakwaters are typically located on relatively weak forecastle structures that lack substantial transverse bulkheads.
- It is difficult to align V-shaped breakwaters with the pattern of typically transverse girders under the deck.
- Vane type breakwaters require support to the tops of the individual vanes, typically by means of a transverse beam. This structure requires discrete supports from the deck below.
- Double skin breakwaters typically require closely spaced support from the structure below, which is not always consistent with the pattern of transverse stiffening.

Detailed design issues for the breakwater itself suggest the use of less complex and more cost effective designs. Thus the use of simple V shaped breakwaters is commonplace due to the conventional ship construction techniques employed, similar to bulwarks. Whilst vane type breakwaters may be efficient and impose much less load on the ship (Buchner, 1996, 2002), such structures are typically

more complex to construct and may require discrete strengthening to the deck below.

The design option of either adopting a breakwater or modifying (above water) ship bow, therefore, should be based on the overall evaluation of how effective each plan is. Extensive analysis and practical inputs must be integrated to provide a reassurance of the choice selected. From a research point of view, it is useful to establish a methodology for optimising the design of a breakwater for a given ship. Further investigation into effects of the bow features on green water performance is, nonetheless, always encouraged.

In this research, evaluation of both design options is implemented and conclusions will be drawn based on the output results.

2.6 Summary

On overall, green water has proved to be a highly complex phenomenon that depends on many non-linear factors both related to ship and environmental conditions. Any subtle changes in these factors could lead to significant changes in the way green water takes place or its behaviour. Investigation via both theoretical and experimental approaches has seen a variety of opinions and conclusions that are far from unanimous. To sum up, the literature review has revealed the following:

- Deck wetness is a highly complex phenomenon, of which evaluation would involve comprehensive hydrodynamic knowledge and vast experimental database.

- Deck wetness is primarily a function of relative motion between deck and free water surface. The relative motion forms the basis on which deck

wetness or green water can be estimated for both occurrence frequency and severity by methods such as probabilistic or time-domain.

- Except for freeboard height, effects of other above water bow features such as bow flare, overhang, knuckle and rake angle are not yet fully understood. There is a scatter of opinions in the influence of these features on the ability to deal with green water.

- Nevertheless, green water loading can be approximated by using several empirical formulae derived from experimental investigation.

- For more detailed analysis, CFD and VOF technique can be applied to simulate green water flow on deck with good degree of accuracy. Even though more validation and better setup are still required, the results so far have been highly encouraging.

- Most CFD investigations carried out so far were focusing on FPSO models which were stationary at sea. For ships travelling at some velocity, green water behaviour can be very different and it is the goal of this project to investigate this factor on green water and its loading effects.

- Finally, the choice of either adopting a breakwater or modifying above water ship bow to tackle green water is debatable. Extensive analysis and vast practical inputs are needed in order to make a good decision and to obtain a reassurance of the opted plan.

Chapter 3:
Time Domain Strip Theory for Predicting the Occurrence of Deck Wetness

3.1 Introduction

Green water, as previously mentioned, is a function of relative motions. The prediction of when green water is going to take place, therefore, starts with the prediction of ship motions in waves. There are several standard models for calculating ship motions and all of these models can be used to estimate the relative motion between the bow and free water surface.

This section intends to present an example mathematical model in which the relative motions, and subsequently, the occurrence of green water are predicted in time-domain. This model is based on non-linear strip theory from the work initiated by Lloyd (1983, 1984) and Lloyd et al. (1985) and later expanded by Crossland and Johnson (1998). The validation is later presented in Chapter 5.

3.2 Theories

3.2.1 Ship motions

Heave and pitch are most influential types of motion to deck wetness phenomenon. Even though surge and roll motions can make certain contributions to the problem, these are ignored in the present theory for simplicity. Equations of heave and pitch are referred to Crossland and Johnson (1998). In order to account for the non-linearity corresponding to the current water line at each strip, the buoyancy force is obtained by integrating elementary pressures on the hull around the instantaneous wetted area of the strip.

The main calculation in ship motions by strip theory is to determine the values of local hydrodynamic coefficients. In standard strip theory, these coefficients are calculated based on the coefficients for a circular cylinder by Ursell (1949b) combined with hull form transformation and conformal mapping techniques. Classical examples can be found in the works of Korvin-Kroukovsky (1955, 1957) and Tasai (1959, 1960, 1961b). There are also experimental studies in determining these coefficients for particular types of ships. Empirical equations are subsequently developed for numerical applications.

3.2.2 Relative motions

Once heave and pitch motions have been calculated, the absolute vertical displacement, velocity and acceleration can be calculated as:

$$s = \eta_3 + x\eta_5 \tag{3.2.1}$$

$$\dot{s} = \dot{\eta}_3 + x.\dot{\eta}_5 + U.\eta_5 \tag{3.2.2}$$

$$\ddot{s} = \ddot{\eta}_3 + x.\ddot{\eta}_5 + 2U.\eta_5 \tag{3.2.3}$$

The relative motion, in turn, can be found by subtracting the absolute motion by the surface wave.

$$r = s - \zeta \tag{3.2.4}$$

Crossland and Johnson (1998) referred to this as '*notional relative motion*' in which other disturbances due to radiated waves, for example, are not taken into account. In reality, the incident wave is disturbed by a variety of factors, which include bow wave, and dynamic swell-ups in both longitudinal and transverse directions. Beck (1982) stated that these components are linearly additive to the ship motions. The corrected elevation of disturbed wave is, therefore, the superposition of these components:

$$\zeta_c = \zeta + \zeta_{sux} + \zeta_{suy} + \zeta_{bw} \tag{3.2.5}$$

The methods to evaluate the disturbances are discussed in the subsequent sections.

3.2.3 Calm water bow wave

As a ship advances on a straight course in calm water, the stem of the ship penetrates the water and generates a steady wave train that begins at the bow and progresses aft. Shearer (1950) used a line of sources at the ship centreline to resemble a moving ship body. The co-ordinate system has origin on calm water surface, in mid-ship plane and centreline plane. x-ordinate is positive in the direction of motion and z positive vertically upwards. If sectional areas of the strips are denoted as A_i's, each strip surface was approximated by a source of strength:

$$\varphi_i = \frac{U}{4\pi}\left(A_{i+1} - A_i\right) \tag{3.2.6}$$

The source is located at a depth z_φ equal to the depth of the effective centroid between the centroids of areas A_{i+1} and A_i. The bow wave profile ζ_{bw} at any distance x from the origin comprises of two components. The first component, denoted as ζ_w, is the wave disturbance due to the source. The second component, ζ_{nw}, is the non-wave or local disturbance. Their expressions are as below:

$$\zeta_w = \frac{8.g.\varphi_i}{U^3} \times \Psi_1 \tag{3.2.7}$$

$$\zeta_{nw} = \frac{8\varphi_i}{z_{\varphi_i}.U} \times \Psi_2 \tag{3.2.8}$$

where Ψ_1, Ψ_2 are values of integrals that are calculated over a range of independent variables (Shearer, 1950). In numerical simulation, these values are stored in a look-up table and intermediate values can be interpolated for use at the intermediate draught.

Note that ζ_w is zero ahead of the source (or positive x) and ζ_{nw} has the same sign as x. The calm water bow wave profile can then be computed with adequate precision by:

$$\zeta_{bw} = \zeta_w + \zeta_{nw} \tag{3.2.9}$$

This was later validated by Blok and Huisman (1983) after they conducted calm water experiments with a compact frigate model. They found that Shearer's method of predicting bow wave profile was practically adequate for engineering purpose. Even though it underestimated the bow wave, the discrepancy was acceptable. Blok and Huisman (1983) also compared the results with those

calculated by Raven (1980). Shearer's method showed a slightly better prediction and hence was concluded to be preferable for use.

3.2.4 Dynamic swell-up

3.2.4.1 Lateral swell-up

When the ship body harmonically oscillates in water expressed by equation:

$$s = s_o \cos \omega_e t \tag{3.2.10}$$

a surface disturbance will be set up in which a train of standing waves and a train of progressive waves are generated. According to Tasai (1961), the surface elevation at the side of the ship ζ_s was a function of the amplitude of the far field radiated wave ζ_{0f}:

$$\zeta_s = \zeta_{0f} . \Theta_0 \cos(\omega_e t + \phi) \tag{3.2.11}$$

where

$$\Theta_0 = \frac{1}{\pi}\sqrt{E_1^2 + E_2^2}$$

$$E_1 = \phi_{S0}\left(\frac{\pi}{2}\right) + \sum_1^{\infty} (-1)^m . q_{2m}$$

$$E_2 = \phi_{C0}\left(\frac{\pi}{2}\right) + \sum_1^{\infty} (-1)^m . p_{2m}$$

$$\varepsilon = \tan^{-1}\left(\frac{E_2}{E_1}\right)$$

$(\phi_{C0} + i.\phi_{S0})$ = potential by the 2D source at origin

$(p_{2m} + i.q_{2m})$ = potential of the component multipole strength

The far field radiated wave can be calculated as in Tasai (1959). The ratio of the far field radiated wave amplitude to the oscillating amplitude of the strip was:

$$\frac{\zeta_{0f}}{s_0} = \frac{\pi\omega^2 B}{2g} \times \frac{1}{\sqrt{C_1^2 + C_2^2}} \tag{3.2.12}$$

where C_1 and C_2 depended on stream functions at the origin and the component multipole strengths. The full expressions of C_1 and C_2 can be found in Tasai (1959).

At the presence of waves, Gallagher and Rainey (1992) applied these equations and replaced the absolute vertical motion in (3.2.12) with the notional relative motion from (3.2.4).

3.2.4.2 Longitudinal swell-up

Longitudinal swell-up was introduced by Crossland and Johnson (1998) based on observations during both the experiments and real sea trials. Due to the pitching motion of the ship, a train of waves appears to be generated every time the bow pitches down into the incident wave. The interaction of these two trains of waves tend to increase the height of the latter. Therefore, along side with swell-up associated with heaving motion on sides of ship, there exists a 'so-called' longitudinal swell-up generated by the bow in the immediate vicinity of the stem. This swell-up is calculated using similar method used to predict transverse swell-up as discussed above.

3.2.5 Corrected relative motions

The corrected elevation of disturbed wave is, therefore, the synthesis of the incident wave and disturbance factors, i.e. bow wave and swell-up (see equation (3.2.5)). The corrected relative motion can be approximated as the resultant of absolute ship motions relative to disturbed incident wave:

$$r_c = s - \zeta_c \tag{3.2.13}$$

3.2.6 Wetness occurrence and classification

Once the relative motion of the main deck to the free surface is calculated, the exceedance of freeboard can be evaluated in time domain. It has been reported that the freeboard exceedance and the subsequent green water event are highly sensitive to the above water bow form. All ship motion theories so far have only considered the under water bow form and assumed an extension of a vertical wall above calm water draught. For this reason, the effects of above water hull form have generally been dealt with in qualitative manner rather than quantitatively.

By using generic equations to calculate hydrodynamic and swell-up coefficients, Crossland and Johnson (1998) managed to calculate the motions at the instantaneous wetted surface. The influence of the above water hull form in this regard was therefore accounted for even though further validation of those generic equations for a frigate hull form is necessary. By setting up a series of threshold criteria, they also initiated a method to include the above water hull form into investigating the occurrence of deck wetness and subsequently classifying the degree of wetness.

3.2.6.1 Freeboard exceedance

The freeboard is exceeded when the relative motion between the water surface and the bow is greater than the freeboard at calm water surface:

$$r_c > FB \tag{3.2.14}$$

The exceedance of freeboard is used in probabilistic method (see Section 2.2) as the indication of deck wetness. However, both seafarers and several researchers such as Maruo and Song (1994) and Wu et al. (2000) have reported that there were situations in which the freeboard was exceeded but no subsequent deck wetness took place. The following sections are based on the work by Crossland and Johnson (1998) in which the evaluation of the deck wetness based on the above water hull form was implemented.

3.2.6.2 Green water

Crossland and Johnson (1998) claimed that green sea wetness or green water occurred if the undisturbed or notional relative motion exceeds the local freeboard at any station:

$$r = (s - \zeta) > FB \tag{3.2.15}$$

This criterion appeared to correspond with the observations in green water experiments carried out by the author which will be presented Chapters 4 and 5.

3.2.6.3 Spray wetness

Spray wetness is relatively difficult to be defined mathematically. It should be a function of the water mass shipped on board, the velocity of rising water and local effects that are related to the above water hull form. However, genuine spray

cannot be deduced from modelling and experimental data since the spray in the experiments cannot represent the spray in reality due to scale effects and viscosity. The principle concept of spray wetness adopted in Crossland and Johnson (1998) was that if the disturbed water was thrown upwards in the air and could manage to land on deck subsequently, the spray wetness was resulted in. In order to land back on the deck, the transverse trajectory of water particle should be less than the increase in local beam as the ship travels forwards. Detail can be found in Appendix B, which is part of the work by Lloyd (1994).

3.3 Summary

Chapter 3 has introduced a methodology based on strip theory to calculate ship motions and surface disturbances around the ship bow. The outputs were integrated subsequently to find out the actual relative motion between ship deck and disturbed free water surface. Method for predicting and classifying deck wetness by Crossland and Johnson (1998) was then described as a way to evaluate the occurrence of green water. Even though no improvement to this method is made from this research, it is an intent, by quoting this method as an example, to propose an encapsulate model (see Chapter 9) for evaluating green water and its loading effects. The numerical results of this method will be validated in Chapter 5.

Chapter 4:
Model Testing of Different Bow Shapes and Rectangular Breakwaters

4.1 Introduction

The main objectives of the model testing are to investigate the physics of green water and its loading effects and to establish a suitable hydraulic modelling framework for simulating green water on deck. Effects of the above water bow form are also part of the investigation programme. Experimental data acquired are used to validate the results from the simulation. A good agreement from this comparison verifies the applicability of the modelling framework.

The experiments also look at the possibility of reducing green water loading on breakwaters by testing generic protective breakwaters fitted on forecastle deck. Numerical modelling is also executed and verified with experimental data to confirm the applicability of the developed modelling framework.

4.2 Model testing of different bow shapes

The purpose of carrying out green water tests using generic bow sections is to assess the effects of bow features on green water. Bow parameters which influence deck wetting include freeboard height, bow flare, bow knuckle and stem overhang. As illustrated in Figure 4.2.1, bow flare is defined to be the angle made by the tangent to the station at the intersection with the deck edge. Bow knuckle is referred to the knuckles that are introduced in the station of the bow section. Generally, bow knuckles define a chine in the bow section. Stem overhang is the horizontal projected distance between the intersecting point of waterline and stem

curve, and the stem head. In order to assess the effects of these features, the under-water body of the bow was kept unchanged. Above water bows were interchangeable.

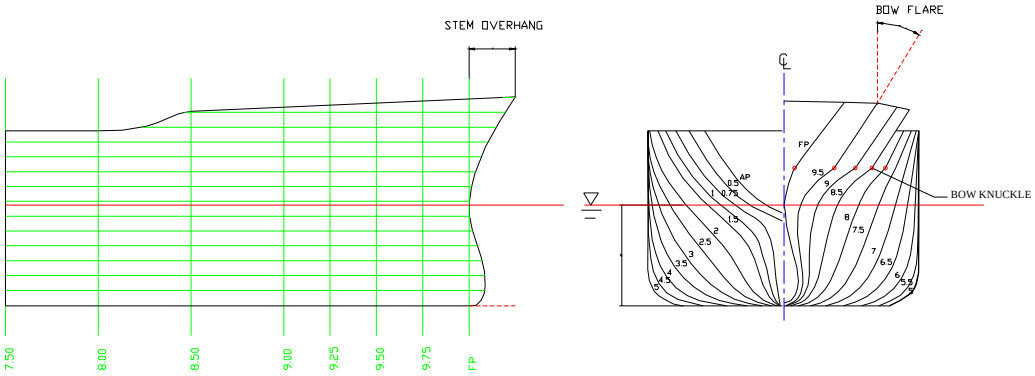

Figure 4.2.1 Definitions of bow flare, bow knuckle and stem overhang.

From this perspective, three generic bow shapes were produced and tested. The parent ship was a 1:70 scale model of the conventional container hull form S175. Principal particulars of the parent hull at both full scale and model scale are as in Table 4.2.1. At model scale, the parent hull (Bow 1) has a stem overhang of 62 mm, no knuckle and a bow flare of approximately 45 degrees at station 9½. The freeboard at the stem head was 146 mm or 10.22m at full scale.

Bow 2 was the modified bow from parent bow in which knuckles were added to stations 8 up to the stem curve. The knuckles were introduced at a height equal to half of freeboard at midship section. The bow flare at station 9½ was reduced by 10 degrees at the deck edge but increased by 15 degrees at the knuckle. The stem overhang was maintained the same as the original stem overhang.

Bow 3 had the stem overhang doubled to 124 mm from the original 62 mm. However, the bulwark was removed (Figure 4.2.4) and this resulted in a reduction in freeboard at the stem head of 15mm.

Table 4.2.2 summarises the bow features of the three bows and their lines plans are as in Figure 4.2.2. Figures 4.2.3 and 4.2.4 show the photos of the bow shapes in front and profile views.

Table 4.2.1 Principal particulars of full-scale and 1:70 model-scale S175 containership.

Particulars	**Full-Scale**	**Model**
Lpp (m)	175.0	2.5
B (m)	25.4	0.363
D (m)	15.4	0.22
d (m)	9.5	0.136
Δ (t)	24 742	0.07213
GM (m)	1.0	0.014
Cb	0.5716	0.5716
Kyy/Lpp	0.24	0.24
Kxx/B	0.328	0.328

Table 4.2.2 Summary of ship bows tested.

Bow	**Bow flare at station 9½ (degs.)**	**Bow knuckles**	**Stem Overhang (mm)**
Parent bow (Bow 1)	45.0	No	62.0
Bow 2	35.0	Yes	62.0
Bow 3	45.0	No	124.0

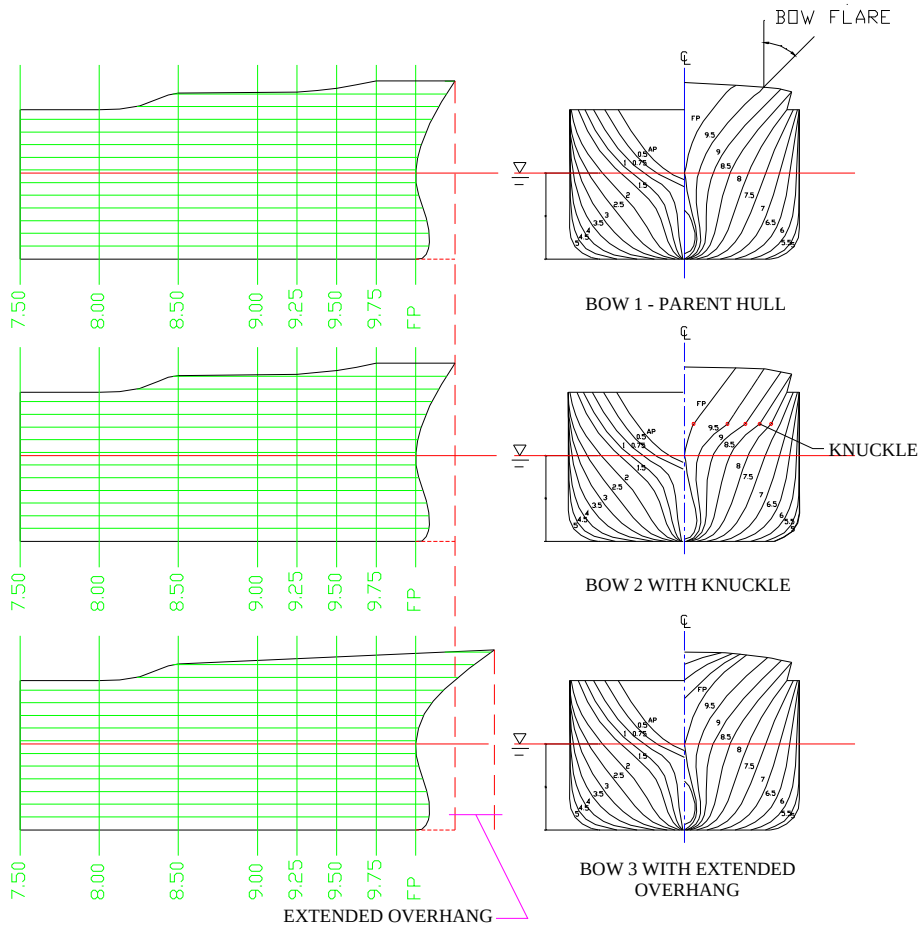

Figure 4.2.2 Lines plans of three bow shapes tested.

Figure 4.2.3 Front views of three ship bows.

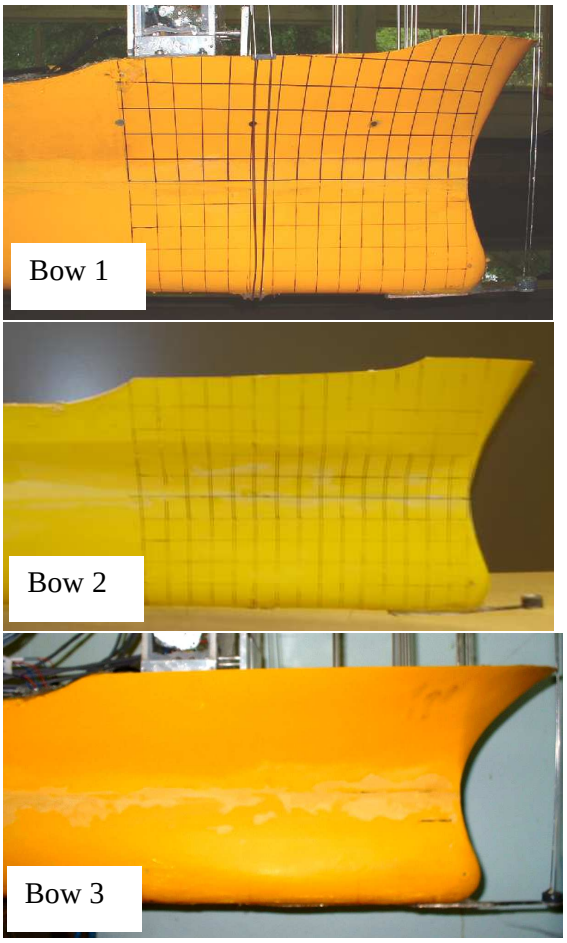

Figure 4.2.4 Profile views of three ship bows.

All the models were built out of Glass Reinforced Plastic (GRP) at the model-making workshop at the Centre for Marine Hydrodynamics, Universities of Glasgow and Strathclyde.

4.3 Towing tank

The model experiments were conducted in the Hydrodynamics Laboratory at the Universities of Glasgow and Strathclyde. The tank dimensions were 70m×4.6m×2.4m. The setup of the tank is as in Figure 4.3.1, standard with a beach at one end and a wave-making system at the other. The wave-making system consists of one hinged flap and software control allowing both regular or random wave generation. Railway is fitted on the sides of the tank to guide a mobile carriage that accommodates the workstation (Figure 4.3.2). The velocity of the carriage is controlled and monitored electronically to ensure that the desired velocity can be achieved and maintained in the tests.

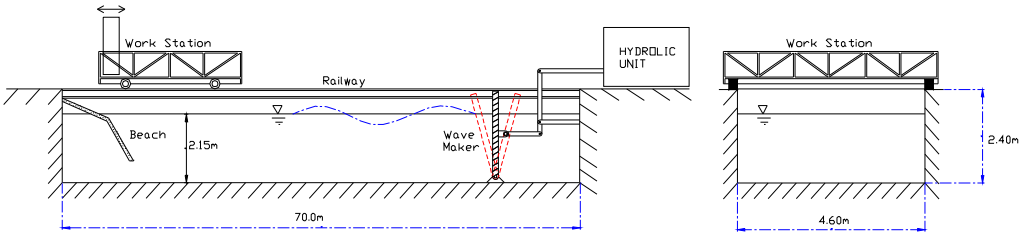

Figure 4.3.1 Towing tank configuration.

Figure 4.3.2 Snapshots of towing tank with the mobile carriage and hinged flap wave maker.

4.4 Measurements

To assess the occurrence of green water, its behaviour on deck and severity of green water loading, experiments were set up. The following measurements were undertaken:

- Heights of generated waves and encountered waves
- Ship motions in vertical plane
- Relative motions between deck and water surface at stem head and at the ship side in station 9
- Elevation of green water on deck when green water takes place
- Green water loading on vertical surfaces
- Green water loading on breakwater
- Green water loading on main deck
- Visual monitoring of the test via video tracking for qualitative assessment

Only motions in vertical plane were taken into account in green-water assessment. Inclusion of rolling in green water assessment would complicate the process and for simplification purpose, rolling was excluded from tests.

4.5 Instrumentation

Based on the measurements that were required, devices were built and set up. The following sections described the instruments that were used.

4.5.1 Generated waves and encountered waves

Generated waves are waves produced from the programmed motions of the wave maker. In the pilot tests, both regular and irregular waves were used in testing. However, due to the forward velocity of the ship, the test time was only limited to a maximum of 70 seconds when tests were carried out at low velocity of 0.75 m/s (equivalent to Fn = 0.15 or 12.2 knots at full scale). The ITTC recommend procedure suggests that for a reliable set of experimental results in irregular seas, a minimum test time duration equivalent to one hour of full-scale trial is required. Given the scaling of 1:70, a required test time in irregular seas should be no less than 430 seconds, indicating tests in irregular waves unsuitable. Multiple runs in different irregular waves having the same spectrum can be spliced to produce the wave trains of required duration. However, this is expensive both in terms of test time and resources. Therefore, this could not be implemented. As the result, only test in regular waves were carried out.

Before the start of experiments, calibration of waves was carried out to obtain the calibration factors required to achieve wave amplitude and period. During the tests, generated waves were measured by a resistance wave probe located at approximately twenty metres from the wave maker. This was outside the zone that could be effected by standing waves caused by the wave maker. During the test, the ship model was moved at a forward velocity, it encountered incident waves at an '*encounter frequency*' which was higher than the frequency of the generated waves. The motions of the model significantly depend on this encountered frequency.

The encountered waves were measured by a wave probe which was fixed on the carriage and transversely aligned to the forward perpendicular of the ship (Figure 4.5.1). It was also set at a distance away from the ship to ensure that the encountered waves at the location it measured was not disturbed by the presence nor the motions of the ship.

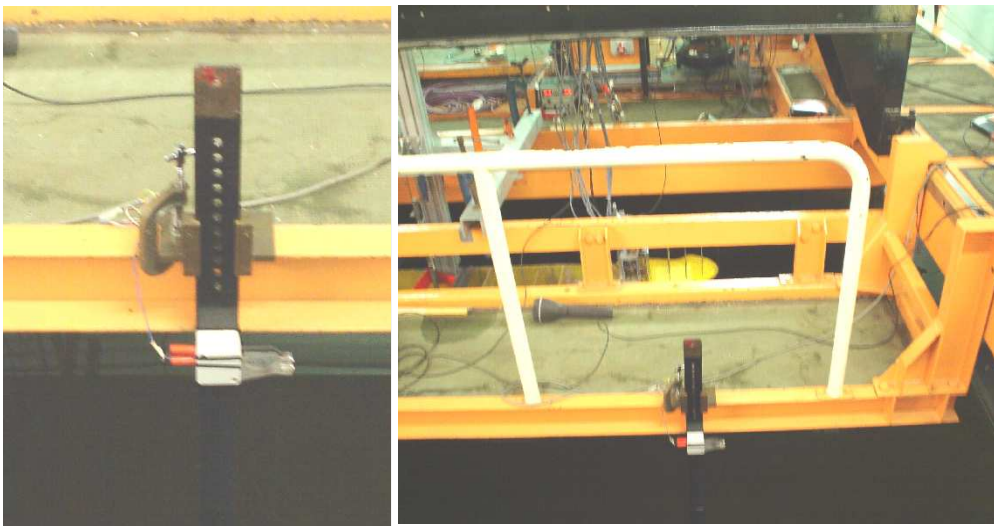

Figure 4.5.1 Wave probe fixed on carriage to measure encountered waves.

4.5.2 Ship motions

Ship motions were fundamental to the relative motions between ship bow and water surface. As mentioned earlier, only heave and pitch motions were interested and measured in these experiments. The ship motions were measured using a system consisting of two linear variable differential transformers (LVDT). The first LVDT was mounted above the longitudinal centre of gravity of the ship and the second at the aft perpendicular as in Figure 4.5.2.

The ship motions or heave and pitch in particular can be derived from the relative measures from these two LVDT's. The derivation of heave and pitch is referred to Section 4.9 which explains the analysis of the experimental data.

Figure 4.5.2 LVDT's to measure ship motions, one at LCG (left) and another at aft perpendicular (right).

4.5.3 Relative motions

Measurement of relative motions was carried out at two locations, i.e. one at the stem head and the other at station 9 (Figure 4.5.3) where the load cells were mounted (see Section 4.5.4). Both wave probes were extended vertically from keel to a height well above the forecastle deck to ensure that a large range of relative motions was recorded. Note that when the keel emerged out of water due to substantial vertical motions, the whole wave probes would be out of water and the signals indicated a cut-off in the time history curves during the time this happens. Keel emergence (and its duration) or keel slamming could therefore be detected via these indicative signals.

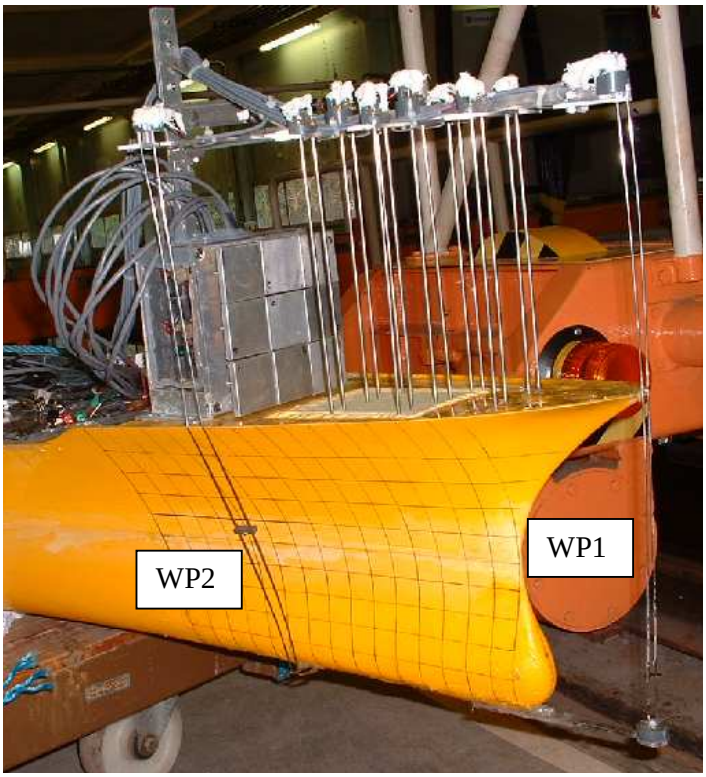

Figure 4.5.3 Wave probes at stem head (WP1) and at station 9 (WP2) to measure relative motions.

4.5.4 Green water elevation on deck

When green water happens, it is helpful to understand the distribution and behaviour of green water flow on deck. Knowledge of green water heights, their distribution on deck and the approximate velocity of the water flow is undoubtedly valuable in understanding green water characteristics and physics.

In order to obtain these data and taking into account the dimensions of the forecastle deck, a system of eight wave probes were set up (Figure 4.5.3). The general setup is as in Figure 4.5.4. The wave probes on the forecastle were arranged in three rows. The first row at the forward perpendicular comprised of two wave probes. The next two rows had three wave probes in each and the

distance between two adjacent rows was set at 78 mm. In each row, the wave probes were 50.8mm (2 inches) apart.

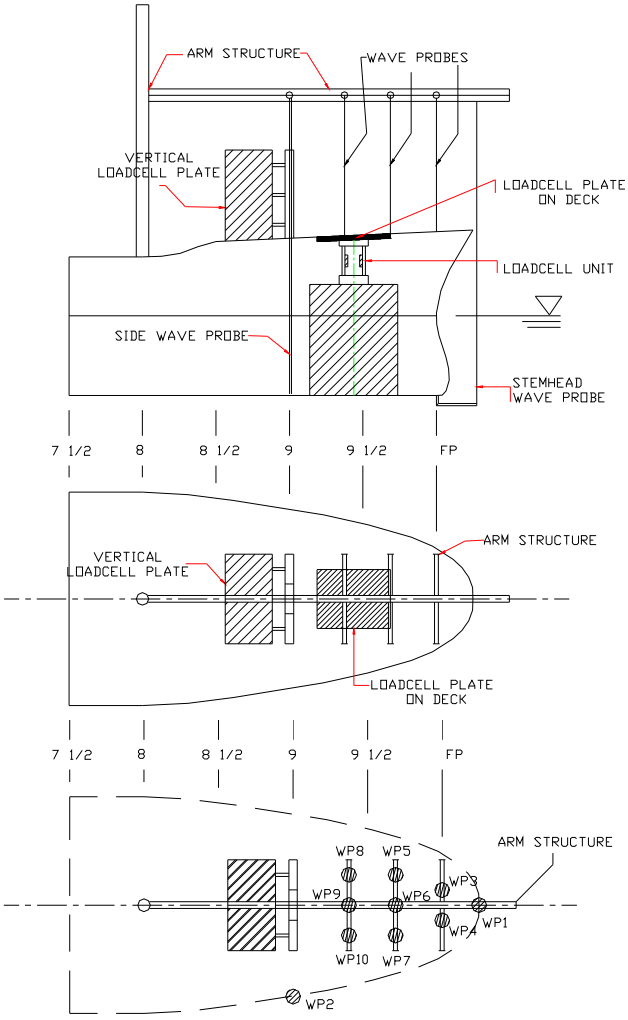

Figure 4.5.4 General setup of green water tests at the bow.

Measuring the translating velocity of green water on deck proved to be a difficult task. Buchner and Cozjin (1997) used wave probes that were arranged parallel to the main deck to measure both the entry velocity and the translating velocity. However, the splashing water during the shipment of green water onto deck caused problems in their interpretation of the data afterwards. In this thesis, the author approximated the velocity of green water flow via the time lag between the

recordings of two wave probes aligned along the centreline of deck. This velocity was then treated as the average velocity when in fact the motions of the deck meant that velocity of green water did vary along the deck due to the sloping of the deck and gravity effects.

4.5.5 Green water loading on vertical surface

One of the major effects caused by green water that has attracted serious concerns in safety and operability of the ship is the loading on vertical surfaces on forecastle deck. In order to investigate the severity of this loading, a vertical structure comprising of nine load cells was assembled and fitted on deck as in Figure 4.5.4. Figure 4.5.5 details the structure of the load cells and their arrangement. Figure 4.5.6 shows the photo of this unit and its installation on deck.

Basically, the vertical load cell unit was mounted on forecastle deck at station 9. It was a 15cm×15cm vertical load cell wall (representing objects on deck such as superstructure or containers) on which nine 5cm×5cm load cells arranged in a 3×3 array were fitted. All the strain gauges were waterproofed, housed and protected inside a plastic box. When green water impact loading took place, the loading on each load cell panels was transmitted through the back shafts and was measured by strain gauges.

The load cells were calibrated to measure the maximum load of five kilograms (approximately 50N) and was considered sufficient for the conditions investigated. The lower limit that could be measured was at approximately 0.5N. Loads below this limit could be interfered by noises, giving disturbed and unreliable signals. This loading is equivalent to the pressure of approximately 1.4m water head at full-scale and may be regarded a non-threat to the integrity of the structure.

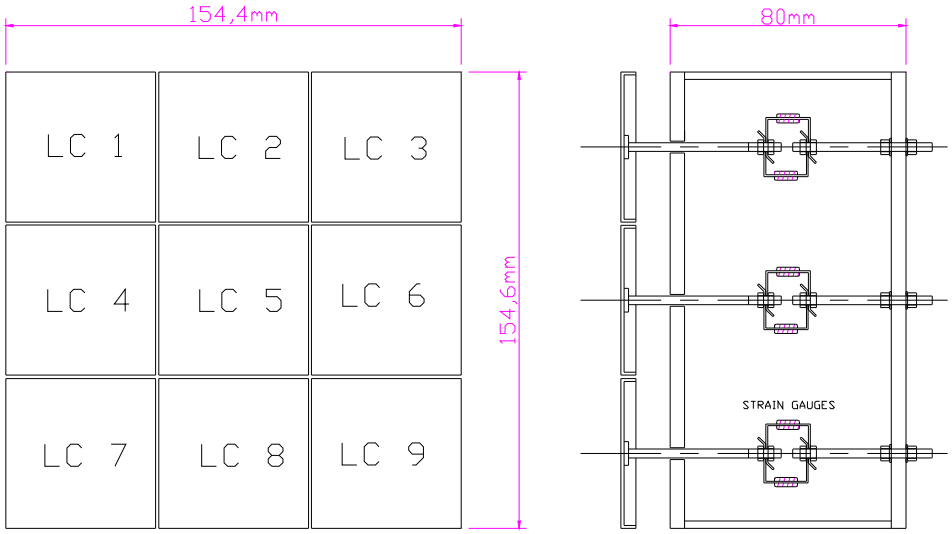

Figure 4.5.5 Load cell structure.

Figure 4.5.6 Load cell box.

4.5.6 Green water loading on deck

As green water is shipped onto deck, its weight as well as its dynamics on deck creates a pressure that may endanger the deck plating. In one investigation on the forecastle deck of a ship, a set-down of 300mm was recorded following a green water spell (Olsen, 2005). This gives an example of how damaging green water may cause to the deck plating. In order to measure this loading, a rectangular area at the centre of the forecastle deck and in front of the vertical load cell unit was cut off and replaced by an aluminium plate. This plate was in turn connected to a high frequency load cell mounted under forecastle deck. The dimensions of the aluminium plate were 98.36mm×123.28mm×8.00mm and the weight was measured at 270 grams. Figure 4.5.4 shows the overview of this setup and Figure 4.5.7 shows the setup for experiments. In order to waterproof the unit, a thin rubber sheet was attached on deck covering the aluminium plate as in Figure 4.5.8. The deck load cell was calibrated to measure loading up to ten kilograms which is adequate for the chosen test conditions.

Figure 4.5.7 Deck load cell unit located under forecastle deck.

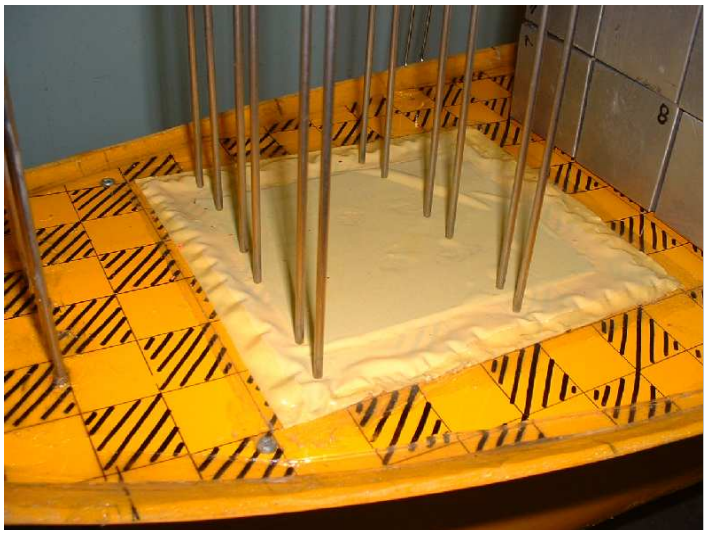

Figure 4.5.8 Yellow rubber sheet covering aluminium plate and deck load cell unit.

4.5.7 Green water loading on breakwater

Protective breakwater is employed to reduce the loading that would be sustained by the structure in early stage. The idea of using a breakwater as a protection on ship might have been inspired by the success of the application of breakwater in coastal engineering. Compared to ship, breakwaters in coastal engineering have a far longer history. Man-made breakwaters were found thousands of years ago, built out of rock and other natural materials. The first modern coastal breakwater was constructed at Cherbourg, France at the end of the 18th century (Tanimoto and Goda, 1991). The concept of building a porous wall in order to reduce the wave motions in front of the breakwater was initiated by Jarlan (1961). By introducing the perforations on the wall, part of the potential energy was dissipated through the formation of multiple water jets behind the perforated wall. The loading on the breakwater is therefore reduced. This could be the inspiration to the application of the Jarlan-type breakwater on ships in recent years.

The experiments were only performed on rectangular breakwaters because of its popular application to containerships recently. Generic rectangular breakwaters were fitted in front of the vertical load cell unit and loading on both structures were recorded in order to see the effectiveness of breakwater in protecting the structure behind it. Perforations were also introduced to resemble the Jarlan-type breakwater to investigate the advantages.

4.5.7.1 Generic rectangular breakwater designs

The generic rectangular breakwaters were designed as a protective structure to the vertical load cell unit. The width of the breakwaters was to cover the width of the vertical load cell unit and this width was fixed. It was obvious that the protection to load cell unit was decided by the height of the breakwater. Higher breakwater meant larger protective area. Breakwaters essentially act as a sacrificial structure to cargo or deck structures since it takes on the loading which would have been sustained by these objects.

Green water loading is severe and by absorbing most of this loading breakwaters need strong foundations to support it. The higher the breakwater, the larger overturning moment caused by green water loading. Supporting structure will need to be stronger as a result. It is therefore necessary to seek an optimal height for the breakwater to balance the degree of protection and the structural reinforcement required for the foundation.

As discussed above, following Jarlan's design of perforated breakwater in coastal engineering, recent breakwaters used on ships have been perforated in order to reduce green water loading by dispersing the water concentration and allowing some water to pass through.

Taking all these concepts into account and also the dimensions of the vertical load cell unit, the generic rectangular breakwaters were designed and they are

summarised in Table 4.5.1 and Figure 4.5.9. Figure 4.5.10 shows the photos of the manufactured breakwaters used for testing. Note that tests were carried out for the last three breakwaters presented in Figure 4.5.10. However, location of perforations on these breakwaters was not consistent with those on other perforated breakwaters. Therefore, the test results were not used for comparison based on this inconsistency, generically.

The breakwater was mounted at a distance of 37 mm from the vertical load cell unit. This distance is equivalent to 2.5 m at full-scale which was regarded a reasonable distance between the breakwater and stacks of containers or deck structure in real case.

Table 4.5.1 Matrix of generic breakwaters designed for testing.

Breakwater number	**Dimensions in mm (width × height)**	**Perforation diameter (mm)**	**Number of rows of perforations**	**Permeability(*) of breakwater in percentage**
1	203.2 × 50.8	No	No	0.0%
2	203.2 × 50.8	10.5	2	11.7%
3	203.2 × 50.8	14.0	2	20.9%
4	203.2 × 50.8	17.5	2	32.6%
5	203.2 × 76.2	No	No	0.0%
6	203.2 × 76.2	10.5	3	11.7%
7	203.2 × 76.2	14.0	3	20.9%
8	203.2 × 76.2	17.5	3	32.6%
9	203.2 × 101.6	No	No	0.0%

(*) Ratio between total area of perforations to area of breakwater including perforations.

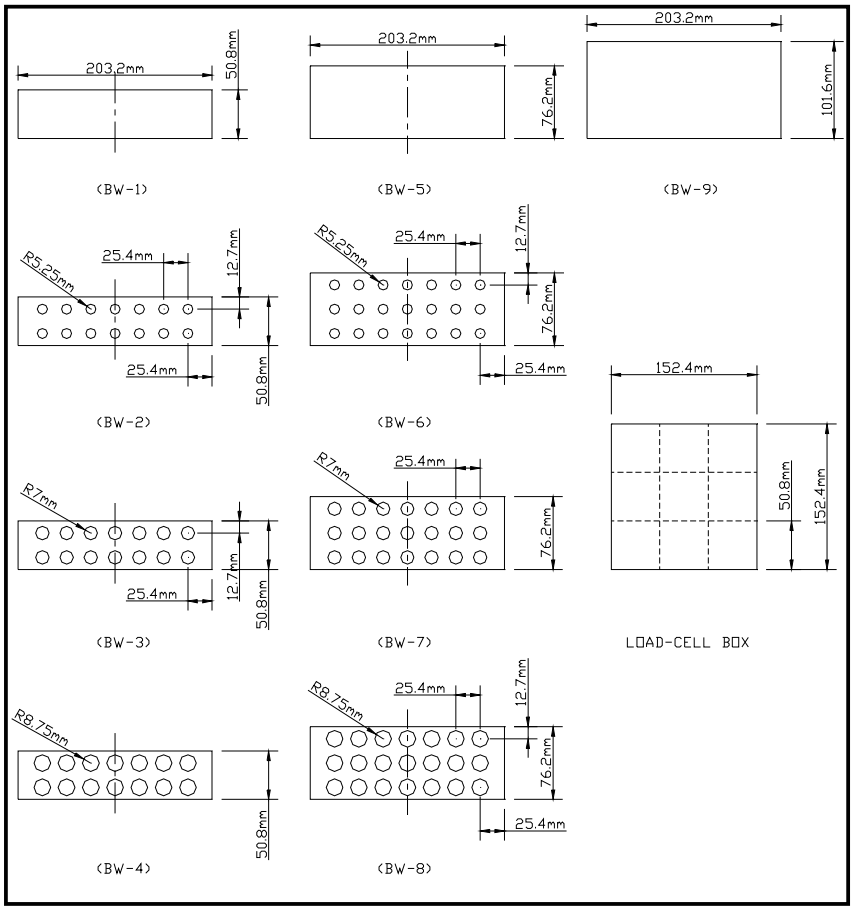

Figure 4.5.9 Designs of generic rectangular breakwater.

Figure 4.5.10 Manufactured rectangular breakwaters used for testing.

4.5.7.2 Measuring load on breakwater

To measure the load on the breakwater, a load cell similar to the deck load cell was used and fitted under forecastle deck. It was mechanically connected to the breakwater so that load acting on the breakwater could be directly transferred to the load cell (Figure 4.5.12). Figure 4.5.11 shows a perforated rectangular breakwater fitted on forecastle deck in front of the vertical load cell unit.

Figure 4.5.11 Breakwater fitted on forecastle deck.

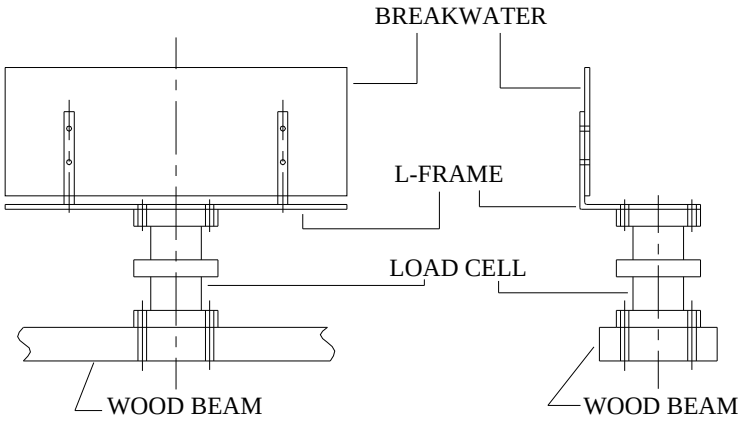

Figure 4.5.12 Connection between breakwater and load cell unit.

4.5.8 Video tracking

Video tracking of green water as it happens is very important for qualitative assessment of the phenomenon. To observe green water on deck , a waterproof camera was fitted on the metal arm as in Figure 4.5.13. Another camera was also used and it was fixed on carriage to capture the ship image from side.

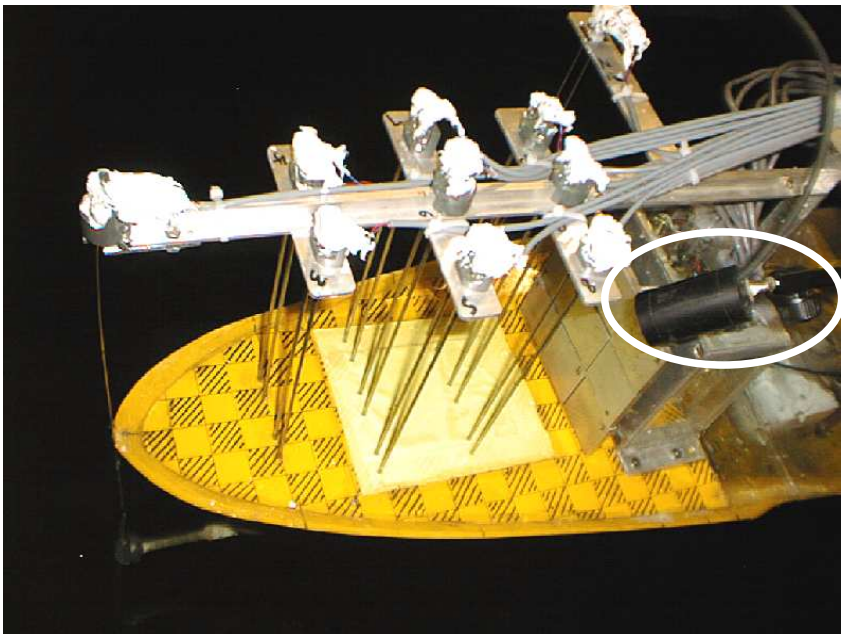

Figure 4.5.13 Deck-mounted camera.

4.6 Connection of model to carriage

As mentioned earlier, only heave and pitch motions were considered in this research. The connection between the model ship and the carriage was therefore designed to satisfy these requirements. An overview of the connection is as in Figure 4.6.1. In order to allow the ship to heave freely whilst surge was restrained, a vertical sliding mechanism was set up with the lower end of the slider bar being connected to ship. This slider bar was allowed to slide vertically along a set of

roller wheels which were fitted to an aluminium framework that was , in turn, clamped to the carriage (Figure 4.6.3).

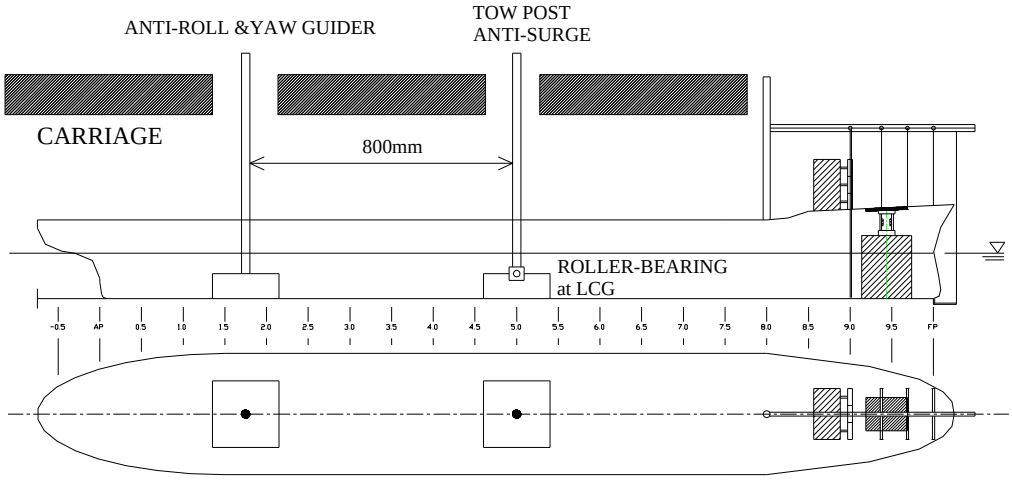

Figure 4.6.1 Overview of the connection between model and carriage.

Figure 4.6.2 Overview of connection between model ship and carriage.

To allow for pitching motions, at the connection point between the model ship and the slider bar, a roller bearing was used. To restrain the ship from rolling and

yawing, two anti-roll and yaw guiders were used. The first guider was the tow post at the LCG. The second guider was fixed at the centreline, 800mm at the back of the first guider (Figures 4.6.1 and 4.6.2). These two posts were then held at the upper ends by two roller bearings which allow the vertical motions of the posts but would stop them from any horizontal motions.

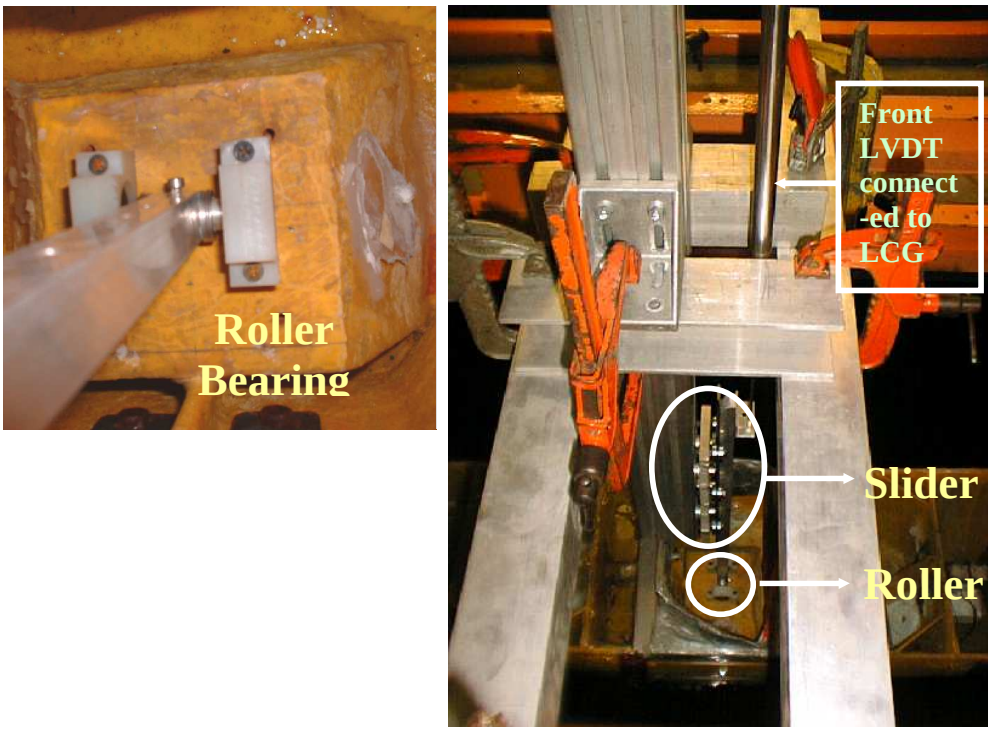

Figure 4.6.3 Ship model was connected to carriage at LCG via a sliding mechanism.

4.7 Data acquisition and calibration of devices

4.7.1 Data acquisition

Figure 4.7.1 illustrates briefly the facilities utilised to acquire test data. Altogether, twenty three data channels and two high-frequency amplifiers were used. Collected data were stored in a PC. Two VCR's were used to monitor the tests. Signals to wave maker were sent via a separate computer.

Figure 4.7.1 Data acquisition system.

4.7.2 Calibration of devices

4.7.2.1 Wave probes

Figure 4.7.2 shows the calibration process of wave probes fitted to the bow section. Three depths with an increment of 50mm were calibrated and the results gave a linear behaviour. The calibration factors were then calculated and applied to the data acquisition system.

Figure 4.7.2 Calibration of wave probes that were fitted to bow section.

4.7.2.2 Load cells

The load cells were also calibrated before and after the experiments to ensure that the calibration factors remained consistent through out the experiments. Ten weights with increment of 100g were calibrated and the results showed almost linear behaviour. The average slopes of the curves was then calculated and used as calibration factors. The calibration process is illustrated in Figures 4.7.3 and 4.7.4.

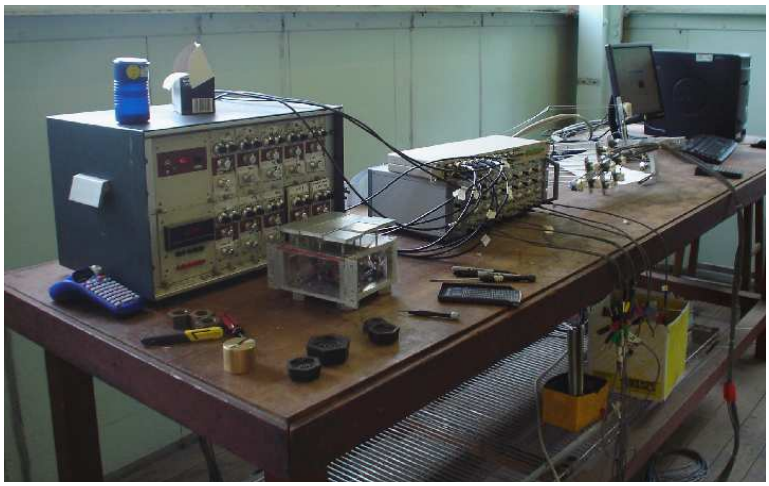

Figure 4.7.3 Calibration of vertical load cells.

Figure 4.7.4 Calibration of deck load cell.

It was important to bear in mind that the ship hull did have a natural frequency when responding to loads acting on the hull. If this frequency was somewhere near to the natural frequencies of either the deck load cell or the vertical load cells, the recorded data would be influenced by the noise coming from the responses of the hull and that could mislead the interpretation of green water loading. During the calibration process, all these frequencies were measured. The natural frequency of hull was measured at 40Hz whilst natural frequencies of the vertical load cells were measured at 130Hz and that of the deck load cell was 150Hz which was sufficiently high to avoid the influence of the hull vibration on green water loading recorded.

4.8 Test conditions

The water level was measured at 2.235 m and the draught of the ship corresponded to fully loaded condition of 136 mm (9.5m at full scale).

The tests were carried out with variation of parameters including carriage velocity, generated wave height and wave periods. For tests without breakwaters, Table 4.8.1 presents the matrix of the tested conditions. For tests with breakwaters, the tested conditions are as in Table 4.8.2.

Still water tests were also conducted at different velocitys to measured sinkage, trim and bow waves at station 9.

Table 4.8.1 Matrix of test conditions for test without breakwaters.

	Full-scale	**Model-scale**
Velocity	12.2 (knots)	0.75 (m/s)
	16.3 (knots)	1.00 (m/s)
	20.4 (knots)	1.25 (m/s)
	24.4 (knots)	1.50 (m/s)
Wave height	3.0 (m)	43 (mm)
	4.0 (m)	57 (mm)
	6.0 (m)	86 (mm)
	8.0 (m)	114 (mm)
Wave period	10 (s)	1.96 (s)
	11 (s)	1.31 (s)
	12 (s)	1.43 (s)
	13 (s)	1.55 (s)
	14 (s)	1.67 (s)
	15 (s)	1.79 (s)

Table 4.8.2 Matrix of testing conditions for tests with breakwaters.

	Full-scale	**Model-scale**
Velocity	20.4 (knots)	1.25 (m/s)
	24.4 (knots)	1.50 (m/s)
Wave height	8.0 (m)	114 (mm)
Wave period	12 (s)	1.43 (s)
	13 (s)	1.55 (s)

4.9 Data analysis

4.9.1 Introduction

Once the experiment has been carried out and data collected, it is important to have a transparent interpretation of the data. To achieve that, the data must be analysed correctly. This section explains the analysis of test data collected from experiments.

4.9.2 Noise filter and data truncation

The experimental data are always interfered by noises. The sources of these noises could come from the motor that drove the carriage, the vibration of the ship hull, etc. To get good data for analysis, the noise is to be filtered off. The filtering was carried out using built-in function *filtfilt*(b,a,x) in MATLAB software in which the cut-off frequency was set to 30Hz.

As explained in MATLAB User's Manual, function *filtfilt*(b,a,x) performs zero-phase digital filtering by processing the input data in both the forward and reverse directions. After filtering in the forward direction, it reverses the filtered sequence and runs it back through the filter. The resulting sequence has precisely zero-phase distortion and double the filter order. *filtfilt* minimises start-up and ending transients by matching initial conditions, and works for both real and complex inputs.

As far as the truncation was concerned, it should be noted that data recorded during the run covers both the pre-run and post-run data which were essentially unnecessary. At the beginning, after encountering the first waves, the ship motions would be affected by its natural frequency. This would diminish quickly and the ship motions would be dominated by the encountered wave frequency. Also, toward the end of the run when the ship decelerated, the ship motions would

change due to the change in encountered frequency. Except for the data recorded still water at the beginning which were used as the datum for zero correction, the data must be sensibly truncated.

4.9.3 Waves

Before the tests, wave calibration was carried out to ensure that waves generated during the experiments would have the height and frequency close to what were wanted. From the wave data, the period could be lifted straight from the wave histories. The wave height was calculated from the standard deviation of wave data:

$$H_w = 2\sqrt{2} \times \text{stddev}(\text{Wave\_Data}) \tag{4.9.1}$$

4.9.4 Ship motions

Since LVDT-1 is located at LCG, its measurements was equal to heave motions:

$$\eta_3 = -\text{LVDT}_1 \tag{4.9.2}$$

Pitch was calculated from the recordings of the two LVDTs using equation:

$$\eta_5 = \sin^{-1}\left(\frac{\text{LVDT}_2 - \text{LVDT}_1}{\ell}\right) \tag{4.9.3}$$

where ℓ is the distance between the two LVDT's.

4.9.5 Relative motions

Relative motion between stem head and free water surface was recorded using a wave probe (WP1 in Figure 4.5.4). The freeboard in still water at this location was calculated based on the depth from keel and the draught mark. By comparing the relative motion with the available freeboard, it could be figured out when and by how much the freeboard was exceeded.

The amount of free surface water exceeding the freeboard is very important since it is a strong indication of the severity of green water shipping. The first derivative of the relative vertical motion would give the relative vertical velocity between the bow and the water surface. Faltinsen et al. (2005) noted that the type of green water flow on deck could be governed by the ratio between the relative vertical velocity and the relative longitudinal velocity between the bow and the water. The latter could be derived from the water particle velocity and the velocity of the ship. In the analysis, these velocities were compared in order to evaluate the relation between this factor and the behaviour of green water flow onto the deck.

4.9.6 Green water elevation on deck

The green water elevations at various locations on deck were recorded by the wave probe system described earlier in Section 4.5.4. It should be noted that these recordings only indicated the maximum elevations that green water flow reached at that particular location at the time rather than the water heads above the deck level. Intuitive observation during the tests revealed that for ship such as containerships with forward velocity, high flare angle and bulwark, green water was shipped on board in two ways:

The first type of green water was somewhat similar to the spray wetness described in Chapter 3. As the ship pitched into the water, there was a water run-up at high velocity upwards the ship sides. When this run-up water reached the deck edge, it

was shed upwards and outwards in the direction normal to the deck edge (Figure 4.9.1). As soon as this water left the deck edge, water particles in the air followed a path that was similar to a ballistic trajectory. Due to the concaveness or the flaring of the ship sides, the take-off velocity of these water particles had a component in positive x-direction (i.e. forward the ship). This magnitude of this velocity component depended on the flare angle and the tangential velocity of the run-up water.

If this velocity was smaller than the forward velocity of the ship, the water would be caught up by the ship (Figure 4.9.2). As it landed back on the deck, it caused green water to happen (Figure 4.9.2). The whole process is summarised in Figure 4.9.3. If this water was caught up early by the ship, it could reach relatively high level before falling down on the deck (Figure 4.9.4). Therefore, if a wave probe was located at the same place on deck, it might record relatively high value of green water elevation. This value should not be perceived as the real water head above the deck because of the air gap underneath the water.

If the velocity component in x-direction of shed water was greater than the forward velocity of the ship (for example in the case of stationary ship in waves), this water would land back into the open water and green water of this type would not take place.

From observation, the amount of green water caused by shed water was normally small compared with the second type of green water that is described later. At full scale when viscosity is less influential, green water caused by shed water may take the form of spray. It represents green water that takes place in small quantities and its physics can be explained as in Section 3.2.6.3. This type of green water may take place even when the freeboard is not exceeded by surrounding water (see Section 5.4.5).

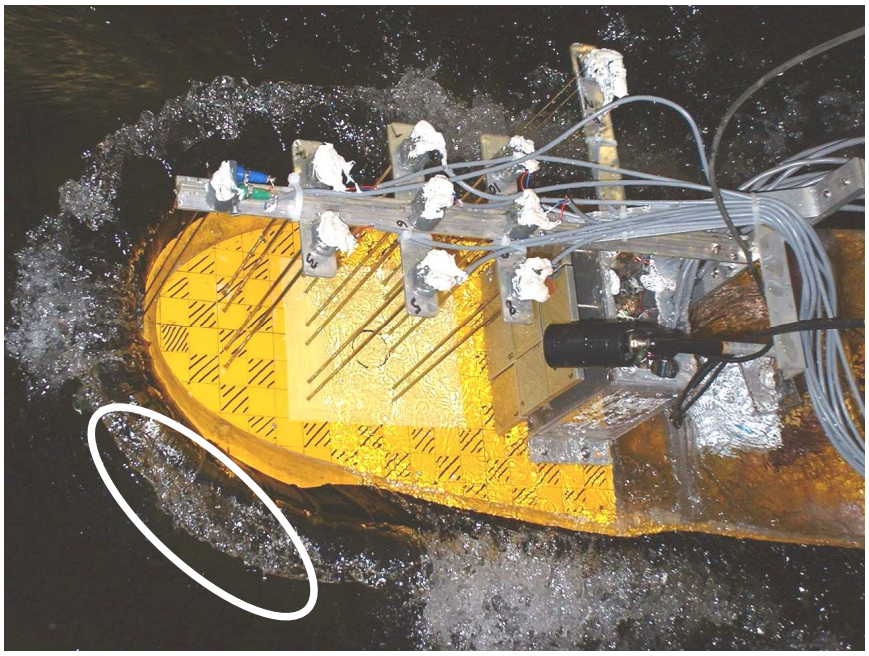

Figure 4.9.1 Run-up water (marked) shed upwards off the deck edge in the direction normal to the deck edge.

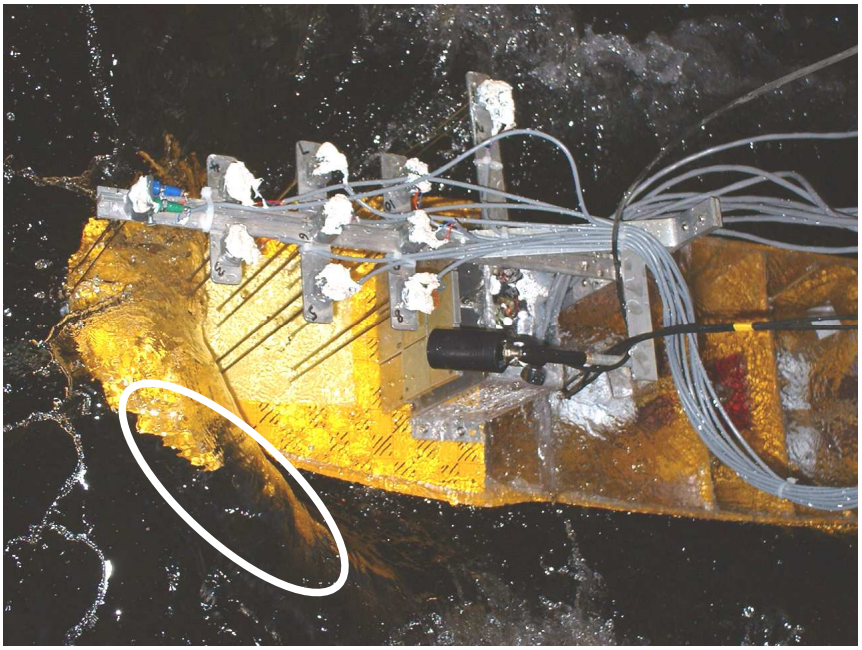

Figure 4.9.2 Due to forward velocity of the ship, shed water (marked) was overtaken and landed back inside forecastle deck.

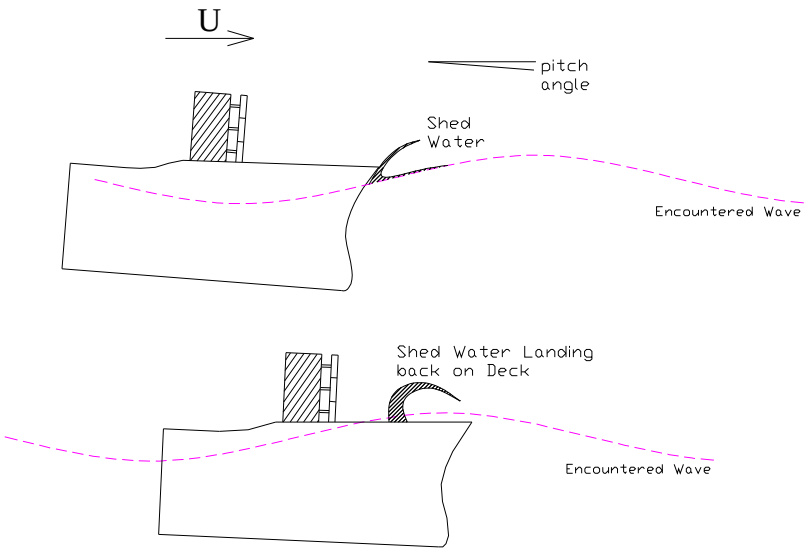

Figure 4.9.3 Shed water due to ship pitching into the water landed back on deck causing green water.

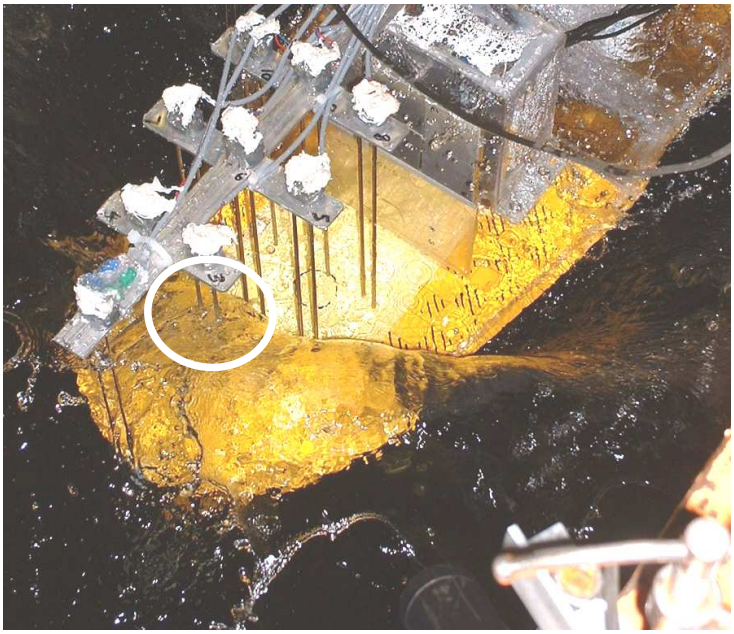

Figure 4.9.4 Shed water (marked) could reach high elevation and result in large recordings by wave probes.

The second type of green water was the in-flow of solid mass of water when the deck level was lower than the surrounding free surface (Figures 4.9.5 and 4.9.6). This corresponds to the green sea wetness described by Crossland and Johnson (1998). These flows entered the deck area from the direction normal to the deck edge. Due to the bulwark and the relative motions between the bow and the surrounding water, the inflows of green water normally had a vertical velocity component. Therefore, green water flows tended to take off the deck edge before plunging back on deck, resulting in an air gap or air entrapment immediately behind the deck edge or the bulwark (Figure 4.9.7).

Collectively, green water on deck was the combination of these two types of green water shipments. In heavy conditions, green water can take place in both forms (Figure 4.9.8). If the ship velocity is low, solid green water may be the only form that is shipped onboard. In light conditions, green water may take place as spray.

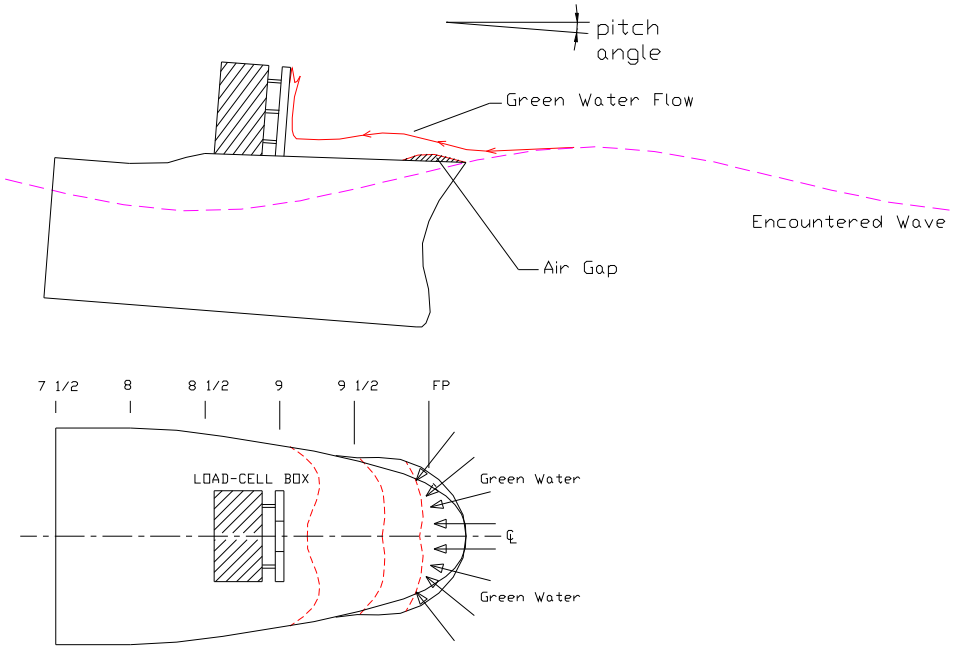

Figure 4.9.5 Green water enters deck area in form of water inflows in the direction normal to deck edge.

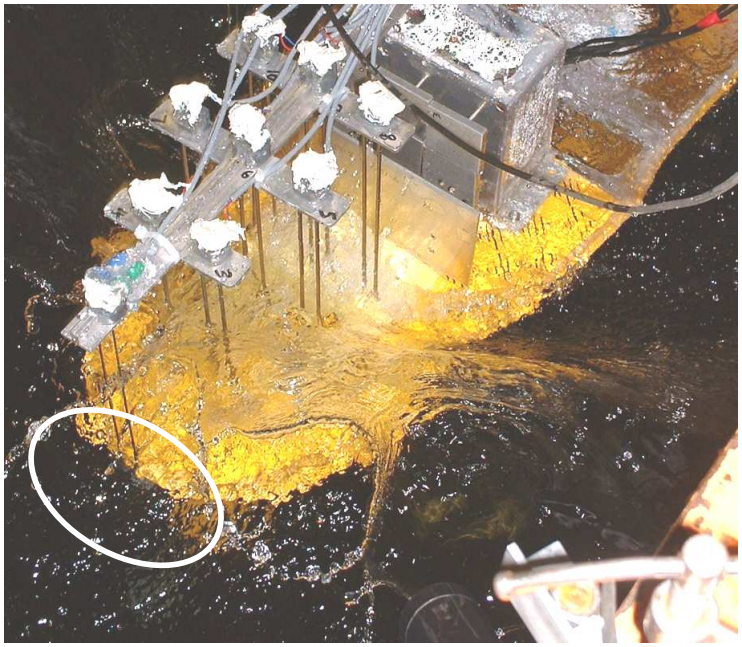

Figure 4.9.6 Solid mass of green water (marked) flows into the deck area as the water exceeds the deck.

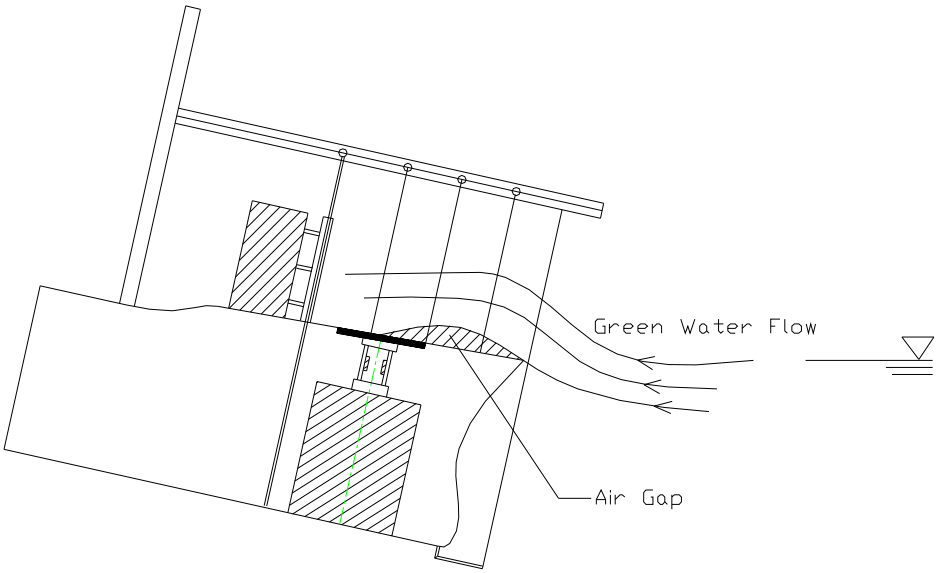

Figure 4.9.7 Behaviour of solid green water flow as it enters the deck area.

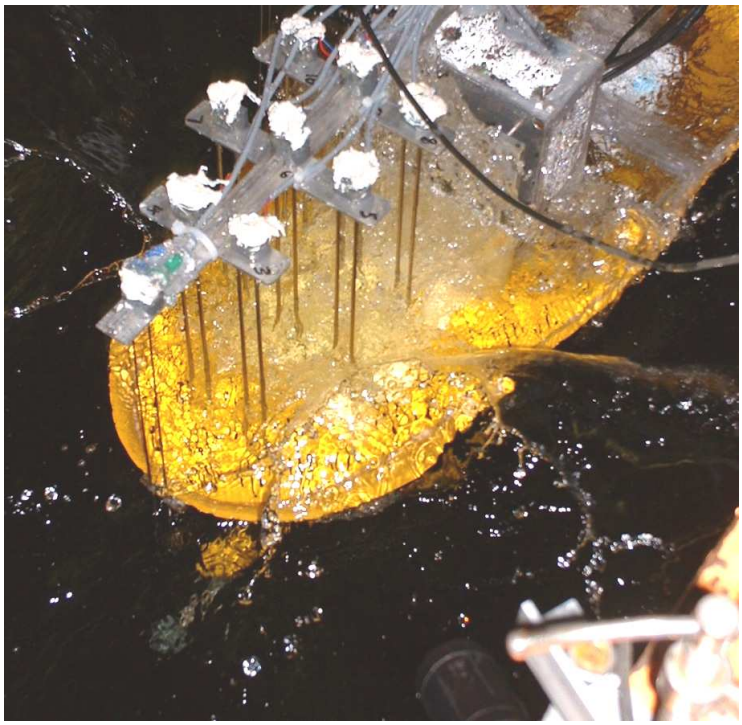

Figure 4.9.8 Collective green water comprises of both shipment of solid mass of green water and the shed water that manages to land back on the deck.

Analysis should distinguish these two types of green water since it may affect the way green water is simulated and loading evaluated. In terms of loading, it appeared that the major loads were resulting from the solid green water mass rather than splash or spray green water. The experimental results showed that when only spray green water took place, both the loads on deck and vertical surfaces were small and could be ignored. The simulation of green water was therefore focused on the shipment of solid green water mass on to deck.

4.9.7 Estimation of velocity of green water flow on deck

The velocity of green water flow on deck is of paramount importance since it is closely related to the impact pressure on the surface (see equation (2.3.3) in Chapter 2). The estimation of this value was therefore a target in this research. Due to the limited deck space available and also the concern over the obstruction to green water flow, no velocimeter was used to measure green water velocity directly. This velocity was therefore estimated from the translation of green water on deck via the recordings by the deck wave probes. Figure 4.9.9 shows the detailed arrangement of wave probes. Recordings from wave probes 6 and 9 (denoted as WP6 and WP9, respectively) were used since they were located along the centreline of the ship and closest to the deck load-cell unit. The distance between WP6 and WP9 was 78mm. If the time lag between the fronts of the curves by WP6 and WP9 was Δt seconds, green water flow velocity could be estimated as:

$$v_{gw} = \frac{78 \times 10^{-3}}{\Delta t} (m/s) \tag{4.9.4}$$

It is also useful to compare this velocity with other velocities such as carriage velocity, wave celerity, relative horizontal velocity between water particle and ship, etc. to see if there was any correlations between any of these velocities.

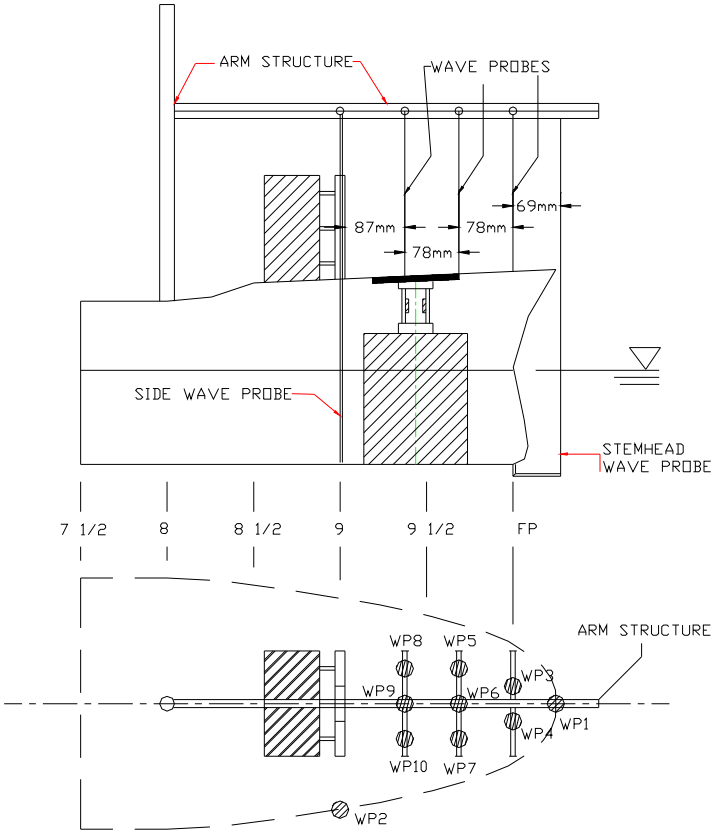

Figure 4.9.9 Arrangement of wave probes on the deck.

4.9.8 Green water loading on vertical surfaces

Green water loading on vertical surfaces was measured by nine load cells which were assembled together to form a vertical unit as described in Section 4.5.5. Loads measured at various locations were compared with each other to assess the effects of green water on different areas and locations on a vertical structure. When breakwater was fitted, the variations in these loads indicated the degree of protection provided by the breakwater. The load on the breakwater was also measured and compared with the total reduction in the load on the vertical load-cell unit as a whole in order to see the transition of loading from the protected surface to the breakwater and vice versa.

4.9.9 Green water loading on deck load cell

Green water loading on deck was measured by the deck load cell described in Section 4.5.6. This loading indicates how much green water could affect the deck plating structure. The experimental data were also used to validate the equation by Buchner (1995a, 2002) in which three components that contributed to the total pressure on deck were identified, namely

- Pressure due to green water mass (denoted as P1).
- Pressure due to the vertical acceleration of the deck (denoted as P2).
- Pressure due to the changing of green water elevation (denoted as P3).

If v_{deck} is defined as the vertical velocity of the deck with regard to earth and H_{GW} is green water height at the location where deck pressure is assessed, the deck pressure according to Buchner (1995a, 2002) can be expressed as:

$$P_{deck} = \underbrace{\rho.g.H_{GW}.\cos(\eta_5)}_{(P1)} + \underbrace{\rho.H_{GW}.\left(\frac{\partial v_{deck}}{\partial t}\right)}_{(P2)} + \underbrace{\rho\left(\frac{\partial H_{GW}}{\partial t}\right).v_{deck}}_{(P3)} \qquad (4.9.5)$$

As reported by Buchner (2002), component P3 made a very significant contribution (more than 50 percent in the cases studied) to the total pressure on deck. This pressure should, therefore, not be excluded from the calculation for deck pressure due to green water.

4.10 Summary

Chapter 4 has described the setup of green water experiments which were carried out at the Centre for Marine Hydrodynamics, University of Glasgow. Three ship bows were produced and appropriate instrumentation was installed to take the targeted measurements in the tests. The tests were carried out in various wave conditions and ship velocities. The analysis of the collected data was also explained accordingly.

Chapter 5:
Experimental Results on Different Bow Shapes and Rectangular Breakwaters

5.1 Introduction

In this Chapter, experimental results are presented. At first, all phases leading to a green water event are illustrated. When green water takes place, investigation focuses on loads on deck and on vertical surfaces. Comparisons with theoretical results are also carried out, followed by comparison of experimental data obtained for different bows. This Chapter also presents the benefits by using protective breakwaters on deck. Finally, repeatability of the experiments is evaluated.

5.2 Wave height and frequency

Generated wave heights and frequencies were measured and then compared with the wave heights and frequencies required for the tests. The results are as in Figure 5.2.1. The wave frequencies were controlled by controlling the frequency of the wave maker. They matched exactly with the frequencies required for the tests. Figure 5.2.1 compared the wave heights generated in the tests for the three bows.

Table 5.2.1 shows the mean errors and the standard deviations of the generated wave heights in three test series with three interchangeable bows. The precision was very good in the first test series with bow 1. Reasonable results were obtained for bows 2 and 3. The generated wave heights did not fluctuate much (standard deviations were within 5 percent) showing a consistency in the results.

Table 5.2.1 Mean error and standard deviation of generated wave heights.

Ship bow	Mean error (%)	Standard deviation (%)
Bow 1	3.50	2.11
Bow 2	5.23	4.37
Bow 3	9.14	5.03

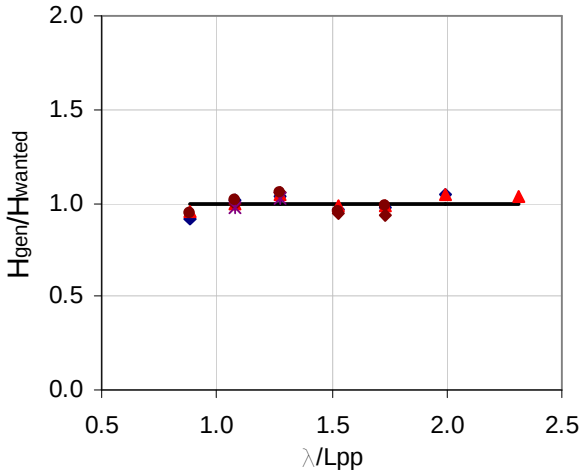

Figure 5.2.1 Ratio between generated wave height and required wave height for waves tested with bow 1.

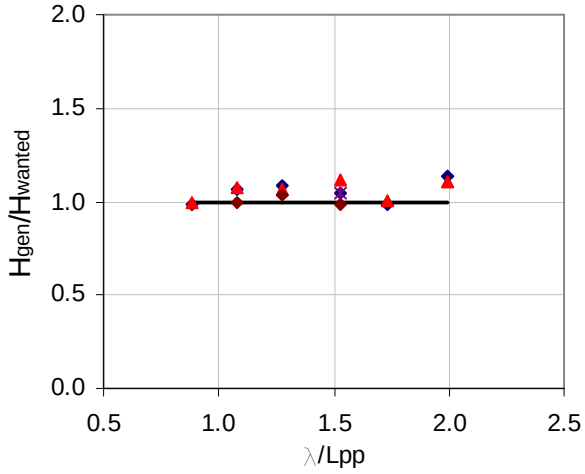

Figure 5.2.2 Ratio between generated wave height and required wave height for waves tested with bow 2.

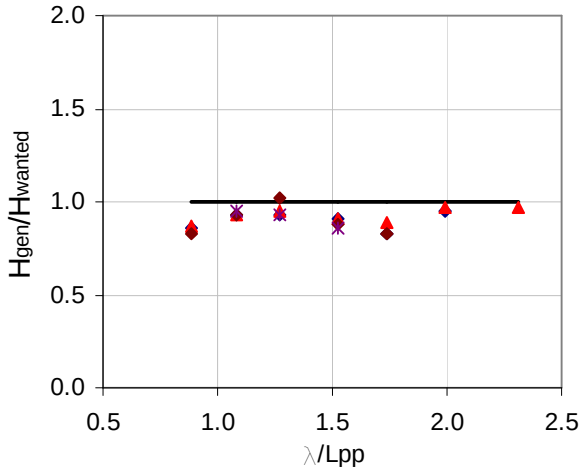

Figure 5.2.3 Ratio between generated wave height and required wave height for waves tested with bow 3.

5.3 Ship motions

5.3.1 Sinkage and trim in still water

When running in still water, ships normally experience some sinkage and trim. This is caused by the unevenly distributed pressure on the hull due to water flow passing the hull. Depending on velocity and hull shape, the values of these terms can be large and they can make significant contribution to the overall relative motions. Sinkage and trim in still water were therefore measured for all three bow shapes.

Since only the above-water part of the ship bow was interchangeable and the under-water body remained the same for all three bows, the sinkage and trim in still water are expected to be similar for all three bow shapes. If the sign conventions for heave and pitch are defined as in Figure 5.3.1, the sinkage and trim in still water are as in Figures 5.3.2 and 5.3.3. As expected, the sinkage and trim values did not vary much between the bows tested.

Figure 5.3.3 shows that trim caused by ship running in still water was not significant, staying well under 10 percent of a degree. Sinkage, however, was considerable especially at higher velocity. It reached nearly 10mm, or approximately 7.4 percent of the draught, at velocity of 1.50m/s or Fn = 0.30 (Figure 5.3.2).

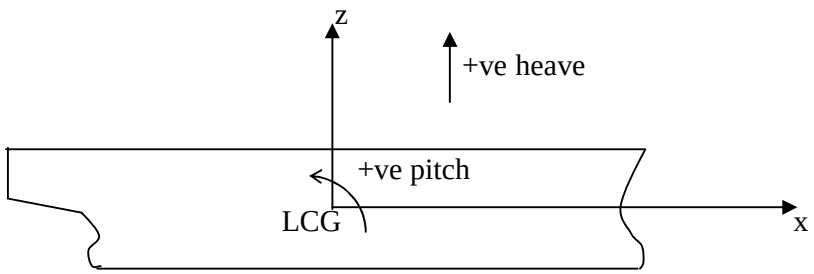

Figure 5.3.1 Sign conventions of heave and pitch.

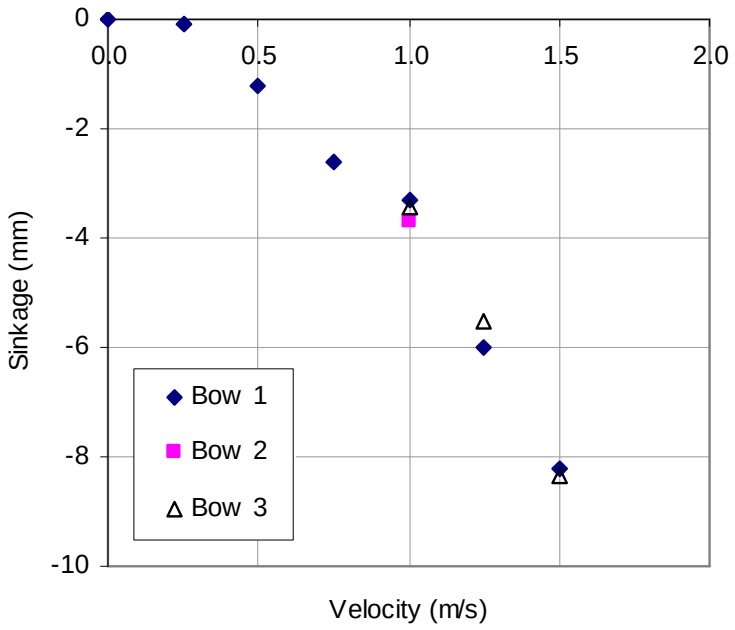

Figure 5.3.2 Sinkage of ship running in still water.

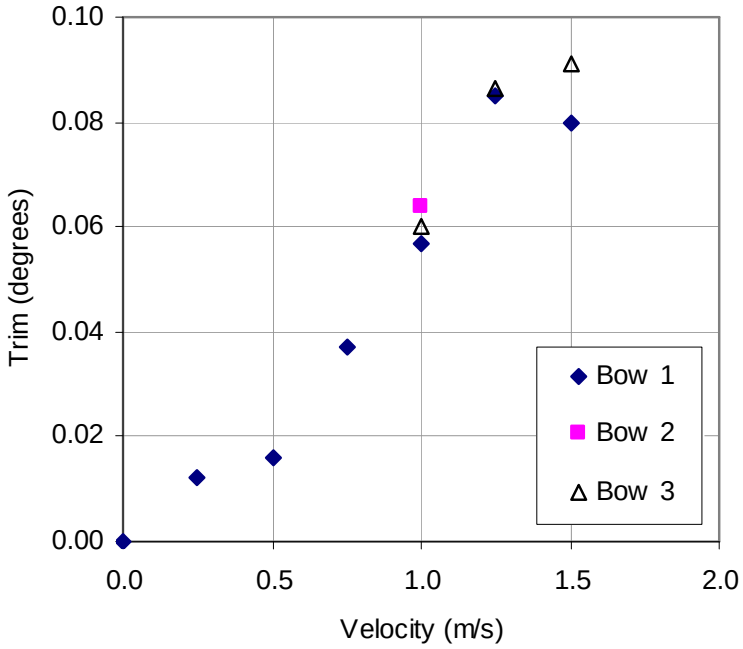

Figure 5.3.3 Trim of ship running in still water.

5.3.2 Ship motions in waves

Ship motions were measured by the LVDT's as described in section 4.9.4. Normally, green water is likely to take place when water surface exceeds freeboard. The ship experiences vigorous motions and this is usually the case in aggressive sea conditions. Many non-linearities are involved in such cases. They are associated with the local effects, bow geometry, etc. which are difficult to include in the prediction. High discrepancy between predicted data and experimental data for ship motions in hostile weather conditions, therefore, exist, causing the assessment of green water incident to become a genuine hardship.

Figures 5.3.4 to 5.3.9 compare the heave and pitch RAO's from experiments with predicted values using non-linear strip theory method by Crossland and Johnson (1998). It is noted that the strip-theory method actually predicted the motions in large-amplitude waves better than in smaller-amplitude waves. For wave heights

of 43mm and 57mm, which were equivalent to 3m and 4m at full scale, respectively, the strip theory over-predicted the pitch RAO's by up to 33 percent and the heave RAO's by up to 25 percent. At larger wave heights of 86mm and 114mm (6m and 8m at full scale, respectively), the over-prediction was only up to about 15 percent for heave and 20 percent for pitch RAO's.

It was noticed during the tests that green water was likely to happen in the (λ_e/L_{pp}) range of 0.4 to 0.6. Note that λ_e, defined as encountered wave length, was used for ease of relating relation between the distance that the ship travelled from one a wave peak to the next with the ship length. λ_e was calculated based on encountered frequency ω_e. It was the combination of steep waves and large motions that resulted in green water. At smaller wavelength, the wave steepness was larger but the ship motions were smaller resulting in a non-critical condition and hence no green water took place. At larger wavelength, the motion could be larger but the waves were less steep. As a result, green water might not occur.

5.3.3 Effects of green water on ship motions

The shipment of green water onto deck did affect the ship motions as indicated by Dillingham (1981) and Liut et al. (2002). With its mass and its dynamics, green water did create extra pressure on deck and this influenced the motions equations. This influence could clearly be seen in Figures 5.3.4 to 5.3.9. For most ship motion theory without green water on deck, linear theory is assumed in which the transfer functions or the RAO's were derived and used to find out the motion amplitudes based on the wave/wave slope amplitudes. According to this assumption, the RAO's do not change with the wave height; and in fact for smaller waves (H = 43mm and H = 57mm in Figures 5.3.4 to 5.3.9), the experimental data more or less verify this behaviour. However, at higher wave heights (H = 86mm and 114mm in Figures 5.3.4 to 5.3.9), when green water took place in the (λ_e/L_{pp}) range of 0.4 to 0.6, the motion amplitudes reduced considerably by more than 10 percent. This clearly implied that the mass of green

water did actually apply the loading on the deck, causing a compensating moment around the midship. Pitching moment was relieved to some extent as a result and this reduced the ship motions. Also, non-linear buoyancy due to above water hull form and non-linear damping in cases of excessive relative ship motions could play considerable part in this behaviour.

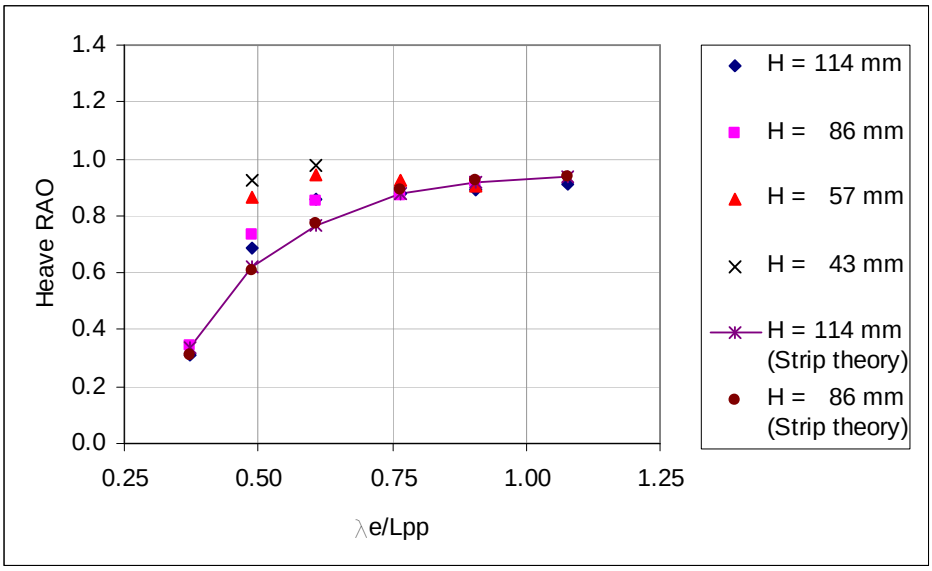

Figure 5.3.4 Heave RAO's of bow 1 at Fn = 0.20.

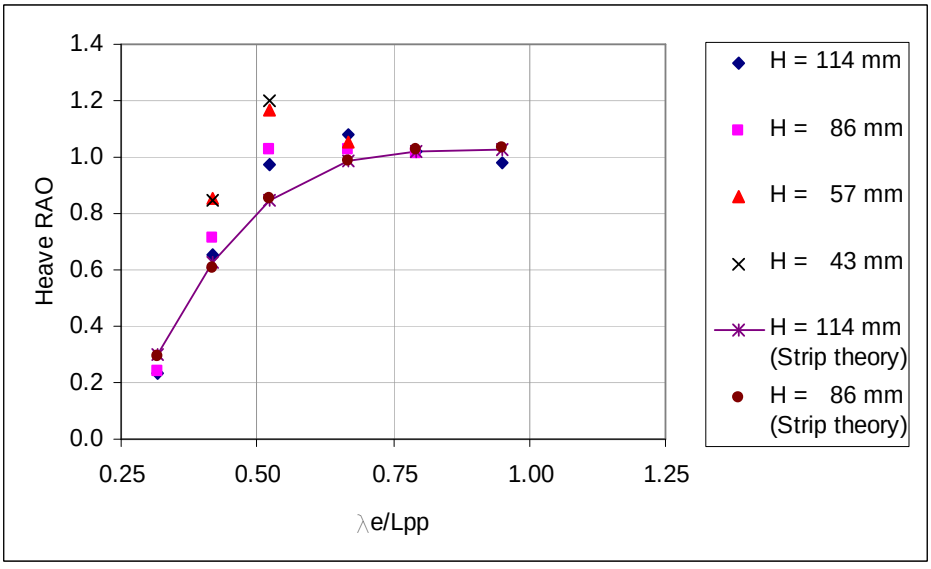

Figure 5.3.5 Heave RAO's of bow 1 at Fn = 0.25.

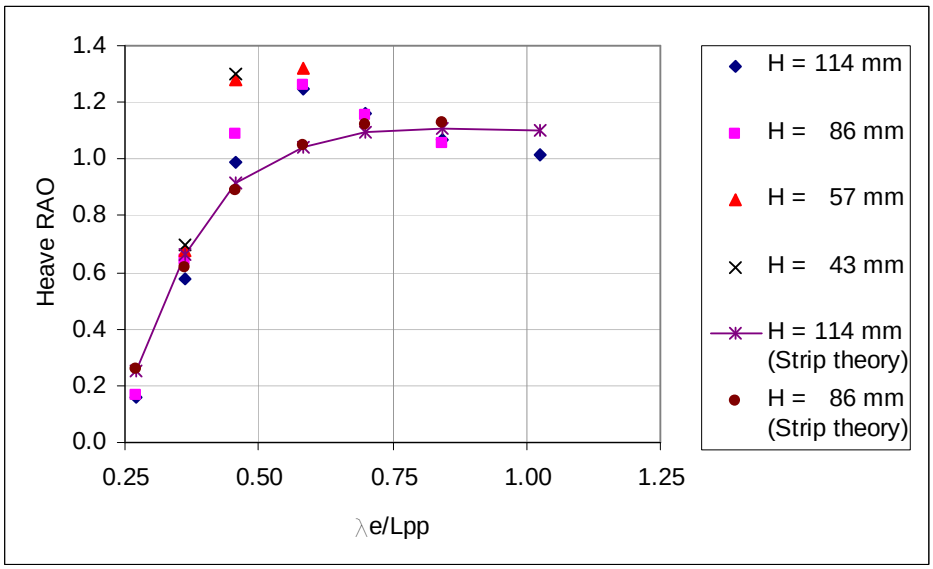

Figure 5.3.6 Heave RAO's of bow 1 at Fn = 0.30.

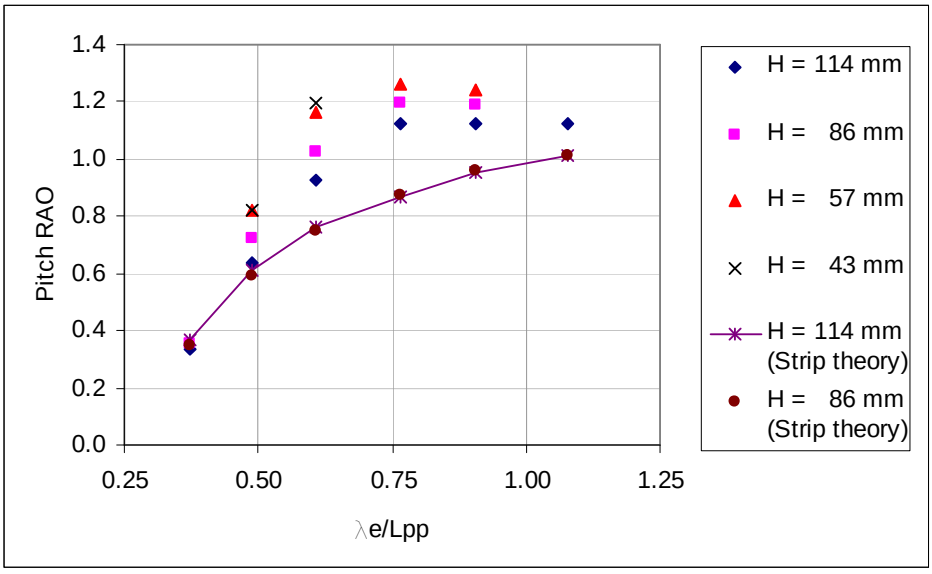

Figure 5.3.7 Pitch RAO's of bow 1 at Fn = 0.20.

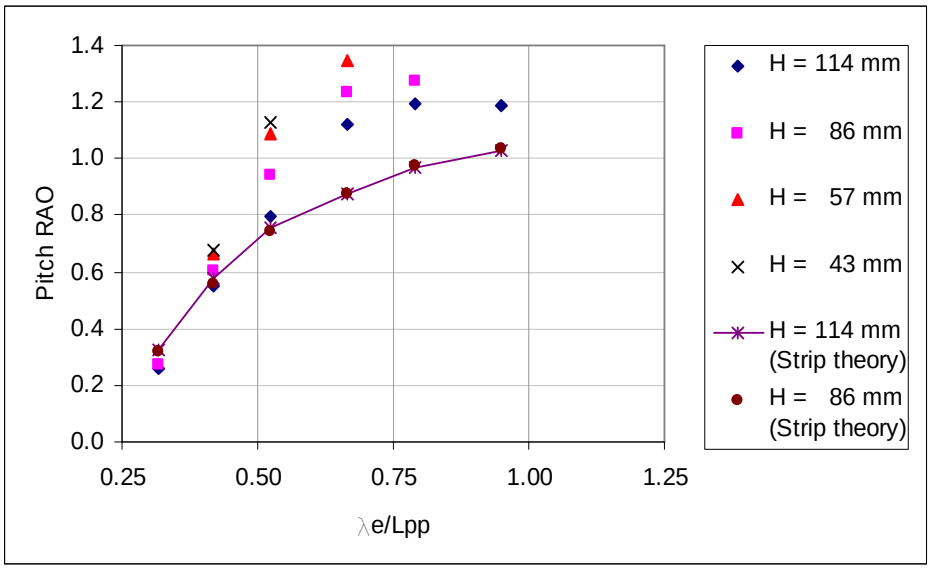

Figure 5.3.8 Pitch RAO's of bow 1 at Fn = 0.25.

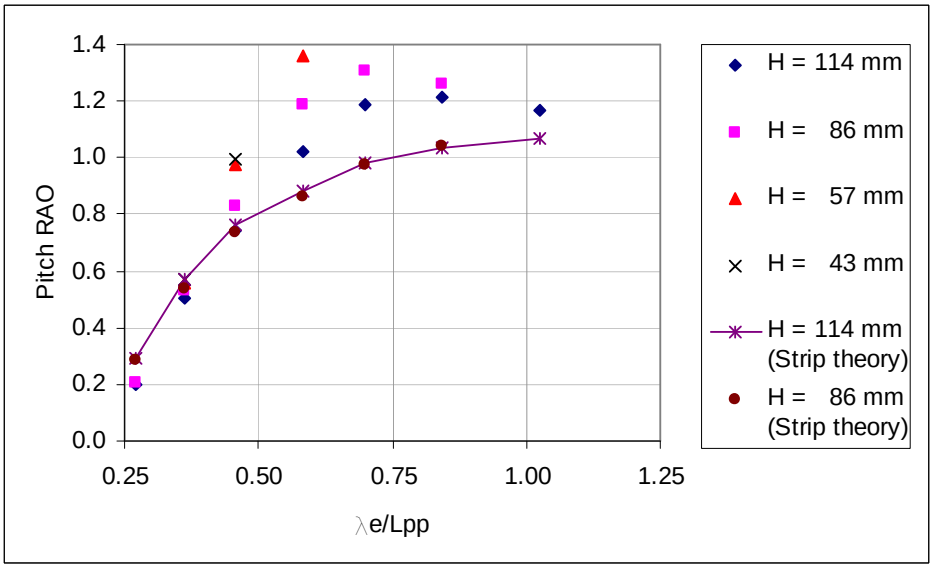

Figure 5.3.9 Pitch RAO's of bow 1 at Fn = 0.30.

5.4 Relative motions

As discussed before in Chapter 3, relative motions between main deck and free water surface are instrumental for occurrence of green water. Fundamental elements that contribute to these relative motions include ship motions, incident waves, bow waves and diffracting waves. The following Sections present the relative motions and its components.

5.4.1 Uncorrected relative motion

From the ship motions measured, the uncorrected or notional relative motions could be found by subtracting the ship motions by the elevation of undisturbed incident waves:

$$r = s - \zeta \tag{5.4.1}$$

where s represents the absolute motion response and ζ is the incident wave:

$$s = \eta_3 + x\eta_5 \tag{5.4.2}$$

η_3 = heave displacement
η_5 = pitch displacement
x = longitudinal distance forward of centre of gravity

The freeboard of the point where the relative motions need to be calculated is then added to equation (5.4.1) to find the relative motions between the free surface and the point of interest:

$$r = s - \zeta + FB \tag{5.4.3}$$

Equation (5.4.3) would give the relative motions between the location of interest and the free water surface if the incident wave were not disturbed. However, due to the presence of the ship, the incident wave does get affected by disturbances referred to as swell-ups in Chapters 2 and 3. The components of water swell-up around the ship include the bow wave, the lateral radiated wave as a result of the ship heaving and the longitudinal radiated wave at the bow due to ship pitching into the water.

Based on equations (5.4.2) and (5.4.3), notional relative motions could be derived from experimental data for various locations. Figures 5.4.1 shows exemplary results of the notional relative motion at the stem head in one of the test.

This notional relative motions was then combined with the swell-ups to get the corrected relative motions between the location of interest and the free water surface.

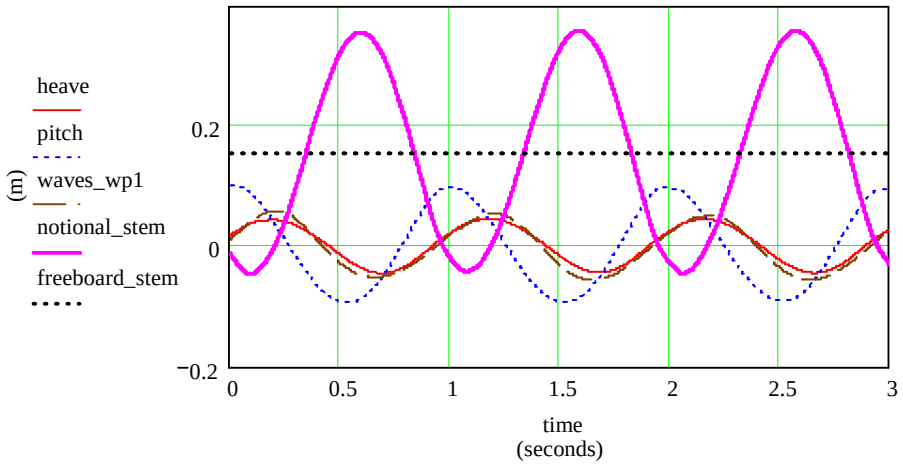

Figure 5.4.1 Notional relative motions between stem head and free water surface when ship travelled at Fn = 0.20 corresponding to regular full-scale waves of 8.0m height and 12.0s period.

5.4.2 Calm water bow wave

Figure 5.4.2 shows the bow wave heights at the locations of wave probe 1 and wave probe 2. Note that the bow wave should essentially be measured at the ship side surface. Experimentally, this was difficult due to the curvature at the ship side. If the wave probe was faired and attached right on the ship side surface, there will be a difficulty in converting the recorded values into the height of the bow wave because the curvature of the ship side is not mathematically known. The values in Figure 5.4.2, therefore, only give a qualitative expression of what a bow wave could have generated. These values should not be treated as the bow wave used in equation (3.2.5) for calculating the corrected relative motions between ship bow and free water surface.

Regarding Figure 5.4.2, since wave probe 1 was located at a distance (equivalent to the overhang) ahead of the front end of the wetted length, it was not affected by any hull-born disturbance to the free surface because the ship was travelling forward. Therefore, the measurements of the bow wave at this location were all zeros. However, at the front end of the wetted length, video tracking revealed that large bow wave was generated and this wave train progressed aft. The amplitude of this bow wave was proportional to velocity of the ship. Estimation via the chequered lines on the side of the ship bow indicated that the bow wave reached a height of approximately 40mm at Fn = 0.30.

Recordings by wave probe 2 at the starboard side of station 9 were the radiated bow wave as it was progressing away. As seen, at the beginning, the bow wave height at this location increased as the velocity increased. However, as the velocity reached 1.0m/s, bow wave height at this location dropped before it increased again. This behaviour should not be seen as the general behaviour of the bow wave since the wave probe was at a distance from the ship side surface (see Figure 5.4.3). As the velocity changed, not only did the amplitude of the bow

wave changed, the wavelength also changed. If wave probe 2 happened to be at the trough of this wave train, the measurement could be low as noticed.

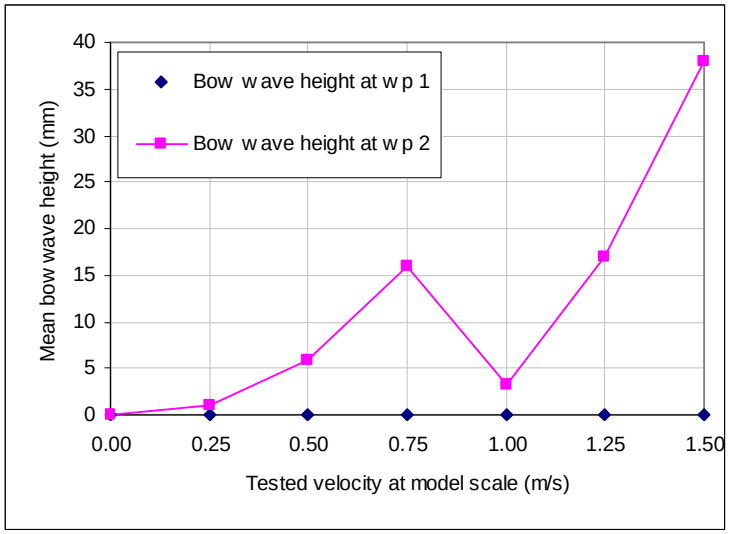

Figure 5.4.2 Bow wave recorded at wave probes 1 (stem head) and 2 (station 9).

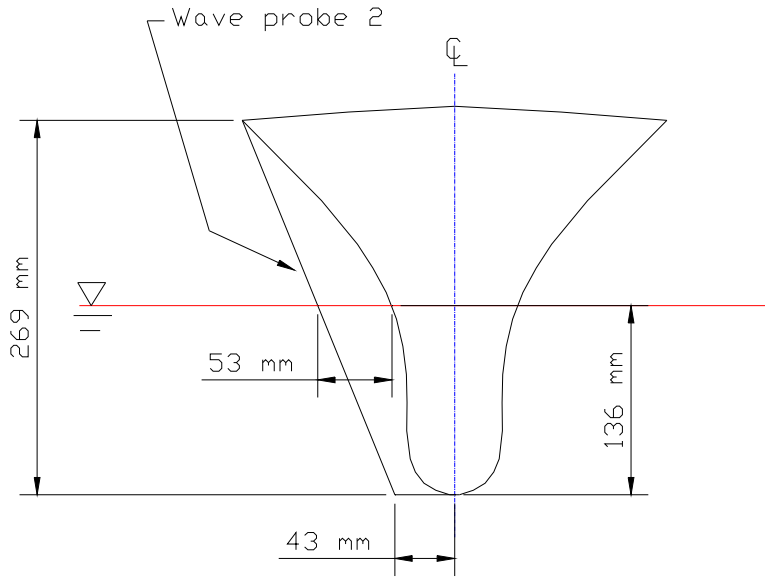

Figure 5.4.3 Relative position of wave probe 2 to ship surface at station 9.

5.4.3 Dynamic swell-up

Measuring of dynamic swell-up requires a fully dedicated experimental setup which is outside the scope of this research. However, from the recordings of relative motions by wave probes 1 and 2, the effects of dynamic swell-up could be interpreted to certain extent.

Blok and Huisman (1984) evaluated the relative wave motions around a frigate bow. Based on the earlier work by Tasai (1961), they presented a dynamic swell-up coefficient (SUC) for the relative wave motions calculated with linear strip theory:

$$r_S = SUC \times r_o \tag{5.4.4}$$

r_S is the relative wave motion including swell-up and r_0 is the relative wave motion as a result of heave, pitch and undisturbed incident wave. Using equation (5.4.4) as the basis, swell-up coefficients were calculated from the exact relative motions measured by wave probes 1 and 2 and the notional relative motions based on equations (5.4.1). These coefficients are plotted in Figures 5.4.4 to 5.4.9 for bow 1. Even though SUC's were also measured in the tests with bow 2 and bow3, the inclusion of all the data in this thesis proved to be too extensive. Within the scope of this research, comparison could only be made for key parameters. The main focus was on the developing a hydraulic model and modelling framework to simulate green water on deck.

Wave probe 1, as mentioned earlier, was located at a distance ahead of the front end of the wetted length. The disturbance due to bow wave and dynamic swell-up due to the pitching motion was relatively small. Since the ship was moving at forward velocities, the radiated wave train due to the ship bow pitching into the water was even less likely to catch up with wave probe 1. The swell-up coefficient at this location should, therefore, essentially be close to unity (Figures 5.4.4 to

5.4.6) and the corrected relative motions were virtually fully dominated by the notion relative motions at the location.

It should be noted that after green water was shipped onto deck, it would start to drain away off the deck due to deck camber and the pitching motion which led to deck sloping. Wave probe 2 was located at the starboard side of station 9 and it was standing in the way of green water that drained away. As this happened, wave probe 2 would give the signal as if the deck had been exceeded at this location. There were, of course, cases when the deck at wave probe 2 was really exceeded. However, it is really difficult to distinguish the two events. Relative motion and swell-up coefficient at wave probe 2 were therefore only derived for the cases when green water did not take place.

As discussed earlier in Section 5.4.2, depending on the velocity, the bow waves at wave probe 2 could be anything between a crest and a trough. The swell-up coefficients measured at wave probe 2 might, therefore, not be the maximum swell-up that could have been.

Figures 5.4.7 to 5.4.9 show that the swell-up coefficients fluctuated considerably about the mean values. There was not any obvious difference between the mean values between different velocities. If plotted together, the mean value for swell-up coefficient for three velocities tested was approximately 1.81 and the standard deviation was 21.84 percent. This strongly indicated that swell-up significantly contributed to relative motions and it was highly sensitive to the encountered frequency.

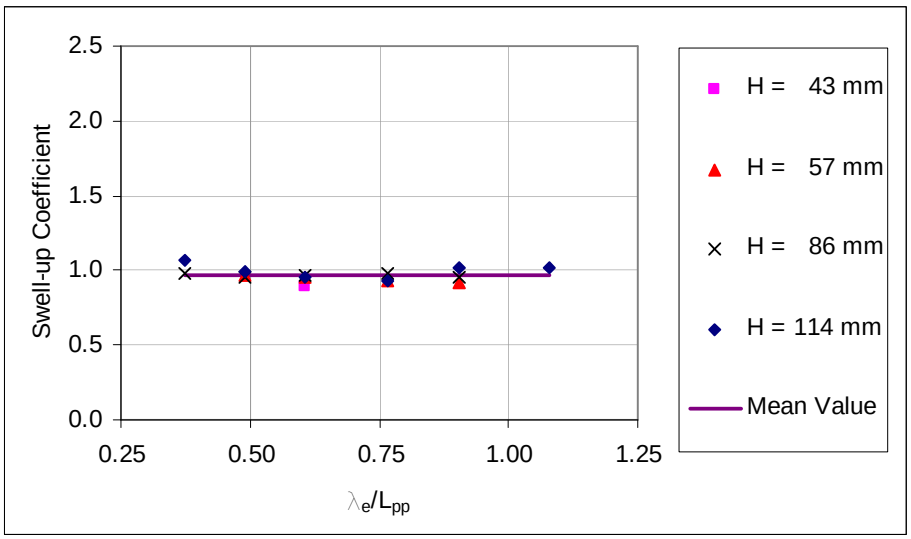

Figure 5.4.4 Swell-up measured by wave probe 1 (stem head) at test velocity equivalent to Fn = 0.20.

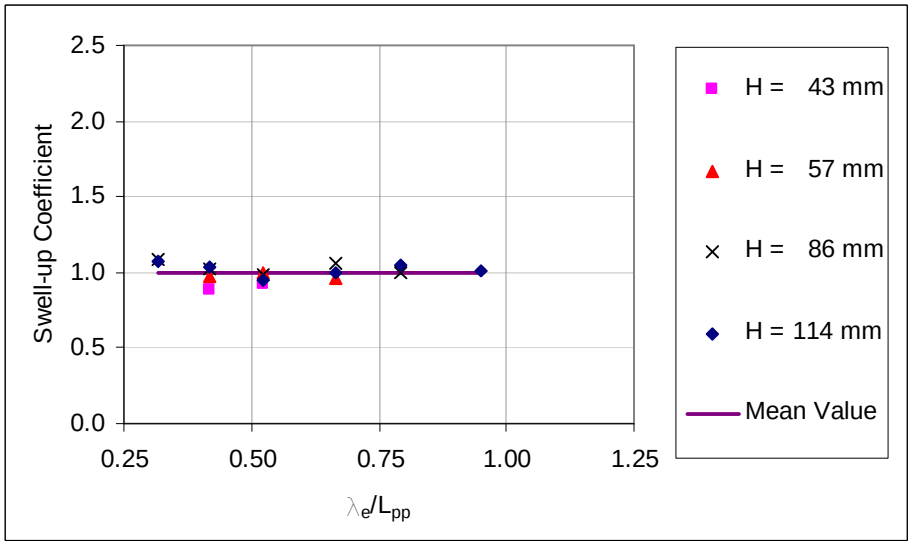

Figure 5.4.5 Swell-up measured by wave probe 1 (stem head) at test velocity equivalent to Fn = 0.25.

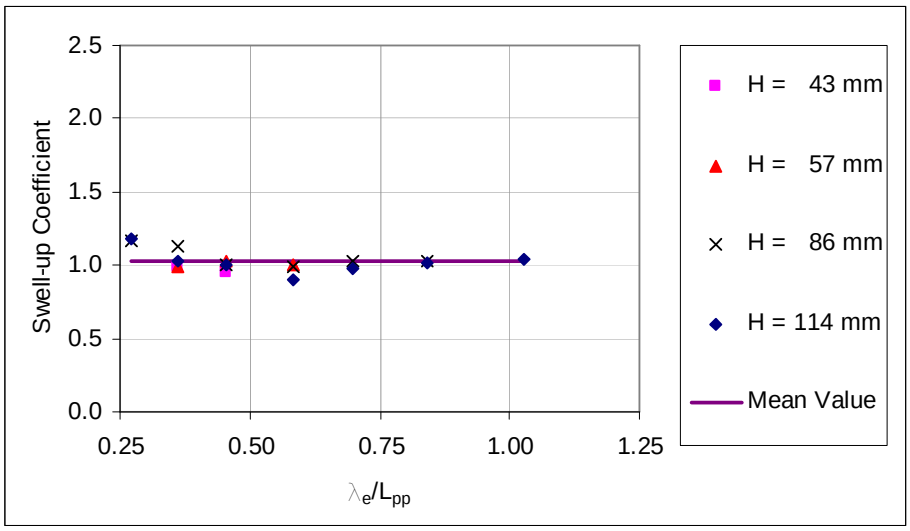

Figure 5.4.6 Swell-up measured by wave probe 1 (stem head) at test velocity equivalent to Fn = 0.30.

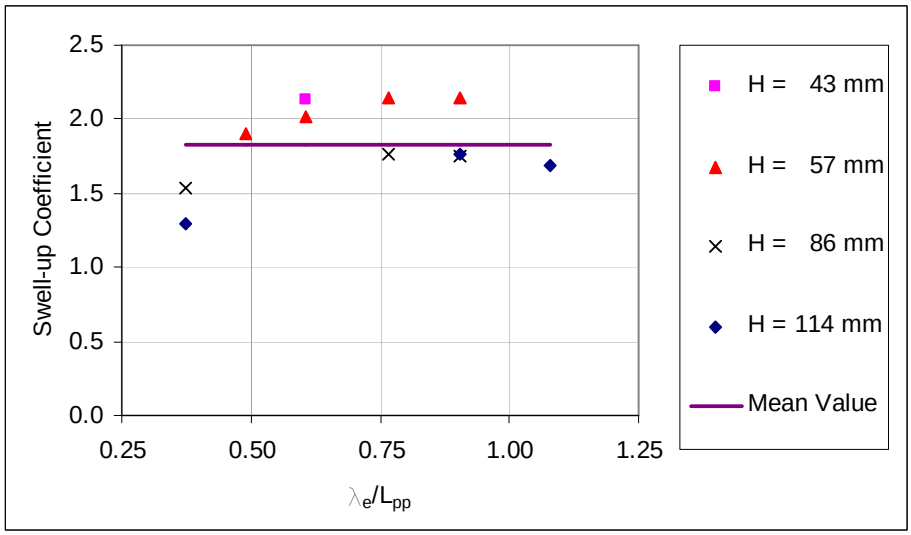

Figure 5.4.7 Swell-up measured by wave probe 2 (station 9) at test velocity equivalent to Fn = 0.20.

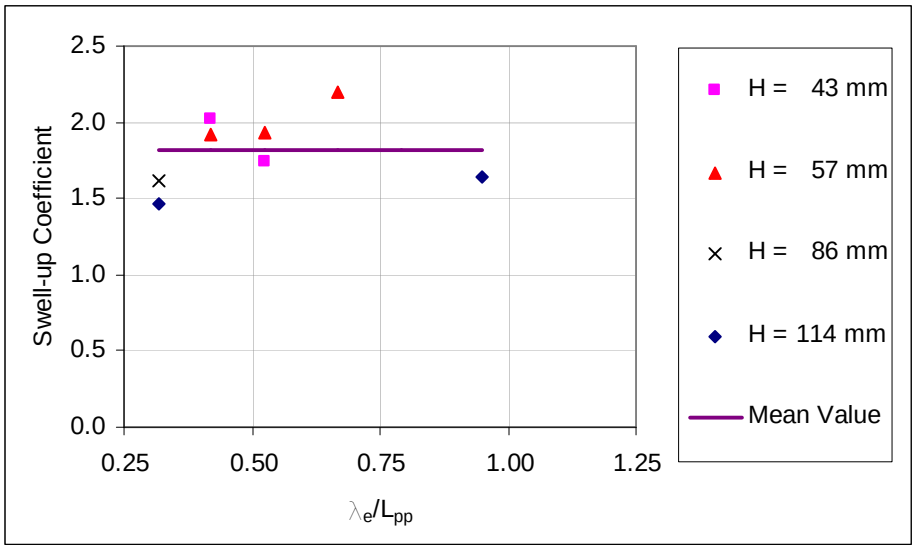

Figure 5.4.8 Swell-up measured by wave probe 2 (station 9) at test velocity equivalent to Fn = 0.25.

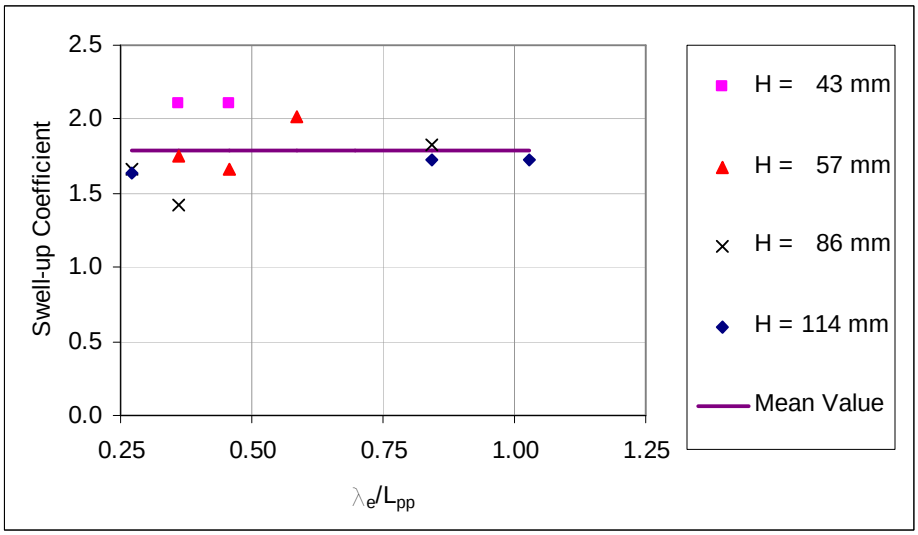

Figure 5.4.9 Swell-up measured by wave probe 2 (station 9) at test velocity equivalent to Fn = 0.30.

5.4.4 Corrected relative motions

As explained in Section 3.2.2 of Chapter 3, the corrected elevation of disturbed wave is the synthesis of the incident wave and disturbance factors, i.e. bow wave and swell-ups (see equation (3.2.5)). Subtracting this from the absolute motion of the ship will give the corrected relative motions between the bow and free water surface (see equation (3.2.13)). Figure 5.4.10 shows the waves, notional relative motion and corrected relative motion of the stem head with respect to water surface. The freeboard of the stem head in still water was also plotted. The flat peaks in the corrected relative motion curve corresponded to keel emergence events when the whole wave probe 1 was out of the water and the signals were cut off. Free board exceedance was also noticed as the curve goes below zero, which means that the stem head went below the free water surface.

Figures 5.4.11 and 5.4.12 show the corrected relative motions of the water surface with respect to the stem head and deck at station 9, respectively. The conditions were the same as in Figure 5.4.10. Freeboard can be seen exceeded by water surface at both locations. By expanding the curve for a close-up view, it could be noticed that at the stem head, there was a sharp rise of water elevation prior to freeboard exceedance. This could be due to the swell-up of local water. At that time, wave probe 1 was closest to the stem and the swell-up could be picked up. At station 9, freeboard was also exceeded and this was followed by the draining of green water off the deck at this location. It explained the broad peaks in the curves.

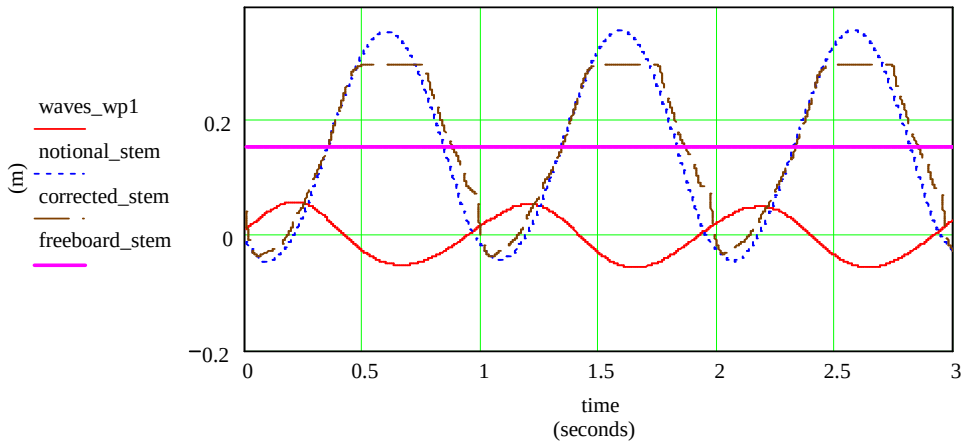

Figure 5.4.10 Notional and corrected relative motions between stem head and free water surface when ship travelled at Fn = 0.20, and equivalent regular full-scale waves of 8.0m height and 12.0s period.

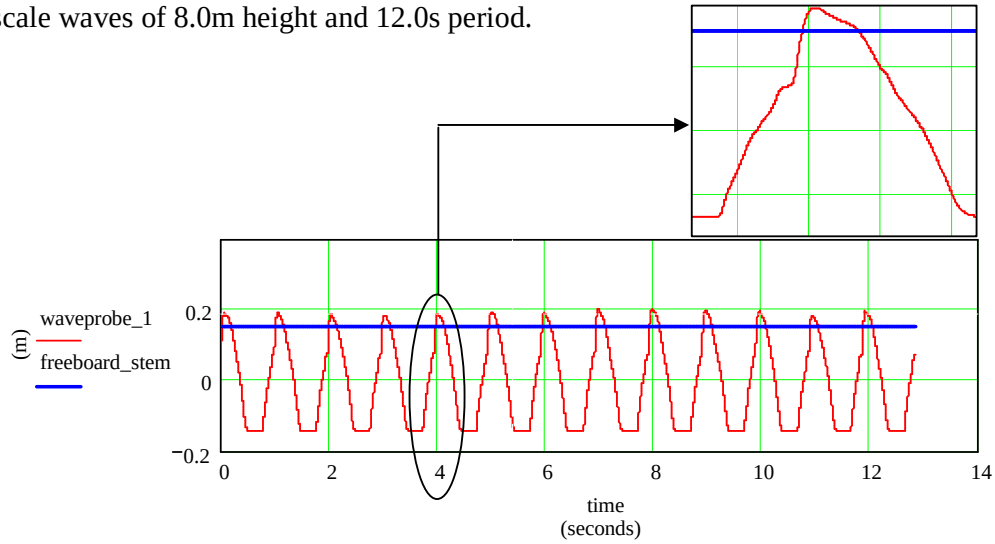

Figure 5.4.11 Relative motion at stem head.

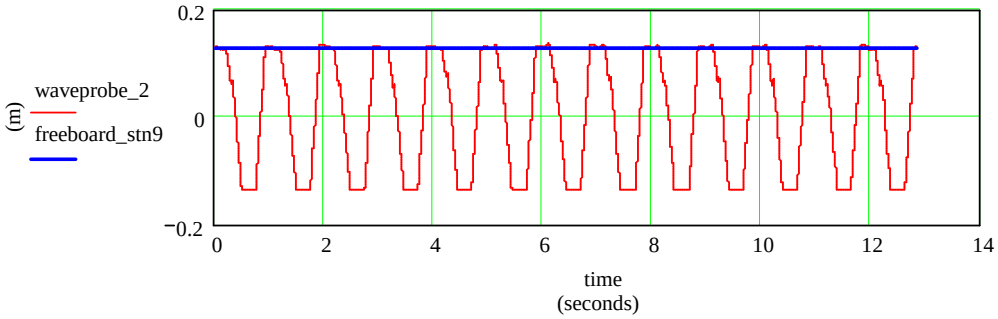

Figure 5.4.12 Relative motion at station 9 on starboard side.

5.4.5 Relative motions and green water occurrence

When relative motions between any point on the deck and free water surface are large, water is likely to enter the deck. In the experiments, the easiest way to detect a green water event was by observing the recordings of wave probes located in the deck area (WP3 to WP10 in Figure 4.5.4 or Figure 4.9.9). In this research, wave probes 3 and 4 were used for detecting green water events because they were closest to the stem head and the signals were, therefore, clearest. Sample results are as in Figure 5.4.13.

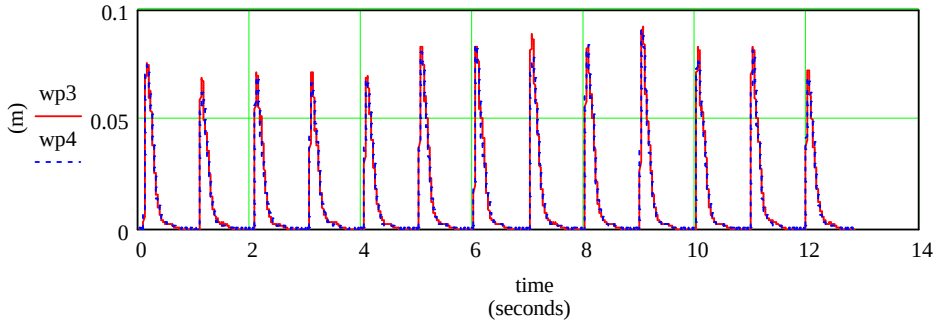

Figure 5.4.13 Recordings of wave probes 3 and 4 from which green water could be detected when ship travelled at Fn = 0.20 in regular waves of equivalent height of 8.0m and period of 12.0s at full scale.

Combining Figure 5.4.11 with Figure 5.4.13, it was clear that in this situation, green water took place every time freeboard at the stem head was exceeded. However, it was interesting to notice during the experiments that in some conditions, water did not actually exceed the deck at the stem head but green water did take place. Figures 5.4.14 and 5.4.15 show one such example. The stem head was not exceeded by water (Figure 5.4.14) but green water was definitely recorded by wave probes 3 and 4. The average height of green water was approximately 3mm which indicated a very small quantity of green water. Tracing the video monitoring, it appeared that green water took place in the first type as described in Section 4.9.6. When pitching into the upcoming waves, water ran up and was shed upwards off both sides of the bow. Wave probe 1 did not pick up

this water run-up since the water was not passing the stem head. However, the water that was shed off the sides of the bow landed back on the forecastle deck due to the forward velocity of the ship and resulted in a green water event Hence, it was the combination of water run-up at the bow and the forward velocity of the ship that led to the occurrence of green water in this situation.

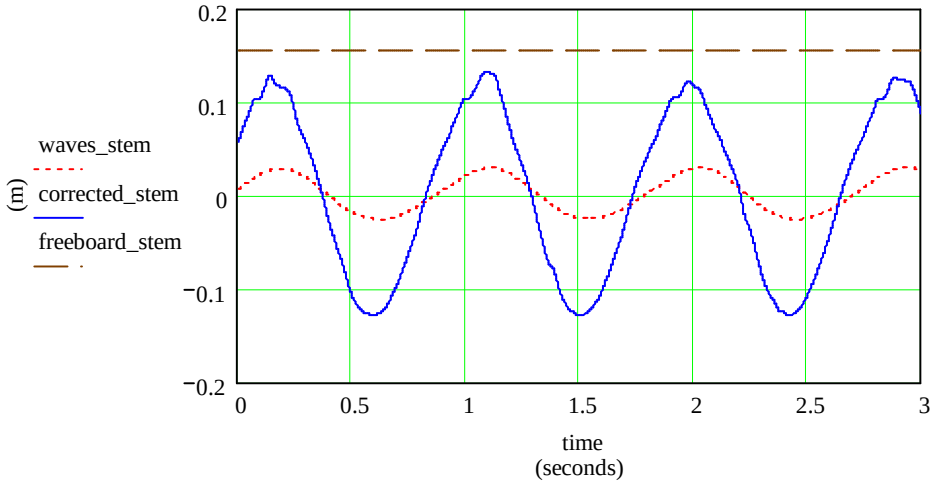

Figure 5.4.14 Free surface as recorded by wave probe 1 in comparison to free board at stem head when ship travelled at Fn = 0.25 in regular waves of equivalent height of 4.0m and period of 12.0s at full scale.

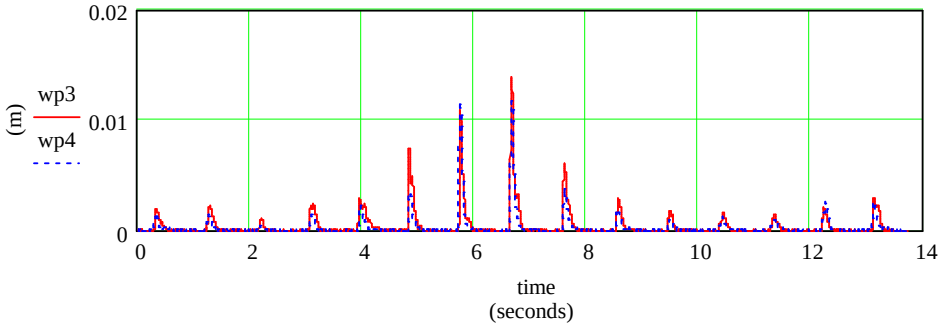

Figure 5.4.15 Recordings of wave probes 3 and 4 when ship travelled at Fn = 0.25 in regular waves of equivalent height of 4.0m and period of 12.0s at full scale.

5.4.6 Relative motions and keel slamming occurrence

Bottom slamming can take place when the relative motion is large and the keel emerges, out of the water. Slamming could be seen in Figures 5.4.11 and 5.4.12 at the time the troughs of the corrected relative motions went flat. The water surface at these times went below the keel, and hence, out of the range of wave probes 1 and 2. The signals were therefore cut off. Slamming, however, is not the target in this research and no further investigation was carried out.

5.5 Relation between relative vertical velocity and relative longitudinal velocity between stem head and free water surface

Greco et al. (2005) stated that the type of flow was governed by the ratio between the relative vertical velocity and the relative longitudinal velocity between the bow and the water. If this ratio is large, a dam-break flow could be expected. When the relative vertical velocity was comparable to, or smaller than, the relative longitudinal velocity, the water might enter as a plunging breaker. The plunging breaker could create a cavity or air gap near the edge of the deck. At a later stage, when this cavity had collapsed, the flow had similarities to the dam-breaking flow Greco et al. (2007).

The relative vertical velocity was derived by taking the derivative of the relative vertical motion between the bow and the water surface with regard to time. Since stem head was usually where green water first took place, the relative motion at this location was used to derive the relative vertical velocity between bow and water. Correction for pitching was also made to get the vertical velocity component.

The relative longitudinal velocity between bow and water at the stem head was difficult to measure because of the disturbances in free surface around this location. Therefore, relative longitudinal velocity between bow and undisturbed

incident wave at the stem head was used for comparison. This velocity was equal to the addition of the ship's velocity and the horizontal particle velocity of undisturbed incident wave.

Figures 5.5.1 and 5.5.3 show sample results of relative vertical and longitudinal velocities (denoted by zvel and xvel, respectively) plotted alongside recorded relative motions of the stem head. When wave height was small and no green water took place (Figure 5.5.1), both velocities were relatively sinusoidal. Relative vertical velocity showed some slight dynamic behaviour at high frequency but it was small compared with overall variation. The ratio of relative vertical velocity to relative longitudinal velocity in this case was plotted in Figure 5.5.2. As seen, this ratio in small wave heights was less than one.

When wave height was large and green water took place (Figure 5.5.3), relative horizontal velocity remained relatively sinusoidal and was dominated by the velocity of the ship. Relative vertical velocity, however, showed considerable dynamic behaviour.

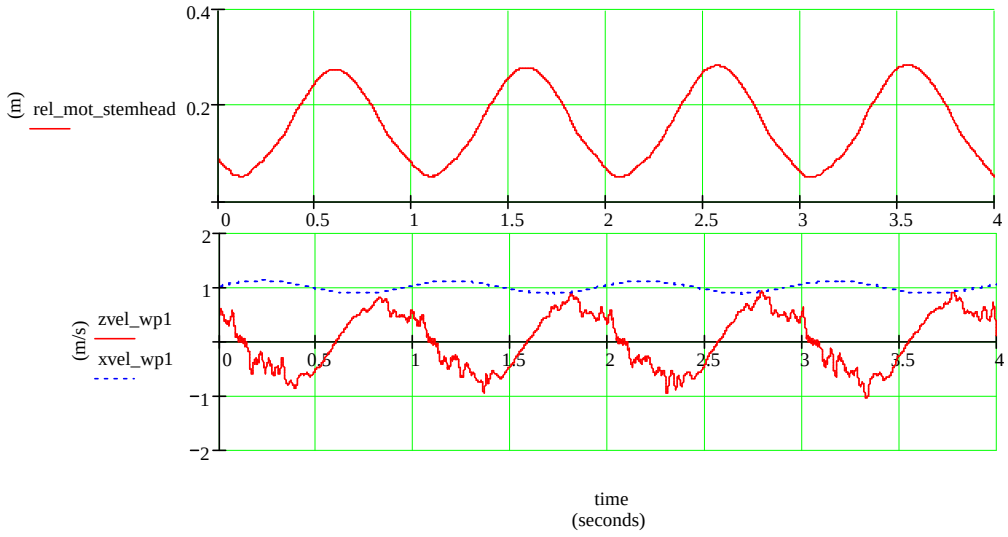

Figure 5.5.1 Relative vertical and longitudinal velocities along with relative motions recorded by wave probe 1 when ship travelled at Fn = 0.20 in regular waves of equivalent height of 4.0m and period of 12.0s at full-scale.

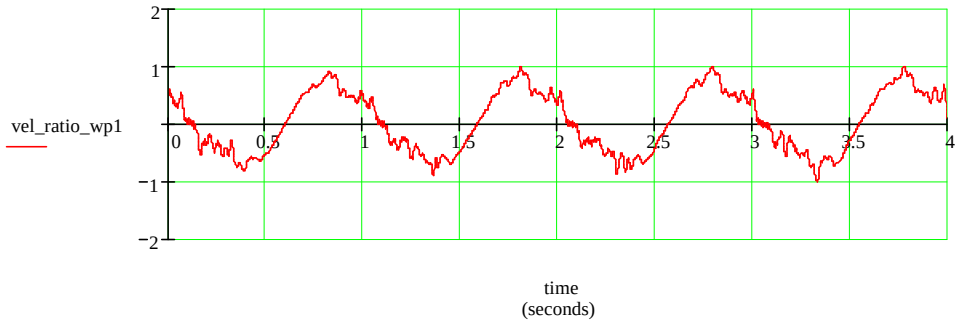

Figure 5.5.2 Ratio of relative vertical velocity to relative longitudinal velocity when ship travelled at Fn = 0.20 in regular waves of equivalent height of 4.0m and period of 12.0s at full-scale.

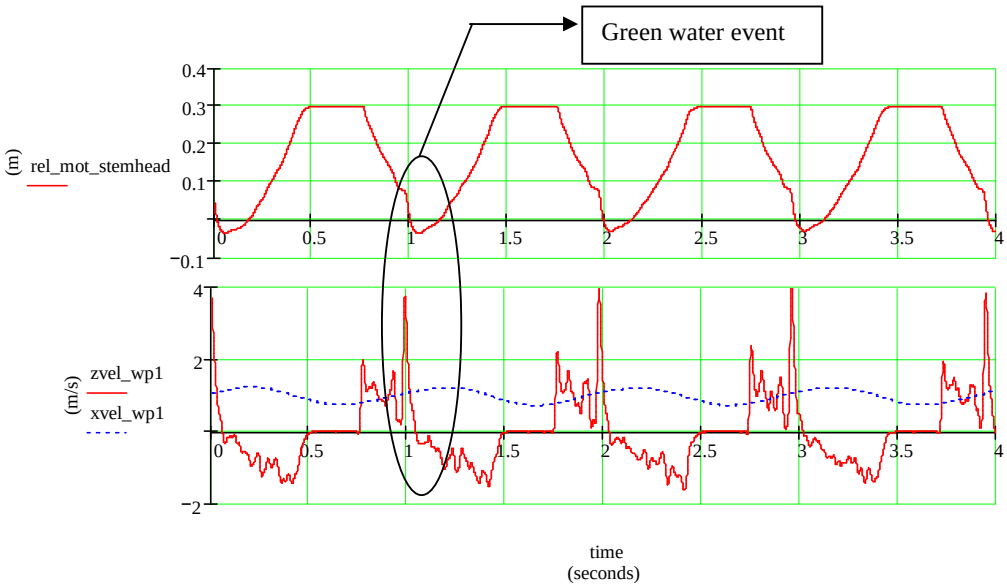

Figure 5.5.3 Relative vertical and longitudinal velocities along with relative motions recorded by wave probe 1 when ship travelled at Fn = 0.20 in regular waves of equivalent height of 8.0m and period of 12.0s at full-scale.

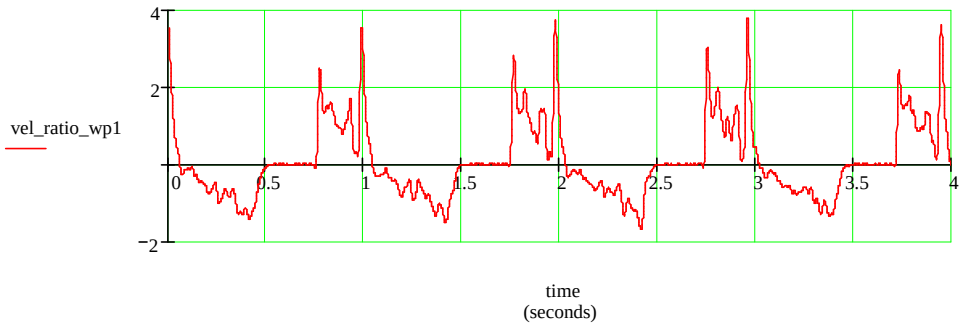

Figure 5.5.4 Ratio of relative vertical velocity to relative longitudinal velocity when ship travelled at Fn = 0.20 in regular waves of equivalent height of 8.0m and period of 12.0s at full-scale.

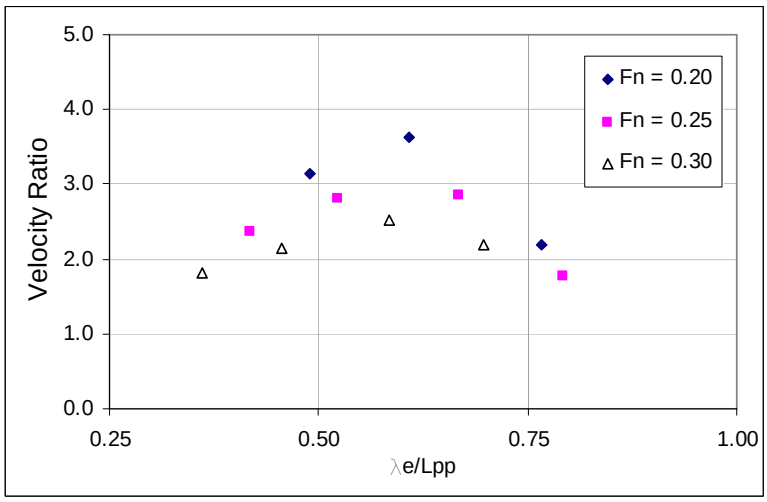

Figure 5.5.5 Maximum ratios of relative vertical velocity to relative longitudinal velocity when ship travelled in regular waves of equivalent height of 8.0m at full scale.

Before a green water event took place (Figure 5.5.3), the relative vertical velocity increased sharply over a short time, resulting in a high ratio (average at 3.62 times) between the two relative velocity components (Figure 5.5.4). According to Greco et al. (2005), green water in such case should be treated as a dam-break model. Figure 5.5.5 plotted the maximum ratios of relative vertical velocity to relative longitudinal velocity in the conditions when green water was shipped onto

deck as solid mass. Note that at higher velocities (Fn = 0.25 and 0.30), green water shipment became more severe but the ratios between the two relative velocities were smaller. In Section 5.3.3, it was discussed that green water mass on deck helped to reduce the motions of the ship. In other words, the vertical motions of the ship bow were subdued by green water on deck. This reduced the vertical velocity of the deck as the ship pitched out of the water. As a result, the relative vertical velocity reduced and so did the ratios in Figure 5.5.5. Figure 5.5.5 showed that the relative vertical velocity at the stem head was approximately 2.5 times higher than the relative longitudinal velocity. The flow characteristics, as reported by Greco et al. (2005), were dominated by the dam-break model.

5.6 Velocities of green water flow on forecastle deck

As described in Section 4.9.7, the longitudinal velocities of green water flow on forecastle deck could be approximated from the recordings of the two wave probes aligned along the deck.

Firstly, the entry velocity of green water was estimated based on the time lag between the recordings by wave probe 1 and wave probes 3 and 4. Note that wave probes 3 and 4 were not directly behind wave probe 1 along the centreline. Instead, they were symmetrically located on either side of wave probe 1. The average measurements of wave probes 3 and 4 was used as an approximation. The projected distance on x-axis between wave probe 1 and wave probes 3 and 4 was 70mm. Dividing this distance by the time lag gives the approximate entry velocity of green water.

Figure 5.6.1 plots the ratios between the magnitude of the absolute entry velocity (with respect to earth) and the ship velocity for various wave frequencies. Only occasions when solid mass of green water was shipped onto the deck were plotted in Figure 5.6.1. The wave height was therefore the largest and it was equivalent to 8.0m at full scale. In other occasions when green water took place in small

quantities, green water entered the deck in a different manner and this is discussed later. The mean value of the ratios in Figure 5.6.1 is 0.87 and the standard deviation is 14.3 percent. This indicates a fluctuation of the data. Nevertheless, the entry velocities were very close to the ship velocities. The fact that the average entry velocity was slightly smaller than the ship velocity implies that the water was pushed back when the ship pitched into the water. This was quite reasonable considering the large flare of the bow.

Likewise, the magnitude of the absolute translation velocity of green water flow on deck was also approximated via the time lag between the recordings by wave probe 6 and wave probe 9. As shown in Figure 4.9.9, wave probe 9 was directly behind wave probe 6 in the centreline. The velocity was obtained by dividing the distance between these two probes (77.5mm) by the time lag. It was then non-dimensionalised by the ship velocity and the result is plotted in Figure 5.6.2. The mean ratio is 1.24 and the standard deviation is 14.4 percent. The fact that green water was translating in the opposite direction to the ship at higher velocity really meant that if somebody stood on the deck, he would see the water come towards himself. Comparing Figure 5.6.2 with 5.6.1, it was observed that green water accelerated on deck after it had entered. This acceleration could be attributed to several factors. Firstly, green water entered the deck when the ship pitched deepest into the water. Then, the ship started to pitch out of the water and the deck would soon slope backwards. The green water, now on the deck, would therefore start to accelerate due to gravity:

$$a_{gravity} = g \times \sin(\eta_5) \tag{5.6.1}$$

Secondly, when translating along the deck, the height of green water also reduced (see Section 5.9). Part of the potential energy was transformed into kinetic energy and the velocity of the water flow increased.

For the cases such as in Figure 5.4.15 when green water took place in small quantity, similar technique could also be used to estimate the relative longitudinal velocity between green water and the ship. In practice, severe green water usually forces involuntary reduction of velocity. In doing so, the ship may get itself out of the aggressive encountered frequency range and hence, avoid the threat of severe green water.

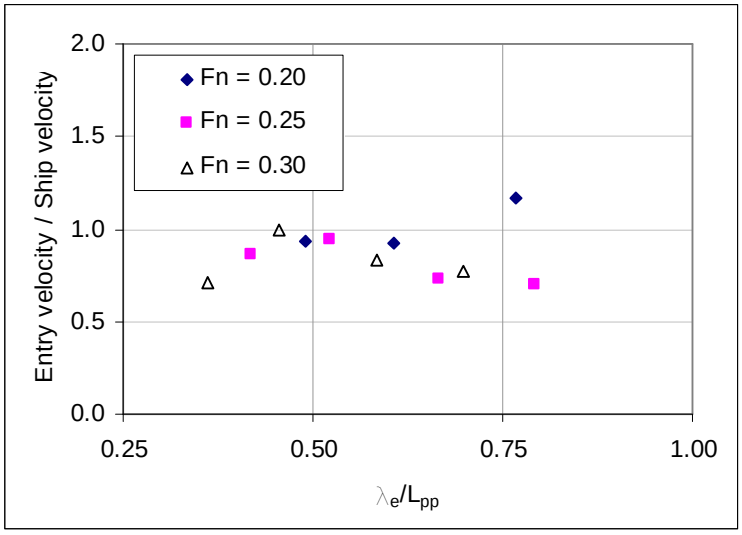

Figure 5.6.1 Entry velocities of green water flow into the deck area.

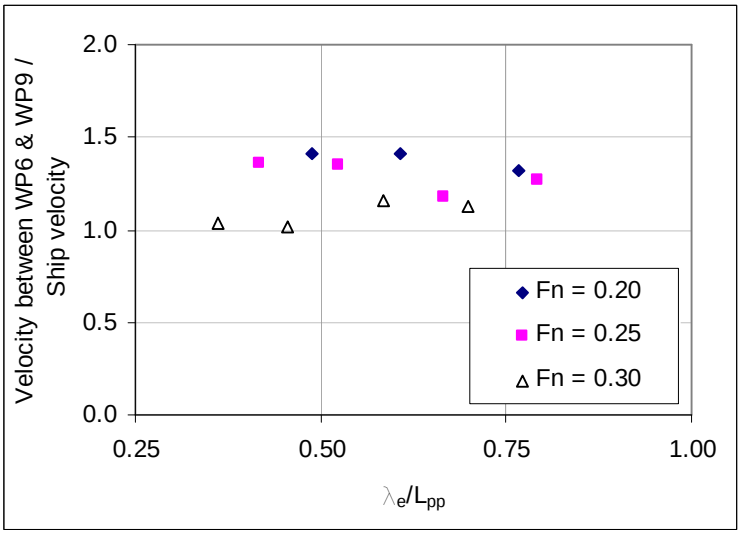

Figure 5.6.2 Translation velocity between wave probe 6 and wave probe 9.

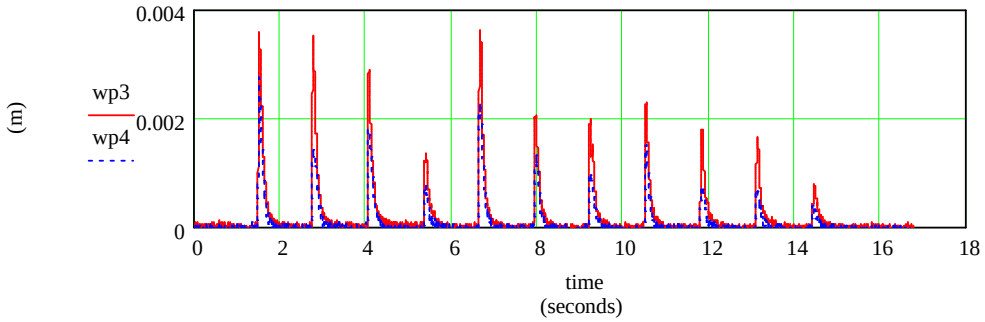

Figure 5.6.3 Recordings of wave probes 3 and 4 when ship travelled at Fn = 0.05 in regular waves of equivalent height of 8.0m and period of 12.0s at full scale.

Figure 5.6.3 shows the recordings of wave probes 3 and 4 when the ship model was travelling at 0.25m/s (equivalent to Fn = 0.05). Compared with Figure 5.4.13 when the ship model was running at 1.0m/s (Fn = 0.20), the average green water height was reduced by 75 percent from 77mm to 18mm.

5.7 Relation between freeboard exceedance and green water height on forecastle deck

In this Section, the relation between freeboard exceedance and green water height on forecastle deck is investigated. By subtracting the vertical relative motions measured at wave probe 1 by the freeboard at stem head, the freeboard exceedance was obtained. Note that there were cases when freeboard was not exceeded at the stem head but at a nearby location (see Section 5.4.5 and Figure 5.4.15). However, since the relative motion was only measured at the stem head in this research, comparison was made at this location accordingly. For more detailed investigation in this regard, more wave probes are suggested to be mounted around the front area of the forecastle deck.

Green water heights on forecastle deck were taken directly from the wave probes located at the centreline of the ship. At the forward perpendicular location (Figure 4.9.9) where there was no wave probe located at the centreline, the mean value of wave probes 3 and 4 was taken for comparison.

Buchner (2002) analysed the test data with FPSO models and concluded that the relation between the free board exceedance at bow centreline and water height on deck was almost linear,

$$H_{GW} = a_0 \times FBE \tag{5.7.1}$$

where H_{GW} represents green water elevation on deck and FBE represents free board exceedance at bow centreline or stem head. Coefficient a_0 was determined with least square fit through the measurement points in regular waves (Buchner, 2002). Note should be taken that for FPSO, green water tests were carried out without any forward velocity. The interaction between ship hull and waves were therefore less severe. The shipment of water onto deck, as a result, could be more random and scattering in nature.

Figures 5.7.1 to 5.7.9 shows the variation of the average green water heights on deck measured by wave probes along the ship centreline with the freeboard exceedance at stem head. It could be seen that overall, the relation between green water height on deck and freeboard exceedance was relatively linear and took the form of:

$$H_{GW} = a_0 \times FBE + b_0 \tag{5.7.2}$$

where both values of a_0 and b_0 are positive and are as in Table 5.7.1. The interesting point noticed for all the cases was that green water could take place when freeboard at stem head was not exceeded at all. This was contrast to Equation (5.7.1) by Buchner (2002) which implied that for the stationary ship like

FPSO, green water only took place when the freeboard at stem head was exceeded. As described in section 5.4.5, green water events when stem head was not exceeded by water were usually caused by water running up the sides of the ship. Even though such green water events were of small quantity, they did indicate that green water could take place when the freeboard was not essentially exceeded.

Figures 5.7.1 to 5.7.9 show that the linearity was clearest for wave probe 9. Data from wave probes 3/6 and 6 show more scattering patterns. This could be attributed to the presence of shed water mentioned in Section 4.9.6. Recall that collectively, green water on deck comprised of two components. The first component was the water that was shed off the deck edge and later caught up by the ship. The second component was the water that flushed onto the deck as the forecastle deck went below the water surface. The former was essentially similar to a splashing of water. It was normally small in quantity and was, therefore, more random in nature. Wave probes 3/4 and 6 were closer to the stem so they were more likely to catch this water splash. Their recordings were, as a result, more influenced by this random water. At lower velocity, the interaction between ship and water was less severe and so was this water splash. The water height on deck was more dominated by the influx of solid mass of green water and its relation with the freeboard exceedance became more linear (compare Figure 5.7.4 with Figures 5.7.5 and 5.7.6 for wave probe 6).

At furthest back, wave probe 9 was least influenced by this water splash and therefore its recordings were much less scattering. A methodology to determine the coefficients a_0 and b_0 in equation (5.7.2) proved to be difficult since physically, they depended on many factors. These included bow shape, deck area, ship velocity, wave conditions, etc.

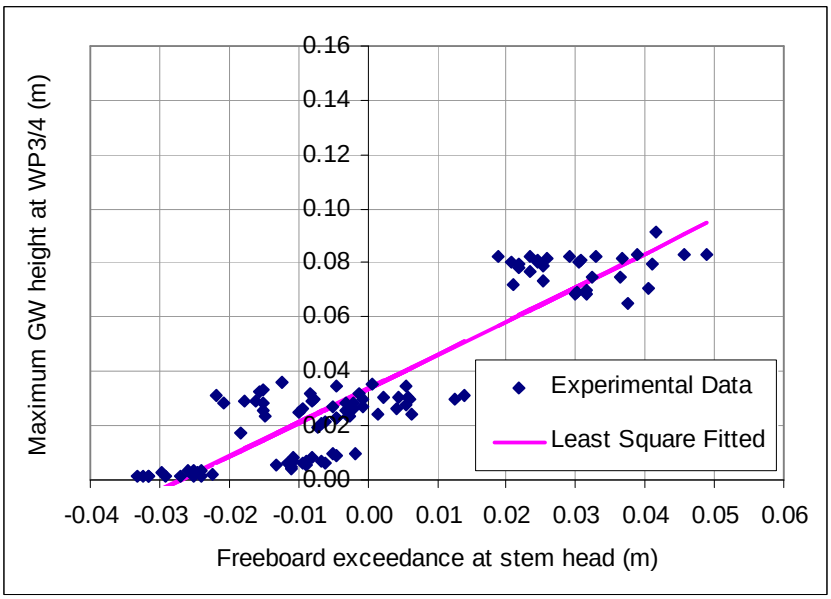

Figure 5.7.1 Relation between free board exceedance at stem head and maximum green water height at the wave probes 3 and 4 when ship travelled at velocity equivalent to Fn = 0.20.

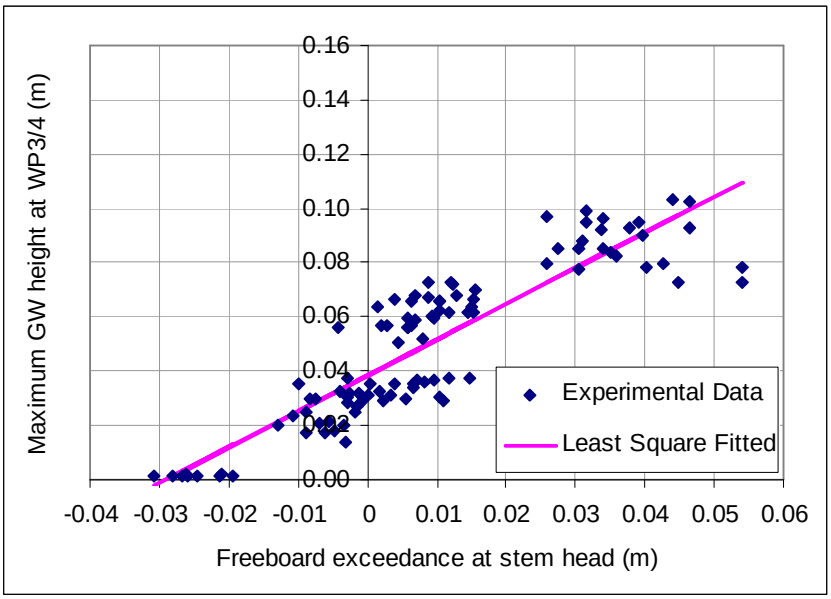

Figure 5.7.2 Relation between free board exceedance at stem head and maximum green water height at the wave probes 3 and 4 when ship travelled at velocity equivalent to Fn = 0.25.

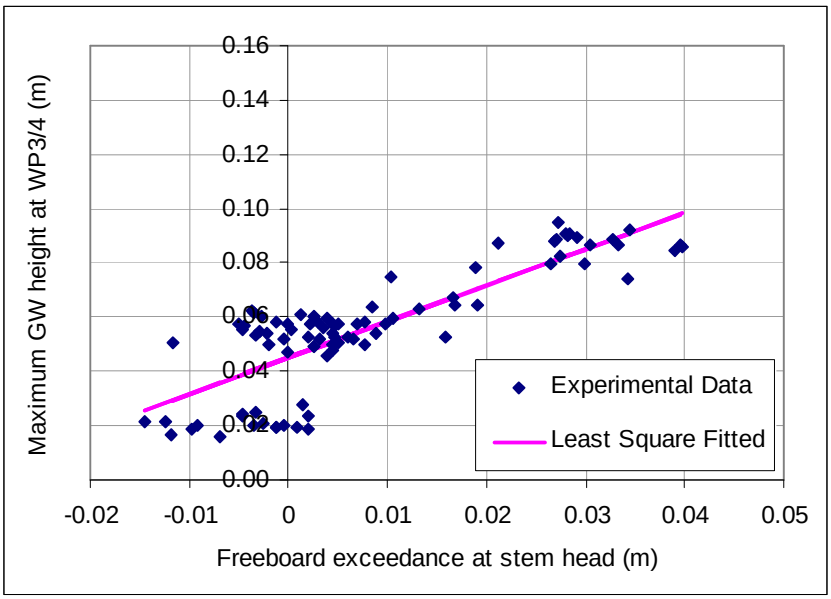

Figure 5.7.3 Relation between free board exceedance at stem head and maximum green water height at the wave probe 3/4 when ship travelled at velocity equivalent to Fn = 0.30.

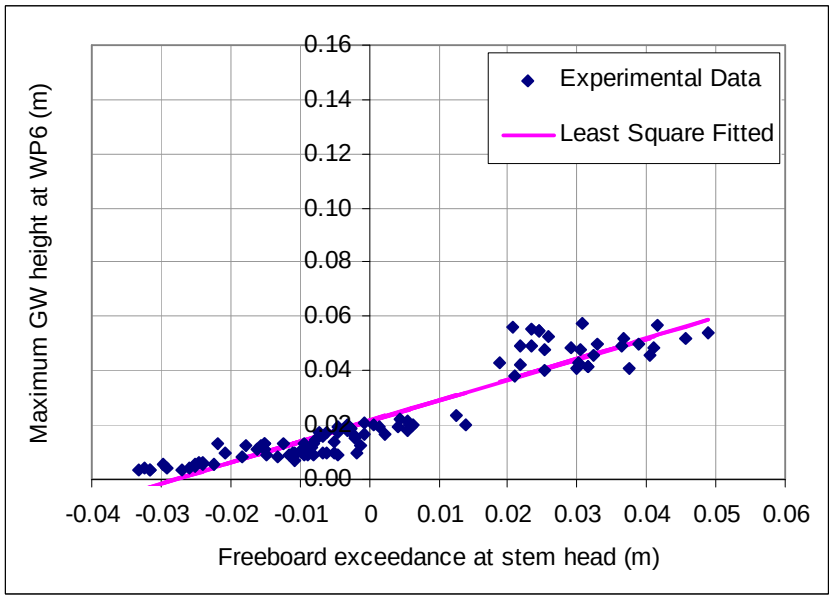

Figure 5.7.4 Relation between free board exceedance at stem head and maximum green water height at the wave probe 6 when ship travelled at velocity equivalent to Fn = 0.20.

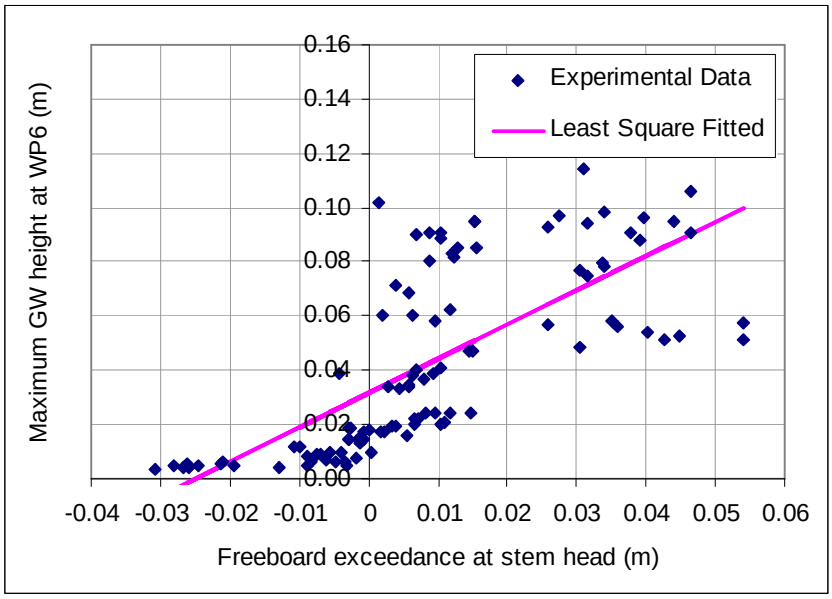

Figure 5.7.5 Relation between free board exceedance at stem head and maximum green water height at the wave probe 6 when ship travelled at velocity equivalent to Fn = 0.25.

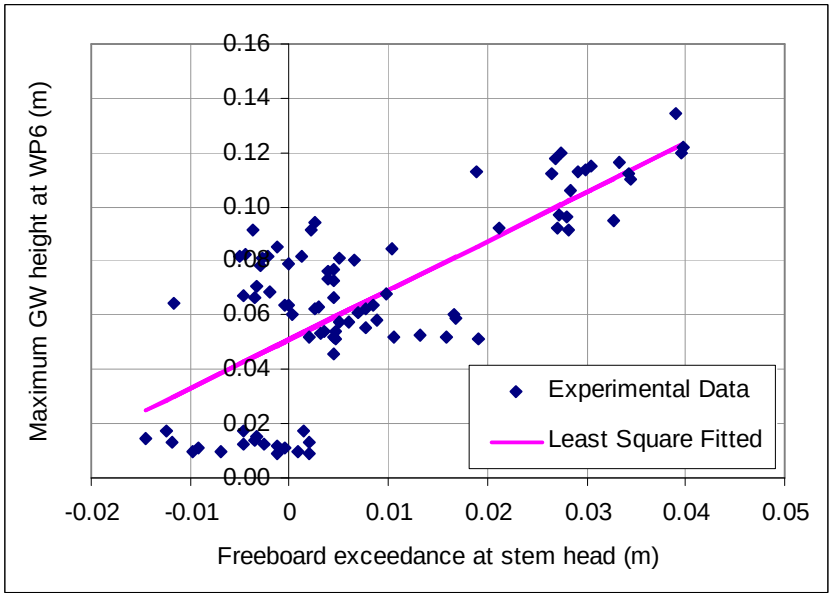

Figure 5.7.6 Relation between free board exceedance at stem head and maximum green water height at the wave probe 6 when ship travelled at velocity equivalent to Fn = 0.30.

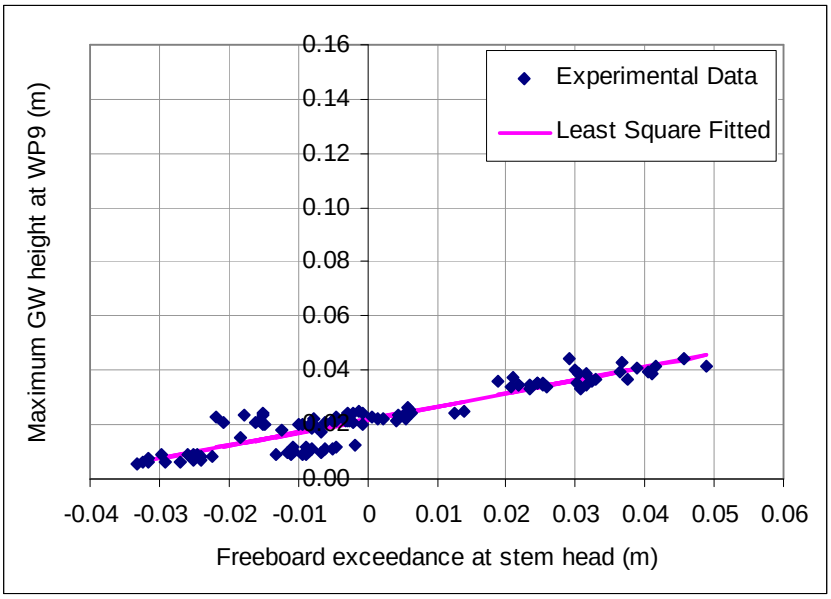

Figure 5.7.7 Relation between free board exceedance at stem head and maximum green water height at the wave probe 9 when ship travelled at velocity equivalent to Fn = 0.20.

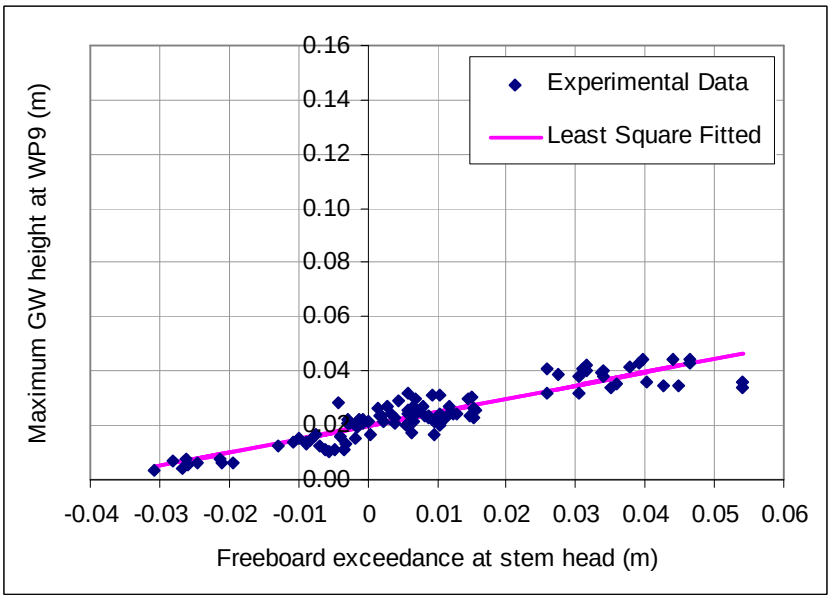

Figure 5.7.8 Relation between free board exceedance at stem head and maximum green water height at the wave probe 9 when ship travelled at velocity equivalent to Fn = 0.25.

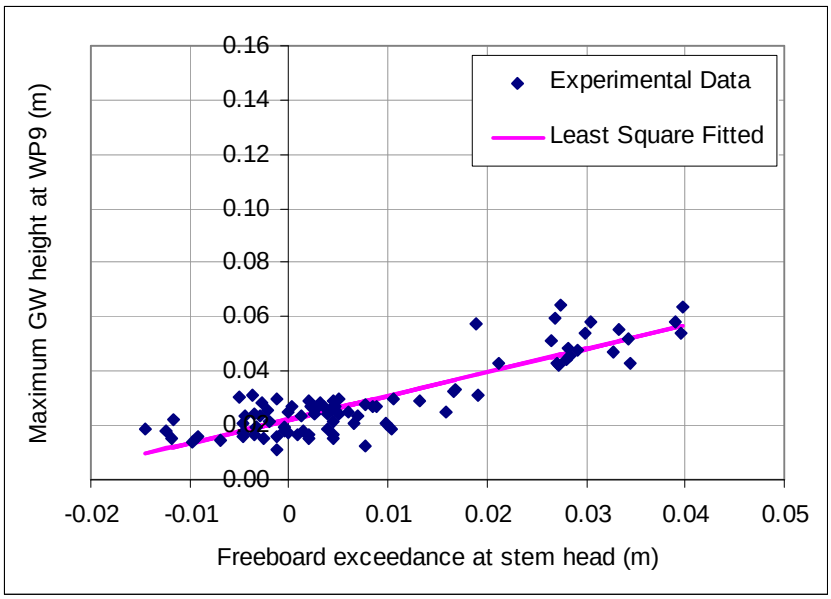

Figure 5.7.9 Relation between free board exceedance at stem head and maximum green water height at the wave probe 9 when ship travelled at velocity equivalent to Fn = 0.30.

Table 5.7.1 Polynomial coefficients of the least-square fitted lines.

	Fn = 0.20		**Fn = 0.25**		**Fn = 0.30**	
	a_0	b_0	a_0	b_0	a_0	b_0
WP3/4	1.2485	0.0335	1.3202	0.0384	0.04505	1.3316
WP6	0.7623	0.0214	1.2655	0.0316	1.8083	0.0511
WP9	0.4806	0.0219	0.4941	0.0198	0.0222	0.8691

5.8 Green water height at different locations on forecastle deck

Containership S175 has a relatively parabolic forecastle deck (Figure 5.8.1). When the bow pitched into the water, water started to enter the deck in the direction relatively normal to the deck edge. Having a transverse velocity component, water tended to head towards the centreline of the ship bow. This led to a concentration of green water along the centreline. In other words, along a line drawn athwart ship on the forecastle deck, green water height at the centreline would be larger than green water heights on either side. This trend was well reflected by experimental data.

Figures 5.8.2 and 5.8.3 present the ratios of the water heights measured by wave probes 5 and 7 to that by wave probe 6. Note that wave probes 5, 6 and 7 were located athwart ship with wave probe 6 at the centreline and wave probes 5 and 7 on the sides (Figure 4.9.9). As seen, in all the cases, these ratios were smaller than 1.0. This strongly indicated that there was a concentration of green water along the centreline of the deck. This is further consolidated by Figures 5.8.4 and 5.8.5 where the ratios of green water heights measured by wave probes 8 and 10 to that by wave probe 9 are presented.

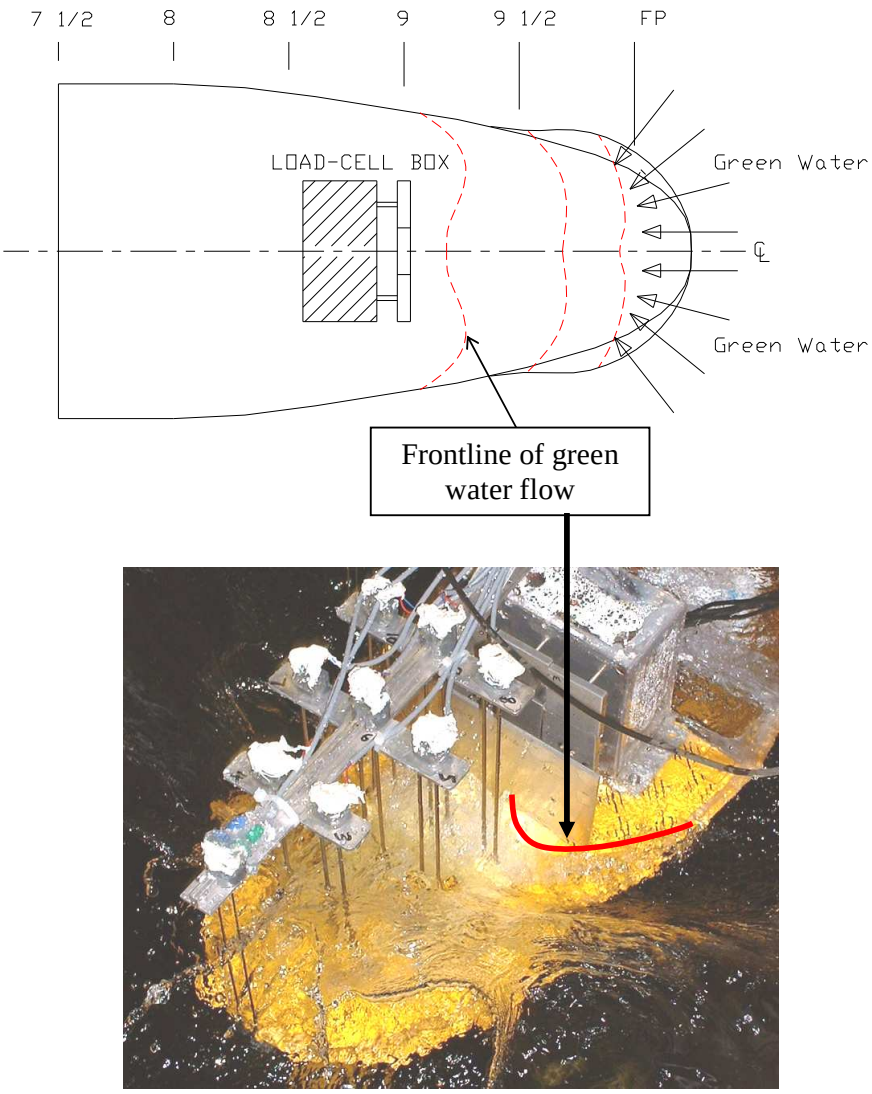

Figure 5.8.1 Approximate visualisation of intrusion direction of green water and shapes of frontlines of green water on forecastle deck.

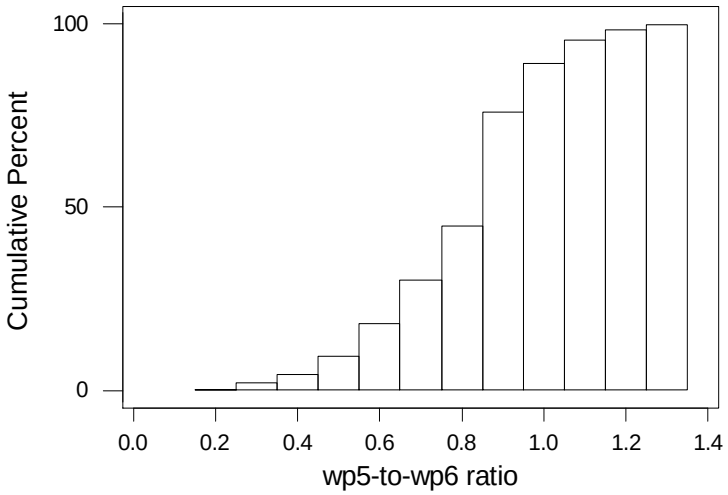

Figure 5.8.2 Ratios between maximum green water elevation measured by wave probe 5 and that by wave probe 6.

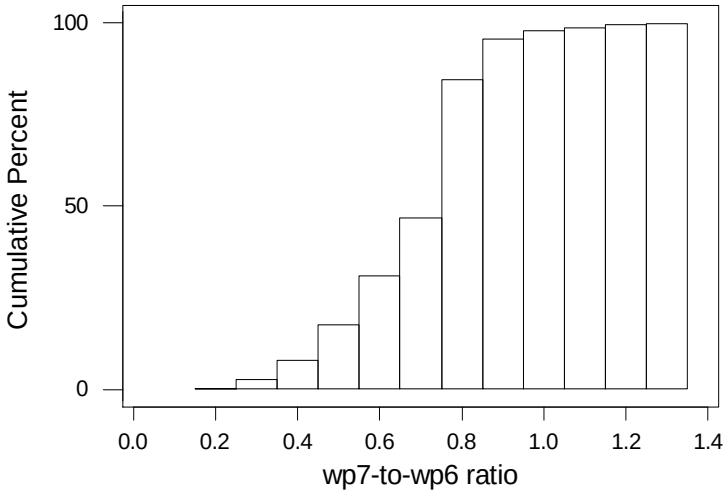

Figure 5.8.3 Ratios between maximum green water elevation measured by wave probe 7 and that by wave probe 6.

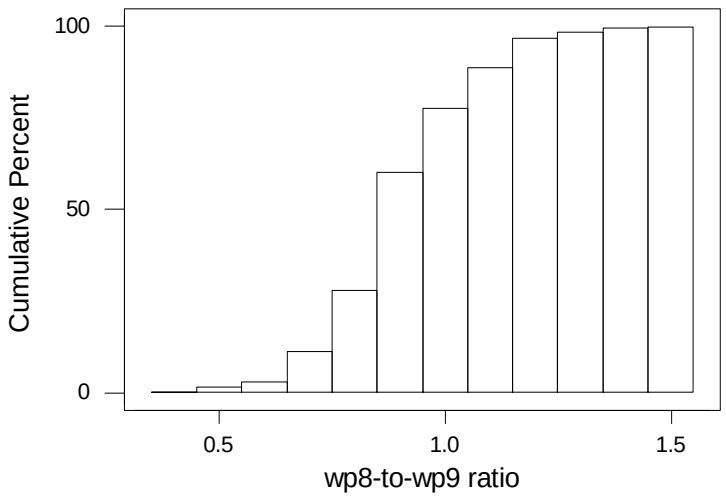

Figure 5.8.4 Ratios between maximum green water elevation measured by wave probe 8 and that by wave probe 9.

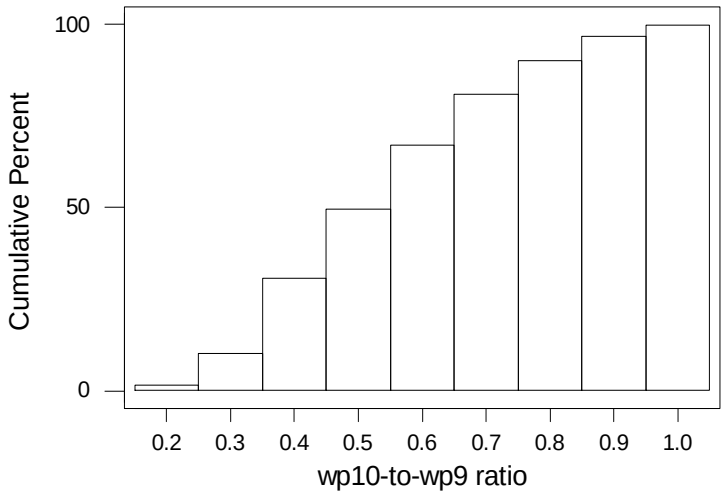

Figure 5.8.5 Ratios between maximum green water elevation measured by wave probe 10 and that by wave probe 9.

5.9 Longitudinal green water loading

Longitudinal green water loading can be referred to as the loading on vertical surfaces on deck. Before going further into the analysis of this parameter, it is noted that during the tests without breakwaters, the loads measured by load cells on the top row of the load cell box (load cells 1, 2 and 3) were smaller than the lower limit of the measuring range (see Section 4.5.5). The signals from these load cells were, therefore, dominated by the noise and were subsequently ignored. The analysis was therefore carried out only for the middle row and bottom row of load cells on the load cell box (i.e. load cells 4 to 9 in Figure 4.5.5). Figures 5.9.1 and 5.9.2 show examples of the longitudinal green water loads recorded by these load cells.

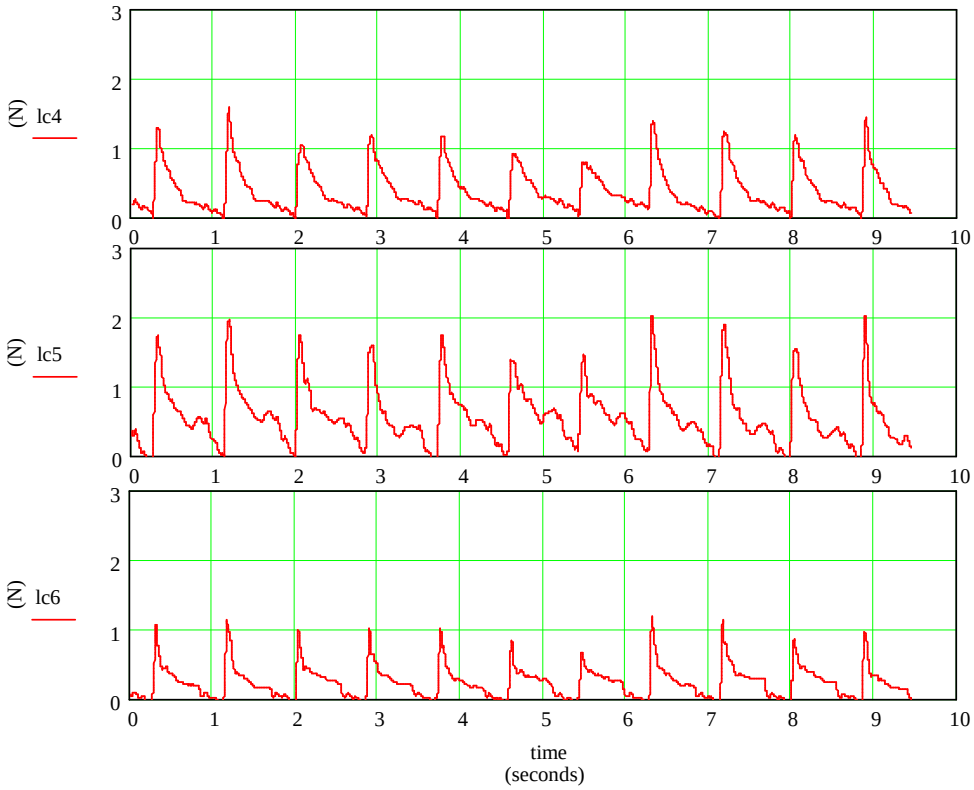

Figure 5.9.1 Longitudinal green water loads on middle-row load cells (load cells 4, 5 and 6, respectively) when ship was travelling at Fn = 0.30 in regular waves having height and period equivalent to 8.0m and 12.0s at full scale.

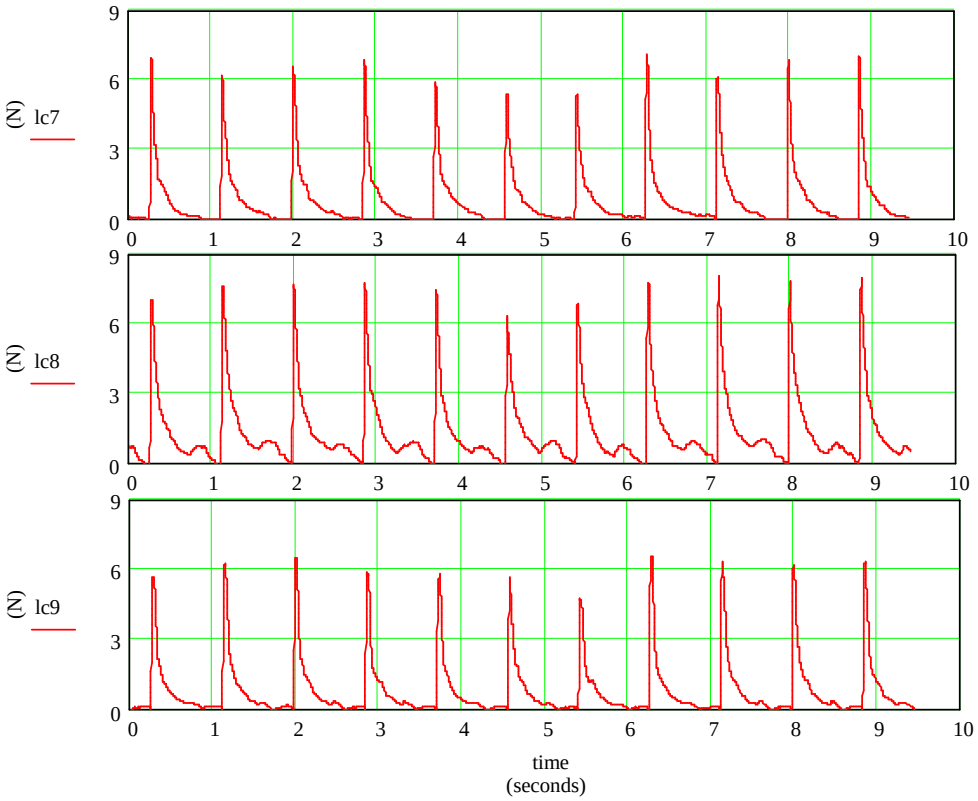

Figure 5.9.2 Longitudinal green water loads on bottom-row load cells (load cell 7, 8 and 9, respectively) when ship was travelling at Fn = 0.30 in regular waves having height and period equivalent to 8.0m and 12.0s at full scale.

Figure 5.9.3 shows a typical impact load (extracted from the time history of impact load on load cell 8 in Figure 5.9.2). This load curve has three key characteristics, i.e. the primary peak load, the rise time to this peak load and the secondary peak load. After being shipped onto the forecastle deck, green water forms a bore and surges towards the load-cell unit. Due to the pitching motion, the velocity of green water flow increases along the way. For surfaces that directly face the water bore like load cell 8, the impact may be treated as the impinging of a water jet on a flat surface (see Section 2.3.2). The peak impact load is then a function of the squared velocity of the front water. The kinetic energy of the front water was absorbed by the vertical surface over a short time, resulting in the primary peak impact load. The time taken to reach the primary peak impact load is

referred to as the rise time. Rise time is very important as it results in vibration in the structure. If the natural frequency of the structure happens to be the same as the inverse of the rise time, unwanted resonance may take place.

After the primary peak, water accumulated in front of the surface and the load becomes more of a quasi-static nature. Therefore, the loading reduces quickly. Note that the accumulated water also helps to direct follow-up water to upper locations and thereby creates the water run-up in front of the vertical structure. Kinetic energy transformed into potential energy as the water runs up. At some point, this water will start to fall back on the deck and in front of the vertical surfaces before dispersing away. At the time the accumulated mass of water in front of the surface closest to deck (like load cell 8) was largest, the secondary peak load takes place. The load was more or less due to static pressure.

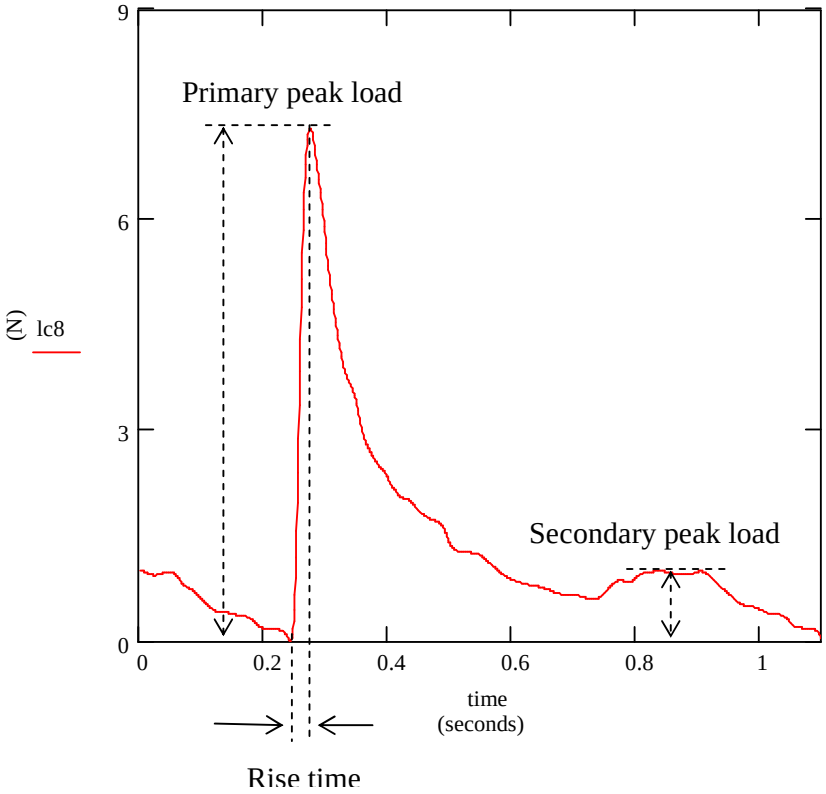

Figure 5.9.3 Typical time history of a green water impact load recorded (equivalent to Fn = 0.30, H = 8.0m and T = 12.0s at full scale).

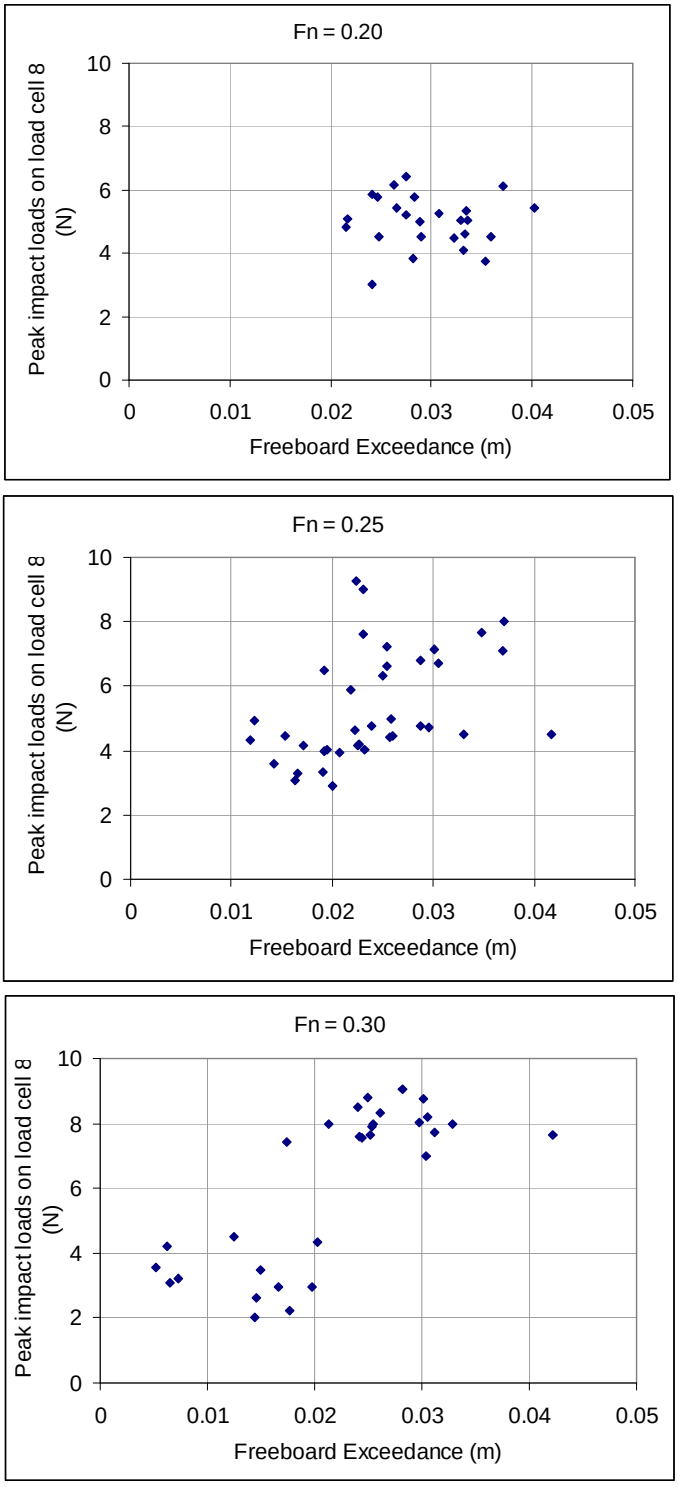

Figure 5.9.4 Relation between peak impact load on load cell 8 and freeboard exceedance.

In order to investigate the relation between impact load at location close to deck level and the freeboard exceedance (FBE), Buchner (2002) reported that it is quadratic in the form:

$$F_{impact} = a_F \times FBE^2 \tag{5.9.1}$$

where a_F is a constant that could be found by empirical method. Figure 5.9.4 plotted the variation of peak impact loads on load cell 8 with the freeboard exceedance at three ship velocities. The data indicated a relatively scattering pattern that surely did not reflect the relation in Equation (5.9.1). Note that the experiments carried out by Buchner (2002) used stationary FPSO models whilst the models tested in this research had forward velocities. This could be the factor that accounted for this difference.

Going back to the problem of a water jet impinging on a flat surface, Suhara et al. (1973) proposed the following empirical formula for estimating the peak impact pressure:

$$P = C\rho U_{gw}^2 \tag{5.9.2}$$

C was set at 1.40 for bottom slamming situations. In an attempt to re-evaluate this equation, peak impact pressures on load cell 8 were plotted against estimated green water velocities (see Section 5.6) in Figure 5.9.5. Similar to what was noticed by Buchner (2002), the use of C = 1.4 in equation (5.9.2) would overestimate the peak impact pressure on a panel of the size of load cell 8 (5cm×5cm at model scale or 3.5m×3.5m at full scale). The maximum impact pressure corresponded to C = 0.8.

Buchner (2002) also stated that the peak force per metre breadth was an important parameter because it expressed the rate of change of linear momentum at the moment the maximum water height at the deck reaches the structure:

$$\frac{F_{peak}}{breadth} = \rho.H_{max}U_{gw}^2 \qquad (5.9.3)$$

Figure 5.9.6 plotted this relation and water height used for equation (5.9.3) was the water height measured by wave probe 9 (closest to load cell 8). The least square fitted line had a slope of 0.57 whilst the maximum slope was approximately 1.42. The corresponding slopes quoted by Buchner (2002) based on his experimental data for FPSO's were 0.40 and 1.25, respectively. This means that the rate of change of linear momentum in this research were higher in the case for FPSO by approximately 14 percent. The difference could be due to the forward velocity of the ship.

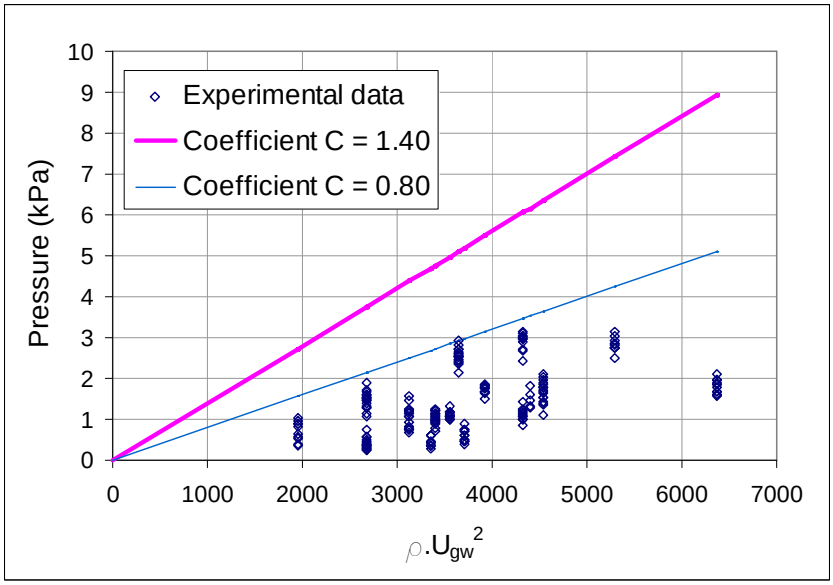

Figure 5.9.5 Peak impact pressure on load cell 8 as a function of the square of the water front velocity U_{gw}.

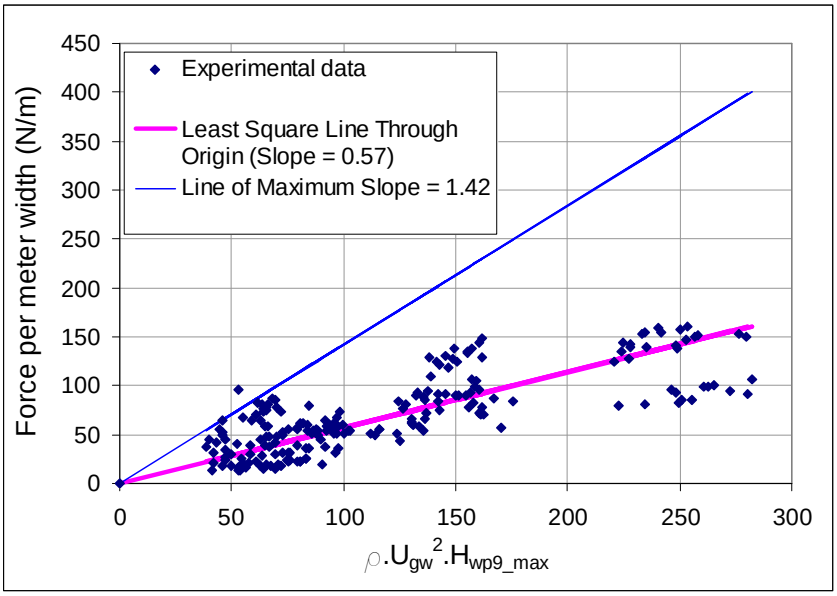

Figure 5.9.6 Peak force per metre breadth on load cell 8 as a function of maximum green water height measured by wave probe 9 multiplied by the square of the water front velocity.

Returning to equation (5.9.2), it is indicated that the impact loading is highly dependent on the incident velocity of the water. If the water jet impinges the flat plate at an incident angle θ, equation (5.9.2) can be re-written as:

$$P = C.\rho U_{gw}^2 \cos\theta \qquad (5.9.4)$$

As described above, after the initial impact between green water and the vertical surfaces, the water accumulated in front of the vertical structure and directed the follow-up water upwards. As the water moved upwards, its kinetic energy was transformed into potential energy so the velocity was reduced. The impact between this run-up water and the upper vertical surfaces therefore happened at lower velocity and also at an incident angle $\theta > 0$ degrees. The impact pressure, as a result, reduced quickly. Examples can be seen by comparing Figure 5.9.1 with Figure 5.9.2. Figure 5.9.7 plotted the loads recorded by load cells 2 and 5 as the

percentage of load by load cell 8 in the test conditions that corresponded to Figures 5.9.1 and 5.9.2. It is clear that green water loading reduced quickly with height. At load cell 5, the peak load decreased by approximately 80 percent. At load cell 2 on the top row directly above load cell 8, the load reduced by more than 95 percent.

Figures 5.9.8 to 5.9.11 show the maximum impact loads measured by load cells in the middle row as percentage of the maximum impact loads measured by load cells in the bottom row. On average, the maximum impact load on middle row of load cell box was only about 15 percent of the maximum impact load on the bottom row.

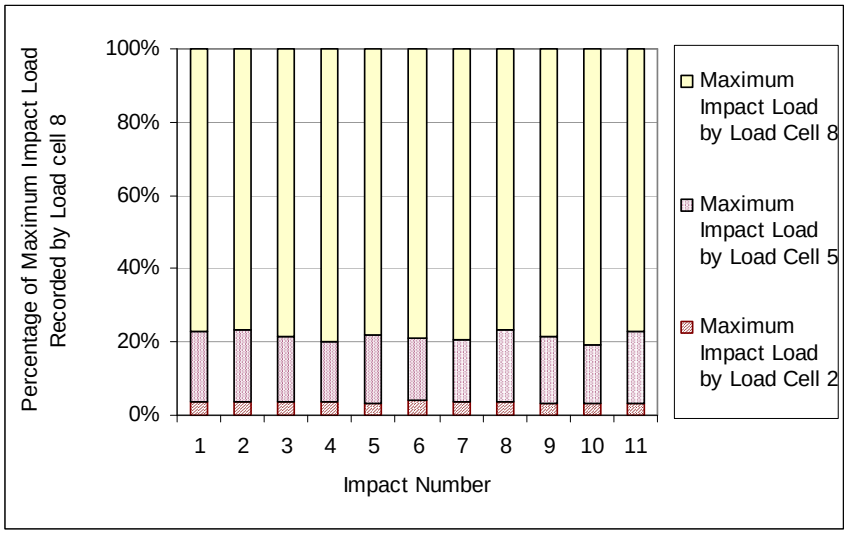

Figure 5.9.7 Maximum impact loads decreased with increased height of load cell (based on measurements of load cells in middle column of the load cell box).

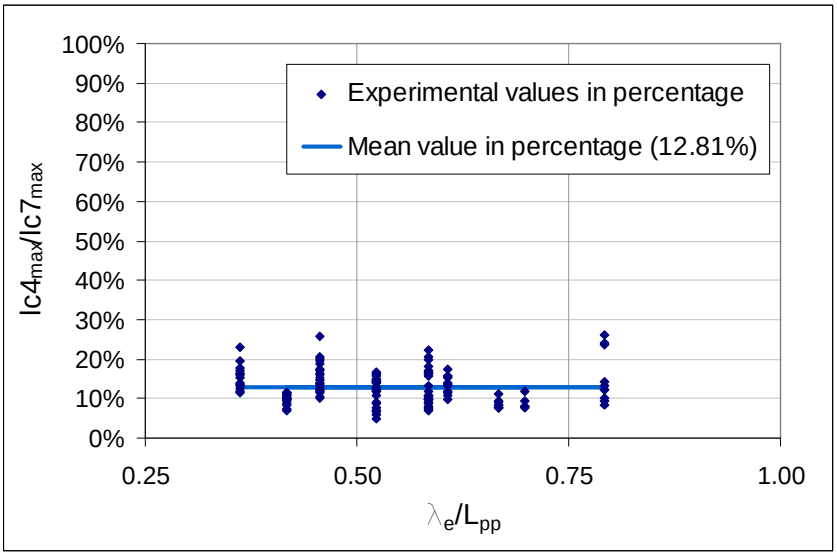

Figure 5.9.8 Maximum impact load measured by load cell 4 as percentage of maximum impact load measured by load cell 7.

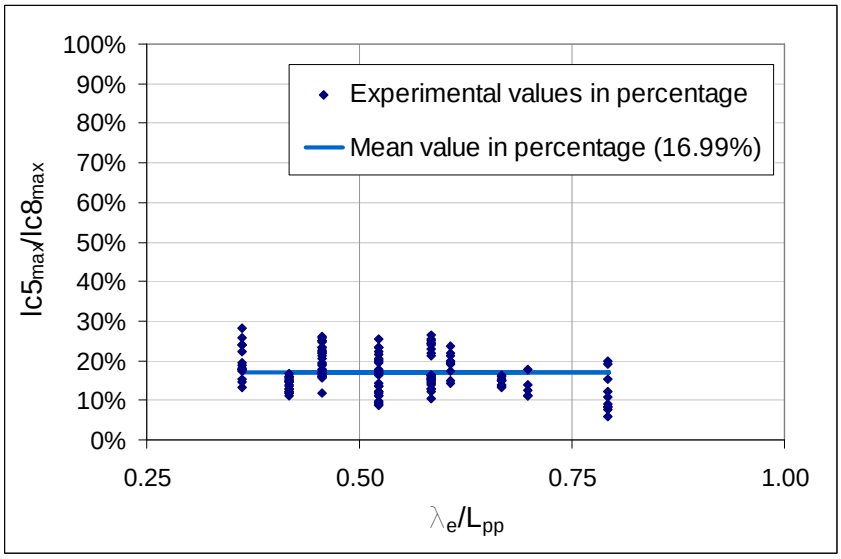

Figure 5.9.9 Maximum impact load measured by load cell 5 as percentage of maximum impact load measured by load cell 8.

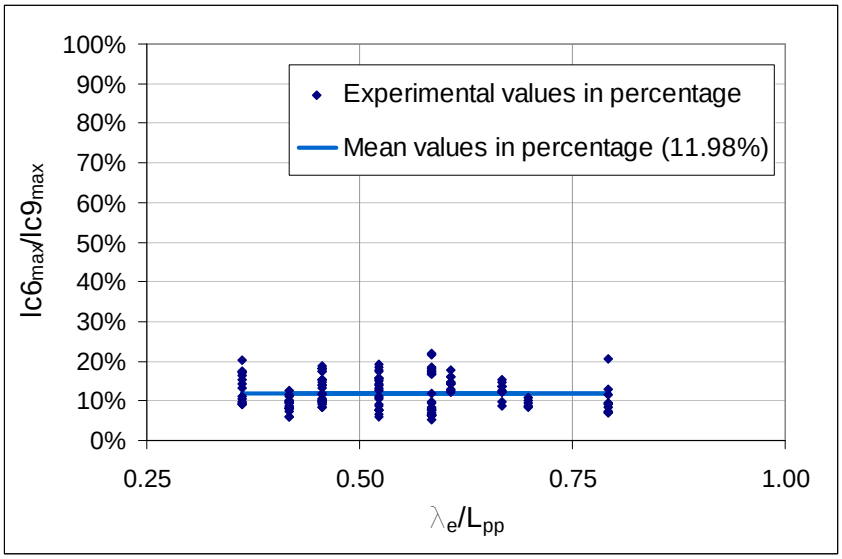

Figure 5.9.10 Maximum impact load measured by load cell 6 as percentage of maximum impact load measured by load cell 9.

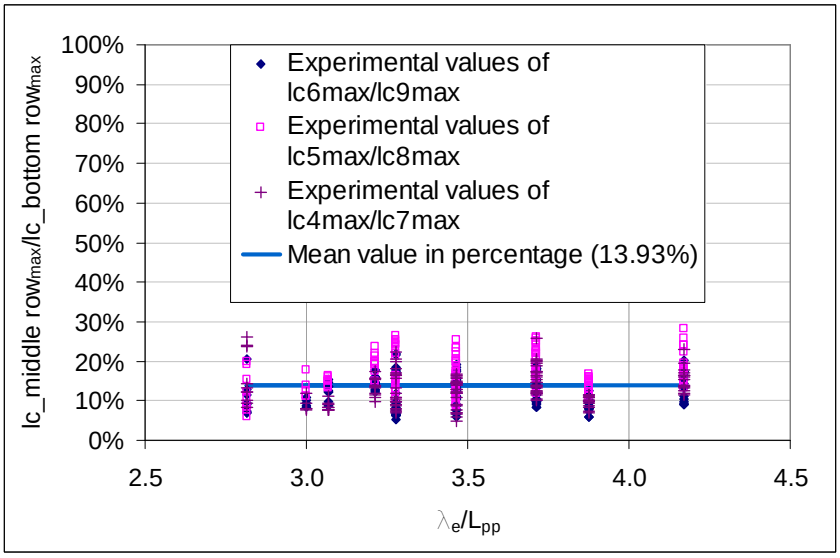

Figure 5.9.11 Maximum impact loads measured by load cells in middle row of the load cell box as percentage of maximum impact loads measured by corresponding load cells in bottom row of load cell box.

5.10 Vertical green water loading

Measured green water loading was used to verify equation (4.9.5) for vertical deck pressure by Buchner (1995a, 2002). For the third term in equation (4.9.5), green water height measured by wave probe 9 was chosen to represent H_{gw} because it was located near the centroid of the deck load cell plate (see Figures 4.5.8 and 4.9.9). Note that the dimensions of the deck load cell plate was relatively sizeable (98.36mm × 123.36mm). It might not be ideal for this verification because the change of green water height over such a large plate could not be as homogenous as wanted (see Section 5.8) to apply equation (4.9.5) properly. The comparison, therefore, only aimed to provide some approximate correlation between the experimental data and the calculated results by this semi-empirical formula. Figure 5.10.2 shows these calculated pressure components, their total and the actual deck pressure measured for comparison.

With the mean values of peak pressures being 1.58kPa for calculated and 1.45kPa for experimental results, there was a good correlation between the two sets of data. Figure 5.10.1 summarises the ratios between calculated peak pressure and measured peak pressure. In general, they stayed close to 1.0 for 75 percent of all green water cases. Recall that the large size of the deck plate might not be ideal for the cases when the change of green water height on the plate was not homogenous. Examples of such cases were when green water shipments were of small quantity and shipped water was splashing on forecastle deck. The non-homogenous variation of green water height on the deck plate also could also explain why the impulses of the measured deck pressure were broader.

Nonetheless, Figures 5.10.1 and 5.10.2 imply that deck pressure by equation (4.9.5) could give a relatively good estimate of green water pressure when the water shipment was amassed. In the cases when the water shipment was scattering, it should only be used locally.

Figure 5.10.2 shows that the pressure component due to the change in green water height was very important. Indeed, in this particular case, it defined the characteristics of the deck pressure. As noticed, the peak pressures due to gravity and due to vertical deck acceleration accounted for only 33 percent and 16 percent of the total peak pressure, respectively. Peak pressure due to the change of water height amounted to 72 percent (note that since the peak pressures of component pressures did not take place at the same time, the addition of these percentages did not necessarily equal to 100 percent). Note that P_gravity is pressure due to gravity; P_accel is pressure due to vertical acceleration of forecastle deck; P_δwp9 is pressure due to variation of water height at location of wave probe 9.

If converting Figure 5.10.2 to full scale, it could be figured out that for this particular case, there was an average peak pressure equivalent to 10 tons per square metre distributed over a deck area of 7m×8.6m along the centreline.

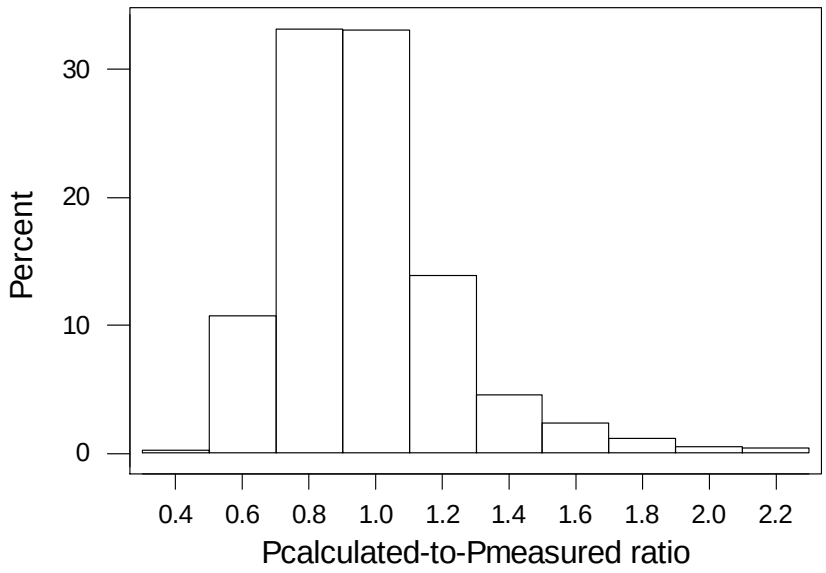

Figure 5.10.1 Distribution of ratios between calculated peak pressure and measured peak pressure on deck plate due to green water.

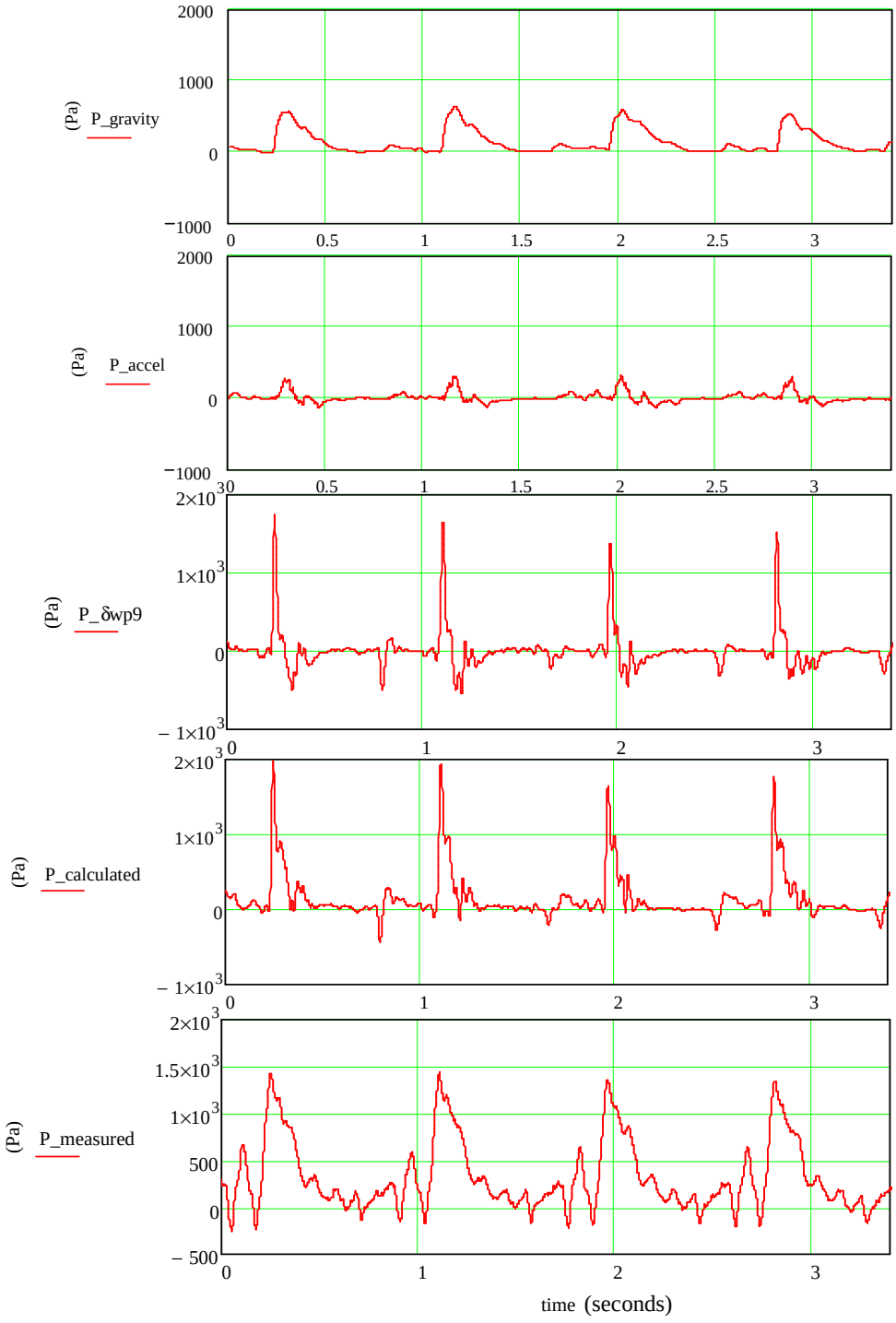

Figure 5.10.2 Deck pressure components, their calculated total against measured total pressure on deck load cell plate in the case corresponding to Fn = 0.30, H = 8.0m and T = 12.0s at full scale.

5.11 Configuration of green water model

Amongst the main objectives of this research is to find a hydraulic model that can well simulate green water on deck. From the analysis of experimental data so far, the characteristics of green water can be summarised as:

- Green water is made up by direct shipment of solid mass of water when the deck is submerged and the water that is shed off the deck edge and later caught up with by the ship due to its forward velocity.

- Due its small quantity, the shed or splashing water is relatively random. Even though it can reach high locations on deck, the loading effects of this splashing water can be assumed to be small.

- The real threat of loading comes from the shipment of the solid mass of green water. This water entered the deck at a velocity slightly less than the advance velocity of the ship. This was due to the front water being pushed backwards when the ship pitched into the water prior to green water taking place.

- Once on deck, green water flow accelerated due to the ship pitching out of the water which created a backward sloping in the forecastle deck.

- Green water concentrated along the centreline and surged down the forecastle deck. If crashing against a vertical surface, the resulted impact load would highly depend on the velocity of the front water and the water height.

To help visualise green water profile on deck, green water velocity derived from Section 5.6 was multiplied with the time history of green water elevation recorded by wave probe 9. The result gave green water elevation against the distance along

the centreline or the water profile at the centreline as it passed wave probe 9. Figure 5.11.1 gives an example of such water profile when the ship was travelling at Fn = 0.25 in regular waves of height and period equivalent to 8m and 12s at full scale. On overall, the water profile was relatively trapezoidal in shape.

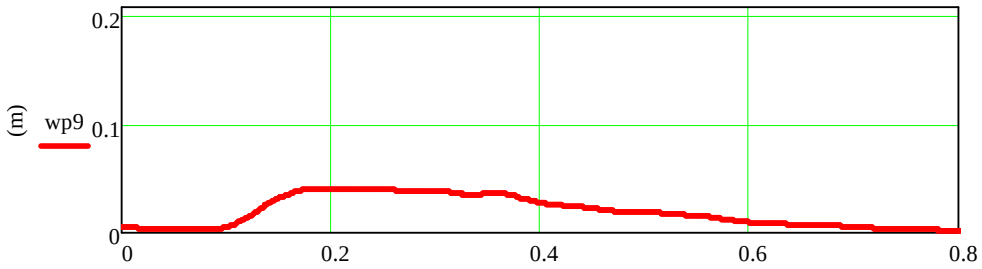

Figure 5.11.1 Approximate shape of green water flow translating on deck.

Buchner (2002) stated that green water flowing into deck could be simulated using a dam-break model in which the initial dam-break height was equivalent to 9/4 times the freeboard exceedance at the stem head. This was derived based on the experiments with stationary FPSO models. For ship with forward velocity, the model requires some modification and the natural modification is to incorporate this relative velocity between ship and water behind the dam into the simulation. This appears to agree with the observations in this research where the entry velocity of green water was found to be relatively close to the advance velocity of the ship.

Having an approximate visualisation of green water flow on deck as in Figure 5.11.1 as a guideline, the configuration of the water mass at the beginning before it enters the deck can be approximated for simulation. A schematic configuration of this water mass is detailed in Chapter 6.

5.12 Efficiency of protecting breakwaters

5.12.1 Design missions for breakwaters

A popular way of preventing green water from damaging deck structures is to use protecting breakwaters. Depending on the available deck area and the potential severity of green water, breakwater can be designed differently. If deck area is limited, breakwater can simply be designed like a vertical rectangular wall. In such cases, the loading on the breakwater can be substantial. If deck area is sufficient, other breakwaters can be designed not to block green water in full face. Green water can be diverted to the sides of the ship and thereby the impact load can be reduced. Examples of these breakwaters include V-shape breakwater which is relatively common in use and vane-type breakwater.

The design missions of breakwater, in general, are:

- Effectively break or deflect green water flow so that impact loading on critical structures can be minimised.

- Strongly withstand the impact loading caused by green water.

The limited deck area in the models tested in this research meant that only one type of breakwater was suitable for experiments, i.e. rectangular breakwater. This is also the common practice in the construction of containerships nowadays. With the high priority for accommodating more containers on deck, the space available for deck machineries and other appendages is left very limited.

5.12.2 Observations

After entering the forecastle deck, green water flow accelerated quickly along the deck and crashed into the breakwater. Blocked by the breakwater, green water built up in front of the breakwater and directed the follow-up water upwards. There was water that overcame the top edge of the breakwater and struck the vertical load cells at the back. Due to the high velocity of water flow, the impact could be relatively violent. Figure 5.12.1 shows a stochastic behaviour of green water during the impact with breakwater.

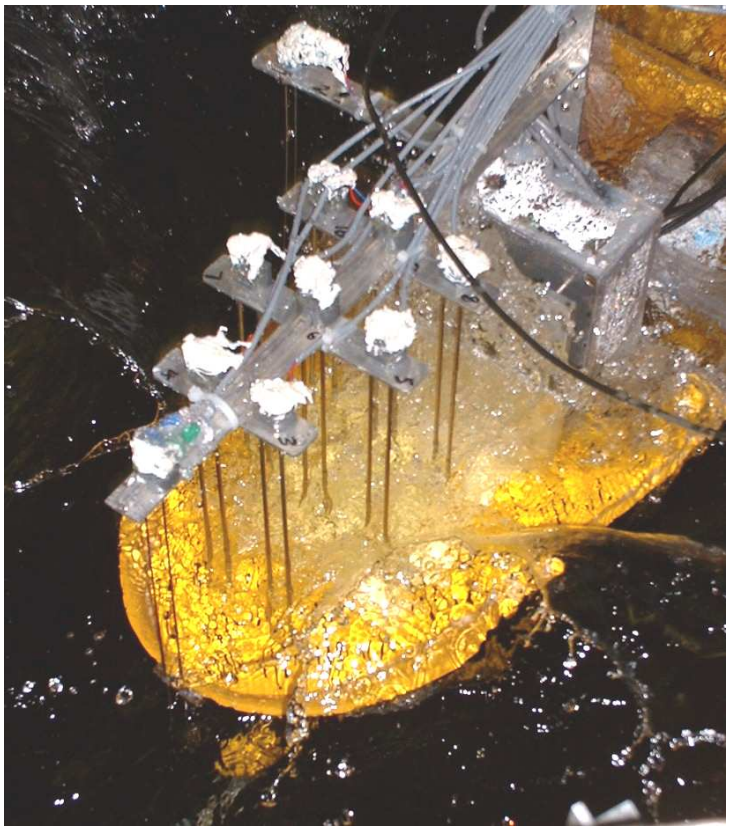

Figure 5.12.1 Green water crashing against breakwater, resulting in run-up water and scattered water.

To reduce the force of the impact, Jarlan-type or perforated breakwater has been adopted in many ships. The perforations in the breakwater allow part of the incident water to go through. The momentum imparted on the breakwater is, therefore, reduced and so is the load on the breakwater. However, this also means that the protected cargo will have to face larger loads caused by the water that goes through the breakwater. Figure 5.12.2 gives an example of the impact between green water and perforated breakwater.

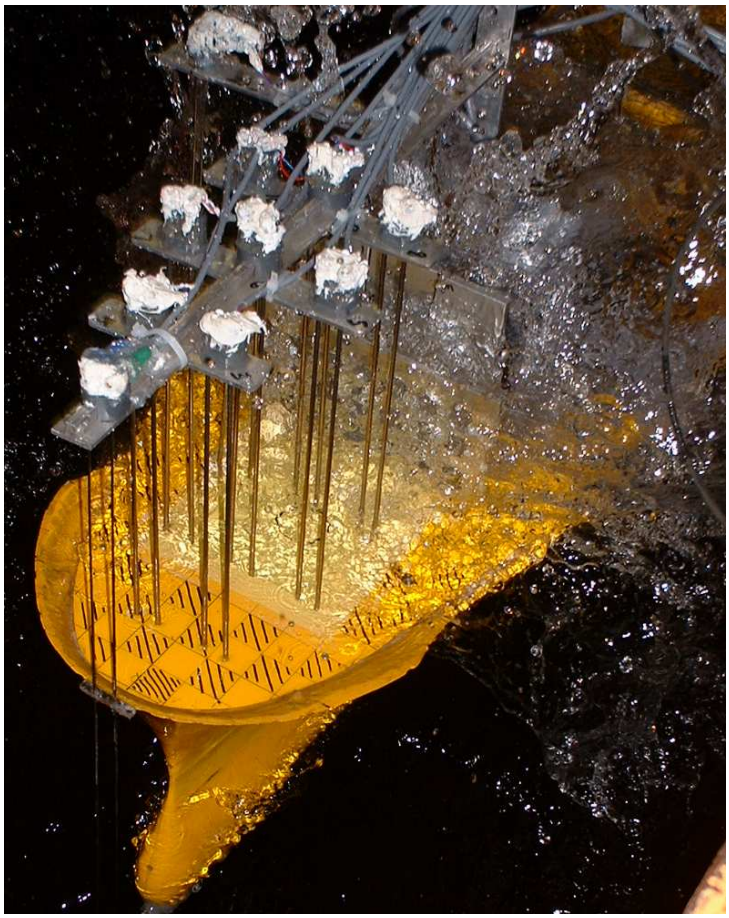

Figure 5.12.2 Green water flow was divided by perforations in the breakwater, resulted in some sub-flows being blocked by the breakwater and others going through and impact with deck structures.

5.12.3 Protective efficiency of breakwater

In order to evaluate the protection by breakwaters, mean values of peak impact loads on load cells 2, 5 and 8 (along the centreline of load-cell unit) were plotted for comparison. Peak values of total load on the load-cell unit were also compared and results are as in Figures 5.12.3 to 5.12.10. For convenience in identifying the breakwaters, they were coded based on the heights and diameters of perforation. For example, breakwater H051D10 was referred to breakwater height of 51mm with perforation diameter of 10mm (10.5mm to be exact). Full dimensions of the breakwaters are listed in Table 4.5.1 of Section 4.5.7.

Without doubt, the breakwaters considered helped to reduce to total load on the vertical structure by at least 50 percent. Most of the reduction went to the load cell closest to deck (load cell 8). Breakwaters could increase the peak impact loads on upper load cells (load cell 2 and 5) but such increase was small compared to the total load.

When the heights of breakwaters increased (Figures 5.12.7 to 5.12.10), the longitudinal green water loads reduced.

Figures 5.12.11 and 5.12.12 show the variation of green water peak load on load cell 8 with variation in breakwater permeability. The height of load cell 8 was smaller than the breakwater height in all these cases. In other words, load cell 8 was fully covered by breakwater in the x-direction. Both Figures indicate that the load on load cell 8 steadily increased with increased permeability. The relation was not linear and rather quadratic.

If the total load on the load-cell unit was considered instead of load cell 8, the behaviours of this load are as in Figures 5.12.13 and 5.12.14. It can be seen that for breakwater height of 76mm, the total longitudinal load steadily increased with the increased permeability like the case for load cell 8. However, for breakwater

height of 51mm, the variation shows a more fluctuating behaviour. Chapter 8 will discuss in detail the explanation for such behaviour. Basically, green water load on the load-cell unit comprised of two components. The first component was related to water that passed through the perforations in the breakwater. The second component was caused by the water that overcame the breakwater. The higher the breakwater, the lesser this water and smaller impact load. As a result, the first component would dominate the characteristics of the load on the load-cell unit. Since the first component depended on amount of water that could pass through the breakwater, the total load (dominated by the first component) would be proportional to the permeability as noticed.

For lower breakwater height, the effects of permeability become less obvious since the impact load caused by overriding water starts to become more influential on the total impact load. At breakwater height of 51mm, the amount of water that overcame the breakwater became comparable to amount of water that passed through the breakwater. The total load, as a result, was fluctuating because neither component had a clear dominance over the other.

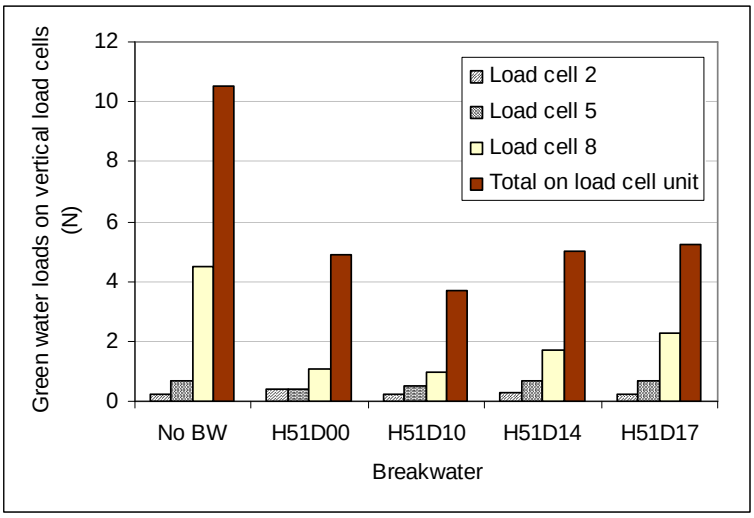

Figure 5.12.3 Effects of breakwater on longitudinal green water loads when model was tested at Fn = 0.25 in waves of equivalent full-scale height and period of 8m and 13s, respectively.

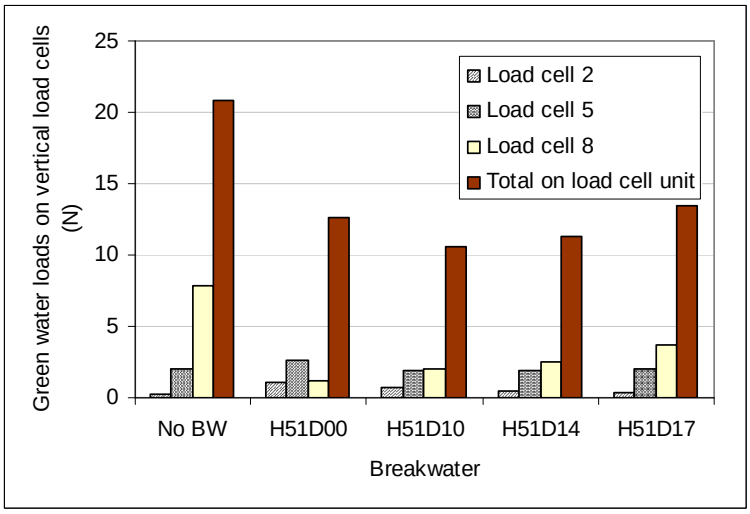

Figure 5.12.4 Effects of breakwater on longitudinal green water loads when model was tested at Fn = 0.30 in waves of equivalent full-scale height and period of 8m and 13s, respectively.

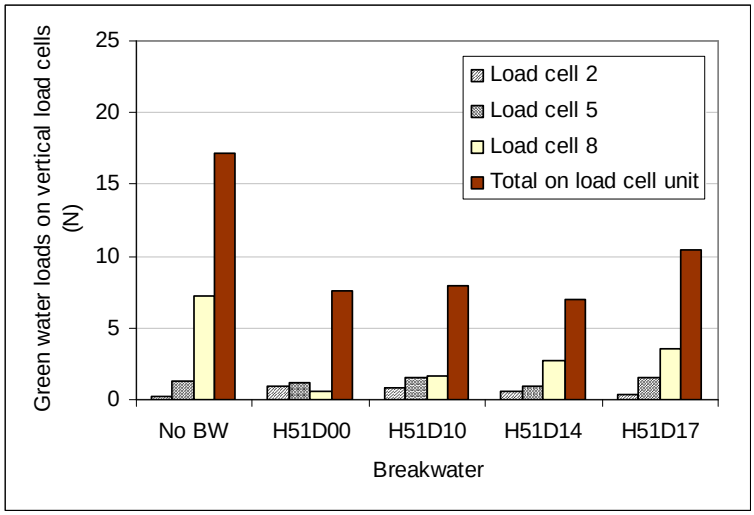

Figure 5.12.5 Effects of breakwater on longitudinal green water loads when model was tested at Fn = 0.25 in waves of equivalent full-scale height and period of 8m and 12s, respectively.

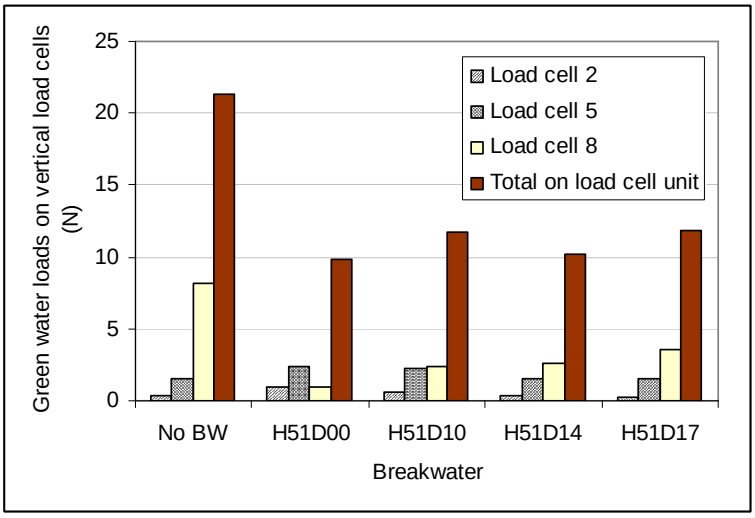

Figure 5.12.6 Effects of breakwater on longitudinal green water loads when model was tested at Fn = 0.30 in waves of equivalent full-scale height and period of 8m and 12s, respectively.

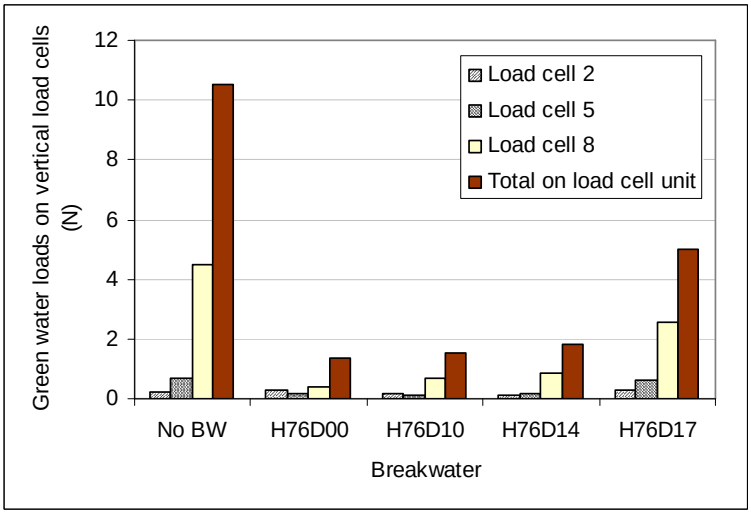

Figure 5.12.7 Effects of breakwater on longitudinal green water loads when model was tested at Fn = 0.25 in waves of equivalent full-scale height and period of 8m and 13s, respectively.

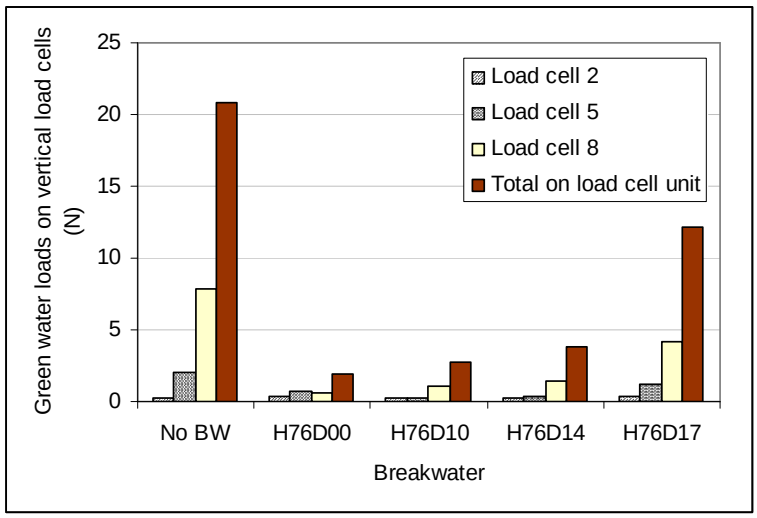

Figure 5.12.8 Effects of breakwater on longitudinal green water loads when model was tested at Fn = 0.30 in waves of equivalent full-scale height and period of 8m and 13s, respectively.

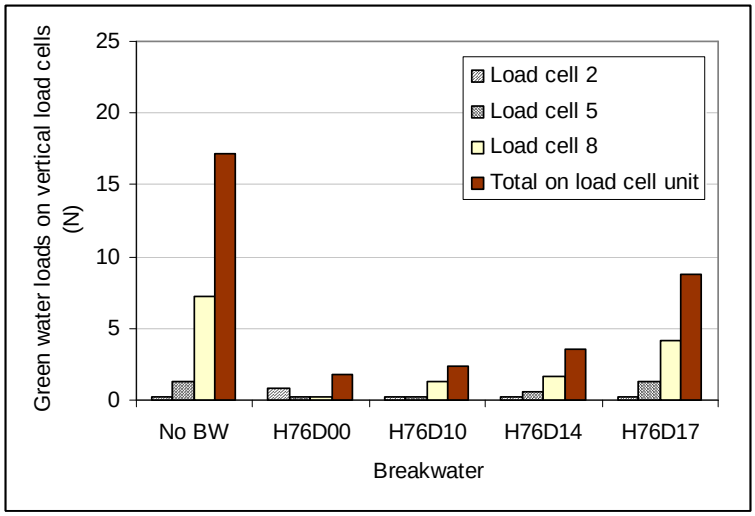

Figure 5.12.9 Effects of breakwater on longitudinal green water loads when model was tested at Fn = 0.25 in waves of equivalent full-scale height and period of 8m and 12s, respectively.

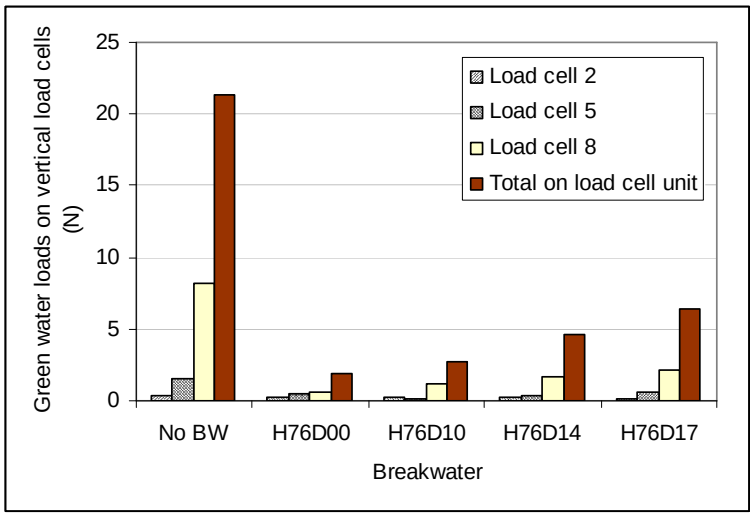

Figure 5.12.10 Effects of breakwater on longitudinal green water loads when model was tested at Fn = 0.25 in waves of equivalent full-scale height and period of 8m and 12s, respectively.

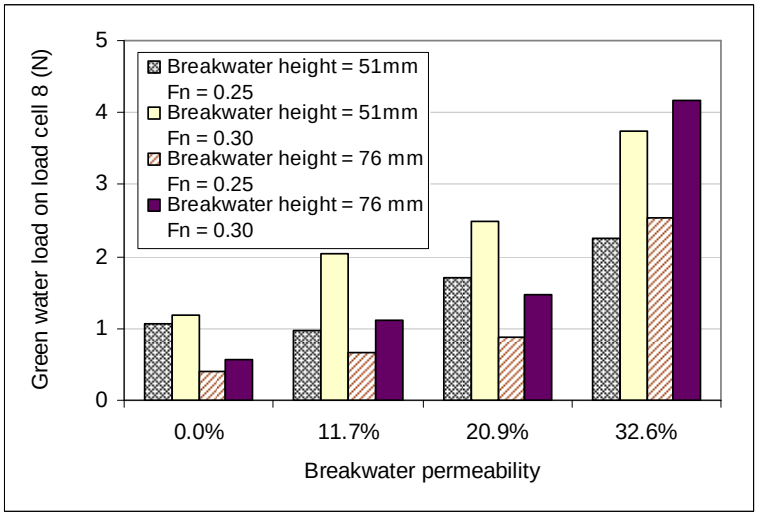

Figure 5.12.11 Effects of breakwater permeability on longitudinal green water loads when model was tested in waves of equivalent full-scale height and period of 8m and 13s, respectively.

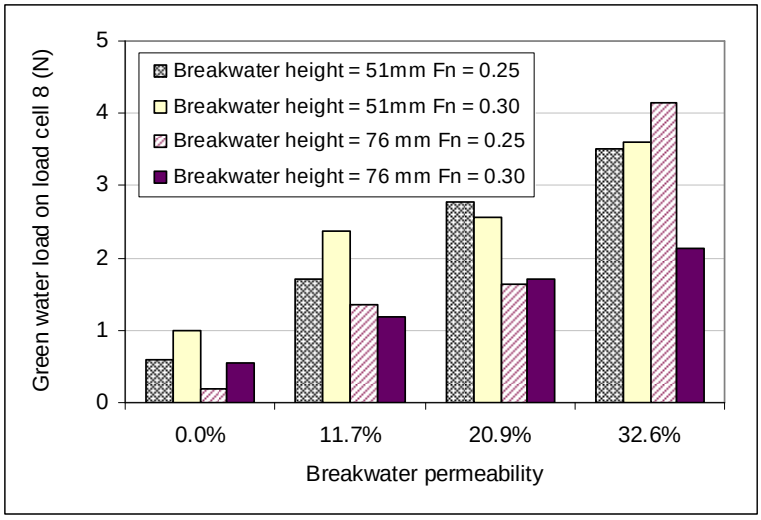

Figure 5.12.12 Effects of breakwater permeability on longitudinal green water loads when model was tested in waves of equivalent full-scale height and period of 8m and 12s, respectively.

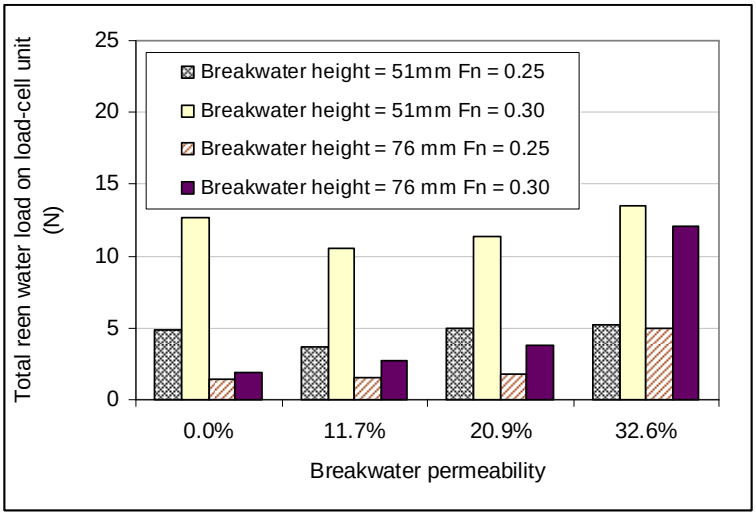

Figure 5.12.13 Effects of breakwater permeability on total longitudinal green water load when model was tested in waves of equivalent full-scale height and period of 8m and 13s, respectively.

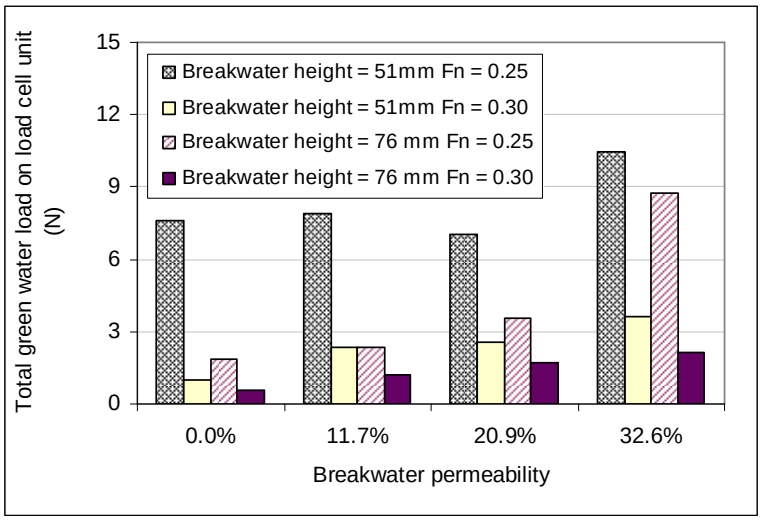

Figure 5.12.14 Effects of breakwater permeability on total longitudinal green water load when model was tested in waves of equivalent full-scale height and period of 8m and 12s, respectively.

5.12.4 Influence of the breakwater height

It is observed that for higher breakwater height, more water is blocked and less load is imposed on the protected vertical structure. Figures 5.12.15 and 5.12.16 show the influence of increased breakwater height on the longitudinal loads measured by load cells 2, 5, 8 and the load-cell unit as a whole. Four non-perforated breakwater heights were compared (the case of no breakwater was seen as a breakwater with zero height).

It can be seen that longitudinal green water load on the load-cell unit reduced very quickly with the increased height of the breakwater and the reduction was not linear. Since the breakwaters were not perforated, green water load was caused solely by the water that overcame the breakwater. The amount of water was not linearly dependent on the height of the breakwater and should be best found by simulation.

As mentioned earlier, load cell 8 was fully covered by the breakwater because of its smaller height. The load on this load cell was reduced most since it was located at deck level. It would have directly faced green water if the breakwater had not been present.

At intermediate height, load cell 5 was subject to direct impact from the water that overcame the breakwater. Therefore, the load it faced might increase compared with no breakwater present (Figure 5.12.16).

On overall, it was shown that breakwater height did indeed have a strong influence over green water load on vertical surfaces.

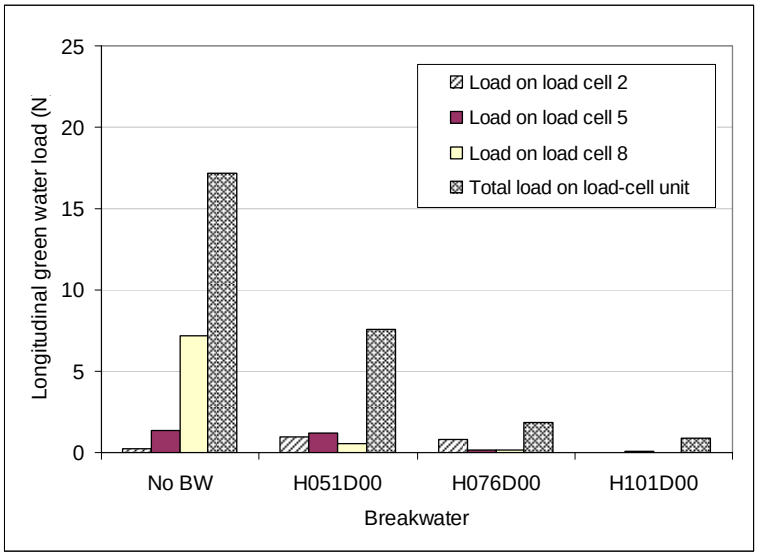

Figure 5.12.15 Effects of breakwater height on the peak longitudinal loads when ship model was tested in waves of equivalent full-scale height of 8m and period of 13s.

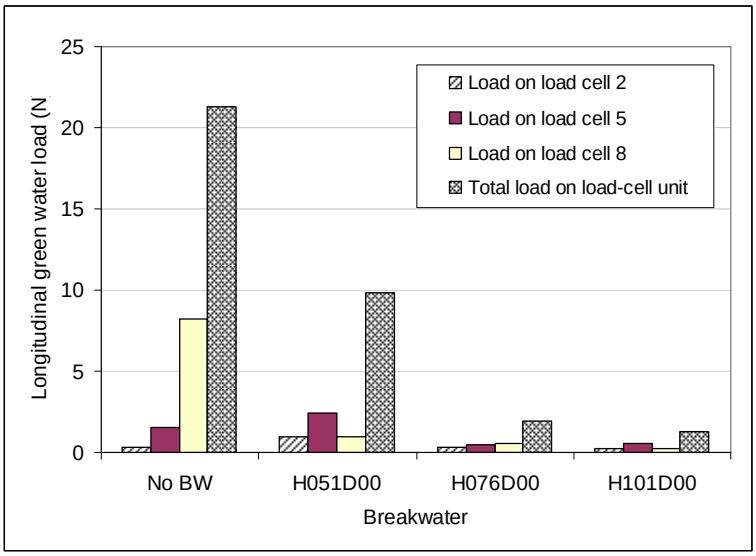

Figure 5.12.16 Effects of breakwater height on the peak longitudinal loads when ship model was tested in waves of equivalent full-scale height of 8m and period of 12s.

5.13 Effects of modified bow features

This section is dedicated to evaluating the effects of the changes in the above-water bow shape described in Section 4.2. Though ignored by most ship motion theories, the above-water bow form does indeed affect the buoyancy force, added mass and damping when the ship pitches in water. This subsequently affects ship motions and green water.

5.13.1 Effects on motions

The RAO's of heave and pitch motions with bow 1 were already presented in Section 5.3.2 so only RAO's of heave and pitch at different tested velocities for bow 2 and bow 3 are shown in this Section (Figures 5.13.1 to 5.13.12).

By looking at the heave and pitch RAO's of bow 1 and bow 3 (Figures 5.3.4 to 5.3.9 vs. Figures 5.13.7 to 5.13.12, respectively), it was noticed that motions of

these two bows were relatively similar. This is quite reasonable considering the bow shapes in the two cases. Except for the stem overhang being extended, the above-water bow shapes are almost similar. Figure 4.2.2 shows the lines plans of the two bows and it can be seen that up to the forward perpendicular, all stations are the same for the two bows. The extra hull volume caused by the extended overhang was very small compared with the volume of the above-water bow. Therefore, motions of the two bows are similar. However, it must be made clear that this does not necessarily mean the relative motions at the stem head stay the same. Being further away from the centre of floatation, the stem head of bow 3 would experience larger relative motions.

Bow 2 has a knuckle or a chine line introduced between station 7½ and the forward perpendicular (Figure 4.2.2). As a result, its above-water bow form becomes fuller than bow 1 and bow 3 as in Figure 4.2.3. This, consequently, affects pitch motions of the ship and it did. By comparing Figures 5.13.4 to 5.13.6 with Figures 5.3.7 to 5.3.9 (bow 1) and Figures 5.13.10 to 5.13.12 (bow 3), respectively, it is observed that the pitch RAO's of bow 2 were much larger, especially towards the critical encountered wave length equivalent to one ship length.

In all cases, the strip theory under-predicted the ship motions by quite a large margin, especially for pitch RAO's. Even though the method took into account the instantaneous wetted surface of the ship in its calculation, the fully non-linear effects of the bow shapes were not reflected. The positive point was that at larger wave amplitudes, the predicted motions got closer to the experimental data.

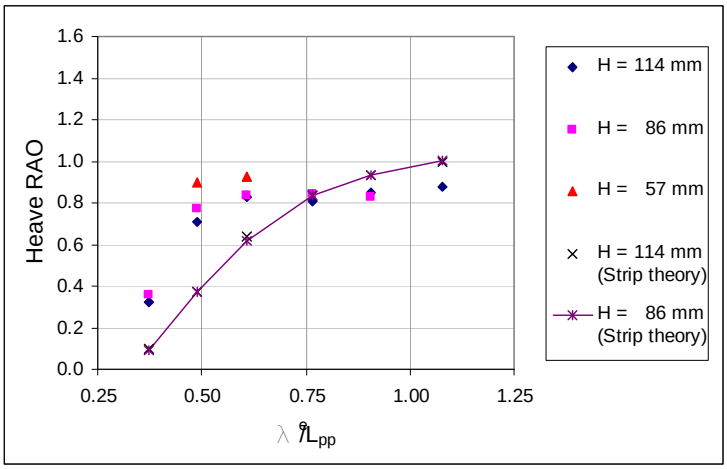

Figure 5.13.1 Heave RAO's of bow 2 at Fn = 0.20.

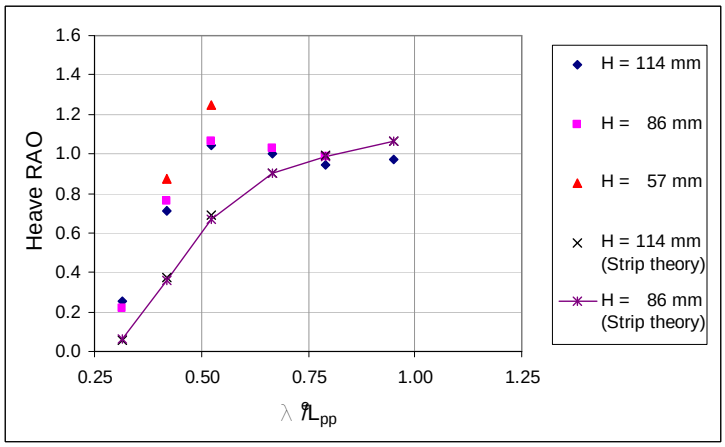

Figure 5.13.2 Heave RAO's of bow 2 at Fn = 0.25.

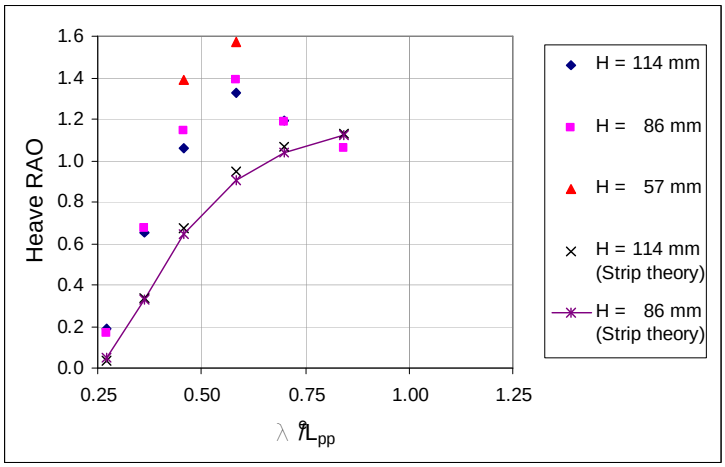

Figure 5.13.3 Heave RAO's of bow 2 at Fn = 0.30.

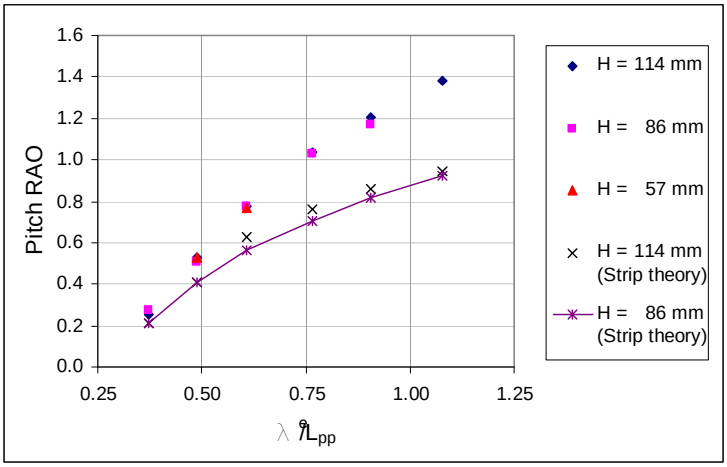

Figure 5.13.4 Pitch RAO's of bow 2 at Fn = 0.20.

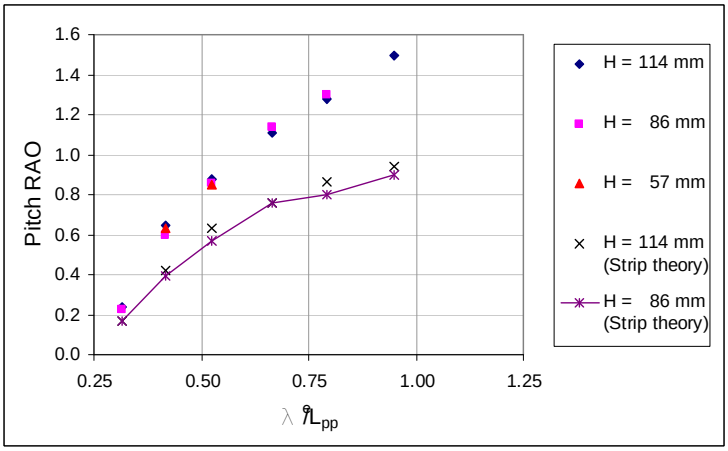

Figure 5.13.5 Pitch RAO's of bow 2 at Fn = 0.25.

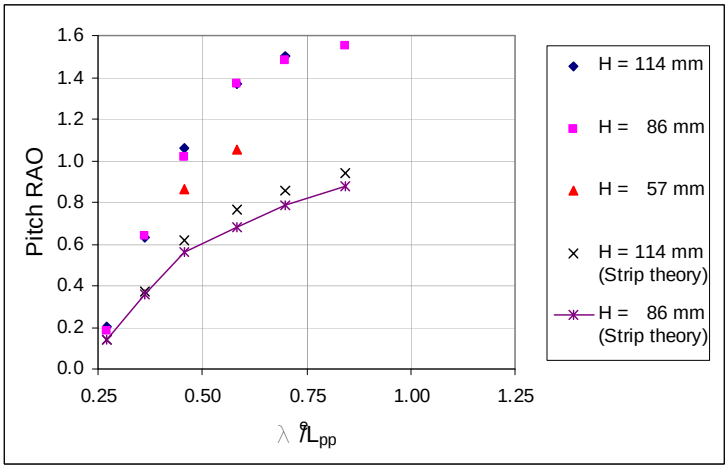

Figure 5.13.6 Pitch RAO's of bow 2 at Fn = 0.30.

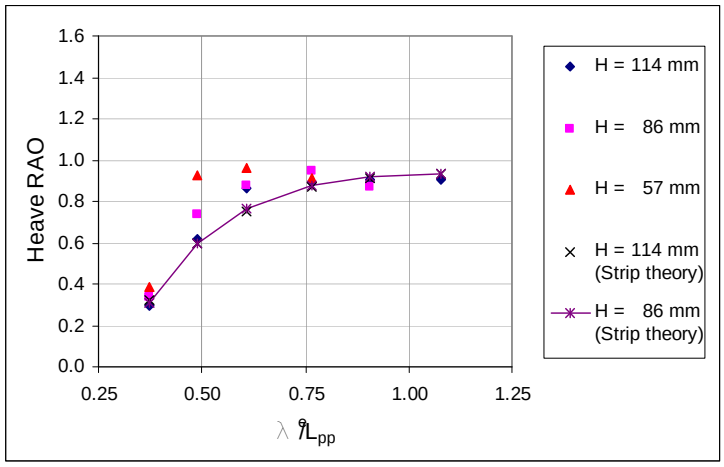

Figure 5.13.7 Heave RAO's of bow 3 at Fn = 0.20.

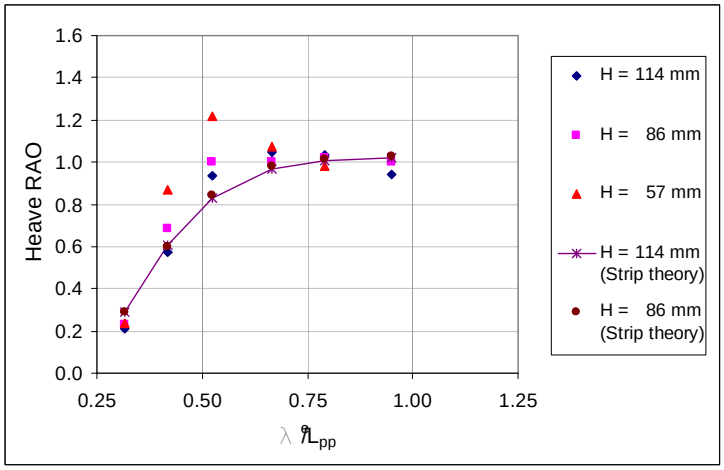

Figure 5.13.8 Heave RAO's of bow 3 at Fn = 0.25.

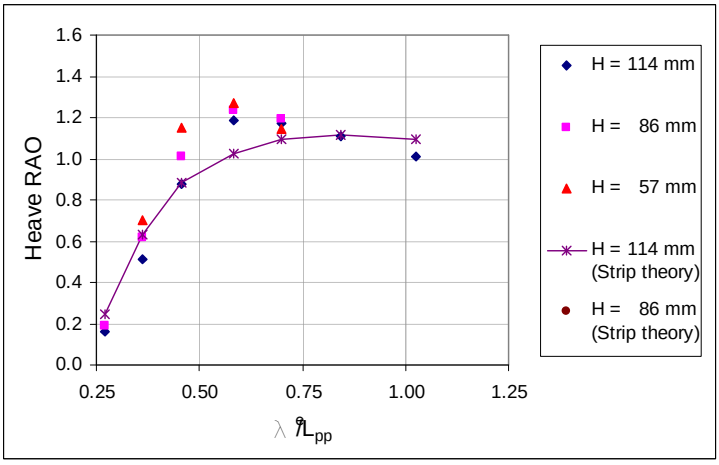

Figure 5.13.9 Heave RAO's of bow 3 at Fn = 0.30.

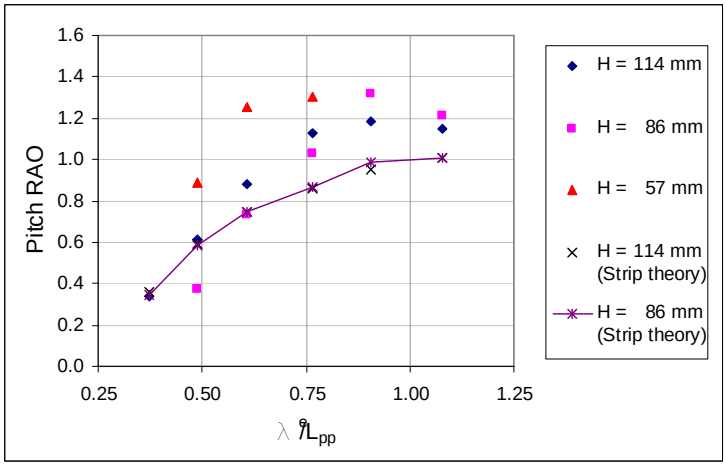

Figure 5.13.10 Pitch RAO's of bow 3 at Fn = 0.20.

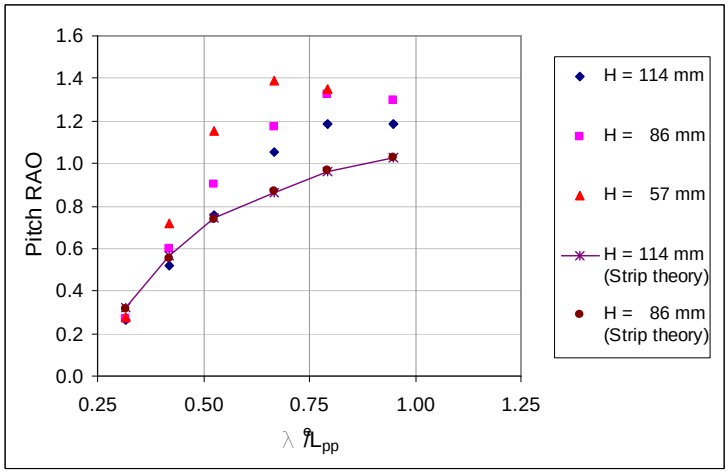

Figure 5.13.11 Pitch RAO's of bow 3 at Fn = 0.25.

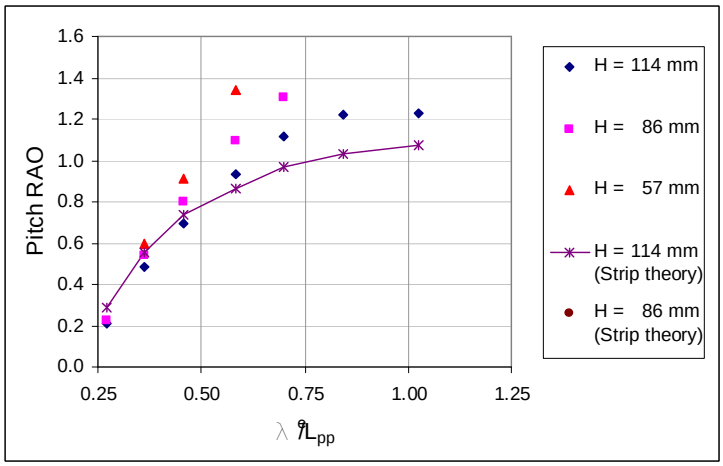

Figure 5.13.12 Pitch RAO's of bow 3 at Fn = 0.30.

5.13.2 Effects on the occurrence of green water

Since no experiment was carried out in irregular waves for the reason mentioned in Section 4.5.1, the effects of above-water bow shape on green water frequency could not be evaluated. The aim of the experiments, therefore, changed to investigating the threshold conditions at which green water started to take place.

Table 5.13.1 shows the conditions and green water results for three bows. All the parameters were converted to full scale for ease of interpretation. Note that it was observed in the experiments that the critical wave periods at which green water was most likely to happen were 12s and 13s. In waves of 3m height, green water did not take place for all three bows regardless of the encountered wave period. At wave height of 4.0m and wave period of 12.0 seconds, for bows 1 and 2, green water did not take place before ship velocity reached 20.0 knots. For bow 3, green water started at lower velocity of 16.0 knots. Likewise, at the same wave height but wave period of 13.0 seconds, green water on bow 3 started at 20.0 knots whilst for bows 1 and 2, this velocity was 24.0 knots. As far as the start-up of green water was concerned, bow 3 with extended overhang and reduced freeboard appeared to perform more poorly than bows 1 and 2.

The occurrence of green water could be a function of both the encountered wave slope and encountered wavelength. It appeared that for the ranges of test conditions chosen, the critical encountered wavelength was between 0.5 and 0.6 times the ship length. Within this range, for higher or steeper waves, it was more likely that green water event would occur.

Tables 5.13.2 to 5.13.4 validate the prediction of green water occurrence using method by Crossland and Johnson (1998). ‘Yes’ is referred to a deck wetness event (green water or spray wetting) whilst ‘No’ indicates no deck wetness taking place. There are some discrepancies (shaded cells in Tables 5.13.2 to 5.13.4). However, these discrepancies were all found in spray wetting conditions. The

mechanism behind spray wetting, as described in Section 3.2.6.3, is highly complex and subject to many non-linearities as well as local effects. The prediction can, therefore, be regarded as good given the circumstances. Green water events, on the other hand, were predicted very well.

Table 5.13.1 Effects of above water bow shape on the occurrence of green water.

Equivalent full-scale wave height (m)	Equivalent full-scale wave period (s)	Equivalent full-scale velocity (knots)	Occurrence of Green Water			Encountered wave slope (deg.)	λ_e/L_{pp}
			Bow 1	Bow 2	Bow 3		
3.0	12.0	16.0	No	Not tested	No	4.62	0.61
3.0	12.0	20.0	Not tested	Not tested	No	5.50	0.52
3.0	12.0	24.0	No	No	No	6.40	0.46
3.0	13.0	24.0	Not tested	Not tested	No	5.05	0.58
4.0	12.0	16.0	No	No	Yes	6.22	0.61
4.0	12.0	20.0	Yes	Yes	Yes	7.36	0.52
4.0	13.0	20.0	No	Not Tested	Yes	5.78	0.67
4.0	13.0	24.0	Yes	Yes	Yes	6.59	0.58

Table 5.13.2 Validation of prediction of green water occurrence to Bow 1.

Wave height	**Wave period**	**Fn = 0.20**		**Fn = 0.25**		**Fn = 0.30**	
		Test	**Simulation**	**Test**	**Simulation**	**Test**	**Simulation**
3m	11s	No	No	No	No	No	No
	12s	No	No	No	No	No	No
4m	11s	No	Yes	No	Yes	No	Yes
	12s	No	No	Yes	Yes	Yes	Yes
	13s	No	No	No	No	Yes	Yes
6m	10s	No	Yes	No	Yes	No	Yes
	11s	Yes	Yes	Yes	Yes	No	Yes
	12s	Yes	Yes	Yes	Yes	Yes	Yes
	13s	Yes	Yes	Yes	Yes	Yes	Yes
	14s	No	No	No	Yes	Yes	Yes
	15s	No	No	No	No	No	No
	16s	No	No	No	No	No	No
8m	10s	No	No	No	Yes	No	Yes
	11s	Yes	Yes	Yes	Yes	Yes	Yes
	12s	Yes	Yes	Yes	Yes	Yes	Yes
	13s	Yes	Yes	Yes	Yes	Yes	Yes
	14s	Yes	Yes	Yes	Yes	Yes	Yes
	15s	No	No	Yes	Yes	Yes	Yes
	16s	No	No	No	No	No	No

Table 5.13.3 Validation of prediction of green water occurrence to Bow 2.

Wave height	Wave period	Fn = 0.20		Fn = 0.25		Fn = 0.30	
		Test	Simulation	Test	Simulation	Test	Simulation
3m	12s	-	No	-	No	No	No
4m	12s	No	Yes	Yes	Yes	-	No
	13s	-	No	-	No	Yes	Yes
6m	10s	No	Yes	No	Yes	No	Yes
	11s	Yes	Yes	Yes	Yes	Yes	Yes
	12s	Yes	Yes	Yes	Yes	Yes	Yes
	13s	Yes	Yes	Yes	Yes	Yes	Yes
	14s	No	Yes	Yes	Yes	Yes	Yes
	15s	No	No	No	Yes	No	Yes
	16s	No	No	No	No	No	No
8m	10s	No	Yes	No	Yes	No	Yes
	11s	Yes	Yes	Yes	Yes	Yes	Yes
	12s	Yes	Yes	Yes	Yes	Yes	Yes
	13s	Yes	Yes	Yes	Yes	Yes	Yes
	14s	Yes	Yes	Yes	Yes	Yes	Yes
	15s	Yes	Yes	Yes	Yes	Yes	Yes
	16s	-	No	-	Yes	No	Yes

Table 5.13.4 Validation of prediction of green water occurrence to Bow 3.

Wave height	Wave period	Fn = 0.20		Fn = 0.25		Fn = 0.30	
		Test	Simulation	Test	Simulation	Test	Simulation
3m	10s	No	No	No	No	No	No
	11s	No	No	No	Yes	No	No
	12s	No	No	No	No	No	No
	13s	No	No	No	No	No	No
4m	10s	No	Yes	No	No	No	No
	11s	Yes	Yes	No	Yes	No	Yes
	12s	Yes	Yes	Yes	Yes	Yes	Yes
	13s	Yes	No	Yes	No	Yes	Yes
	14s	-	No	No	No	No	No
6m	10s	No	Yes	No	Yes	No	Yes
	11s	Yes	Yes	Yes	Yes	Yes	Yes
	12s	Yes	Yes	Yes	Yes	Yes	Yes
	13s	Yes	Yes	Yes	Yes	Yes	Yes
	14s	Yes	No	Yes	Yes	Yes	Yes
	15s	-	No	Yes	No	Yes	Yes
	16s	-	No	-	No	No	No
8m	10s	Yes	Yes	No	Yes	No	Yes
	11s	Yes	Yes	Yes	Yes	Yes	Yes
	12s	Yes	Yes	Yes	Yes	Yes	Yes
	13s	Yes	Yes	Yes	Yes	Yes	Yes
	14s	Yes	Yes	Yes	Yes	Yes	Yes
	15s	Yes	Yes	Yes	Yes	Yes	Yes
	16s	-	No	Yes	No	Yes	No

5.13.3 Effects on green water height on deck

Apart from the effect on when green water starts, the above-water bow shape can also influence the severity of green water. This Section looks at the change in green water height on deck following changes in bow shape.

Measurements by wave probe 9 were selected for comparison based on several reasons. Firstly, wave probe 9 was located at the centreline where green water concentrated. It therefore represented the most severe event. Secondly, green water on deck comprised of two components described in Section 4.9.6, i.e. run-up water off the deck edge and water inflow due to the submergence of the bow. Being located furthest at the back, measurements of wave probe 9 were least interfered by the run-up water which could give a false sense of the actual water height on deck.

Comparison was carried out in conditions corresponding to wave height at full scale of 8m, and in two critical wave periods of 12s and 13s (equivalent to wave frequencies at model scale of 0.70Hz and 0.64Hz, respectively). The results are as in Figures 5.13.13 and 5.13.14. It could be seen that green water heights on bow 3 were consistently higher than on bows 1 and 2 for all conditions. Bow 1 appeared to be slightly better than bow 2.

The experimental results showed that neither of the bow modifications (i.e. added knuckle and extended overhang) improved the performance of the ship against green water. As the data have indicated so far, it either increased the motions (bow 2) or intensified green water problem (bow 3) without bringing in any obvious advantages.

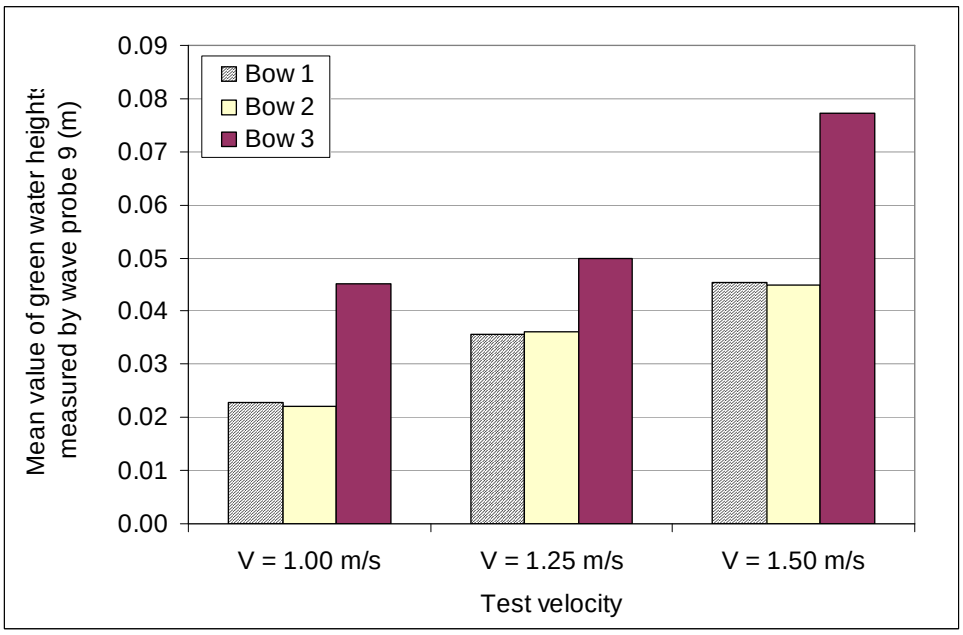

Figure 5.13.13 Effects of above water bow shape on the green water height on deck (wave frequency of 0.64Hz).

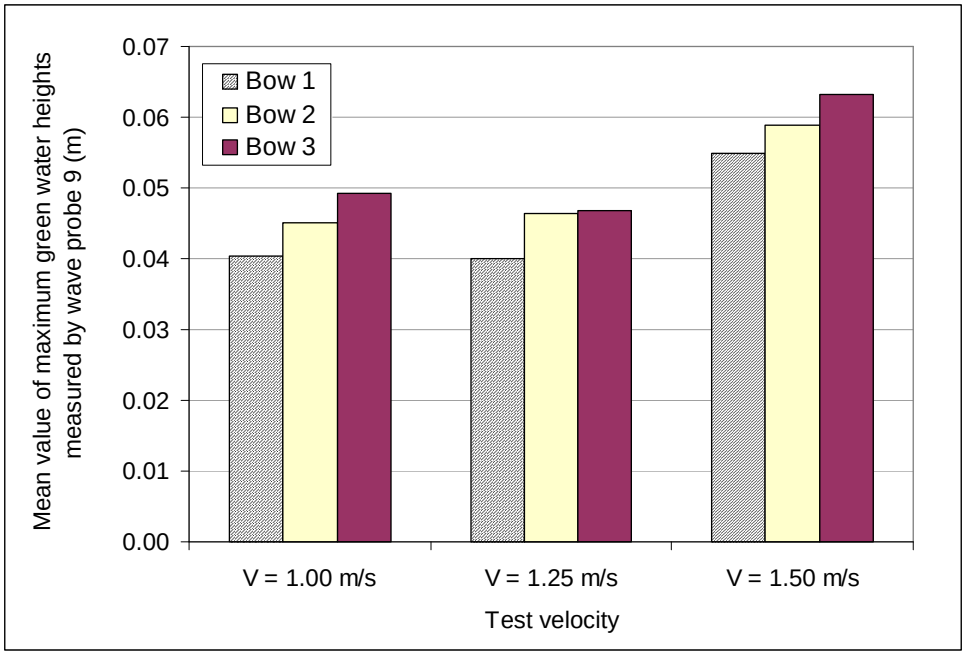

Figure 5.13.14 Effects of above water bow shape on the green water height on deck (wave frequency of 0.70Hz).

5.13.4 Effects on longitudinal green water loading

In order to obtain an overview of the effects of above-water bow shape on longitudinal green water loading, the total load measured by the vertical load-cell unit was compared between the ship bows. To get this load, component loads measured by individual vertical load cells were added together and the peak value was lifted.

For similar test conditions mentioned in Section 5.13.3, the mean values of these peak loads were compared between the three bows and the results are as in Figures 5.13.15 and 5.13.16.

Following the outcomes in Sections 5.13.2 and 5.13.3, longitudinal green water loading on the load-cell unit for bow 3 was, as expected, the largest for all conditions. The loading for bow 2, on the other hand, was smaller than for bow 1 despite the fact that green water height at wave probe 9 being slightly higher (Section 5.13.3). This implied that the green water height at wave probe 9 for bow 2 could be interfered by the splashing water or water that was shed off the deck edge.

Results shown in Figures 5.13.15 and 5.13.16 provide further evidence that the extended overhang and reduced freeboard to S175 containership hull intensified green water problem on the forecastle deck.

Despite increasing ship motions of the ship, the added knuckle appeared to help lessen green water loading on vertical surfaces.

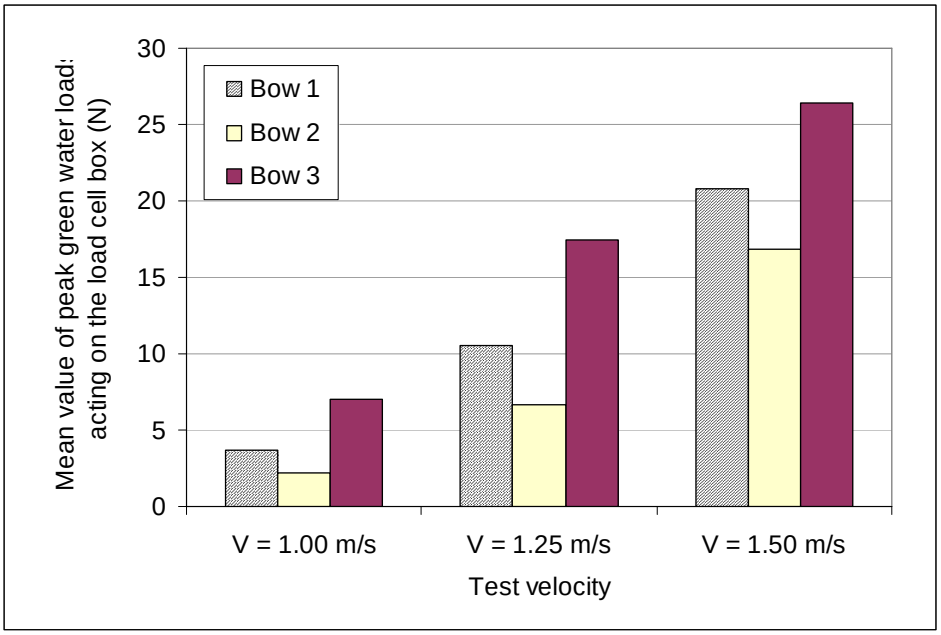

Figure 5.13.15 Effects of above water bow shape on longitudinal green water loading on load cell box (frequency = 0.64Hz).

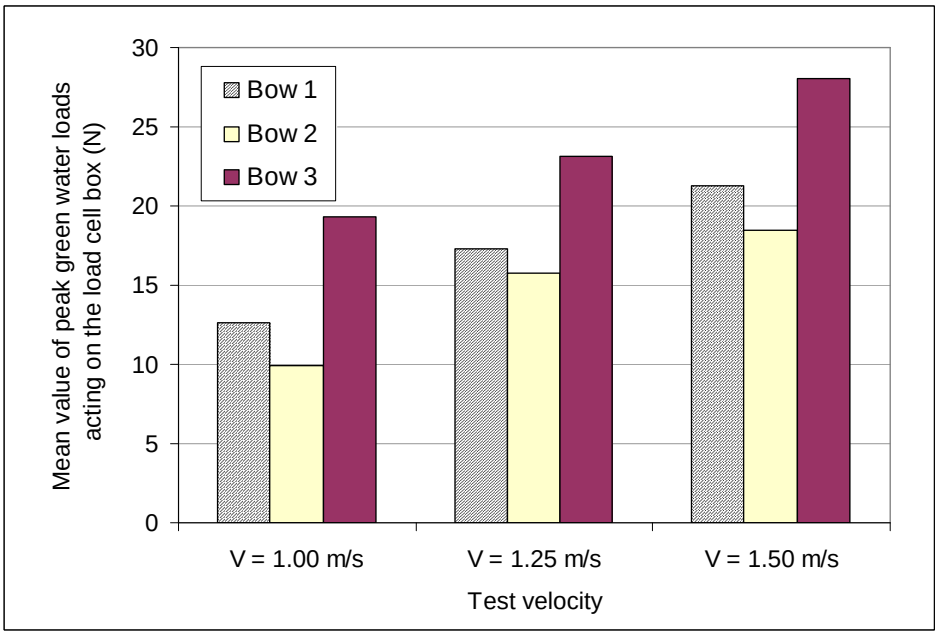

Figure 5.13.16 Effects of above water bow shape on longitudinal green water loading on load cell box (frequency = 0.70Hz).

5.13.5 Effects on vertical green water loading

Due to problems with deck load cell during the tests with bow 2, vertical green water loading or deck loading was not recorded properly in these tests. The results were, therefore, presented only for bow 1 and bow 3 as in Figures 5.13.17 and 5.13.18.

Despite the extended overhang, the reduced freeboard in bow 3 appeared to result in more water shipped on board when green water event took place (see Section 5.13.3). As a consequence, the longitudinal loading was increased (Section 5.13.4) and so was the vertical loading on deck load cell. At tested wave frequency of 0.64Hz (13s wave period at full scale), the load on deck load cell for bow 3 was consistently higher by approximately 30 percent on average. At tested wave frequency of 0.70Hz, the margin was not as large but still indicatively showed that green water deck loading for bow 3 was greater.

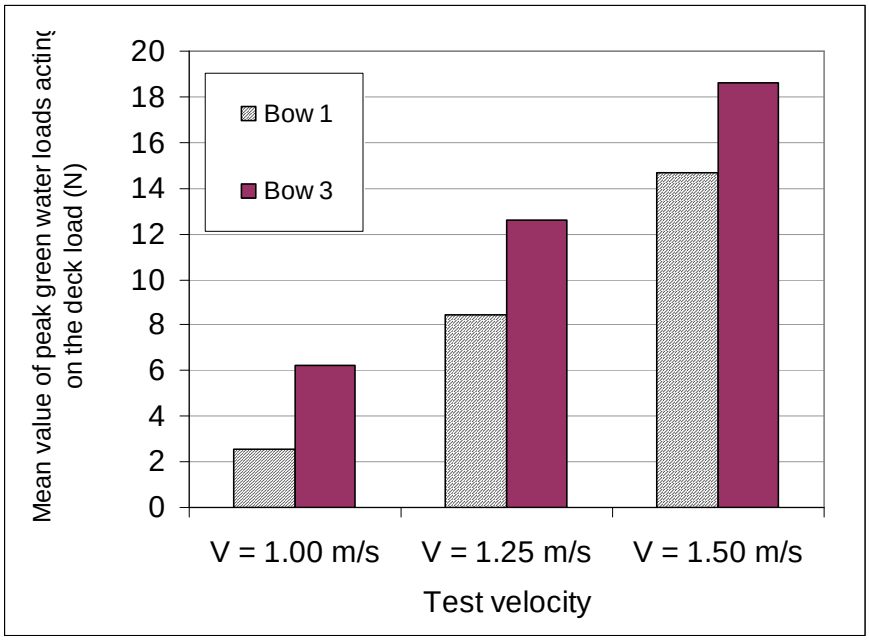

Figure 5.13.17 Effects of above water bow shape on vertical green water loading measured by deck load cell (frequency = 0.64Hz).

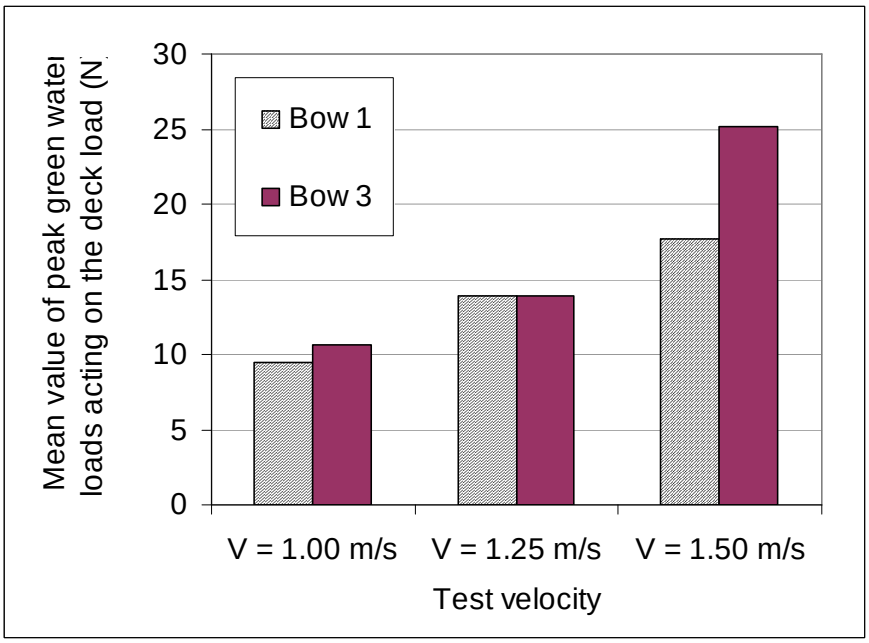

Figure 5.13.18 Effects of above water bow shape on vertical green water loading measured by deck load cell (frequency = 0.70Hz).

5.14 Repeatability

This Section aims to check the repeatability of the experiments. The repeatability of the data was evaluated based on the ratio between the standard deviation and the mean value. This ratio is referred to as repeatability index $\Re$:

$$\Re = \frac{\left[\frac{1}{n-1}\sum_{1}^{n}\left(x_i - \bar{x}\right)^2\right]^{1/2}}{\bar{x}} \tag{5.14.1}$$

where

$$\bar{x} = \frac{1}{n}\sum_{i=1}^{n} x_i \tag{5.14.2}$$

$\Re$ = 0 will indicate a perfect repeatability of the measurements. The larger the value of $\Re$, the poorer the repeatability implies.

Repeatability tests were carried out for both test series with and without breakwaters. In each case, the following data were checked for repeatability:

- Encountered wave
- Relative motion at stem head
- Green water heights on deck at wave probes 3, 6 and 9.
- Vertical green water load
- Longitudinal green water loads on load cells 2, 5 and 8.

The results are discussed in the following sub-sections.

5.14.1 Repeatability check for test series without breakwaters

A representative test run was selected and it was associated with the following test conditions:

- Wave height of 114mm which was equivalent to 8m full scale.
- Wave frequency of 0.70Hz which corresponded to wave period of 12s at full scale.
- Model ship velocity of 1.25m/s which was equivalent to Fn = 0.25 or 20.3knots at full scale.

Figures 5.14.1 to 5.14.3 plot the peak values measured by the channels listed above. The mean values, standard deviations and repeatability indices of these channels are as in Table 5.14.1. The waves were generated with good precision. As indicated by Figure 5.14.1, the measurements of relative motion (wave probe 1), and water heights on deck at wave probes 3 and 9 were also relatively consistent with the repeatability indices of around 5 percent. The water height at wave probe 6 appeared to be most affected by the water splashing. As a result, its measurement shows some scattering behaviour with a repeatability index of nearly 10 percent.

Due to the complicated interaction between the water and the load cell surfaces, the measurements of green water loads appear to be more scattered. The repeatability indices of load cells 5, 8 and deck load cell were all greater than 10 percent but less than 20 percent.

By comparing the standard deviations of the wave probes and load cells with the standard deviation of the encountered wave, it can be seen how sensitive green water event could be to changes in test conditions. With the test velocities and wave frequencies being well controlled, the only external changes appeared to be

in the wave amplitude. A variation of within 3 percent of wave amplitude resulted in up to nearly 20 percent change in green water loads.

On overall, given the complicated nature of the tests and the violent interactions between water and solid surfaces, the repeatability of the experiments was considered reasonable.

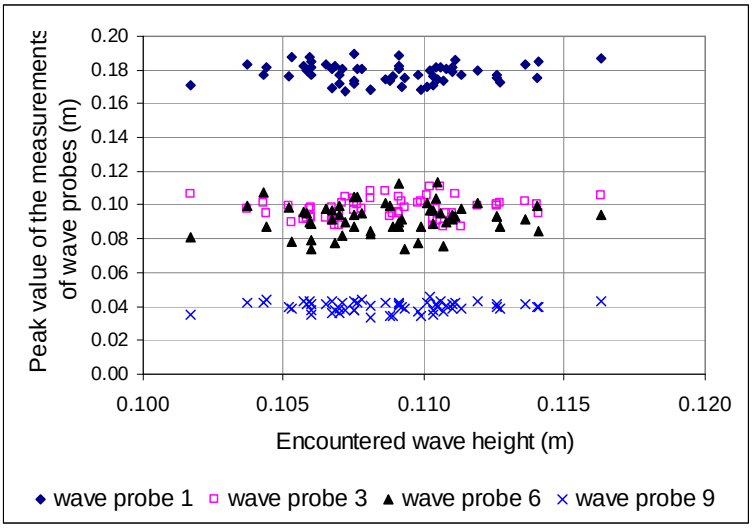

Figure 5.14.1 Repeatability of the wave probe measurements.

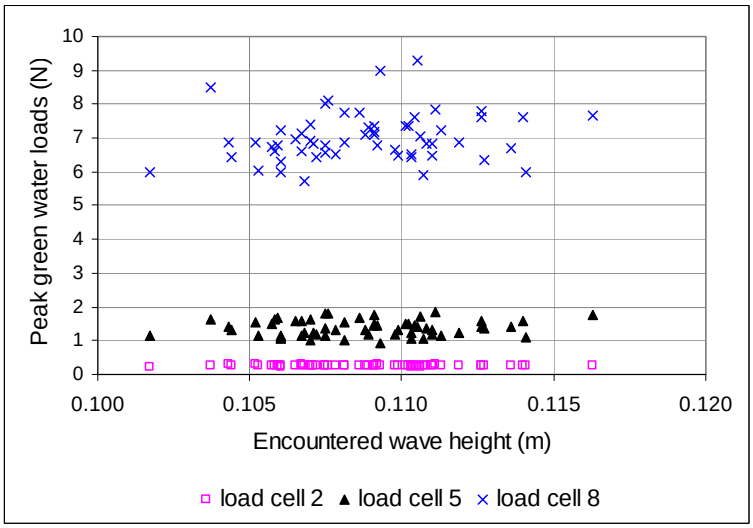

Figure 5.14.2 Repeatability of the vertical load cell measurements.

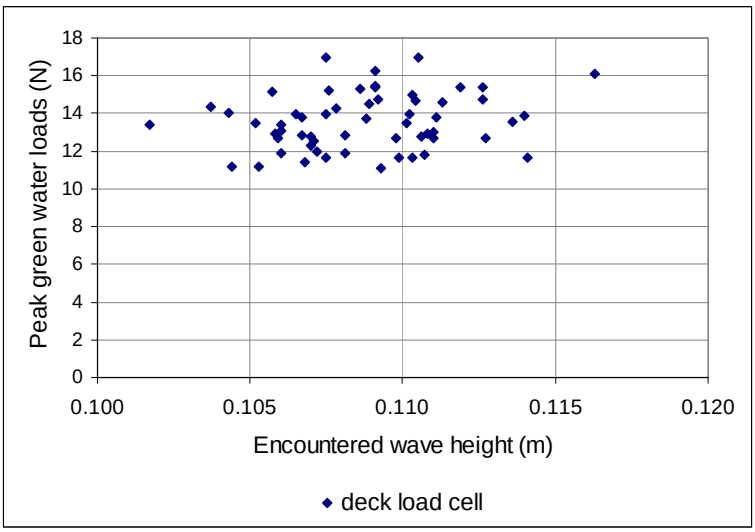

Figure 5.14.3 Repeatability of the deck load cell measurement.

Table 5.14.1 Repeatability indices of selected test measurements.

	Mean value	**Standard deviation**	**Repeatability index**
Encountered wave	0.109m	0.003m	2.63%
Wave probe 1	0.178m	0.006m	3.16%
Wave probe 3	0.098m	0.006m	6.19%
Wave probe 6	0.092m	0.009m	9.75%
Wave probe 9	0.040m	0.003m	7.37%
Deck load cell	13.561N	1.483N	10.94%
Load cell 2	0.266N	0.015N	5.75%
Load cell 5	1.377N	0.236N	17.17%
Load cell 8	7.017N	0.716N	10.21%

5.14.2 Repeatability check for case of green water shipment in large quantities

The selected test run for repeatability check in this case was associated with the following test conditions:

- Wave height of 114mm which was equivalent to 8m full scale.
- Wave frequency of 0.70Hz which corresponded to wave period of 12s at full scale.
- Model ship velocity of 1.50m/s which was equivalent to Fn = 0.30 or 24.4knots at full scale.
- Breakwater height of 51mm with perforation diameter of 10.5mm.

The peak values of the measurements listed for checking are plotted in Figures 5.14.3 to 5.14.6. Their mean values, standard deviation and repeatability indices are as in Table 5.14.2. In general, the measurements of the wave probes were relatively consistent, having repeatability indices around 5 percent. Wave probe 9, however, appeared to be affected by the water splashing instead of wave probe 6 as in Section 5.14.1. Note that the test velocity was higher than that in Section 5.14.1 and this could be the reason.

With the perforated breakwater present on deck, the interaction between green water and deck structures became further complicated due to serial impacts. Figures 5.14.5 and 5.14.6 show scattering behaviour of the load cells. Their repeatability indices were between 10 percent and 25 percent. As explained in Section 5.12.3, green water loads on load cell 8 were dominated by the impact with the water that went through the perforations. The repeatability of load cell 8 was, therefore, relatively better than load cells 2 and 5. The loads on load cells 2 and 5 were comprised of the impact with water that overcame the breakwater and the pressure due to water running up the load-cell unit. Since both green water loads resulted from secondary interactions after the primary impact between green

water and breakwater, their behaviours became more random and scattering as seen.

However, with all the indices below 25 percent, the repeatability could be seen as reasonable.

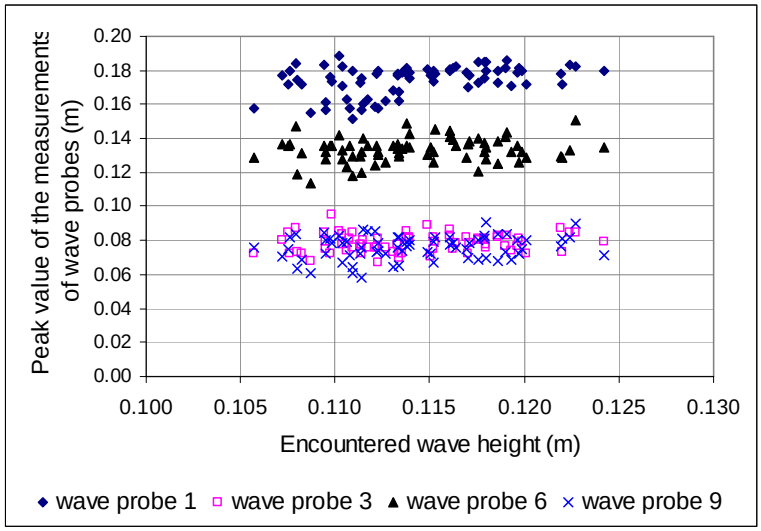

Figure 5.14.4 Repeatability of the wave probe measurements.

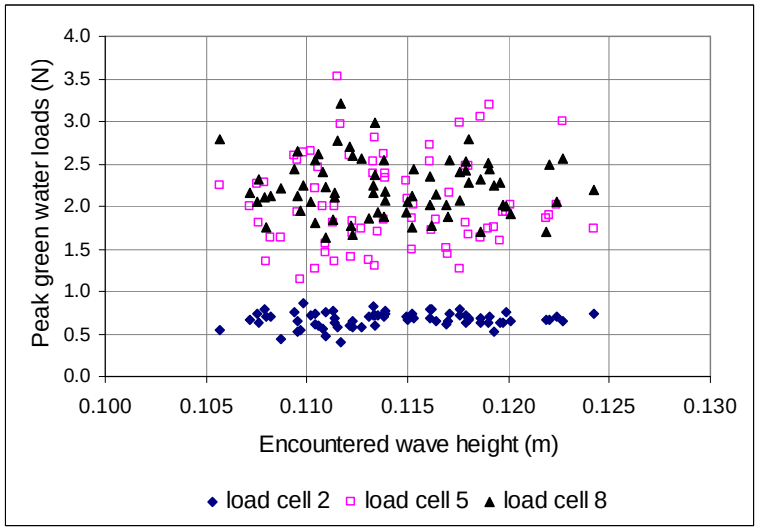

Figure 5.14.5 Repeatability of the vertical load cell measurements.

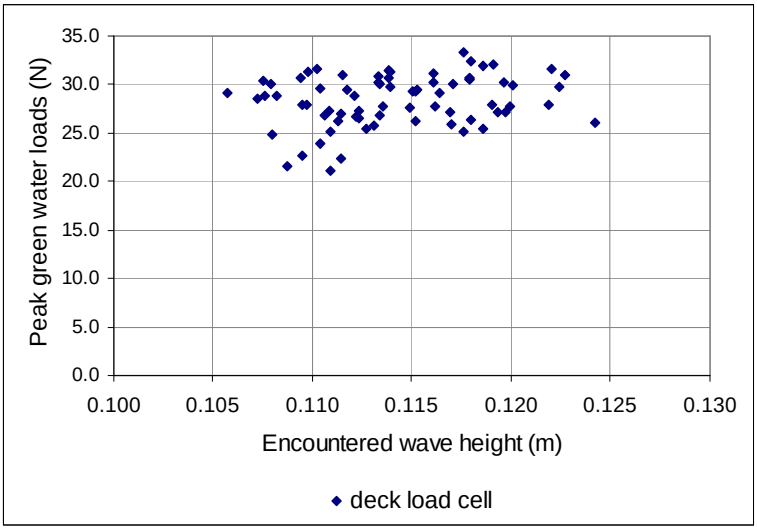

Figure 5.14.6 Repeatability of the deck load cell measurement.

Table 5.14.2 Repeatability indices of selected test measurements.

	Mean value	Standard deviation	Repeatability index
Encountered wave	0.114m	0.004m	3.80%
Wave probe 1	0.174m	0.009m	5.08%
Wave probe 3	0.079m	0.005m	6.87%
Wave probe 6	0.133m	0.007m	5.30%
Wave probe 9	0.076m	0.007m	9.30%
Deck load cell	28.349N	2.639N	9.31%
Load cell 2	0.669N	0.087N	12.98%
Load cell 5	2.049N	0.525N	25.64%
Load cell 8	2.218N	0.333N	14.99%

5.15 Summary

This Chapter has presented the experimental data obtained from green water tests carried out at the Centre for Hydrodynamics, Universities of Glasgow and Strathclyde. All the data related to the development of green water were shown. Later, the behaviour of green water on deck was evaluated and a hydraulic model that could best represent green water flow was configured. Based on the experimental data, effects of breakwaters on green water loading were discussed. The influence of the above water bow features was also evaluated on both ship motions and green water behaviour. Prediction of the occurrence of green water using method by Crossland and Johnson (1998) was found matching relatively well with experimental results. Finally, the repeatability of the experiments was investigated which showed reasonable behaviour. Green water problem was found to be a highly complex process which could be sensitive to small changes in the external conditions.

The next objective is to find a suitable modelling environment to simulate green water flow on deck and to test the hydraulic model that was configured in Section 5.11.

Chapter 6:
CFD Numerical Model Development

6.1 Introduction

As discussed in Chapter 5, green water is a highly complex process. To model this properly, a powerful modelling tool is needed so that the complicated interaction between green water flow and deck structures can be correctly reproduced.

There have been several approaches in dealing with green water simulation. One of such approaches was via Lagrangian technique in which the hydrodynamic properties of specific masses of fluid are tracked and updated during the simulation. The method is very popular in geophysics and has achieved successes in simulating the shifting of particulate substances like soil and gravel. In the piloting research, Pham et al. (2003b) tested this method in simulating the dam-break model and the model of a water jet striking a vertical wall. Even though the gross characteristics of the flows were found reasonable, the method showed difficulties in reproducing hydrodynamic properties of the water, impact loading and subtle interactions with solid surfaces. The tracking of multiple water masses/volumes also appeared to be very expensive in computation, especially for 3D simulation. Extensive efforts in improving the method and adapting it to hydrodynamic problems can also be found in the works of Gesteria et al. (2003), Iglesias et al. (2004) and Koshizuka and Shibata (2005). However, the results were still limited to the qualitative assessment of the problems. With lack of validation, this approach, therefore, has not proved to be a comprehensive tool for modelling complex hydrodynamic problems such as green water.

The second approach is based on Computational Fluid Dynamics (CFD) and Volume of Fluid (VOF) technique as in Chapter 2. CFD is based on Eulerian

approach to find the properties of fluid inside predefined volumes in space. The method has been used by various researchers for evaluation of green water problem. Validation was also carried out and the results have been found to agree fairly well (Pham and Varyani, 2004, 2005, 2006a, 2006b). Following Sections describe the numerical process, benchmark modelling and validation.

6.2 Governing equations

For incompressible, invicid flow, the governing equations are simplified to:

$$\left.\begin{aligned}
&\frac{\partial u}{\partial x}+\frac{\partial v}{\partial y}+\frac{\partial w}{\partial z}=0\\
&\frac{\partial(\rho u)}{\partial t}+\nabla.(\rho u\mathbf{V})=-\frac{\partial p}{\partial x}+\rho f_x\\
&\frac{\partial(\rho v)}{\partial t}+\nabla.(\rho v\mathbf{V})=-\frac{\partial p}{\partial y}+\rho f_y\\
&\frac{\partial(\rho w)}{\partial t}+\nabla.(\rho w\mathbf{V})=-\frac{\partial p}{\partial z}+\rho f_z
\end{aligned}\right\} \qquad (6.2.1)$$

Detail of the derivation of these equations is referred to Appendix A which is part of the work by Anderson (1995).

6.4 Solutions of the differential equations

Even in simplified form, analytical solutions to incompressible and inviscid flow are impossible. Numerical solutions are therefore developed to provide an estimate as close to the actual solutions as possible.

6.4.1 Integration and discretisation

As mentioned above, the Finite Volume Method (FVM) divides the domain into a large number of infinitesimally small fluid cells or control volumes. This process is normally termed '*grid/mesh generation*' and is performed in a pre-processing program such as **Gambit** for **Fluent** processor. **Fluent 5** processor is selected for simulation in this research.

Fluent 5 (ANSYS Inc., 2006) uses a control-volume-based technique to convert the governing equations to algebraic equations that can be solved numerically. This control volume technique consists of integrating the governing equations about each control volume, yielding discrete equations that conserve each quantity on a control-volume basis.

Fluent 5 stores discrete values of the scalar quantities (like pressure and velocity, etc.) at the cell centres. However, face values are required for the convection terms and must be interpolated from the cell centre values. This is accomplished using a differencing scheme. With regard to differencing scheme, Anderson (1995) noted that equations to *incompressible* flow problem are derived based on equations for *compressible* flow problem and this may lead to the thought that differencing scheme to solve for solutions to the former can also be used to deal with the latter. However, the difference stays in the fact that the Mach's number of compressible fluid is finite whilst that of incompressible fluid approaches infinite in theory. This makes differencing schemes such as central differencing (which works well for compressible flow problem) become highly unstable and

convergence time consuming when applied to incompressible flow. To address this issue, upwind differencing scheme is developed (and it is included in **Fluent 5**) to deal with incompressible flow problems. Upwinding means that the face value is derived from quantities in the cell upstream, or "upwind," relative to the direction of the normal velocity. There were several upwind schemes for use, i.e. first-order upwind, second-order upwind, power law, and QUICK (Quadratic Upwind Interpolation of Convective Kinematics).

6.4.1.1 First order upwind scheme

When first-order accuracy is desired, quantities at cell faces are determined by assuming that the cell-centre values of any field variable represent a cell-average value and hold throughout the entire cell; the face quantities are identical to the cell quantities. Thus when first-order upwinding is selected, the face value is set equal to the cell-centre value in the upstream cell.

6.4.1.2 Second order upwind scheme

When second-order accuracy is desired, quantities at cell faces are computed using a multidimensional linear reconstruction approach. In this approach, higher-order accuracy is achieved at cell faces through a Taylor series expansion of the cell-centred solution about the cell centroid.

6.4.1.3 Quadratic Upwind Interpolation of Convective Kinematics (QUICK)

QUICK scheme is only applicable to quadrilateral and hexahedral meshes where unique upstream and downstream faces and cells can be identified. It is based on a weighted average of second-order-upwind and central interpolations of the variable. The QUICK scheme is typically more accurate on structured grids aligned with the flow direction. However, due to the complexity of the simulation model in this research, the grid was hybrid and it was found during the simulation

process that the use of QUICK scheme led to high instability. The QUICK scheme was therefore not used in the simulation for this thesis.

6.4.1.4 Pressure interpolation scheme

The default scheme in **Fluent 5** interpolates the pressure values at the faces using momentum equation coefficients. This procedure works well as long as the pressure variation between cell centres is smooth. When there are jumps or large gradients in the momentum source terms between control volumes, the pressure profile has a high gradient at the cell face, and cannot be interpolated using this scheme. If this scheme is used, the discrepancy shows up in overshoots/undershoots of cell velocity.

Flows for which the standard pressure interpolation scheme will have trouble include flows with large body forces, such as in strongly swirling flows, in high-Rayleigh-number natural convection and the like. In such cases, it is necessary to pack the mesh in regions of high gradient to resolve the pressure variation adequately.

Another source of error is that **Fluent 5** assumes that the normal pressure gradient at the wall is zero. This is valid for boundary layers, but not in the presence of body forces or curvature. Again, the failure to correctly account for the wall pressure gradient is manifested in velocity vectors pointing in/out of walls.

Several alternate methods are available for cases in which the standard pressure interpolation scheme is not valid:

- The linear scheme computes the face pressure as the average of the pressure values in the adjacent cells.

- The second-order scheme reconstructs the face pressure in the manner used for second-order accurate convection terms (see Section 6.4.1.2 for Second-Order Upwind Scheme). This scheme may provide some improvement over the standard and linear schemes, but it may have some trouble if it is used at the start of a calculation and/or with a bad mesh.

- The body-force-weighted scheme computes the face pressure by assuming that the normal gradient of the difference between pressure and body forces is constant. This works well if the body forces are known a priori in the momentum equations. When large body forces (e.g., gravity or surface tension forces) exist in multiphase flows, the body force and pressure gradient terms in the momentum equation are almost in equilibrium, with the contributions of convective and viscous terms small in comparison. Segregated algorithms converge poorly unless partial equilibrium of pressure gradient and body forces is taken into account. **Fluent 5** provides an optional "implicit body force" treatment that can account for this effect, making the solution more robust.

- The PRESTO! (PREssure STaggering Option) scheme uses the discrete continuity balance for a "staggered" control volume about the face to compute the "staggered" (i.e., face) pressure. However, the PRESTO! scheme is available only for quadrilateral and hexahedral meshes. For a hybrid grid that was developed in this simulation, PRESTO! was not valid to use.

Fluent 5 suggested that for problems involving large body forces, the body-force-weighted scheme was recommended. The second-order scheme was recommended for compressible flows which was not the case for this simulation.

6.4.1.5 Pressure-velocity coupling method

Fluent 5 provides the option to choose among three pressure-velocity coupling algorithms:

- Semi-Implicit Method for Pressure-Linked Equations (SIMPLE)
- SIMPLEC (SIMPLE-Consistent)
- Pressure-Implicit with Splitting of Operators (PISO)

Steady-state calculations will generally use SIMPLE or SIMPLEC, while PISO is recommended for transient calculations. PISO may also be useful for steady-state and transient calculations on highly skewed meshes.

The Pressure-Implicit with Splitting of Operators (PISO) pressure-velocity coupling scheme is based on the higher degree of the approximate relation between the corrections for pressure and velocity. One of the limitations of the SIMPLE and SIMPLEC algorithms is that new velocities and corresponding fluxes do not satisfy the momentum balance after the pressure-correction equation is solved. As a result, the calculation must be repeated until the balance is satisfied. To improve the efficiency of this calculation, the PISO algorithm performs two additional corrections: neighbour correction and skewness correction.

The main idea of the PISO algorithm is to move the repeated calculations required by SIMPLE and SIMPLEC inside the solution stage of the pressure-correction equation. After one or more additional PISO loops, the corrected velocities satisfy the continuity and momentum equations more closely. This iterative process is called a momentum correction or "neighbour correction". The PISO algorithm takes a little more CPU time per solver iteration, but it can dramatically decrease the number of iterations required for convergence, especially for transient problems.

For meshes with some degree of skewness, the approximate relationship between the correction of mass flux at the cell face and the difference of the pressure corrections at the adjacent cells is very rough. Since the components of the pressure-correction gradient along the cell faces are not known in advance, an iterative process similar to the PISO neighbour correction described above is desirable. After the initial solution of the pressure-correction equation, the pressure-correction gradient is recalculated and used to update the mass flux corrections. This process, which is referred to as "skewness correction", significantly reduces convergence difficulties associated with highly distorted meshes. The PISO skewness correction allows **Fluent 5** to obtain a solution on a highly skewed mesh in approximately the same number of iterations as required for a more orthogonal mesh. For these merits, PISO algorithm was used for the pressure-velocity coupling method.

6.4.2 Boundary conditions

In order to come up with a unique solution of the conservation equations, the domain boundaries are to be defined. In general, there are two types of boundary conditions that are popular in use, i.e. Dirichlet and Neumann. Dirichlet condition specifies the value of the function on a surface; for example, pressure at free surface is equal to ambient pressure. Neumann condition specifies the value of the normal derivative of the function on a surface; for example, for wall boundary to an incompressible flow, the normal derivative of pressure is equal to zero. To set up the modelling, appropriate boundary conditions are to be specified at the beginning. Details of the boundary conditions set up for the simulations in this research are described in Chapter 7.

6.4.3 Solutions of linear equation system

The **Fluent 5** solver uses a segregated solution algorithm with implicit formulation to solve Reynolds-Averaged Navier-Stokes equations for time-dependent solutions of momentum and hence loading on interested surfaces. Using this approach, the governing equations are solved sequentially (i.e., segregated from one another). Because the governing equations are non-linear (and coupled), several iterations of the solution loop must be performed before a converged solution is obtained. Each iteration goes through steps illustrated in Figure 6.4.1 and outlined below:

1. Fluid properties are updated, based on the current solution. (If the calculation has just begun, the fluid properties will be updated based on the initialised solution.).

2. The **u**, **v**, and **w** momentum equations are each solved in turn using current values for pressure and face mass fluxes, in order to update the velocity field.

3. Since the velocities obtained in Step 1 may not satisfy the continuity equation locally, a "Poisson-type" equation for the pressure correction is derived from the continuity equation and the linearised momentum equations. This pressure correction equation is then solved to obtain the necessary corrections to the pressure and velocity fields and the face mass fluxes such that continuity is satisfied.

4. A check for convergence of the equation set is made.

These steps are continued until the convergence criteria are met.

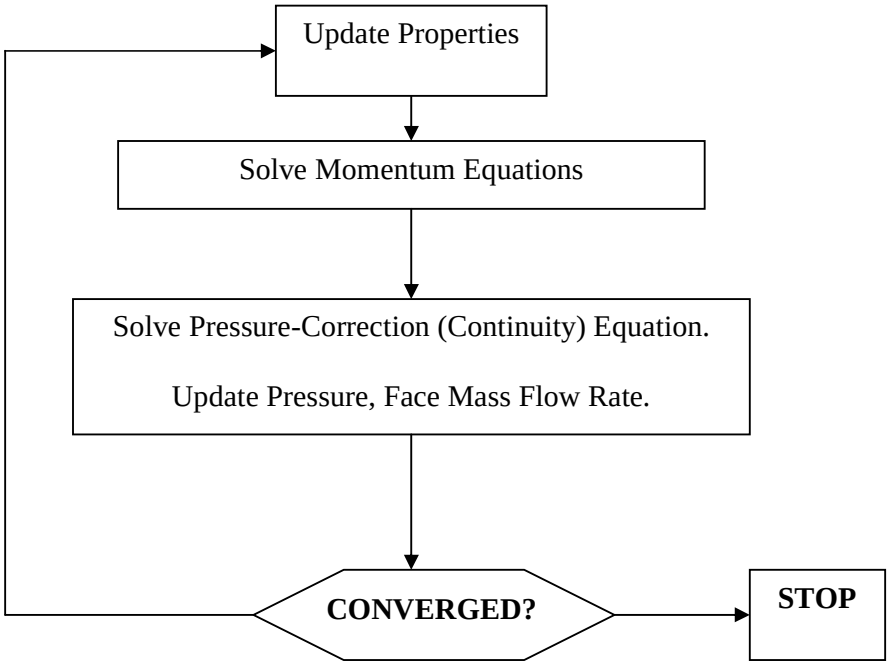

Figure 6.4.1 Overview of the segregated solution method.

6.5 Free surface modelling

In the simulation of problem such as green water, there is an interface between different fluids (water and air in this case). Due to severe interaction between green water and solid structures, this interface is expected to change dramatically during the course of the simulation. In general, there are two methods for dealing with free surface or fluid interfaces in CFD, namely, surface tracking and surface capturing.

The surface tracking method is essentially an explicit representation of the surface. In other words, the grid is adapted to the free surface and it is updated at every time step to track the new location of the free surface by means of a height function that describes the new elevation of the free surface. The limitation of surface tracking is in the fact that it is unable to deal with complex surface geometries and overturning waves due to the problems of the nodes getting

clustered and entangled, etc. This automatically sidelines the surface tracking technique from modelling green water problem because of the severity involved.

Surface capturing method is a different approach and there are several techniques available in CFD applications. **Fluent 5** adopts the Volume of Fluid (VOF) technique which involves a scalar that indicates the filling level of a cell. This scalar field is integrated in time by solving a transport equation.

6.5.1 VOF concepts

In **Fluent 5** the standard interpolation schemes are used to obtain the face fluxes whenever a cell is completely filled with one phase or another. When the cell is near the interface between two phases, the geometric reconstruction scheme is used.

The geometric reconstruction scheme represents the interface between fluids using a piecewise-linear approach. It is generalized for unstructured meshes. It assumes that the interface between two fluids has a linear slope within each cell, and uses this linear shape for calculation of the advection of fluid through the cell faces. The first step in this reconstruction scheme is calculating the position of the linear interface relative to the centre of each partially-filled cell, based on information about the volume fraction and its derivatives in the cell. The second step is calculating the advecting amount of fluid through each face using the computed linear interface representation and information about the normal and tangential velocity distribution on the face. The third step is calculating the volume fraction in each cell using the balance of fluxes calculated during the previous step.

6.6 Benchmark problems

Despite having a sound mathematical foundation, simulation results by CFD processor or **Fluent 5** solver in this project are to be verified via benchmark studies. Successful benchmark validations will certainly give confidence of upgrading the simulation towards dealing with more complex problems.

Two benchmark problems are considered relevant to this project. The first problem is the classic dam-break problem. In many researches such as Buchner (2002), green water on deck has been described to resemble a dam-break problem. The second problem is the water entry of a wedge section. This problem is relevant to the evaluation of green water problem because it features a substantial interaction between fluid and solid structure. The resulting fluid surface becomes very complex and overturning waves can be developed as in the case for green water. If **Fluent 5** is found to model these problems well, there will be a clear suggestion that it is also able to model green water problem.

6.6.1 Dam-break problem confined in a tank

6.6.1.1 Introduction

The dam-break problem is well known in civil engineering. As its name suggests, it describes the problem of a collapsed dam leading to outflow of water that was held by the dam before. Due to its importance in civil engineering as well as its resemblance to other engineering problems, the dam-break problem has been the topic of numerous researches both theoretically and experimentally. Details of the mathematical model of the dam-break model can be found in Stoker (1957). Out of many experimental investigations in dam-break, experimental data by Zhou et al. (1999) will be used for validation purposes.

6.6.1.2 Experimental setup

To describe the experiments carried out by Zhou et al. (1999), Figure 6.6.1 sketches the set up that was constructed by Zhou et al. (1999). Locations H1, H2 and H3 were positions at which the water heights were monitored. P2, P3 and P4 were three pressure transducers mounted on the impact plate to record the pressures at these locations during the experiment. Before the test, the reservoir was filled with a water head of 600mm. To start the experiment, the flap was lifted at high speed and water was allowed to crash out into the flow area.

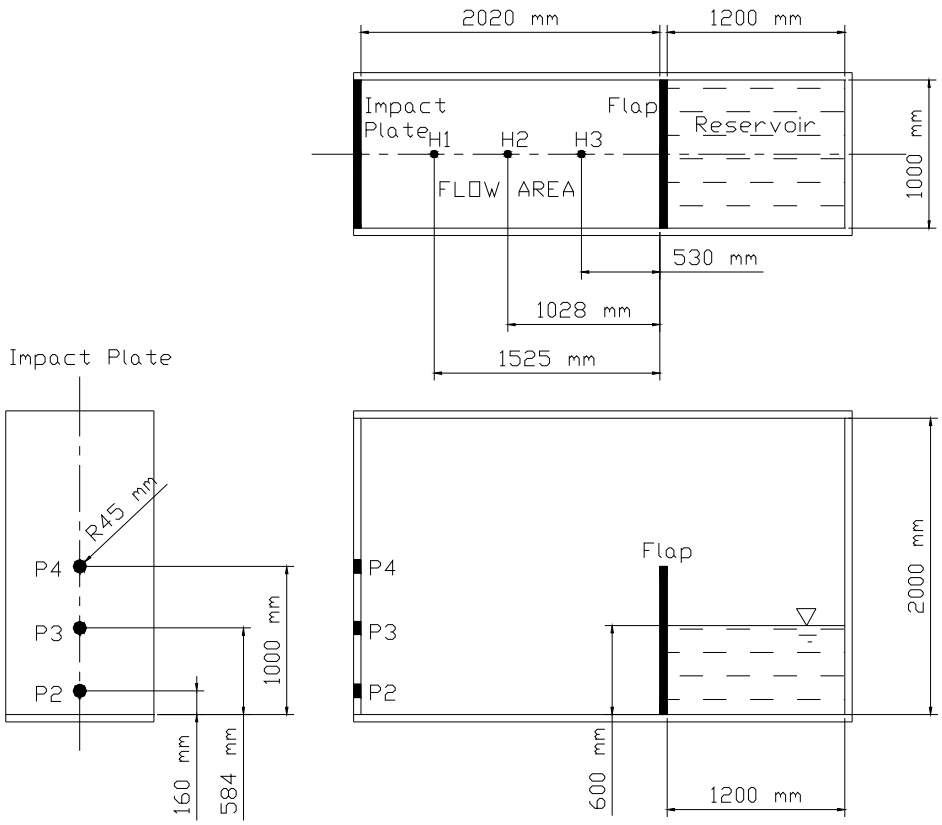

Figure 6.6.1 Dam-break experiment setup by Zhou et al. (1999).

6.6.1.3 CFD modelling setup

The dam-break experiment by Zhou et al. (1999) was modelled in the mesh generator **Gambit** and later solved in **Fluent 5** solver. Due to the scale of the experiment, it was thought suitable to simulate the problem in 2D so that the grid can be refined to give better results. A domain of similar dimensions was constructed and the boundaries were defined as in Figure 6.6.2. All the confining boundaries were defined as non-slip walls at which the incident fluid flow will be totally reflected. Viscosity is neglected in this problem so no boundary layer was included. Initial mass of water was contained at the start by two walls at the bottom and at the back and two internal boundaries. These internal boundaries were 'virtual' and were used only to define the shape of the water mass prior to simulation. When the simulation commenced, these internal boundaries did not interfere with the translation of the water whatsoever. The rest of the space was filled with air. Note also that three small walls were created on the left hand side to represent three pressure transducers P2, P3 and P4. Three small walls were also modelled corresponding to three positions H1, H2 and H3. The static pressure on these walls gave the water heights at these locations.

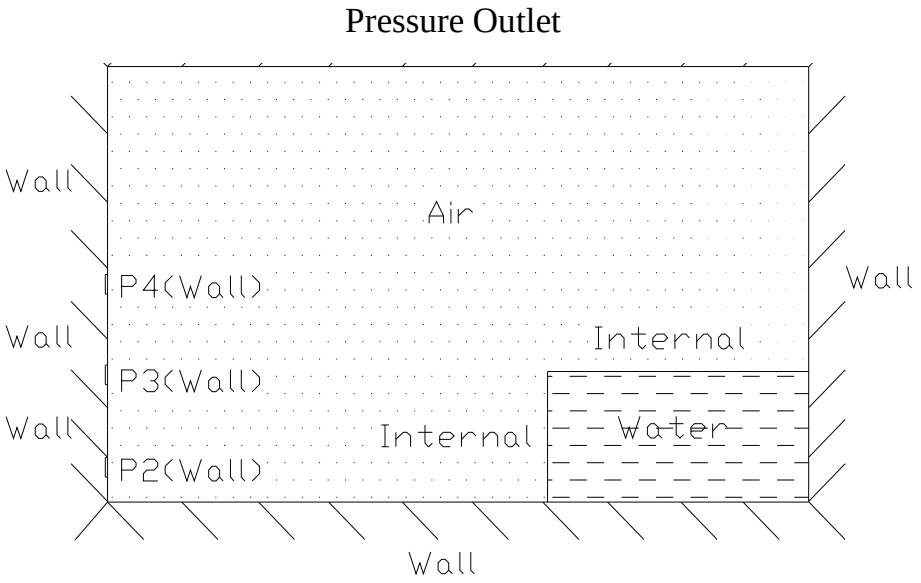

Figure 6.6.2 Boundary definition in modelling of dam-break problem.

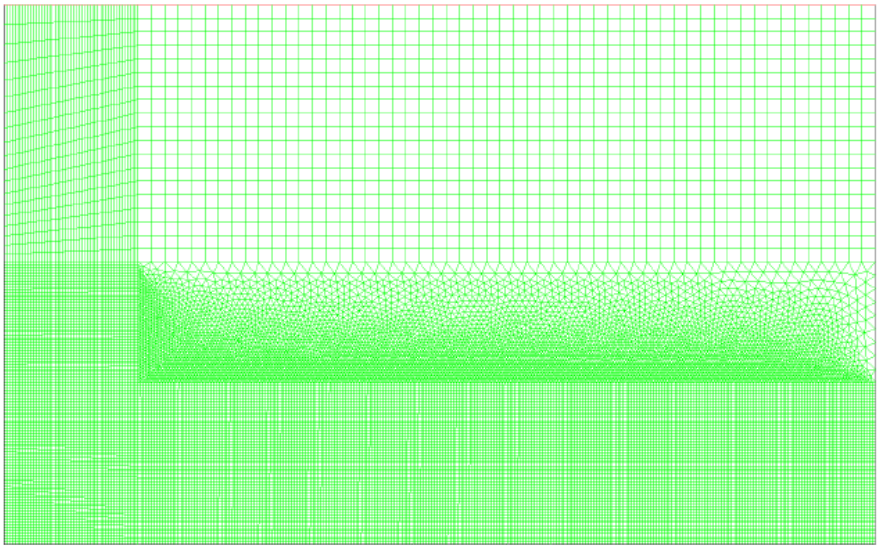

Figure 6.6.3 Grid of the dam-break model.

The structured grid was then generated following the boundary-fitted co-ordinate system. Note that the accuracy and numerical stability of the simulation are largely dependent on the quality of the grid. If the grid is coarse, the representation of the problem will be poor and so are the numerical results. On the other hand, if the grid is too dense, excessive computational effort will be required, sometimes, unnecessarily. An optimal grid can only be obtained via parametric studies or assessment of discretisation error. The common practice to optimise the grid generation is to construct dense clusters of cells at critical areas where the interaction is most active. The density of cell is then reduced toward areas where interaction is less active. The grid for the dam-break simulation is as in Figure 6.6.3.

The constructed grid with defined boundaries was then exported to **Fluent 5** solver for processing. **Fluent 5** offers two solvers, namely, coupled solver and segregated solver. The former is coded for high-speed compressible applications and the latter for incompressible lower speed flows. For multiphase problems, segregated solver is the only option and it was used for this modelling.

6.6.1.4 Numerical results and validation

Figure 6.6.4 shows the visualisation of the water during the simulation. As noticed, after impact with the left wall, the behaviour of water became very complex with overturning waves and subsequent sloshing of water.

The limited released data meant that the comparison of numerical results with experimental data could only be made for pressure at P2 and the water height at H1. There was a fair agreement between the two sets of data as shown in Figures 6.6.5 to 6.6.7. Note that in their report, Zhou et al. (1999) stated that the experiment data were relatively scattering. In fact, they used hydrostatic pressure to compare with the experimental data which made the type of pressure transducers they were using questionable. In order to measure the high-frequency impact load, a high-frequency load cell or pressure transducer should be used. Figure 6.6.8 shows the simulation results of the total pressure at P2. Recalling equation (5.9.2) in Section 5.9, peak impact load by a water jet against a vertical surface can be approximated by $P = C\rho u^2$. In this formula, u is the velocity of the front water. In the case of dam-break problem, if taking u as the velocity of the water particles at P2, the following formula is given by Stoker (1957):

$$u = \frac{2}{3}\left(\frac{x}{t} + \sqrt{g.H_0}\right) \tag{6.6.1}$$

where x = 2.02m is the distance of P2 from the dam, H_0 = 0.6m is the initial water height behind the dam. The time t taken for water to reach the height of P2 can be approximated from Figure 6.6.8 at the peak pressure (t = 0.71s). The value of u can then be estimated as:

$$u = \frac{2}{3}\left(\frac{2.02}{0.71} + \sqrt{9.81 \times 0.6}\right) = 3.51(m/s) \tag{6.6.2}$$

Substituting this value into equation (5.9.2) and using C = 1.4 as suggested by Suhara et al. (1973), the peak impact pressure is:

$$P = 1.4 \times 1000 \frac{kg}{m^3} \times \left(3.51 \frac{m}{s} \right)^2 \approx 17.25 kPa \qquad (6.6.3)$$

Comparing this with the peak value of 9.135 kPa in Figure 6.6.8, the use of C = 1.4 is relatively conservative as noted in Section 5.9.

If using C = 0.88 as derived from experimental data shown in Section 5.9, the peak value estimated by equation (5.9.2) becomes 10.7 kPa which correlates with numerical result.

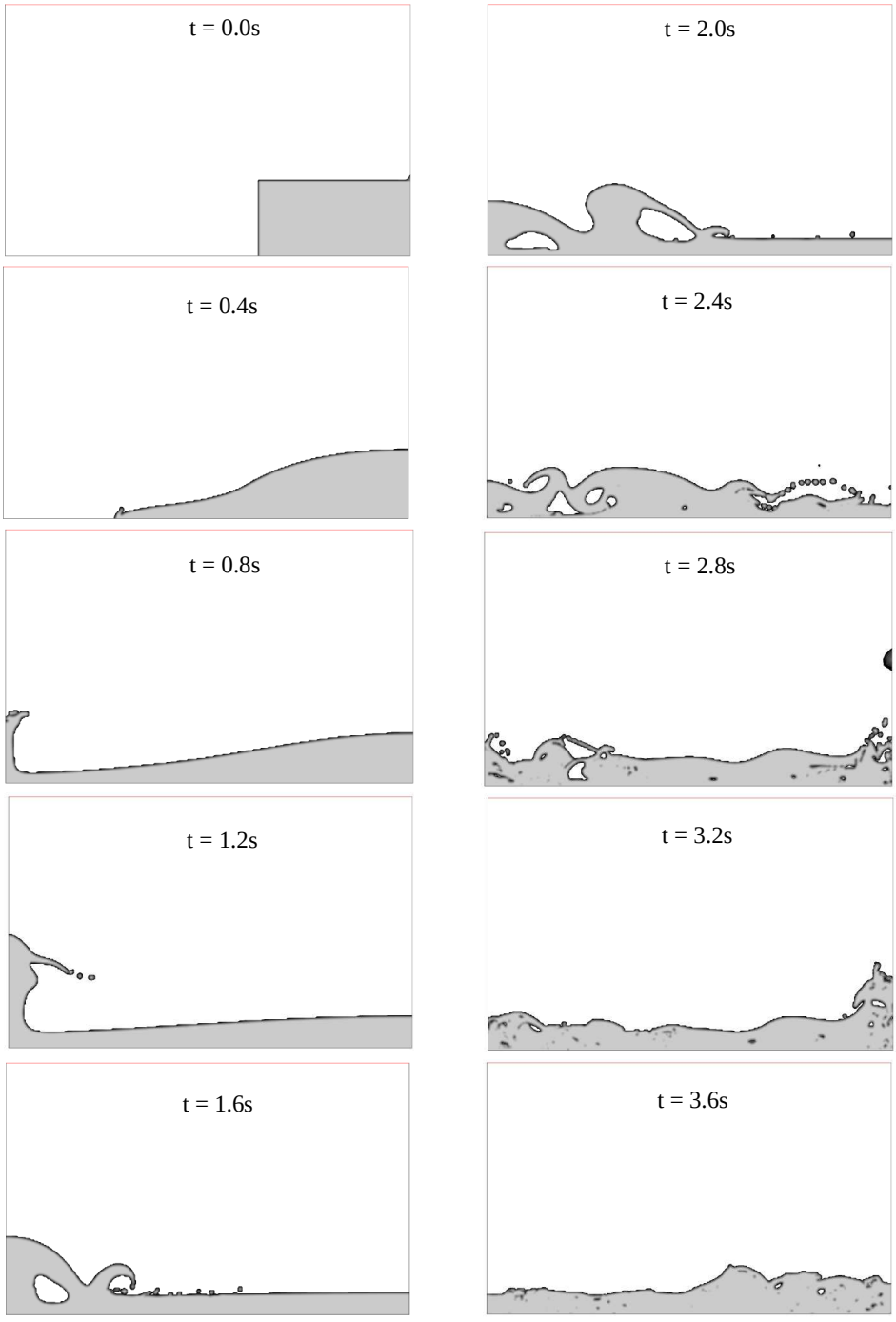

Figure 6.6.4 Visualisation of the dam-break simulation.

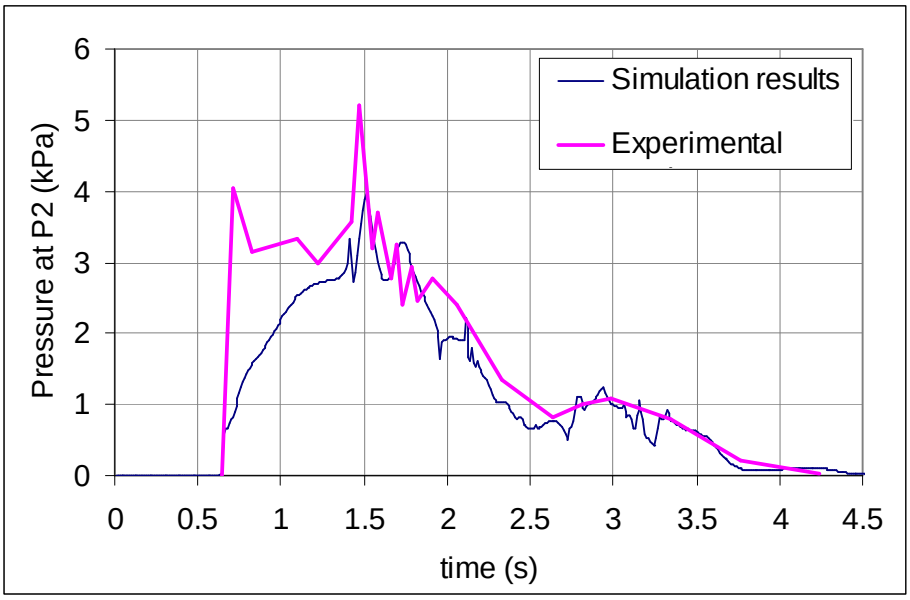

Figure 6.6.5 Comparison of pressures at P2.

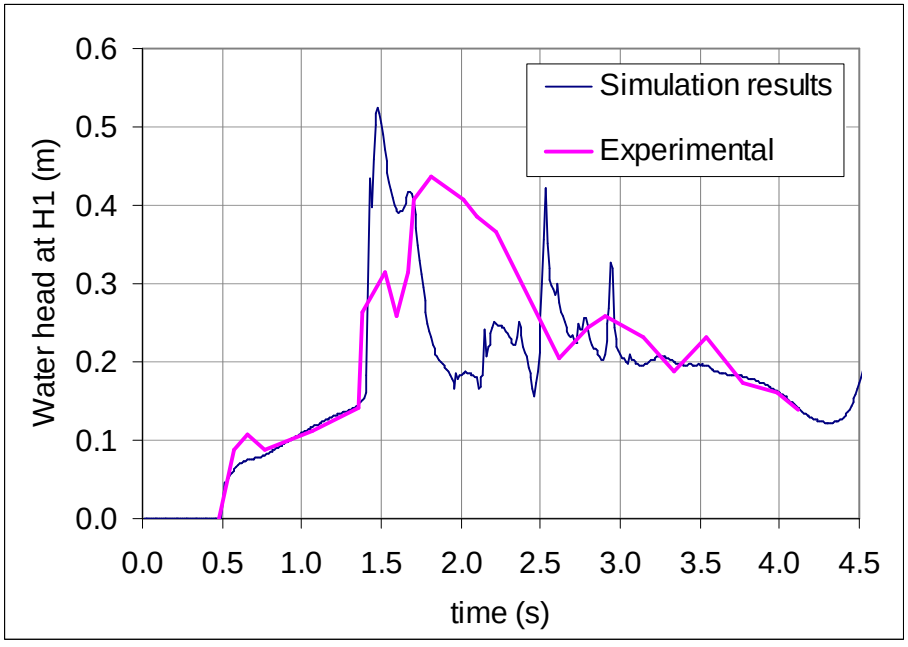

Figure 6.6.6 Comparison of water heads at H1.

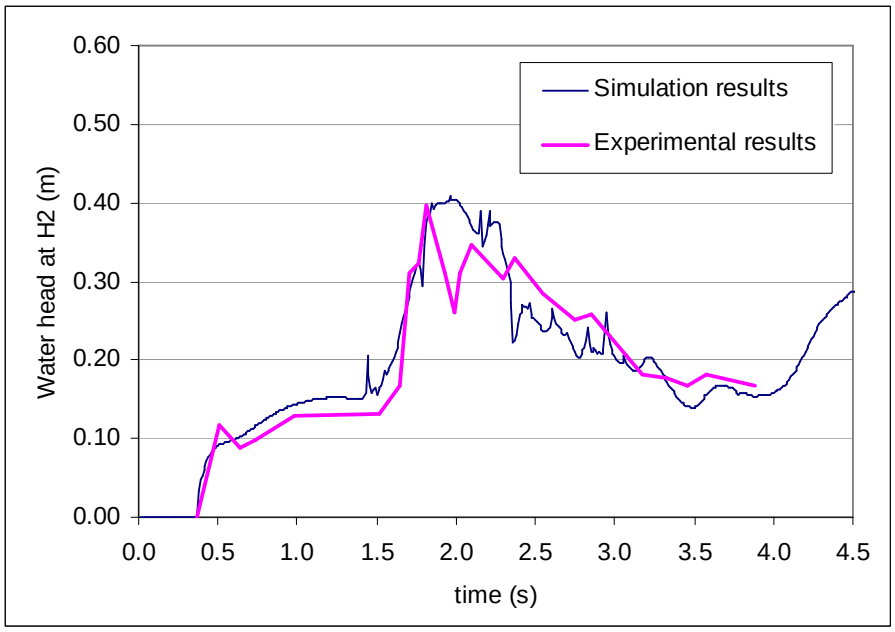

Figure 6.6.7 Comparison of water heads at H2.

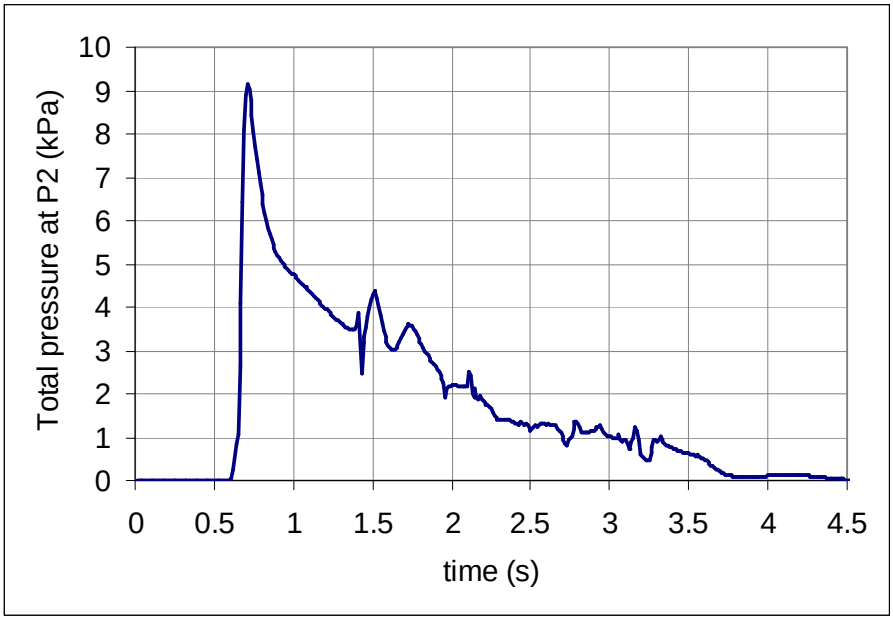

Figure 6.6.8 Total pressure at P2.

6.6.2 Water entry of a wedge section

6.6.2.1 Introduction

The water entry of a wedge section is another approach to understand the hydrodynamics of a planing craft travelling at high speed or slamming in general. Overturning waves normally occur in that case and the loading is a high-frequency impact. To simplify this slamming, the problem is modelled as a 2D wedge section intruding the water at some velocity. No gravity effect is accounted for. Only hydrodynamic force is considered.

Water entry of a wedge-section and green water shares the complication in their hydrodynamics which involves complex interaction between water flow and solid structures. A successful representation of the former will certainly develop confidence in modelling green water problem with CFD. This section looks at the modelling of the water entry of a wedge-section using **Fluent 5** and the validation of the simulation results with experimental data by Tveitnes (2001).

6.6.2.2 Experimental setup

The detailed experimental setup is referred to the thesis by Tveitnes (2001). This section only describes in brief the mechanism which was applied to carry out the experiment. As seen in Figure 6.6.9, the test section was attached to a model carrier via load sensors. The model carrier was, in turn, connected to a guide and drive combo system. A pair of vertical guide shafts were used to ensure linear motion of the structure. Each of these shafts ran through two guide bearings that were attached to an A-frame support structure. A servo-motor was installed to drive the structure vertically up and down via rotating the threaded shaft. The rotational speed was calibrated to obtain the desired axial velocities for testing.

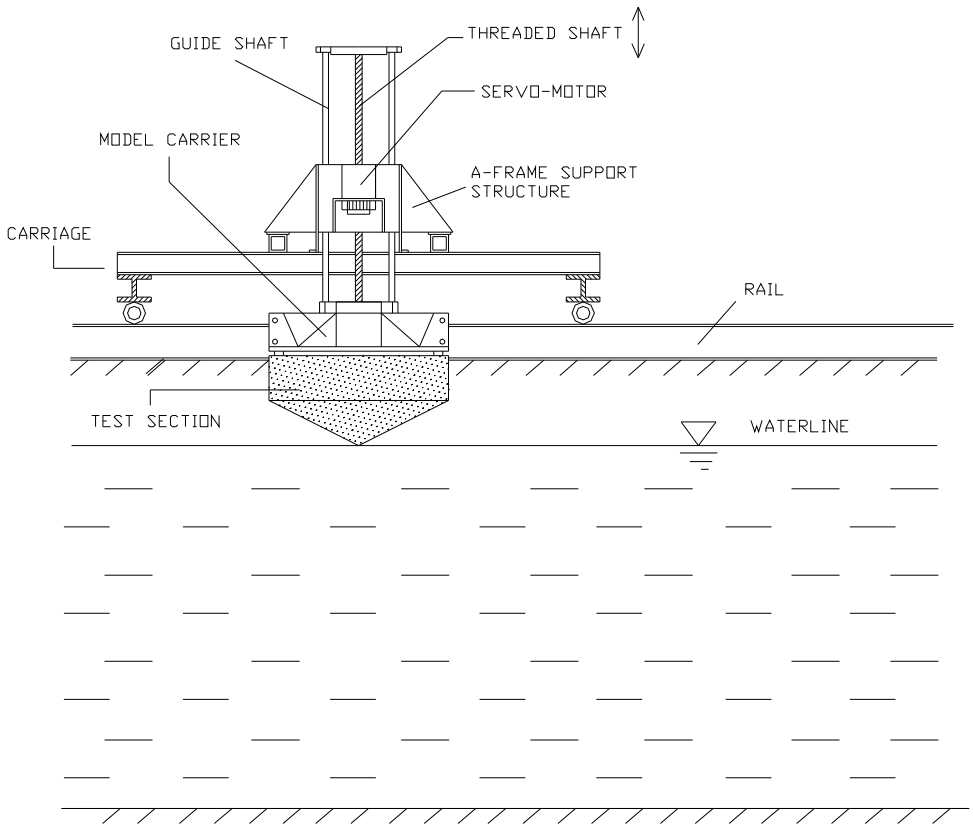

Figure 6.6.9 Experimental setup of water entry of a wedge section (Tveitnes, 2001).

To capture the disturbance of the water surface in the test, a video camera was used. All the control and data acquisition units were located on a separate carriage to reduce noise. The wedge entered water at a constant velocity.

6.6.2.3 CFD modelling setup

Figure 6.6.10 defines setup and the boundary conditions of the model as it was constructed in the mesh generator **Gambit**. Dimensions of the sample test section are as in Figure 6.6.11. The structured grid is illustrated in Figure 6.6.12. Note that elements were clustered around the area where interaction between water and test

section was most active. Further away, pressure gradients were not varying as much, the grid could be coarser so that the simulation could be optimised in terms of computational time. The completed mesh was exported to **Fluent 5** solver for processing.

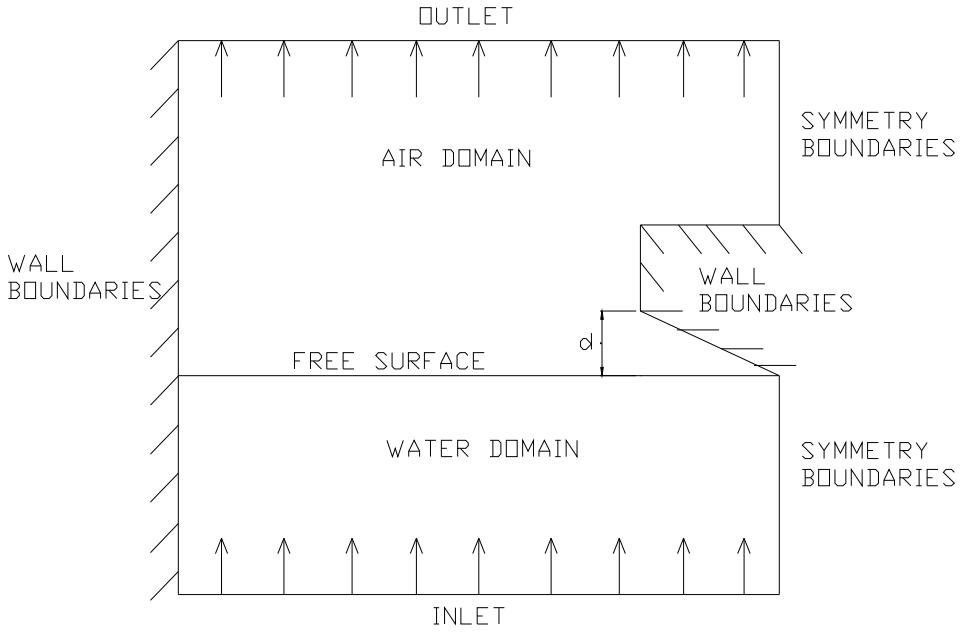

Figure 6.6.10 Boundary definition of the water entry of a wedge section problem.

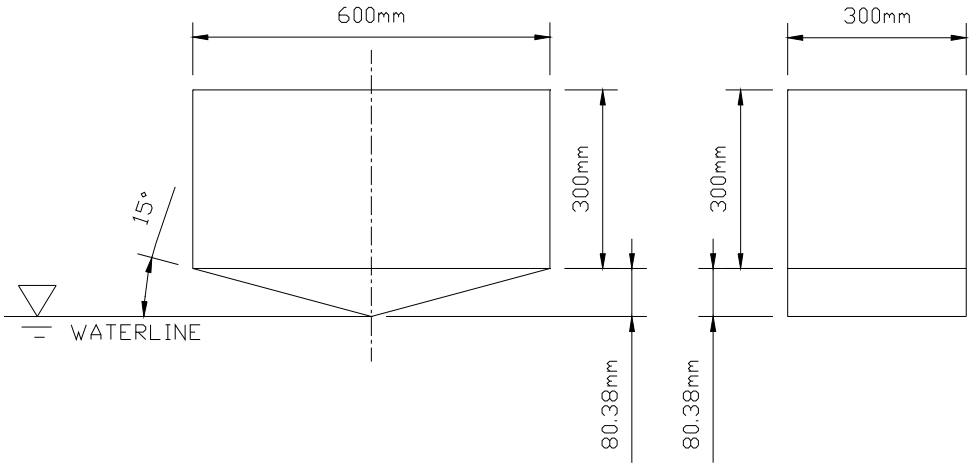

Figure 6.6.11 Dimensions of wedge section tested (Tveitnes, 2001).

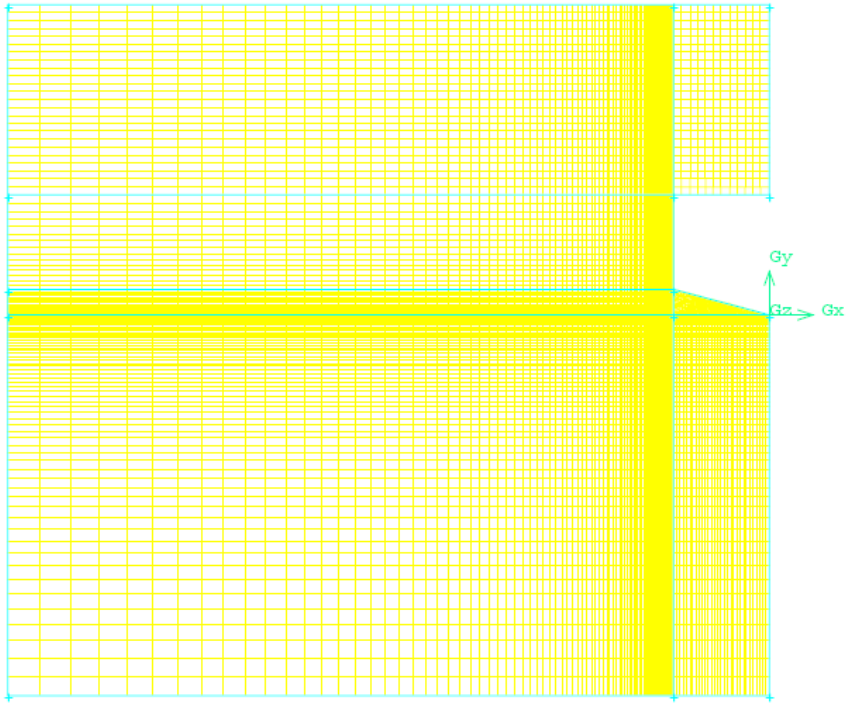

Figure 6.6.12 Grid of water-entry simulation.

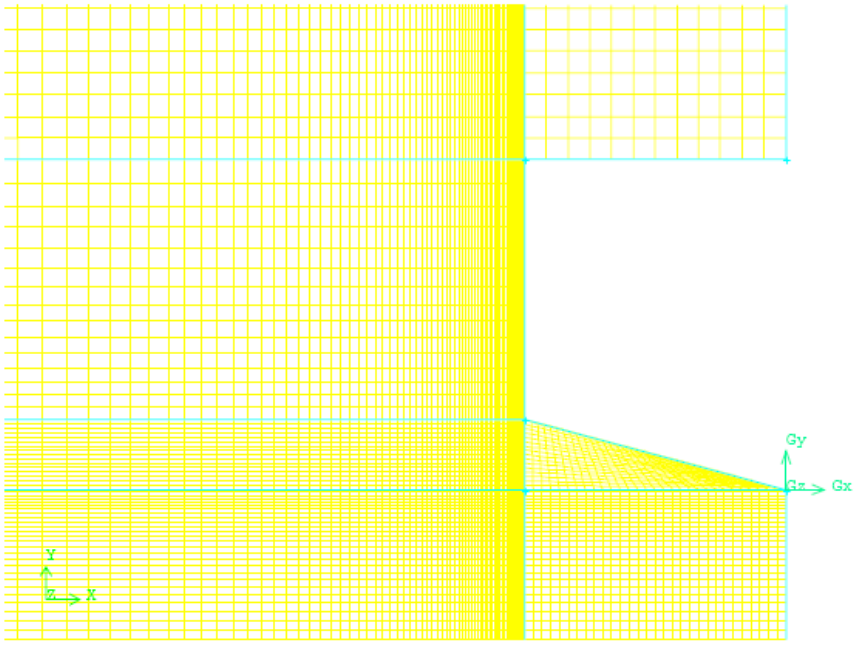

Figure 6.6.13 Enlarged view of grid around ship section of water-entry simulation.

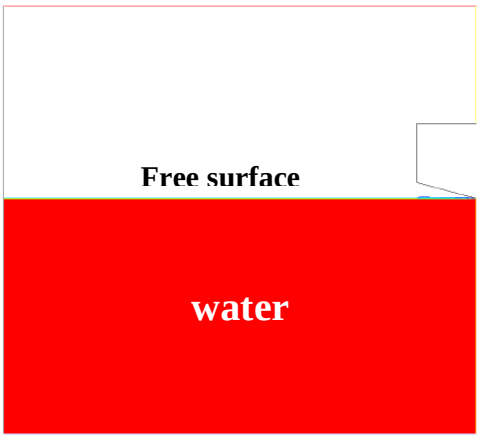

Figure 6.6.14 Capture of initial setup of water-entry simulation.

6.6.2.4 Numerical results and validation

The initial state before the simulation began is as in Figure 6.6.14. Figure 6.6.16 shows the visualisation of the interaction between water and wedge section during simulation. In this case, severe slamming led to a jet of water to be created and shed away.

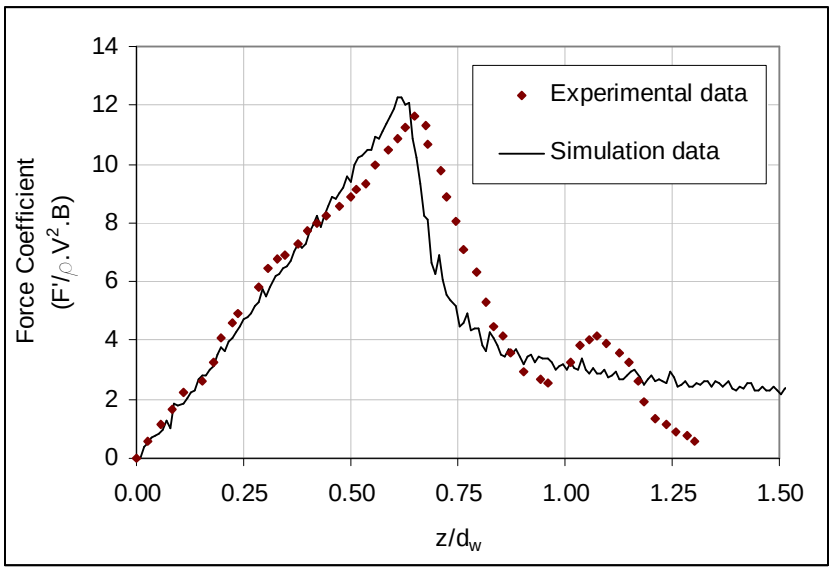

Figure 6.6.15 Comparison of impact force acting on bottom plating of a water-entry wedge (water-entry velocity of 0.72 m/s).

In terms of loading, Figure 6.6.15 shows the numerical results compared with experimental data by Tveitnes (2001). As seen, there is a fairly good correlation between the two sets of data.

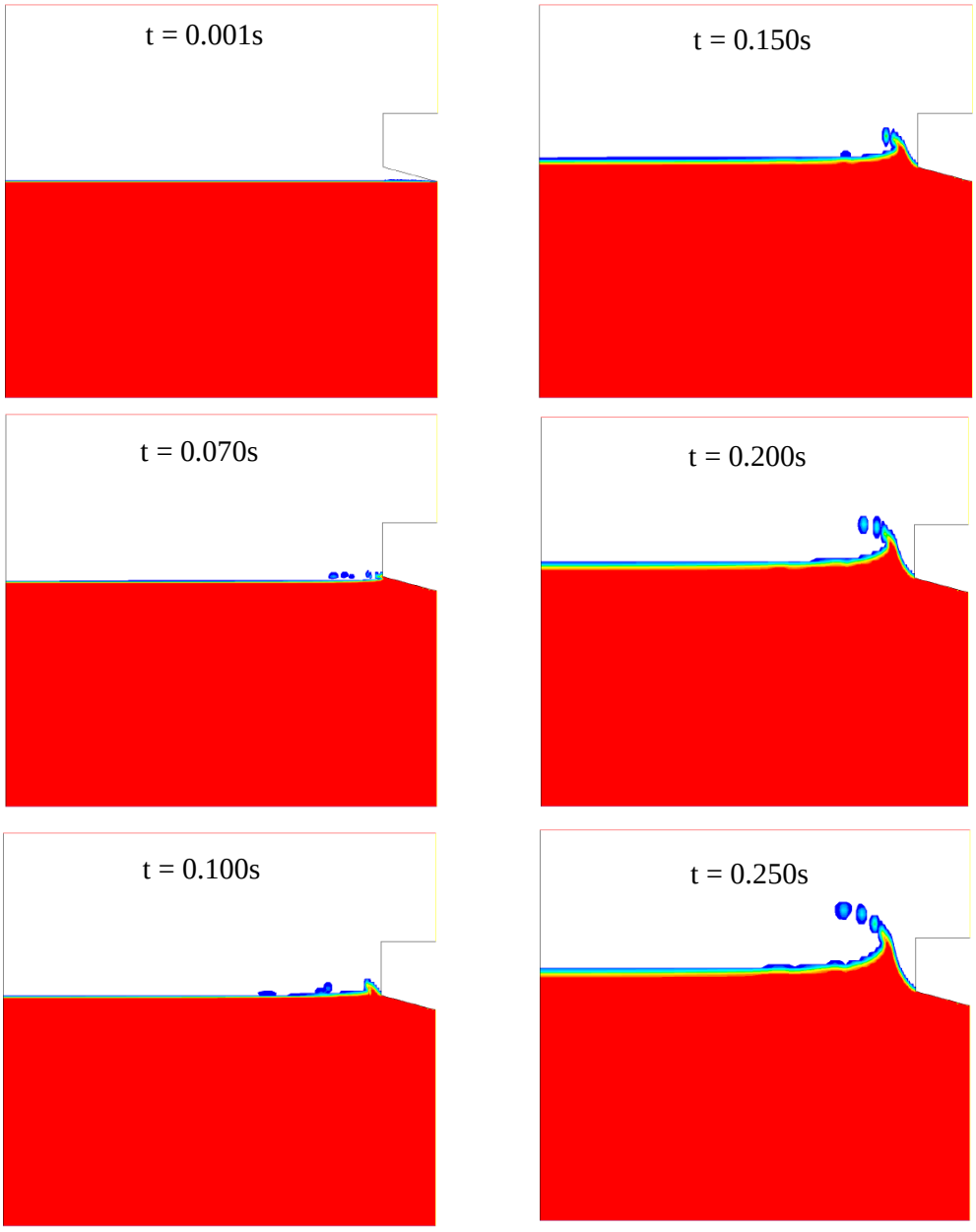

Figure 6.6.16 Snapshots of interaction between water and wedge structure during the water-entry of the wedge section at the velocity of 0.72 m/s.

6.7 Summary

Chapter 6 has presented a theoretical background on which the CFD is built on. In order to prove that CFD was suitable for simulating green water flow, two benchmark problems of similar characteristics were evaluated. The first problem was the dam-break model and the second problem was the water entry of a 2D wedge section. In both cases, the CFD modelling setup was explained and numerical results were compared with published experimental results. The correlation was fairly good for both the dam-break model and water entry of a 2D wedge section. Based on this outcome, it can be interpreted that CFD is capable of simulating hydrodynamic problems of complex nature such as green water.

Chapter 7:
Numerical Prediction of Green Water Flow on Deck Using CFD

7.1 Introduction

Based on the outcomes of Chapters 5 and 6, this Chapter expands on the setup of the hydraulic model to represent green water flow on deck. The general theory of the dam-break model is briefly introduced. Since the ship has a forward velocity, some modification is then needed to account for this parameter. The setup process begins with a 2D model for simplification. It is later extended to 3D in which all the geometrical parameters that define green water mass are explained. Steps leading to the start of simulation are elaborated.

7.2 Hydrodynamic models for green water flow

7.2.1 Dam-break model

As discussed in earlier Chapters, from the analysis of green water problem of FPSO's, Buchner (2002) reported that green water flow on deck could be well simulated by a dam-break model. Stoker (1957) described in details the theory of dam-break problem based on the assumptions that the problem was similar to a shallow water wave. If initially at time t = 0 seconds, the dam water height is denoted as H_0 metres, the water height H at a distance x downstream at time t > 0 seconds (Figure 7.2.1) is:

$$H(x,t) = \left\{ \frac{2}{3}\sqrt{H_0} - \frac{x}{3\sqrt{g}.t} \right\}^2 \qquad (7.2.1)$$

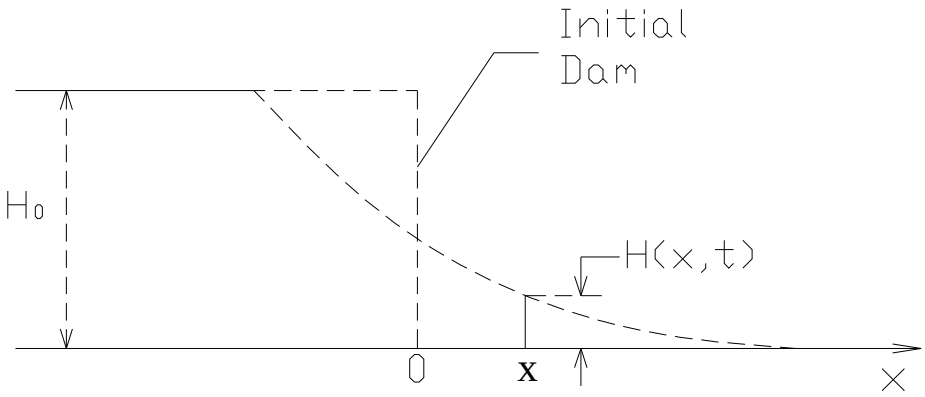

Figure 7.2.1 Illustration of the theoretical dam-break model.

Buchner (2002) used green water height measured at stem head as the effective green water height on deck. The longitudinal distance x in equation (7.2.1) would be close to zero and therefore, the initial water head of the imaginary dam would be:

$$H_0 = \frac{9}{4} H_{stem\_head} \tag{7.2.2}$$

The green water downstream can also be approximated from the velocity of the water particles in the flow, which is given by Stoker (1957) as:

$$u = \frac{2}{3}\left\{\frac{x}{t} + \sqrt{g.H_0}\right\} \tag{7.2.3}$$

Buchner (2002) stated that since dam-break flow resembles a shallow water wave, the velocity distribution over the height of the flow at one point is considered to be constant. It means that velocity given by (7.2.3) can be seen as the horizontal velocity of the flow at time t and position x over the complete height H of the flow at this position (Figure 7.2.2). By rearranging equation (7.2.3), it can be obtained:

$$\frac{x}{t} = \frac{3}{2}u - \sqrt{g.H_0} \tag{7.2.4}$$

Also, rearranging (7.2.1) gives:

$$\frac{x}{t} = 2\sqrt{g.H_0} - 3\sqrt{g.H} \tag{7.2.5}$$

Equating (7.2.5) to (7.2.4) and rearranging the terms, it gives:

$$u = 2\sqrt{g}\left(\sqrt{H_0} - \sqrt{H}\right) \tag{7.2.6}$$

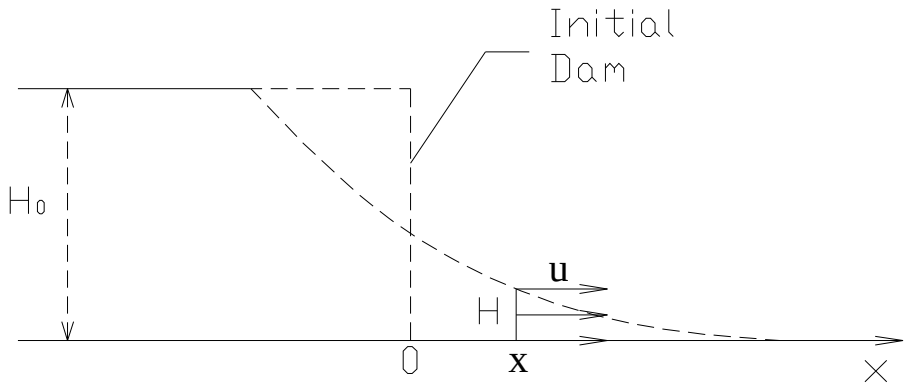

Figure 7.2.2 Distribution of particle velocity of water flow in dam break model at a fixed location (Buchner, 2002).

Equations (7.2.1) to (7.2.6) are the fundamental equations of a dam-break model. In the case when ship is travelling with a velocity, these equations are subject to changes which are discussed in the next section.

7.2.2 Dam-break model with initial velocity

FPSO's are stationary during operation whilst containerships have forward velocities. If green water occurs, there will be a relative velocity between the ship and the water shipment. If the velocity is assumed constant during the time the shipment of water takes place, a person standing on the forecastle deck would see the water moving in at a velocity equal to ship velocity. If the ship was modelled as a fixed object, green water could resemble a dam-break model with an initial velocity equal to ship velocity.

7.3 Setup of 3D simulation of green water flow

7.3.1 Introduction

In order to simplify the explanation of the setup of a 3D simulation of green water flow, a 2D setup is first described. It is then extended into 3D at later stage.

7.3.2 Set up of two-dimensional (2D) simulation of green water flow

7.3.2.1 Water mass profile

The water height of the dam can be calculated by equation (7.2.2). In the theoretical dam break problem, the water mass behind the dam is infinite. In green water problem, only a limited volume of water was shipped onto the deck. Therefore, the water mass behind the dam needs to be configured. From the approximated profile of green water on deck derived in Section 5.11, the water mass behind the dam can be assumed to take a simplified shape of a trapezoid ABCD in Figure 7.3.1. The height AD is the initial water height behind the dam H_0. Important parameters to be configured are the top edge AB and the bottom edge CD.

In Section 5.6, it was pointed out that before green water event occurs, the water front was pushed backwards due to the ship pitching into the water. Angle ADC in Figure 7.3.1 should, as a result, be less than 90 degrees. Note that as the ship pitches into the water, the run-up water is shed away tangentially to the flare. Edge AD is, therefore, assumed to be tangential to the stem of the ship at the deck edge. Point A then becomes point A' as in Figure 7.3.1.

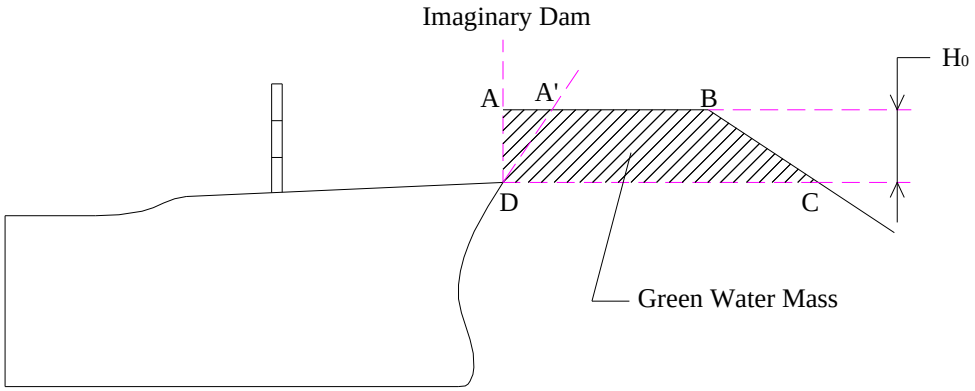

Figure 7.3.1 Water mass ABCD behind the dam needs to be configured.

As mentioned above, green water is part of the incident wave and as a result, green water mass should be derived based on the configuration of the wave itself. As the ship pitches at a frequency equal to encountered wave frequency, it is presumed that the profile of encountered wave could be used to configure green water mass. A sample encountered wave profile is as in Figure 7.3.2. If tangents at the zero-crossing points and the peak point of the waves are drawn and joined together, a trapezoid EFGH can be obtained. This trapezoid envelops the wave peak as seen. The configuration of green water mass is based on the configuration of the wave. In other words, trapezoid A'BCD in Figure 7.3.1 is derived from trapezoid EFGH in Figure 7.3.2. For simplification, it is assumed that top edge A'B in Figure 7.3.1 is equal to top edge FG in Figure 7.3.2. From the known encountered wave height H_e, wavelength λ_e and maximum α_e, the length of these edges can be calculated as:

$$b_{gw} = \frac{1}{2}\lambda_e - \frac{H_e}{\tan(\alpha_e)} \tag{7.3.1}$$

Slope of edge BC is also presumed to be the same as slope of edge GH which is the maximum encountered wave slope α_e. The final configuration of green water mass is as in Figure 7.3.3. Edge BC is extended to the lower boundary MN of the control volume. The detail on how the control volume is selected follows in Section 7.3.2.2.

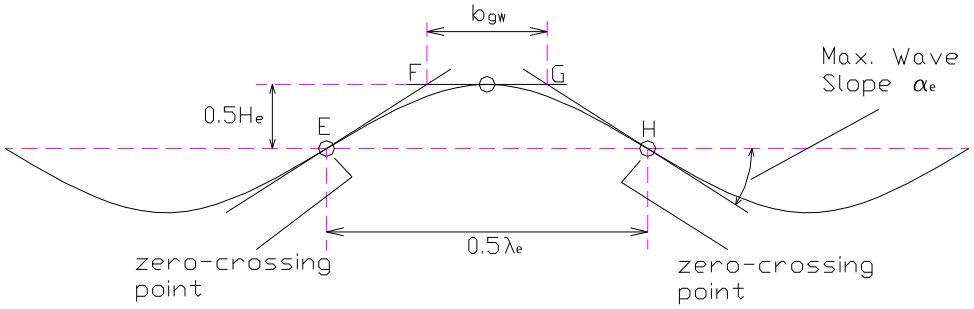

Figure 7.3.2 Encountered wave profile for deriving the shape of green water mass.

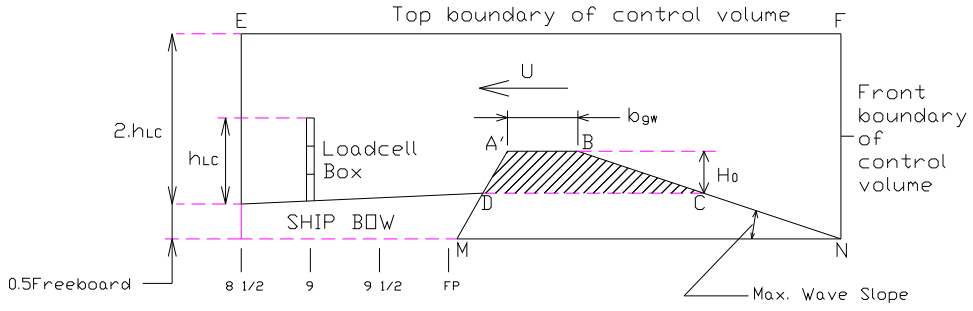

Figure 7.3.3 Water mass modelled in 2-D CFD simulation.

7.3.2.2 Control volume

Control volume is the encapsulating domain in which the dynamics of the fluid or interaction between fluid and structures is simulated. Control volume is defined by boundaries and the conditions of these boundaries are carefully selected so that reality is reflected. Usually, a large control volume is desirable because it can capture more interactions between fluid and structure. If the boundaries are walls, the further they are from the interaction zone, the less reflection effects will be exerted on the fluid. However, it also means that the pressure/velocity field to be processed becomes larger. The computational requirement will, as a result, be more intensive.

Selection of an optimal control volume that best compromises the computational effort and reduction in boundary interference could be a subject on its own. The selection of control volume for simulation in this research was based on simulation experiences, experimental observation and advices from previous researchers as well as review of simulations of similar nature. Spatial boundaries of the control volume were then selected as described below.

Only the above water bow section was modelled in the simulation. So above water body from station 8½ towards the stem was modelled (Figure 7.3.3). The lower boundary MN was set at a distance of 0.5 times the freeboard at stem head. The top boundary EF was set at a height of twice the height of the load cell box h_{lc} from the deck. The front boundary of the control volume depended on the slope of edge BC.

7.3.2.3 Initial velocity of water mass

In reality, the ship travels at a forward velocity of U. However, in CFD, simulation of moving boundaries is an extremely demanding and unstable process in terms of computation. And the computational requirement will be multiplied

when the simulation becomes 3D. This was solved by assigning the water mass with an initial velocity equal but opposite to ship velocity U.

7.3.3 Setup of 3D model of green water flow

To extend the 2D configuration into 3D, the 2D profile of green water mass in Figure 7.3.3 was used as the basis. At the centreline plane, the sectional view of the setup was exactly the same as in Figure 7.3.3. By sweeping edges A'B and BN to port side of the ship by a distance of 1.5 times ship's breadth, surfaces $A'BB_1A_1$ and BNN_1B_1. Note that away from the ship body, the water surface was less disturbed so it was assumed that the front surface of the water volume was equal to the maximum encountered wave slope α_e. Therefore, edge $A'A_1$ was swept to create a surface that made an angle of α_e to the horizontal plane. Edge A'D was also swept along the deck edge to create a surface that represented the water that was shed off the deck edge. The intersection of these two surfaces was found and together with the surfaces that had been created, it helped define the volume of water on the port side of the ship. Similarly, the volume of water on the starboard side of the ship could be defined. Altogether, the water volume that contained green water mass to be shipped on board was defined as in Figure 7.3.4. Figure 7.3.5 shows the visualisation of this water volume together with the ship body modelled in **Fluent 5**.

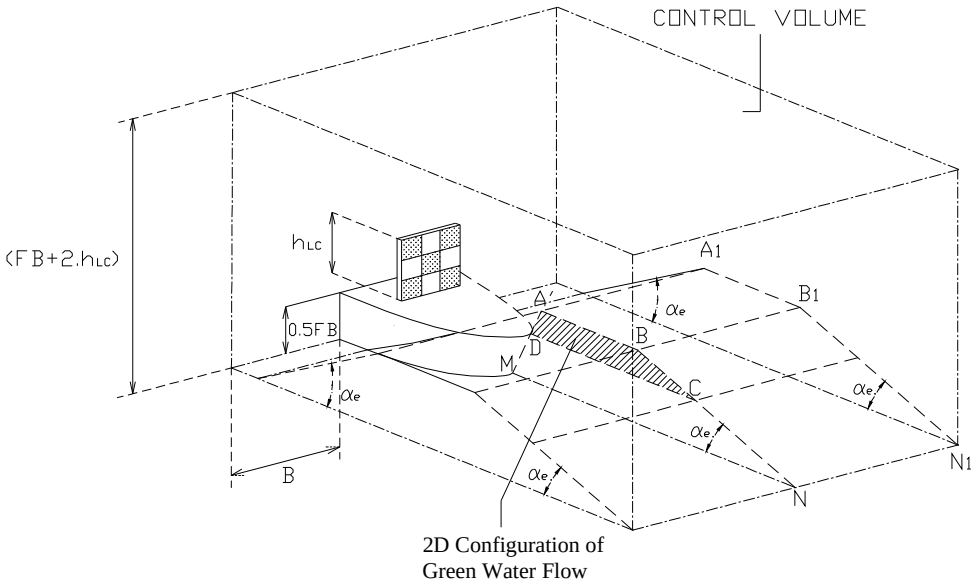

Figure 7.3.4 3D setup of green water flow based on the 2D configuration.

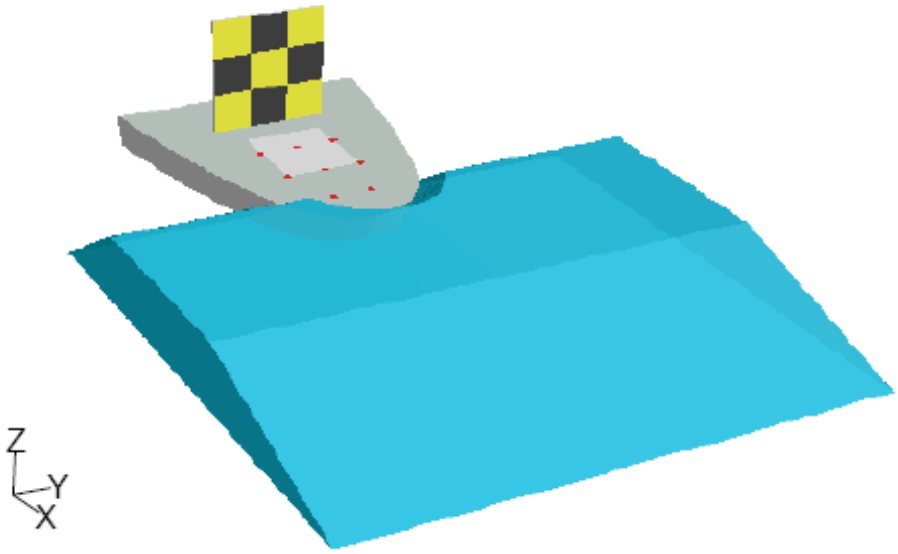

Figure 7.3.5 Visualisation of the 3D setup of green water flow at the initial stage in **Fluent 5**.

7.3.4 Grid generation

As the model was symmetrical about the centreline, only half the control volume shown in Figure 7.3.4 was modelled in the simulation. The grid was constructed in the mesh generator **Gambit** and it was structured in such a way that there was a dense cluster of cells in the space on the deck where green water flow translated and interacted with the vertical structures (load-cell unit and breakwater). Further out, either the fluid-structure interaction was less or there was no water translation at all, the cell size could be larger without losing significant numerical accuracy. The pressure/velocity gradients in these areas did not change much. All the grids consisted of approximately 900,000 elements and this was appropriate for obtaining good numerical results (see Appendix C for detail). Figures 7.3.6 and 7.3.7 give example visualisation of the grid generated for simulation.

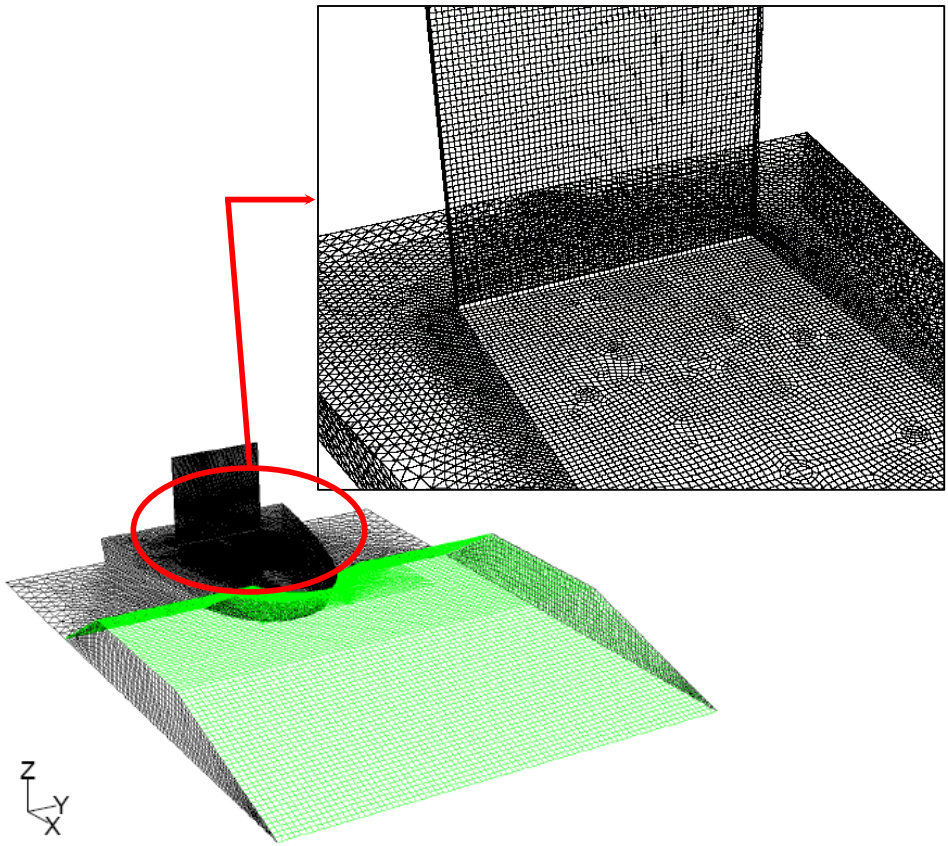

Figure 7.3.6 Example of grid – front view.

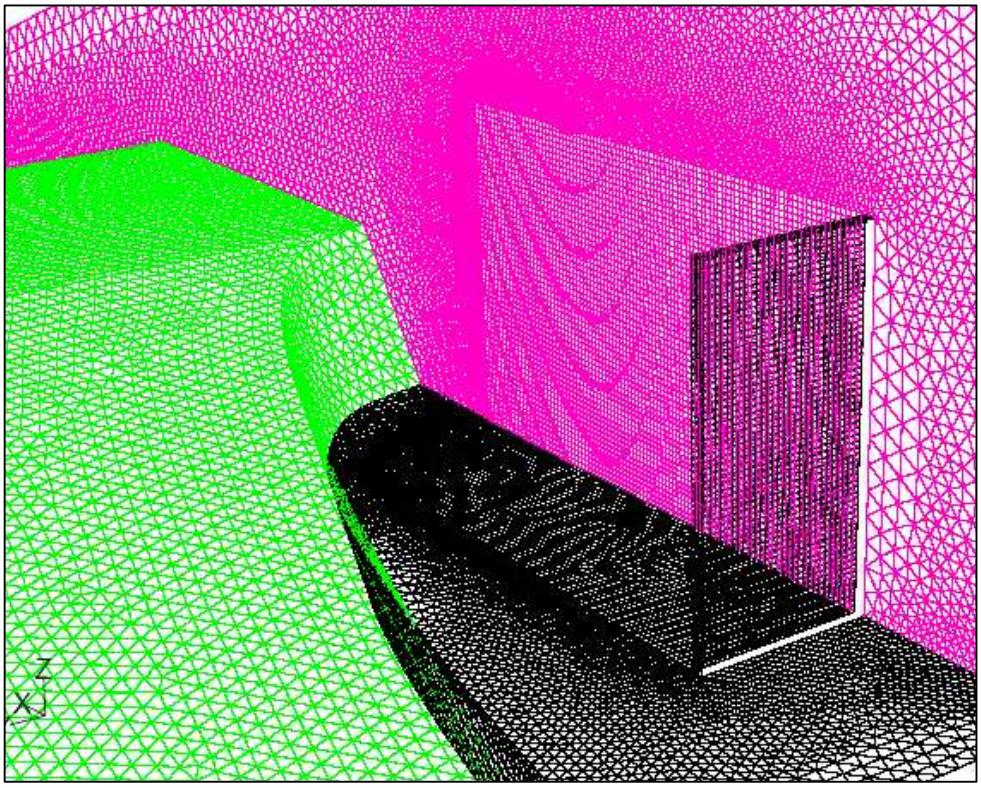

Figure 7.3.7 Example of grid – back view.

7.3.5 Boundary Conditions

As mentioned above, boundary conditions are important and need to be carefully defined. Initial boundary conditions provide the values of pressure or fluid velocity at the boundaries. They then help to solve the differential equations and find solutions of pressure/velocity in other cells within the control volume. The defining of boundary conditions in this research was based on a rational judgement of the hydraulic model, backed up by consultation with specialists and inputs from research over other works of similar type. Figures 7.3.8 and 7.3.9 illustrate the definition of boundary conditions in the simulation.

All the surfaces that defined ship body, load cells and breakwater (if modelled) were defined as non-slip walls. The bottom, side and front surfaces of the control

volume were also defined as non-slip walls so that the water was not dispersed away before it reached the vertical structures. The back and top surfaces of the control volume were defined as pressure outlet surfaces. That allowed fluid splashing to exit the control volume (as it would in experiments) after the interaction with vertical structures rather than falling back to the control volume.

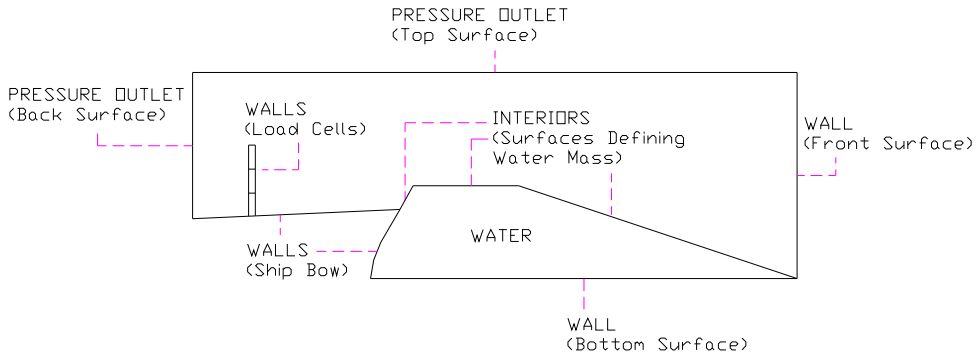

Figure 7.3.8 Definition of boundary conditions in profile view.

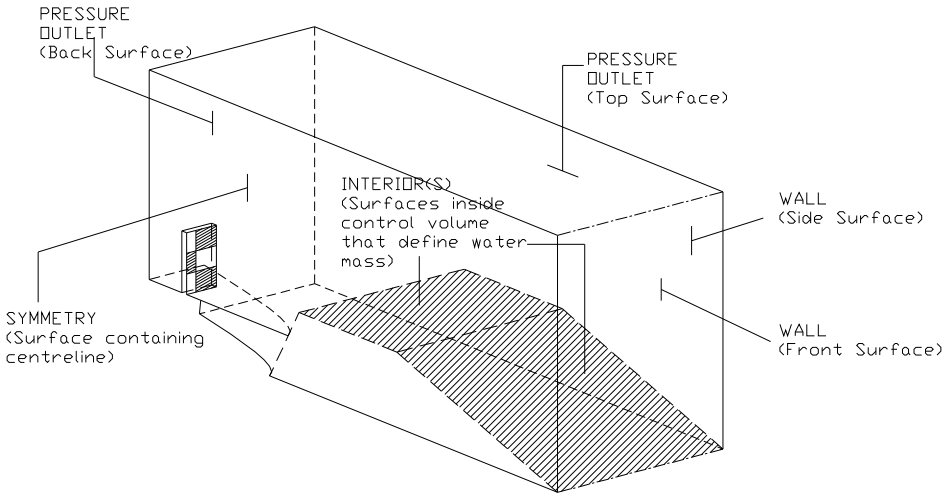

Figure 7.3.9 Definition of boundary conditions in 3D view.

All the surfaces that defined the initial shape of water mass/volume were defined as interior surfaces. They did not interfere with fluid once the iteration began. Their presence was just to define a domain that contained a fluid of different properties such as water in this simulation. The vertical surfaces at the centreline

were defined as a symmetry surface because the model was symmetric about these surfaces.

7.3.6 Discretisation schemes

Following the description in Section 6.4, the selection of discretisation schemes is as follows:

- Discretisation of momentum equations: First Order Upwind scheme.
- Discretisation of pressure equations: Body Force Weighted scheme.
- Pressure-Velocity coupling: PISO.

7.3.7 Time stepping

The selection of appropriate time step is important to ensure the simulation is stable. The Courant number is a dimensionless number that compares the time step in a calculation to the characteristic time of transit of a fluid element across a control volume. In other words, it is a measure of how far inside a cell a fluid element travels per time step.

For explicit formulations, the maximum value of the Courant number for a solution to be stable is one. This is referred to as the Courant-Friedrichs-Lewy criterion. However, in most cases the Courant number required to achieve numerical stability is below 0.25. Using initial velocity of water mass and the minimum vertical distance between horizontal grid lines to calculate the Courant number, it was found that this number had to be less than 0.50 for all the case to be stable. The default value of 0.25, therefore, was used for all the cases.

7.3.8 Fluid properties

Multiphase model was selected in which the primary fluid was air and the secondary fresh water. At room temperature, the densities of air and water in use were 1.293kg/m^3 and 998.2kg/m^3, respectively.

7.3.9 Initialisation

At the beginning of the solving process, properties of fluid, their occupancy and initial state were to be initialised. If these initial values were closer to the actual solutions, fewer iterations would be required. The solving would, in turn, be faster.

7.3.10 Convergence

The process of obtaining a converged solution is of great importance in the simulation. For monitoring this process, **Fluent 5** provides a running report of the residuals for each equation at every iteration. The residuals are measures of how closely each finite difference equation is balanced, given the current state of the solution. During the solving process, a level is set to which the sum of the normalised residuals must drop to before going on to the next time step. For most problems, the default convergence criterion in **Fluent 5** is sufficient. For the present analysis, the default convergence criteria for velocities and continuity were 10E-3. These criteria were reset to 10E-4 for more accurate solutions.

To ensure that these criteria were adequate for the simulation, the total pressure forces on the vertical load cells in the bottom row of the load-cell box were plotted against the number of iterations. The peak pressure was then checked with pressure approximated by simple equation such as equation (5.9.2) in Section 5.9.

7.4 Summary

Chapter 7 has explained the establishment of the hydraulic model to simulate green water flow on deck. Using the dam-break model as the basis, green water mass behind the dam was initialised with the ship velocity so that the relative velocity between the ship and green water could be included at the start. Configuration of the water mass behind the dam was also described in detail. For CFD simulation, the grid of the model was constructed with the mesh generator **Gambit** and later exported to **Fluent 5** solver. Boundary conditions were defined and descretisation schemes were selected. Appropriate time-step was also chosen to ensure the simulation was stable. Some notes on convergence criteria and checking were finally discussed to provide guidelines for monitoring the simulation process.

Chapter 8:
Comparison and Discussion of Results

8.1 Introduction

This Chapter focuses on verifying numerical results described in Chapter 7 using experimental data. The validation was carried out for experiments with and without breakwater on forecastle deck. The test conditions are listed in Tables 4.8.1 and 4.8.2 in Section 4.8, Chapter 4. Ideally, the same number of simulations should be implemented to perform a complete validation. However, due to the limited computation resources (especially demanding for 3D simulation), the substantial amount of data analysis work that would be required, and the scope of the thesis, it was believed that adequate validation was carried out over nine representative tests without breakwater and nine representative tests with breakwaters.

For tests without breakwaters, validation was undertaken for the conditions that correspond to equivalent full-scale wave height of 8m and periods of 11s, 12s and 13s. The velocities in use were equivalent to Fn = 0.20, 0.25 and 0.30. These were the most severe conditions of the test series and green water was likely to pose most serious threat.

For tests with breakwater, due to a number of breakwaters involved in the testing (ten breakwaters), the wave height was fixed at 8m (full scale) and wave period 12s. The ship velocity was equivalent to Fn = 0.25 or approximately 20 knots at full scale.

In Chapter 5, it had already been shown that green water loading on a vertical structure varies with the height of the structure above the deck. The closer to deck

level, the greater green water loading the structure was likely to face. Three separate levels or heights were used for comparison of green water loading on the load cell box:

- Load cells in the bottom row of the load-cell box: load cells 7, 8 and 9;
- Load cells in the middle row of the load cell box: load cells 4, 5 and 6;
- Load cells in the top row of the load cell box: load cells 1, 2 and 3.

Note that in Section 4.5.5, it was already mentioned that any load smaller than 0.5N could be interfered by noise and is assumed doubtful. When that was the case, either the results were assumed to be trivial and ignored or they could be presented for illustrating the loading behaviour. The peak values might not be exact due to the filtering of the data for clarity.

It should also be noted that due to the severe nature of the tests and under severe wet conditions, the load cells were subject to high risks of getting damaged by water and as a result malfunctioned. When this happened, the comparison was performed with either the data from the load cell on the other side, symmetrical to it or from the central load cell if that load cell was also out of order.

Since the main purpose of this Chapter is to validate the numerical results, the results are shown at model scale values rather than full-scale. The test conditions are, however, mentioned at full scale for convenience of interpreting the sea conditions. The validation is presented in the following Sections.

8.2 Comparison of longitudinal green water loading without breakwater

Due to the number of load cells involved in the tests and the location they were mounted, the comparison of longitudinal green water loading was categorised in four groups (refer to Figure 4.5.5 for the arrangement of load cells). The first group included the three load cells (7, 8 and 9) in the bottom row of the load cell box. The second group were three load cells (4, 5 and 6) in the middle row. The third group included the load cells located in the top row (1, 2 and 3) and finally the comparison looked at the sum of all the load cells or, in other words, the total loading on the load-cell box as a whole.

In order to facilitate the comparison process, Table 8.2.1 re-listed green water height measured at wave probe 9 for comparison with corresponding load. Also, in order to identify the tests, runs were coded systematically based on the test conditions at full scale. The data used for coding the runs include wave height, wave period and ship velocity represented by Froude number. Illustration of the coding is as in Figure 8.2.1.

Table 8.2.1 Green water heights measured at wave probe 9.

Test run	Green water height at model scale (mm)
H08T11Fn020	35
H08T12Fn020	40
H08T13Fn020	23
H08T11Fn025	23
H08T12Fn025	40
H08T13Fn025	36
H08T11Fn030	24
H08T12Fn030	56
H08T13Fn030	46

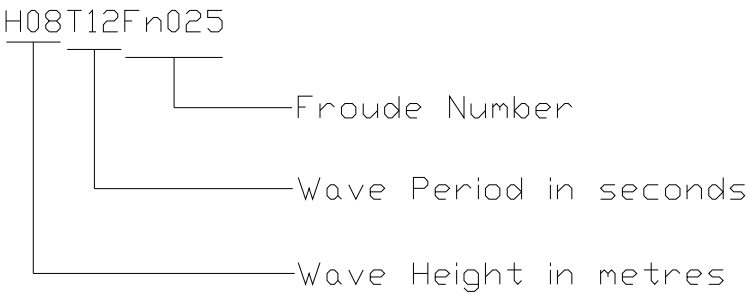

Figure 8.2.1 Coding of test run without breakwater.

8.2.1 Longitudinal green water loading on load cells in bottom row

Figures 8.2.6 to 8.2.14 show the comparison between green water loads on load cells in the bottom row with experimental data. Figure 8.2.2 summarises the ratios of the peak load by simulation to the peak load by experiment. Generally speaking, the simulation data predicted relatively well the behaviour and peak values of the loads. The mean error of only 3.9 percent and the standard deviation of 12.1 percent indicated good agreement. Numerical results fluctuated within approximately 10 percent of the experimental results.

By combining results in Figures 8.2.6 to 8.2.14 with Table 8.2.1, it could be seen that at the same ship velocity, green water loading really increased with the water height on deck. Also, all the Figures consistently show that the load on the central load cell (load cell 8) was higher than those on the sides (load cells 7 and 9). This reconfirmed that there was a concentration of green water along the centreline of the ship. Figure 8.2.3 shows the sectional views of green water flow on deck at the time of peak impact loads at load cells 7, 8 and 9. As seen, the water appeared to enter the deck as a plunging breaker at the beginning, similar to what was described by Greco et al. (2005, 2007). The water can also be seen to concentrate along the centreline of the ship (Figure 8.2.3 left).

One of the drawbacks of the simulation results was that after the peak values were reached, the numerical load curves tended to reduce more slowly than in experiment. This was attributed to the fact that in experiment the ship started to pitch out of the water at this stage. Green water could have drained away and off the deck faster due to the sloping of the main deck. The pitch motion could not be simulated and this led to a greater pile-up of green water in front of the bottom load cells. The extra hydrostatic pressure consequently accounted for this difference between the two load curves. The dispersion of green water could also be fastened by extending the control volume transversely.

One way of addressing this issue is to reduce green water at the tail of the green water volume in the simulation. This curtailing should not compromise the peak load caused by green water because the peak load, as explained at later stage, was mostly caused by green water at the front. With such alteration, (which could not be accomplished in this research), the simulation is believed to reflect reality. Nonetheless, the most critical part of green water loading was the peak load and the rise-time (time taken by the load to reach maximum from zero at the impact) and they both were predicted at reasonably good level of accuracy as seen.

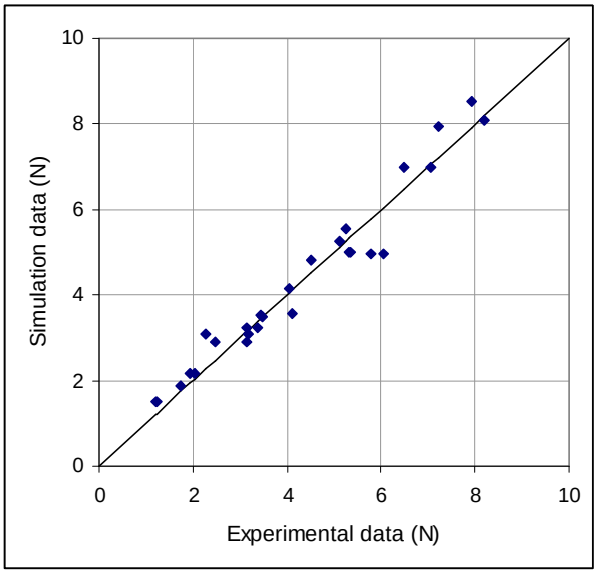

Figure 8.2.2 Comparison of peak loads on the load cells in the bottom row.

Extending the width of the control volume could also reduce the difference between simulation data and experiment data. Parametric investigation into this is recommended for future work.

In Figure 8.2.3, it was evident that maximum impact loads took place almost at the time of the first water impact. It was the front water that resulted in the peak load. This is consistent with the equation (5.9.2) in which the peak impact loads on structures were proportional to squared velocity of the front water on deck. Equation (5.9.2) indicates that the peak load normally takes place at the initial impact when the velocity of the water is highest.

After the initial impact, green water piled up in front of the load-cell box, creating a buffer that consequently directed the follow-up water upwards (Figure 8.2.4). Figure 8.2.5 shows the velocity vectors at the foot of the load-cell box. It could be seen that near the corner, velocity of water was almost zero. Further out, following the direction of the velocity vectors, it was evident that the follow-up water was steered upwards at almost the same velocity as the incident velocity. The pressures on load cells 7, 8 and 9 started to become more hydrostatic and therefore reduced as shown in Figures 8.2.6 to 8.2.14.

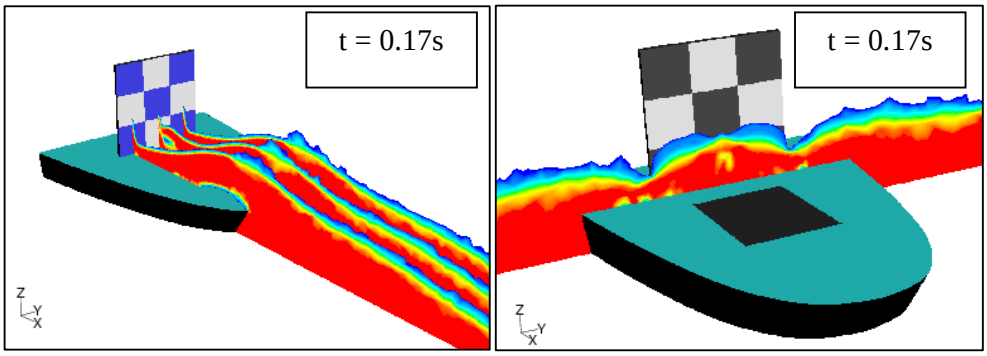

Figure 8.2.3 Sectional views of green water on deck (longitudinally and transversely) corresponding to maximum loads on load cells 7, 8 and 9 when ship was running in regular waves of 8m height and 13s period at a velocity equivalent to Fn = 0.25.

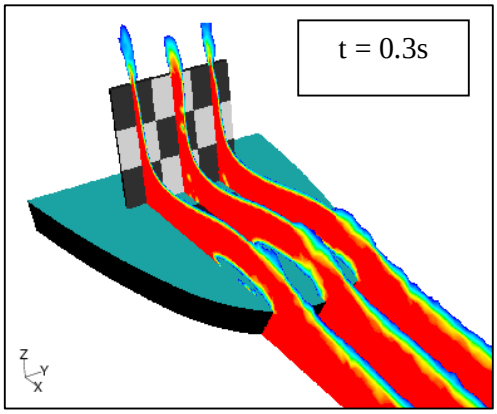

Figure 8.2.4 Longitudinal sectional views of green water running up the load-cell box.

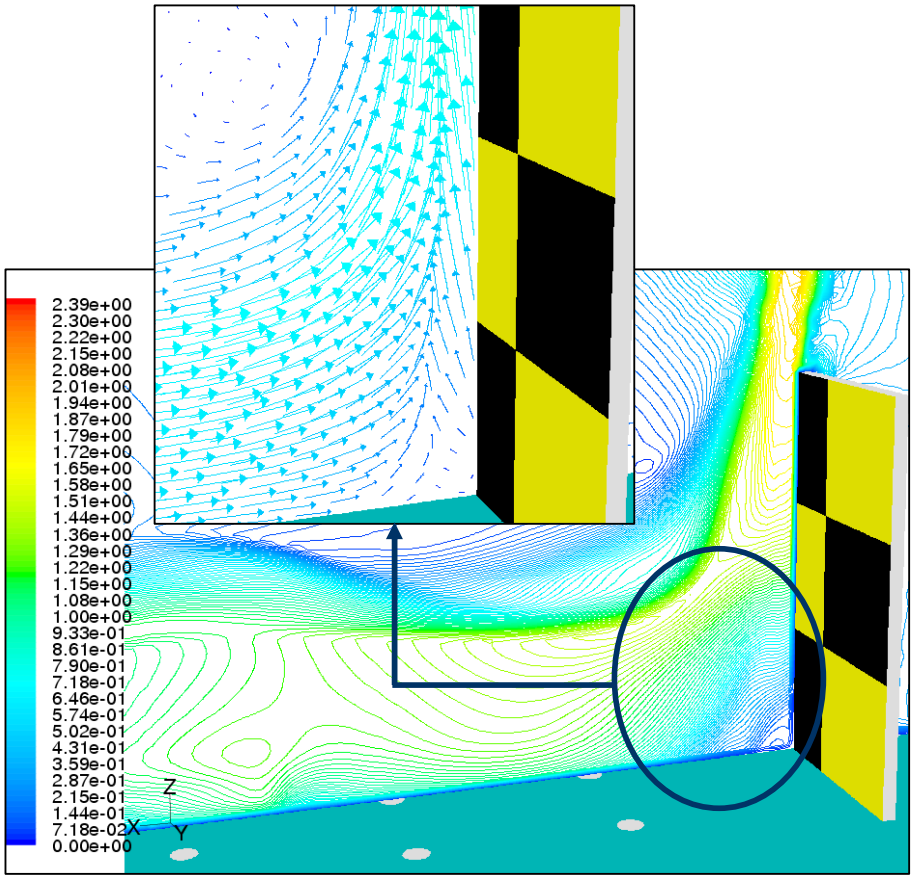

Figure 8.2.5 Velocity contours and vector field of fluid around the corner of load-cell box and main deck.

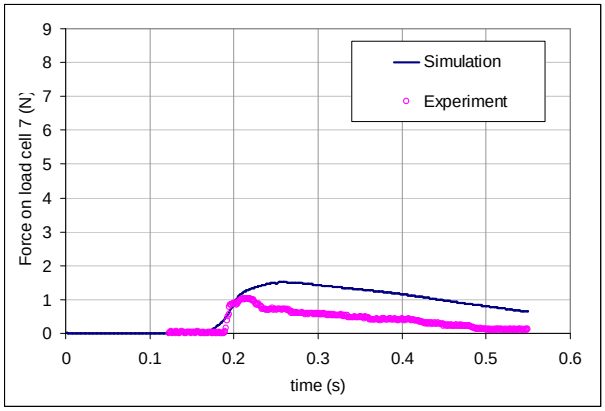

(A)

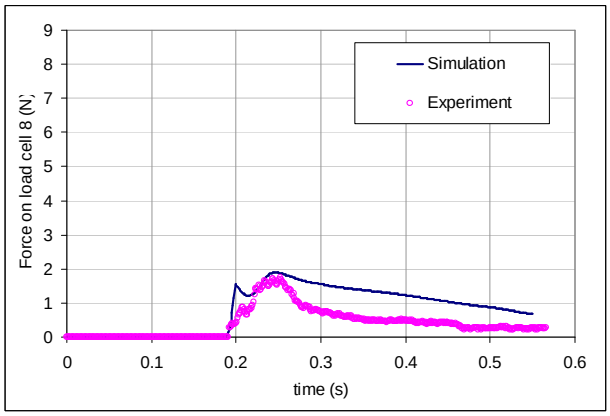

(B)

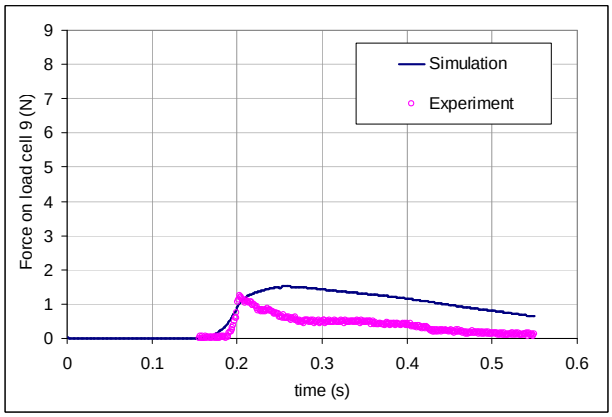

(C)

Figure 8.2.6 Comparison of green water loading on load cells 7, 8 and 9, respectively when ship was travelling at Fn = 0.20 in waves of equivalent full-scale height of 8.0m and period of 13 seconds.

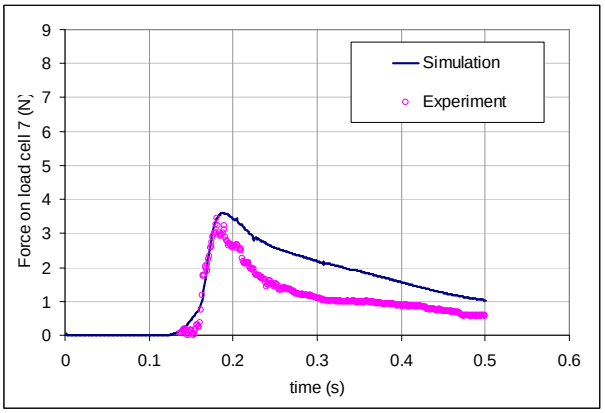

(A)

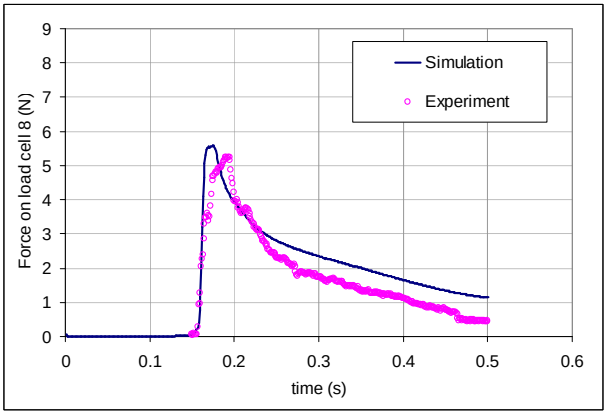

(B)

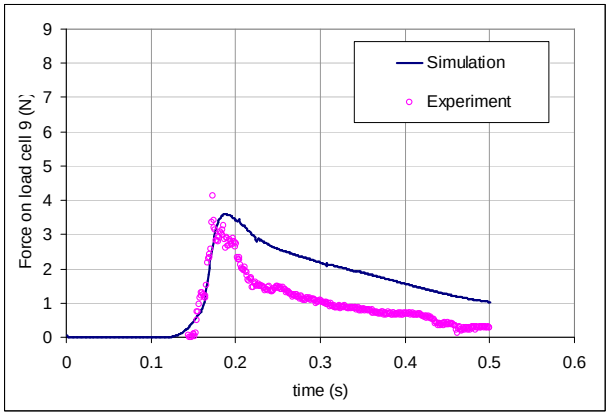

(C)

Figure 8.2.7 Comparison of green water loading on load cells 7, 8 and 9, respectively when ship was travelling at Fn = 0.20 in waves of equivalent full-scale height of 8.0m and period of 12 seconds.

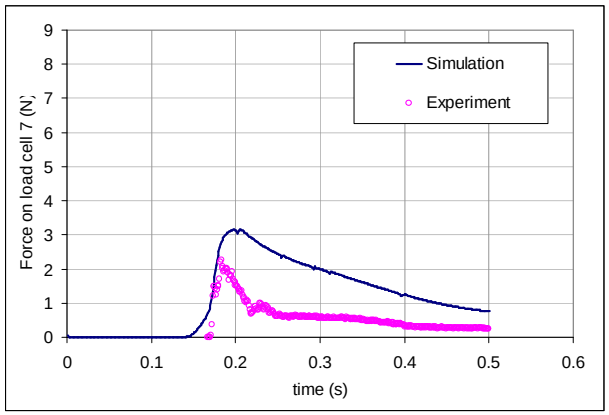

(A)

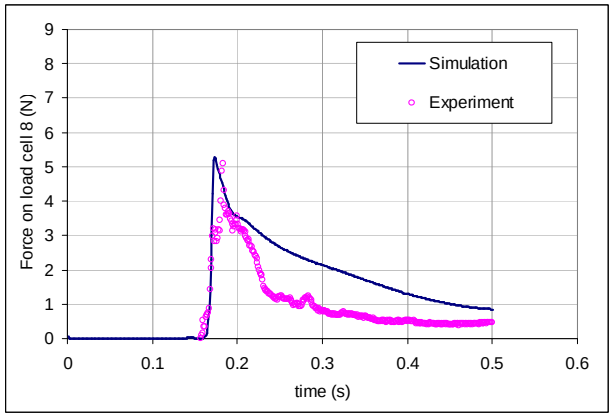

(B)

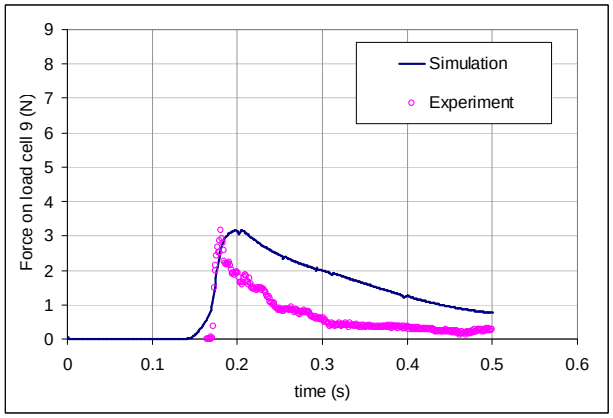

(C)

Figure 8.2.8 Comparison of green water loading on load cells 7, 8 and 9, respectively when ship was travelling at Fn = 0.20 in waves of equivalent full-scale height of 8.0m and period of 11 seconds.

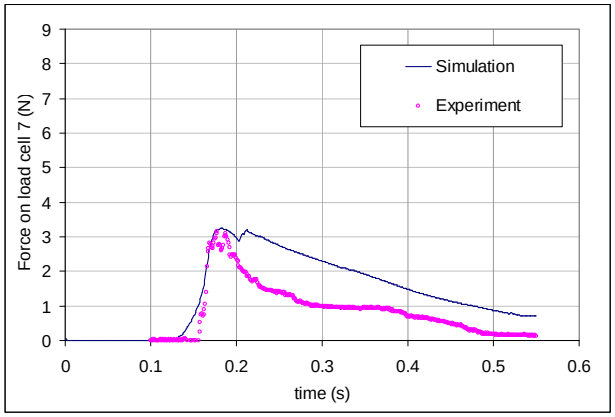

(A)

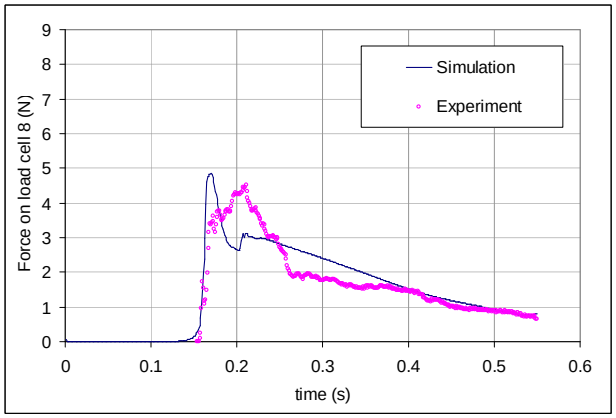

(B)

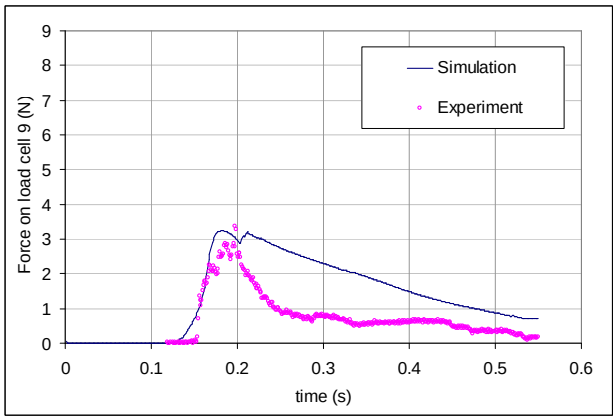

(C)

Figure 8.2.9 Comparison of green water loading on load cells 7, 8 and 9, respectively when ship was travelling at Fn = 0.25 in waves of equivalent full-scale height of 8.0m and period of 13 seconds.

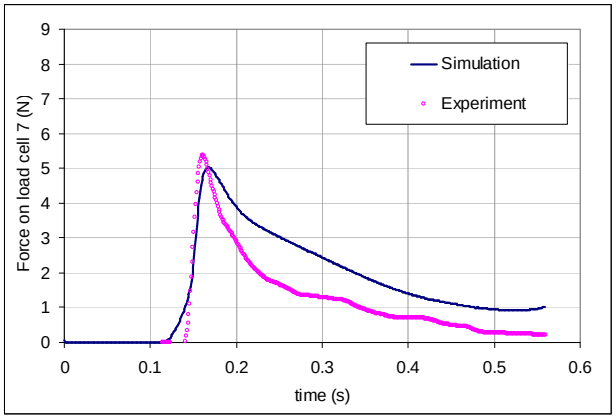

(A)

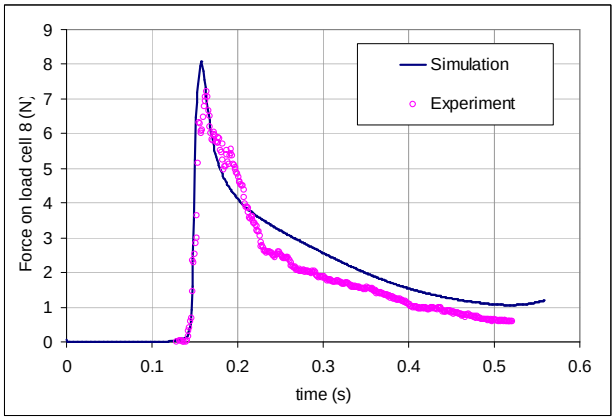

(B)

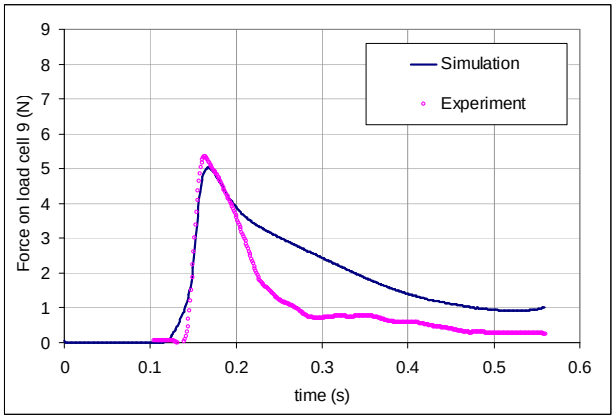

(C)

Figure 8.2.10 Comparison of green water loading on load cells 7, 8 and 9, respectively when ship was travelling at Fn = 0.25 in waves of equivalent full-scale height of 8.0m and period of 12 seconds.

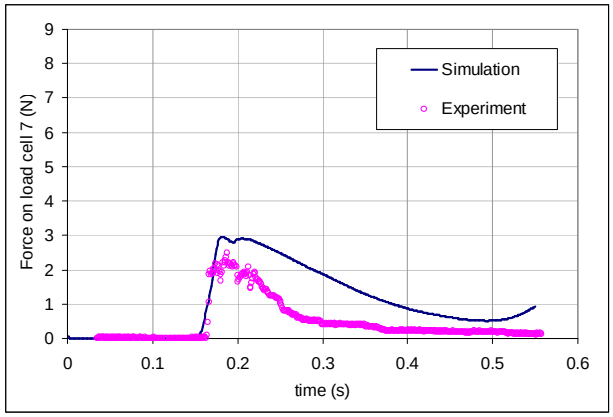

(A)

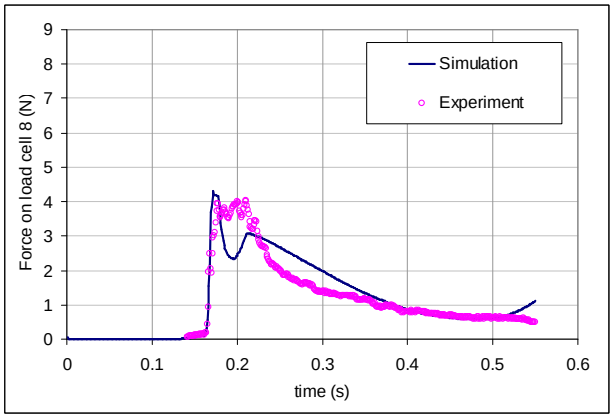

(B)

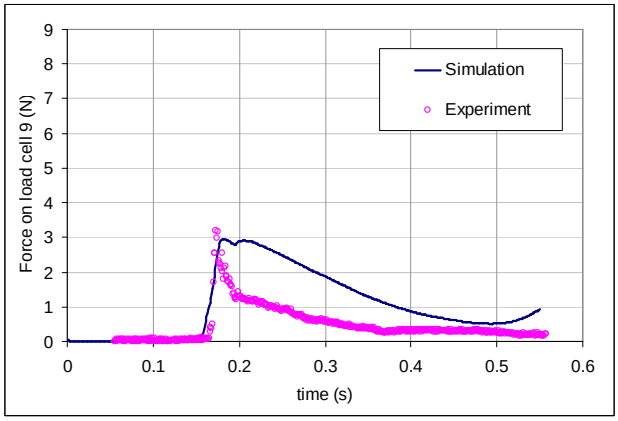

(C)

Figure 8.2.11 Comparison of green water loading on load cells 7, 8 and 9, respectively when ship was travelling at Fn = 0.25 in waves of equivalent full-scale height of 8.0m and period of 11 seconds.

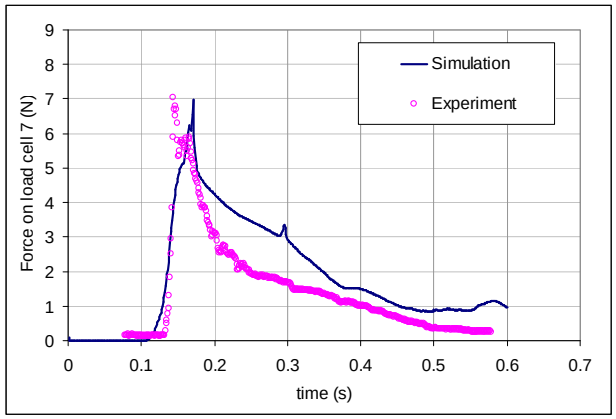

(A)

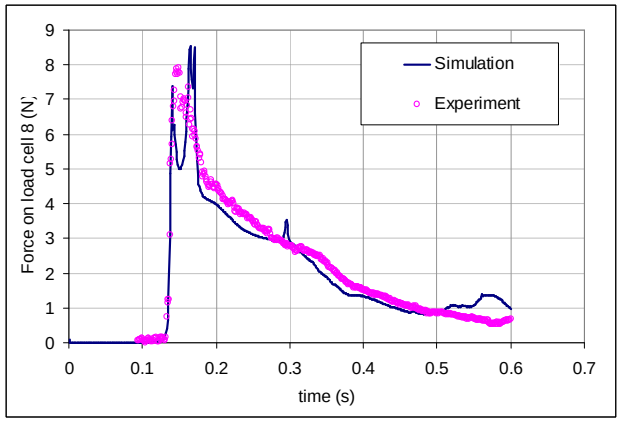

(B)

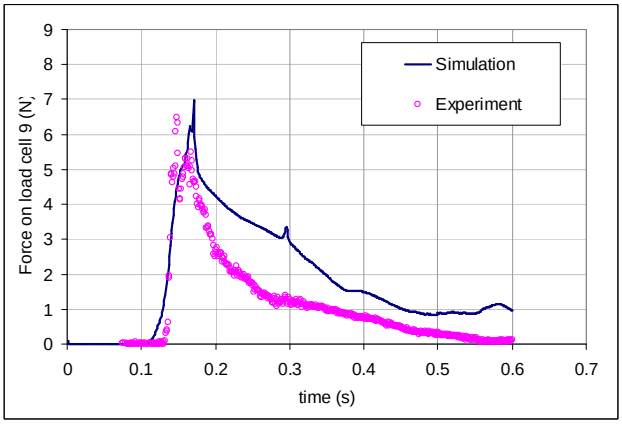

(C)

Figure 8.2.12 Comparison of green water loading on load cells 7, 8 and 9, respectively when ship was travelling at Fn = 0.30 in waves of equivalent full-scale height of 8.0m and period of 13 seconds.

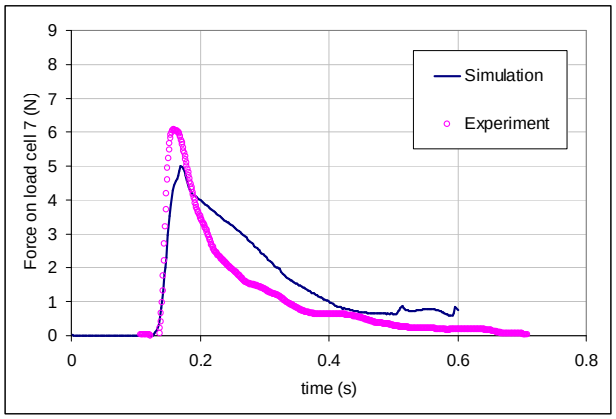

(A)

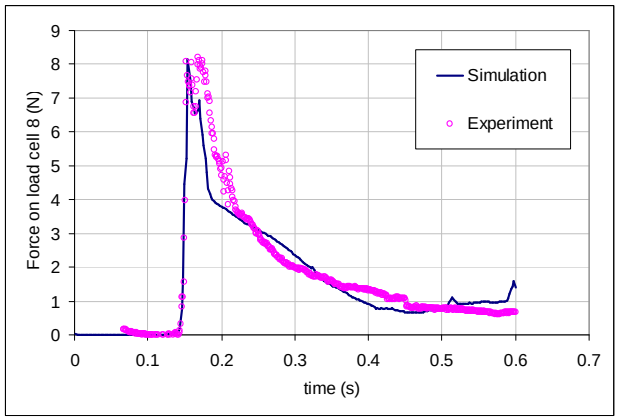

(B)

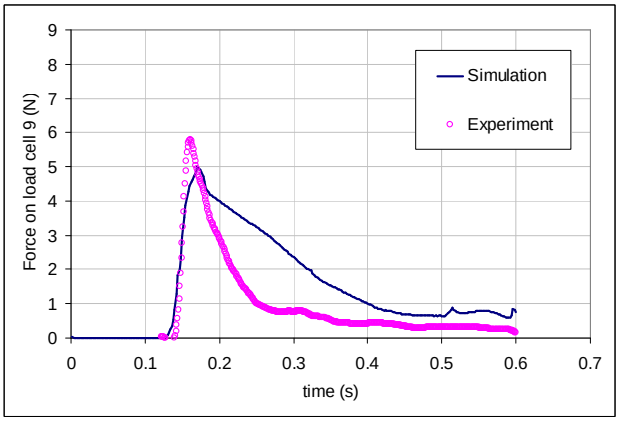

(C)

Figure 8.2.13 Comparison of green water loading on load cells 7, 8 and 9, respectively when ship was travelling at Fn = 0.30 in waves of equivalent full-scale height of 8.0m and period of 12 seconds.

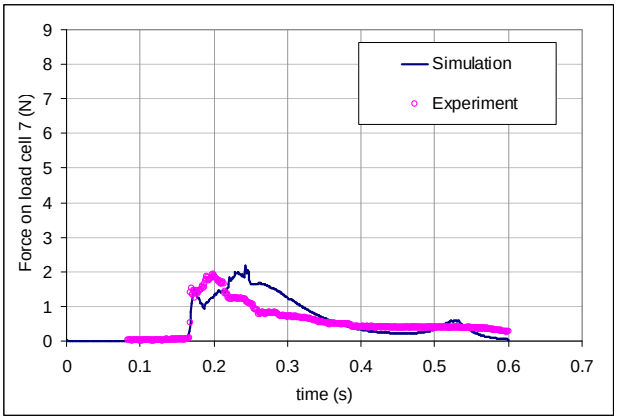

(A)

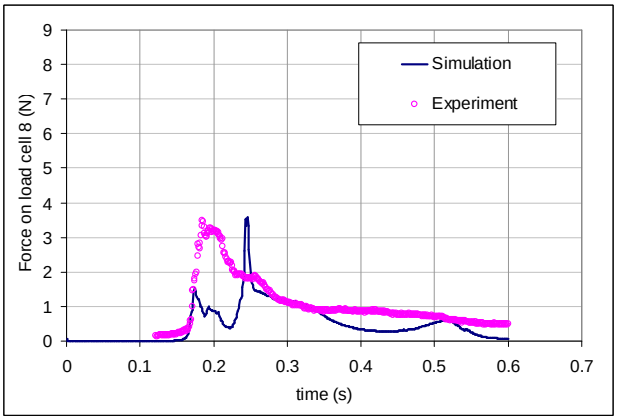

(B)

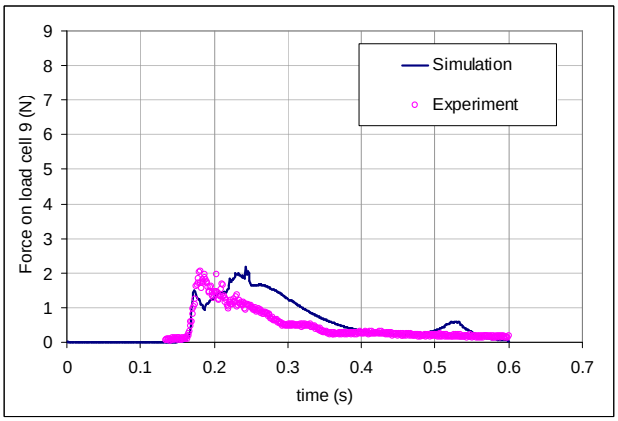

(C)

Figure 8.2.14 Comparison of green water loading on load cells 7, 8 and 9, respectively when ship was travelling at Fn = 0.30 in waves of equivalent full-scale wave of 8.0m and period of 11 seconds.

8.2.2 Longitudinal green water loading on load cells in middle row

Green water load on vertical structures decreases with increased height. Section 5.9 reported that for tests without breakwaters, the longitudinal green water loading on load cells in middle row were only around 20 percent of the loading on bottom row. This is re-confirmed herein when comparing Figures 8.2.18 to 8.2.26 in this Section to Figures 8.2.6 to 8.2.14 of Section 8.2.1, respectively.

As the lower limit of load cells' measurement was 0.5N, any loads smaller than this limit were likely to be interfered by noises and may not be inadequate for validation purpose. Comparison should really be carried out for loads greater than 0.5N only. Figure 8.2.15 compares the peak loads by simulation and experiment. Generally speaking, there was a fair agreement between the two sets of data. The mean error was 8 percent. A standard deviation of 20.6 percent, however, indicates a scattering of numerical data.

For small loads, direct comparison between simulation and experiment can be misleading since a large discrepancy in percentage may not be significant in terms of loading. If both of these values are compared with loads on bottom row, the difference may not be as much. In light of this, the loads in middle row were compared with each other as percentages of the load measured by load cell 8 (usually the largest load faced by the a single load cell in the load-cell box). Table 8.2.2 shows that mean error between numerical and experimental results is reduced to 1.7 percent and standard deviation is around 3.8 percent.

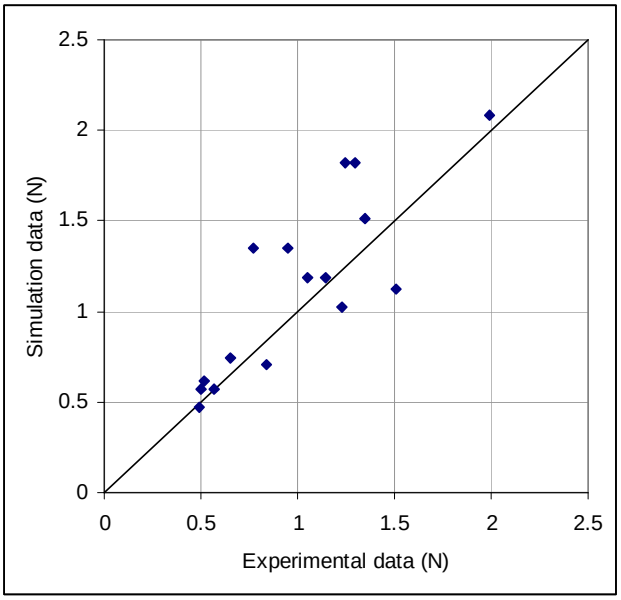

Figure 8.2.15 Comparison of peak loads on the load cells in the middle row.

Table 8.2.2 Comparison of peak loads on the load cells in the middle row in terms of percentage of load recorded by load cell 8.

	Run	Experiment (N)	Simulation (N)	Load by load cell 8 (N)	% of load cell 8 by experiment	% of load cell 8 by simulation	Discrepancy in %
Load cell 4	H08F076V100	0.5026	0.57	5.105	9.8%	11.2%	1.3%
	H08F070V125	0.77	1.353	7.21	10.7%	18.8%	8.1%
	H08F064V150	1.244	1.82	7.916	15.7%	23.0%	7.3%
	H08F070V150	1.14	1.187	8.208	13.9%	14.5%	0.6%
Load cell 5	H08F070V100	1.23	1.02	5.242	23.5%	19.5%	-4.0%
	H08F076V100	0.835	0.71	5.105	16.4%	13.9%	-2.4%
	H08F064V125	0.652	0.74	4.517	14.4%	16.4%	1.9%
	H08F070V125	1.35	1.51	7.21	18.7%	20.9%	2.2%
	H08F076V125	0.49	0.47	4.044	12.1%	11.6%	-0.5%
	H08F064V150	1.99	2.08	7.916	25.1%	26.3%	1.1%
	H08F070V150	1.51	1.12	8.208	18.4%	13.6%	-4.8%
	H08F076V150	0.52	0.618	3.479	14.9%	17.8%	2.8%
Load cell 6	H08F076V100	0.566	0.57	5.105	11.1%	11.2%	0.1%
	H08F070V125	0.95	1.353	7.21	13.2%	18.8%	5.6%
	H08F064V150	1.3	1.82	7.916	16.4%	23.0%	6.6%
	H08F070V150	1.053	1.187	8.208	12.8%	14.5%	1.6%
					Mean error:		**1.7%**
					Standard deviation:		**3.8%**

Regarding the behaviour of green water on deck, Figure 8.2.16 shows the sectional views of green water flow on deck near the load-cell box when the loads on middle row are maximum. It is seen that maximum loads on middle row occurred shortly after the follow-up water was diverted to the middle row by the water piling up in front of the bottom row. Figure 8.2.17 shows the vector field around load cell 5 and it could be seen that the high velocity stream at this time directly impacted load cell 5. This explains why the maximum load was reached at this point. However, it could also be noticed that the impact was at an angle much smaller than 90 degrees (which indicates a head-on impact). This could partly explain why the impact load on load cell 5 was much smaller than that on load cell 8 when the impact was almost at the right angle (Figure 8.2.5).

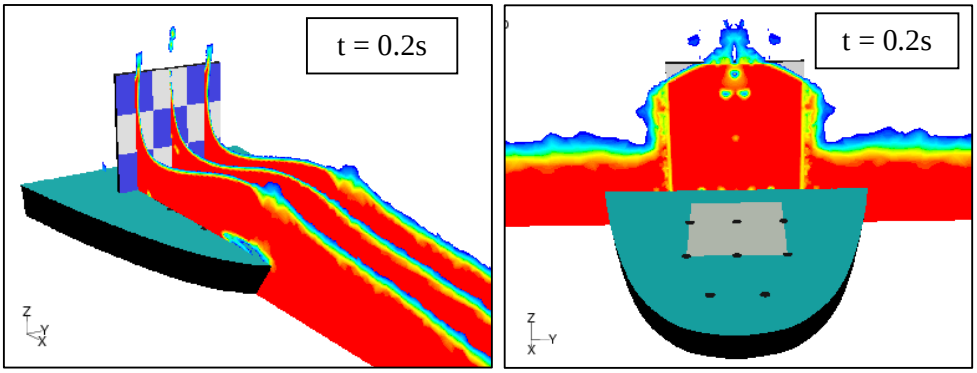

Figure 8.2.16 Sectional views (longitudinally and transversely) of green water on deck at the time when loads on load cells 4, 5 and 6 were maximum in run H08T12Fn025.

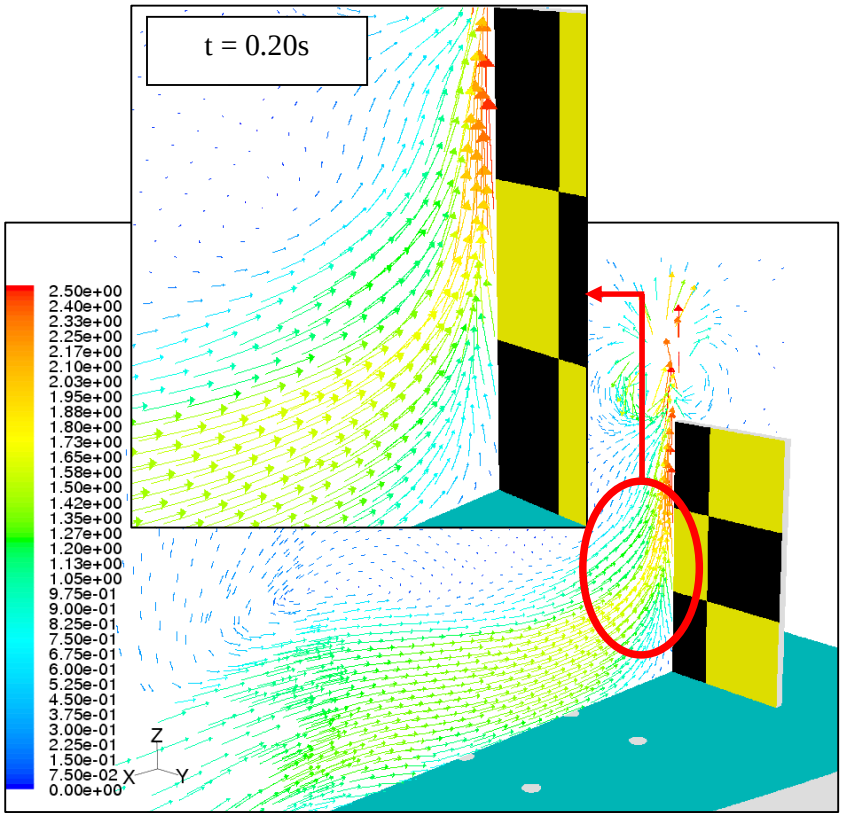

Figure 8.2.17 Velocity vector field around load cell 5 when the load on this load cell was maximum in run H08T12Fn025.

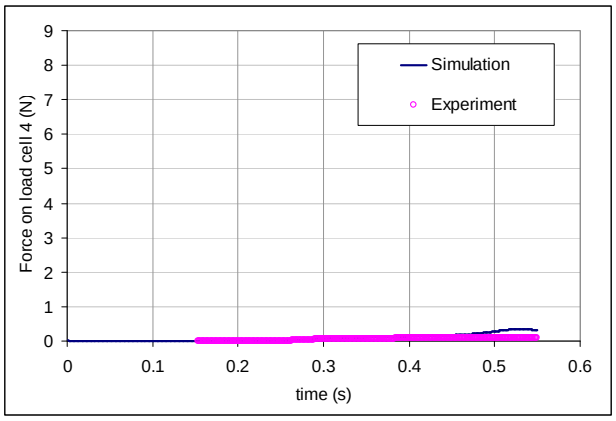

(A)

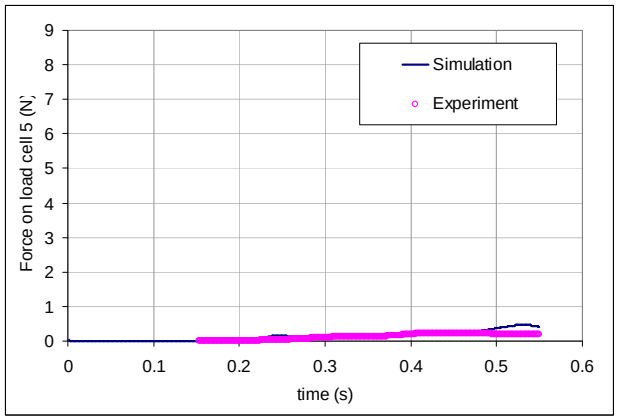

(B)

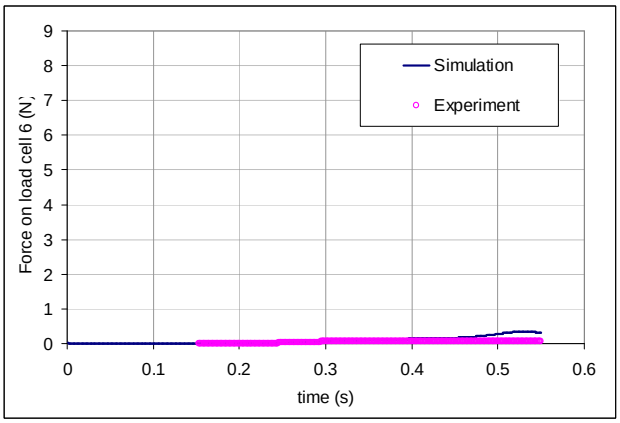

(C)

Figure 8.2.18 Comparison of green water loading on load cells 4, 5 and 6, respectively when ship was travelling at Fn = 0.20 in waves of equivalent full-scale height of 8.0m and period of 13 seconds.

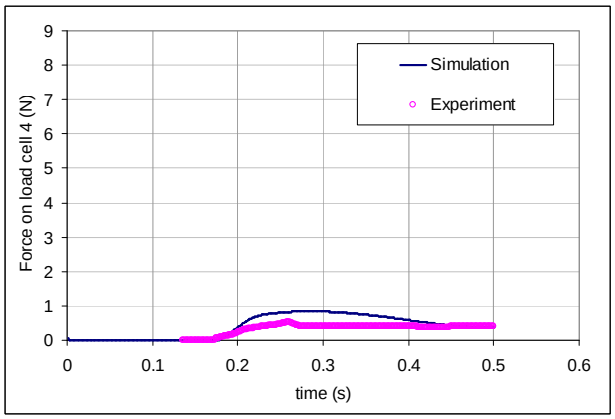

(A)

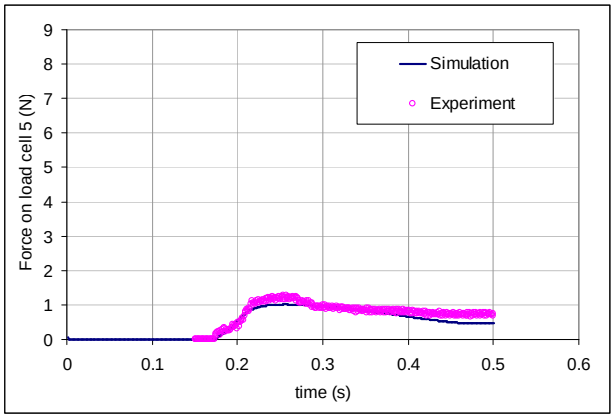

(B)

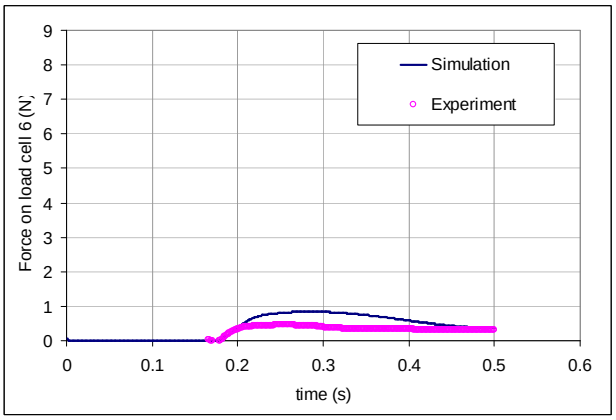

(C)

Figure 8.2.19 Comparison of green water loading on load cells 4, 5 and 6, respectively when ship was travelling at Fn = 0.20 in waves of equivalent full-scale height of 8.0m and period of 12 seconds.

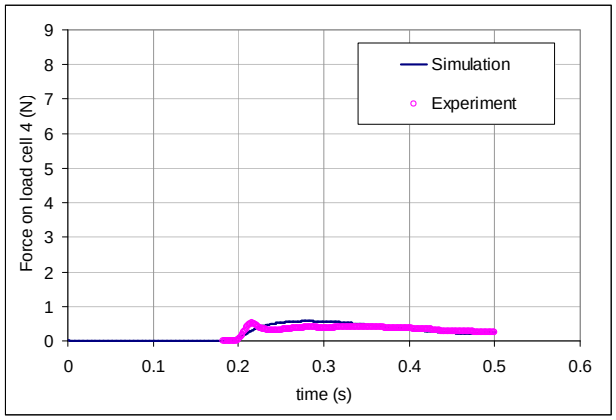

(A)

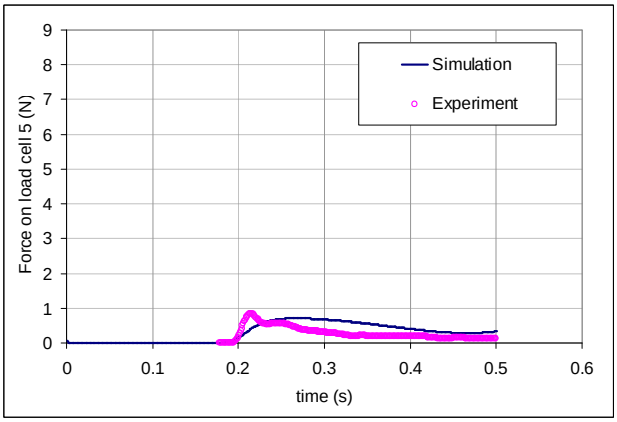

(B)

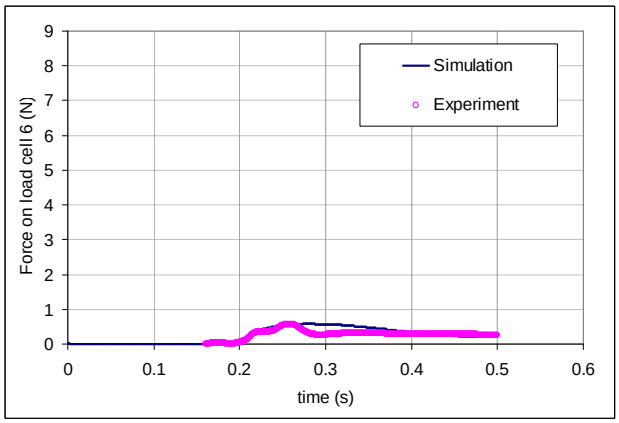

(C)

Figure 8.2.20 Comparison of green water loading on load cells 4, 5 and 6, respectively when ship was travelling at Fn = 0.20 in waves of equivalent full-scale height of 8.0m and period of 11 seconds.

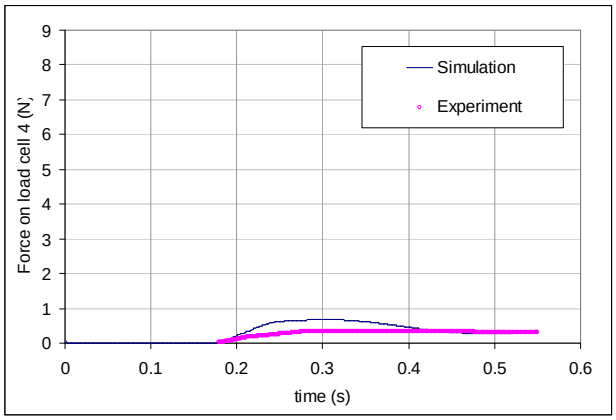

(A)

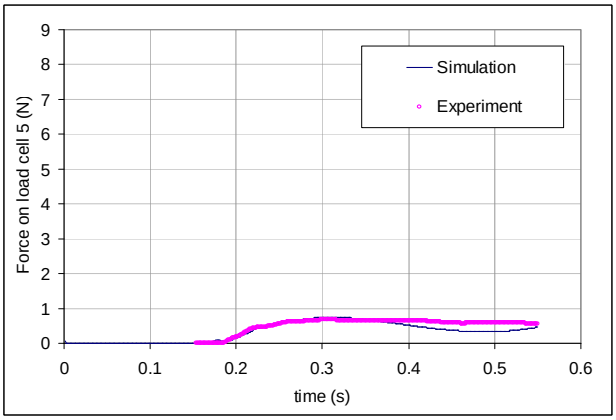

(B)

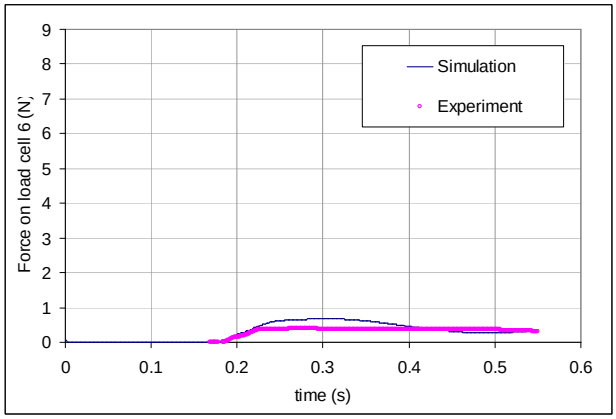

(C)

Figure 8.2.21 Comparison of green water loading on load cells 4, 5 and 6, respectively when ship was travelling at Fn = 0.25 in waves of equivalent full-scale height of 8.0m and period of 13 seconds.

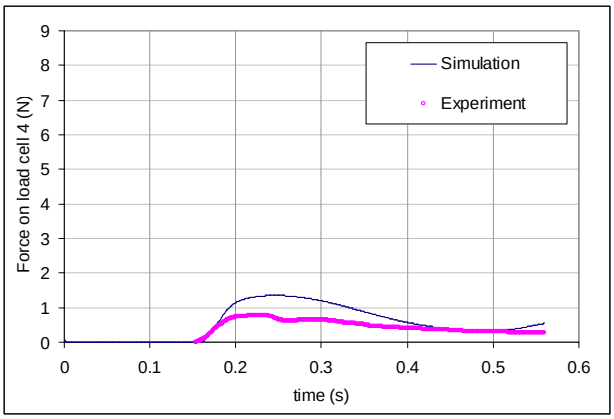

(A)

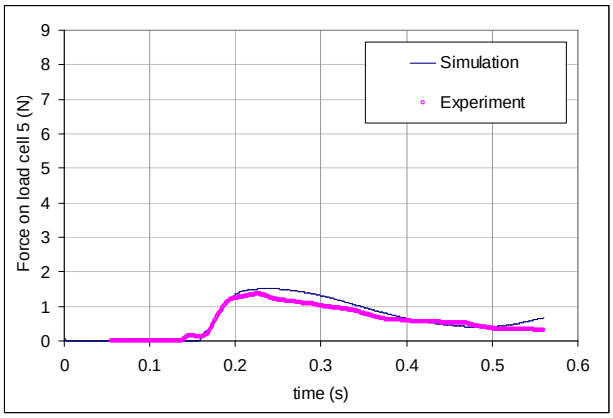

(B)

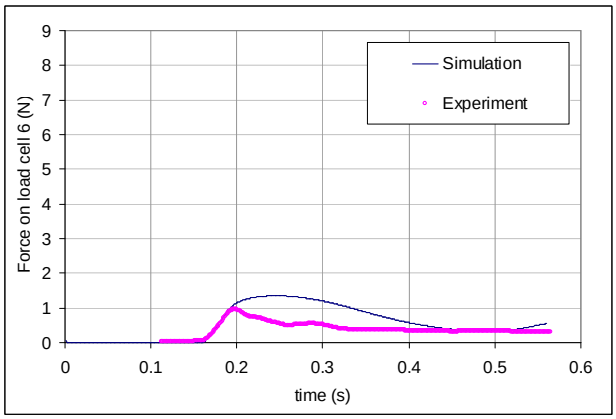

(C)

Figure 8.2.22 Comparison of green water loading on load cells 4, 5 and 6, respectively when ship was travelling at Fn = 0.25 in waves of equivalent full-scale height of 8.0m and period of 12 seconds.

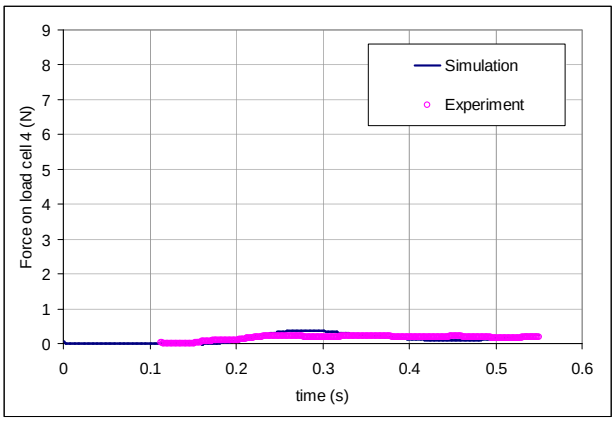

(A)

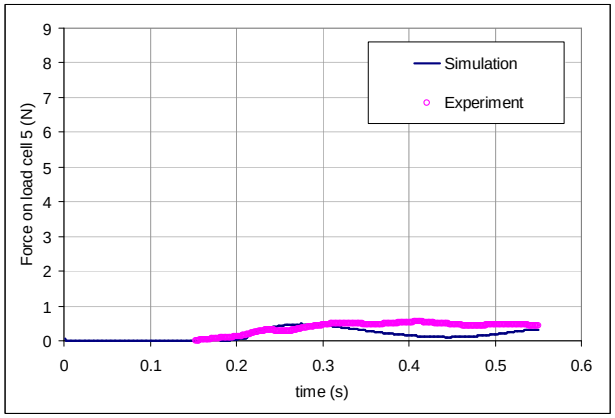

(B)

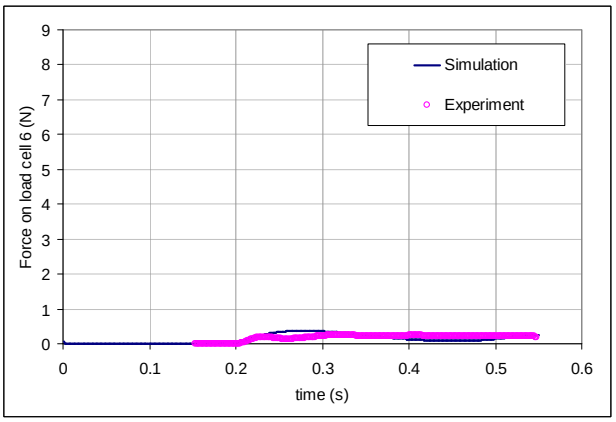

(C)

Figure 8.2.23 Comparison of green water loading on load cells 4, 5 and 6, respectively when ship was travelling at Fn = 0.25 in waves of equivalent full-scale height of 8.0m and period of 11 seconds.

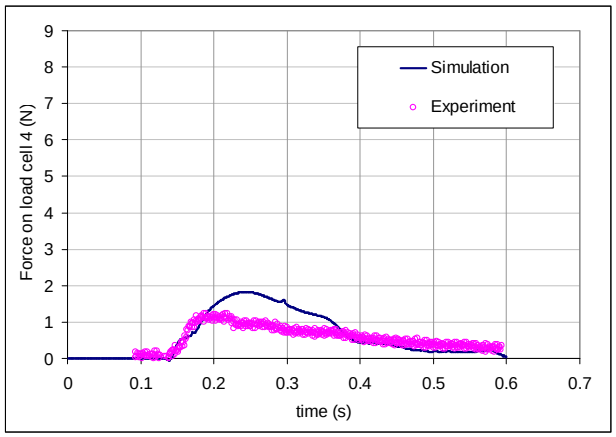

(A)

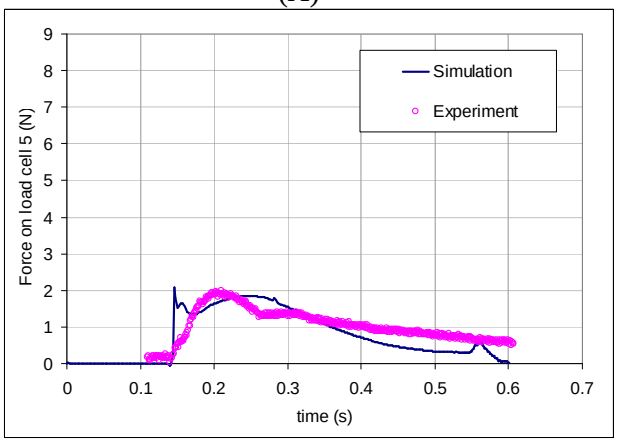

(B)

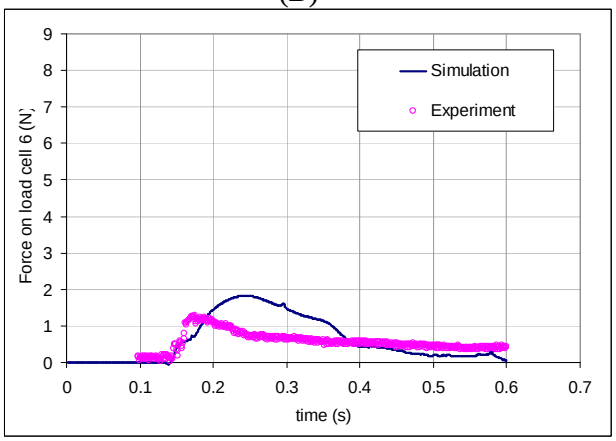

(C)

Figure 8.2.24 Comparison of green water loading on load cells 4, 5 and 6, respectively when ship was travelling at Fn = 0.30 in waves of equivalent full-scale height of 8.0m and period of 13 seconds.

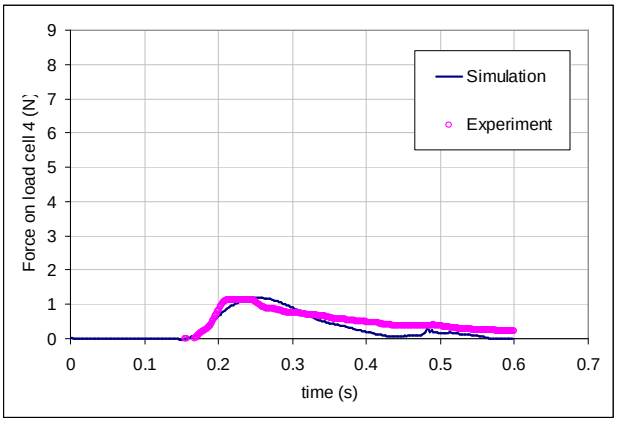

(A)

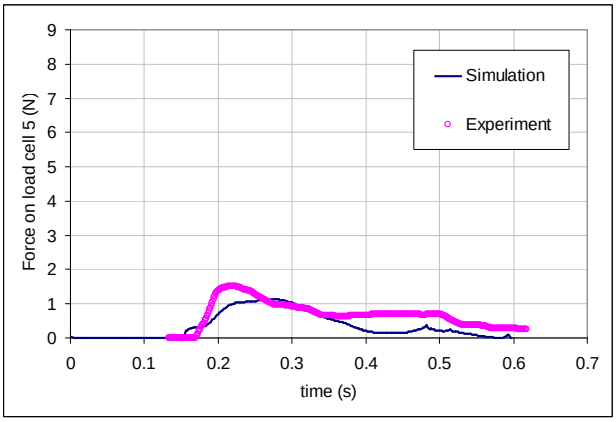

(B)

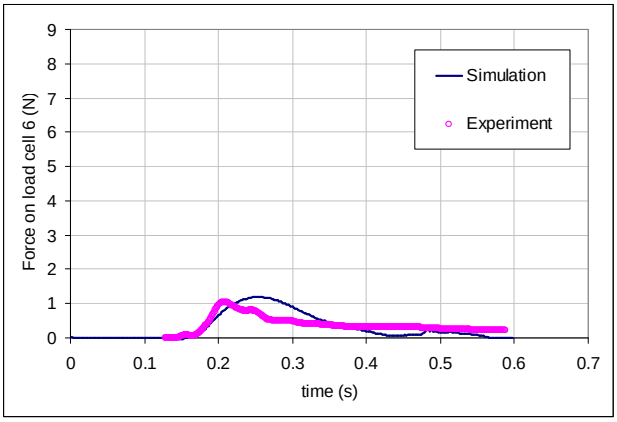

(C)

Figure 8.2.25 Comparison of green water loading on load cells 4, 5 and 6, respectively when ship was travelling at Fn = 0.30 in waves of equivalent full-scale height of 8.0m and period of 12 seconds.

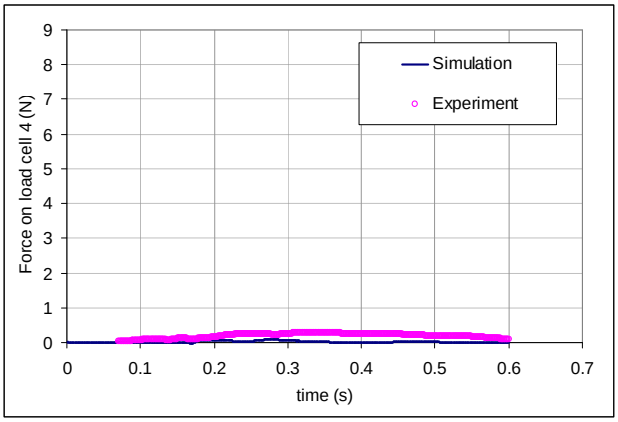

(A)

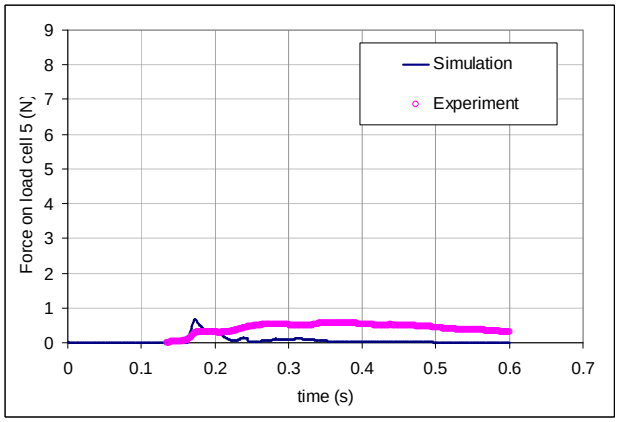

(B)

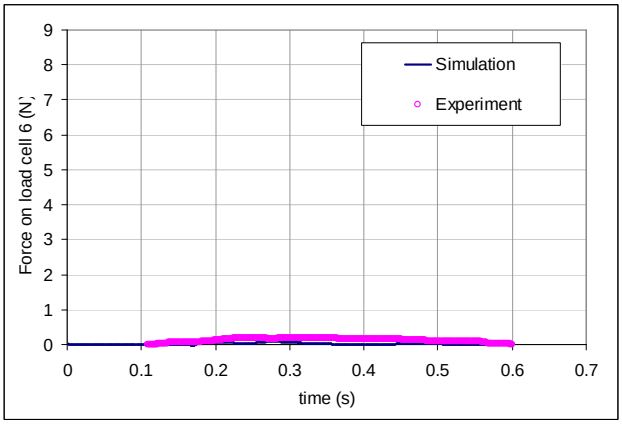

(C)

Figure 8.2.26 Comparison of green water loading on load cells 4, 5 and 6, respectively when ship was travelling at Fn = 0.30 in waves of equivalent full-scale height of 8.0m and period of 11 seconds.

8.2.3 Longitudinal green water loading on load cells in top row

It was noticed both in experiments and in simulation that for the cases of no breakwaters, green water loads on top row of load-cell box were very small (well less than the lower limit of 0.5N). The comparison was therefore found unnecessary and the results were assumed to be insignificant (see also Figure 5.9.7 in Section 5.9, Chapter 5).

Figure 8.2.27 shows the capture of the moment in simulation when green water load on load cell 2 was maximum and Figure 8.2.28 shows the vector field at this time. As Figure 8.2.28 indicated, the water in front of load cell 2 was the run-up water from load cell 5. The velocity of the water passing load cell 2 was relatively high, around 1.5 m/s at model scale. However, this water was running almost parallel to the surface and therefore there was no significant pressure imposed on the surface. The longitudinal loading, as a result, was low as noticed.

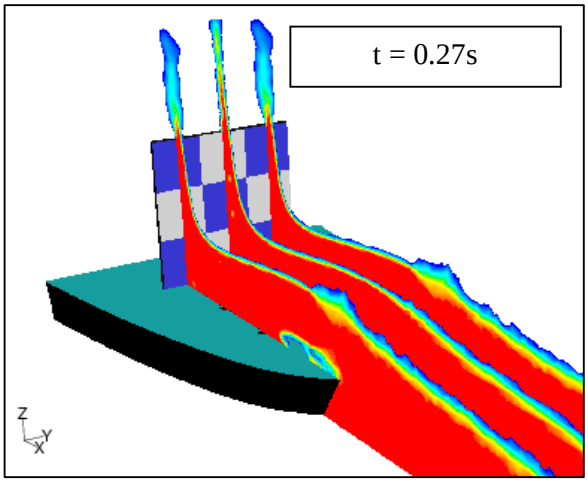

Figure 8.2.27 Snapshot corresponding to maximum loads on load cells 1, 2 and 3 in run H08T12Fn025.

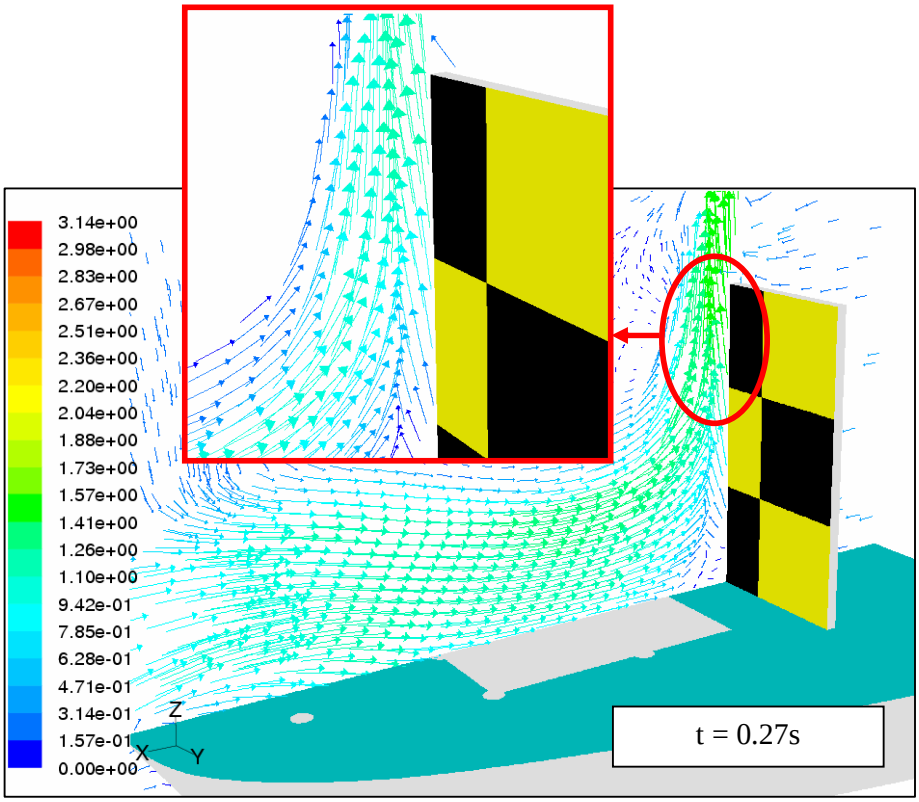

Figure 8.2.28 Vector field around load cell 2 at the time green water load on this load cell was maximum in run H08T12Fn025.

8.2.4 Total longitudinal green water loading on load-cell box

With green water loading on the top row being trivially small, the total green water loading on load cell box was mostly made up from the loads on middle row and bottom row. Figures 8.2.31 to 8.2.39 compared the total load on load-cell box measured in experiment with that in simulation. There was a good agreement in terms of peak loads, the rise time and the general behaviour of the loads. As already mentioned in Section 8.2.1, the numerical results herein also indicate some over-prediction of the loading after the peak load had been reached. The reason, as already explained, was the pitching motion of the ship during the test which helped to drain green water faster.

Figure 8.2.29 compared the peak loads by simulation with those by experiments. It showed a fair agreement with a mean error of 7 percent and standard deviation of 17 percent.

Figure 8.2.30 shows example views of green water flow at the time the total load on load-cell box reached maximum. Since the majority of this load came from load on bottom row, the moment the peak load was reached relatively coincided with the moment the loads on bottom row reached maximum (i.e. around the time of impact between front water and the load-cell box).

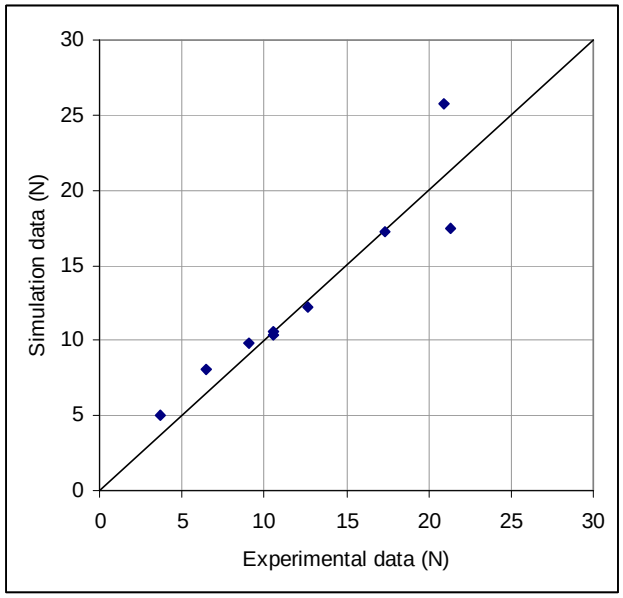

Figure 8.2.29 Comparison of peak loads on the load-cell box in total.

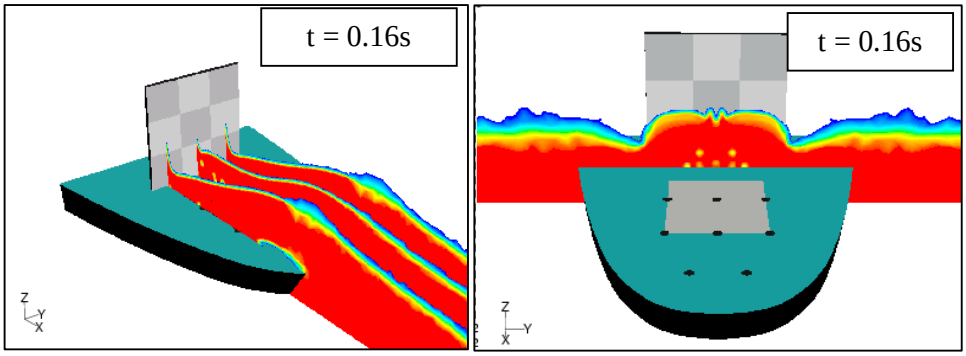

Figure 8.2.30 Sectional views of green water flow at the time when total green water load on load-cell box reached maximum for run H08T12Fn025.

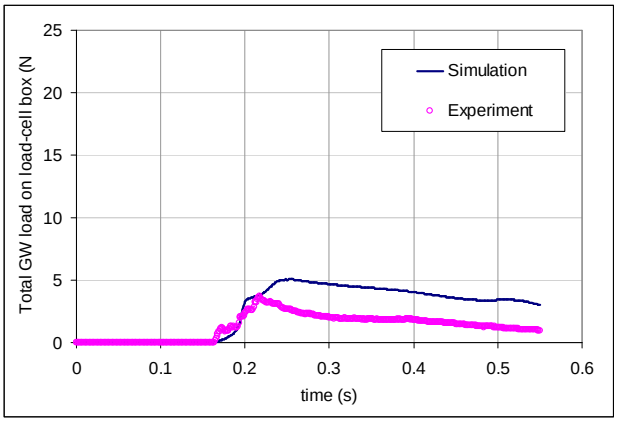

Figure 8.2.31 Ship was travelling at Fn = 0.20 in waves of equivalent full-scale wave height of 8.0m and wave period of 13 seconds.

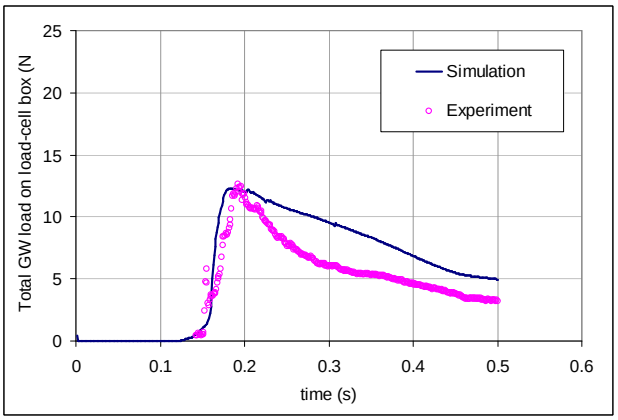

Figure 8.2.32 Ship was travelling at Fn = 0.20 in waves of equivalent full-scale wave height of 8.0m and wave period of 12 seconds.

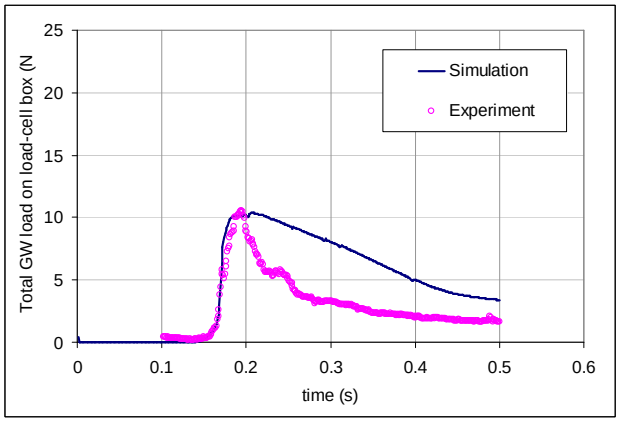

Figure 8.2.33 Ship was travelling at Fn = 0.20 in waves of equivalent full-scale wave height of 8.0m and wave period of 11 seconds.

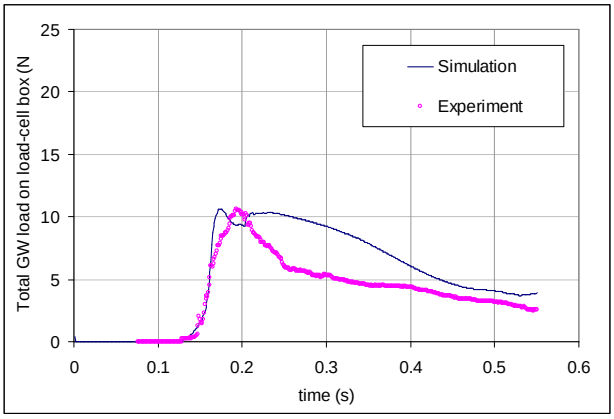

Figure 8.2.34 Ship was travelling at Fn = 0.25 in waves of equivalent full-scale wave height of 8.0m and wave period of 13 seconds.

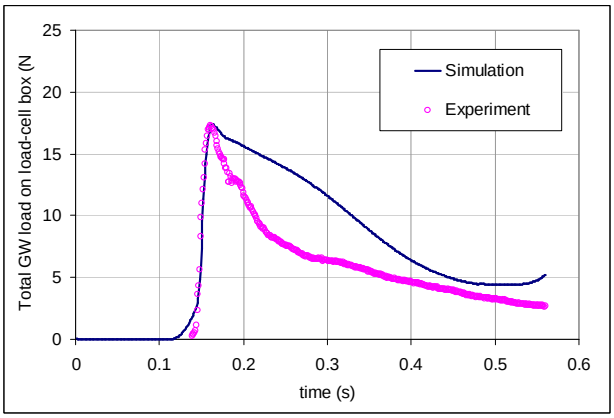

Figure 8.2.35 Ship was travelling at Fn = 0.25 in waves of equivalent full-scale wave height of 8.0m and wave period of 12 seconds.

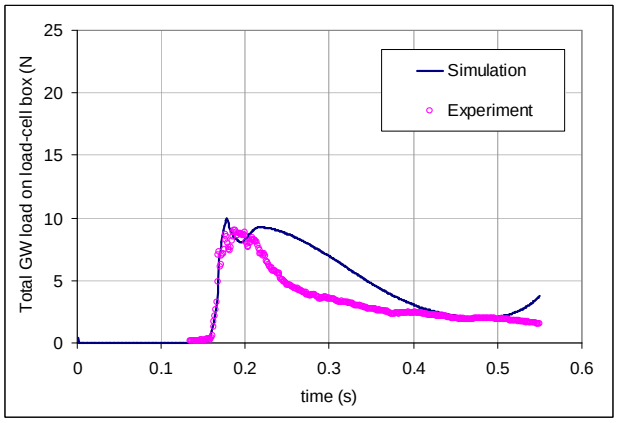

Figure 8.2.36 Ship was travelling at Fn = 0.25 in waves of equivalent full-scale wave height of 8.0m and wave period of 11 seconds.

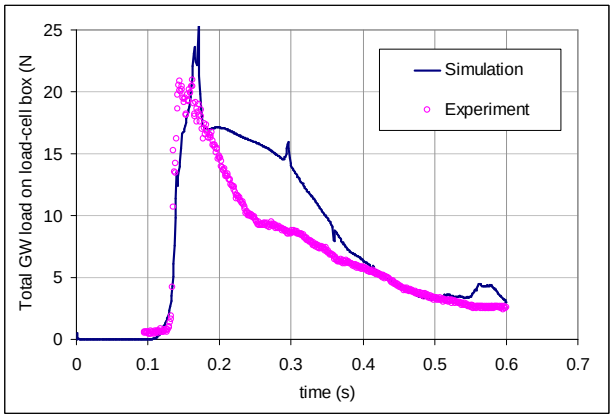

Figure 8.2.37 Ship was travelling at Fn = 0.30 in waves of equivalent full-scale wave height of 8.0m and wave period of 13 seconds.

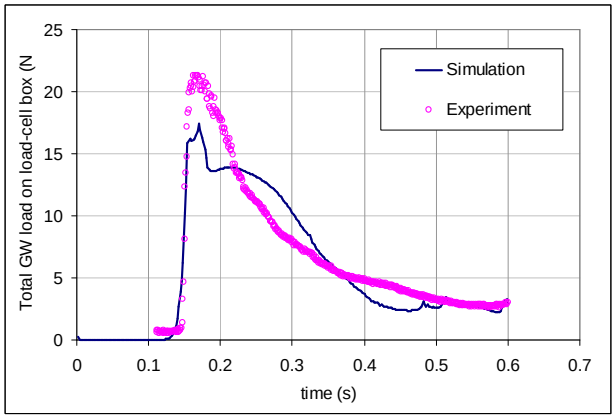

Figure 8.2.38 Ship was travelling at Fn = 0.30 in waves of equivalent full-scale height of 8.0m and period of 12 seconds.

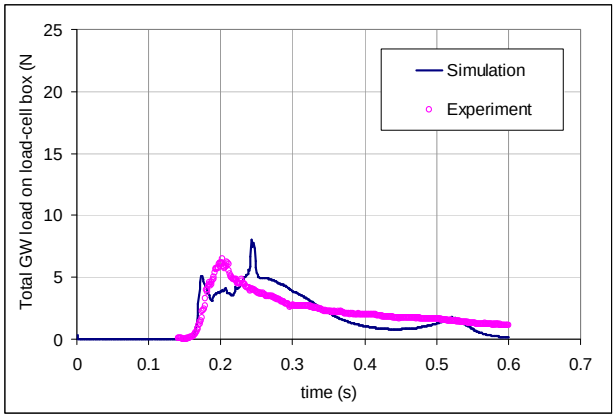

Figure 8.2.39 Ship was travelling at Fn = 0.30 in waves of equivalent full-scale height of 8.0m and period of 11 seconds.

8.3 Comparison of vertical green water loading in case of no breakwater on board

When shipped onto the main deck, green water does not only cause damage to vertical structures, it also results in substantial loading on the deck plating. As discussed in Section 4.9.9, this loading comprises of three components:

- Gravity or the weight of the water mass that lands on deck.
- Loading caused by the acceleration of the deck itself.
- Loading caused by the change in height of green water.

In simulation, the acceleration of the deck could not be simulated due to limited computational resources. Therefore, the second component was not included in the simulation results. The comparison between experiment and simulation results is as in Figure 8.3.3 to 8.3.11. Note that the deck panel used for monitoring deck loading was relatively large. At model scale, the dimensions were 98.36mm×123.28mm (equivalent to approximately 25 percent of the deck area between forward perpendicular and station 9). The reason for using such a large panel was due to limited number of load cells that could be used. In this test series, only one deck load cell was available. It was decided that global loading would be measured rather than local loading which might not reflect the general behaviour of the vertical green water loading.

Comparison shows that on overall, both experimental and simulation data showed similar order of deck loading even though the characteristics of the load curves appeared to differ to certain extent. Experimental data indicated that there was noise interference of a frequency of approximately 10Hz in the signals. Investigation into this noise interference revealed that it could be attributed to the natural frequency of the ship hull in bending. Post-experiment calibration showed that when an impulsive load was applied to the deck load cell, the signals did get influenced by the natural frequency of the hull. This could only be addressed by

stiffening the hull. Attempts were undertaken to filter out this noise but the outcome was not as reliable. Hence, the experimental data were smoothed such that up to the peak load, the data were kept intact. After that, a best-fit curve was fitted to the data and the results are as in Figures 8.3.3 to 8.3.11.

The simulation results showed some impulsive characteristics in the load curves, especially at the beginning when the water started to land on the deck. The experimental data, on the other hand, showed a more gradual increase in load curve at the time the water was shipped onto the deck. This could be related to the hull stiffness which helped to dampen the deck loading. In simulation, all the ship surfaces were assumed to be solid walls, which meant that the stiffness of the hull was essentially infinite. The complete impulsive behaviour of the load curves could therefore be picked up in the simulation. If focusing on the peak loads and the general trend of the loading, the simulation results could reproduce a reasonable picture of how green water loading might affect the deck panel.

Figure 8.3.2 shows the sectional views of green water flow at the time the deck loads were maximum. When green water flow on deck was greater in mass, the prediction was better. For lesser quantity, green water flow was more scattering when it was shipped on board. Figure 8.3.2 (G) gives an example in run H08T11Fn030. The simulation in this case actually showed that due to the high velocity and small quantity of green water, the water impinged the deck in a projectile manner. It impacted the bottom row of the load-cell box before reflecting and landing on the deck load cell. Review of the video recording also implied a similar behaviour of water. The loading behaviour consequently became more complicated and difficult to predict precisely (Figures 8.3.10 and 8.3.11). In other cases when green water was in larger quantities, the general behaviour of green water was predicted at a reasonable level of accuracy (note that load component due to deck acceleration was not included).

Figure 8.3.1 compares the peak loads by simulation and experiment. The standard deviation of 28 percent implied a scattering of data around the mean value. However, with the mean error of minus 9 percent, the prediction was relatively fine and slightly under-estimating. In about 50 percent of the cases considered, the agreement was good. The interference of the natural frequency of the hull and the lacking of load component due to deck acceleration appeared to play primary roles in the discrepancies noticed herein.

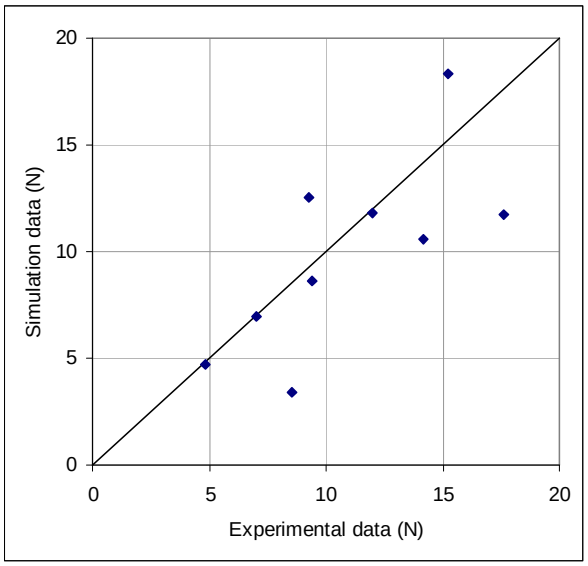

Figure 8.3.1 Comparison of peak loads on the deck load cell.

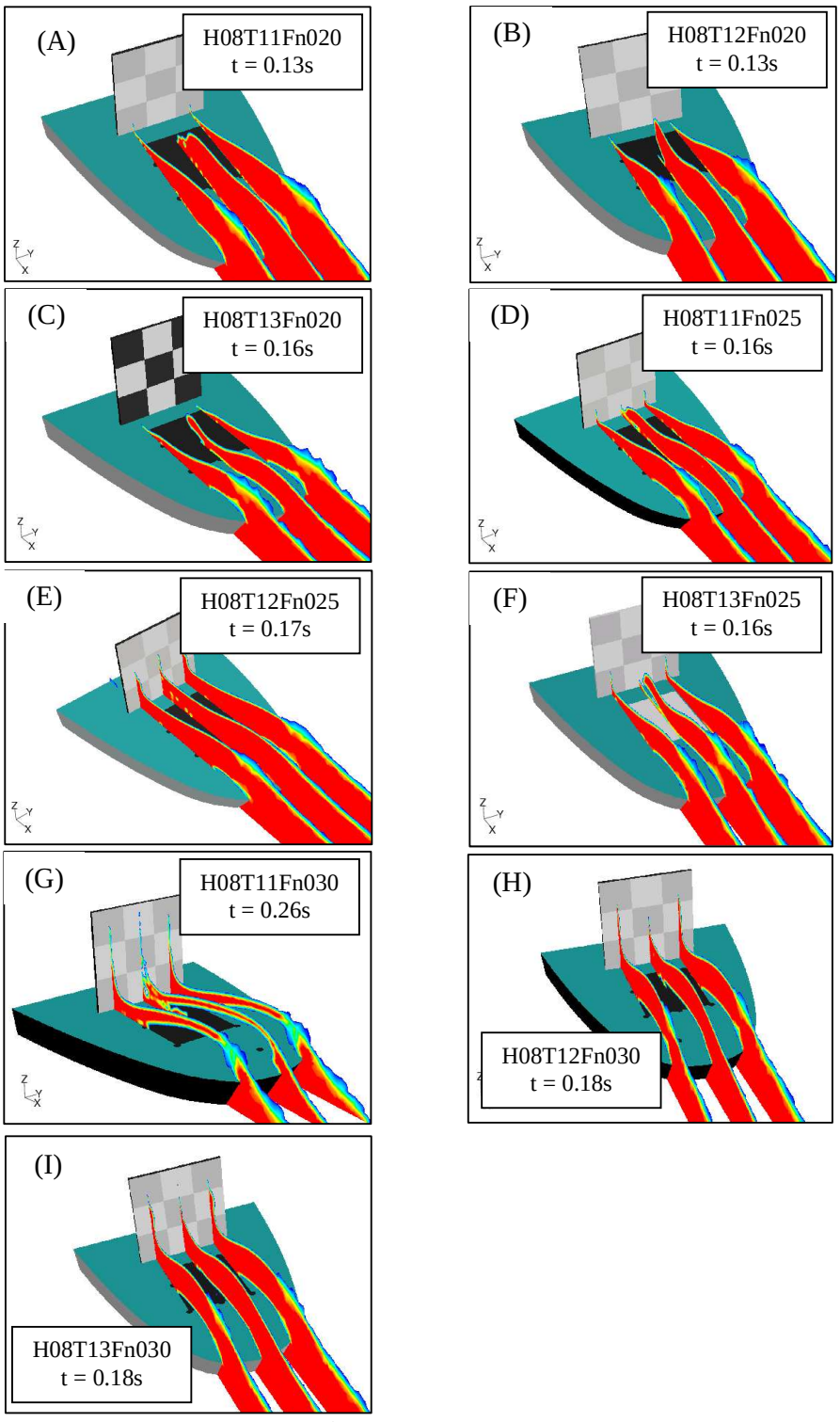

Figure 8.3.2 Green water flows corresponding to maximum loading on deck load cell.

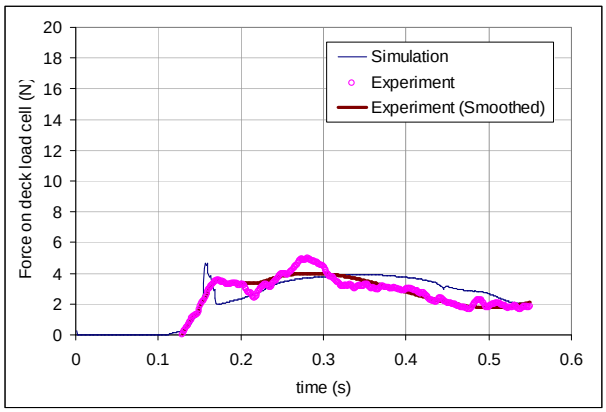

Figure 8.3.3 Ship was travelling at Fn = 0.20 in waves of equivalent full-scale height of 8.0m and period of 13 seconds.

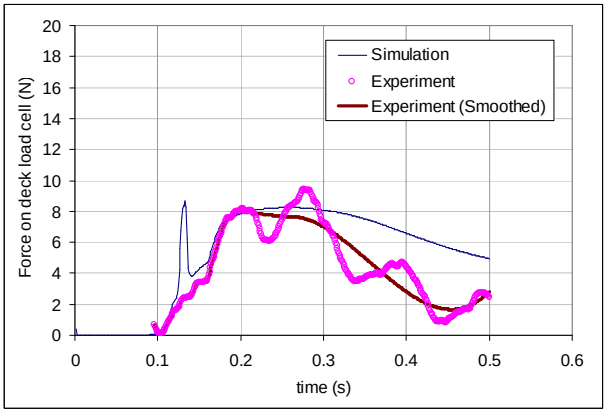

Figure 8.3.4 Ship was travelling at Fn = 0.20 in waves of equivalent full-scale height of 8.0m and period of 12 seconds.

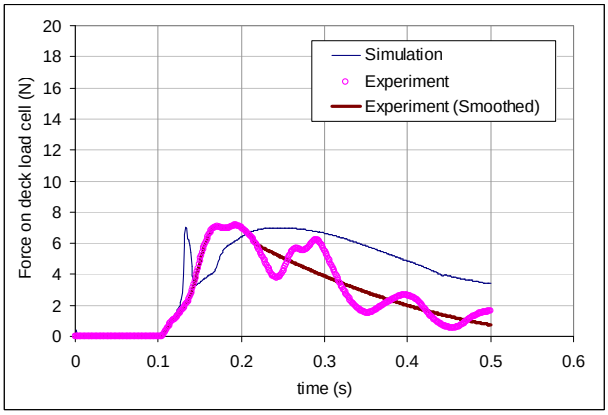

Figure 8.3.5 Ship was travelling at Fn = 0.20 in waves of equivalent full-scale height of 8.0m and period of 11 seconds.

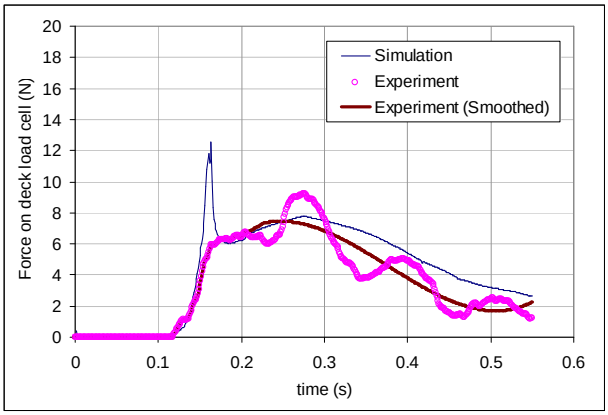

Figure 8.3.6 Ship was travelling at Fn = 0.25 in waves of equivalent full-scale height of 8.0m and period of 13 seconds.

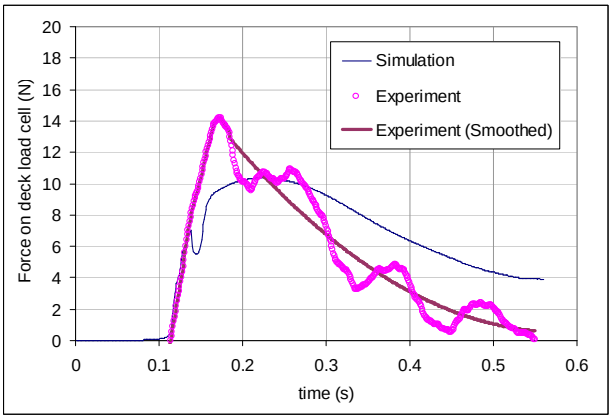

Figure 8.3.7 Ship was travelling at Fn = 0.25 in waves of equivalent full-scale height of 8.0m and period of 12 seconds.

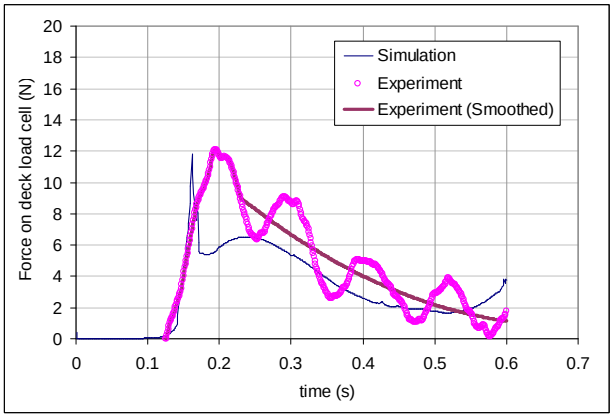

Figure 8.3.8 Ship was travelling at Fn = 0.25 in waves of equivalent full-scale height of 8.0m and period of 11 seconds.

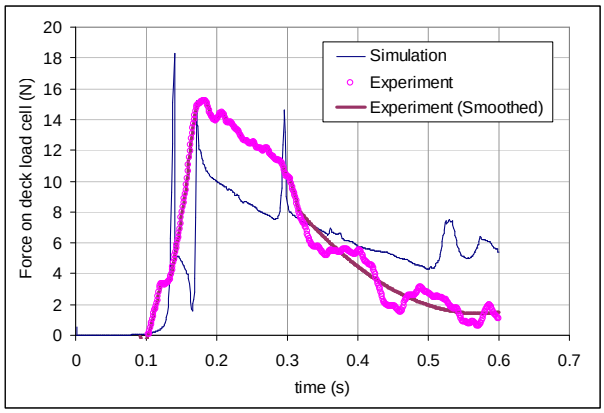

Figure 8.3.9 Ship was travelling at Fn = 0.30 in waves of equivalent full-scale height of 8.0m and period of 13 seconds.

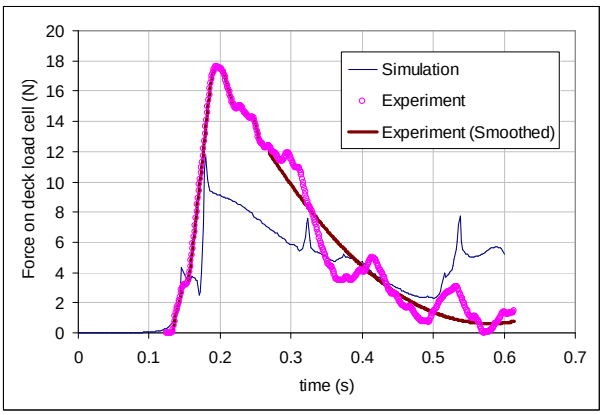

Figure 8.3.10 Ship was travelling at Fn = 0.30 in waves of equivalent full-scale height of 8.0m and period of 12 seconds.

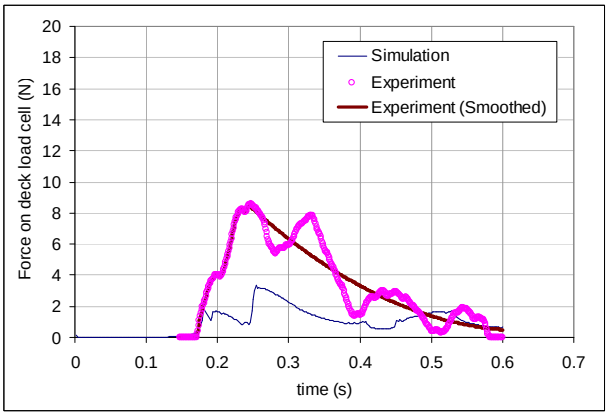

Figure 8.3.11 Ship was travelling at Fn = 0.30 in waves of equivalent full-scale height of 8.0m and period of 11 seconds.

8.4 Longitudinal green water loading when breakwaters are fitted

From this Section, the cases when breakwaters were fitted on the forecastle deck are analysed. With a large number of 10 generic breakwaters tested and due to the limitation in computational resources available, not all the conditions listed in Table 4.8.2 could be simulated and verified. Having taken all aspects into consideration, it was decided that for the best interests of validation without losing much generality, one representative condition was chosen for simulation with 10 breakwaters. This condition was when the ship travelled at Fn = 0.25 (approximately 20 knots at full scale) in regular head waves of equivalent full-scale height of 8m and period of 12s.

In the piloting researches using CFD analysis, Pham and Varyani (2004, 2006a) and Varyani et al. (2005) reported that the presence of the breakwater could create a water jet that overrode the breakwater and impacted the structures at greater height on the deck. This essentially meant that higher locations behind the breakwater could be exposed to larger green water loading. This was true in all types of breakwaters that Pham and Varyani (2004, 2006a) and Varyani et al. (2006) analysed, including V-type, Vane-type and rectangular breakwater with and without perforations. This Section will re-inspect this behaviour to ensure consistency of the results reported previously.

Due to a large number of load cells, the comparisons are carried out in several stages. Firstly, the loads on the load-cell box are compared. Then green water loading on the breakwater is validated. Finally, comparison of vertical green water loads is carried out. In order to identify the test runs, the experiments were denoted based on the test parameters specific to the test. Because the validation was carried out only in one wave condition and one ship velocity (Section 8.1), the parameters used in coding the test runs included only the height of the breakwater and the diameter of the perforations. In case of no perforations on the

breakwater, the diameter was referred to as zero. Table 8.4.1 lists the codes of the test runs and their associated identity parameters.

Table 8.4.1 Denotation of test runs in the test series with breakwaters

Run Code	Height of Breakwater (mm)	Diameter of Perforations (mm)
h051D000	51.0	0.0
h051D105	51.0	10.5
h051D140	51.0	14.0
h051D175	51.0	17.5
h076D000	76.2	0.0
h076D105	76.2	10.5
h076D140	76.2	14.0
h076D175	76.2	17.5
h101D000	101.6	0.0

8.4.1 Breakwater height of 51mm and no perforations

Without the perforations, there was no water passing through the breakwater and structures at the level close to the main deck are better protected. Figure 8.4.1 shows the front view of the breakwater and the load-cell box and Figures 8.4.4 to 8.4.10 shows the comparison between the simulation and experiment. At a height of 51mm (model scale), the breakwater was one third of the height of the load-cell box. It should be noted that, during the course of the experiments, load cells 1, 4 and 9 mal-functioned and therefore the comparison could only be carried out on other load cells. Also, in this particular experiment, signals from load cell 7 were very low due to small loading and were dominated by noise. To keep consistency in the comparison process, the load on load cell 7 was assumed to be equal to that on load cell 8.

In general, the simulation predicted relatively well the experiment results including the trend, peak values and the rise-times. The peak loads matched within an error of approximately 10 percent. Measurements from load cells 7 and 8

indicated that the loads at this height were low due to protection by breakwater. As mentioned before, loading of under 0.5N could be dominated by noises and could not well reflect the actual process. As a result, it was ignored.

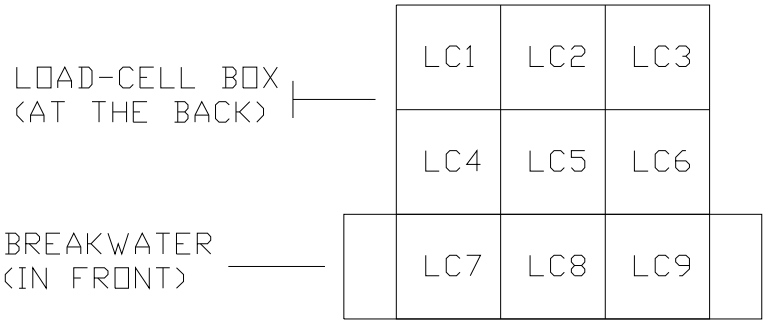

Figure 8.4.1 Front view of breakwater and load-cell box.

Figures 8.4.4 and 8.4.5 show that the top row of load-cell box recorded larger loads than lower rows (Figures 8.4.6 to 8.4.9). Recalling Section 8.2, in which the tests were without breakwaters, the loads on load cells in the top row were so small that they were assumed insignificant and ignored. With a breakwater, the results indicated that there was a green water impact at top row of load-cell box. This was investigated from simulation outputs and Figure 8.4.2 shows the sectional view of green water flow at the time green water loads on the top row were maximum. It is clear that when interacting with the breakwater, green water flow formed a water jet which took off and directly impacted the top row of load-cell box. This resulted in the loading as in Figures 8.4.4 and 8.4.5.

The first green water impact on the load-cell box was the most aggressive. Later, the follow-up water attenuated and the take-off angle of the water jet started to reduce. The water jet then began to hit the load cells at lower levels. Figure 8.4.3 captures the view of green water flow at the time the loads on the middle row were maximum. Comparing Figures 8.4.6 and 8.4.7 with Figures 8.2.22 indicated that green water loads on the middle row were of similar order to the case when no breakwater was used.

Overall, the breakwater helped to reduce the total load on load-cell box substantially. By comparing Figure 8.4.10 with Figure 8.2.35, it is noticed that the reduction was more than 50 percent. Most of this reduction came from the load cells in the bottom row where the loads were reduced by approximately 90 percent. Even though the load cells in the top row faced greater loads, they were well offset by the reduction on the bottom row.

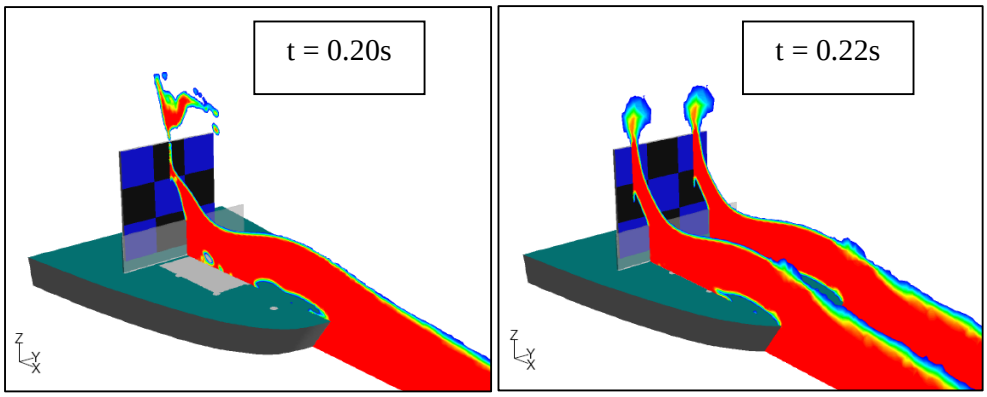

Figure 8.4.2 Snapshots corresponding to maximum impact loads on load cell 2 (left) and load cell 3 (right).

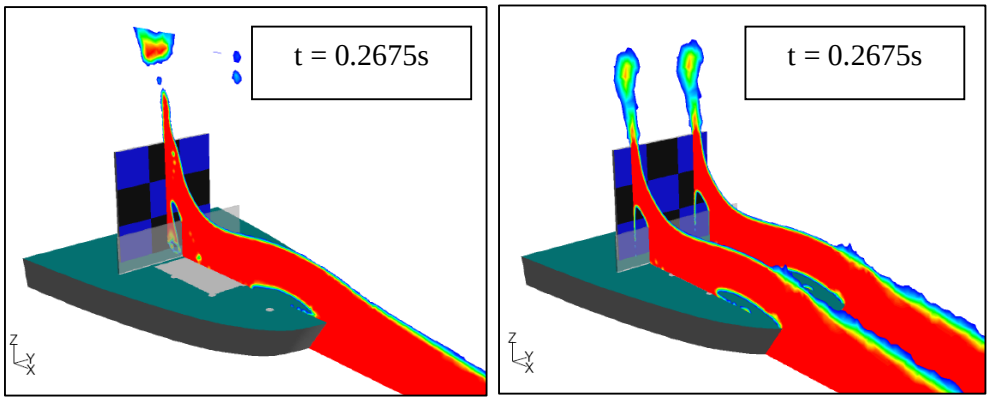

Figure 8.4.3 Snapshots corresponding to maximum impact loads on load cell 5 (left) and load cell 6 (right).

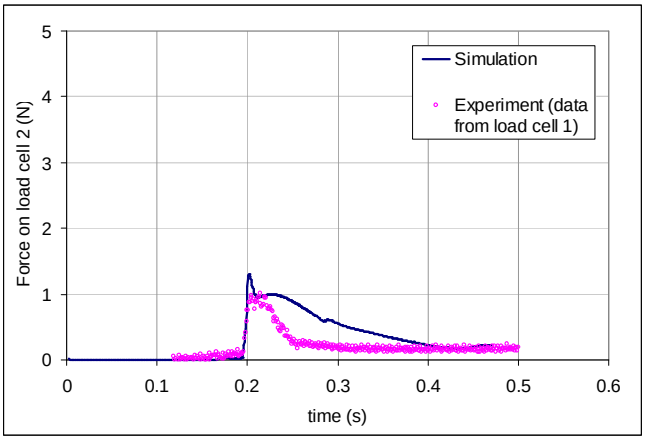

Figure 8.4.4 Comparison of green water loading on load cell 2.

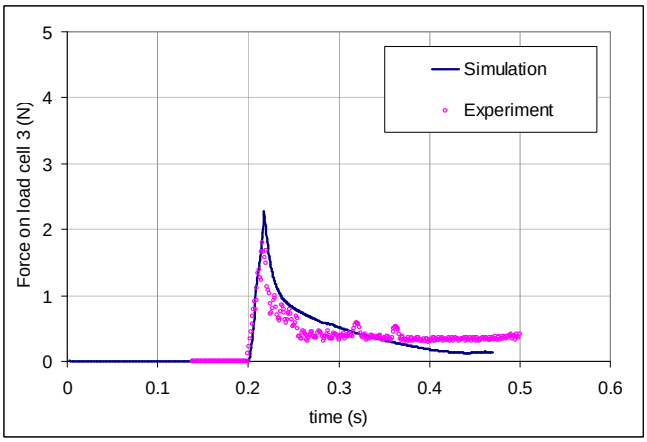

Figure 8.4.5 Comparison of green water loading on load cell 3.

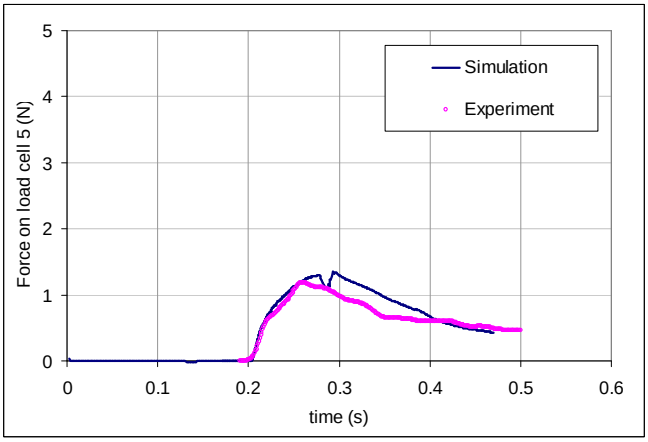

Figure 8.4.6 Comparison of green water loading on load cell 5.

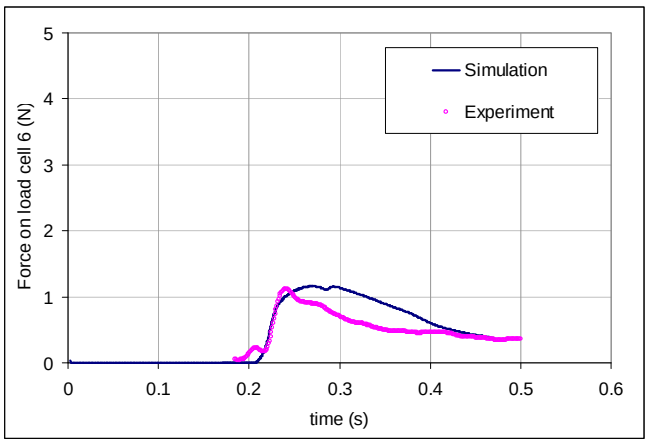

Figure 8.4.7 Comparison of green water loading on load cell 6.

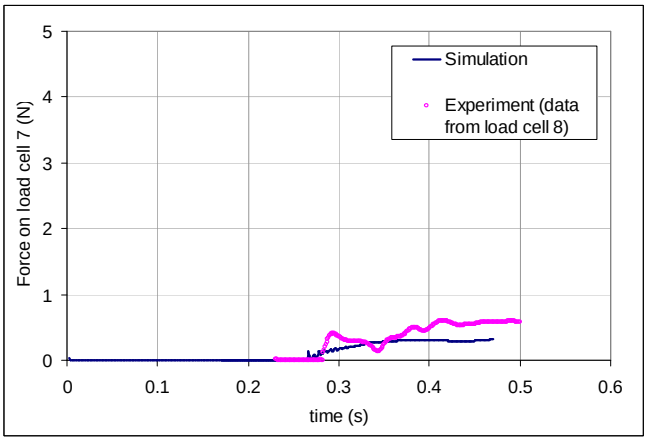

Figure 8.4.8 Comparison of green water loading on load cell 7.

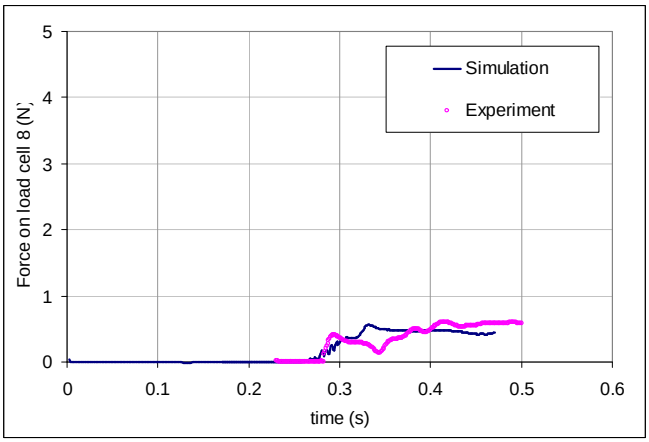

Figure 8.4.9 Comparison of green water loading on load cell 8.

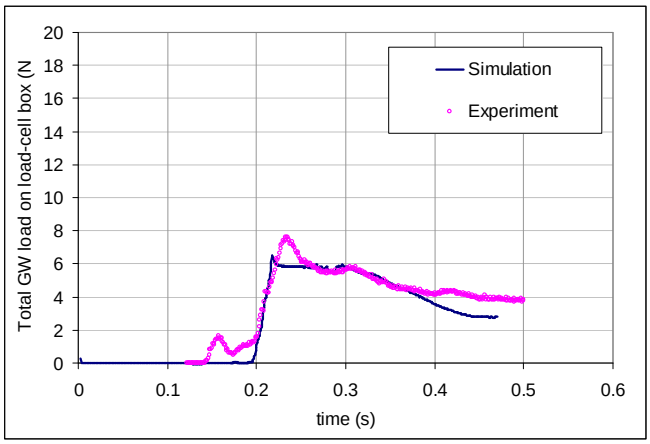

Figure 8.4.10 Comparison of total green water loading on load-cell box.

8.4.2 Breakwater height of 51mm and perforation diameter of 10.5 mm

The perforations on the breakwater (Figure 8.4.11) would create passages for water to pass through (Figure 8.4.14). As described by Pham and Varyani (2004, 2006a) and Varyani et al. (2006), the breakwater could hold back a large amount of the front water. And as this water piled up in front of the breakwater, this created a buffer of stagnant water that diverted the follow-up water upwards. A water jet was then created and overrode the breakwater (Figures 8.4.12 and 8.4.13). Since this water jet was formed by the follow-up water, it normally reached the structures behind the breakwater later than the water that went through the perforations (Figure 8.4.14). By comparing the impact times in Figures 8.4.15 to 8.4.18 with Figures 8.4.19 and 8.4.20, it was observed that the impacts on load cells 7 and 8 were caused by the water that passed through the breakwater and they were 0.06 seconds earlier than the impacts on load cells 2 to 6 which were caused by the overriding water. This time lag created a step in the total load curve on the load-cell box as a whole (Figure 8.4.21). The simulation could actually predict this behaviour relatively well.

As far as validation is concerned, the simulation predicts quite well the behaviour, magnitude and the rise-times of green water loads on individual load cells. Even

though the loads on bottom row were slightly under-estimated (Figures 8.4.15 and 8.4.16), on overall, the mean difference in the peak loads was approximately 10 percent.

Figures 8.4.12 to 8.4.14 show the sectional views of green water flow when the loads on top, middle and bottom rows were maximum, respectively. These events took place at the time the water first impacted the load cells. Similar to observation in Section 8.4.1, the overriding water caused by the breakwater led to an increased loading on the top row (Figures 8.4.15 and 8.416 compared with trivial loads on the top row noted in Section 8.2.3).

Maximum loading on the bottom row was mostly caused by water that passed through the perforations (Figure 8.4.14). However, compared with Figure 8.2.10, it was reduced by 80 percent. The overall load on the load cell box was therefore reduced by approximately 55 percent in total due to the breakwater (comparing Figure 8.4.21 with Figure 8.2.35).

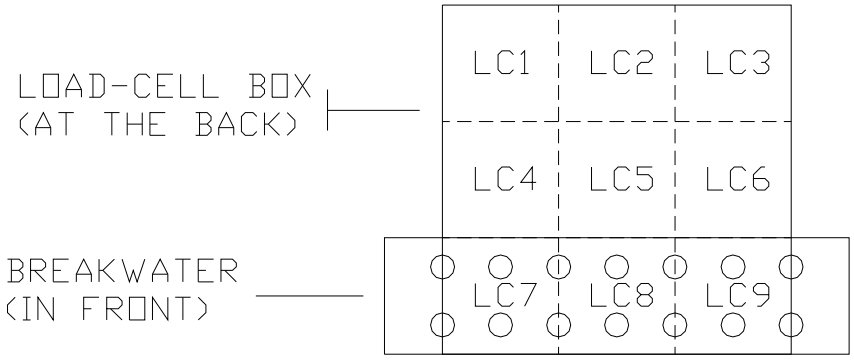

Figure 8.4.11 Front view of breakwater and load-cell box.

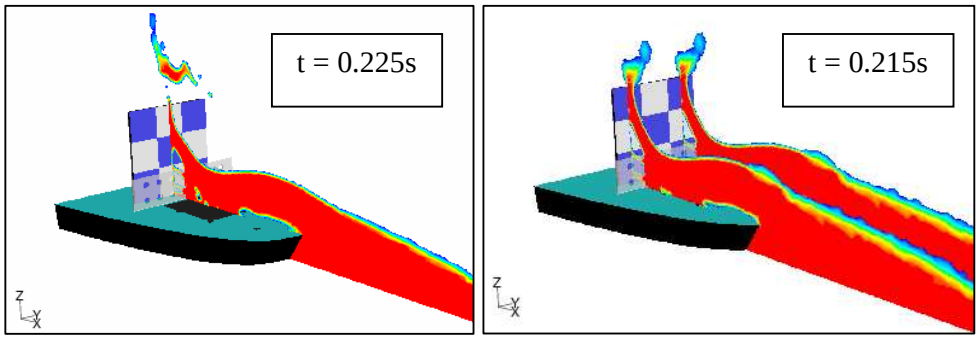

Figure 8.4.12 Snapshots corresponding to maximum impact loads on load cell 2 (left) and load cell 3 (right).

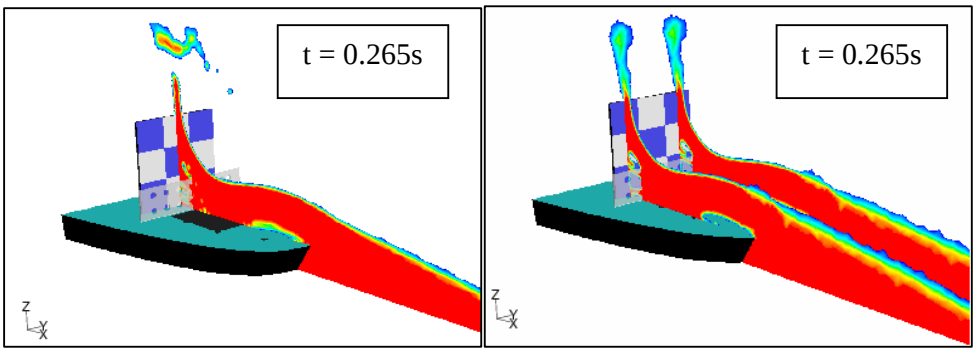

Figure 8.4.13 Snapshots corresponding to maximum impact loads on load cell 5 (left) and load cell 6 (right).

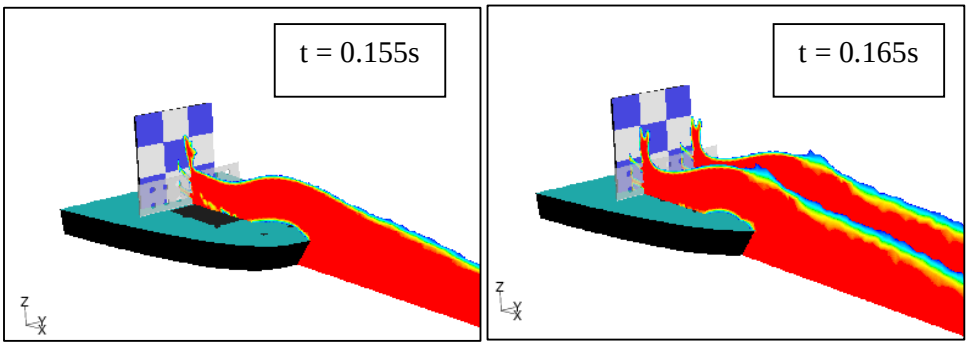

Figure 8.4.14 Snapshots corresponding to maximum impact loads on load cell 7 (right) and load cell 8 (left).

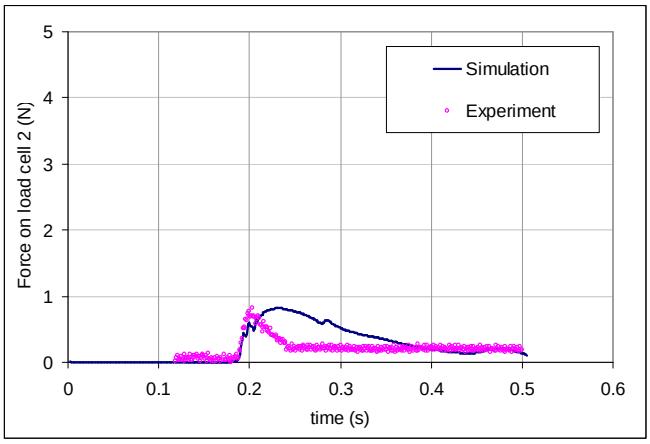

Figure 8.4.15 Comparison of green water loading on load cell 2.

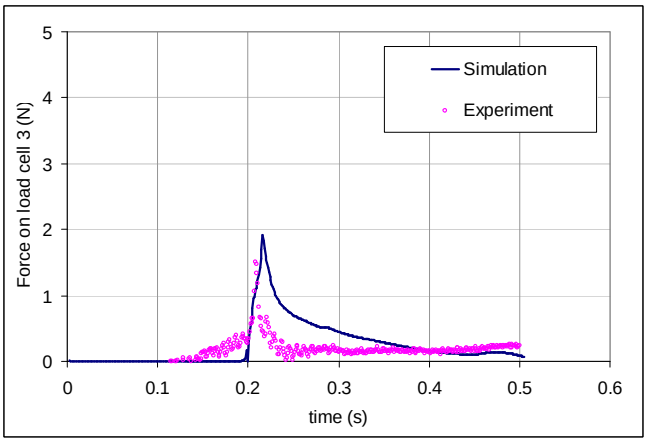

Figure 8.4.16 Comparison of green water loading on load cell 3.

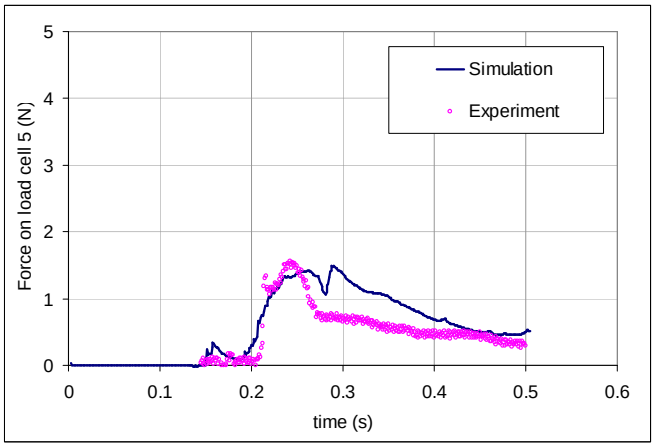

Figure 8.4.17 Comparison of green water loading on load cell 5.

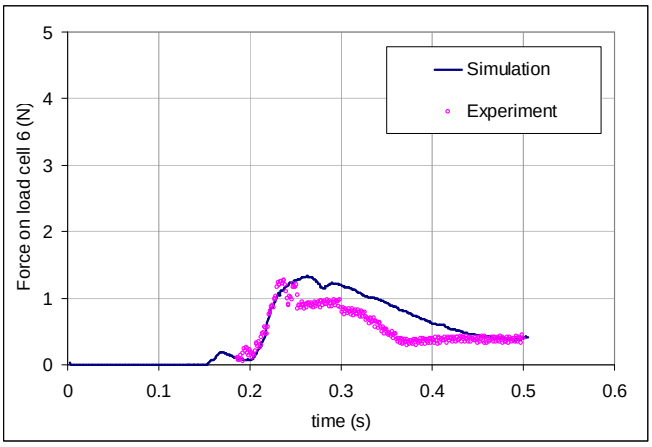

Figure 8.4.18 Comparison of green water loading on load cell 6.

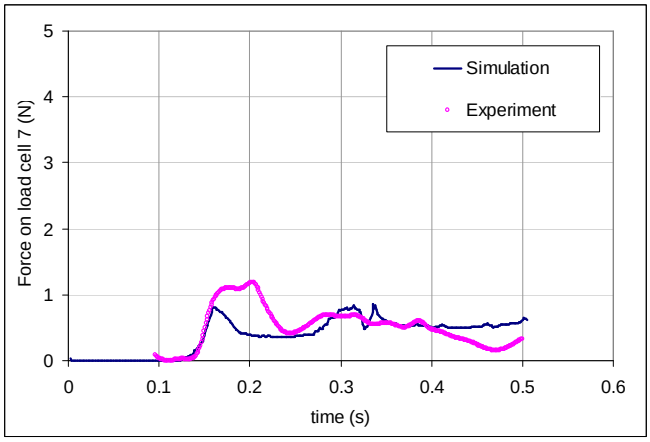

Figure 8.4.19 Comparison of green water loading on load cell 7.

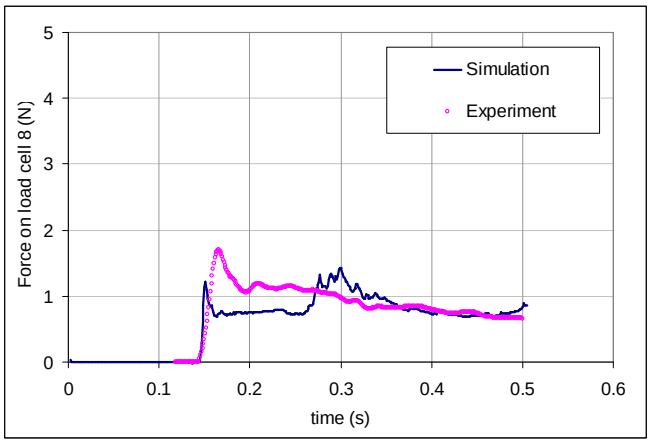

Figure 8.4.20 Comparison of green water loading on load cell 8.

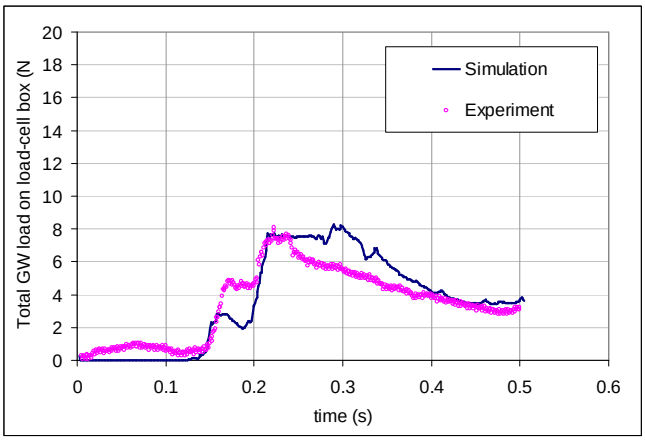

Figure 8.4.21 Comparison of total green water loading on load-cell box.

8.4.3 Breakwater height of 51mm and perforation diameter of 14.0 mm

The front view of the breakwater and load-cell box in this case is as in Figure 8.4.22 and comparison of longitudinal green water loads is as in Figures 8.4.27 to 8.4.33. In general, the simulation predicted the behaviour of green water loading relatively well even though the peak loads were slightly over-predicted for load cells at higher levels (load cells 2 to 6). The loads on bottom row (Figures 8.4.31 and 8.4.32) were well predicted.

As the perforation diameter was increased to 14.0mm, there was more green water passing through the breakwater. The green water loading on load cells 7 and 8, as a result, increased (comparing Figures 8.4.31 and 8.4.32 with Figures 8.4.19 and 8.4.20, respectively). As more water was allowed to pass through the breakwater, there was less water that overrode the breakwater and the water jet became less aggressive. As a result, the height reached on the load-cell box was lower (comparing Figure 8.4.23 with Figure 8.4.12).

Interestingly, the load curves of load cells 5 and 6 showed a double-peak characteristic and this was well reproduced by simulation (Figures 8.4.29 and 8.4.30). Using simulation data to analyse this observation, it revealed that the

double peak actually came from the double impacts on these load cells. The first impact was caused by the water that passed through the upper perforations (Figures 8.4.24 and 8.4.25). The second impact was from the water that overrode the breakwater. Since the overriding water was greater in mass (Figures 8.4.24 and 8.4.25), the second peak load was larger than the first as noticed in both numerical and experimental data.

Due to the breakwater, the loads on bottom row of load-cell box were reduced by approximately 70 percent. The middle row still faced the loads of similar order. The loads on the top row were, however, larger than when no breakwater was fitted. As explained earlier, this was due to the impact with the water that overrode the breakwater. Overall, the total load on the load-cell box was reduced approximately by 58 percent.

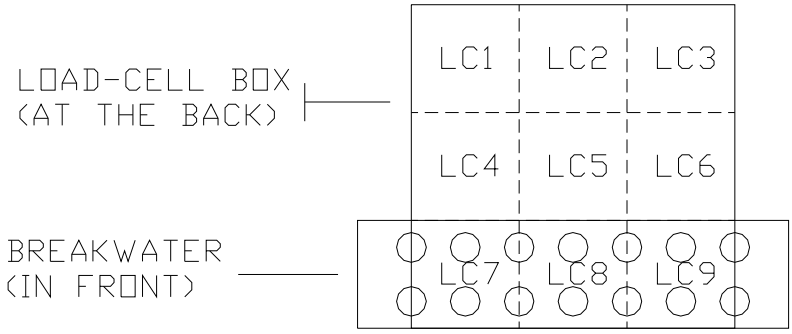

Figure 8.4.22 Front view of breakwater and load-cell box.

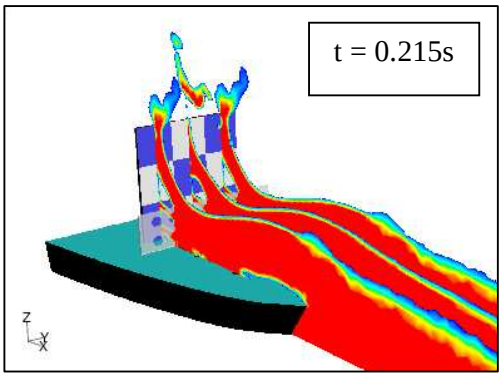

Figure 8.4.23 Snapshot corresponding to maximum impact loads on load cells 1, 2 and 3.

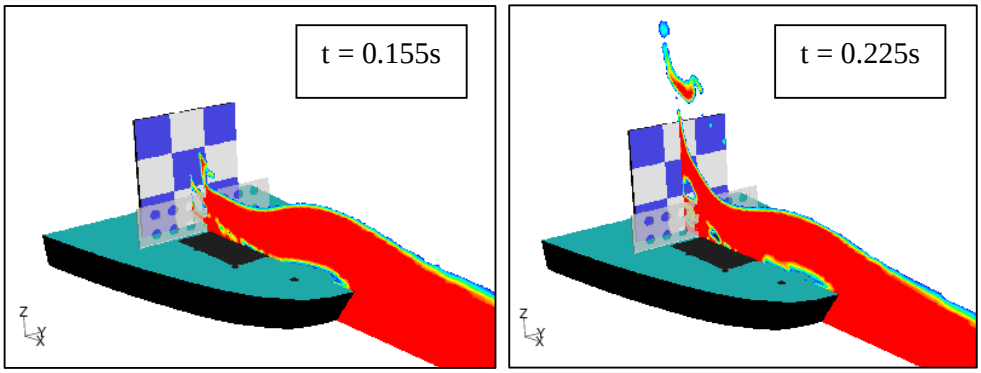

Figure 8.4.24 Snapshots corresponding to double impact loads on load cell 5.

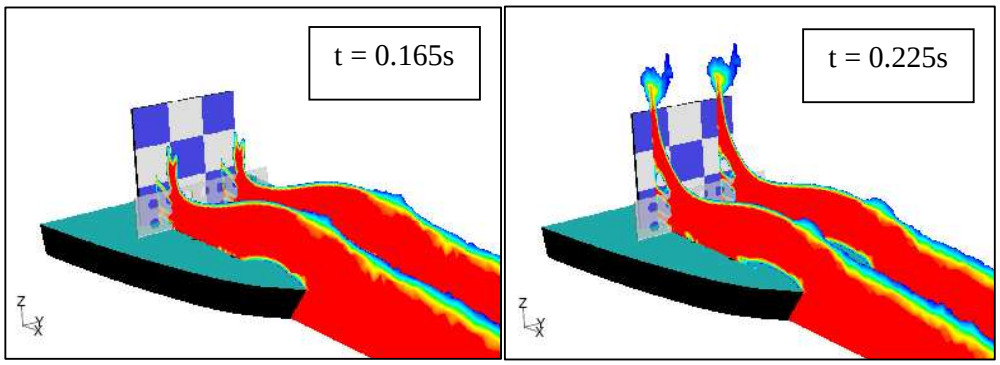

Figure 8.4.25 Snapshots corresponding to double impact loads on load cell 6.

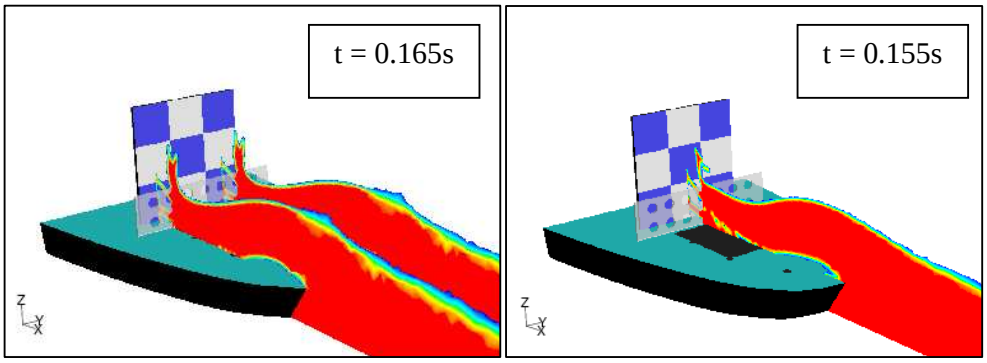

Figure 8.4.26 Snapshots corresponding to maximum impact loads on load cell 7 (left) and load cell 8 (right).

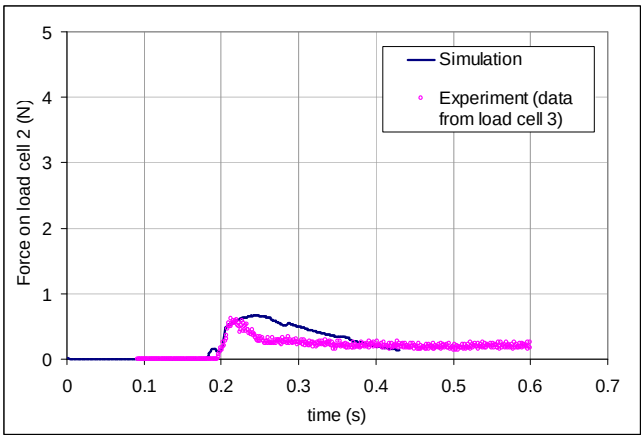

Figure 8.4.27 Comparison of green water loading on load cell 2.

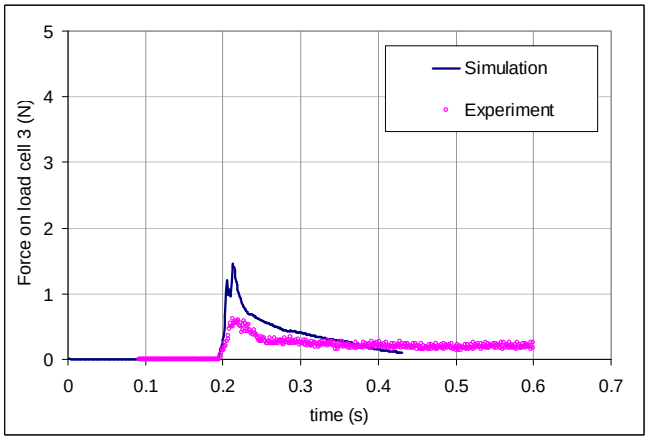

Figure 8.4.28 Comparison of green water loading on load cell 3.

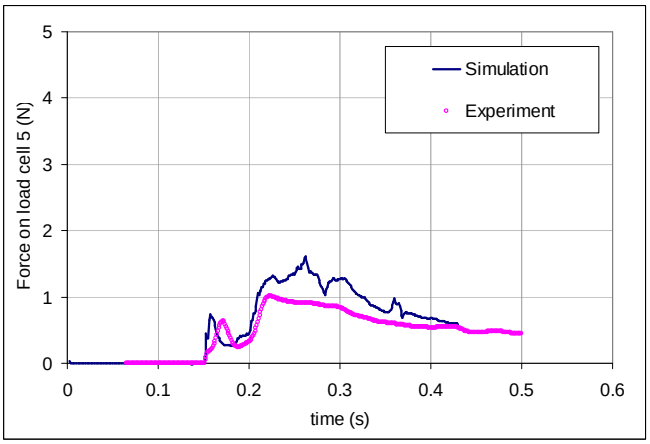

Figure 8.4.29 Comparison of green water loading on load cell 5.

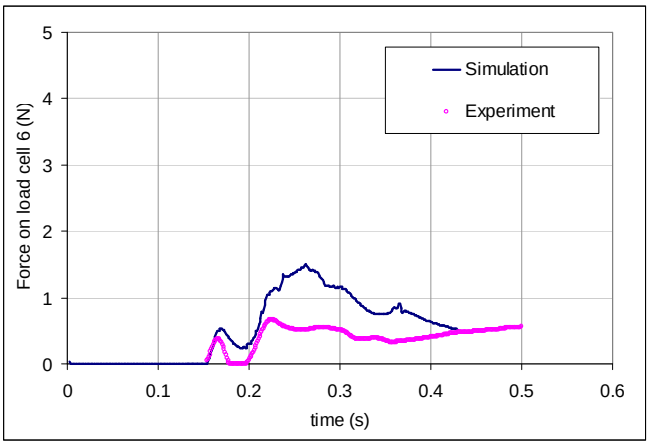

Figure 8.4.30 Comparison of green water loading on load cell 6.

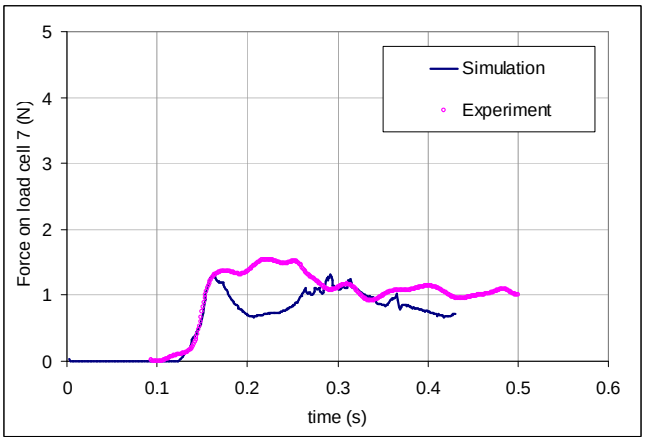

Figure 8.4.31 Comparison of green water loading on load cell 7.

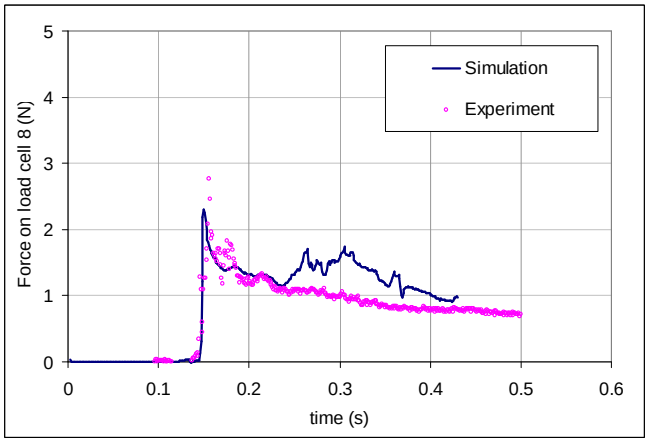

Figure 8.4.32 Comparison of green water loading on load cells 8.

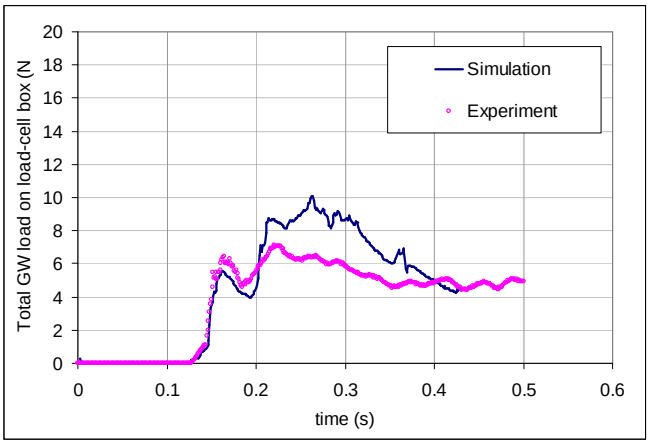

Figure 8.4.33 Comparison of total green water loading on load-cell box.

8.4.4 Breakwater height of 51mm and perforation diameter of 17.5 mm

Figure 8.4.34 shows the front view of the breakwater and the load-cell box aligned on deck. The validation between simulation and experiment is as in Figures 8.4.39 to 8.4.45. Except for loads on the top row where they were too small for an adequate validation, the other loads showed a relatively good agreement between the simulation and the experiment. All the behaviour, peak loads and rise time of the load curves were well predicted by the simulation. The mean error of predicted peak loads fell within 10 percent of the experimental values. Nevertheless, the simulation results showed some over-prediction at the tail of the load curves (behind the peak loads). The reason was as explained in Section 8.2.1, related to the pitching motion of the ship which could not be modelled in the simulation.

Characteristics of green water flow were relatively similar to observations in Section 8.4.3. The increased diameter of the perforations meant that more water could pass through the breakwater. This means that the strength of overriding water caused by the presence of the breakwater was reduced. As a result, the impact point on the load-cell box was lower, towards the middle row of load cells (Figure 8.4.34). It means that middle row had to face direct impact with the overriding water. However, since the strength of overriding water reduced, the

loading on the middle row was not necessarily higher (comparing Figures 8.4.41 and 8.4.42 with Figures 8.4.29 and 8.4.30, for example).

The bottom row definitely faced larger impact load since more water could pass through the breakwater (Figure 8.4.38). The double-peak in load curve of load cell 6 was well predicted by simulation (Figure 8.4.42). The first and minor peak was caused by the water that passed through the upper perforations (Figure 8.4.37 (left)) and the second (and major) peak was from the impact with overriding water (Figure 8.4.37 (right)).

With the use of breakwater, the loading on bottom row was reduced by approximately 50 percent (comparing Figures 8.4.43 and 8.4.44 with Figures 8.4.9 and 8.4.10, respectively). The total load on load-cell box, as a result, was reduced by approximately 40 percent (comparing Figure 8.4.45 with Figure 8.2.35).

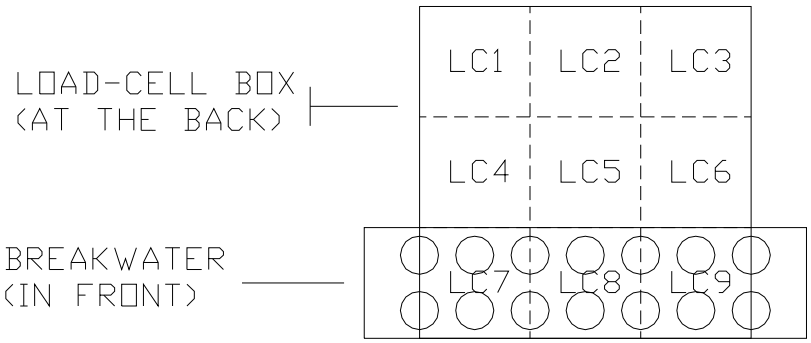

Figure 8.4.34 Front view of breakwater and load-cell box.

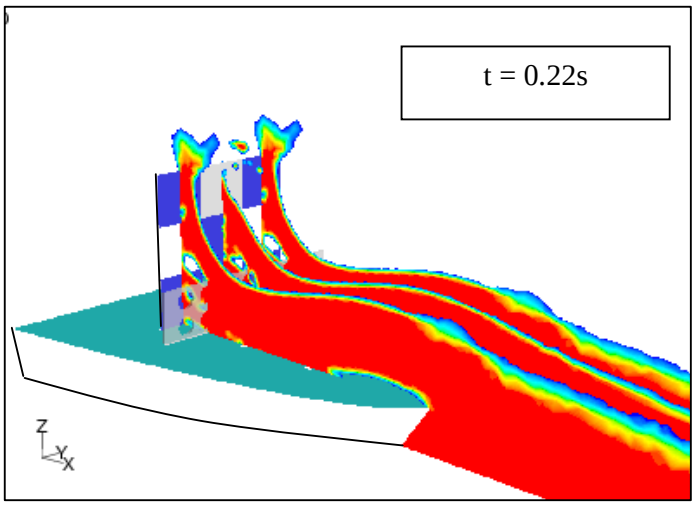

Figure 8.4.35 Snapshot corresponding to maximum impact loads on load cells 1, 2 and 3.

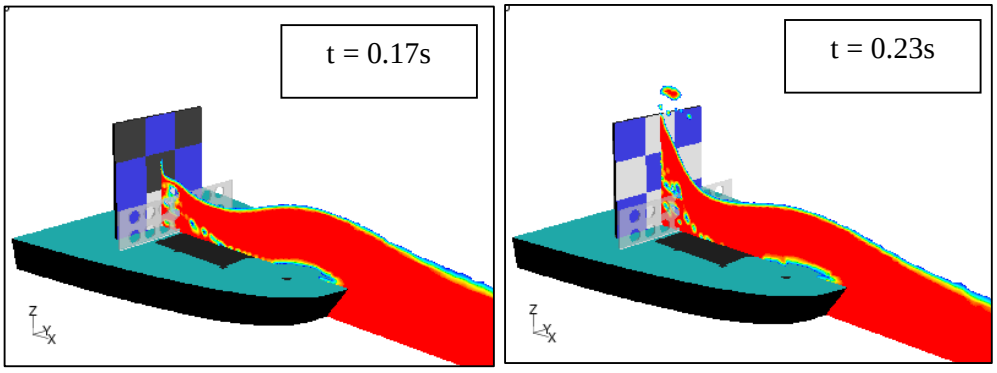

Figure 8.4.36 Snapshots corresponding to double impact loads on load cell 5.

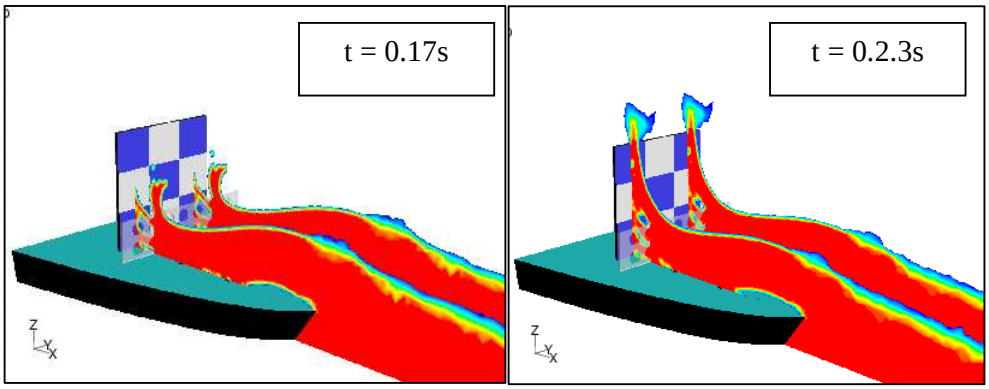

Figure 8.4.37 Snapshots corresponding to double impact loads on load cell 6.

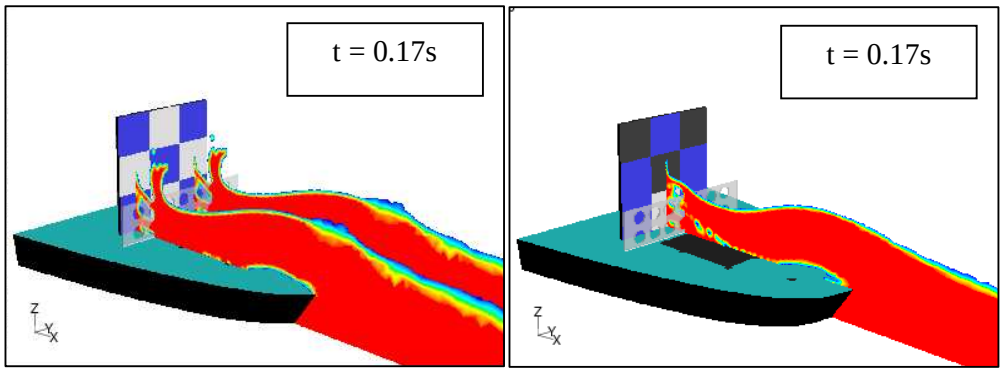

Figure 8.4.38 Snapshots corresponding to maximum impact loads on load cell 7 (left) and load cell 8 (right).

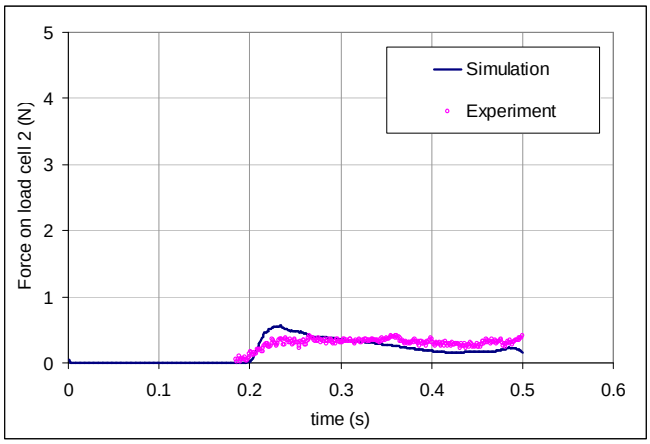

Figure 8.4.39 Comparison of green water loading on load cell 2.

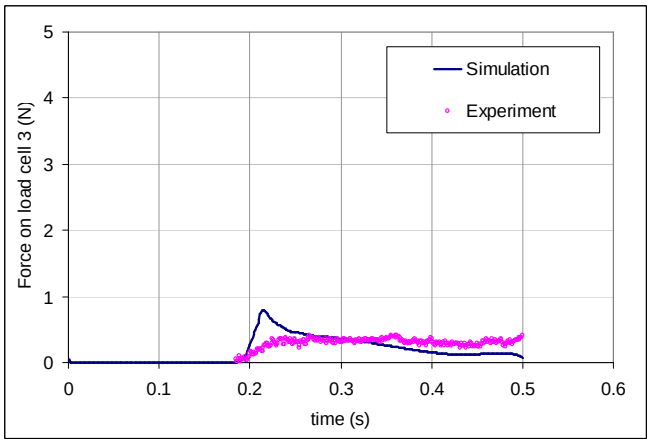

Figure 8.4.40 Comparison of green water loading on load cell 3.

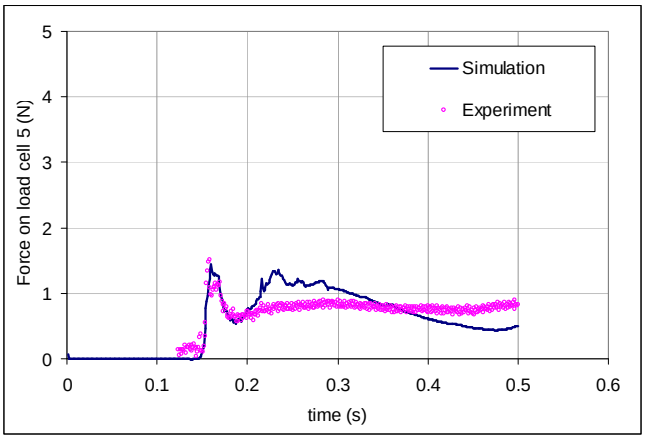

Figure 8.4.41 Comparison of green water loading on load cell 5.

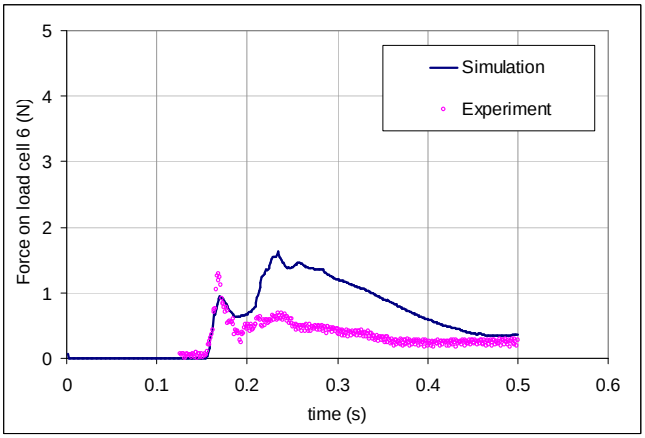

Figure 8.4.42 Comparison of green water loading on load cell 6.

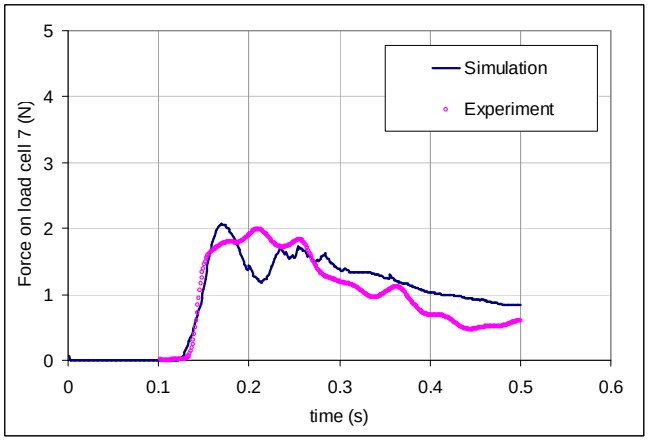

Figure 8.4.43 Comparison of green water loading on load cell 7.

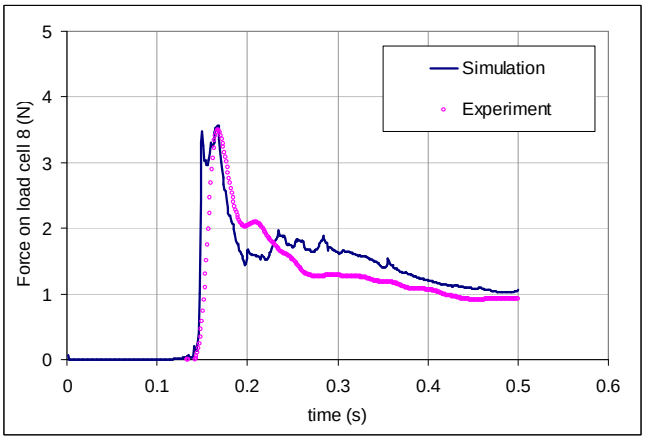

Figure 8.4.44 Comparison of green water loading on load cell 8.

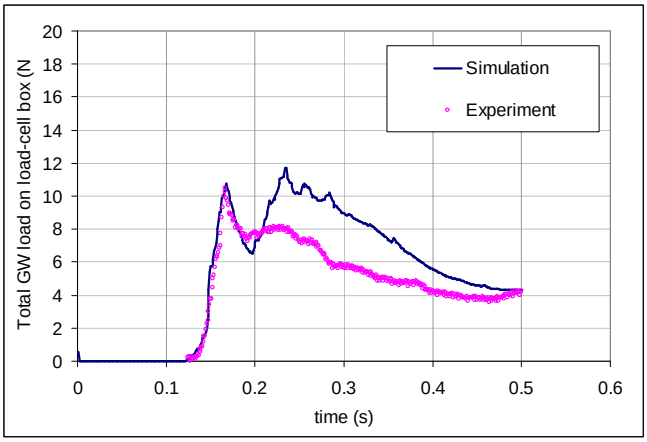

Figure 8.4.45 Comparison of total green water loading on load-cell box.

8.4.5 Breakwater height of 76.2mm and no perforations

The front view of the breakwater and the load-cell box is as in Figure 8.4.46. The height of the breakwater was increased to half the height of the load-cell box. The amount of protection to the load-cell box was more than previous cases as observed through experimental and simulation. Longitudinal loads on individual load cells became very small. Figure 8.4.49 plotted the total load on the load-cell box as a whole and it could be seen that the maximum load was only 2N (model scale). Comparing this with Figure 8.2.35, it was only around 10 percent of the maximum load faced by the load-cell box when no breakwater was fitted. Validation on individual load cells was not carried out since the loads were insignificant. Figure 8.4.49 indicates an agreement between simulation and experiment.

Figure 8.4.47 shows the moment when green water impacted the top row. Similar to other cases, the pile-up of water in front of the breakwater accounted for the overriding of green water which took off at the back of the breakwater in the form of a water jet. The increased height of the breakwater meant that the water jet took off at higher location. It was therefore likely to reach higher areas on the load-cell box (comparing Figure 8.4.2 with Figure 8.4.47). However, as the water went higher, kinetic energy transformed into potential energy so the velocity of the water jet reduced as a result. The time of impact was also later which meant that the impact in this case came from the water further at the tail of the green water mass. Since the energy of the water dissipated during its translation, the impact caused by this water became less severe. As a result, the impact on the top row of load-cell box became much weaker than that when the breakwater height was lower (see Section 8.4.1 for example). Figure 8.4.48 demonstrated the stage when the water jet attenuated and water started to descend to the deck. At this stage, more water was observed in front of the load-cell box but the loads on the load cells were low since they were merely due to hydrostatic pressure.

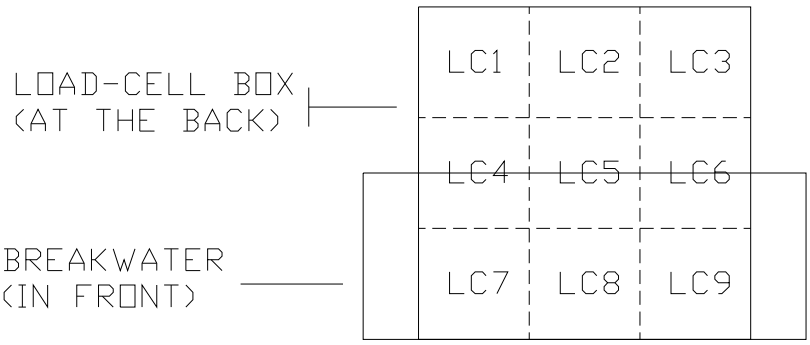

Figure 8.4.46 Front view of the breakwater and load-cell box.

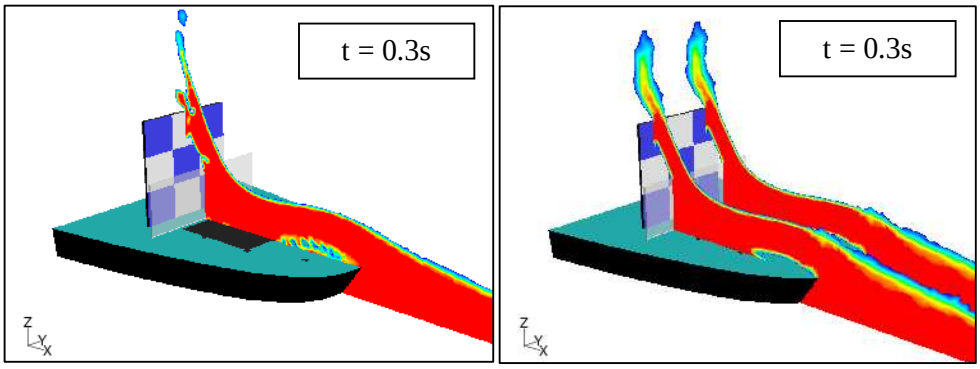

Figure 8.4.47 Snapshots corresponding to maximum load on load-cell box with water jet impacting load cell 2 (left) and load cells 1 and 3 (right).

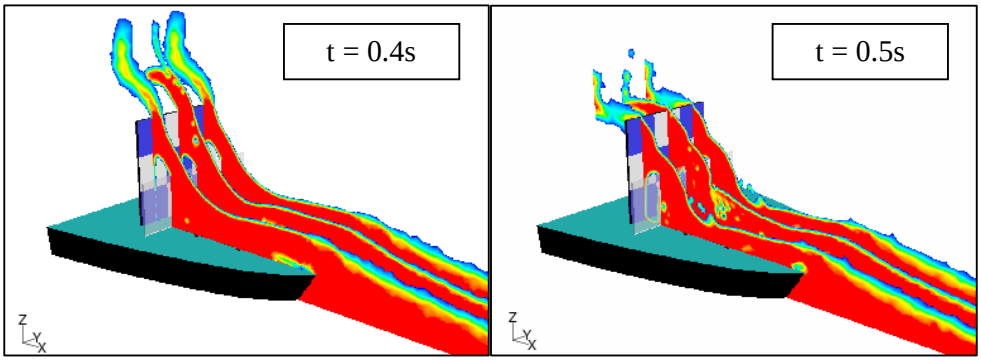

Figure 8.4.48 Snapshots showing water behaviour at time of 0.4s (left) and 0.5s (right), respectively.

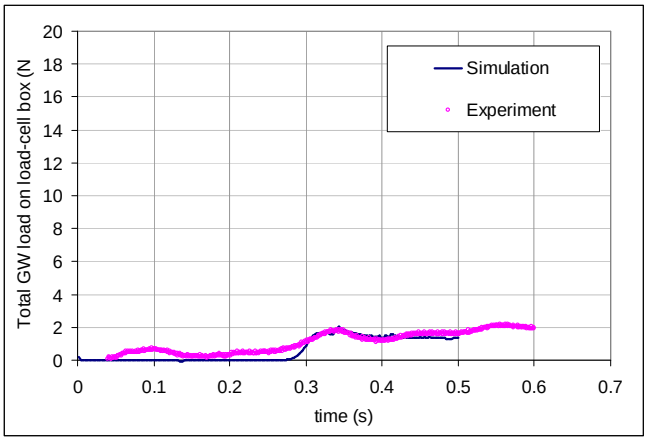

Figure 8.4.49 Comparison of total green water loading on load-cell box.

8.4.6 Breakwater height of 76.2mm and perforation diameter of 10.5mm

With three rows of perforations of 10.5mm diameter (Figure 8.4.50), water would pass through the breakwater and directly strike the load cells at low levels (Figures 8.4.51 and 8.4.52). Compared with the previous case in Section 8.4.5, the loads on these load cells were greater (Figures 8.4.57 and 8.4.58). However, as in Section 8.4.2, these loads were much smaller than when no breakwater was fitted. Most of green water loading caused by the front water was taken by the breakwater. The water jet that overrode the breakwater was mostly made up by the follow-up water further down the tail of the water flow. As explained in Section 8.4.5, this water did not carry high kinetic energy. The impact caused was therefore far less severe than when lower breakwater of similar design was used (Section 8.4.2).

From the validation point of view, prediction of loads on all the load cells was relatively good as in Figures 8.4.53 to 8.4.58. The peak loads and the behaviour of green water flow matched reasonably well. Regarding the protection performance, the breakwater in this case helped to reduce the loads on bottom row by more than 80 percent. The load on the load-cell box in total was also reduced by the same margin (comparing Figure 8.4.59 with Figure 8.2.35).

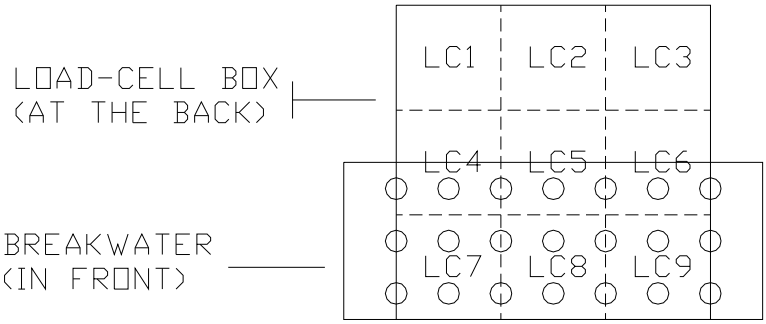

Figure 8.4.50 Front view of the breakwater and load-cell box.

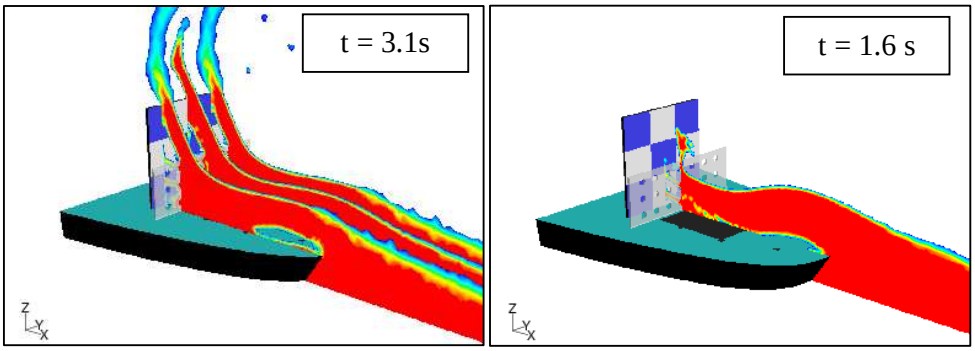

Figure 8.4.51 Snapshots corresponding to maximum impact loads on load cells 1, 2, 3 (left) and load cells 5, 8 (right).

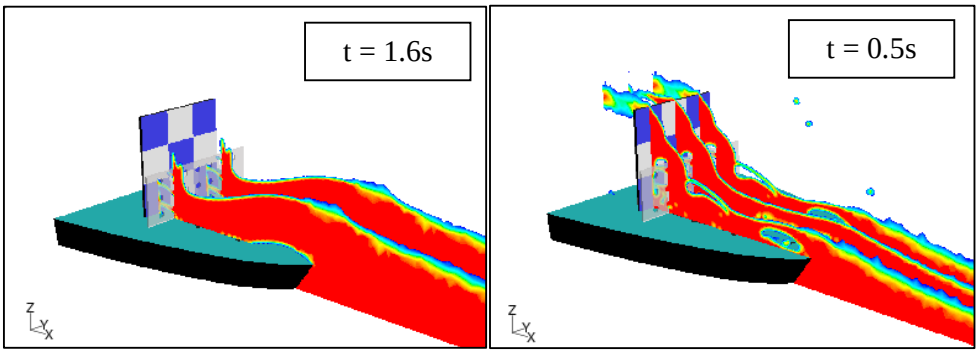

Figure 8.4.52 Snapshot corresponding to maximum impact loads on load cells 6, 7 (left) and water behaviour at time of 0.5s (right).

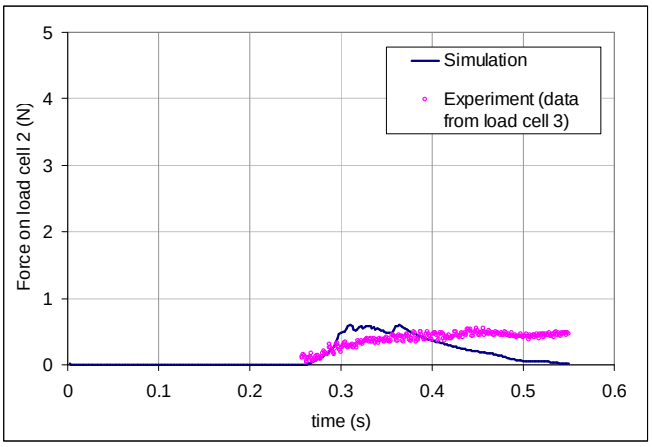

Figure 8.4.53 Comparison of green water loading on load cell 2.

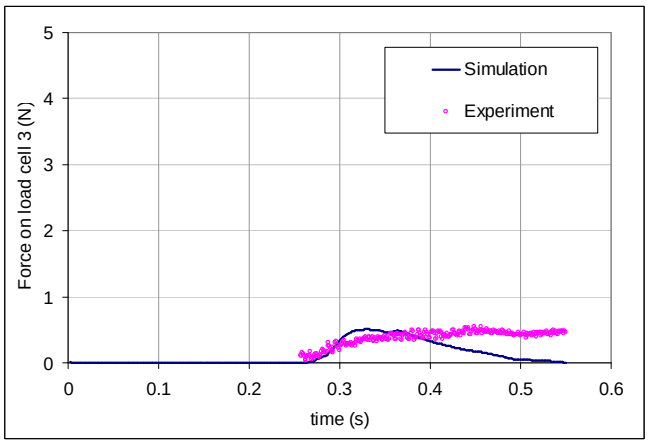

Figure 8.4.54 Comparison of green water loading on load cell 3.

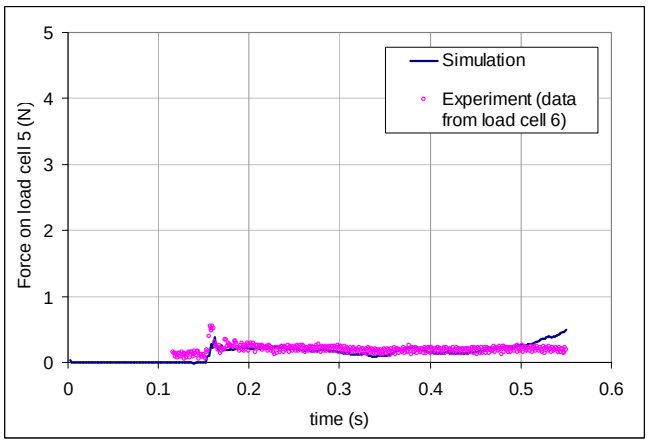

Figure 8.4.55 Comparison of green water loading on load cell 5.

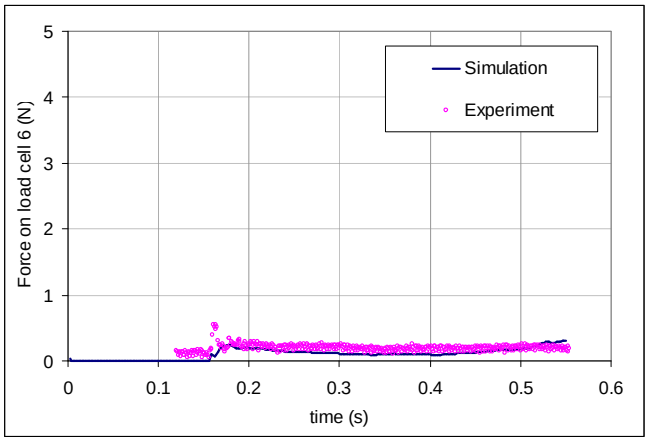

Figure 8.4.56 Comparison of green water loading on load cell 6.

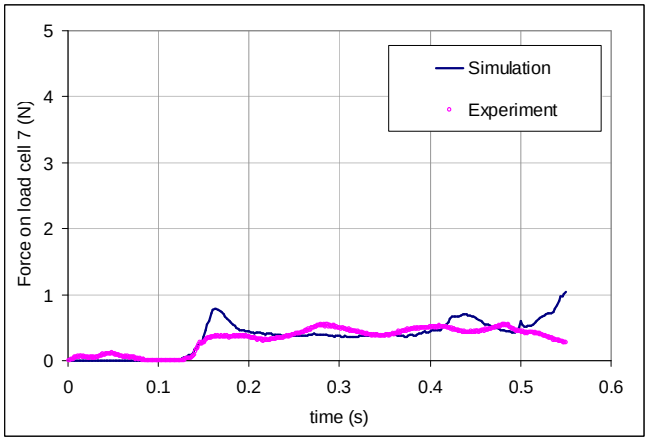

Figure 8.4.57 Comparison of green water loading on load cell 7.

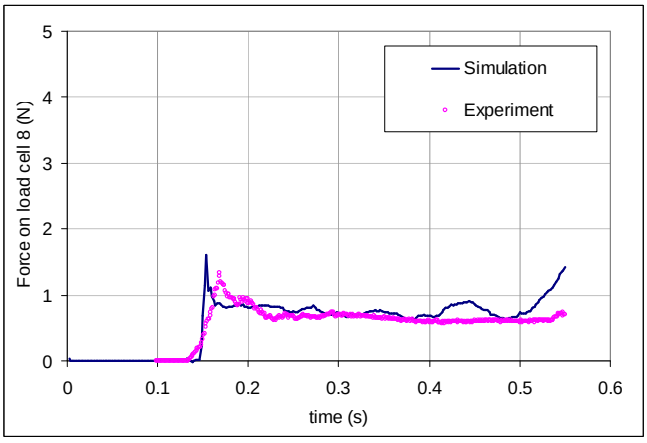

Figure 8.4.58 Comparison of green water loading on load cell 8.

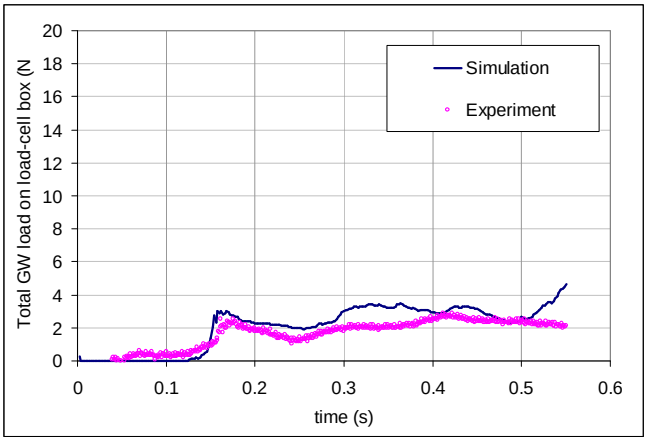

Figure 8.4.59 Comparison of total green water loading on load-cell box.

8.4.7 Breakwater height of 76.2mm and perforation diameter of 14.0mm

With larger perforations (Figure 8.4.60), more green water passed through the breakwater and the loads on the load cells increased as a result. Figures 8.4.63 to 8.4.69 show that the numerical results matched well with the experimental data. The load on load cell 8 could be slightly over-predicted but on overall, there was good agreement. Figures 8.4.61 (right) and 8.4.62 (left) show that all the impulsive loads on middle and bottom rows were caused by green water flows that passed the breakwater through the perforations. There was an impact on the top row caused by the overriding water jet. However, despite large amount of overriding water (Figure 8.4.61 (left)), velocity of the water was low (approximately 0.75m/s from simulation results) and the impact was not severe. The loads on the top row, as a result, were low (Figures 8.4.63 and 8.4.64).

As far as the effectiveness of the breakwater was concerned, the breakwater helped to reduce the total load on the load-cell box by approximately 70 percent (Figure 8.4.69 verse Figure 8.2.35). The loads on bottom row, in particular, was reduced by around 75 percent.

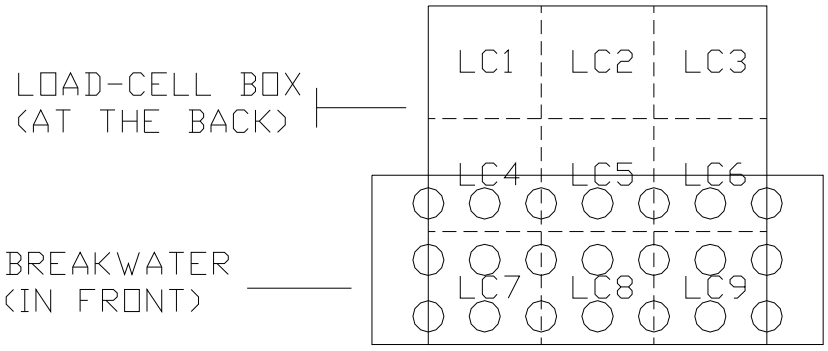

Figure 8.4.60 Front view of breakwater and load-cell box.

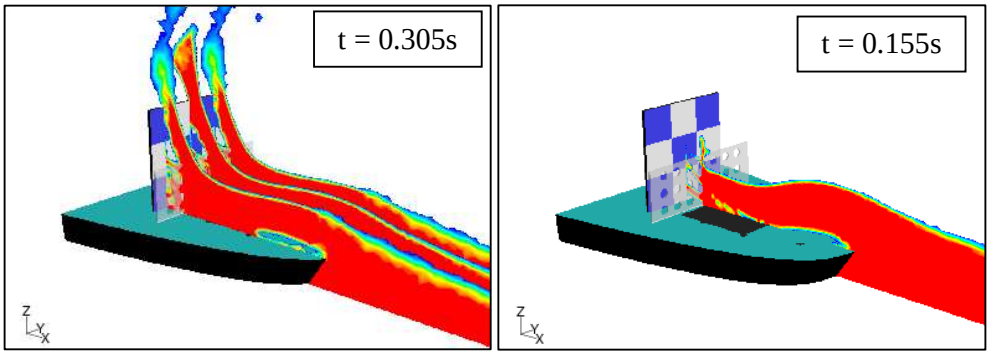

Figure 8.4.61 Snapshots corresponding to maximum loads on load cells 1, 2, 3 (left) and on load cells 5, 8 (right).

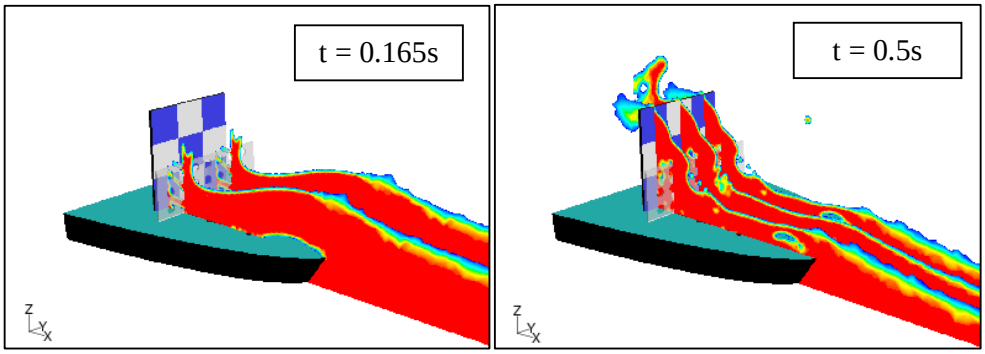

Figure 8.4.62 Snapshots corresponding to maximum loads on load cells 6, 7 (left) and water behaviour at time of 0.5s (right).

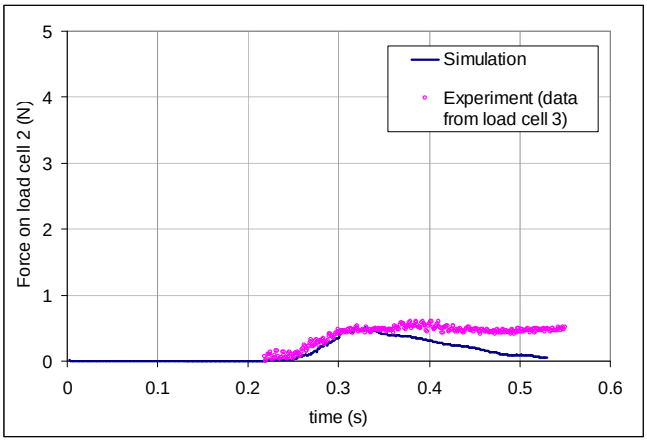

Figure 8.4.63 Comparison of green water loading on load cell 2.

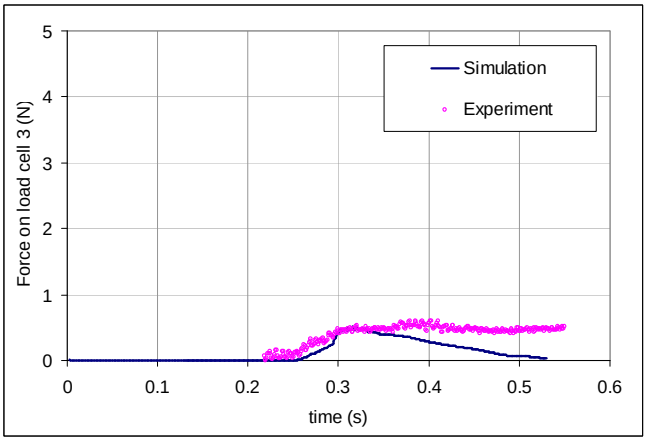

Figure 8.4.64 Comparison of green water loading on load cell 3.

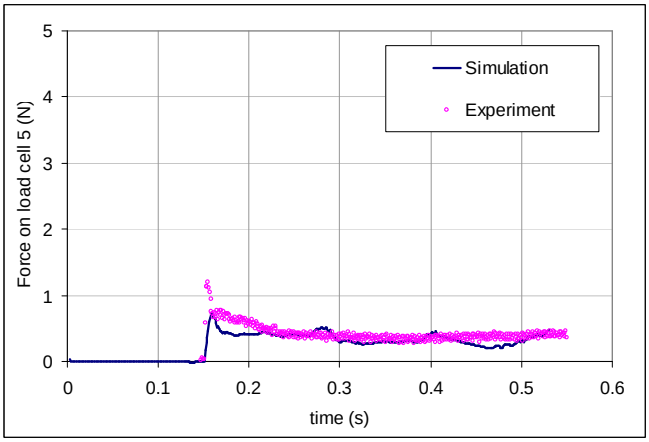

Figure 8.4.65 Comparison of green water loading on load cell 5.

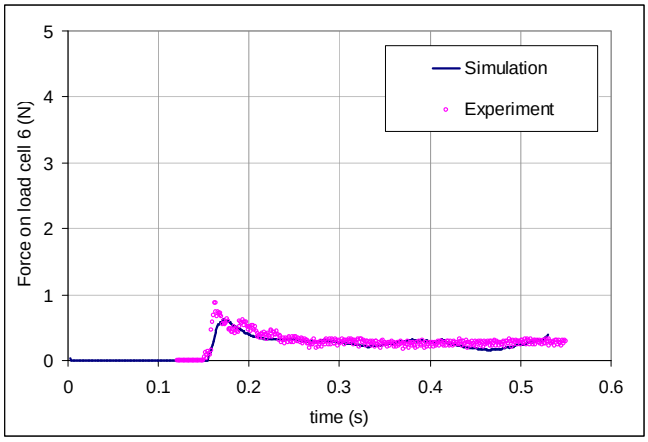

Figure 8.4.66 Comparison of green water loading on load cell 6.

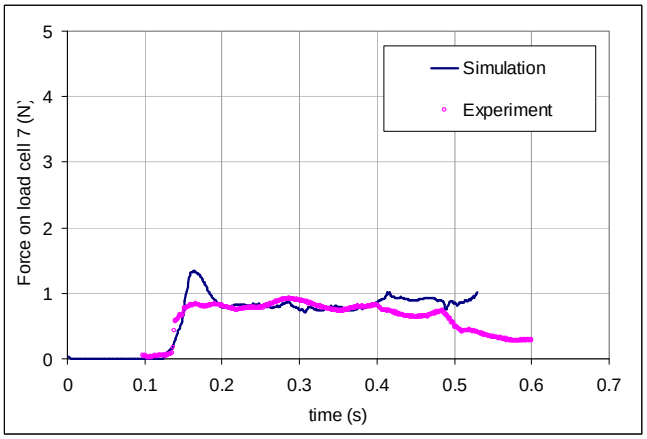

Figure 8.4.67 Comparison of green water loading on load cell 7.

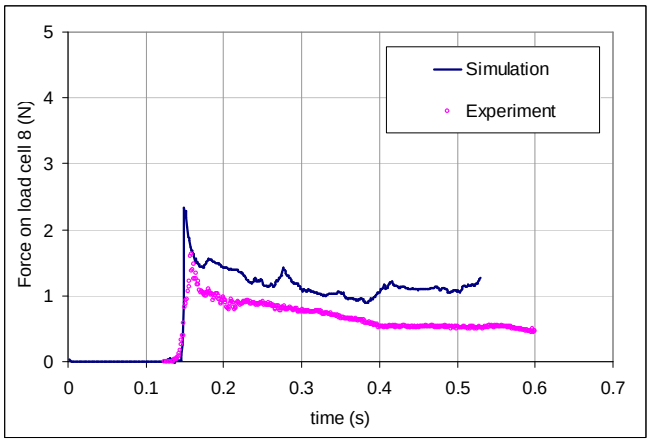

Figure 8.4.68 Comparison of green water loading on load cells 8.

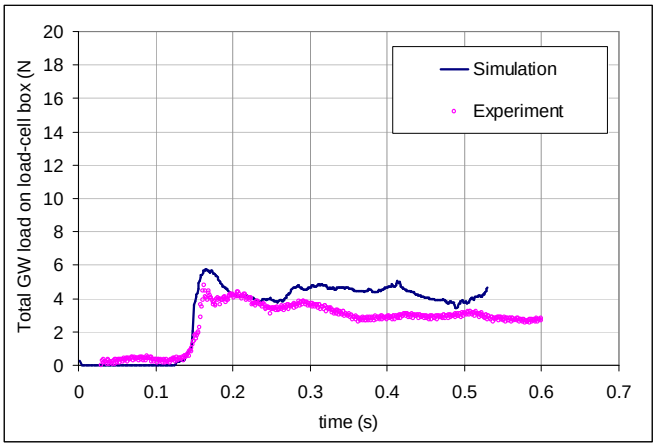

Figure 8.4.69 Comparison of total green water loading on load-cell box.

8.4.8 Breakwater height of 76.2mm and perforation diameter of 17.5mm

The breakwater in this case has largest perforations (Figure 8.4.70) and it allowed most green water to pass through. However, since green water loading on the load-cell box also depended on the overriding water, this did not mean that the loads on the load cells would be the largest. Figures 8.4.75 to 8.4.78 showed that compared with breakwaters of similar dimensions but smaller permeability (Sections 8.4.5 to 8.4.7), the loads on middle and bottom rows were higher. They well predicted by the simulation in terms of peak load, rise time and general behaviour. The discrepancies were well below 5 percent of the peak load on load cell 8. Figure 8.4.79 also indicated a good agreement between experiment and simulation in terms of total load on the load cell box. The loads on top row were too small for comparison.

Figures 8.4.71 and 8.4.72 show that all the impulsive loads on middle row and bottom row were due to the impacts of the water jets coming out of the perforations. There was quite a lot of overriding water (Figure 8.4.71 (left)) but the loading on top row remained small due to low velocity of water (approximately 0.6m/s from numerical results). The breakwater in this case helped

to reduce green water loading on bottom row by more than 50 percent. On the load-cell box as a whole, the reduction was 45 percent.

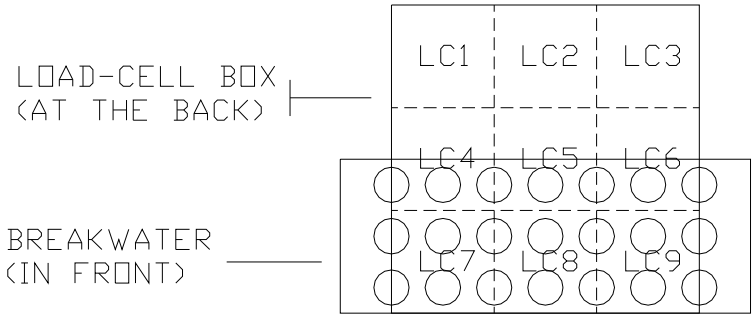

Figure 8.4.70 Front view of the breakwater and load-cell box.

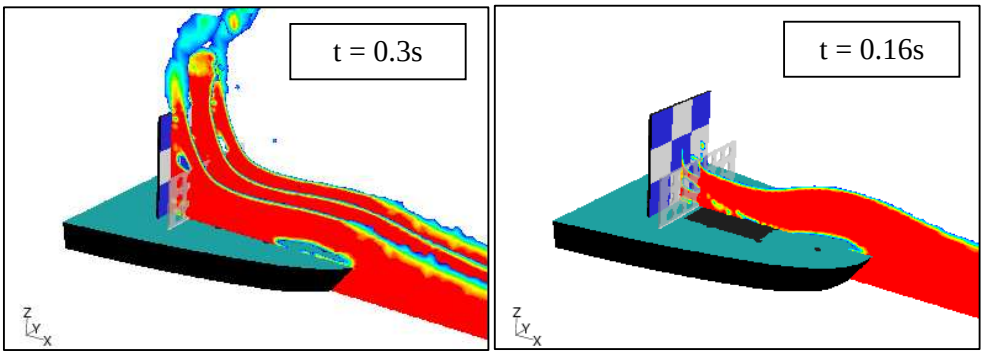

Figure 8.4.71 Snapshots corresponding to maximum loads on load cells 1, 2, 3 (left) and on load cell 5 (right).

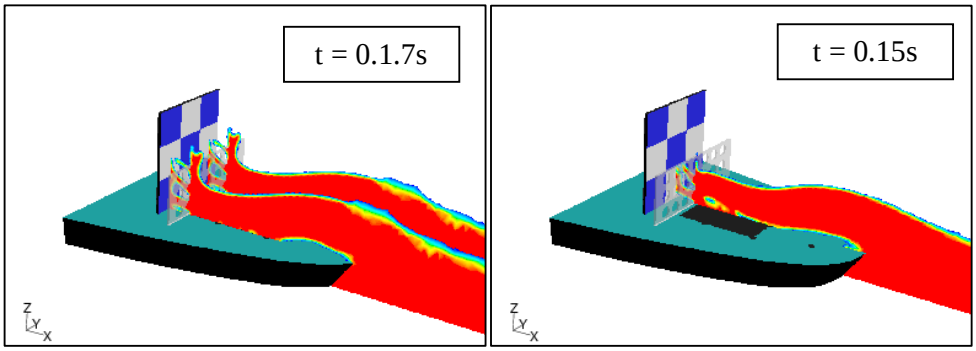

Figure 8.4.72 Snapshots corresponding to maximum loads on load cells 6, 7 (left) and on load cell 8 (right).

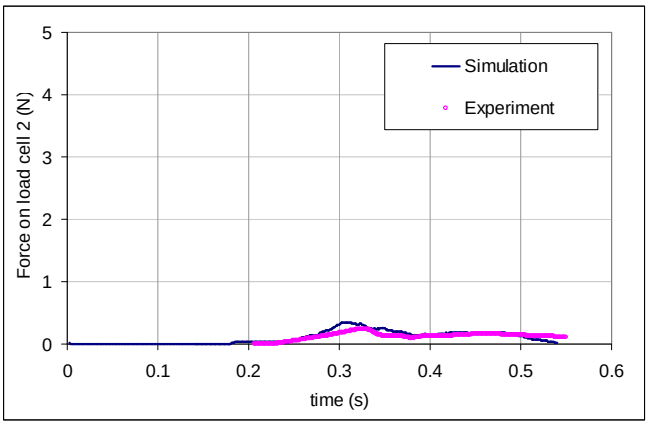

Figure 8.4.73 Comparison of green water loading on load cell 2.

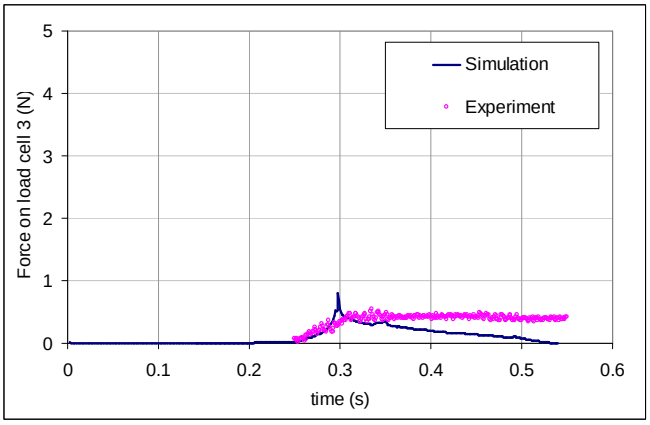

Figure 8.4.74 Comparison of green water loading on load cell 3.

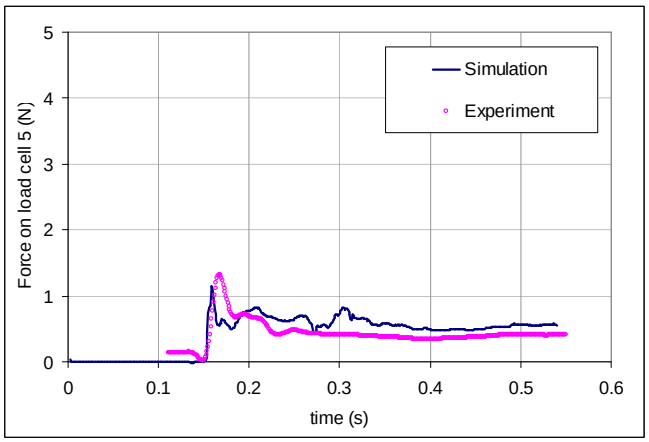

Figure 8.4.75 Comparison of green water loading on load cell 5.

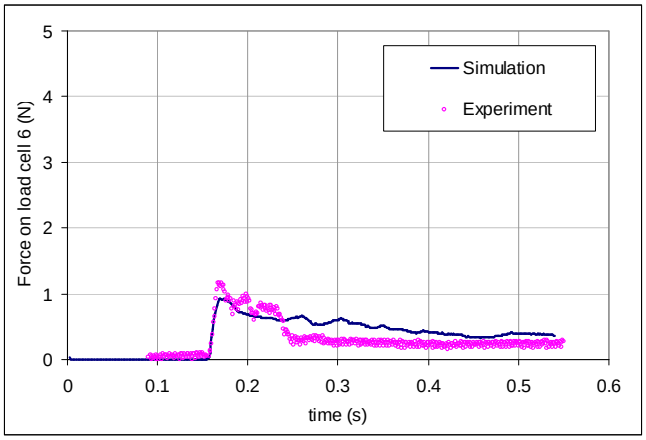

Figure 8.4.76 Comparison of green water loading on load cell 6.

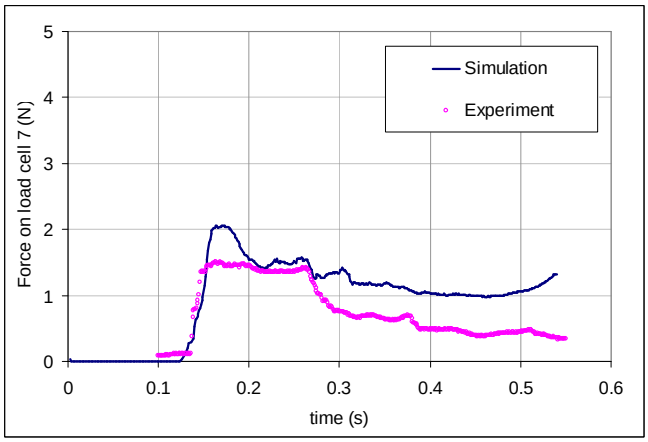

Figure 8.4.77 Comparison of green water loading on load cell 7.

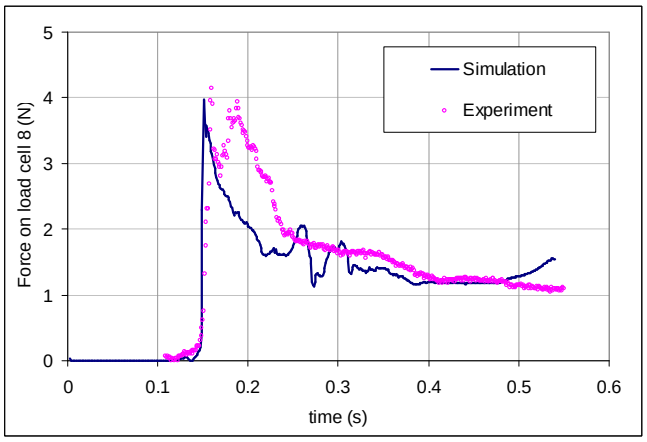

Figure 8.4.78 Comparison of green water loading on load cell 8.

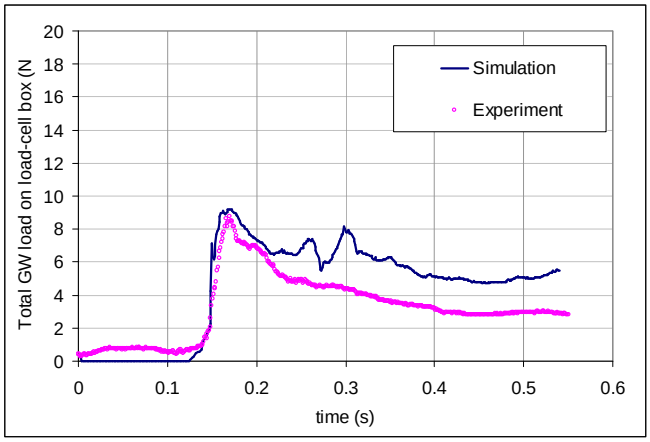

Figure 8.4.79 Comparison of total green water loading on load-cell box.

8.4.9 Breakwater height of 101.6mm and no perforations

The last breakwater of the test series had the height increased to two thirds of the height of the load-cell box as in Figure 8.4.80. No perforations were introduced meant that the green water stopping capability was largest. This is observed in Figure 8.4.83 when the total load on the load-cell box was hardly noticeable (a fractional three percent of the load when no breakwater was on deck). This was observed in both experiment and simulation.

Even though there was water that overrode the breakwater, this took place at a later stage of the impact. Figure 8.4.81 recorded the time of 0.48s at which the overriding water managed to overcome the breakwater and clip the top row of the load-cell box. Due to its low kinetic energy, this water mass soon fell deck-wards and imposed no real loading on the load-cell box. Figure 8.4.82 shows that most of the green water was reflected back from the breakwater and this further explained the low impact load noticed on the load-cell box.

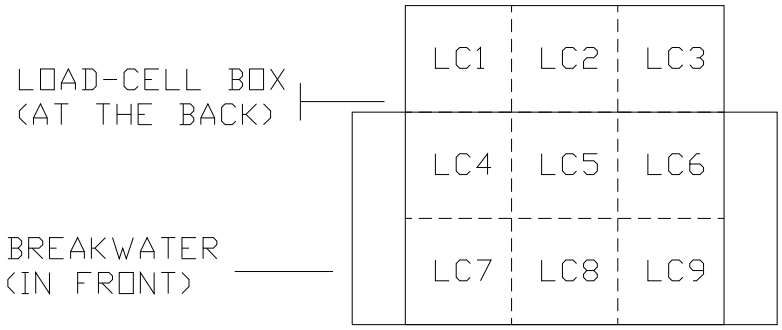

Figure 8.4.80 Front view of breakwater and load-cell box.

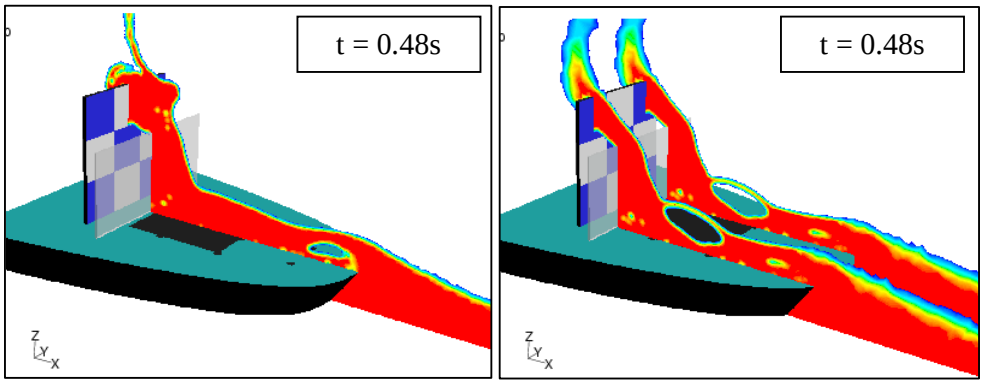

Figure 8.4.81 Snapshots corresponding to maximum impact loads on load cell 2 (left) and load cells 1, 3 (right).

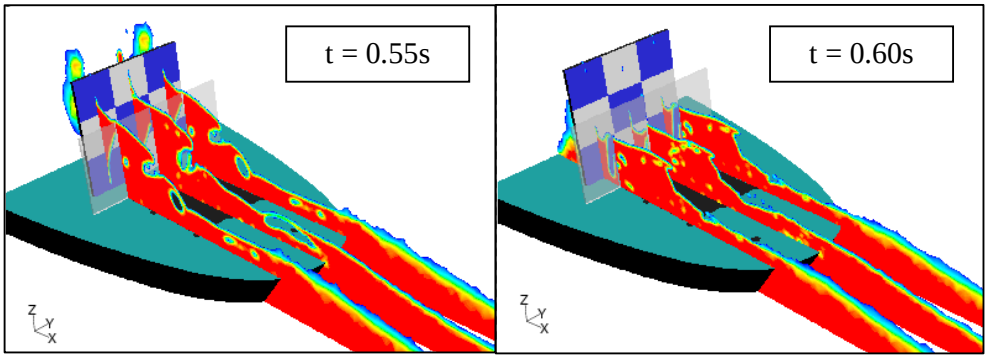

Figure 8.4.82 Snapshots showing water behaviour at time of 0.55s and 0.6s, respectively.

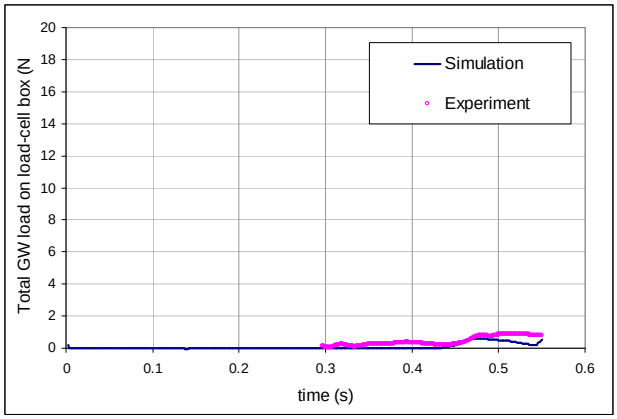

Figure 8.4.83 Comparison of total green water loading on load-cell box.

8.5 Comparison of green water loading on breakwaters

So far the longitudinal green water loads measured by the load-cell box have been compared and the validation has shown a relatively good agreement. The presence of the breakwater no doubt helped reduce green water loading on the vertical structures by at least 40 percent, if not better. In principle, the breakwater acted as a protective or, strictly speaking, sacrificial object that took the severity of green water flow in early stages. The protected structures therefore only faced the secondary green water loading. The investigation in this Section looks at the extent of the load that the breakwater had to face and how well the simulation model could predict it when it happened.

Qualitatively, maximum load on the breakwater came when the front water of green water flow impacted the breakwater. Figure 8.5.1 gives two examples of this moment in two different cases. It was evident that initially, the high kinetic front water interacted with the breakwater, resulting in impulsive load. After the impact, the water piled up in front of the breakwater and acted as a buffer that protected the breakwater from any further impact from the follow-up water. Therefore, water could be seen to accumulate at the breakwater as a result. The loading, dominated by hydrostatic pressure, began to reduce (Figure 8.5.2).

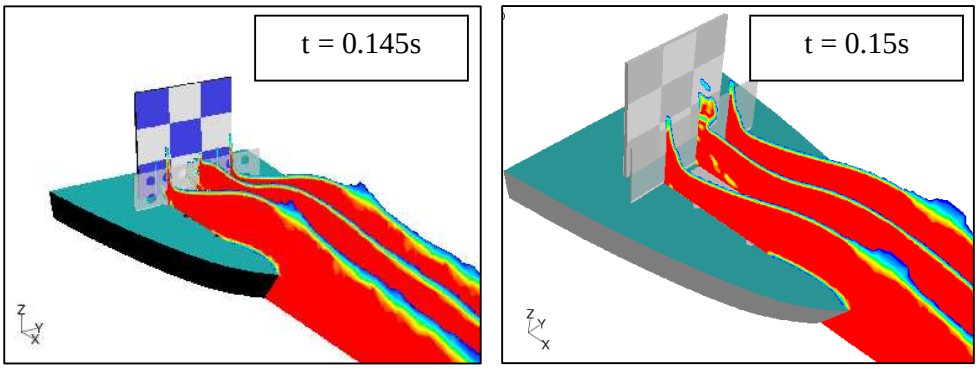

Figure 8.5.1 Snapshots corresponding to maximum impact loads on breakwater of 51mm height with perforations of 14mm diameter (left) and 76.2mm height without perforations (right).

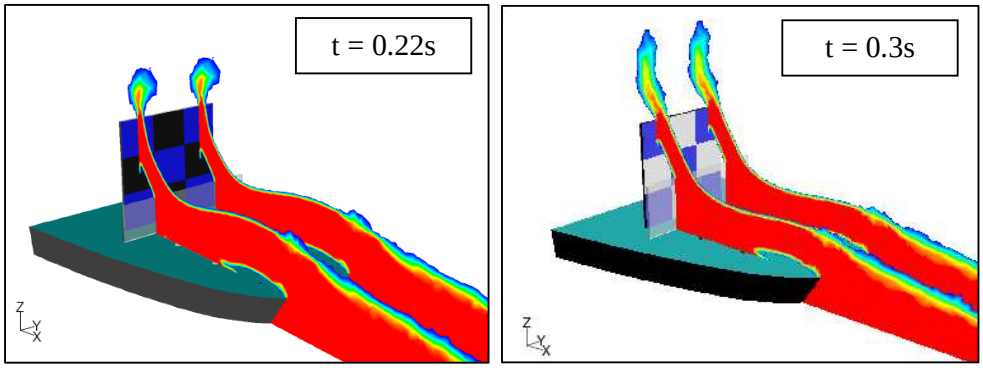

Figure 8.5.2 Water amassed at the breakwater but loading began to reduce (breakwater height of 51mm with perforations of 14mm diameter on the right and breakwater height of 76.2mm without perforations on the left).

Figures 8.5.5 to 8.5.13 show the loads on the breakwaters in nine cases analysed and Figure 8.5.3 compares the peak loads from experiment and simulation. With a mean error of 51.4 percent and standard deviation of 25.2 percent, there was a large discrepancy between numerical and experimental results. A review of the experimental setup was therefore carried out to find out what could have been behind this discrepancy.

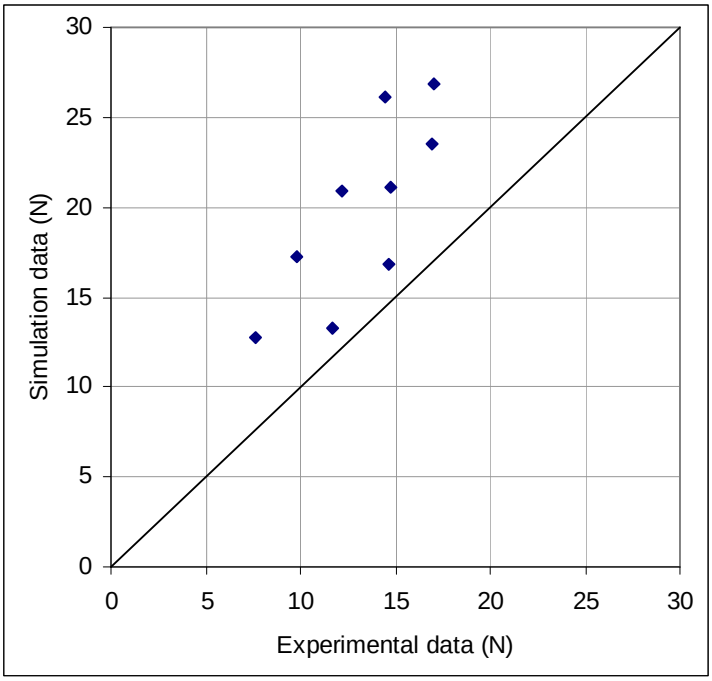

Figure 8.5.3 Comparison of the peak loads on breakwaters.

The loading on the breakwater should follow the same trend as the loads on the bottom row of load-cell box because in principles, they were similar setups. Figure 8.2.10 presented the results for the same conditions as the test series with breakwaters. The rise time and the total load on the bottom row should give an indication of how the load on the breakwater of height of 51mm and without perforations (see Figure 8.4.1) should look like. Figure 8.5.4 combines the simulation data, experimental data with the total load on the bottom row taken from Figure 8.2.10. It then became clear that there appeared to be some flaw in the measuring of green water loading on the breakwater since the measured data showed neither the expected impulsive characteristics nor the adequate peak load. As it stands in Figure 8.5.4, despite having a larger (by 33.33 percent) projected area, the load on the breakwater by experiment was even smaller than the total load on the bottom row of the load-cell box. The rise time of 0.152s compared with 0.03s implied that the measured load on the breakwater was not showing any impulsive characteristics. The simulation results, on the other hand, showed a

better reflection of what could have been the load on the breakwater both in terms of rise time and peak load.

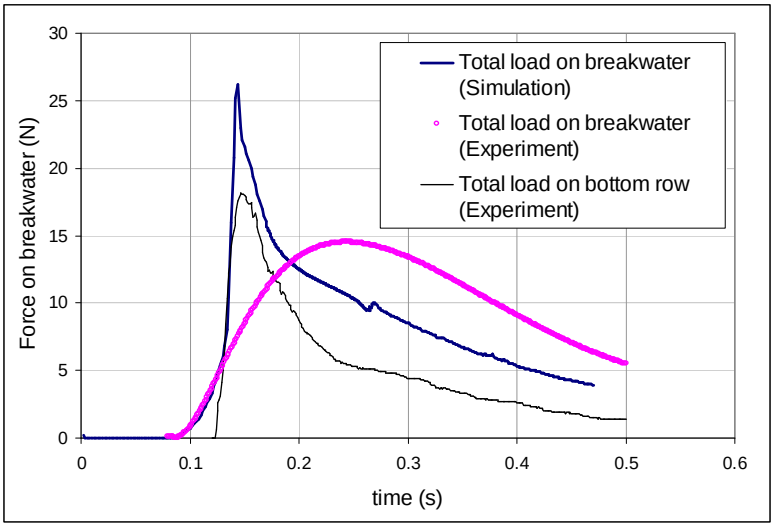

Figure 8.5.4 Review of simulation and experiment data on the loading sustained by the breakwater.

The flaw could be due to the mechanical setup of the deck load cell. Figure 4.5.12 in Chapter 4 shows the setup of the deck load cell. It is possible that the wood beam on which the load cell was mounted was the source of error. Located at approximately 100mm below the forecastle deck, the bending moment caused by green water loading on the breakwater was as high as 2.5Nm. This could cause the beam to twist, resulting in the under-measurement of the load. Nevertheless, Figure 8.5.4 implies that the simulation could have predicted well the load on the breakwater.

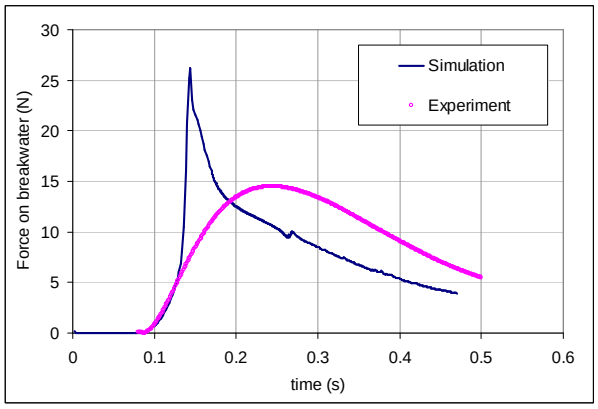

Figure 8.5.5 Comparison of green water loading on breakwater of height 51mm and no perforations.

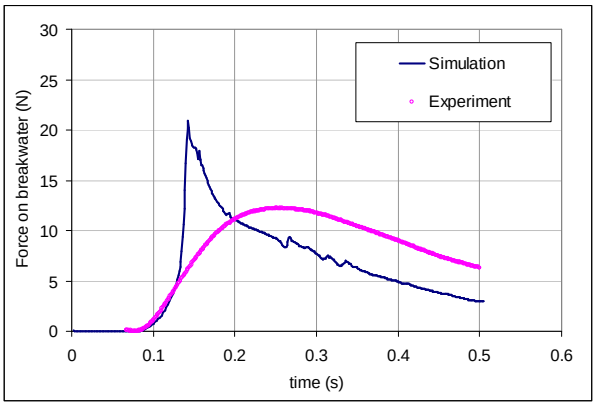

Figure 8.5.6 Comparison of green water loading on breakwater of height 51mm and perforation diameter of 10.5mm.

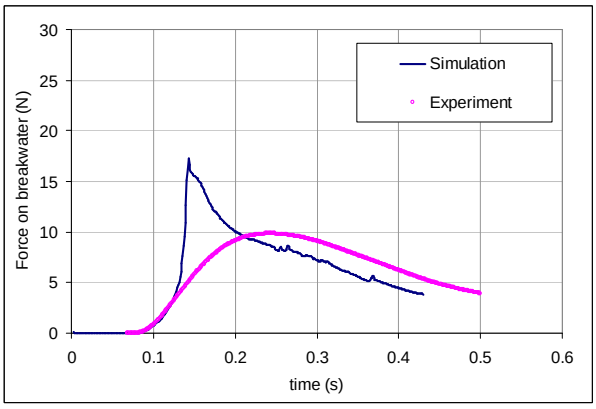

Figure 8.5.7 Comparison of green water loading on breakwater of height 51mm and perforation diameter of 14.0mm.

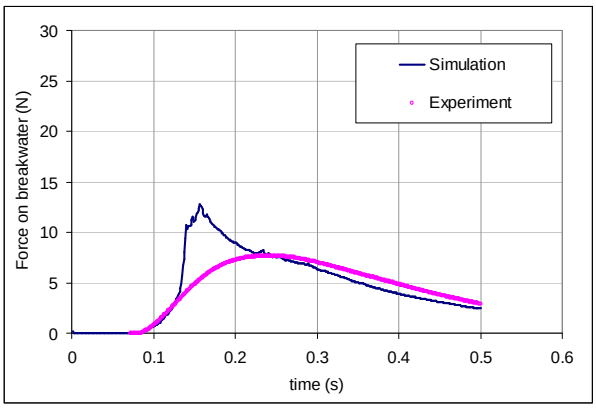

Figure 8.5.8 Comparison of green water loading on breakwater of height 51mm and perforation diameter of 17.5mm.

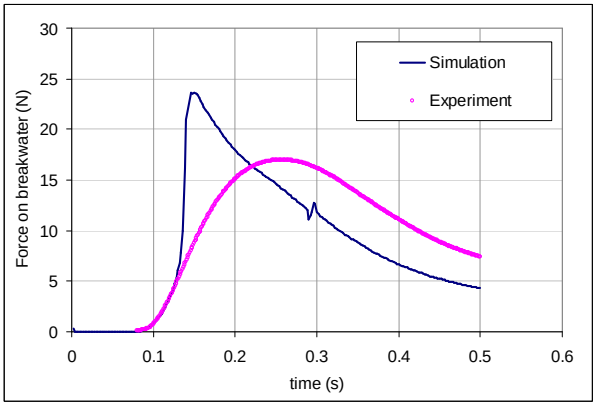

Figure 8.5.9 Comparison of green water loading on breakwater of height 76.2mm and no perforations.

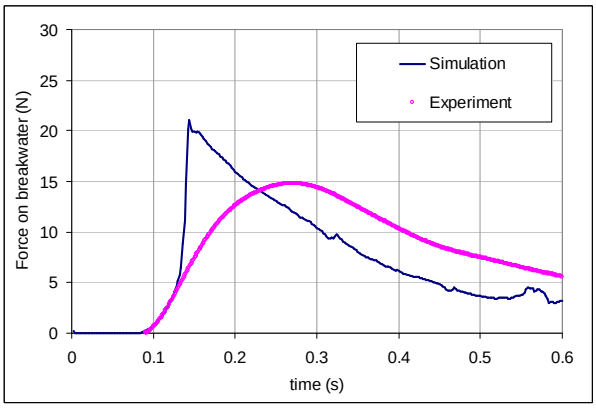

Figure 8.5.10 Comparison of green water loading on breakwater of height 76.2mm and perforation diameter of 10.5mm.

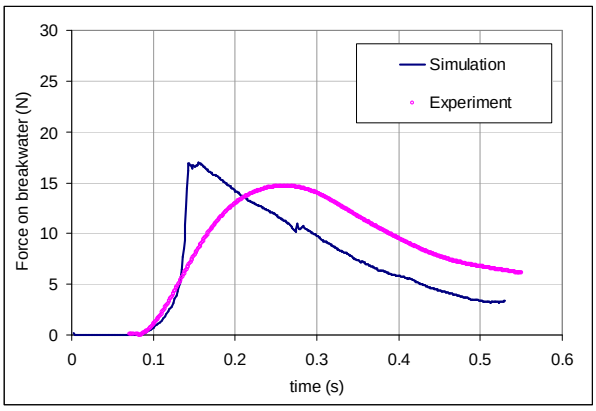

Figure 8.5.11 Comparison of green water loading on breakwater of height 76.2mm and perforation diameter of 14.0mm.

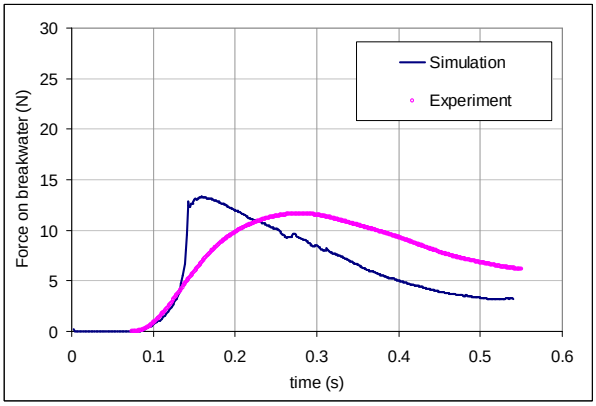

Figure 8.5.12 Comparison of green water loading on breakwater of height 76.2mm and perforation diameter of 17.5mm.

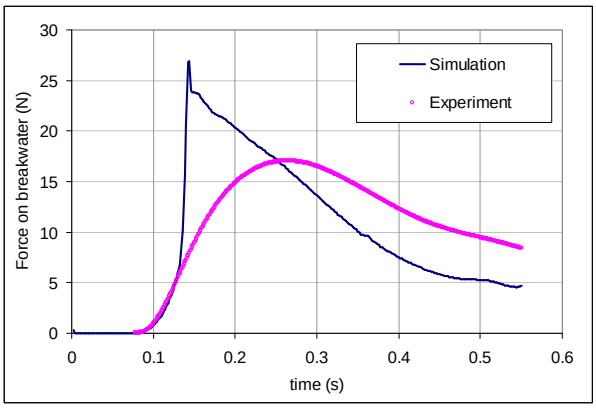

Figure 8.5.13 Comparison of green water loading on breakwater of height 101.6mm and no perforations.

8.6 Vertical green water loading when breakwaters are fitted

Besides posing direct threats on vertical structures, green water was a real danger to the deck plating itself. A case example showed that an amount of approximately 1000 tonnes of sea water was lifted out of the ocean by the ship's forecastle and forward foredeck when rising up from a severe pitch into a head sea, thereby depressing the deck plating and twisting the bed plates of several items of mooring machinery (Olsen, 2005). Massive damage could be predicted in such a situation.

This Section concentrates on validating the load acting on the deck panel described in Section 4.5.6 in Chapter 4. Figure 8.6.1 presents an example of the longitudinal and horizontal views of green water on deck at the time when the load on the deck load cell was maximum. As seen, this took place shortly after green water landed on the deck when the highly kinetic green water mass interacted with the bare deck plating. Later, more water was shipped above the deck plating (Figure 8.6.2). The pressure became more hydrostatic and deck load started to reduce.

Comparison of the loads on the deck load cell was made and the outcome is as in Figures 8.6.6 to 8.6.14. On overall, the simulation gave a relatively good estimation of the loads. The peak loads and the trends of the load curves were both well predicted. Figures 8.6.3 and 8.6.4 compare the peak loads lifted from these load curves together. The mean error was 5.7 percent and the standard deviation 9.1 percent evidently implied a good agreement between experiment and simulation. However, as the load curves in Figures 8.5.6 to 8.5.14 suggested, the peak loads in the simulation were more impulsive than in experiment. This could be attributed to the noise interference coming from the vibration of the hull at its natural frequency as discussed before in Section 8.3. Also, the acceleration of the deck which was not simulated meant that the load component due to the motion of

the deck was not included in the simulation results. This could account for the broadness of the experimental load curves in Figures 8.6.6 to 8.6.14.

The variation in vertical load by both experiment and simulation meant that the deck loading was influenced to a certain extent by the variation of the breakwater. Figure 8.6.5 shows the deck loads when there was no breakwater on board. Compared with Figures 8.6.6 to 8.6.14, it was evident that the presence of the breakwater did lead to an increase in deck loading significantly. This could be due to the water that was reflected backwards, off the breakwater after the initial impact.

The variation of deck loading with the variation in perforation diameter further consolidated this conclusion. Figure 8.5.3 shows that for the same breakwater height, as the perforations were introduced and their diameter increased, the deck loading reduced considerably until the diameter reached 14.0mm. After which, a further increase in diameter to 17.5mm did not bring any further reduction and this was the case for both breakwater heights of 51mm and 76.2mm. This could mean that around this range of perforation diameter, the accumulation of water in front of the breakwater did not necessarily change significantly. The loading therefore stayed relatively steady.

As far as validation was concerned, the simulation showed that it was capable of estimating the behaviour of green water loading on deck even with the changes that followed by variation in breakwater parameters.

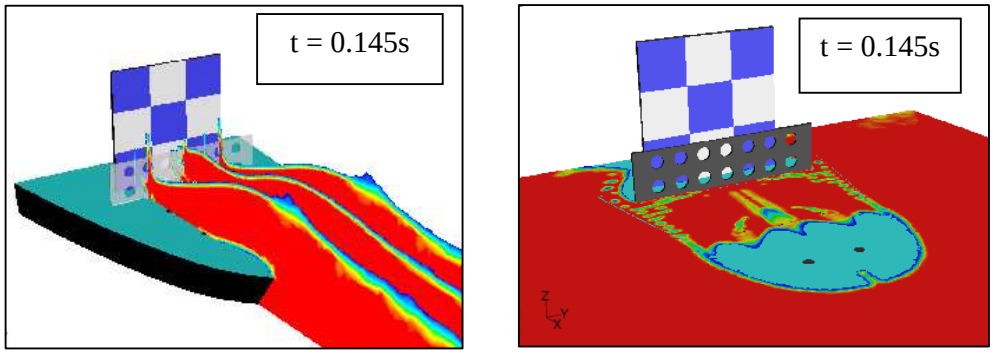

Figure 8.6.1 Sectional views (vertically and horizontally, respectively) of green water on deck at the time maximum impact load on deck load cell was recorded.

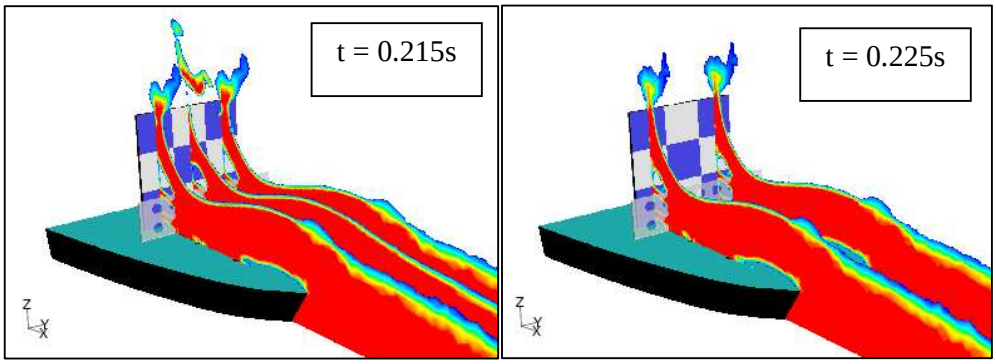

Figure 8.6.2 Water head above the deck load plate was higher but pressure became more hydrostatic and began to reduce.

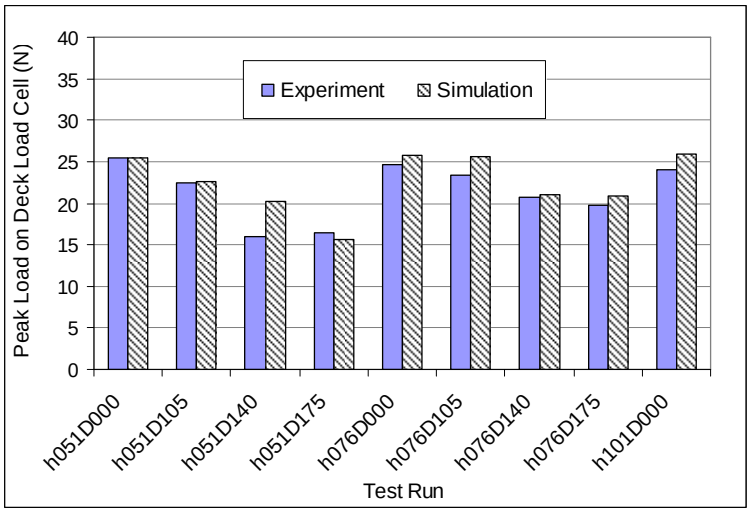

Figure 8.6.3 Comparison of load on deck load cell in test series with breakwaters.

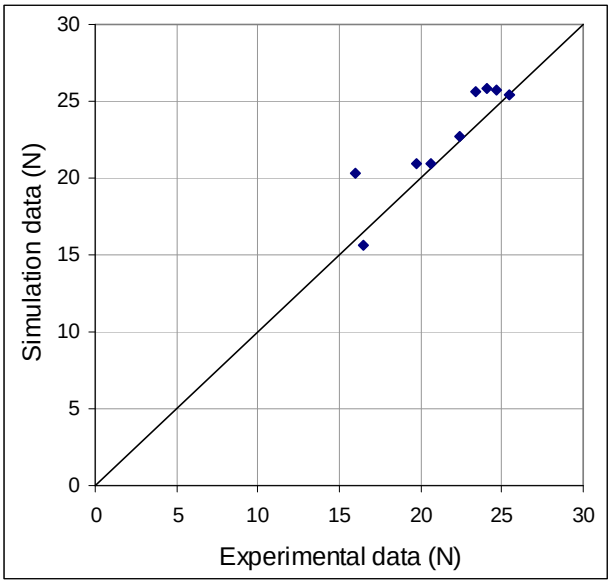

Figure 8.6.4 Comparison of peak loads on the deck load cell.

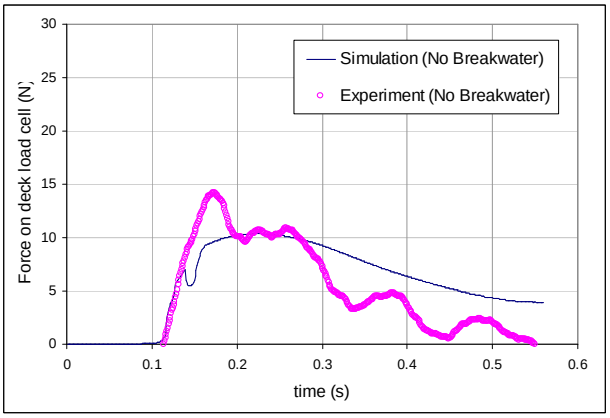

Figure 8.6.5 Comparison of loads on deck load cell when no breakwater was fitted.

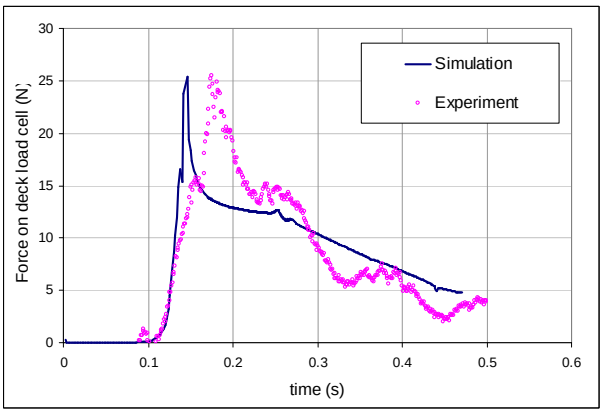

Figure 8.6.6 Comparison of green water loading on deck load cell in case of breakwater height of 51mm with no perforations.

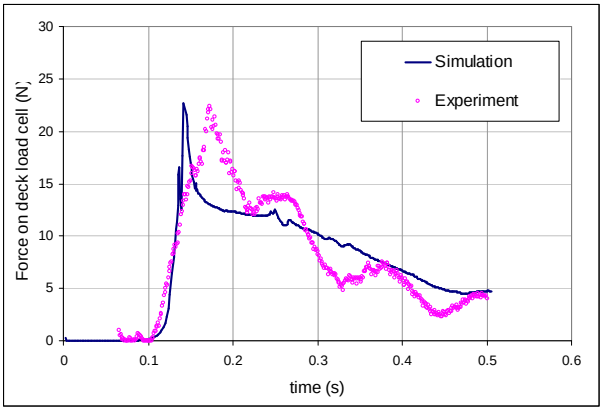

Figure 8.6.7 Comparison of green water loading on deck load cell in case of breakwater height of 51mm and perforation diameter of 10.5mm.

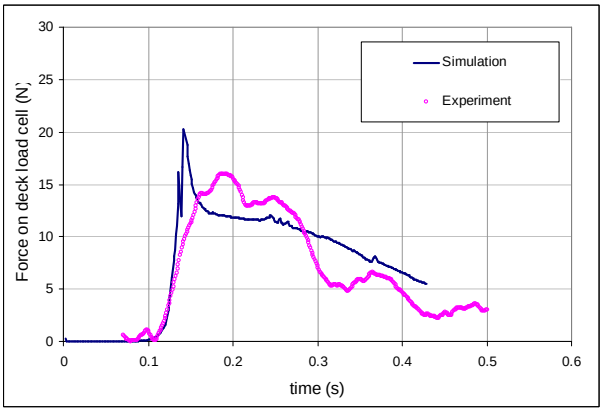

Figure 8.6.8 Comparison of green water loading on deck load cell in case of breakwater height of 51mm and perforation diameter of 14.0mm.

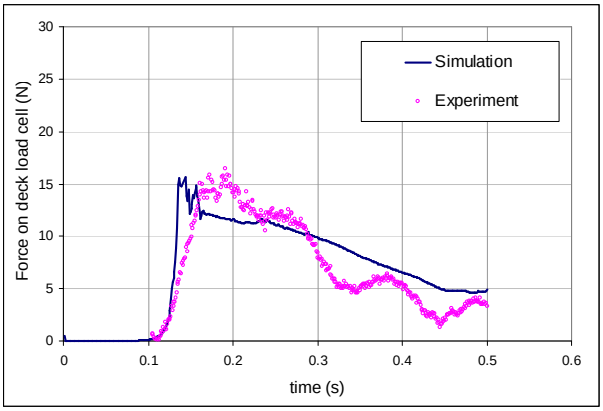

Figure 8.6.9 Comparison of green water loading on deck load cell in case of breakwater height of 51mm and perforation diameter of 17.5mm.

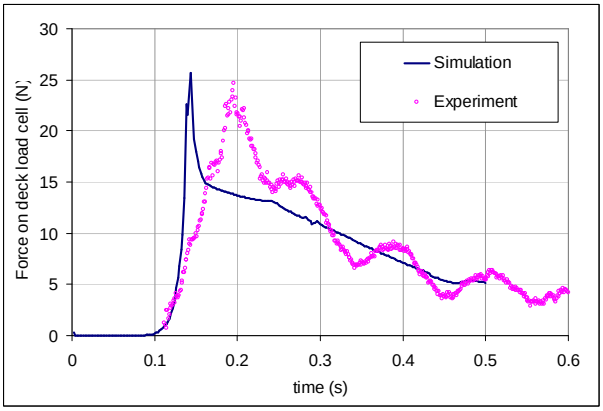

Figure 8.6.10 Comparison of green water loading on deck load cell in case of breakwater height of 76.2mm and no perforations.

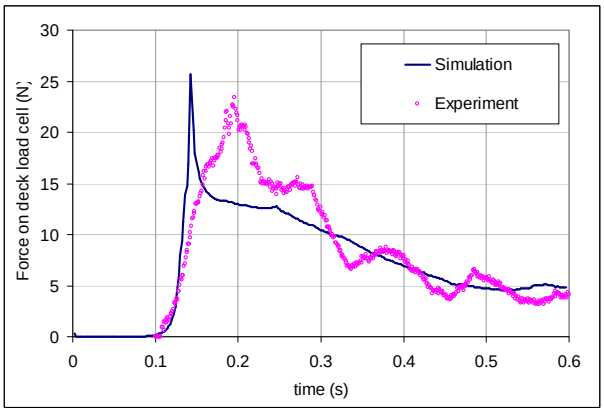

Figure 8.6.11 Comparison of green water loading on deck load cell in case of breakwater height of 76.2mm and perforation diameter of 10.5mm.

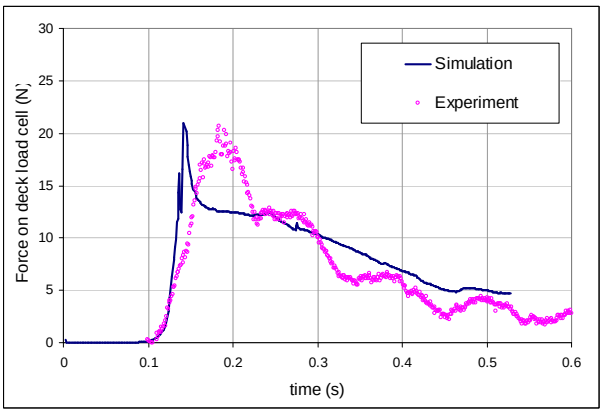

Figure 8.6.12 Comparison of green water loading on deck load cell in case of breakwater height of 76.2mm and perforation diameter of 14.0mm.

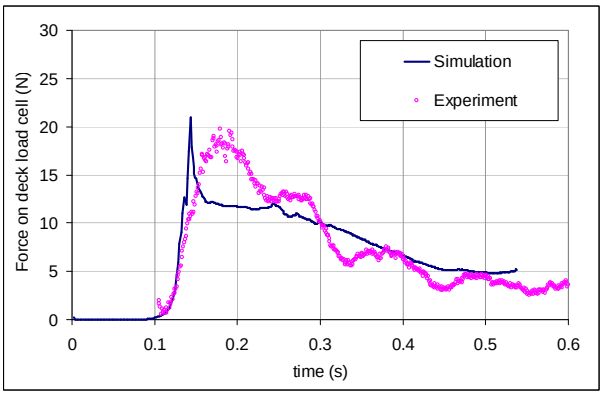

Figure 8.6.13 Comparison of green water loading on deck load cell in case of breakwater height of 76.2mm and perforation diameter of 17.5mm.

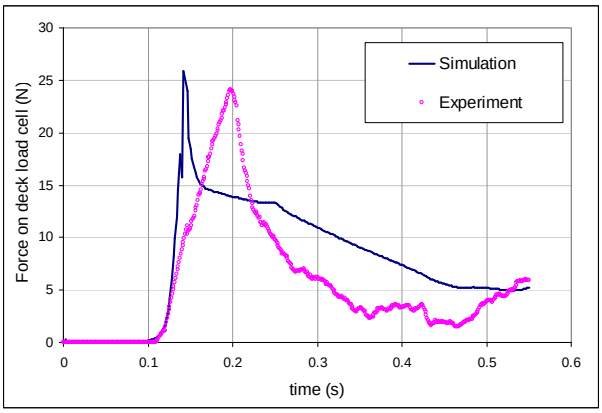

Figure 8.6.14 Comparison of green water loading on deck load cell in case of breakwater height of 101.6mm and no perforations.

8.7 Discussion of results and parametric analyses

Sections 8.2 to 8.6 have compared all aspects related to green water loading with and without the breakwaters on the forecastle deck. Overall, the validation has been relatively good. Despite several minor discrepancies, the agreement between simulation and experiment has been consistent and this leads to the conclusion that the proposed hydraulic model is reliable and works relatively well in reproducing the characteristics of green water on deck.

As an extended analysis, this Section continues with an attempt to conduct several key parametric investigations into other aspects of green water as well as the use of breakwaters in reducing the damages that could be inflicted. There were two sets of data that could be used for these investigations, i.e. experimental and numerical. In order to avoid confusion in the analysis, it was decided that simulation results were more convenient to use since it could provide illustrative images that help to explain the events in detail.

8.7.1 Effects of green water height

If the velocity of the ship is unchanged, the greater water height will undoubtedly inflict more loading and, hence, worse damages to both vertical structures and deck plating of the ship. The question is if there are any other changes that can result from the increased height of green water height other than loading. In order to find the answer for this, three sample cases of green water event were selected and compared with each other in terms of:

- Loading on vertical structures
- Load on deck plating
- Characteristics of green water flow on deck at key stages

These three selected cases corresponded to test runs H08T11Fn020, H08T12Fn020 and H08T13Fn020 as listed in Table 8.2.1. These cases were tested at velocity of Fn = 0.20 (or 16 knots at full scale), wave height of 8m and wave periods of 11s, 12s and 13s, respectively at full scale. The results are presented in model scale for comparison with other Sections. Table 8.7.1 lists green water height in each of these three cases.

Table 8.7.1 Initial green water height on deck in simulation.

Run	Green water height in simulation (mm)
H08T11Fn020	63.7
H08T12Fn020	70.0
H08T13Fn020	33.0

In order to make the Section concise without losing any generality, comparison of loading was carried out only on load cells 5, 8, the total load on the load-cell box and the deck loading. Figures 8.7.1 to 8.7.4 show that, in general, the relation between the peak loads and green water heights were relatively linear for all cases.

Water from greater initial water height reached the load-cell box sooner, as in Figures 8.7.1 to 8.7.3. This was consistent with the dam-break theory when the velocity of the front water is defined in terms of initial water height H_0 by:

$$U_{front} = 2\sqrt{g.H_0} \tag{8.7.1}$$

Equation (8.7.1) means that greater green water height will cause the front water to travel faster. This is confirmed by Figures 8.7.5 to 8.7.7 which show the sectional views of green water flow in three cases when the deck loading reached maximum. To reach the same location on deck, it took 0.16s for the front water in run H08T11Fn020 but only 0.13s in runs H08T12Fn020 and H08T13Fn020.

Figures 8.7.5 to 8.7.7 also indicate that green water entered the deck in a form similar to a plunging breaker as described by Greco et al. (2005, 2007). For small green water height, the water flow appeared to fly deeper into the deck before landing. The air gap or air cavity between the deck and the plunging green water was therefore larger. This can be seen clearly when comparing the dry deck areas surrounded by water in Figures 8.7.5 (right) to 8.7.7 (right).

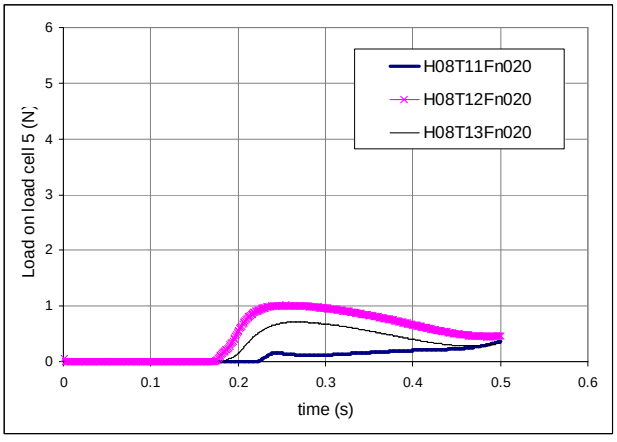

Figure 8.7.1 Effects of green water height on loading on load cell 5.

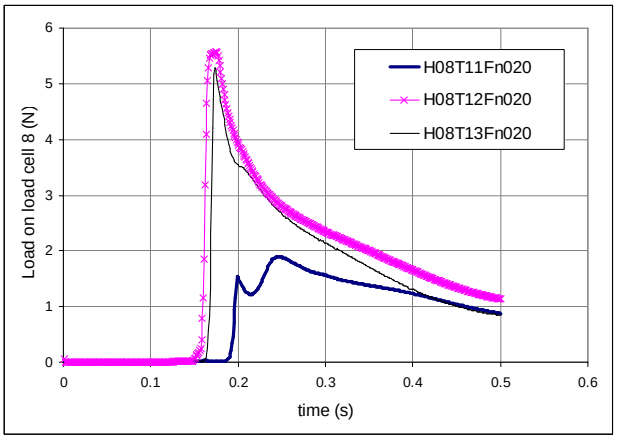

Figure 8.7.2 Effects of green water height on loading on load cell 8.

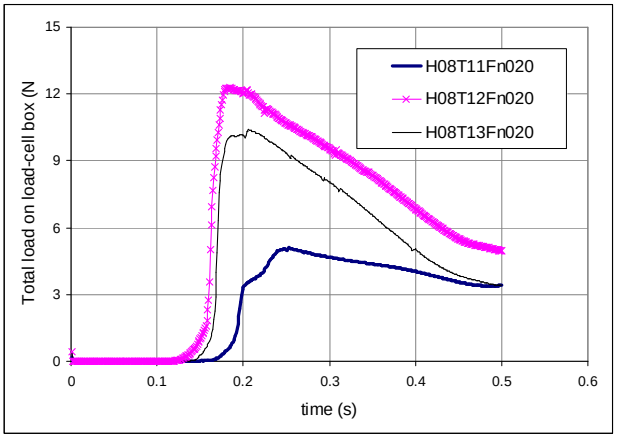

Figure 8.7.3 Effects of green water height on total loading on load-cell box.

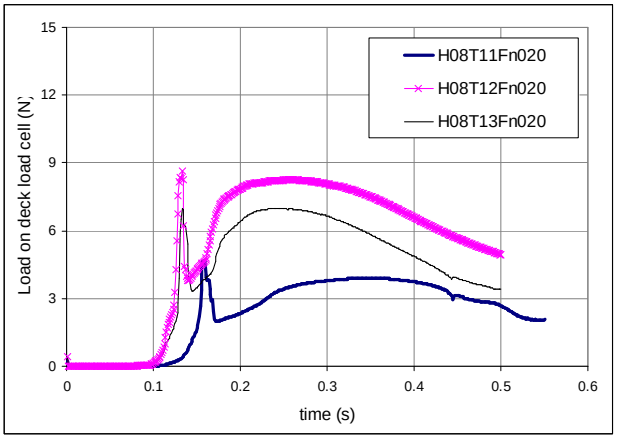

Figure 8.7.4 Effects of green water height on deck loading.

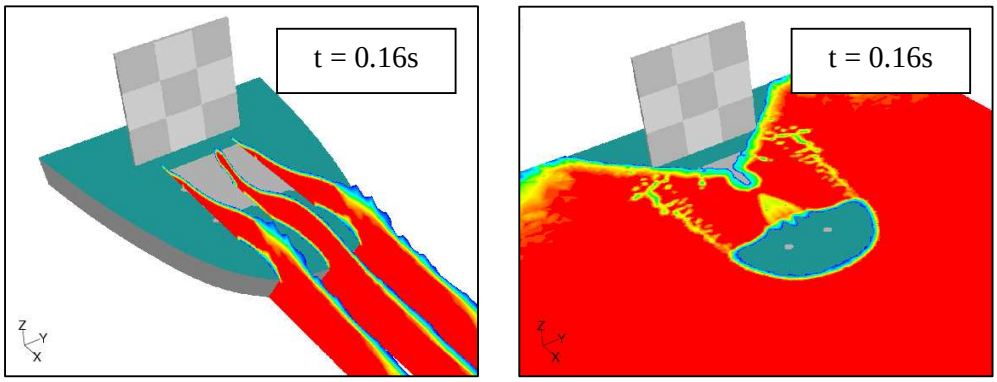

Figure 8.7.5 Sectional views of green water on deck in run H08T13Fn020 at the time the deck loading was maximum.

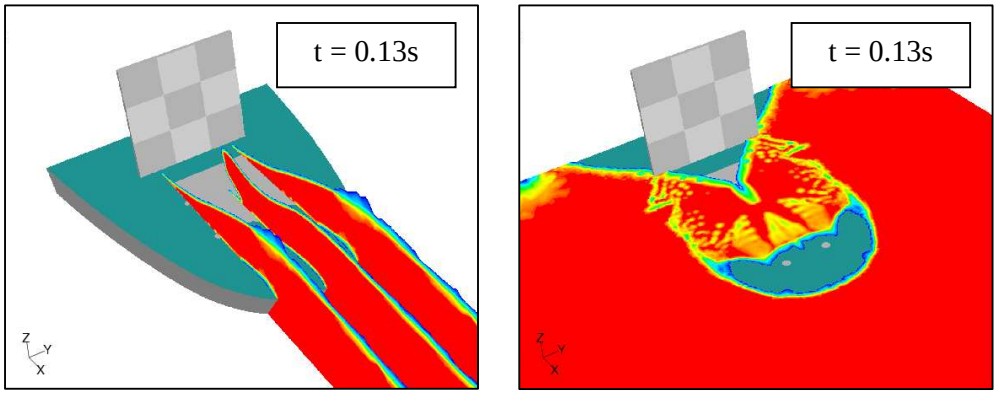

Figure 8.7.6 Sectional views of green water on deck in run H08T12Fn020 at the time the deck loading was maximum.

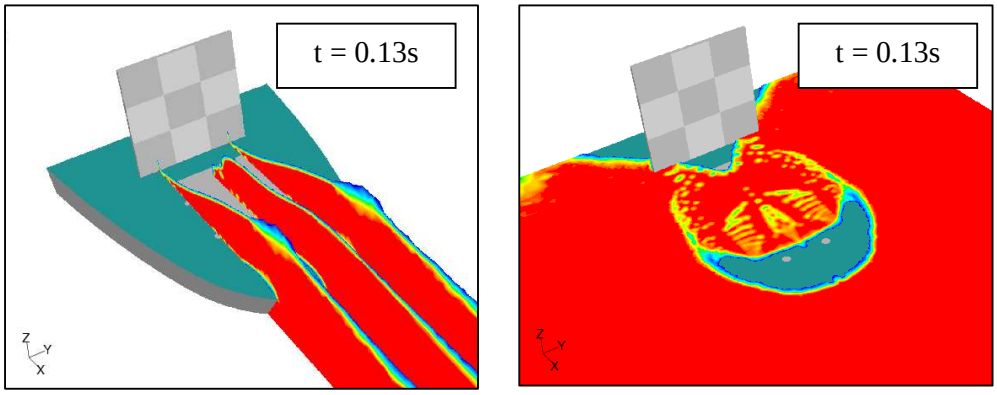

Figure 8.7.7 Sectional views of green water on deck in run H08T11Fn020 at the time the deck loading was maximum.

8.7.2 Effects of ship velocity on green water and loading

When green water height is kept constant, the increased relative velocity between the ship and the green water mass should intensify green water impact. In order to check this and also to investigate the differences in the behaviour of green water flows on deck, two simulations (Table 8.7.2) were implemented and the results compared.

Table 8.7.2 Initial green water height on deck in simulation.

Run	Green water height in simulation (mm)
H08T11Fn020	63.7
H08T13Fn030	64.0

The comparison of loading was carried out on load cells 5, 8, the load-cell box as a whole and deck load cell. The results are as in Figures 8.7.8 to 8.7.11. Figure 8.7.10 clearly shows that by having larger relative velocity, green water flow in run H08T13Fn030 reached the load-cell box earlier by approximately 0.033s. However, Figure 8.7.11 indicated that green water in this case impacted the deck load cell slightly later than in run H08T13Fn020. The answer was found by viewing green water flows at the impact times in the two cases (Figures 8.7.12 and 8.7.13). Indeed, due to its higher velocity and the sharp deck edge, green water flow in run H08T13Fn030 took off the deck at the deck edge. It later landed at the far end of the deck load cell (Figure 8.7.13). Green water flow in run 08T11Fn020, on the other hand, entered the deck at lower velocity. Even though it also took off the deck at the deck edge, it landed back on the deck earlier at the near end of the deck load cell (Figure 8.7.12). Therefore, despite having lower relative velocity, the impact on deck load cell in run H08T11Fn020 actually occurred slightly earlier as seen in Figure 8.7.11.

Higher relative velocity between green water flow and vertical structures would result in larger and more impulsive impact load as suggested by equation (5.9.2) and this was well reflected in Figures 8.7.8 to 8.7.10. Using equation (5.9.2) as an approximate estimation, the ratio between the peak impact loads is to be proportional to the square of the ratio of velocities. The ratio of velocities between run H08T13Fn030 and H08T11Fn020 was 1.5 which implied the ratio between the peak impact loads to be in the order of 2. This was indeed the case when comparing the peak values of the load curves in Figures 8.7.8 to 8.7.10.

In summary, the relative velocity between the ship and green water is closely related to the degree of severity in which green water loading can take place. The velocity also influences the characteristics of green water flow when it enters the deck.

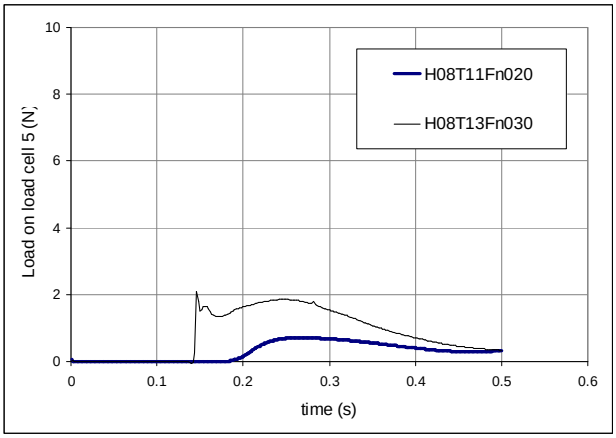

Figure 8.7.8 Effects of ship velocity on loading on load cell 5.

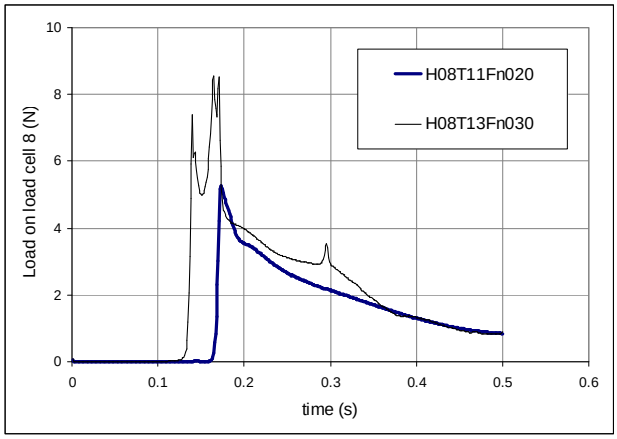

Figure 8.7.9 Effects of ship velocity on loading on load cell 8.

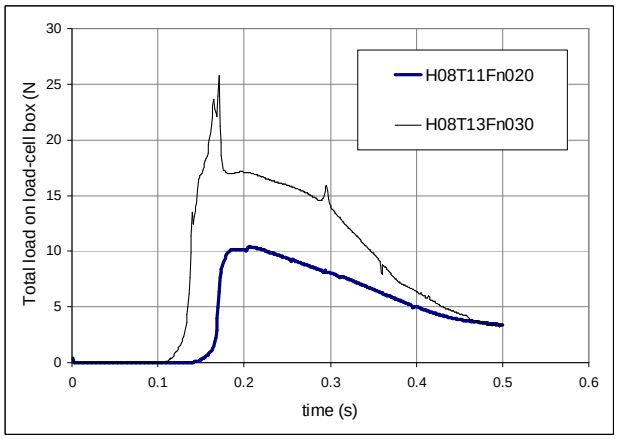

Figure 8.7.10 Effects of ship velocity on total load on load-cell box.

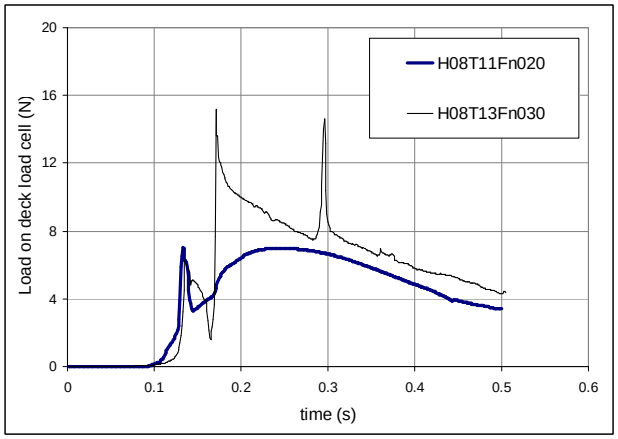

Figure 8.7.11 Effects of ship velocity on total load on deck load cell.

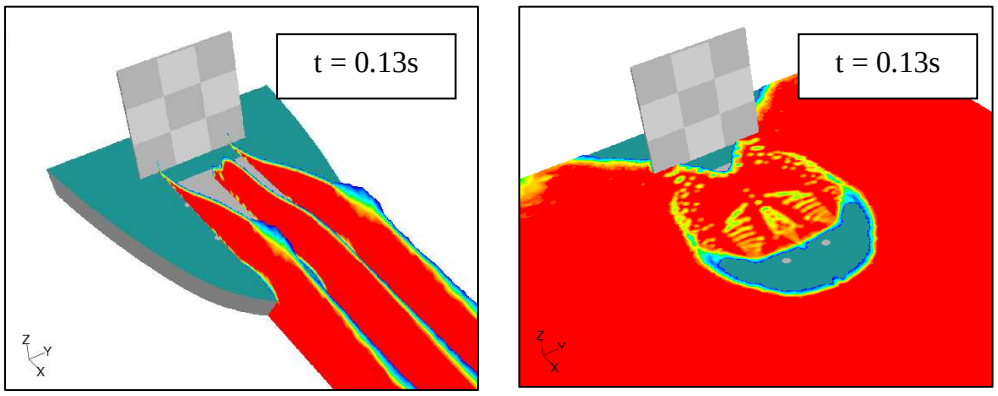

Figure 8.7.12 Sectional views of green water on deck in run H08T11Fn020 at the time the deck loading was maximum.

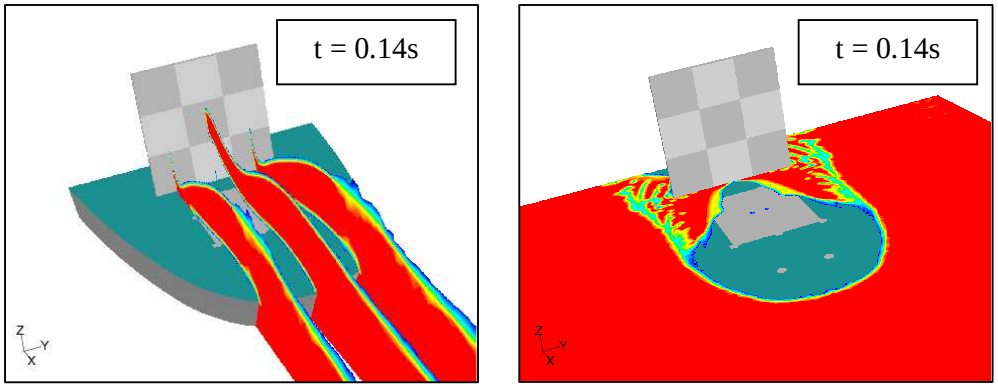

Figure 8.7.13 Sectional views of green water on deck in run H08T13Fn030 at the time the first peak load on deck load cell took place.

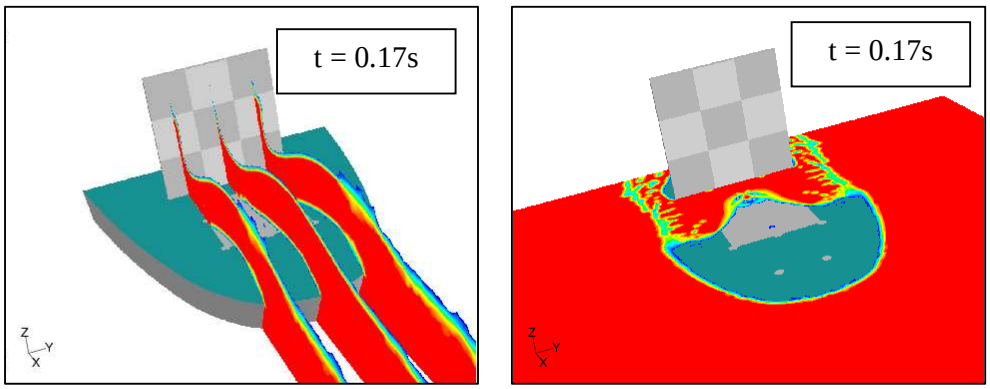

Figure 8.7.14 Sectional views of green water on deck in run H08T13Fn030 at the time when the load on load cell 8 and also on the load-cell box as a whole was maximum.

8.7.3 Effects of breakwater height on green water and loading

Breakwater is designed to obstruct incoming water flow and keep the destructive impact loading away from the protected structures. Higher breakwater means larger cross section area, and hence, more protective breakwater. Larger breakwater, however, comes at the cost of extra material, heavier supporting structure and foundation. Also, up to a certain height, the protection of the breakwater does not significantly increase with any further increase in breakwater height. The design of breakwater will then need to be optimised using CFD tools.

This Section carries out a sample investigation on the effects of breakwater height on the behaviour of green water on deck and the loading on deck structures and plating. Four cases were selected for this investigation and they are listed in Table 8.7.3.

Table 8.7.3 Cases for investigation of the effects of breakwater height on green water and loading.

Case number	Breakwater height (mm)	Breakwater width (mm)	Perforations
No breakwater	0.0	0.0	0
H051D000	51.0	203.2	0
H076D000	76.2	203.2	0
H101D000	101.6	203.2	0

The investigation looked at the following aspects in order to look for relations between the breakwater height and green water both qualitatively and quantitatively:

- Loading on the bottom row of the load-cell box
- Loading on the middle row of the load-cell box
- Loading on the top row of the load-cell box
- Total loading on the load-cell box collectively

- Loading on deck load cell.
- Loading on the breakwater.

The comparisons of these loadings are as in Figures 8.7.15 to 8.7.21. In general, breakwaters helped to substantially reduce green water loading on vertical structures. Figure 8.7.18 indicated that the breakwater with a height equivalent to one third of the structure height (H051D000) reduced the total green water load by more than 60 percent. When the height increased to half of the structure height (H076D000), nearly 90 percent of the load was reduced. When breakwater height was increased to two thirds of the structure height (H101D000), green water load was reduced to almost zero.

Most protection from the breakwater was made to the low-level structures. Well sheltered behind the breakwater, these low-level structures successfully avoided the destructive front water in green water flow. Figure 8.7.16 shows that even with lowest breakwater height, green water load on bottom row of the load-cell box was reduced by a substantial amount of 95 percent. The only load on these structures was related to the hydrostatic pressure of the descending water from upper levels, which was generally insignificant.

Upper-level structures, on the other hand, could face greater green water loads due to the breakwater. The accumulated water in front of the breakwater appeared to create a buffer that diverted the follow-up water upwards. In heavy green water event such as those considered herein, the accumulation of water continued until it reached the top edge of the breakwater. Then, the follow-up water flow would overcome the breakwater in the form of a water jet and could be strong enough to carry on and strike the structures behind the breakwater. If such impact took place, the severity depended on the velocity of the water jet (equation (5.9.4)) and the incident angle of the jet itself.

Figure 8.7.22 captured the moments when green water load on the middle and top rows were maximum for all four cases. The timing of these moments indicated that green water took longer time to overcome higher breakwater. Figures 8.7.22 (B) and (C) showed the direct impacts of green water jets on the top row at similar incident angles. However, the load resulted in (B) was much higher than in (C) as in Figure 8.7.17. This was due to the difference in green water velocities in these two cases. Reviews of vector fields around the top row revealed that green water velocity at the time of impact in (B) was 1.8m/s whilst in (C) it was only 0.5m/s. In the case of no breakwater (Figure 8.7.22 (A)), although the velocity of green water at the top row was relatively high (approximately 1.3m/s), green water load was low. This was because the incident angle or the angle of impact was almost 90 degrees. The water simply ran up the load cells without imposing any significant pressure. Figure 8.7.23 presents the velocity vector field around load cell 2 in the top row of the load-cell box for the case corresponding to Figure 8.7.22 (D). It could be seen that the water was descending along the load cell surface (velocity vector was parallel to the surface). Therefore, even though there was a fair amount of water in front of this load cell, the load was almost as low as in Figure 8.7.17.

Figure 8.7.16 plotted the load curves on middle row of the load-cell box. One interesting fact about the middle row was that it was at intermediate level between the low-level and high-level. The physics behind the load acting on this row was, therefore, relatively sensitive to the height of the breakwater in use. Without the breakwater, incident water accumulated in front of the bottom row and then directed the follow-up water upwards, resulting in an impact with the middle row (Figure 8.7.24(A)). With the breakwater of low height, the load on the middle row was caused by direct impact with the overriding water jet that took off the edge of the breakwater (Figure 8.7.24(B)). When high breakwaters were fitted, the overriding water jet caused an impact at higher location than the middle row. The water after this impact then descended and as it passed the middle row, it imposed some pressure. This pressure is normally insignificant as in Figure 8.7.16.

As far as the loads on vertical structures were concerned, the increased height of breakwater could increase the loads faced by structures at upper levels. However, this increased load, if any, was well offset by a substantial reduction in the loading on low-level structures. Overall, the total loading on the vertical structures reduces.

Figure 8.7.19 shows green water loads acting on the breakwaters and Figure 8.7.20 compares the peak loads on the breakwater with those on the load-cell box. Despite a harmonic transition of green water loads between the breakwater and the load-cell box, it could be seen that for the range of breakwater height in consideration, the peak impact load on the breakwater did not change significantly with breakwater height. In equation (5.9.2), the peak impact loads are proportional to squared velocity of the water front. If the velocity was not changed and as long as the breakwaters were large enough to take on the full impact (Figure 8.7.25), the peak impact loads should stay relatively the same.

After the impact, the water accumulated in front of the breakwater. Higher breakwater meant that more water could be accumulated in this region. The extra hydrostatic pressure would then cause some differences in the load curves and this was observed in Figure 8.7.19.

Figure 8.7.21 compared the loads acting on the deck load cell. As discussed in Section 8.6, due to the reflected water off the breakwater, the load on the deck load cell increased. Since all the breakwaters considered in this Section did not have any perforations and were of similar design, the amounts of reflected water should be similar. The differences between the load curves should therefore be small as in Figure 8.7.21.

For similar design features, the variation in height of the breakwater could change the behaviour of green water. The loading as a result would also change. If all the

breakwaters were large enough to take the full impact from green water flow, any increase in height would not result in any significant changes in loading on the breakwater itself. The loading on deck plating could change depending on its location relative to the breakwater. If the breakwaters are of similar design and large enough, this load would not pose any significant changes.

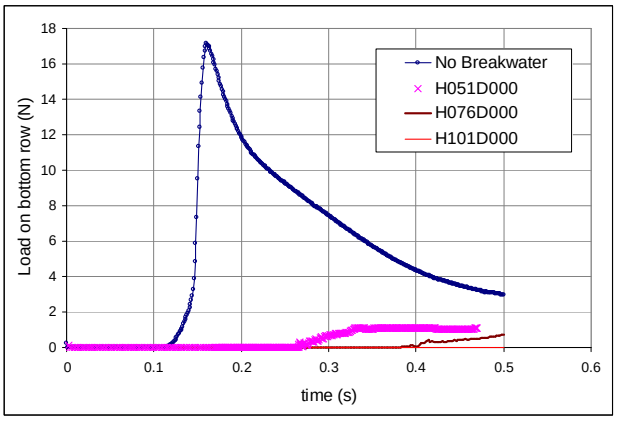

Figure 8.7.15 Comparison of loads on the bottom row of the load-cell box.

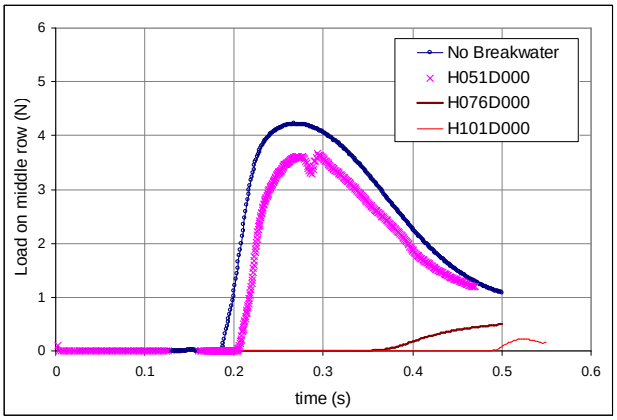

Figure 8.7.16 Comparison of loads on the middle row of the load-cell box.

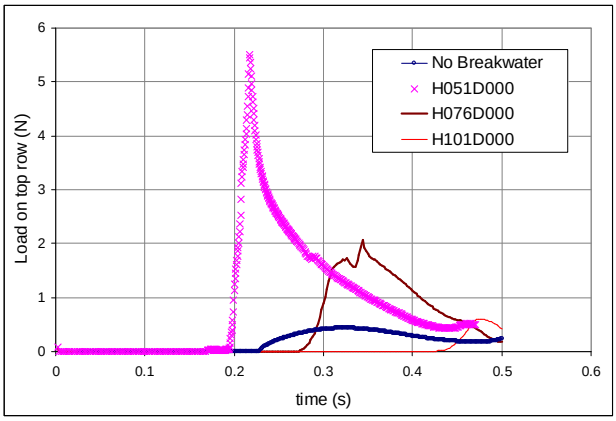

Figure 8.7.17 Comparison of loads on the top row of the load-cell box.

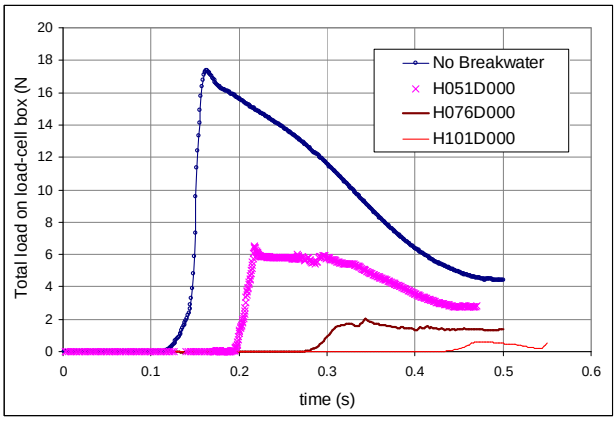

Figure 8.7.18 Comparison of total loads on the load-cell box.

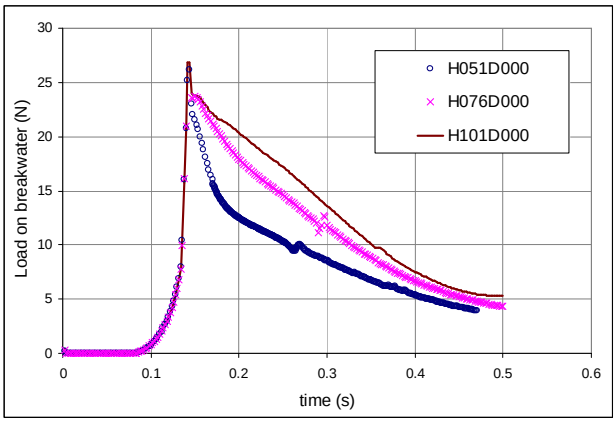

Figure 8.7.19 Comparison of loads on the breakwater.

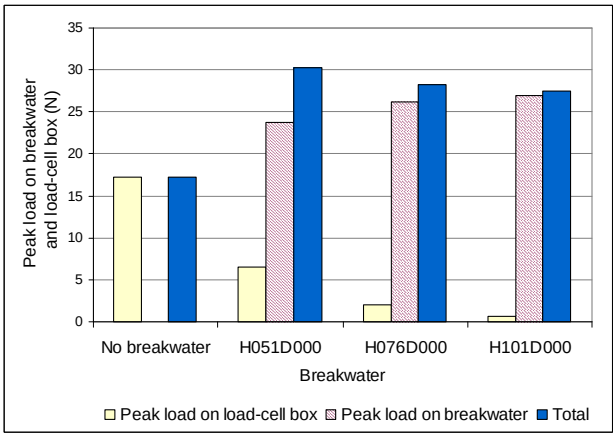

Figure 8.7.20 Peak loads on the load-cell box and on the breakwater.

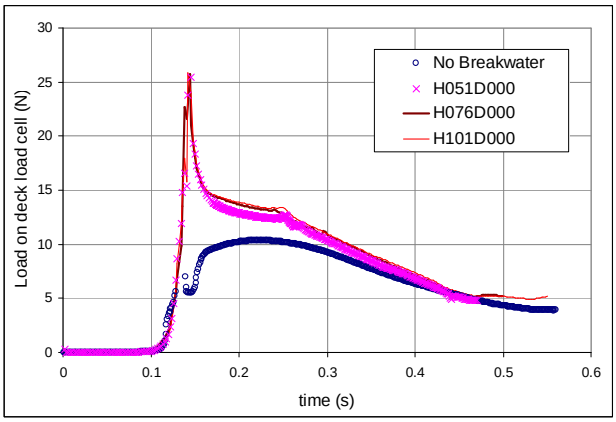

Figure 8.7.21 Comparison of loads on the deck load cell.

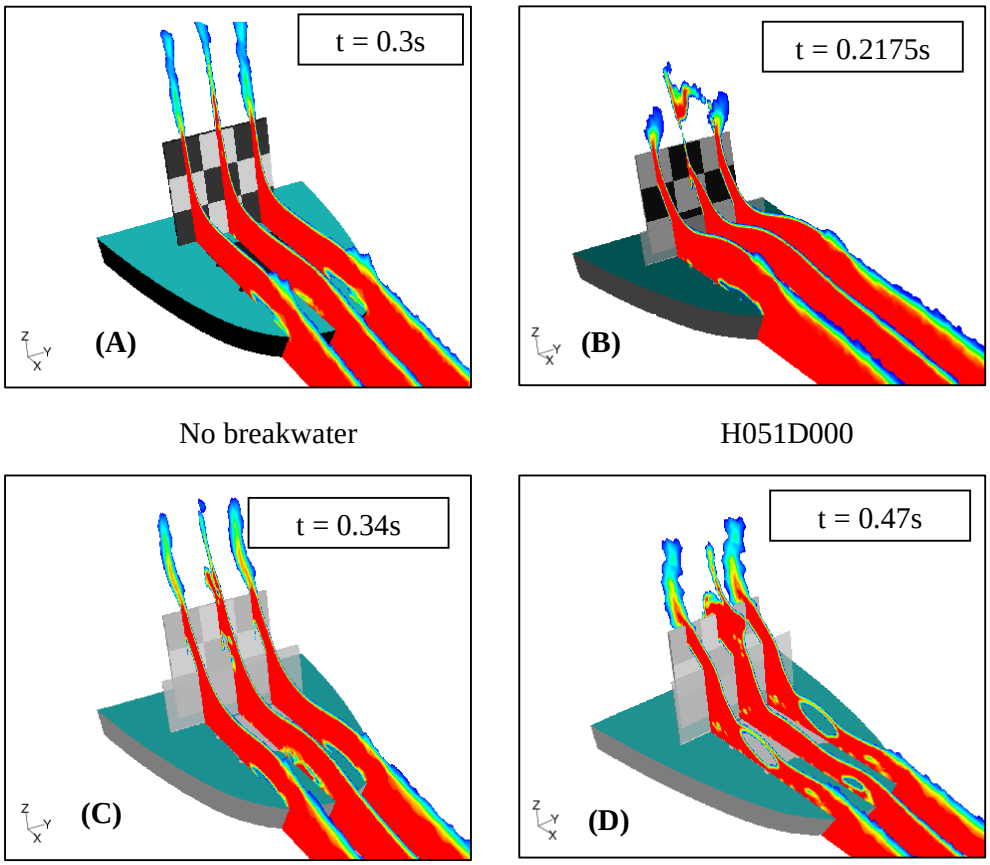

Figure 8.7.22 Green water flows at the time of maximum loads on top row of the load cell box.

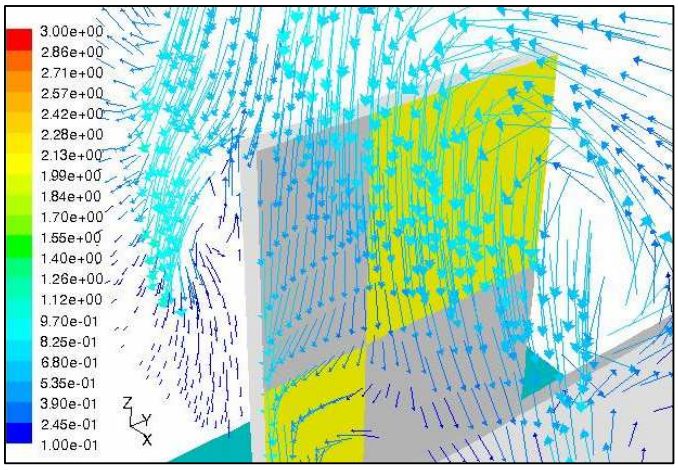

Figure 8.7.23 Velocity vector field around load cell 2 in the top row of the load-cell box in the case corresponding to Figure 8.7.22 (D).

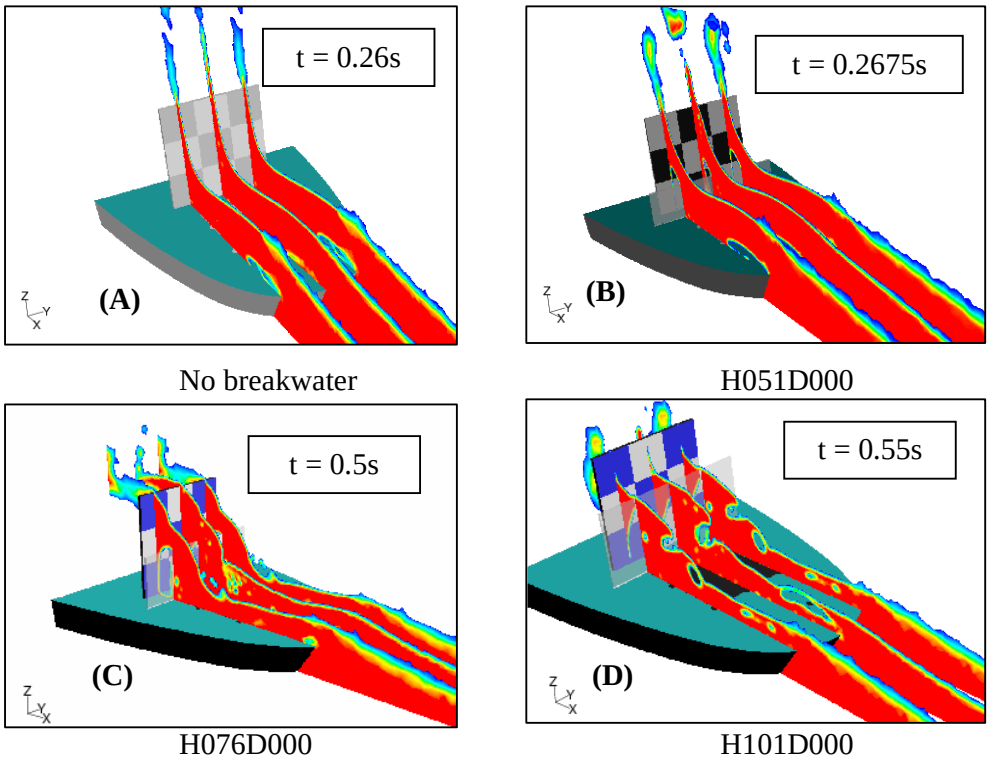

Figure 8.7.24 Green water flows at the time of maximum loads on middle row of the load cell box.

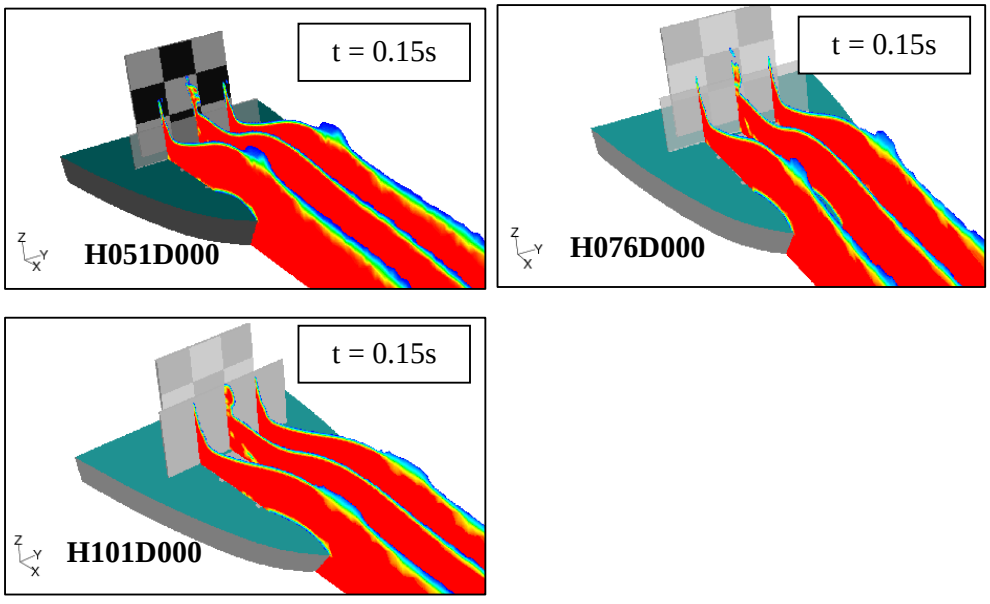

Figure 8.7.25 All the breakwaters were large enough to take the full impact from green water which resulted in maximum loads on the breakwaters.

8.7.4 Effects of breakwater permeability on green water and loading

The effectiveness of a breakwater against green water flow does not only depend on the height, it is also influenced by the degree of permeability of the breakwater. This Section aims to investigate this influence. To achieve this, four breakwaters of different perforation diameters or permeability percentages were selected and they are as in Table 8.7.4. Without losing any generality, the breakwater height selected was 51mm (at model scale).

Table 8.7.4 Specifications of breakwaters for investigating the influence of permeability on green water and loading.

Breakwater	Dimensions (mm)	Rows of perforations	Number of perforations	Perforation diameter (mm)	Permeability percentage
H051D000	51×203.2	2	14	0.0	0.0%
H051D105	51×203.2	2	14	10.5	11.7%
H051D140	51×203.2	2	14	14.0	20.9%
H051D175	51×203.2	2	14	17.5	32.6%

Figures 8.7.26 to 8.7.32 show the variation of loads in various load cells within the influential zone of green water loading. Figures 8.7.26 and 8.7.27 present the load curves from load cells for the lower-level rows. All the load curves had distinct double-peak characteristics which indicated that double impacts took place on these load cells. Figures 8.7.33 to 8.7.36 present the views of green water flow on deck at the times that the peak loads happened. It turned out that the first peak loads were caused by water jets that came out from the perforations. Depending on the dimensions of the perforations, the quantities and velocities of these water jets could vary. When the breakwater was not perforated (H051D000) or, in other words, the perforation diameter was zero, there were no such water jets (Figures 8.7.33(A) and 8.7.35(A)) and the first peak loads in this case were

zero as in Figures 8.7.26 and 8.7.27, respectively. The larger the perforations, the larger the permeability percentage and more water could pass through the breakwater. The loads would therefore increase. Comparison of the first peak loads could be made from Figures 8.7.26 and 8.7.27. For simplification, if the exit velocities (U's) of the water jets were assumed to be similar, the discharge rate Q of each water jet behind the breakwater would then only depend on the area A_p of the perforation:

$$Q = U.A_p \tag{8.7.1}$$

Assume also that the distance between the load-cell box and the breakwater was small enough to ignore any reduction in the water jet velocity, the peak impact load on the load cells F_{impact} could be estimated by the formula:

$$F_{impact} = \rho.Q.U \tag{8.7.2}$$

By substituting (8.7.1) into (8.7.2) and using formula for a disc area based on its diameter D_p, impact force caused by one water jet F_{impact} could be given as:

$$F_{impact} = \frac{1}{4}\rho.\pi.D_p^2.U^2 \tag{8.7.3}$$

Since U was assumed to be constant, the load on the load cells depended on the square of the diameter of the perforations. Ratios between the first peak loads on load the load cell box (Figure 8.7.29) reflected this characteristic.

Figure 8.7.34 show that the second peak loads on the bottom row of the load-cell box were due to the combination of the build-up of water between the load-cell box and the breakwater and the water that continued to come off the perforations.

Figures 8.7.36 and 8.7.38, on the other hand, show that the second peak loads on the middle row were actually due to the water that overrode the breakwater.

Figure 8.7.37 shows the views of green water flows at the times the impact loads on the top row of load-cell box were maximum. Since the top row was well above the influential zone of the water jets that came off the perforations, the double-peak characteristics in the load curves were not present (Figure 8.7.28). This Figure also indicated that the height this water jet could reach on the load-cell box depended on the size of the perforations. Note that the perforations helped to divide the incident water flow via three following ways:

- Letting some of the water pass through.
- Reflecting some of the water back.
- Diverting the rest of the water upwards and away.

The strength of the original water flow was therefore divided accordingly. The strength of the diverted water or the water that overrode the breakwater would depend on the amount of the water that could pass through the breakwater. Also, the accumulation of the reflected water partly affected the strength of the diverted water. If the rate of accumulation of water in front of the breakwater is higher, the follow-up water will be diverted upwards and away more quickly. When the breakwater was not perforated, the rate of water accumulation was highest and the overriding water was the strongest. It reached the load-cell box at higher location on the top row. As the perforation diameter increased, it was evident in Figure 8.7.37 that the overriding water reached the load-cell box at lower location. The impact load was then shared between the top row and the middle row. Therefore, even though the velocity of this water did not necessarily change much (Table 8.7.5), the peak impact load on the top row reduced (see also Table 8.7.5). For perforation diameter of 17.5mm, the velocity of overriding water did reduce significantly. Together with the lower impact area on the load-cell box, this

resulted in a considerable decrease in peak impact load on the top row (see Table 8.7.5 and Figure 8.7.28).

Figure 8.7.30 present the loads imposed by green water on the breakwaters and Figure 8.7.31 plot the peak values of these loads along with the peak impact loads on the load-cell box as a whole. In Section 8.7.3, it was already shown that there was a transition between the load on the load-cell box and the load on the breakwater when the breakwater area was varied. Larger breakwater area would see less loading on the load-cell box but more loading on the breakwater itself. Similar trend was noticed as in Figure 8.7.31. Figure 8.7.39 shows the moments when the peak loads on the load-cell box occurred.

Figure 8.7.32 compares the loads acting on the deck load cells when the perforation diameter was varied. It could be noticed that the load curves were very much the same except for the impulsive peak loads at the beginning when the water first landed on the deck load cell. Slight differences could be noticed and these were due to the hydrostatic pressure caused by the reflected water from the breakwater. Larger permeability percentage meant smaller breakwater area and less reflected water. The load on the load cell was, as a result, smaller.

In summary, the permeability of the breakwater could greatly affect green water and its loading. Generally, for larger permeability, more loading was faced by the protected load-cell box and less loading on the breakwater.

Table 8.7.5 Velocity of overriding water on impact the top row of load-cell box and peak impact load on top row.

Breakwater	Velocity range of overriding water on impacting the top row (m/s)	Peak impact load on the deck load cell (N)
H051D000	1.30-1.50	25.43
H051D105	1.35-1.50	22.67
H051D140	1.35-1.55	20.28
H051D175	1.10-1.30	15.62

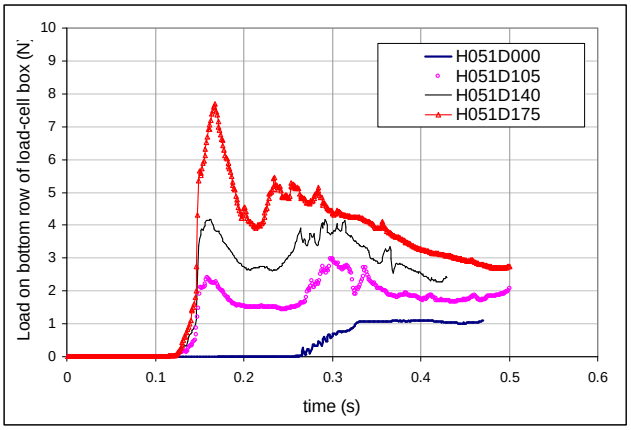

Figure 8.7.26 Comparison of loads on the bottom row of the load-cell box.

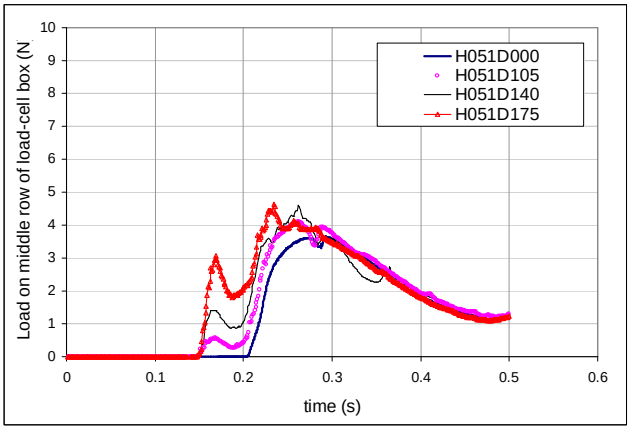

Figure 8.7.27 Comparison of loads on the middle row of the load-cell box.

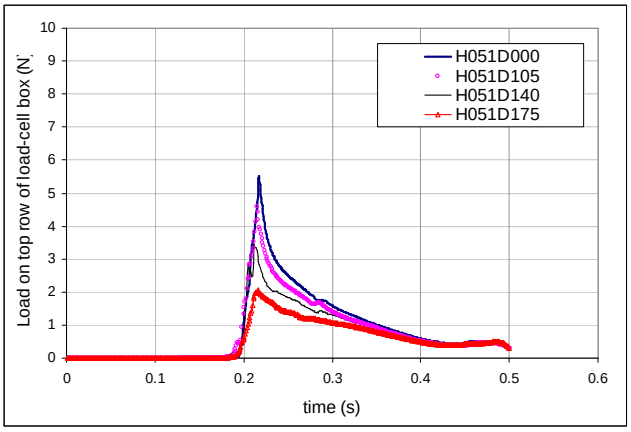

Figure 8.7.28 Comparison of loads on the top row of the load-cell box.

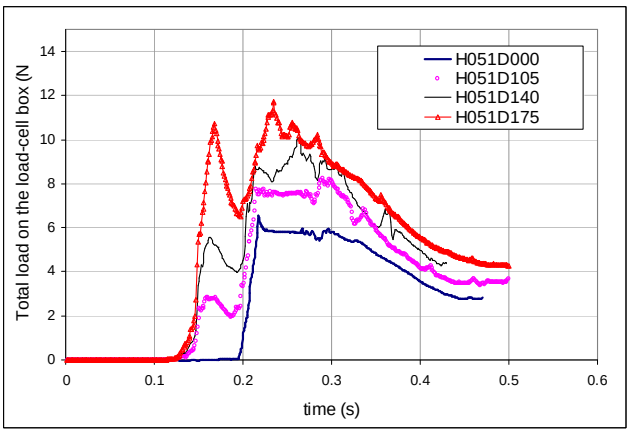

Figure 8.7.29 Comparison of total loads on the load-cell box.

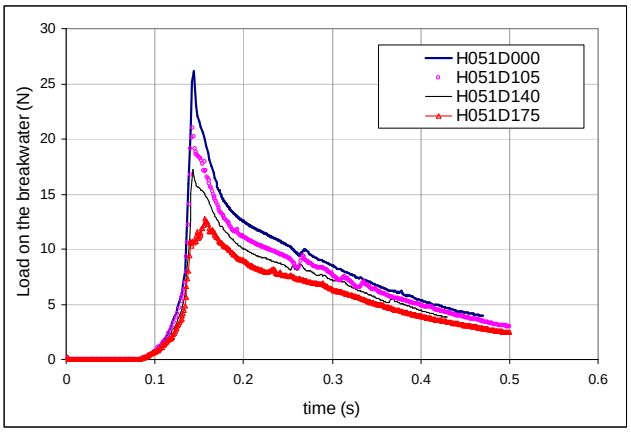

Figure 8.7.30 Comparison of loads on the breakwater.

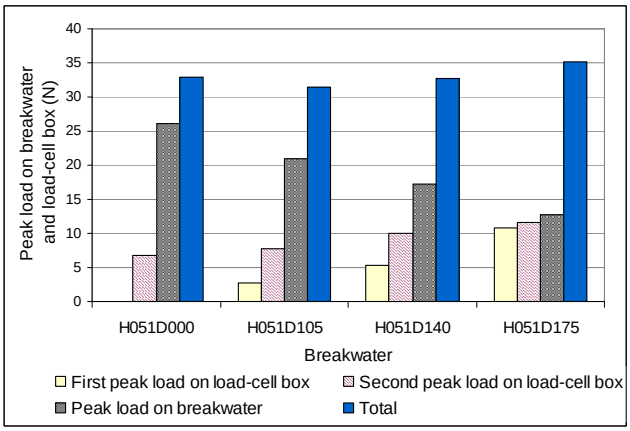

Figure 8.7.31 Peak loads on the load-cell box and on the breakwater.

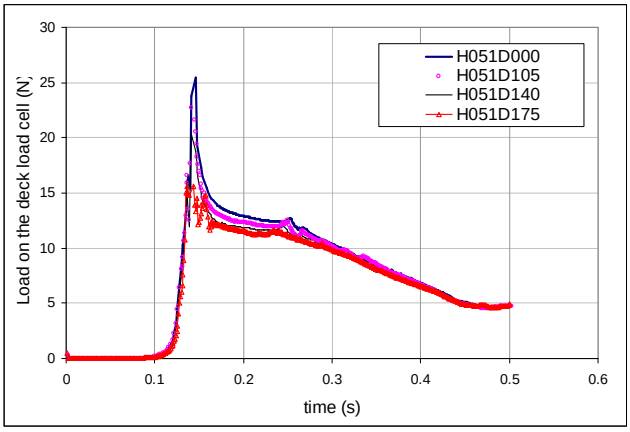

Figure 8.7.32 Comparison of loads on the deck load cell.

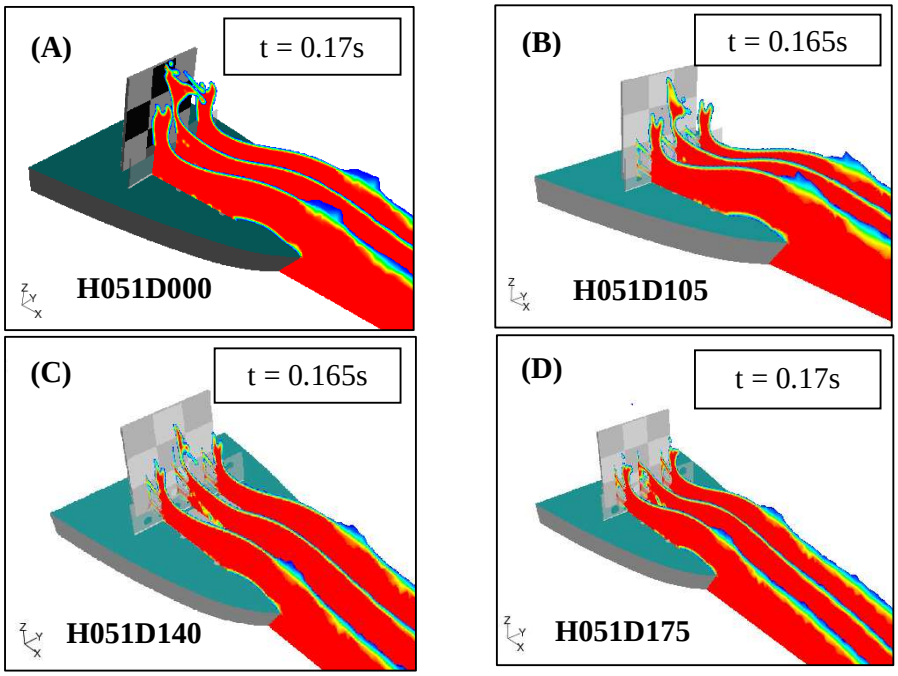

Figure 8.7.33 Green water flows at the time of the first peak loads on bottom row of the load-cell box and also on the load-cell box as a whole.

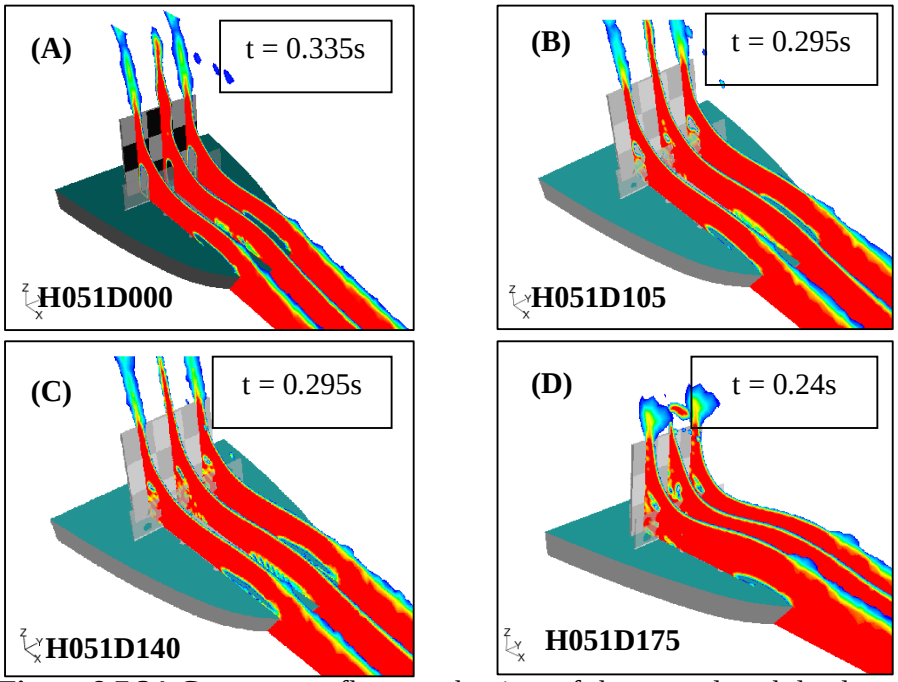

Figure 8.7.34 Green water flows at the time of the second peak loads on bottom row of the load cell box.

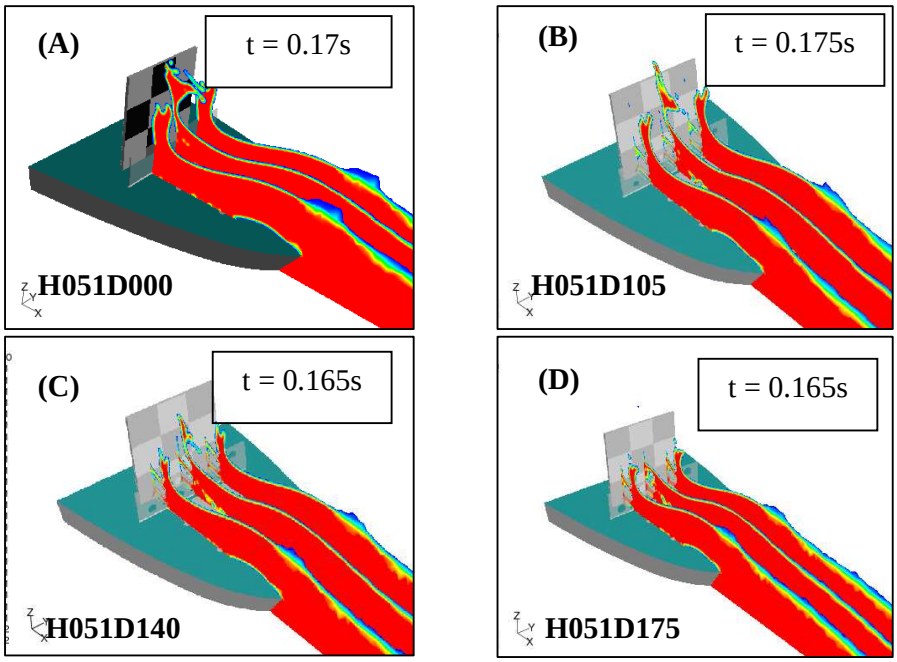

Figure 8.7.35 Green water flows at the time of the first peak loads on middle row of the load cell box.

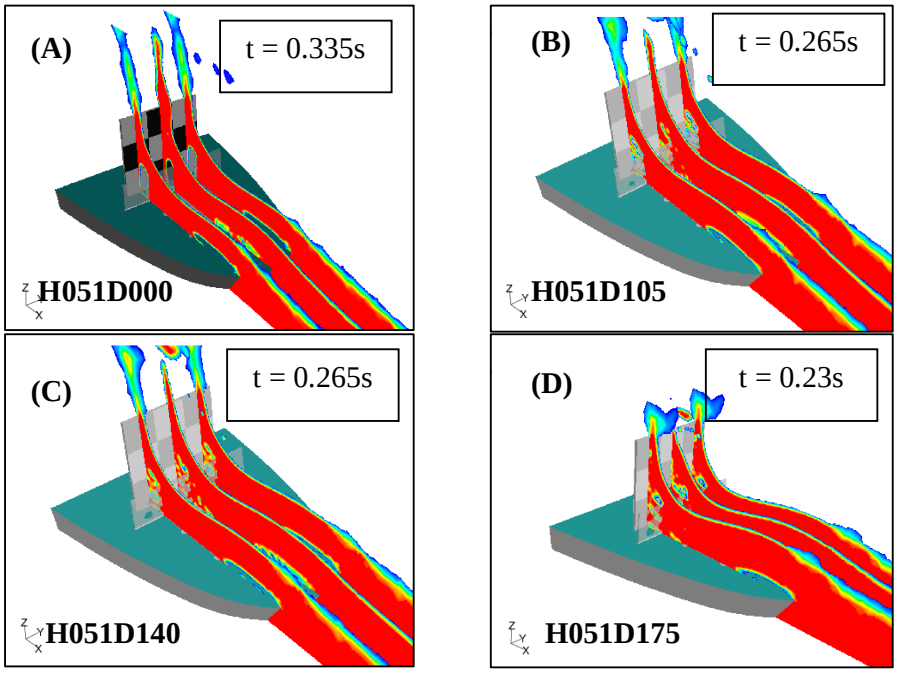

Figure 8.7.36 Green water flows at the time of the second peak loads on middle row of the load cell box.

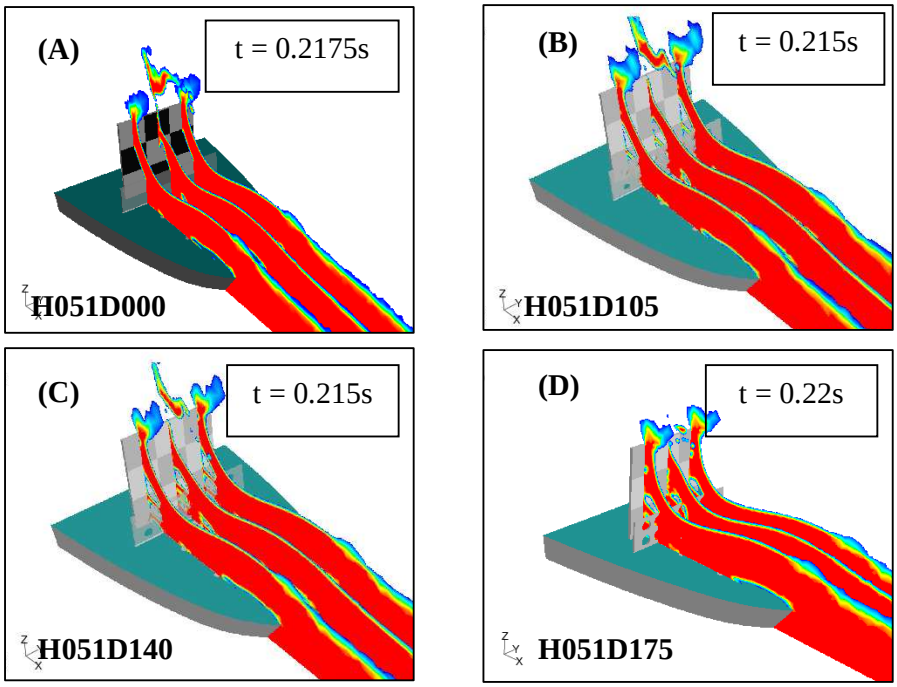

Figure 8.7.37 Green water flows at the time of the peak loads on top row of the load cell box.

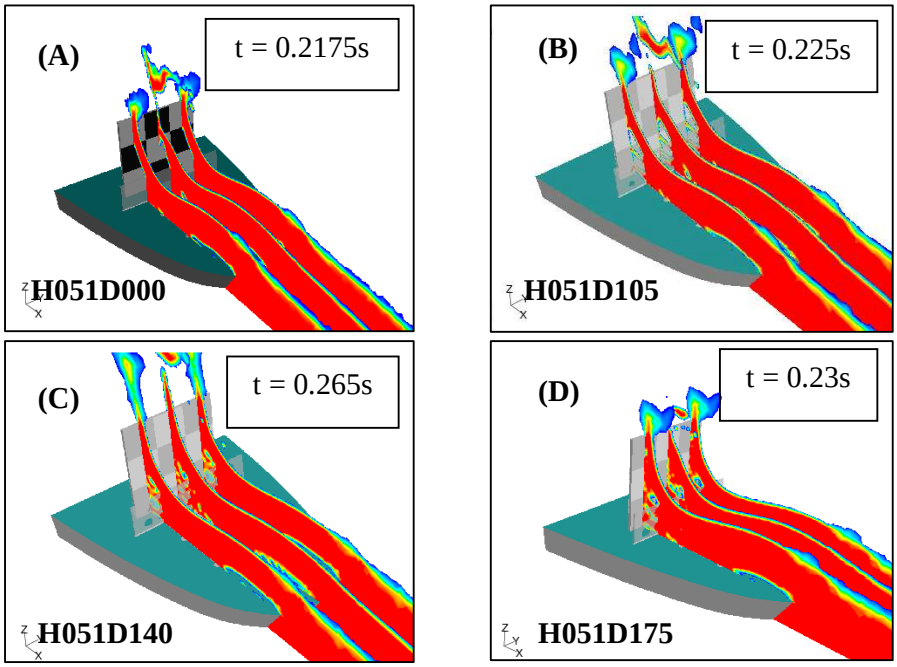

Figure 8.7.38 Green water flows at the time of the second peak loads on the load cell box.

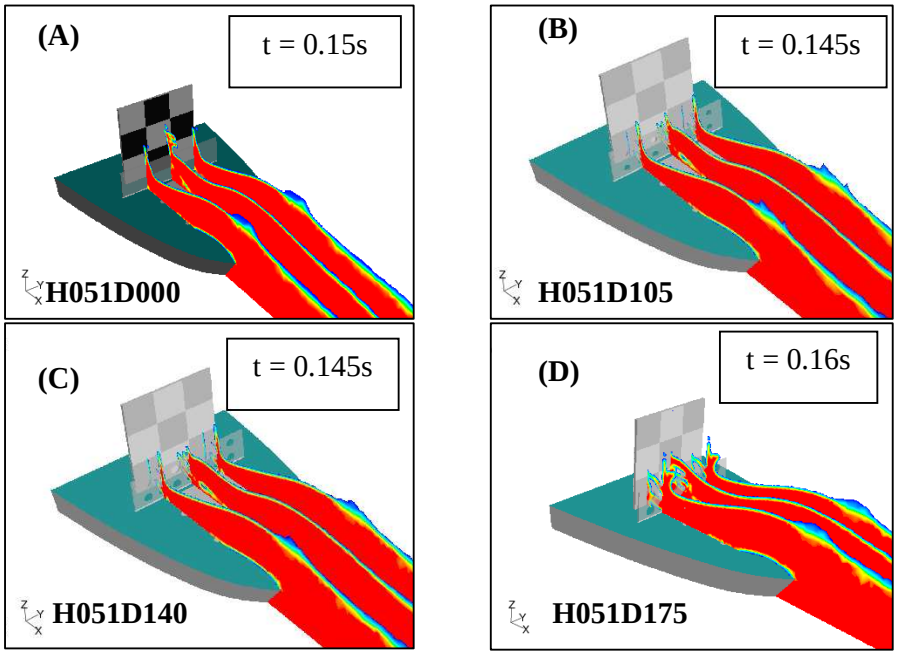

Figure 8.7.39 Green water flows at the time of the second peak loads on the load cell box.

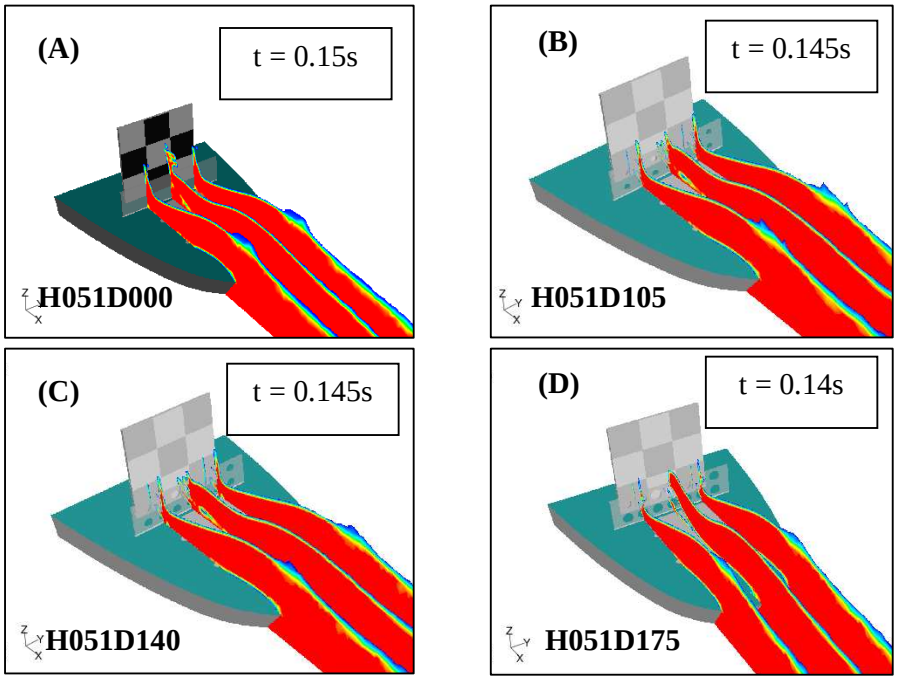

Figure 8.7.40 Green water flows at the time of the peak loads on the deck load cell.

8.8 Summary

In this Chapter, the numerical results based on CFD simulation were validated by experimental data obtained from the model tests. Either with or without breakwater on forecastle deck, there was good agreement between the two streams of data. The simulation produced well green water behaviour on deck for all test conditions considered and for all the variations of breakwaters. Breakwaters proved to be an effective way of dealing with green water on deck. They were shown to help reduce green water loading on vertical surfaces by substantial amounts. A sensible selection of permeability for the breakwater could bring in optimal balance of loads faced by the breakwater and protected structures. Following successful validation of numerical results, this Chapter carried out numerical parametric studies on effects of green water height and breakwater design features. It was found out that green water height and ship velocity could increase green water loading significantly. In terms of breakwater design, both the dimensions and permeability of the breakwater had considerable influence on the characteristics of green water on deck. Green water loading was basically reduced when the protective area on the breakwater was larger. This included either increased breakwater height (with breakwater breadth fixed) or reduced breakwater permeability.

Chapter 9:
Review and Applications of Simulation Model

9.1 Introduction

The simulation model tested in this project has been a simplified version of what could actually have happened in reality. Even though the validation has been encouraging, there are limitations. This Chapter, firstly, aims to review the methodology of the modelling framework for simulating green water on the deck of a containership at high speed. Ranges of applicability of this model are then specified. Secondly, this Chapter looks at practical applications of the model. Several examples of these applications are presented to demonstrate the applicability the hydraulic model.

9.2 Review of simulation model

From preceding Chapters, the analysis model for green water event can be summarised as in Figure 9.2.1. The review process was carried out at every step of the analysis model.

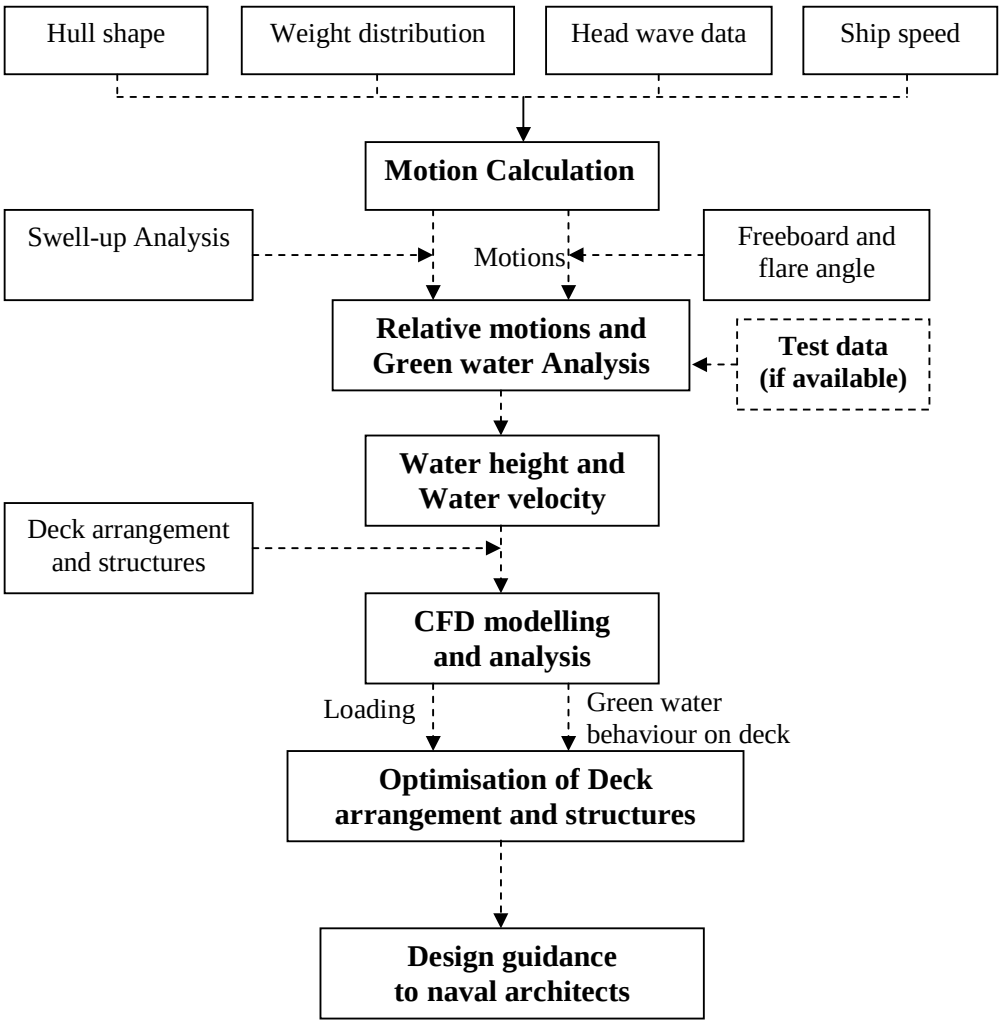

Figure 9.2.1 Outline of the semi-empirical design evaluation method.

9.2.1 Review of ship motion prediction theory

Note that the validation in Chapter 8 was based on a semi-empirical process in which the measured freeboard exceedance was used to build the simulation for CFD analysis (see also Chapters 6 and 7). If no experimental data are available, the freeboard exceedance is to be calculated from the relative motions between the forecastle deck and free water surface as in Chapter 3 for instance. Care should then be taken in using these numerical results. Firstly, most of ship motion theories available are based on the assumptions of small wave amplitude and other linear assumptions. Despite efforts to bridge the gap between numerical and experimental results, the motions of ship in large waves involve many non-linearities and these were not included fully in the numerical solutions. Unfortunately, green water normally takes place in large and steep waves. The ship motions in such scenarios are excessive and highly non-linear as in Chapter 5. This is further complicated by the shipment of water on board and keel/flare slamming. The comparison between experiment and simulation in such rough conditions can foresee discrepancies that can only be rectified by enhancement factors which may be unique to a particular ship.

Type of ship hull is another factor that should be considered when adopting some numerical analysis for ship motions. Containership hull normally comes with a bulbous bow and this causes difficulty in most of the ship motion theories. For example, the ship motion results used for comparison in Chapter 5 were calculated based on strip theories. The added mass and damping coefficients were estimated based on generic equations developed from test data using frigate ship hulls. Despite the fact that hydrodynamic coefficients could be calculated for instantaneous wetted surface area, the differences in hull shape resulted in considerable discrepancies in the ship motion results. This subsequently affected the calculations of relative motions, freeboard exceedance, and finally, the prediction of deck wetting and CFD analysis as a whole.

Therefore, if theoretical estimation is to be used, a method that is as close to fully non-linear as possible has to be chosen and correction factors may be necessary to ensure the discrepancies can be sensibly reduced.

9.2.2 Review of swell-up analysis theories

Similar to ship motions, swell-ups of water around the bow are fundamental components to freeboard exceedance and occurrence of green water. As in Chapter 3, two types of swell-up (namely, static and dynamic) were treated independently and then superimposed to obtain the total swell-up. Coupling effects were ignored for simplification when they, indeed, exist.

The bow waves were calculated using the theory proposed by Shearer (1950). In this theory, the ship was assumed slender and the calculation used the sectional areas of the strips at the constant draught. When the ship travels in waves, it pitches. The sectional areas of the strips therefore change and this means the bow waves will change as a result. However, this was not fully included in the suggested deck wetness evaluation model.

The dynamic swell-up were estimated using the theory by Tasai (1961). The generated radiating waves were calculated based on small harmonic heaving of a cylinder. The ship motions associated with green water were normally large and non-linearities are inevitable. Together with the discrepancies incurred through the transformation techniques, the swell-up calculation can be a significant source of error and its use must be taken with care.

9.2.3 Review of relative motions and green water occurrence

The relative motions between a point on deck and the free water surface were calculated based on the calculated motions and estimated swell-ups around the bow. Discrepancies in those two processes will collectively add up to the discrepancies in the relative motions.

The methods in Chapter 3 for detecting the occurrence of green water and classifying the event as it happens were based on the simplified laws of physics, observations in tank tests and in reality. Errors were therefore inevitable and improvement on the existing method is always encouraged.

9.2.4 Review of model tests and the use of test data in CFD modelling

The test data used in this project were from the experiments with the containership model. The analysis methodology developed herein is most suitable for containerships. The application to other types of ship hull should be dealt with care and verification is highly recommended.

The tests were conducted in regular head waves only and the model was restrained against all motions other than heave and pitch. The forward velocity of the model meant that tests in random waves would not have achieved valid test time (as suggested by ITTC) for a reliable analysis. Evaluation of green water in random and oblique waves would require a review of the method. In oblique waves, green water may take place at the stern and the sides of the ship, especially when the ship rolls.

Validation was carried out at model scale. Interpretation of loading and form of deck wetting at full scale is to be taken with care. Scale effects existed since velocity terms were derived by Froude scale whilst fluid viscosity υ was more or less similar. Reynold number Rn, defined by:

$$Rn = \frac{\text{Inertial force}}{\text{Viscous force}} = \frac{U.L}{\upsilon} \qquad (9.2.1)$$

was not similar between model and full scales. The characteristics of the flow were therefore different to some extent. In order to understand the scale effects, experiments with larger ship model are needed. The test results can then be compared with current test results for evaluation of scale effects. However, this is outside the scope of this research.

9.2.5 Review of the setup for CFD modelling

In Chapter 7, the setup of the CFD model was based on data obtained from the experiments (see also Chapter 6). Shortfalls present in the existing ship motion theories together with sensitivity of green water to bow shape meant that experimental inputs are still essential in CFD modelling setup and analysis.

Green water mass modelled in CFD had a simplified shape and the water velocity was assumed one-dimensional along the x-axis at the beginning. In fact, the water entered the deck in a direction nominal to the deck edge. Hence, improvements in this area are recommended. The motions of ship body were not simulated due to requirements for computational capability. This led to a certain degree of discrepancy between experiments and simulations as in Chapter 8.

In this research, only part of the ship body was modelled in CFD and so were the waves and surrounding water. If the whole ship body was modelled, sensible adjustment must be made to ensure the problem remains well defined.

9.2.6 Review of the limitations in CFD analysis

CFD has proven to be a powerful tool for solving a variety of industrial problems. However, it still has its own limitations and, therefore, does not give a final solution to complex problems, such as green water. Apart from the fact that the governing equations have already been simplified, the accuracy of the output results from CFD analysis depends largely on the setup of the model. If well posed, the produced solutions will be more reliable and reflect better what could happen in reality. The use of CFD, therefore, requires rigorous and systematic approach for which benchmark tests are essential. Validation with reliable test data is essential for the development of this simulation model.

9.3 Engineering applications of the simulation model

This Section will look at the possible applications of the modelling framework in the field of engineering.

9.3.1 Investigation into the performance of various breakwater designs against green water on deck

Besides rectangular shape with and without perforations, breakwater also comes in many other forms. The conventional V-shape has been a common practice for many years. This design consists of two slender plates which are joined together at one end to form a V-shape as its name suggests. Unlike the rectangular breakwater, the V-shape does not block the incoming water at a right angle. Instead, it spearheads the water flow, divides it into sub-flows and channels these sub-flows to the ship sides. As a result, the breakwater does not encounter the impact head on. The impact load will be less than that faced by a rectangular design of similar dimensions. Geometrically, the V-shape breakwater requires more space than other designs because of its depth. The V-shape breakwater is as in Figures 9.3.1 and 9.3.8.

Vane-type breakwater is another option that was designed aimed at reducing the accumulation of water in front of the breakwater. This breakwater was fabricated from multiple rectangular plates that were arranged one after the other athwart ship. These plates are angled to the direction of the incoming water so that water can be diverted to the sides. This arrangement makes the breakwater resemble a series of vanes assembled together. There are gaps between the vanes which act as passages for incident water to go through. Like the V-shape breakwater, the vanes do not encounter the incoming water at right angles. The angled vanes divide the water flow into multiple sub-flows and channel them to the sides of the ship. Due to the gaps between the vanes, the water does not pile up as much as it would in other breakwater designs. The loading on the breakwater, as a result, will reduce. Also, without the accumulated water in front of the breakwater which acts as a buffer, less water can be expected to overcome the breakwater.

So far, there have been very limited publications on the performances of breakwater of different designs. No concrete methodology of systematically optimising the breakwater design for a ship is known.

The success of the simulation model in predicting the behaviour of green water flow on deck with and without rectangular breakwaters implies that the model works well with other kind of breakwaters, i.e. V-shape and vane-type. Therefore, instead of conducting expensive series of experiments, the established simulation model can be applied to investigate and compare the performances of different breakwaters and optimise the design for a specified ship. To illustrate this concept, CFD analyses have been carried out on green water on deck with V-shape and vane-type breakwaters. The results are then compared with results from rectangular breakwaters and for the case with no breakwater. Simulation conditions corresponded to experimental data when ship model was running at Fn = 0.25, in waves equivalent to full scale height of 8m and period of 12s.

9.3.1.1 Non-inclined V-shape breakwater

In the design of the V-shape breakwater, the plates can either be set vertically or at an angle (normally forward) to the vertical axis. The joining edge of the V will vary accordingly. In this Section, a vertical or non-inclined V-shape breakwater was modelled for CFD analysis. For comparison purposes, it has the same height and projected area (along x-axis) as the non-perforated rectangular breakwater H051D000 (see Table 8.7.4). The positioning of the V-shape breakwater was also at a similar location on deck (Figure 9.3.1): the rectangular breakwater coincides with the median of the V-shape breakwater. The confront angle or V angle was set at 120 degrees.

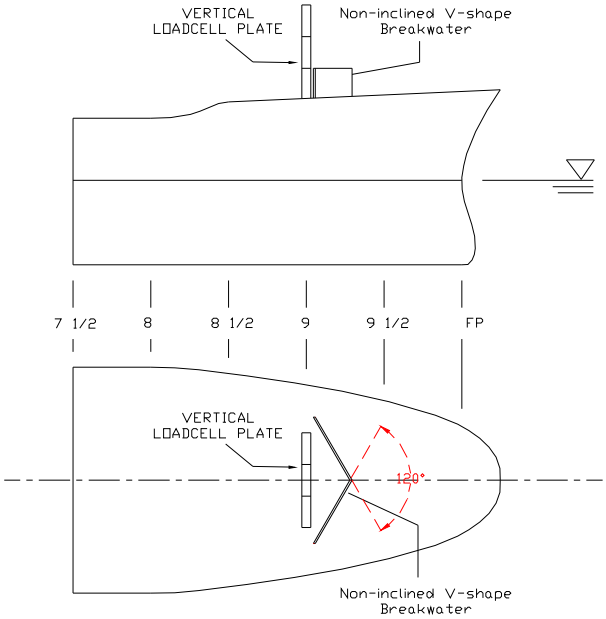

Figure 9.3.1 Setup of the non-inclined V-shape breakwater on the forecastle deck.

Comparison of the loads is as in Figures 9.3.2 to 9.3.7 and Figures 9.3.8 to 9.3.12 show the views of green water flow corresponding to the key points of the load curves. Figures 9.3.13 to 9.3.16 compare the vector fields of green water in front of the V-shaped breakwater with rectangular breakwater. As expected, on

reaching the rectangular breakwater, the water front transferred most of its kinetic energy onto the breakwater and became virtually stagnant (velocity was close to zero as in Figure 9.3.13). The stagnant water meant a pile-up of water in front of the breakwater. The V-shape breakwater, on the other hand, used the sloping of the wing plates to channel the water to the sides of the ship and this was well illustrated by the velocity vectors in Figure 9.3.15. Kinetic energy of the water front was also transferred onto the breakwater since the velocity near the breakwater reduced in magnitude (from 1.25m/s to approximately 0.8m/s). However, the amount of kinetic energy transferred must be less than the rectangular breakwater because the peak impact load on the V-shape breakwater was less as in Figure 9.3.6. Figures 9.3.14 and 9.3.16 show that there was high interaction between water and breakwaters at the centreline. The front water was repulsed off the breakwater and interacted with the follow-up water. This resulted in the follow-up water being pushed upwards at much greater velocity.

In general, Figures 9.3.5 to 9.3.7 show that both types of breakwater helped reduce green water loading on the load-cell box substantially (approximately around 65 percent). Rectangular breakwater sustained higher green water loading due to more water accumulating in front of it.

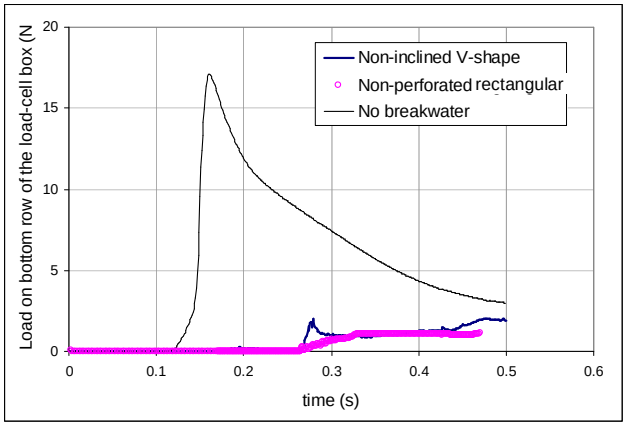

Figure 9.3.2 Comparison of loads on the bottom row of the load-cell box.

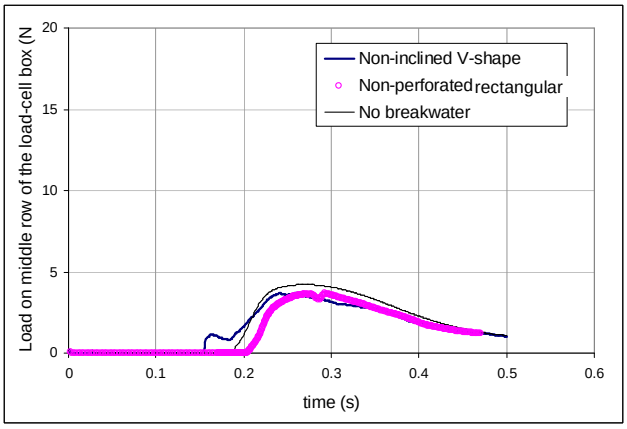

Figure 9.3.3 Comparison of loads on the middle row of the load-cell box.

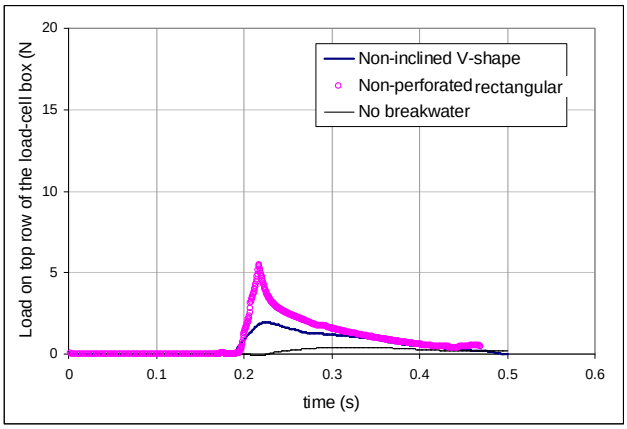

Figure 9.3.4 Comparison of loads on the top row of the load-cell box.

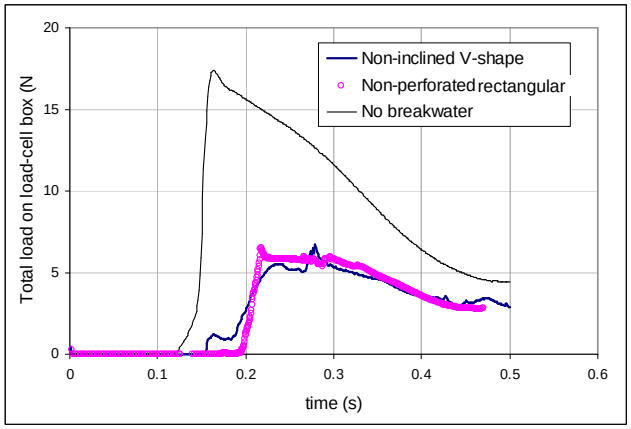

Figure 9.3.5 Comparison of total loads the load-cell box.

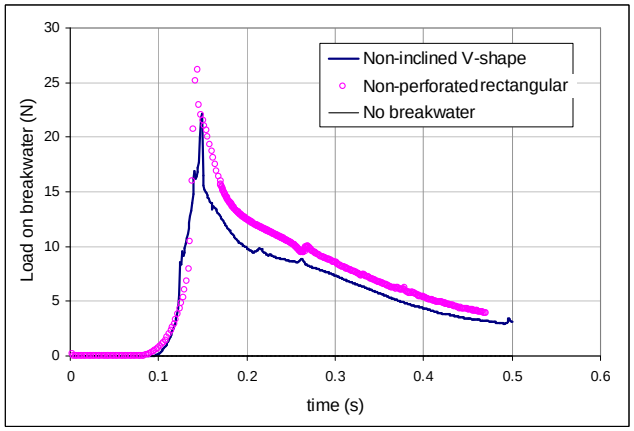

Figure 9.3.6 Comparison of loads on the breakwater in x-direction.

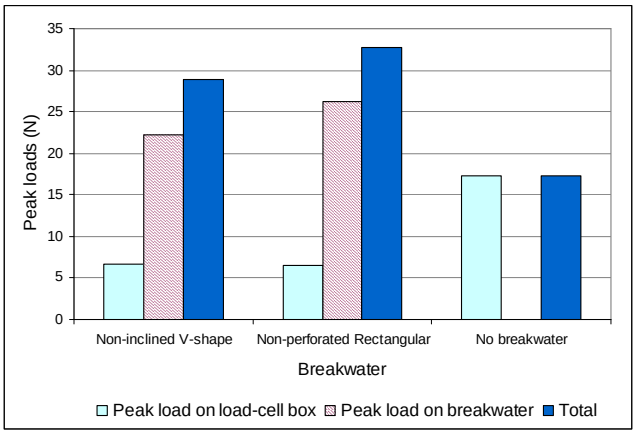

Figure 9.3.7 Comparison of peak loads on the load-cell box and the breakwater.

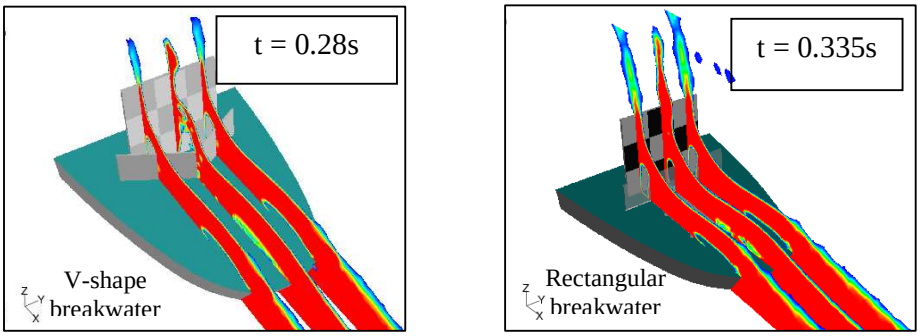

Figure 9.3.8 Sectional views of green water flows at the time of peak loads on the bottom row of the load-cell box.

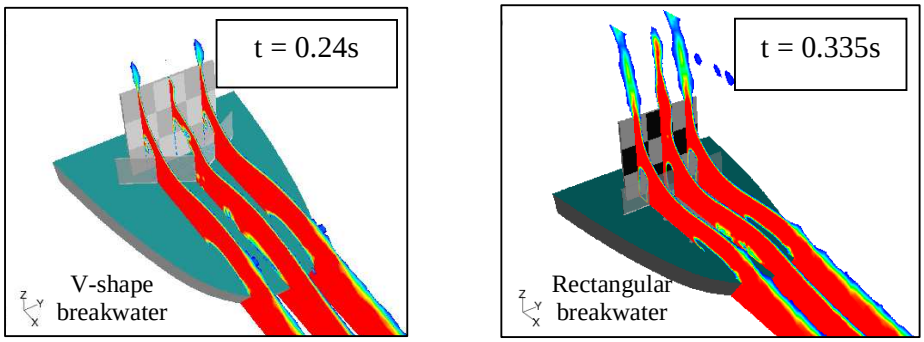

Figure 9.3.9 Sectional views of green water flows at the time of the peak loads on the middle row of the load-cell box.

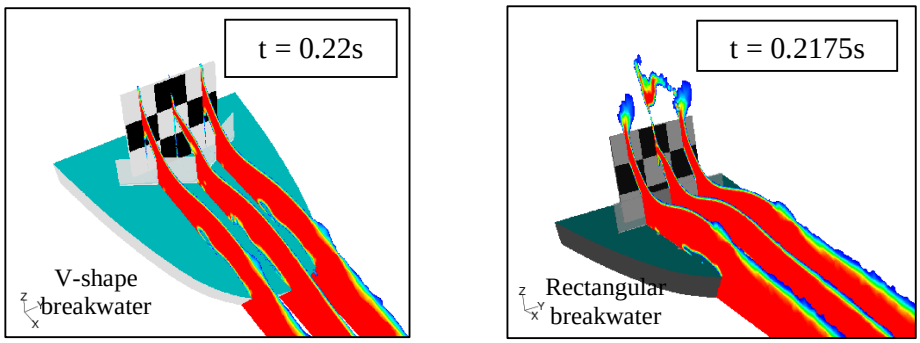

Figure 9.3.10 Sectional views of green water flows at the time of the peak loads on the top row of the load-cell box.

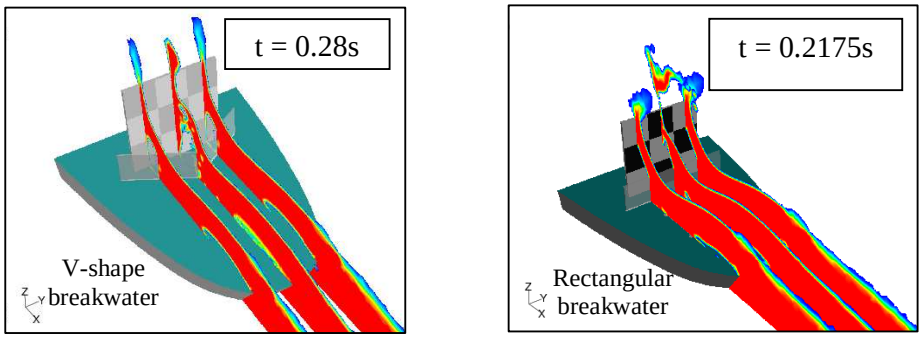

Figure 9.3.11 Sectional views of green water flows at the time of the peak loads on the load-cell box.

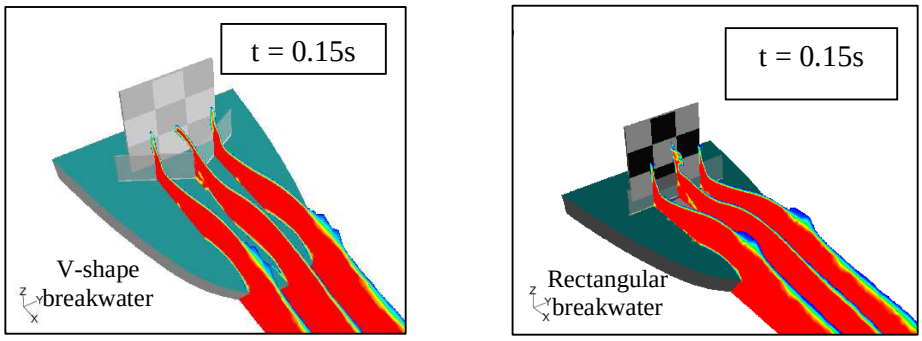

Figure 9.3.12 Sectional views of green water flows at the time of the peak loads on the breakwater.

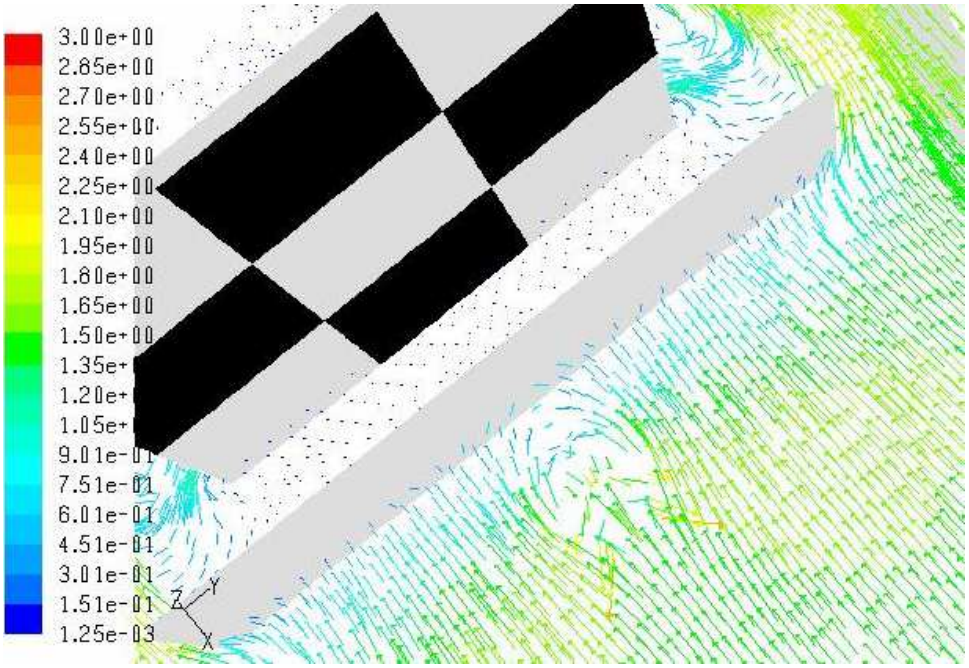

Figure 9.3.13 Horizontal view of water velocity vector field in front of breakwater at the time of maximum load on the rectangular breakwater (t = 0.15s).

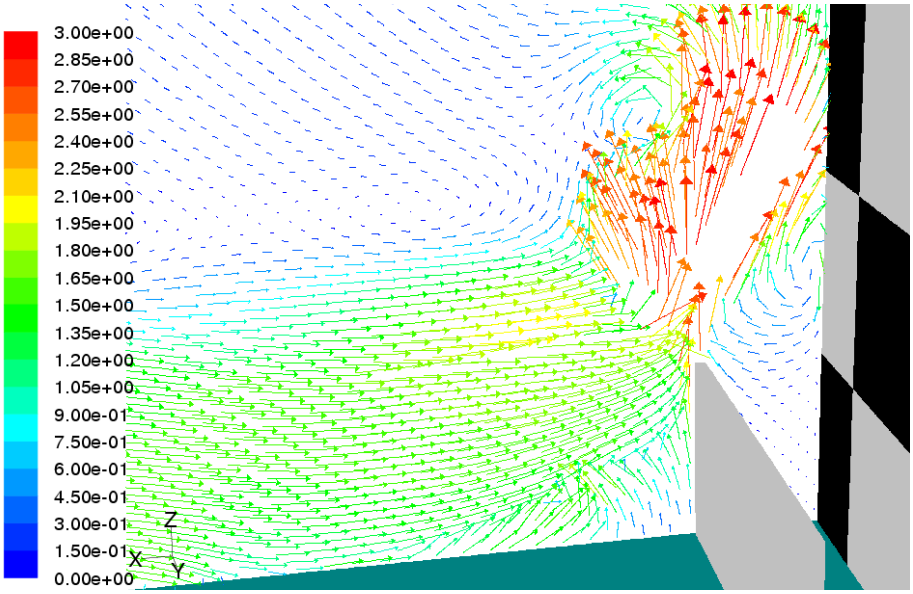

Figure 9.3.14 Vertical view of water velocity vector field in front of breakwater at the time of maximum load on the rectangular breakwater (t = 0.15s).

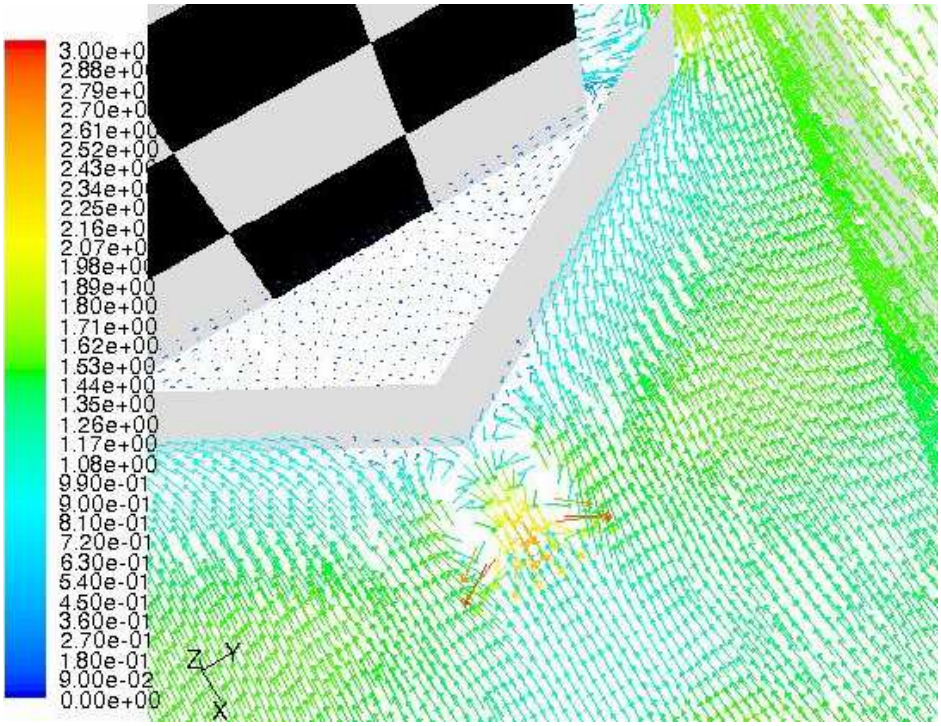

Figure 9.3.15 Horizontal view of the water velocity vector field in front of breakwater at the time of maximum load on the non-inclined V-shape breakwater (t = 0.15s).

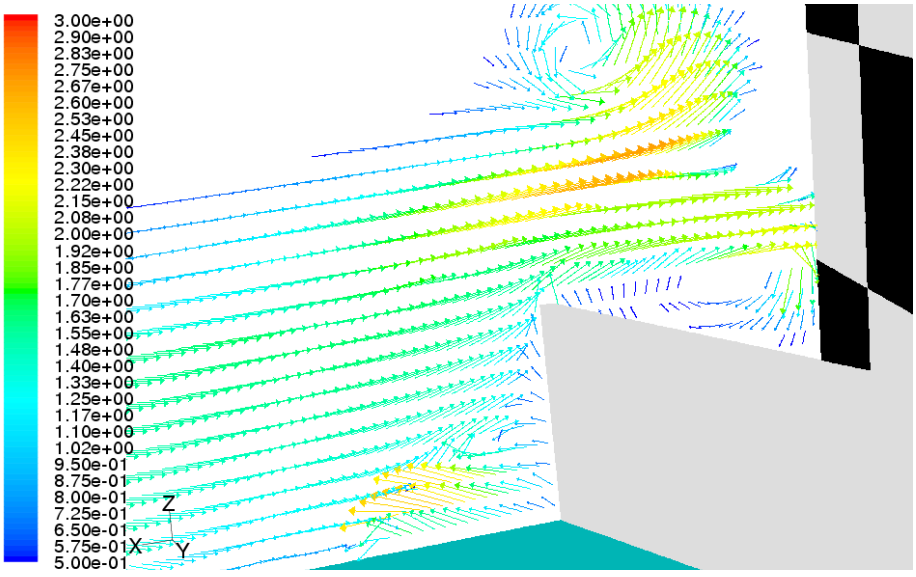

Figure 9.3.16 Vertical view of the water velocity vector field in front of breakwater at the time of maximum load on the non-inclined V-shape breakwater (t = 0.15s).

9.3.1.2 Inclined V-shape breakwater

In this example, the V-shape breakwater in Section 9.3.1.1 was inclined forward by 30 degrees to the vertical axis. The setup of this breakwater on the forecastle deck is as in Figure 9.3.17.

If comparing the loads in Figures 8.3.18 to 8.3.23 to those in Figures 8.3.2 to 8.3.7, it could be seen that the inclined V-shape breakwater also helped reduce green water on the load-cell box, similar to non-inclined V-shape breakwater. The behaviour of green water on deck might differ slightly between the two cases when there was more water overriding the breakwater in the latter. This resulted in more distinct double-peak characteristics in the load curves on the load-cell box (Figure 9.3.21 verse Figure 9.3.5). The reason behind this behaviour could be explained by comparing the water vector fields in front of the breakwaters (Figure 9.3.29 to Figure 9.3.15). Even though water was directed to the sides of the ships in both cases, there was more water piled up in front of the inclined V-shape breakwater. The water velocity in front of this breakwater was reduced down to around 0.5m/s as opposed to 0.8m/s for the non-inclined breakwater. The layer of low-velocity water could also be seen thicker in Figures 9.3.29 and 9.3.30. As a result, more of the follow-up water could overcome the breakwater at early stages and impacted the load-cell box. This created a more distinct first peak impact load on the load curve.

Being less effective in directing the water away also meant that the inclined V-shape breakwater absorbed more loading from the incident water flow. This was evident by comparing Figure 9.3.22 to Figure 9.3.6. In fact, the peak impact load on the inclined V-shape breakwater was even higher than that on rectangular breakwater.

Figures 9.3.24 to 9.3.26 show the water behaviour at the times the impact loads on bottom row, middle row and top row reached maxima, respectively. Figures

9.3.27 and 9.3.28 show the water behaviour at the time when the impact loads on the load-cell box as a whole and on the breakwater were maximum.

Overall, the inclination of the V-shape breakwater did not bring in any real benefits in terms of loading.

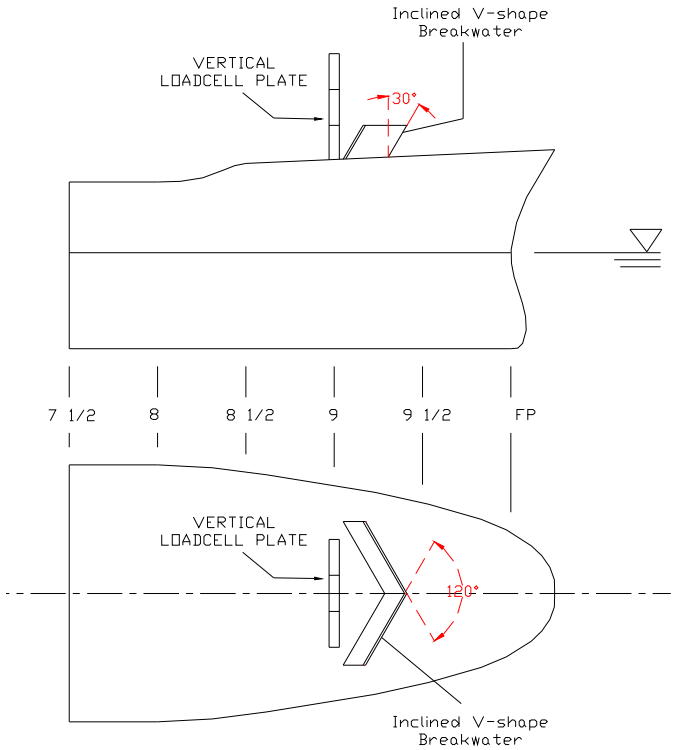

Figure 9.3.17 Setup of inclined V-shape breakwater on the forecastle deck.

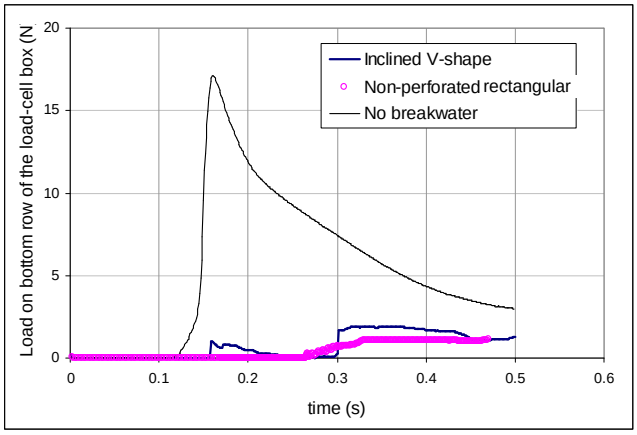

Figure 9.3.18 Comparison of loads on the bottom row of the load-cell box.

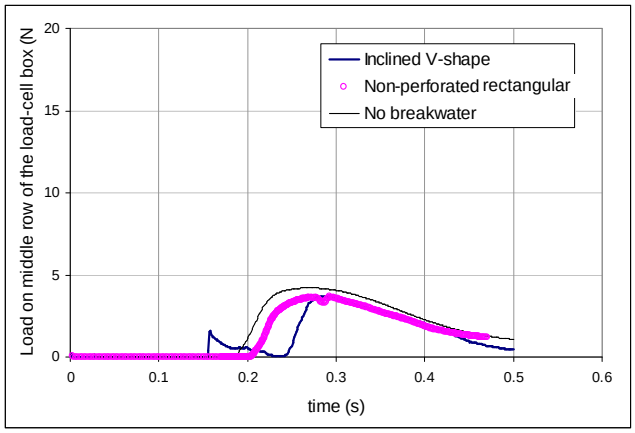

Figure 9.3.19 Comparison of loads on the middle row of the load-cell box.

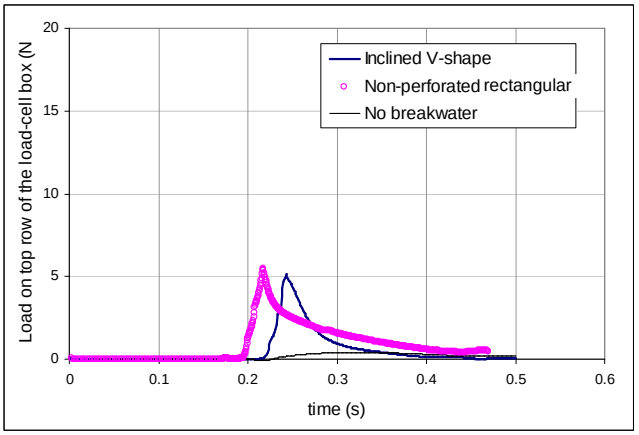

Figure 9.3.20 Comparison of loads on the top row of the load-cell box.

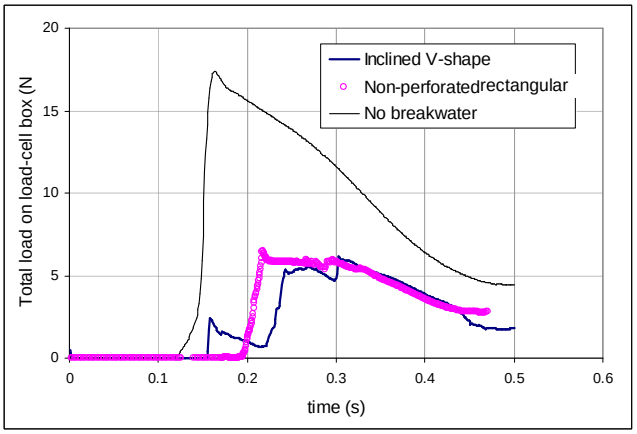

Figure 9.3.21 Comparison of total loads on the load-cell box.

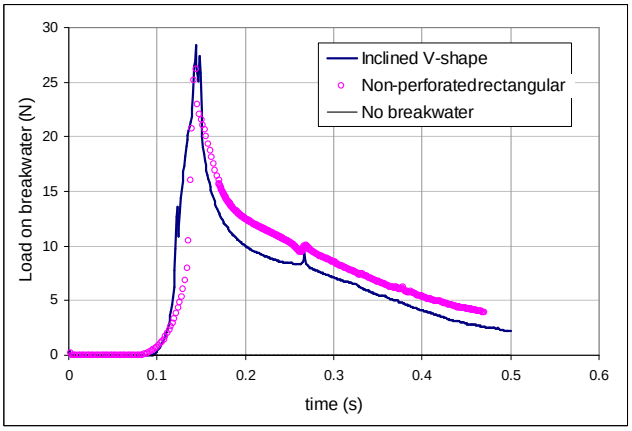

Figure 9.3.22 Comparison of loads on the breakwater.

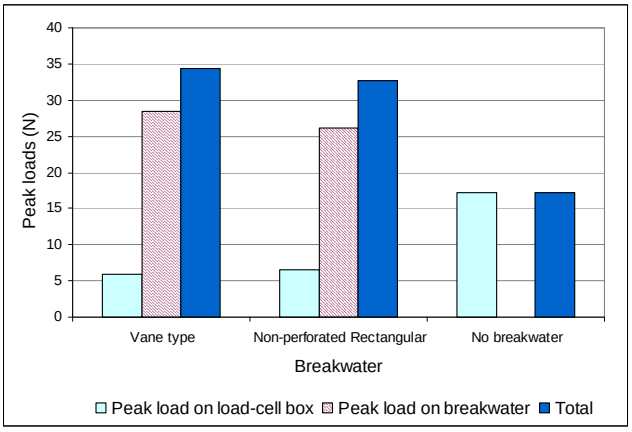

Figure 9.3.23 Comparison of peak loads on the load-cell box and the breakwater.

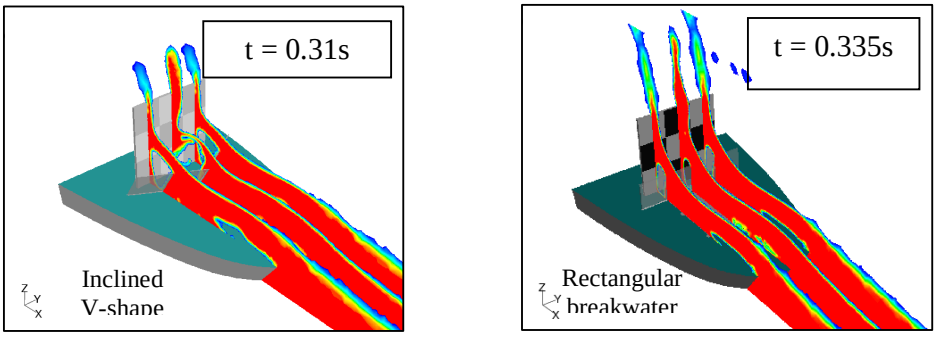

Figure 9.3.24 Sectional views of green water flows on deck at the time of peak loads on the bottom row of the load-cell box.

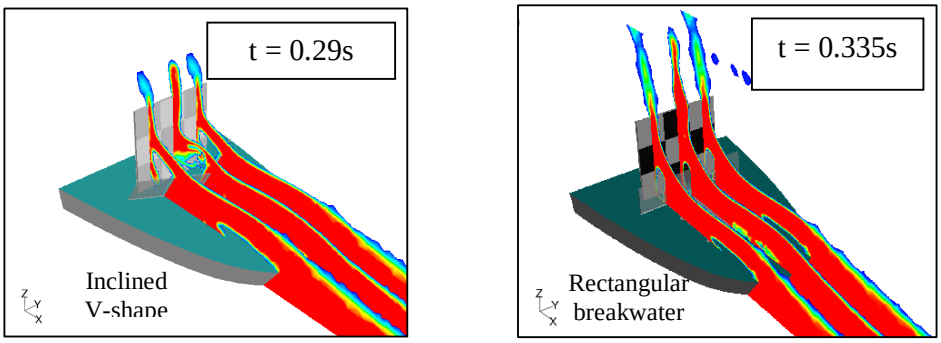

Figure 9.3.25 Sectional views of green water flows on deck at the time of peak loads on the middle row of the load-cell box.

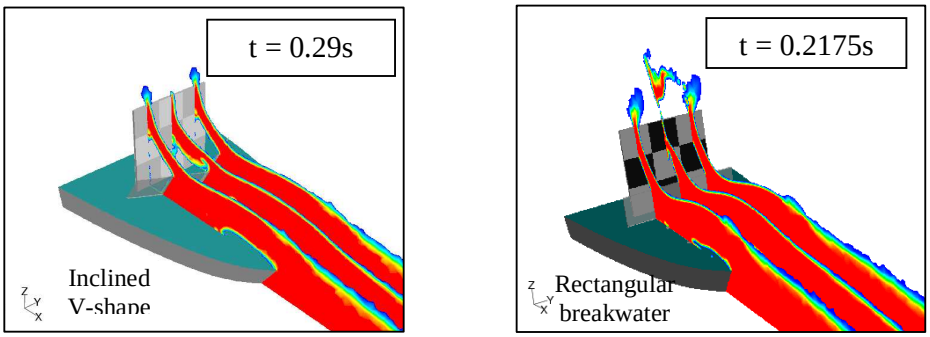

Figure 9.3.26 Sectional views of green water flows on deck at the time of peak loads on the top row of the load-cell box.

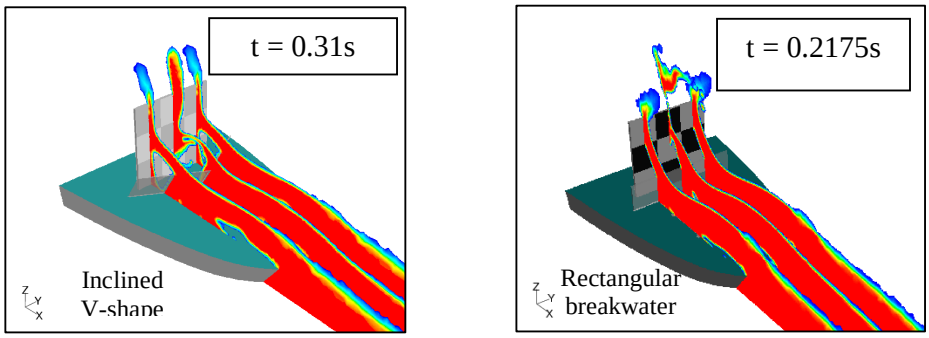

Figure 9.3.27 Sectional views of green water flows on deck at the time of peak loads on the load-cell box.

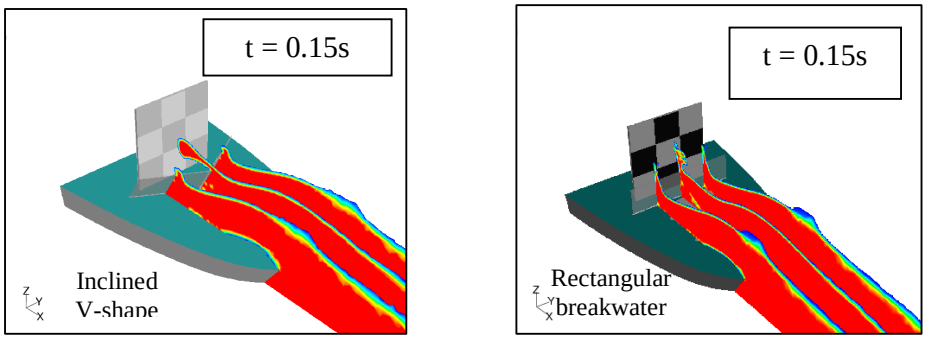

Figure 9.3.28 Sectional views of green water flows on deck at the time of peak loads on the breakwater.

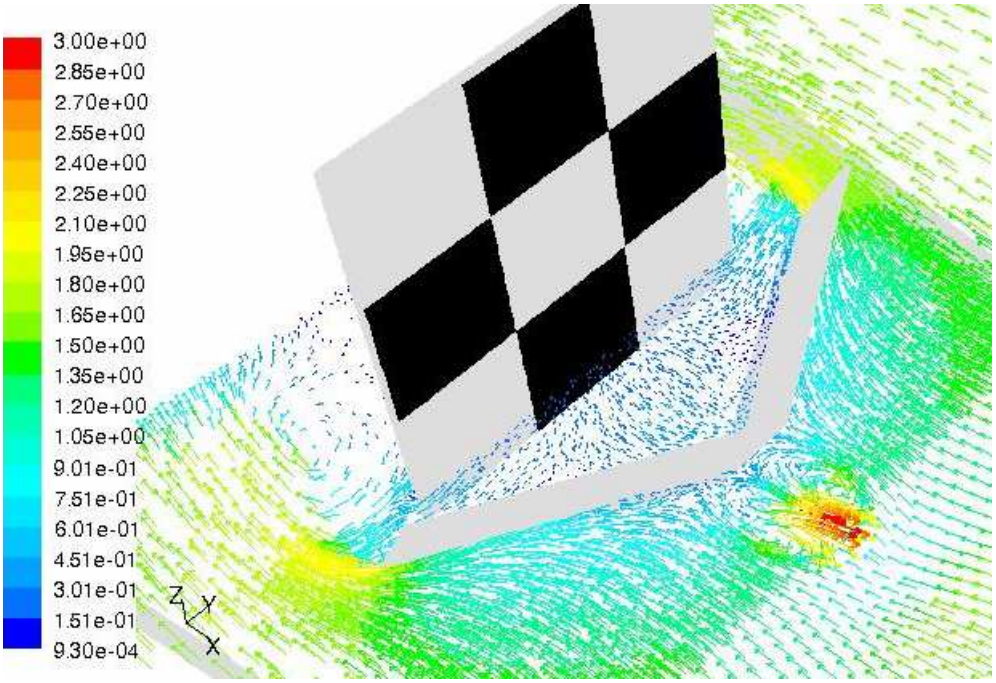

Figure 9.3.29 Horizontal view of water velocity vector field in front of the breakwater at the time of maximum load on the inclined V-shape breakwater (t = 0.15s).

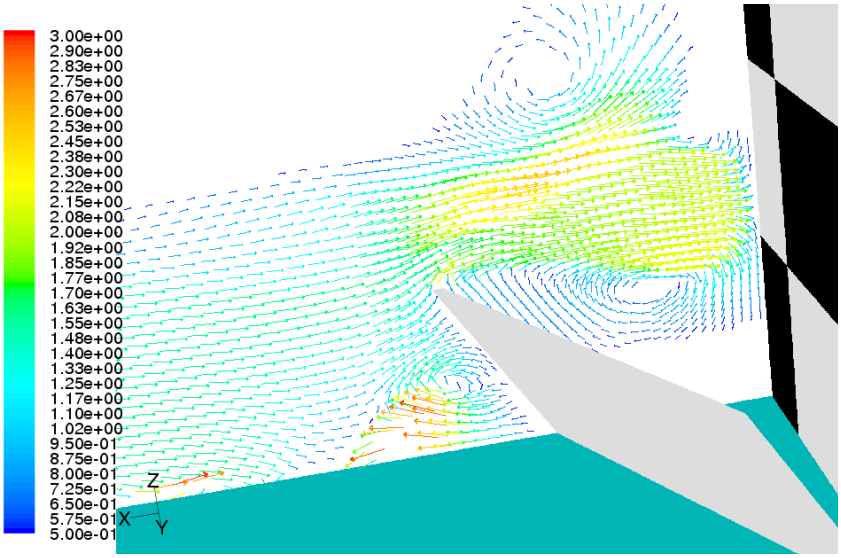

Figure 9.3.30 Vertical view of water velocity vector field in front of the breakwater at the time of maximum load on the inclined V-shape breakwater (t = 0.15s).

9.3.1.3 Vane-type breakwater

Figure 9.3.31 shows the design of the vane-type breakwater and its location on the deck. For comparison purposes, the median of this breakwater was coincident with the rectangular breakwater. The width of individual vane was selected such that its projected length on y-axis was equal to half the width of a load cell on the load-cell box. The angle the vanes were aligned was 30 degrees to the y-axis making the confront angle equal to 120 degrees (same as V angle of the V-shape breakwater). At model scale, the width of each vane was 29.33mm. This was equivalent to approximately 2m at full scale. The height of the breakwater was the same as the height of the rectangular breakwater H051D000, which was 51mm at model scale or 3.6m at full scale. Figures 9.3.38 and 9.3.43 show that the water was channelled through the passages between the vanes and to the sides of the ships. The bottlenecks of these passages meant that each passage was acting similar to a nozzle through which the water was accelerated. When coming out of these passages, the water velocity was higher and this resulted in higher loads at

first impact with the load-cell box (Figure 9.3.32 as opposed to Figures 9.3.2 and 9.3.18). However, in front of the first half of each vane (closer to the centreline), the water slowed down due to the drag resistance from the vane. The build up of water, therefore, took place leading to overriding of water as in Figures 9.3.38 to 9.42. However, water pile-up was less than other cases since the load on the breakwater caused by the overriding water was much lower (Figure 9.3.36 as opposed to Figures 9.3.6 and 9.3.22).

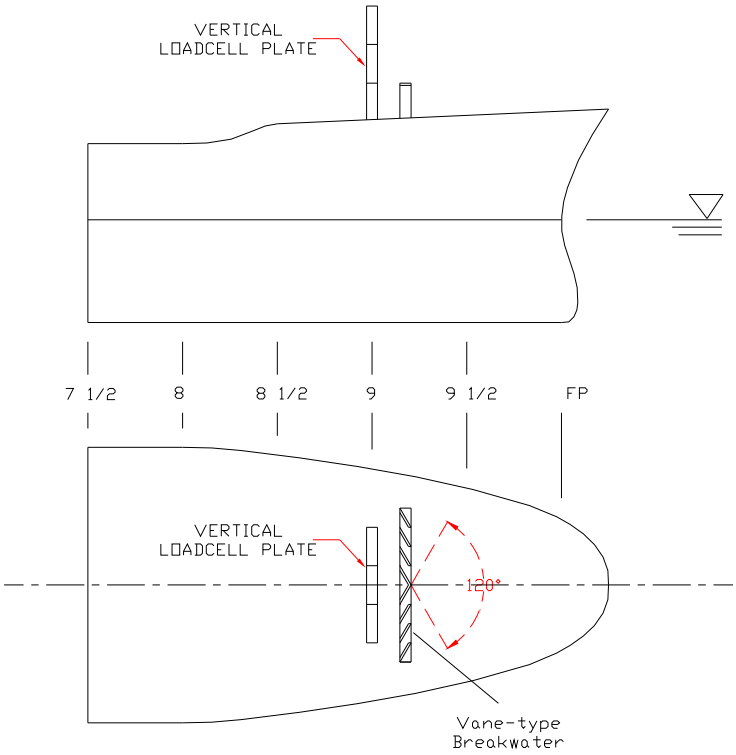

Figure 9.3.31 Setup of inclined vane-type breakwater on the forecastle deck.

By creating a passage for water to go through, the vane-type breakwater lessened the amount of water pile-up and the load it had to sustain. However, in doing so, water flows coming out of the passages reached the load-cell box and this resulted in higher loading on the protected structures. The impacts by multiple sub-flows coming off the passages also led to more dynamic behaviour of the loads on the load cells (Figures 9.3.32 and 9.3.35).

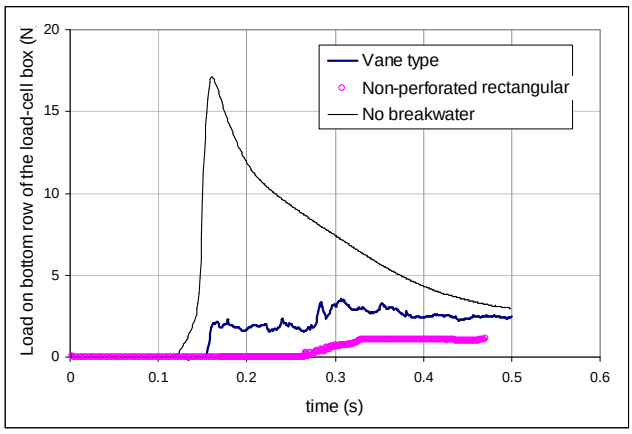

Figure 9.3.32 Comparison of loads on the bottom row of the load-cell box.

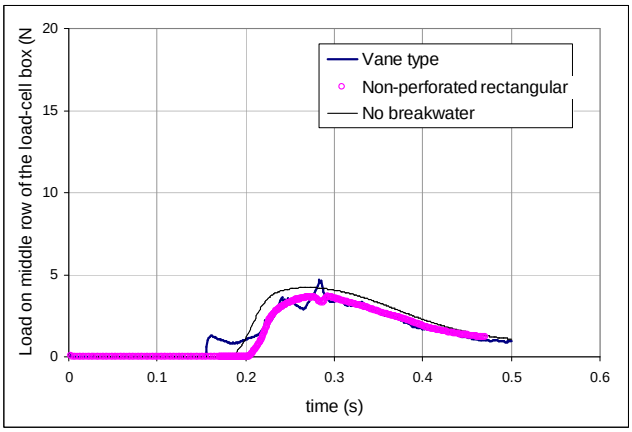

Figure 9.3.33 Comparison of loads on the middle row of the load-cell box.

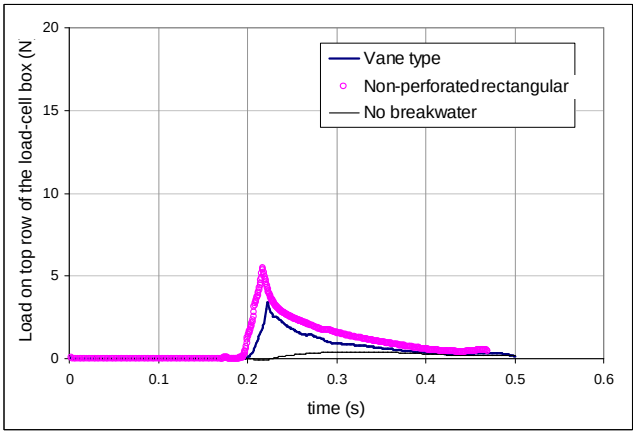

Figure 9.3.34 Comparison of loads on the top row of the load-cell box.

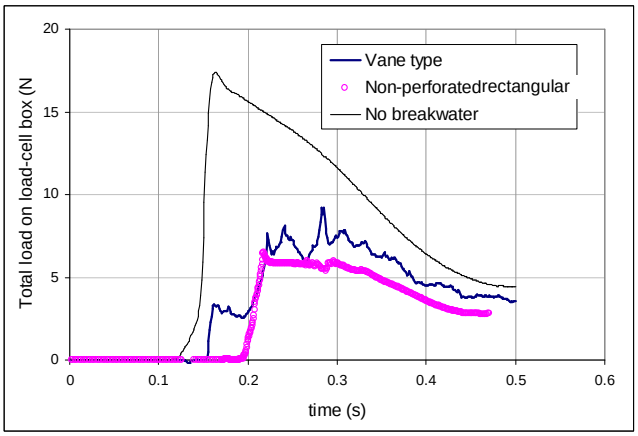

Figure 9.3.35 Comparison of loads on the load-cell box.

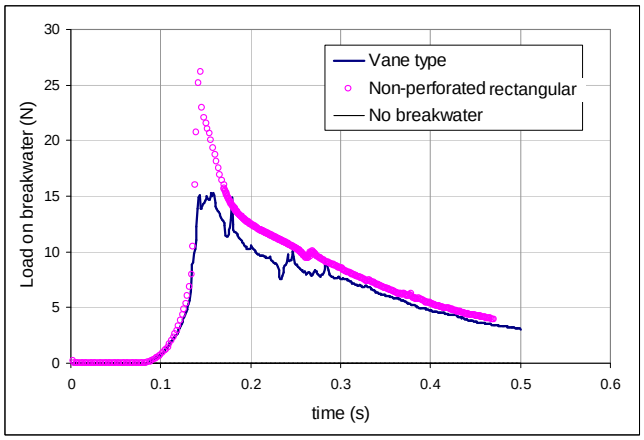

Figure 9.3.36 Comparison of loads on the breakwater.

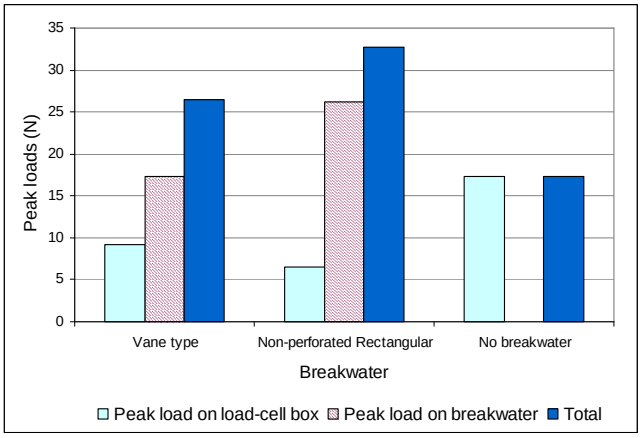

Figure 9.3.37 Comparison of peak loads on the load-cell box and the breakwater.

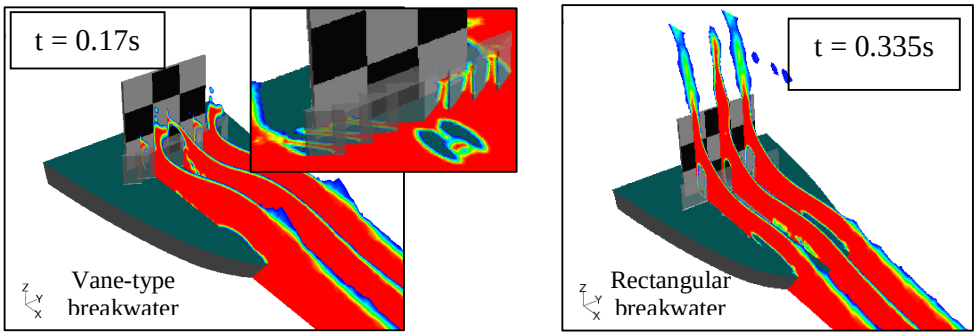

Figure 9.3.38 Sectional views of green water flows on deck at the time of peak loads on the bottom row of the load-cell box.

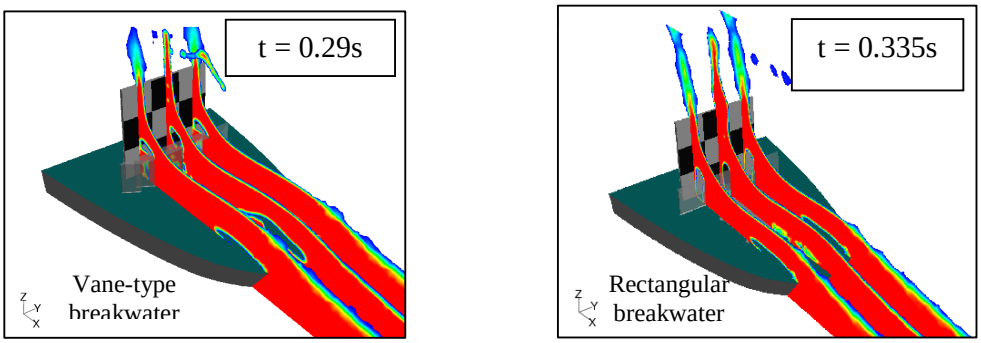

Figure 9.3.39 Sectional views of green water flows on deck at the time of peak loads on the middle row of the load-cell box.

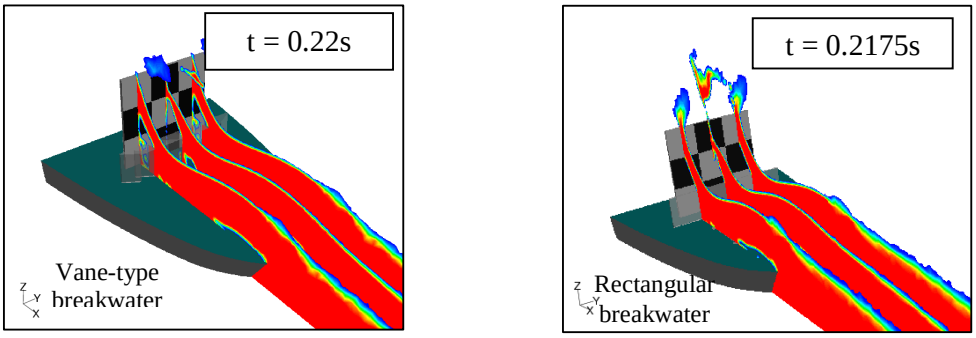

Figure 9.3.40 Sectional views of green water flows on deck at the time of peak loads on the top row of the load-cell box.

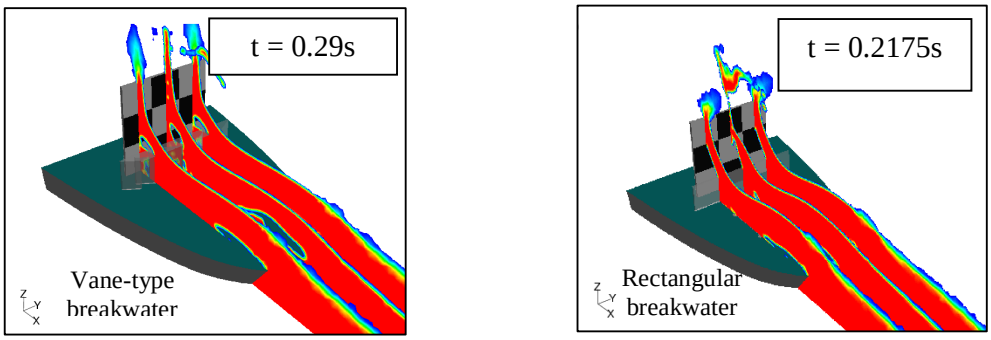

Figure 9.3.41 Sectional views of green water flows on deck at the time of peak loads on the load-cell box.

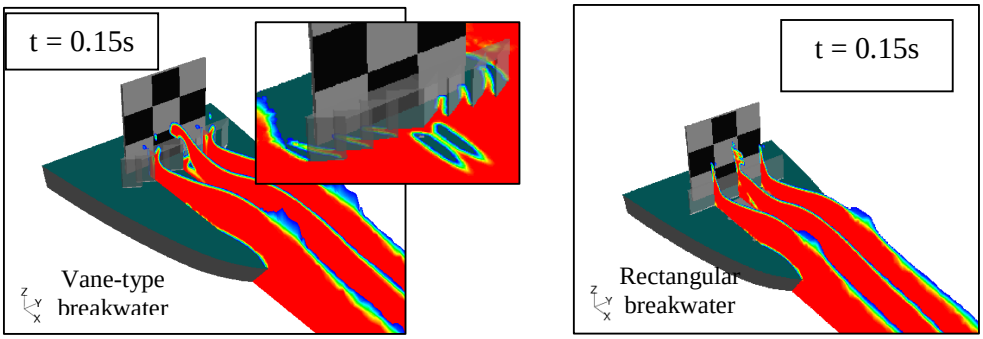

Figure 9.3.42 Sectional views of green water flows on deck at the time of peak loads on the breakwater.

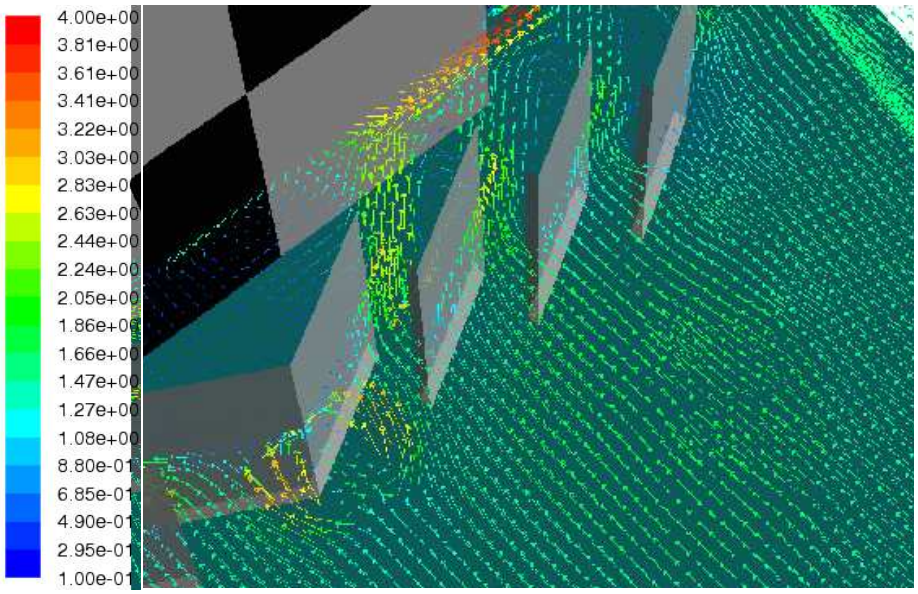

Figure 9.3.43 Horizontal view of water velocity vector field in front of the breakwater at the time of maximum load on the vane-type breakwater (t = 0.15s).

9.3.2 Investigation into the performance of novel bow design against green water: Whale-back forecastle deck

Following the widespread application of cargo-protecting breakwaters on ships in the 1980's, the early 1990's saw new designs of container ships produced with shelter whaleback cover of the forecastle. To add shelter over the forecastle head, thereby protecting both the forward deck machinery and shedding water when the ship is in a short swell and heavy sea condition, does increase confidence when achieving the tight time schedules of the feeder ship. The mariner is, however, likely to have some misgivings relating to the forecastle whaleback shelters. Questions may arise regarding entrapment of crew under the shelter in heavy sea conditions. The aft sloping shape of such shelters may accelerate water flow against container stows extending above the after edge of the shelter and cause damage.

Answers to such uncertainties associated with a novel design like the whale-back can be obtained by carrying the parametric studies using the established simulation model. Comparison of the results with other types of structure can also be done so that a comprehensive picture of the new design may be understood and its practicality evaluated.

Figure 9.3.44 shows a simple design of a whale-back forecastle deck which was made up of three flat platings. For comparison purposes, the height and the width of the central shelter plating (corresponding to triangle BCS) were set equal to the height and width of the rectangular breakwater H051D000. The distance between the edge of the shelter and the load-cell box was also equal to the distance between the rectangular breakwater to the load-cell box. The comparison of green water loads is as in Figures 9.3.45 to 9.3.50. The load curves in Figure 9.3.48 show that the water reached the load-cell box even earlier than in the case of no breakwater or equivalent structure. This strongly indicated that there was an acceleration of green water flow up the sloping of the whale-back. Figure 9.3.56

shows that there was very little disturbance to the water flow running up the whale-back deck. The velocity magnitude actually increased as in Figure 9.3.57.

The resistance to the incident water was much smaller than in other cases of breakwater due to the light sloping of the whale-back (Figure 9.3.49). The impact load on the load-cell box was, therefore, much higher. It was indeed not much smaller than in the case of no breakwater (Figure 9.3.48). The slope of the shelter as in Figure 9.3.44 meant that green water flow was directed straight to the middle row of the load-cell box (Figures 9.3.52 and 9.3.53). Therefore, the impact load on this row was considerably increased compared to other cases (Figure 9.3.46 as opposed to Figures 9.3.19 and 9.3.33). The substantial downfall of this water after the impact also caused considerable damage to the lower level structures as in Figure 9.3.45 (compared with Figures 9.3.18 and 9.3.32). It could also lead to the entrapment of crew inside the shelter.

Overall, with the green water conditions considered in this example, the whale-back deck has shown little advantage over other choices of breakwaters.

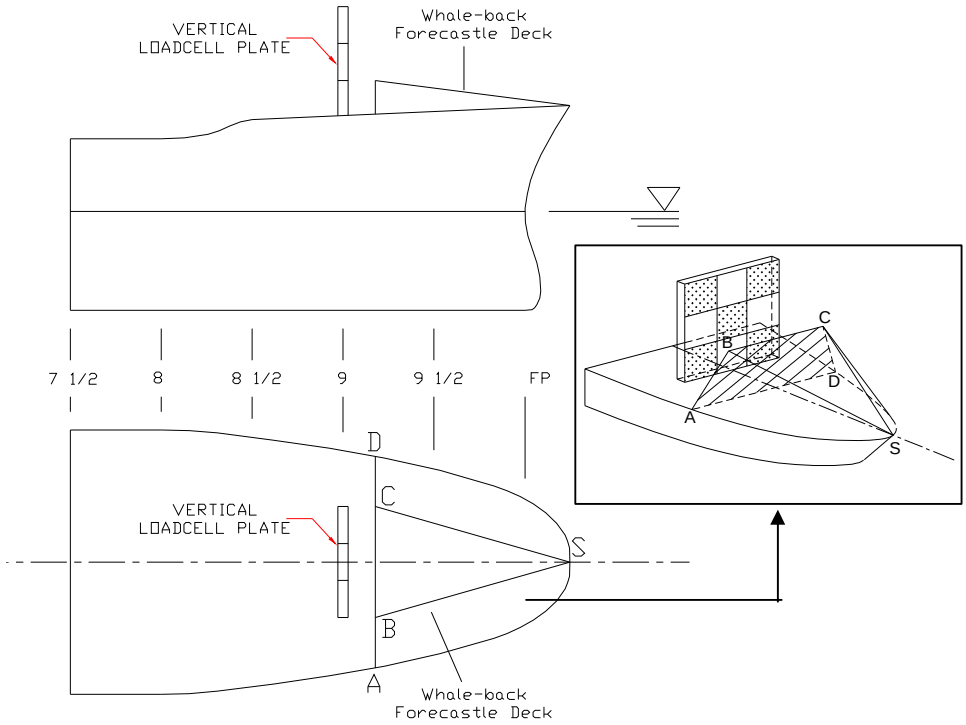

Figure 9.3.44 Setup of whale-back forecastle deck.

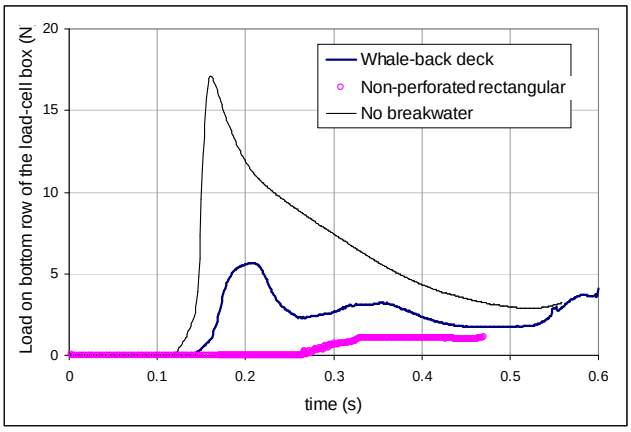

Figure 9.3.45 Comparison of loads on the bottom row of the load-cell box.

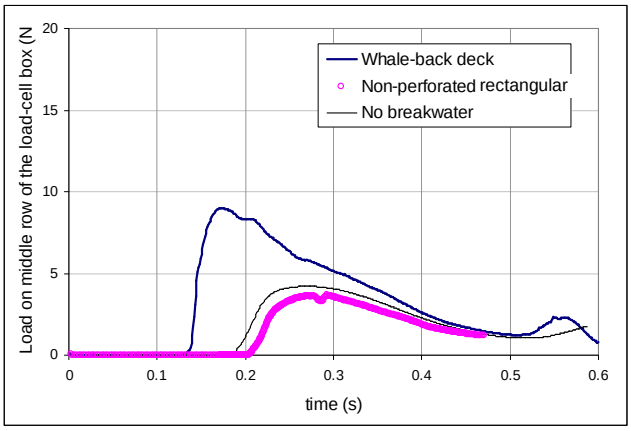

Figure 9.3.46 Comparison of loads on the middle row of the load-cell box.

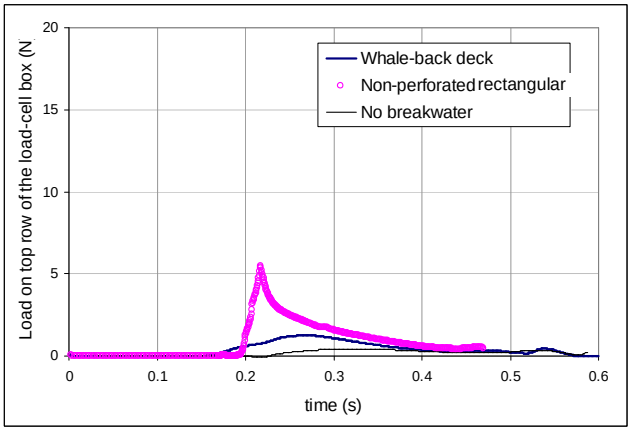

Figure 9.3.47 Comparison of loads on the top row of the load-cell box.

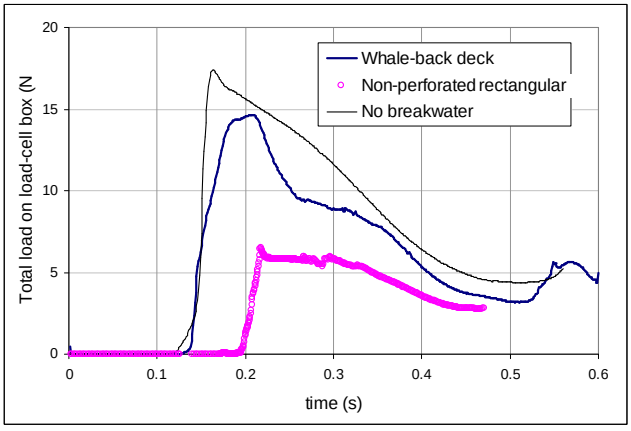

Figure 9.3.48 Comparison of total loads on the load-cell box.

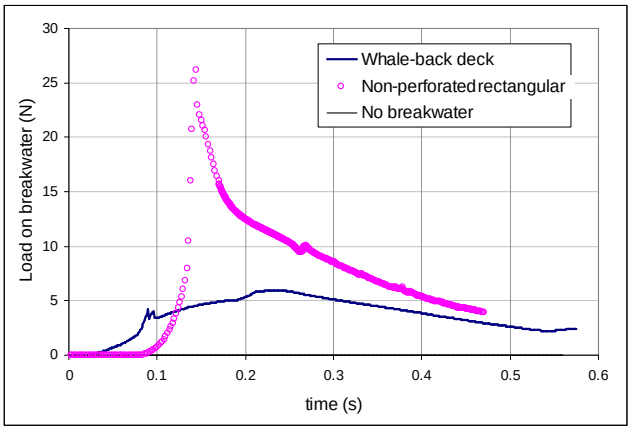

Figure 9.3.49 Comparison of resistance load on the whale back deck.

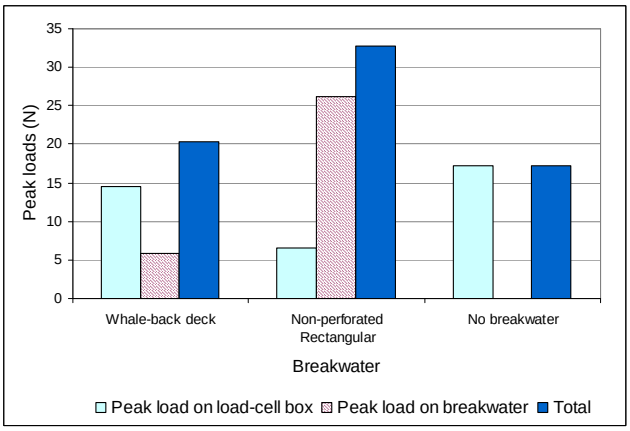

Figure 9.3.50 Comparison of peak longitudinal loads on the load-cell box and the whale back deck.

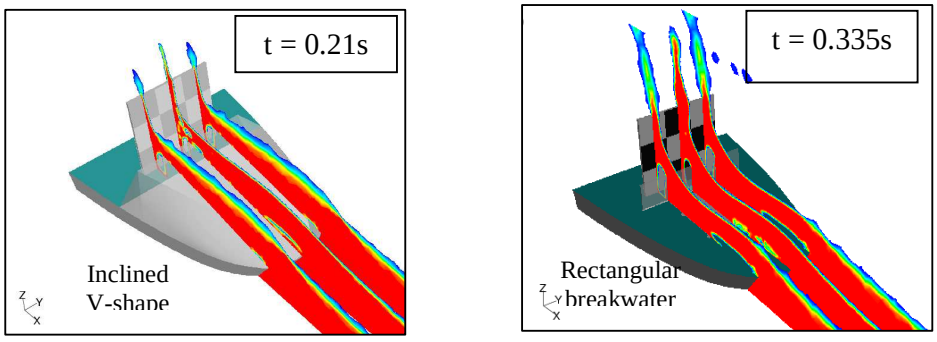

Figure 9.3.51 Sectional views of green water flows on deck at the time of peak loads on the bottom row of the load-cell box.

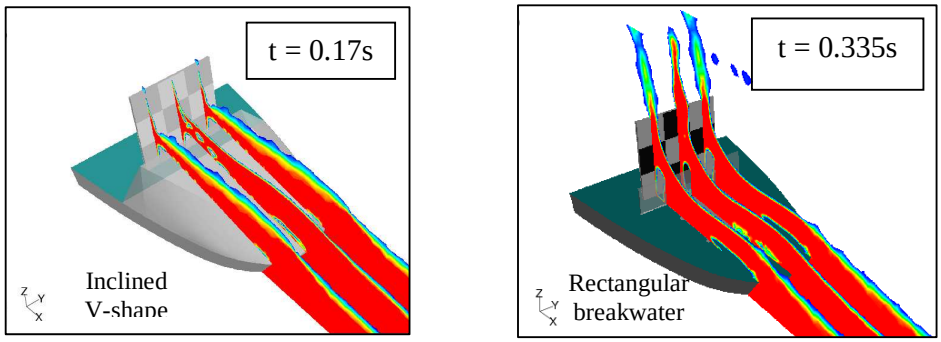

Figure 9.3.52 Sectional views of green water flows on deck at the time of peak loads on the middle row of the load-cell box.

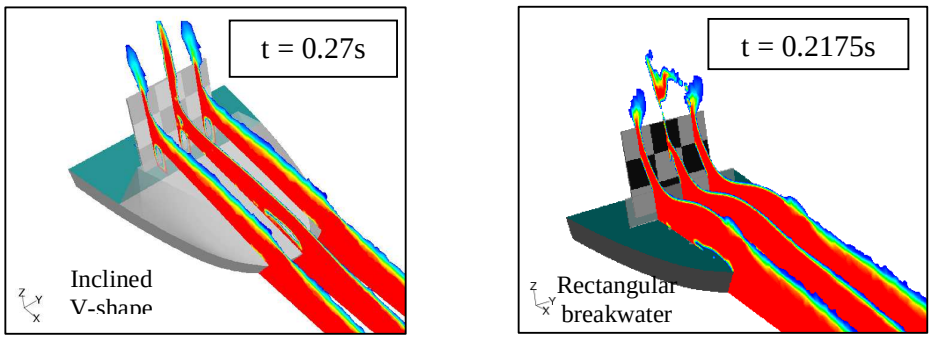

Figure 9.3.53 Sectional views of green water flows on deck at the time of peak loads on the top row of the load-cell box.

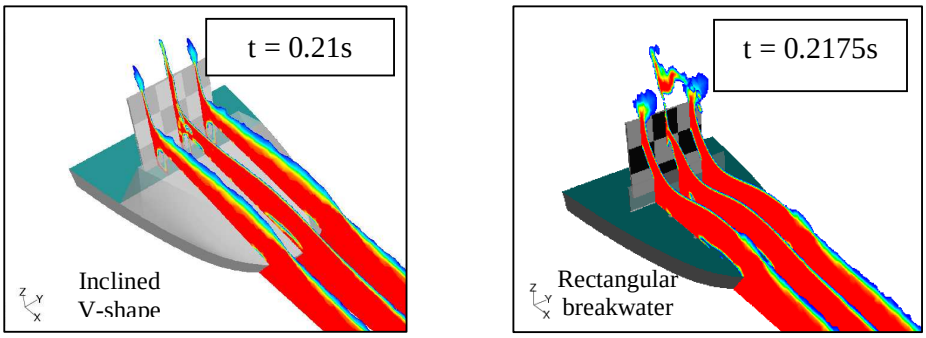

Figure 9.3.54 Sectional views of green water flows on deck at the time of peak loads on the load-cell box.

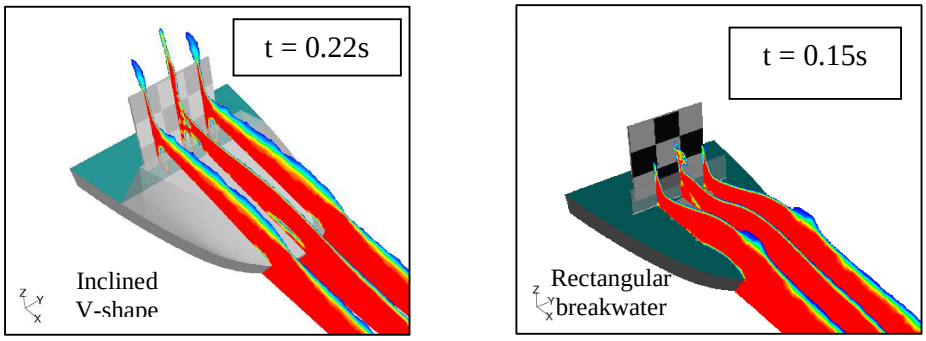

Figure 9.3.55 Sectional views of green water flows on deck at the time of peak loads on the breakwater in x-axis.

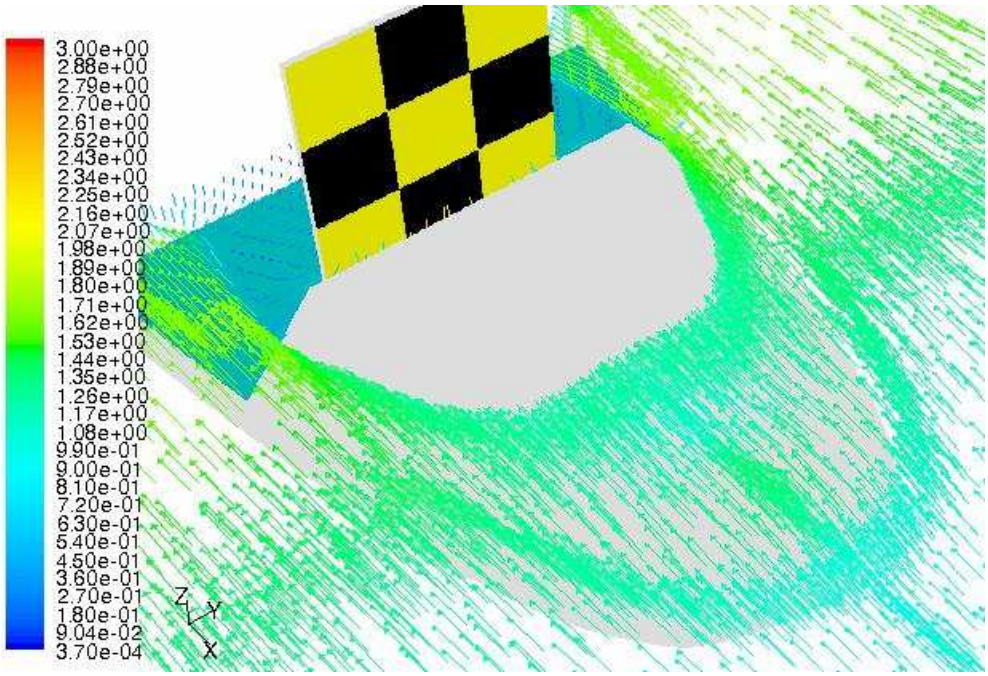

Figure 9.3.56 Water velocity vector field around the whaleback forecastle deck at t = 0.15s.

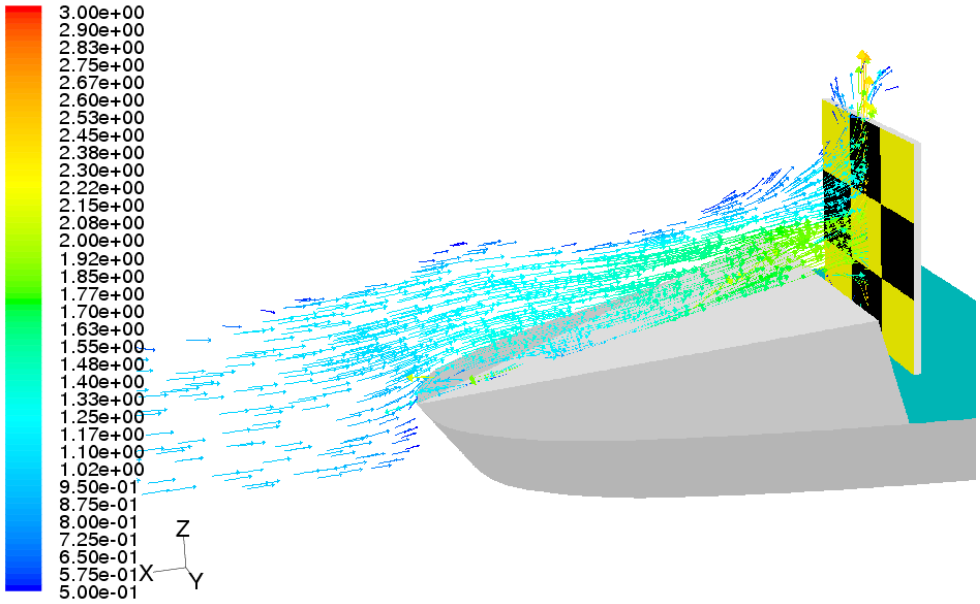

Figure 9.3.57 Vertical view of water velocity vector field along whaleback forecastle deck at t = 0.15s.

9.3.3 Applications in coastal engineering: Coastal Breakwaters

By the time breakwaters were adopted onto ships in the later half of the 20th century, they had already been employed in coastal engineering since as far as the ancient ages of Egypt and Mycenae (Tanimoto and Goda, 1991). From building bays for ships to shelter and seawalls to protecting the land using rocks and other rubbles, construction of coastal breakwaters have evolved substantially through time. Nowadays, they have been taken to another level with cutting-edge technologies to effectively hold off the challenges coming from the open seas. Following the 2004 tsunami disaster resulted from the earthquake off the west coast of Sumatra, Indonesia in which surge of height of as much as 30m was recorded sweeping shoreward, designs of coastal breakwaters are beginning to be revised so that they can cope with extreme conditions of similar scale. Along side with experimental work, simulation of such events can gather valuable data that undoubtedly help coastal engineers to make efficient design of breakwaters. From this point of view, the established simulation model can be adopted to obtain a

preliminary picture of how the water front may behave and the possible damages it may cause. For illustration, a simple 2D model of a sea wall was constructed and simulated using CFD. The general setup is as in Figure 9.3.58 with the initial height of the tsunami assumed to be 20m at 100m away from the seawall. The seawall itself was 16m above the calm sea level and it had square perforations of 2m height and 2m depth. In open sea, the tsunami can travel at a speed of around 500km/h. However, when getting close to shore, it breaks and slows down. The initial speed of the surge simulated was, in this example, assumed to be 180km/h for demonstration purposes. Figure 9.3.59 shows the visualisation of the development of water flow as the water surge approached the seawall and the impact took place. Due to the velocity difference along the height of the water surge, the water surge broke on its way to the seawall.

Figure 9.3.60 shows the vector field in front of the seawall at the time the water started to overcome the seawall. It can be clearly seen that on impacting the seawall, the water repulsed anti-clockwise towards the seabed and formed a large vortex (see also Figure 9.3.61). Follow-up water was then diverted by this vortex and started to overcome the seawall. Due to its high velocity, and sharp take-off angle at the beginning, the water formed a strong water jet which could reach a substantial height above the sea wall as seen in Figure 9.3.59. After the impact, water that overcame the seawall landed back on the back slope of the seawall and the water flow continued to travel at very high velocity. Figure 9.3.62 shows the vector field around this area and it can be seen that water flowed down the back of the seawall at a velocity of approximately 40m/s or 144km/h. Further simulation could be implemented to see the destructive characteristics of the water flow that overcame the seawall and continued to travel deep in land. Due to the scope of this research, the simulation herein was only for demonstration purpose to illustrate the possible application of the simulation model in the area of coastal engineering.

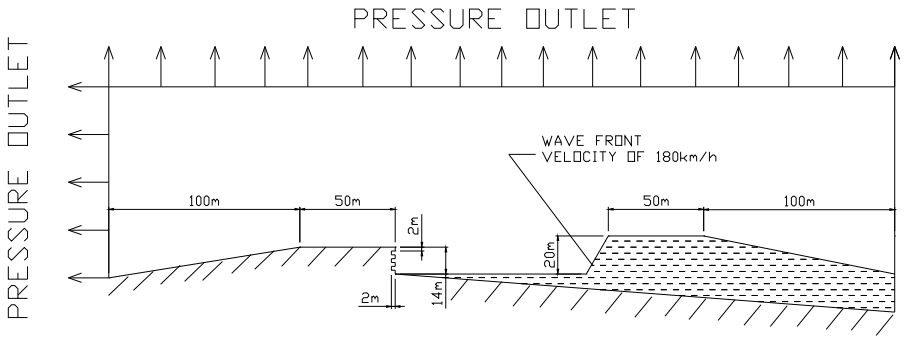

Figure 9.3.58 Setup of seawall for CFD analysis.

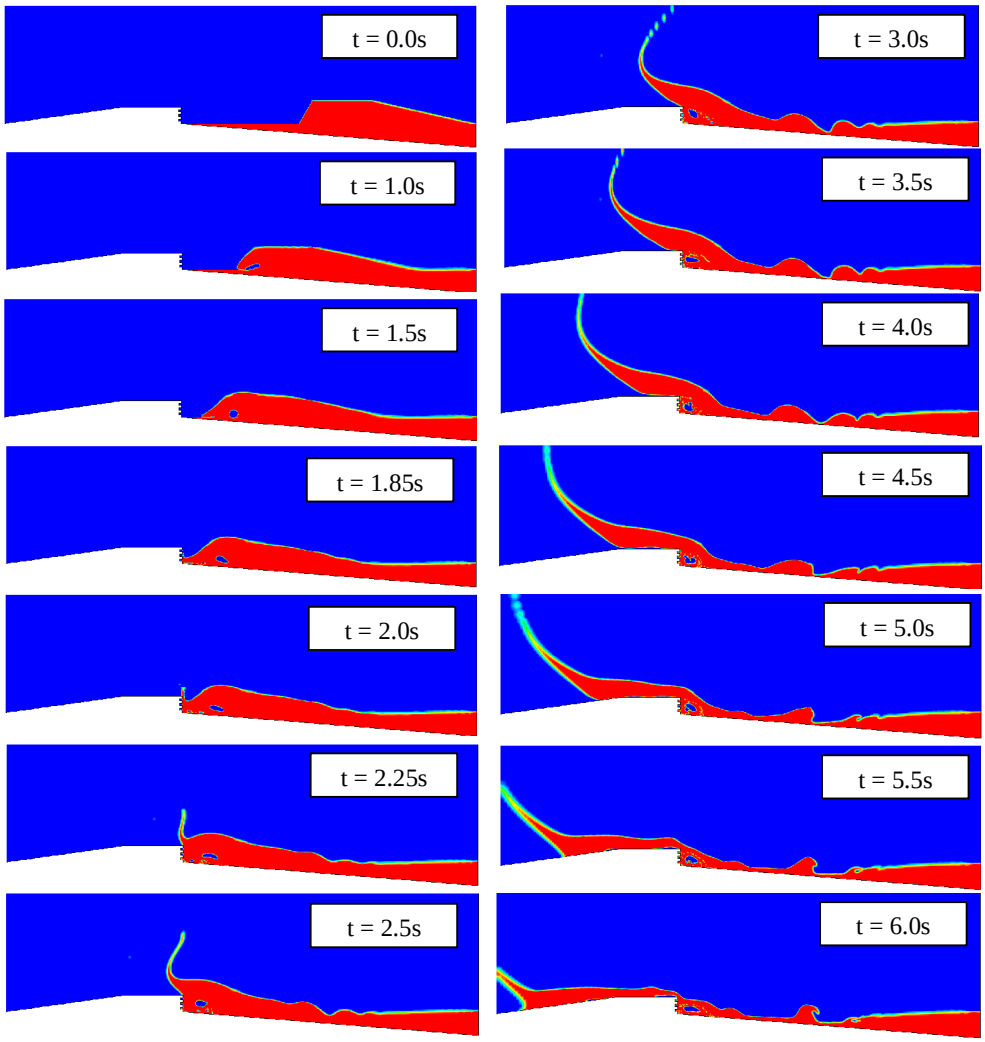

Figure 9.3.59 Visualisation of interaction between water surge and a seawall.

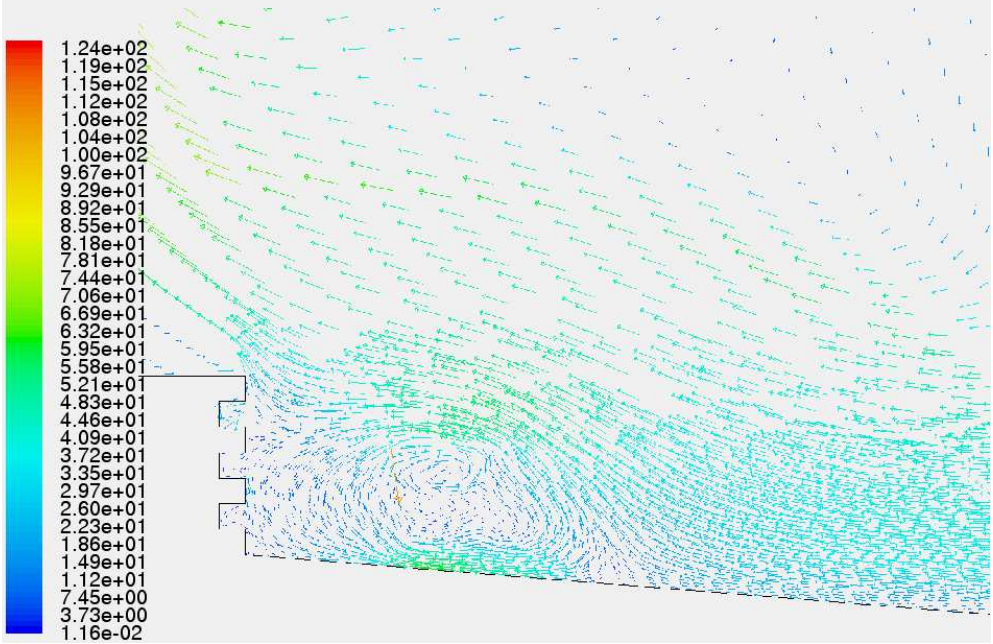

Figure 9.3.60 Vector field in front of the seawall at t = 2.5s.

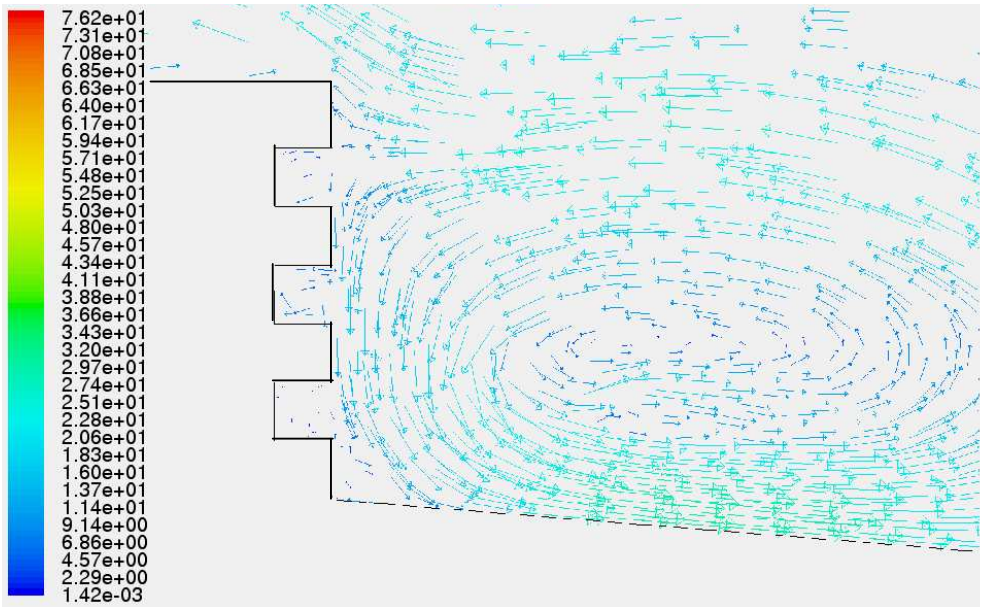

Figure 9.3.61 Vector field in front of the seawall at t = 6.0s.

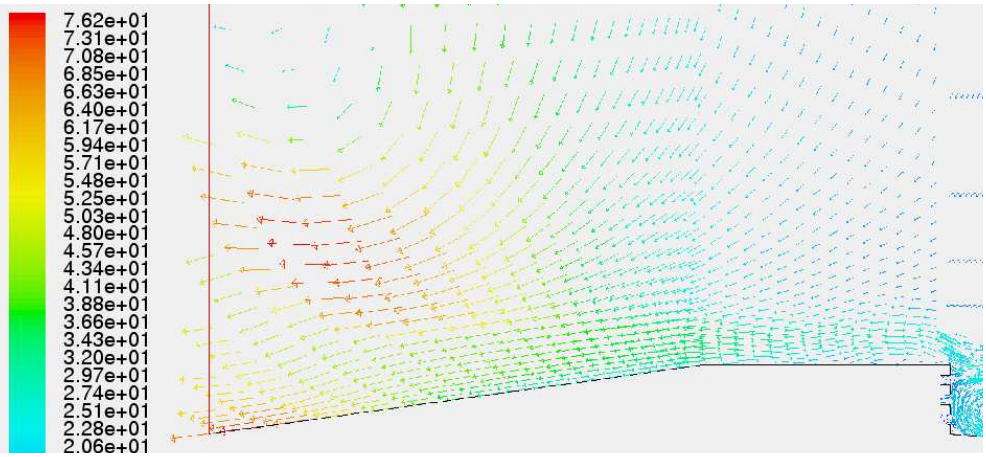

Figure 9.3.62 Vector field at the back of the seawall at t = 6.0s.

9.3.4 Application in practical design of container lashing

A good estimation of green water loading on deck cargo such as containers can be essential to design of securing arrangement and equipment, e.g. lashing. Lloyd's Register (2005) specifies in Part 3, Chapter 14.3 (Rules for Ships) that the design breaking loads of lashings depend on types of lashing and are approximately 35 tonnes on average. At scale model of this research, this load is equivalent to approximately 2N on a single load cell (assuming a standard container having cross section of 8½ft × 8½ft for estimating pressure at full scale; this pressure is then scaled down to get the pressure on load cells). Combining this value with results in Section 8.4 will help designers to work out the amount of container securing equipment required.

9.3.5 Summary of applicability of the model in engineering field

Sections 9.3.1 to 9.3.4 have shown that the applicability of the established model can be wide and practical. It can be adopted for either parametric investigation of various types of breakwater used on ship or heuristic studies in coastal engineering on seawalls and offshore breakwaters. Even though more extensive

validation in these investigations is highly suggested, the success of the outcome will undoubtedly help reduce expensive experimental cost.

9.4 Summary

This Chapter has reviewed the steps in the analysis model for evaluating green water and its loading effects. Green water is a complex problem and the prediction of its characteristics must be carried out systematically and with great care. Semi-empirical approach is at the moment recommended to reduce the sources of errors that could misguide the estimation of green water.

The simulation model established from this research has a wide range of engineering applications. It can be used to evaluate the performance of breakwaters and thereby optimise their designs. It may also be helpful in heuristic studies of novel designs of breakwater or similar structures. Outside naval architecture field, the simulation model can also find itself useful in preliminary studies of seawall and coastal breakwaters.

Chapter 10: Conclusions and Recommendations for Future Work

The thesis has shown a pragmatic application of a non-linear strip method in combination with a RANSE (Reynold-Averaged Navier-Stokes Equations) solver and semi-empirical approach to analyse and discuss several topics related to green water and loading on high-speed container ships operating at sea. As a conclusion, this Chapter summarises the process in which this research was carried out and highlights some of the most important findings. Recommendations to future work are also given.

10.1 Conclusions to present work

This research began by reviewing researches closely related to ship motions, green water and its loading effects on ships and offshore structures. Having gathered relevant information which helped to establish the foundation for this research, a methodology was developed. A semi-empirical approach was considered as an appropriate approach given the complexity and randomness in the nature of green water. On this basis, experiment work followed by CFD analysis was seen as the key to solving the problem of green water.

Before executing this plan, a general background that led to the occurrence of green water and its loading on ship was described in Chapter 3. Strip theory was chosen as a simple demonstrative method to help understand the fundamentals behind green water problem. The physics of green water started with basic motions when the ship travelled in waves. Relative motions between the deck and water surface were due to motions and incident waves. The motions of the ship in

water also created disturbances on water surface and these disturbances, known as swell-ups, contributed further to the relative motions between the deck and the local water surface. These relative motions could be intensified by large wave amplitude and unfriendly wavelengths. As they became larger, the water surface exceeded the deck level and water was seen to be shipped onto the deck. When this happened, the water that entered the deck was referred to as green water. On landing on the deck, green water imposed loads on deck plating under gravity effects and the acceleration of the deck itself. In small quantities, green water took the form of spray and caused disturbance to the manning on forecastle deck. In large quantities, green water could form a rigorous flow of water that rushed down the deck, crashed into structures and objects that happened to be in its path. The damages resulting from this were substantial, including possible rupture of plating or even loss of lives.

With the objective set on predicting green water behaviour on deck and its loading effects, experiments were conducted in order to obtain a physical understanding of green water as well as gathering data for validation purposes at a later stage. A containership model (S175) with two interchangeable bow shapes was selected for testing. A system of ten wave probes was used to monitor the relative motions and green water heights at critical locations. A matrix of nine load cells was also built and installed on deck to record the magnitude of green water loads on vertical structures of different heights and locations. For deck loading, a deck load cell was used and it was mounted under the forecastle deck. By connecting to a deck plating, it could record the load imposed by green water when water landed on deck.

Investigation into the effectiveness of cargo-protecting breakwater was also carried out experimentally. To accomplish this, rectangular breakwaters with and without perforations were installed in front of the protected structures and the changes in loading were monitored. The test was then carried out for a variety of wave heights, wave periods and ship velocities. The output results were analysed

with the aim to understand the physics of green water and to obtain a suitable hydraulic model associated with green water. As far as the behaviour was concerned, green water entered the deck at the time the ship bow pitched deepest into the water. Due to the bow flare and forward velocity of the ship, green water could come onto the deck in two ways.

In the first approach, when the ship pitched into the water, the water started to run up the sides of the bow and got shed due to the bow flare. However, because of the forward velocity, the ship could catch up with part of this shed water and the water ended up landing on the forecastle deck. High relative velocity between the deck and the water surface meant that the shed water could fly off the deck edge to relatively higher levels. However, this form of green water was normally small in quantity and did not pose a serious threat to the structure.

In the second approach, green water could take place when the forecastle deck pitched below the surrounding water. If the ship were stationary, the water would enter the deck in a similar fashion to a dam-break problem (Buchner, 2002). If the ship had a high forward velocity, the water would enter as a plunging breaker at the beginning and behaved like a dam-break flow later on (Faltinsen et al., 2002). On entering the deck, the water velocity direction was normal to the deck edge. Since the deck was relatively parabolic in shape, water had a transverse velocity and tended to translate towards the centreline of the ship. As a result, there was a concentration of water along the centreline of the deck which carried more energy than any other areas of the flow. The impact on vertical structures at the centreline was therefore more severe. The peak impact load took place shortly after the front water reached the structures. Without the protecting breakwater, vertical structures at lower levels sustained most of the impact load in an impulsive manner. Despite the possible high water run-up following the impact, the loads on higher structures were mostly due to quasi-static water pressure. They were gradual and of a smaller magnitude.

The deck pressure or vertical green water loading was a combination of the water head on deck, the pressure induced by the acceleration of the deck and the change in water height on deck. The last component could play a significant part in the overall deck pressure and should not be discounted.

With the breakwater fitted on forecastle deck, green water was blocked at early stages. However, there was an accumulation of green water in front of the breakwater due to blockage. If green water was severe, the follow-up water could be directed upwards by the water pile-up and subsequently overrode the breakwater. The water that overrode the breakwater took off at the top edge of the breakwater like a water jet and headed to higher locations of vertical structures. However, this impact was much less severe than the impact when no breakwater was fitted. Nevertheless, it exposed the higher structures to greater loads.

Breakwaters did help reduce green water load substantially (between approximately 50 percent to 95 percent in the cases considered in this research). Depending on the height and permeability, green water behaviour was changed considerably, as also loading. Larger breakwater area meant that more protection was provided to the structures. Perforations on the breakwater helped lessen the impact load sustained by the breakwater but increased the loads on the protected structures. A sensible choice of perforation size or permeability ratio could give optimal control of loading. Analysis of results from this research showed that 20 to 30 percent permeability appeared to give most advantages in terms of loading.

Green water could be influenced by subtle changes in the above-water bow shape. Experimental results showed that by introduction of knuckles in the bow, benefit in ship motions was gained and possibility of green water was reduced. The extension of overhang, on the other hand, could intensify green water and bow flare slamming.

Following the work by Buchner (2002) on green water on FPSO's, and based on the observed behaviour of green water flow on deck and test data, it was concluded that a hydraulic model similar to dam-break with an initial velocity equal to ship velocity could well represent green water flow on deck. CFD tool was selected for modelling. **Fluent 5** processor supported by mesh generator **Gambit** was adopted for simulation.

Chapter 6 provided a mathematic background on which CFD was built on. In order to justify the option of using CFD to analyse green water problem, two benchmark simulations were carried out and the results were validated using published experimental data. The first benchmark model was the dam-break problem and test data from Zhou et al (1999) were used for verification. The correlation was fair, given the fact that Zhou et al (1999) were using static pressure in their comparison rather than total pressure. The second benchmark model was the water-entry of a wedge section and verification was accomplished using test data by Tveitnes (2002). The agreement between the experiment and simulation was good. Since both benchmark models were relevant and similar in nature to green water problem, the success in using CFD to model suggested that CFD could be used for modelling of green water.

Based on freeboard exceedance recorded in the tests, the encountered frequency and wave height, a hydraulic model was set up together with the above water body of the ship bow and deck arrangement. Firstly, tests without breakwater in which green water took place were simulated. The output results were then compared with experimental results. It was found that in most cases investigated, there was good agreement (within 20 percent) between the two sets of data. All aspects of loading including peak load, rise time and general behaviour of the load curve were relatively well predicted. This meant that the simulation could reflect well the behaviour of green water on deck.

Building on this achievement, simulations with breakwaters fitted on forecastle deck were undertaken. A series of nine generic breakwaters were modelled for verification with experimental results. The breakwaters were rectangular in shape and were perforated by systematically varying the perforation diameters. The permeability of the breakwater varied accordingly. Due to limits in computational resources, only a representative green water condition was chosen for the nine simulations with breakwaters. The results were compared with experimental data and the outcome was encouraging. For both longitudinal loads and vertical loads, there was a good agreement between experiment and simulation. Even though a flawed setup of the load cell to measure loads on the breakwater meant that the comparison of this load was not possible, the results from other comparisons were promising. For a range of breakwaters with varied height and permeability, there was consistent agreement between simulation and test data.

The overall outcome of the validation process strongly confirmed that the hydraulic model worked well in reproducing green water behaviour on deck, both qualitatively and quantitatively. The achievements in simulating green water on deck with rectangular breakwaters meant that similar achievements could be expected for other types of breakwaters and objects on forecastle deck. In order to illustrate this, CFD analyses using a variety of commonly used breakwaters were carried out and comparisons between the performances of these breakwaters were demonstrated in Chapter 9.

In summary, green water is a complex problem arising from many factors, both ship-born and environmentally. It is also sensitive to subtle changes in these parameters. Therefore, a semi-empirical approach to investigate green water and its loading is suggested. A model of dam-break combined with forward ship velocity and waves condition can be used to gain insight into the behaviour of green water and its loading effects on deck. From an application point of view, the model can help carry out parametric investigations and optimisation of breakwater

designs. This application can also be extended to several other engineering areas such as coastal engineering.

10.2 Recommendations for future work

Despite positive achievements in the present research on green water modelling, there are still elements which can considerably improve the outcome of this research and they are as follows:

- **Experiments:**

    - More comprehensive test series with better variety of modification to the above water bow shape will help justify the benefits or disadvantages associated with a particular bow feature.

    - More comprehensive test series with other types of breakwaters will make the validation of the proposed model more complete and provide more confidence in the application of the present modelling methodology.

    - Better setup of load cells to ensure that all loads are reliably recorded. A more complete validation will undoubtedly supply a better picture of the problem.

    - Tests in irregular waves and oblique waves will definitely add new dimensions to the understanding of green water especially when rolling motions are incorporated. Side/stern green water can also be another area of research.

- **Ship motions theories:**

    - It is unquestionable that better ship motion prediction will make the evaluation of green water less dependent on empirical approach. Since ship motions are the building blocks in the physics of green water, improvement in ship motions theories will, in no doubt, provide a platform for the prediction of green water problem.

- **CFD modelling:**

    - For better results, motions of the ship should be included in the CFD simulation. This inclusion will reduce discrepancies caused by slow drainage of green water in the present simulation. In reality, due to the pitching motions, green water on deck could drain away faster. The success of including ship motions in CFD analysis also means that the deck pressure component induced by deck acceleration can be accounted for. The gap between simulation and experiment will, therefore, be bridged.

    - Simulation of a complete ship with surrounding waves will be an ultimate achievement in modelling green water and assessing full interaction between ship and waves. The effects by bow shapes will also be evaluated in such simulations.

    - Finally, the hydraulic model proposed herein is only a simplified model in which many parameters are compromised. A more sophisticated (addressing the limitations of this current model) and more effective model is always encouraged so that green water problem can be dealt comprehensively.

References

American Bureau of Shipping, 2006. Rules for Building and Classing Steel Ships.

Anderson, J.D. Jr., 1995. *Computational Fluid Dynamics*. New Delhi: McGraw-Hill, Inc..

ANSYS Inc. (NASDAQ: ANSS), 2006. FLUENT 5 Software Package.

Bales, N.K., 1978. Procedures Required for Computing the Freeboard Requirements for Displacement Monohulls. *DTNSRDC Report SPD-811-01*. 1978.

Bales, N.K., 1979. Procedures Required for Computing the Freeboard Requirements of Displacement Monohulls. *DTNSRDC Report SPD-811-05*. January 1979.

Bales, N.K., 1979. Minimum Freeboard Requirements for Dry Foredecks: A Design Procedure. *SNAME STAR Symposium*. April 1979.

Bales, N.K., & Watkins, R.M., 1976. Validity of Analytical Predictions of Deck Wetness for an Offshore Supply Vessel in Following Waves. *DTNSRDC Report SPD-726-01*. September 1976.

Beck, R.F., 1982. Relative Motion Components for a Mathematical Form in Regular Waves. *Proceedings of the 14 Symposium on Naval Hydrodynamics*. Ann Arbor, Michigan, USA 1982.

Bishop, C.R., & Bales, N.K., 1978. A Synthesis of Bow Wave Profile and Change of Level Data for Destroyer-Type Hulls with Application to Computing Minimum Required Freeboards. *DTNSRDC SPD-811-01*. January 1978.

Blok, J.J. & Huisman, J., 1983. Relative Motions and Swell-Up for a Frigate Bow. *Transactions of RINA*, 125.

Buchner, B., 1995a. On the Impact of Green Water Loading on Ship and Offshore Unit Design. *PRADS95*. Seoul, Republic of Korea September1995.

Buchner, B., 1995b. Impact of Green Water on FPSO Design. *Offshore Technology Conference*. Houston, Texas, USA. October 1995.

Buchner, B.,1996. Advances in Green Water Effect Prediction for FPSOs. *The Atlantic Frontier Forum 1996*. Aberdeen, UK January 1996.

Buchner, B. & van Ballegoyen, G., 1997. Joint Industry Project: F(P)SO Green Water Loading. MARIN, The Netherlands.

Buchner, B. & Cozjin, J.L., 1997. An Investigation into the Numerical Simulation of Green Water. *The Proceedings of BOSS97*. Delft, The Netherlands 1997.

Buchner, B. 2002. *Green Water on Ship-Type Offshore Structures*. Ph.D. Delft University of Technology.

Bureau Veritas, 2005. *Rules for the Classification of Steel Ships.*

Chan, H.S., 1990. *A Three-Dimensional Technique for Predicting First- and Second-Order Hydrodynamic Forces on a Marine Vehicle Advancing in Waves*. Ph.D. University of Glasgow.

Cox, D.T. & Ortega, J.A., 2001. Laboratory Observations of Green Water Overtopping a Fixed Deck. *Ocean Engineering*, 29, pp.1827-1840.

Cozijn, J.L., 1995. Development of a Calculation Tool for Green Water Simulation. *Delft University of Technology Report No. 1047-SC*.

Crossland, P. & Johnson, M.C., 1998. A Time Domain Simulation of Deck Wetness in Head Seas. *RINA International Conference on Ship Motions and Manoeuvrability*, London.

Det Norske Veritas, 2002. *Rules for Classification of Ships.*

Dillingham, J., 1981. Motion Studies of a Vessel with Water on Deck. *Marine Technology*, 18(1), pp. 38-50.

Edward, J. & Todd, F.H., 1938. Steam Drifters, Tank and Sea Tests. *Institute of Engineers and Shipbuilders in Scotland*. Scotland.

Faltinsen, O. M., Greco, M., & Landrini, M., 2002. Green Water Loading on FPSO, *Journal of Offshore Mechanics and Arctic Engineering*, 124, pp. 94-103.

Faltinsen, O.M., 2005. *Hydrodynamics of High-Speed Marine Vehicles*. Cambridge University Press. London, UK.

Fonseca, N. & Guedes Soares, C., 1998. Time-Domain Analysis of Large-Amplitude Vertical Ship Motions and Wave Loads. *Journal of Ship Research*, 42(2).

Fonseca, N. & Guedes Soares, C., 2005. Experimental Investigation of the Shipping of Water on the Bow of a Containership. *Journal of Offshore Mechanics and Artic Engineering*, 127(4), pp. 322-330.

Gallagher, P., & Rainey, R.C.T., 1992. Final Report into the Prediction of Deck Wetting. *WS Atkins Engineering Services Report No M1389.R05*. UK April 1992.

Gesteria, M.G., Cerqueiro, D., Crespo, C. & Dalrymple, R.A., 2003. Green Water Overtopping Analyzed with a SPH model. *Ocean Engineering*, 30, pp. 2021-2052.

Goda, K., Miyamoto, T. & Yamamoto, Y., 1978. A Study of Shipping Water Pressure on Deck by Two Dimensional Ship Model Test. *Journal of the Society of Naval Architects of Japan*, 143.

Goodrich, G.J., 1964. The Influence of Freeboard on Wetness. *5th Symposium on Naval Hydrodynamics*. Norway 10-12 September 1964.

Greco, M., Faltinsen, O.M. & Landrini, M., 2000a. A Parametric Study of Water On Deck Phenomena, *NAV 2000*. Venice, Italy.

Greco, M., Faltinsen, O.M. & Landrini, M., 2000b. An Investigation of Water on Deck Phenomena. *Proceedings of the 15th International Workshop on Water-Waves and Floating Bodies*. Caesarea, Israel 17 February – 1 March 2000.

Greco, M., Faltinsen, O. M. & Landrini, M., 2000c. Basic Studies of Water on Deck. *23rd Symposium on Naval Hydrodynamics*. Val de Reuil, France September 2000.

Greco, M., Faltinsen, O. M. & Landrini, M., 2001. Green Water Loading on a Deck Structure. *Proceedings of the 16th International Workshop on Water Waves and Floating Bodies*. Hiroshima, Japan 22-25 April 2001.

Greco, M., Landrini, M. & Faltinsen, O.M., 2005. Shipping of Water on a Two-Dimensional Structure. Part 2. *Journal of Fluid Mechanics*, 525, pp. 309-332.

Greco, M., Colicchio, G. & Faltinsen, O.M., 2007. Shipping of Water on a Two-Dimensional Structure. Part 2. *Journal of Fluid Mechanics*, 581, pp. 371-399.

Guedes Soares, C. & Ramos, J., 1997. On the Assessment of Hydrodynamic Coefficients of Cylinders in Heaving. *Ocean Engineering*, 24(8).

Guedes Soares, C. & Pascoal, R., 2005. Experimental Study of the Probability Distributions of Green Water on the Bow of Floating Production Platforms. *Journal of Offshore Mechanics and Artic Engineering*, 127(3), pp. 234-242.

Hamoudi, B. & Varyani, K. S., 1994. Load Prediction due to Green Water on Deck Mounted Equipment for Floating Bodies. *Proceedings of the International Conference on Marine, Offshore and Ice Technology*. Southampton, UK 1994, pp145-152.

Hamoudi, B., 1995. *Dynamic Response of Hull due to Bottom Slamming and Deck Wetness*. Ph.D. University of Glasgow.

Hamoudi, B. & Varyani, K. S., 1997. A New Approach to Wave Loading on Deck Mounted Equipment on Offshore Structures/Vessels. *International Shipbuilding Progress*, 44(440), pp. 321-339.

Hamoudi, B. & Varyani, K. S., 1998. Significant Load and Green Water on Deck of Offshore Units/Vessels. *Ocean Engineering*, 25(8), pp. 715-731.

Haskind, M.D., 1947. Hydrodynamic Methods in the Problem of the Behaviour of Ships in Waves. *Trudy C.A.G.I.*, 603.

Haskind, M.D., 1953. Two Papers on the Hydrodynamic Theory of Heaving and Pitching of a Ship. *Technical and Research Bulletin*. No. 1-12. Society of Naval Architects and Marine Engineers.

Hirt, C.W., & Nichols, B.D., 1981. Volume of Fluid (VOF) Method for the Dynamics of Free Boundaries. *Journal of Computational Physics*, 39, pp. 201-225.

Hong, S.Y., Lee, P.M. & Gong, D.S., 1993. Experimental Study on the Deck Wetting of a Container Ship in Irregular Head Waves. *The Society of Naval Architects of Korea*, 1.

Huijsmans, R.H.M. & van Groesen, E., 2004. Coupling Freak Wave Events with Green Water Simulations. *Proceedings of the 14th International Offshore and Polar Engineering Conference*. Toulon, France 23-28 May 2004.

Iglesias, A.S., Rojas, L.P. & Rodriguez, R.Z., 2004. Simulation of Anti-Roll Tanks and Sloshing Type Problems with Smoothed Particle Hydrodynamics. *Ocean Engineering*, 31, pp. 1169-1192.

Jarlan, G.E., 1961. A Perforated Vertical Wall Breakwater. *Dock and Harbour Authority*, 486, pp.394-398.

Johnson, M.C., 1996, Deck Wetness Experiments with Various Bow Shapes: Validation of the NLWET Computer Simulation. *DRA/SS/SSHE/CR96104* (Unclassified). Defence Research Agency, UK.

Kleefsman, K.M.T, Loots, G.E., Veldman, A.E.P., Buchner, B., Bunnik, T. & Falkenberg, E., 2005. The Numerical Simulation of Green Water Loading Including Vessel Motions and the Incoming Wave Field. *Proceedings of the 24th International Conference on Offshore Mechanics and Artic Engineering*. Halkidiki, Greece 12-17 June 2005.

Korvin-Kroukovsky, B.V., 1955. Investigation of Ship Motions in Regular Waves. *Transactions of The Society of Naval Architects and Marine Engineers*, 63.

Korvin-Kroukovsky, B.V., 1957. Pitching and Heaving Motions of a Ship in Regular Waves. *Transactions of The Society of Naval Architects and Marine Engineers*, 65.

Koshizuka, S. & Shibata, K., 2005. Numerical Analysis of Wave Impact on Ships with Deck Wetness Using a Particle Method. *Proceedings of the 15th International Offshore and Polar Engineering Conference*. Seoul, Korea 19.24 June 2005.

Liut, D.A., Weems, K.W. & Lin, W.M., 2002. Nonlinear Green Water Effects on Ship Motions and Structural Loads. *Proceedings of the 24th Symposium on Naval Hydrodynamics*. Fukuoka, Japan 8-13 July 2002.

Lloyd, A.R.J.M., & Hammond, M.A., 1982. The Effect of Bow Shape on Ship Motions and Deck Wetness. *Report AMTE (H) R82012* (Unclassified).

Lloyd, A.R.J.M, 1983. Deck Wetness Experiments, *Proceedings of the General Meeting of the 20th American Towing Tank Conference*, 2. New Jersey 2-4 August 1983.

Lloyd, A.R.J.M., 1984. Deck Wetness Experiments at the United States Naval Academy. *Report no. AMTE (H) R84213* (Unclassified).

Lloyd, A.R.J.M, Salsich, J.O. & Zseleczky, J.J., 1985. Effect of Bow Shape on Deck Wetness in Head Seas. *Transactions of The Royal Institution of Naval Architects*, 124.

Lloyd, A.R.J.M, March 1994. A Non-Linear Simulation of Deck Wetness. DRA/AW/AWH/TR94003. Defence Research Agency, UK.

Lloyd's Register, 2005. *Rules and Regulations for the Classification of Ships*.

Maruo, H. & Song, W., 1994. Non-linear Analysis of Bow Wave Breaking and Deck Wetness of a High-speed Ship by the Parabolic Approximation. *Proceedings of the 20th Symposium on Naval Hydrodynamics*. Santa Barbara, California 1994.

Mizouguchi, S., 1988. Analysis of Shipping Water with the Experiments and the Numerical Calculations. *Journal of the Society of Naval Architects of Japan*, 163.

Nielsen, K.B., 2003. *Numerical Prediction of Green Water Loads on Ships*, Ph.D. Technical University of Denmark.

Nielsen, K.B., & Mayer, S., 2004. Numerical Prediction of Green Water Incidents. *Ocean Engineering*, 31, pp. 363-399.

Newman, J.N., 1957. On the Damping of Pitch in Waves. *Journal of Ship Research*, 1(2).

Newman, J.N., 1959. The Damping and Wave Resistance of a Pitching and Heaving Ship. *Journal of Ship Research*, 3(1).

Newman, J.N., 1978. The Theory of Ship Motions. *Advances in Applied Mechanics*, 18, pp. 221-283.

Newton, R.N., 1960. Wetness Related to Freeboard and Flare. *Transactions of the Royal Institution of Naval Architects*, 102.

Ochi, K., 1964. Extreme Behaviour of a Ship in Rough Seas – Slamming and Shipping of Green Water. *Transaction of the Society of Naval Architects and Marine Engineers*, 72.

Ogawa, Y., Taguchi, H. & Ishida, S., 1998. A Prediction Method for the Shipping Water Height and its Load on Deck. *Proceedings of the 7th International Symposium on Practical Design of Ships and Mobile Units*. The Hague, The Netherlands 20-25 September 1998.

Ogawa, Y., Taguchi, H., Ishida, S., Wantanabe, I., Sawada, H., Tsujimoto, M., & Minami, M., 2000. Study of a Rational Method of Assigning Freeboard. *Papers of Ship Research Institute*, 37(6). Tokyo: Ministry of Transport.

Ogilvie, T.F., 1972. The Wave Generated by a Fine Ship Bow. *Proceedings of the 9th Symposium on Naval Hydrodynamics*. ACR-203, pp.1483-1525. Office of Naval Research, Washington, D.C.

Oliver, J.C., 1981. Analytical Methods to Predict Transient Loads on Floating Platforms. In D. Faulkner, M.J.Cowling & P.A. Frieze, eds. *Integrity of Offshore Structure*. Applied Science Publishers.

Olsen, E.O., 2005. Application of Double Skin Breakwater with Perforations for Reducing Green Water Loading on High Speed Container Vessels. *Discussion Note*.

Pham, X.P. Varyani, K.S. & Crossland, P., 2003a. Estimation of Horozontal Loading due to Green Water Using Three-Dimensional CFD Simulation. *MARNET Workshop*. Gosport, UK 2003.

Pham, X.P. Varyani, K.S. & Crossland, P., 2003b. Application of Three Dimensional Discrete Element Method in the Prediction of Deck Loading due to Green Water Effect. *MARNET Workshop*. Gosport, UK 2003.

Pham, X.P. & Varyani, K.S., 2004. Influence of Breakwaters in Reducing the Effects of Green Water Loading onboard High Speed Container Vessels

Using CFD. *Proceedings of the 14th International Offshore and Polar Engineering Conference*. Toulon, France, 23-28 May 2004.

Pham, X.P. & Varyani, K. S., 2005. Evaluation of Green Water on High-Speed Containership Using CFD. *Ocean Engineering*, 32(5-6), pp571-585.

Pham, X.P. & Varyani, K.S., 2006a. Generic design of V-Shape and Vane-Type Breakwaters to Reduce Green water Load Effects on Deck Structures and Containers of Ships: Case Study. *Journal of Waterway, Port, Coastal And Ocean Engineering*, 132(1), pp 57-65.

Pham, X.P. & Varyani, K.S., 2006b. Whaleback Forecastle for Reducing Green water Loading on High Speed Container Vessels. *Proceedings of 3rd ASRANet International Colloquium*. Glasgow, UK, 10-12 July 2006.

Price, W.G. & Bishop, R.E.D., 1974. *Probabilistic Theory of Ship Dynamics*. London: Chapman and Hall.

Raven, H.C., 1980. Calculation of Wave Profile and Wave Resistance by the Thin-Ship Theory; the First Order Problem. *NSMB Report No. 50002-1-SR*. November 1980.

Ryu, Y. & Chang, K.A., 2005. Breaking Wave Impinging and Green Water on a Two-Dimensional Offshore Structure. *Proceedings of the 15th International Offshore and Polar Engineering Conference*. Seoul, Korea 19.24 June 2005.

Salvesen, N., Tuck, E.O. & Faltinsen, O., 1970. Ship Motions and Sea Loads. *Annual Meeting of the Society of Naval Architects and Marine Engineers*. New York, USA 12-13 November 1970.

Shearer, J.R., 1950. A Preliminary Investigation of the Discrepancies between the Calculated and Measured Wavemaking of Hull Form. *Transactions of North-East Coast Institute of Engineers and Shipbuilders*, 167.

Schonberg, T. & Rainey, R.C.T., 2002. A Hydrodynamic Model of Green Water Incidents. *Applied Ocean Research*, 24, pp. 299-307.

Stansberg, C.T., Berget, K., Hellan, O., Hermundstad, O., Hoff, J.R. &Kristiansen, T., 2004. Prediction of Green Sea Loads on FPSO in

Random Seas. *Proceedings of the 14th International Offshore and Polar Engineering Conference*. Toulon, France, 23-28 May 2004.

Stoker, J.J., 1957. Water Waves: Pure and Applied Mathematics. In R. Courant, L. Bers & J.J. Stoker, eds., *Water Waves: The Mathematical Theory with Applications*. New York: Inter-science.

Suhara, T., Hiyama, H. & Koga, Y., 1973. Shock Pressure due to Impact of Water Jet and Response of Elastic Plate. *Transactions of the West-Japan Society of Naval Architects*, 46.

Swaan, W.A. & Vossers, G., 1961. The Effect of Forebody Section Shape on Ship Behaviour in Waves. *Transactions of the Royal Institution of Naval Architects*, 103.

Takagi, K. & Niimi, A., 1990. A Theoretical Approach to Bow Deck Wetness of a High-Speed Ship. *Journal of Ship Research*, 34.

Tanimoto, Y. & Goda, Y., 1991. Historical Development of Breakwater Structures in the World. *Coastal Structures and Breakwaters*. Thomas Telford, London, pp. 193-206.

Tanizawa, K., Sawada, H., Hoshino, K. & Tsujimoto, M., 2004. Visualization of Shipping Water on Running Ship Foredeck in Regular Head Seas. *Proceedings of the 14th International Offshore and Polar Engineering Conference*. Toulon, France 23-28 May 2004.

Tasai, F., 1959. On the Damping Force and Added Mass of Ship Heaving and Pitching. *Reports of Research Institute for Applied Mechanics*, 7(26).

Tasai, F., 1960. Damping Force and Added Mass of Ship Heaving and Pitching (continued). *Reports of Research Institute for Applied Mechanics*, 8(31).

Tasai, F., 1961a. Wave Height at the Side of Two-Dimensional Body Oscillating on the Surface of a Fluid. *Reports of Research Institute for Applied Mechanics*. 9(35).

Tasai, F., 1961b. Hydrodynamic Force and Moment Produced by Swaying and Rolling Oscillation of Cylinders on the Free Surface. *Reports of Research Institute for Applied Mechanics*. 9(35).

Tasai, F., 1969. On the Deck Wetness and Slamming of Full Ship Forms. *12th International Towing Tank Conferrence*. Rome 22-30 September 1969.

Tasaki, R., 1963. On Shipment of Water in Head Waves. *10th International Towing Tank Conferrence*. London 4-11 September 1963.

Tucker, M.J., 1991. *Waves in Ocean Engineering*. Ellis Horwood.

Tveitnes, T., 2001. *Application of Added Mass Theory in Planing*, Ph.D. University of Glasgow.

Ursell, F., 1949a. Surface Waves on Deep Water in the Presence of A Submerged Circular Cylinder. *Quarterly Journal of Mechanics and Applied Mathematics*, 2.

Ursell, F., 1949b. On the Heaving Motion of a Circular Cylinder on the Surface of a Fluid. *Quarterly Journal of Mechanics and Applied Mathematics*, 2.

Ursell, F., 1953. Multipole Expansions in the Theory of Surface Waves. *Proceedings of the Royal Society of London*, Series A, 220.

Varyani, K. S., Pham, X. P., & Crossland, P., 2004. Green Water Investigation Onboard Container Ships. *Ship Technology Research (Schiffstechnick)*, 51(4), pp151-161.

Varyani, K.S., Pham, X P., & Olsen, E.O., 2005. Application of Double Skin Breakwater with Perforations for Reducing Green Water Loading on High Speed Container Vessels. *International Shipbuilding Progress*, 52(3), pp273-292.

Varyani, K.S., Hodgson, T. & Pham, X.P., 2006. Effective Breakwater Design for Trading Vessels and FPSO's, *Journal of the Offshore Mechanics and Arctic Engineering*, 128.

Varyani, K.S. & Pham, X.P., 2007. Effective Breakwaters for High-Speed Container Vessels. Proceedings of MARSTRUCT Conference 2007. Glasgow, UK March 2007.

Vosser, G., Swaan, W.A., & Rijken, H., 1960. Experiments with Series 60 Models in Waves. *Journal of the Society of Naval Architects and Marine Engineers*, 68.

Waniewski, T.A., Brennen, C.E. & Raichlen, F., 2002. Bow Wave Dynamics. *Journal of Ship Research*, 46(1), pp.1-15.

Wu, M., Tulin, M.P. & Fontaine, E., 2000. On the Simulation of Amplified Bow Waves Induced by Motion in Head Seas. *Journal of Ship Research*, 44(4).

Yamasaki, J., Miyata, H., & Kanai, A., 2005. Finite-Difference Simulation of Green Water Impact on Fixed and Moving Bodies. *Journal of Marine Science and Technology*, 10(1), pp. 1-10.

Zhang, S., Liut, D., Weems, K. & Lin, W.M., 2005. A 3-D Finite Volume Method for Green Water Calculations. *Proceedings of the 24th International Conference on Offshore Mechanics and Arctic Engineering*. Halkidiki, Greece 12-17 June 2005.

Zhou, Z.Q., De Kat J.O. & Buchner, B., 1999. A Non-linear 3-D Approach to Simulate Green Water Dynamics on Deck. *Proceedings of the 7th International Conference on Numerical Ship Hydrodynamics*. Nantes, France July 1999.

Bibliography

Bhattacharyya, R., 1978. *Dynamics of Marine Vehicles.* New York: Wiley.

Cummins, W.E., 1962. The Impulse Response Function and Ship Motions. *Schiffstechnik,* 9.

Dallinga, R. & Gaillarde, G., 2001. Hatch Cover Loads Experienced by M.V. Derbyshire During Typhoon ORCHID. *Glasgow Marine Fair and International Workshop on Safety of Bulk Carrier*. Glasgow, UK 2001.

De Kat, J.O., 1989. The Simulation of Ship Motions and Capsizing in Severe Seas. *Transactions of SNAME,* 97.

De Kat, J.O., 2001. Revision of the Load Line Convention. *Glasgow Marine Fair and International Workshop on Safety of Bulk Carriers*. Glasgow, UK 2001.

Dillingham, J.T., & Falzarano, J.M., 1986. Three Dimensional Numerical Simulation of Green Water on Deck. *3rd International Conference on the Stability of Ships and Ocean Vehicles.*

Faltinsen, O.M., 1974. A Numerical Investigation of the Ogilvie-Tuck Formulas for Added Mass and Damping Coefficients. *Journal of Ship Research,* 18(2).

Fang, M.C, Lee, M.L. & Lee, C.K., 1993. Time Simulation of Water Shipping for a Ship Advancing in Large Longitudinal Waves. *Journal of Ship Research,* 37.

Faulkner, D. & Buckley, W.H., 1997. Critical Survival Conditions for Ship Design. *International Conference on Design and Operation for Abnormal Conditions*. RINA, Glasgow, UK October 1997.

Faulkner, D. & Williams, R.A., 1996. Design for Abnormal Ocean Waves, *RINA Spring Meeting.*

Gaillarde, G., & Zheng, X., 2001. MARIN Model Tests – Green Seas Hatch Loading on Bulk Carriers. *Transactions of the Royal Institution of Naval Architects*, 140.

Goring, D.G., 1978. Tsunamis – The Propagation of Long Waves onto a Shelf. *Technical Report No. KH-R-38*. California Institute of Technology, W.M.Keck Laboratory of Hydraulics and Water Resources, Pasadena, CA.

Hamoudi, B. & Varyani, K.S., 1992. On the Prediction of Impact Pressure due to Bottom Slamming on a Container Ship. *4th International Conference on Computer Aided Design, Manufacture & Operation in the Marine & Offshore Industries*. Madrid October 1992.

Huang, J., Cong, L., Grochowalski, S., & Hsiung, C. C., 1999. Capsize Analysis for Ships with Water Shipping on and off the Deck. *22nd Symposium on Naval Hydrodynamics*. Washington, DC, USA August 1999.

Huang, Y. & Sclavounos, P.D., 1998. Non-linear Ship Motions. *Journal of Ship Research*, 42(2).

International Ship Structures Congress, 1982. *Report of Committee: Transient Dynamic Loadings and Response*. Gdansk: 8th International Ship Structures Congress.

Kawakami, M., 1969. On the Impact Strength of Ships due to Shipping Green Seas. *Journal of the Society of Naval Architects of Japan*, 125.

Kent, J.L., 1950. The Design of Seakindly Ships. *Transactions of The North-East Coast Institution of Engineers & Shipbuilders*, 67.

Lloyd, A.R.J.M., 1989. *Seakeeping: Ship Behaviour in Rough Weather*. Chichester: Ellis Horwood.

O'Dea, J.F., 1983. Relative Motion and Deck Wetness Investigation of the SL-7 Containership. *DTNSRDC Report SPD-1081-01*. April 1983.

O'Dea, J.F. & Walden, D.A, 1984. The Effect of Bow Shape and Non-linearities on the Prediction of Large Amplitude Motion and Deck Wetness. *Office of Naval Research Symposium*.

SAFE-FLOW Project, 2004. *Summary Report on Design Guidance and Assessment Methodologies for Wave Slam and Green Water Impact Loading*. Glasgow, UK August 2004.

Tao, Z. & Incecik, A., 2000. Nonlinear Ship Motion and Global Bending Moment Predictions in Regular Head Waves. *International Shipbuilding Progress*, 47(452), pp.353-378.

Tucker, M.J., Challenor, P.G. & Carter, D.J.T., 1984. Numerical Simulation of A Random Sea: A Common Error and Its Effect Upon Wave Group Statistics. *Applied Ocean Research*, 6(2).

Van Sluijs, M.F., 1974. Ship Relative Motions and Related Phenomena. *The Proceedings of the International Symposiums on The Dynamics of Marine Vehicles and Structures in Waves*. London, UK 1974.

Vassalos, D., Guarin, L., & Jasionowski, A., 2001. Original Tests on MV Derbyshire and the Seakeeping Investigation Programme on the Safety of Bulk Carriers. *Glasgow Marine Fair and International Workshop on Safety of Bulk Carrier*. Glasgow, UK 2001.

Von Kerczek, C. & Tuck, E.O., 1969. The Representation of Ship Hulls by Conformal Mapping Functions. *Journal of Ship Research*, 13.

Voogt, A. & Buchner, B., 2004. Prediction of Wave Impact Loads on Ship-type Offshore Structures in Steep Fronted Waves. *Proceedings of the 14th International Offshore and Polar Engineering Conference*. Toulon, France 23-28 May 2004.

Yilmaz, O., Incecik, A. & Han, J.C., 2003. Simulation of Green Water Flow on Deck Using Non-Linear Dam Breaking Theory. *Ocean Engineering*, 30, pp. 601-610.

Appendix A:
Governing Equations of CFD Simulation

Numerical modelling in CFD divides the fluid domain into multiple finite control volumes (Finite Volume Method) so that instead of looking at the whole flow field at once, the fundamental physical principles are applied to just the infinitesimally small fluid element itself. By this way, the approximated solutions to these small fluid elements can be found in an easier manner and the discrepancy is also reduced. In order to set up the equations of fluid motion, the following laws of physics are chosen:

- Mass is conserved.
- Momentum is conserved.
- Energy is conserved.

Mathematical equations which embody such physical principles are then extracted and by applying boundary conditions, the solutions to the fluid characteristics in the finite control volume in consideration can be found. Integration process was finally performed to find the solutions to the flow characteristics of the whole fluid flow. The details are explained in the following sub-sections.

A.1 Spatial discretisation

The domain is divided into a number of infinitesimally small control volumes. These control volumes do not overlap one another and they are normally denoted as cells. The whole domain that has been divided into cells is termed computational grid. In 3D simulation, the cells are commonly tetrahedral or hexahedral. By considering each cell and particular conditions in the problem, the

governing equations can be derived and solved for the velocity and pressure fields, which define the behaviour of the flow.

A.2 Continuity equation

To obtain the governing equations, consider, first, the flow model shown in Figure A.2.1: an infinitesimally small element fixed in space, with the fluid moving through it. Taking into account the inflow and outflow of this fluid element (Figure A.2.2) and following the law of conserved mass, the net mass flow out of the element must equal the time rate of decrease of mass inside the element. If denoting the decrease of mass by a negative quantity, it can be obtained that:

$$\left[\frac{\partial(\rho.u)}{\partial x}+\frac{\partial(\rho.v)}{\partial y}+\frac{\partial(\rho.w)}{\partial z}\right]dxdydz=-\frac{\partial\rho}{\partial t}(dxdydz) \qquad (A.2.1)$$

in which u, v and w are velocity components in x-, y- and z-directions, respectively. Dividing both sides by the volume of the fluid element and putting all the terms to the right hand side gives:

$$\frac{\partial(\rho.u)}{\partial x}+\frac{\partial(\rho.v)}{\partial y}+\frac{\partial(\rho.w)}{\partial z}+\frac{\partial\rho}{\partial t}=0 \qquad (A.2.2)$$

Equation (A.2.2) is a partial differential equation form of the continuity equation.

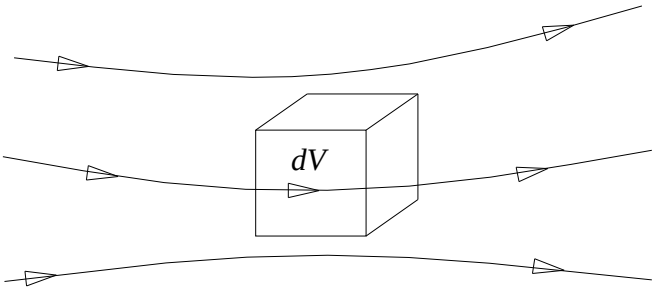

Figure A.2.1 Infinitesimally small fluid element fixed in space with the fluid moving through it (Anderson, 1995).

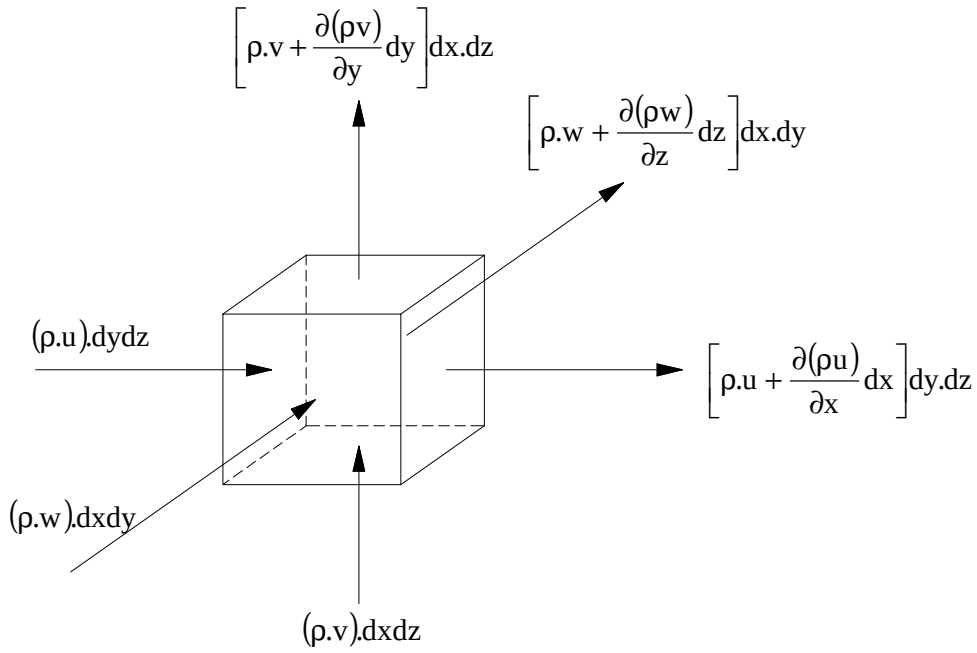

Figure A.2.2 Mass fluxes through the various surfaces of the element (Anderson, 1995).

In the simulation of green water flow, the fluid is water and incompressible. Because the water density is constant, equation (A.2.2) can be re-written as:

$$\frac{\partial u}{\partial x} + \frac{\partial v}{\partial y} + \frac{\partial w}{\partial z} = 0 \qquad \text{(A.2.3)}$$

A.3 Momentum equations

Momentum equations are based on Newton's second law, i.e. **F** = m.**a**. Even though momentum equations can be derived from a Eulerian model of flow (conservation form), i.e. by looking at an infinitesimally small fluid element fixed in space, it is thought to be easier to derive them using a Lagrangian model (non-conservation form), i.e. a moving fluid element model.

Considering only the x-component of Newton's second law $\mathbf{F_x} = m.\mathbf{a_x}$. All forces acting on this fluid element are as in Figure A.3.1. Essentially, there are two sources of forces:

- *Body forces*: act directly on the volumetric mass of the fluid element such as gravitational forces. In mathematic form, it can be written as:

  Body force (in x-direction) = $\rho f_x (dx\, dy\, dz)$ (A.3.1)

  where f_x is the body force per unit mass in x-direction.

- *Surface forces*: act directly on the surface of the fluid element due to pressure distribution imposed by the outside fluid surrounding the fluid element and the shear and normal stress distributions acting on the surface, also imposed by the outside fluid by means of friction. In mathematic form, it can be written as:

  Net surface force (in x-direction) = $\left[-\frac{\partial p}{\partial x} + \frac{\partial \tau_{xx}}{\partial x} + \frac{\partial \tau_{yx}}{\partial y} + \frac{\partial \tau_{zx}}{\partial z} \right] dxdydz$ (A.3.2)

  where τ_{ij} denotes a stress in the j-direction exerted on a plane perpendicular to the i-axis.

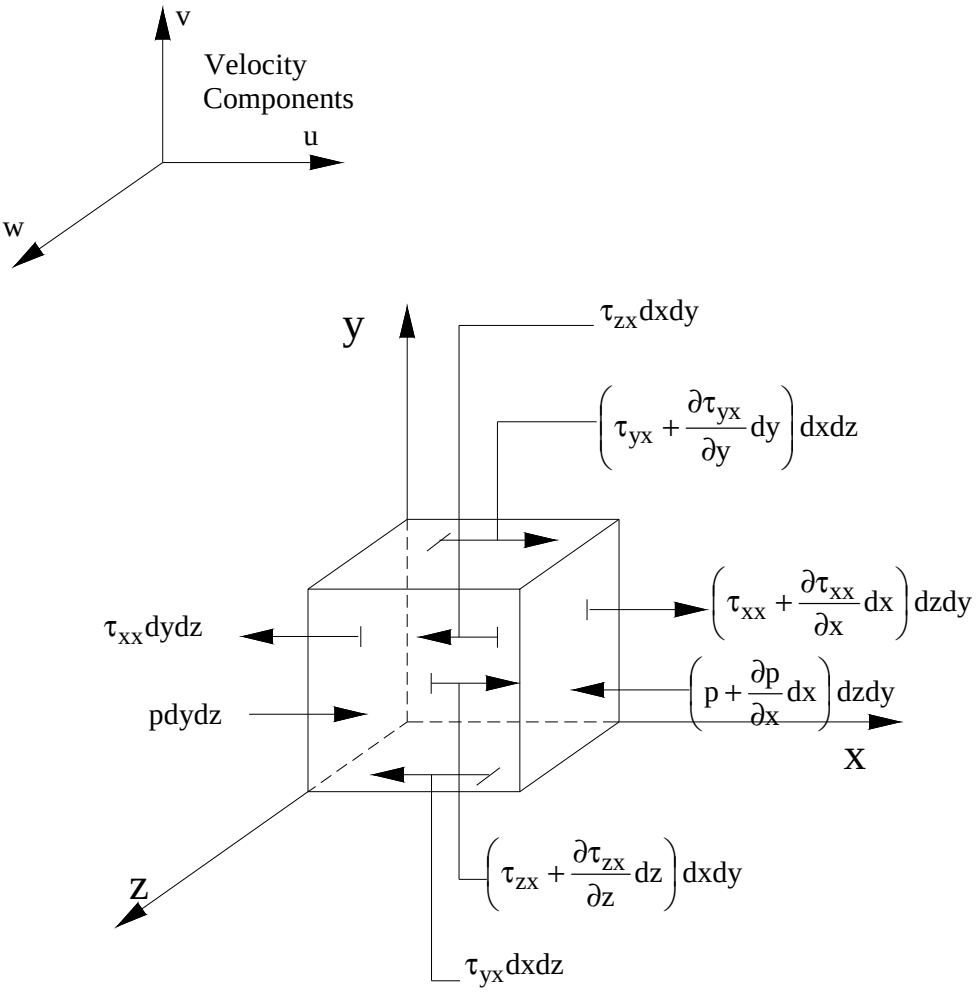

Figure A.3.1 Forces in x-direction acting on infinitesimally small fluid element (Anderson, 1995).

The total force acting on the fluid element will then become:

F_x = *Body force* (in x-direction) + *Net surface force* (in x-direction)

$$= \left[-\frac{\partial p}{\partial x}+\frac{\partial\tau_{xx}}{\partial x}+\frac{\partial\tau_{yx}}{\partial y}+\frac{\partial\tau_{zx}}{\partial z}\right]dxdydz+\rho f_x(dx\,dy\,dz) \qquad (A.3.3)$$

Replace mass of fluid element m = $\rho(dx\,dy\,dz)$ and acceleration in x-direction:

$$a_x = \frac{Du}{Dt} \tag{A.3.4}$$

equation (A.3.3) becomes:

$$\rho\frac{Du}{Dt} = -\frac{\partial p}{\partial x} + \frac{\partial \tau_{xx}}{\partial x} + \frac{\partial \tau_{yx}}{\partial y} + \frac{\partial \tau_{zx}}{\partial z} + \rho f_x \tag{A.3.5}$$

which is the x-component of the momentum equation for a viscous flow. Similarly, the y- and z-components can be obtained as:

$$\rho\frac{Dv}{Dt} = -\frac{\partial p}{\partial y} + \frac{\partial \tau_{xy}}{\partial x} + \frac{\partial \tau_{yy}}{\partial y} + \frac{\partial \tau_{zy}}{\partial z} + \rho f_y \tag{A.3.6}$$

$$\rho\frac{Dw}{Dt} = -\frac{\partial p}{\partial z} + \frac{\partial \tau_{xz}}{\partial x} + \frac{\partial \tau_{yz}}{\partial y} + \frac{\partial \tau_{zz}}{\partial z} + \rho f_z \tag{A.3.7}$$

Equations (A.3.5) to (A.3.7) are the Navier-Stokes equations in non-conservation form. In order to transform them to conservation form, first consider equation (A.3.5). In terms of the definition of the substantial derivative the left hand side can be rewritten as:

$$\rho\frac{Du}{Dt} = \rho\frac{\partial u}{\partial t} + \rho\mathbf{V}.\nabla u \tag{A.3.8}$$

in which $$\rho\frac{\partial u}{\partial t} = \frac{\partial(\rho u)}{\partial t} - u\frac{\partial \rho}{\partial t} \tag{A.3.9}$$

and $$\rho\mathbf{V}.\nabla u = \nabla.(\rho u\mathbf{V}) - u\nabla.(\rho\mathbf{V}) \tag{A.3.10}$$

Substituting (A.3.9) and (A.3.10) into (A.3.8) gives:

$$\rho\frac{Du}{Dt}=\frac{\partial(\rho u)}{\partial t}-u\left[\frac{\partial\rho}{\partial t}+\nabla.(\rho\mathbf{V})\right]+\nabla.(\rho u\mathbf{V}) \tag{A.3.11}$$

The term in square bracket when expanded is actually the right hand side of equation (A.2.2). Therefore, equation (A.3.11) becomes:

$$\rho\frac{Du}{Dt}=\frac{\partial(\rho u)}{\partial t}+\nabla.(\rho u\mathbf{V}) \tag{A.3.12}$$

Substituting (A.3.12) into (A.3.5) gives:

$$\frac{\partial(\rho u)}{\partial t}+\nabla.(\rho u\mathbf{V})=-\frac{\partial p}{\partial x}+\frac{\partial\tau_{xx}}{\partial x}+\frac{\partial\tau_{yx}}{\partial y}+\frac{\partial\tau_{zx}}{\partial z}+\rho f_x \tag{A.3.13}$$

Similarly, in y- and z-directions the following equations are obtained:

$$\frac{\partial(\rho v)}{\partial t}+\nabla.(\rho v\mathbf{V})=-\frac{\partial p}{\partial y}+\frac{\partial\tau_{xy}}{\partial x}+\frac{\partial\tau_{yy}}{\partial y}+\frac{\partial\tau_{zy}}{\partial z}+\rho f_y \tag{A.3.14}$$

$$\frac{\partial(\rho w)}{\partial t}+\nabla.(\rho w\mathbf{V})=-\frac{\partial p}{\partial z}+\frac{\partial\tau_{xz}}{\partial x}+\frac{\partial\tau_{yz}}{\partial y}+\frac{\partial\tau_{zz}}{\partial z}+\rho f_z \tag{A.3.15}$$

Equations (A.3.13) to (A.3.15) are the Navier-Stokes equations in conservation form. In this research, the water is assumed inviscid, or in other words, the dissipative transport phenomena of viscosity, mass diffusion and thermal conductivity are neglected. By removing terms related to friction in equations (A.3.13) to (A.3.15) the momentum equations are simplified to:

$$\frac{\partial(\rho u)}{\partial t} + \nabla.(\rho u \mathbf{V}) = -\frac{\partial p}{\partial x} + \rho f_x \quad \text{(A.3.16)}$$

$$\frac{\partial(\rho v)}{\partial t} + \nabla.(\rho v \mathbf{V}) = -\frac{\partial p}{\partial y} + \rho f_y \quad \text{(A.3.17)}$$

$$\frac{\partial(\rho w)}{\partial t} + \nabla.(\rho w \mathbf{V}) = -\frac{\partial p}{\partial z} + \rho f_z \quad \text{(A.3.18)}$$

If the only body force is gravitational force, therefore $f_x = 0$, $f_y = 0$ and $f_z = -gravity$.

A.4 Energy equations

The energy equations are derived based on the law of conservation of energy. Again, to simplify the process of deriving energy equations, model of an infinitesimally small fluid element moving with the flow is used. The equations will then be transformed into the conservation form thereafter. Physically, the energy equations are based on the following principle:

Rate of change of energy inside fluid element	=	Net flux of heat into element	+	Rate of work done on element due to body force and surface forces	(A.4.1)

Since the water is assumed to be inviscid, the terms related to thermal conduction are removed:

Rate of change of energy inside fluid element	=	Rate of work done on element due to body force and surface forces	(A.4.2)

With the terms involved with friction being neglected, the energy flux diagram associated with an infinitesimally small fluid element moving with flow is as in Figure A.4.1. The net rate of work done by pressure in the x-direction is:

$$\left[up - \left(up + \frac{\partial (up)}{\partial x} dx \right) \right] dydz = - \frac{\partial (up)}{\partial x} dx\, dy\, dz \qquad (A.4.3)$$

On the other hand, the rate of work done by the body forces acting on the fluid element moving along x-direction at a velocity u is $(\rho f_x.u.dx.dy.dz)$. The net rates of work done by pressure and by body force in the y- and z-directions are obtained similarly, giving the total net rate of work done by pressure:

$$\boxed{\text{Rate of work done on element due to body force and surface forces}} = \left[\rho \mathbf{f}.\mathbf{V} - \frac{\partial (up)}{\partial x} - \frac{\partial (vp)}{\partial y} - \frac{\partial (wp)}{\partial z} \right] dx\, dy\, dz \qquad (A.4.4)$$

Considering now the rate of change of energy inside the fluid element, it comprises of two contributions:

- Internal energy due to random molecular motion, *e* (per unit mass).
- Kinetic energy due to translational motion of the fluid element.

In mathematic form, the rate of change of energy inside the fluid element is:

$$\boxed{\text{Rate of change of energy inside fluid element}} = \rho \frac{D}{Dt} \left(e + \frac{V^2}{2} \right) dx\, dy\, dz \qquad (A.4.5)$$

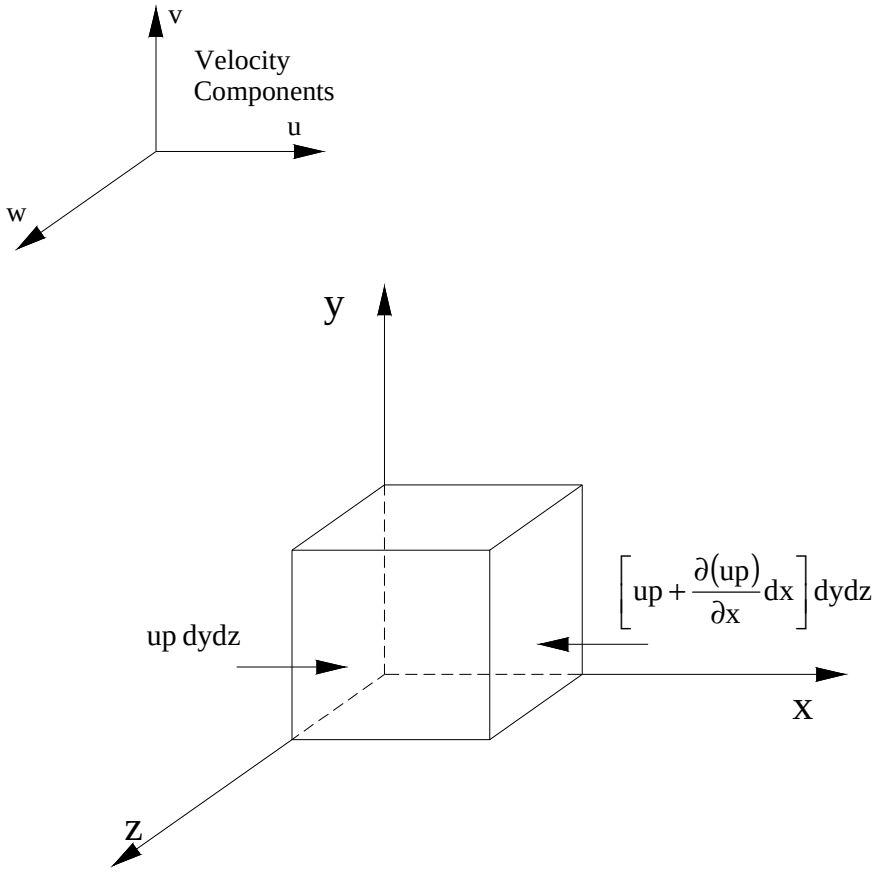

Figure A.4.1 Energy fluxes associates with an infinitesimally small fluid element moving in the flow.

From (A.4.3) to (A.4.5), it can be obtained that:

$$\rho\frac{D}{Dt}\left(e+\frac{V^2}{2}\right)dx\,dy\,dz=\left[\rho\mathbf{f}.\mathbf{V}-\frac{\partial(up)}{\partial x}-\frac{\partial(vp)}{\partial y}-\frac{\partial(wp)}{\partial z}\right]dx\,dy\,dz$$

or

$$\rho\frac{D}{Dt}\left(e+\frac{V^2}{2}\right)=\rho\mathbf{f}.\mathbf{V}-\left[\frac{\partial(up)}{\partial x}+\frac{\partial(vp)}{\partial y}+\frac{\partial(wp)}{\partial z}\right] \qquad (A.4.6)$$

Re-written in the form of conservation, the energy equation for invicid flow is:

$$\frac{\partial}{\partial t}\left[\rho\left(e+\frac{V^2}{2}\right)\right]+\nabla.\left[\rho\left(e+\frac{V^2}{2}\right)\mathbf{V}\right]=\rho\mathbf{f}.\mathbf{V}-\left[\frac{\partial(up)}{\partial x}+\frac{\partial(vp)}{\partial y}+\frac{\partial(wp)}{\partial z}\right] \qquad (A.4.7)$$

A.5 Equations in use for solving green water problem

Solutions to green water flow are achieved through solutions to velocity and pressure fields. For incompressible, inviscid flow, the following system of equations has been derived:

$$\left.\begin{aligned}
&\frac{\partial u}{\partial x}+\frac{\partial v}{\partial y}+\frac{\partial w}{\partial z}=0\\
&\frac{\partial(\rho u)}{\partial t}+\nabla.(\rho u\mathbf{V})=-\frac{\partial p}{\partial x}+\rho f_x\\
&\frac{\partial(\rho v)}{\partial t}+\nabla.(\rho v\mathbf{V})=-\frac{\partial p}{\partial y}+\rho f_y\\
&\frac{\partial(\rho w)}{\partial t}+\nabla.(\rho w\mathbf{V})=-\frac{\partial p}{\partial z}+\rho f_z\\
&\frac{\partial}{\partial t}\left[\rho\left(e+\frac{V^2}{2}\right)\right]+\nabla.\left[\rho\left(e+\frac{V^2}{2}\right)\mathbf{V}\right]=\rho\mathbf{f}.\mathbf{V}-\left[\frac{\partial(up)}{\partial x}+\frac{\partial(vp)}{\partial y}+\frac{\partial(wp)}{\partial z}\right]
\end{aligned}\right\} \quad (A.5.1)$$

Note that the first four equations in equation system (A.5.1) are self-contained, i.e. they are four equations for four dependent variables u, v, w and p. With the assumptions of incompressible and inviscid flow, the energy equation is not required any more and hence is decoupled from the analysis. Therefore, the resulting system of equations for incompressible and inviscid flow is:

$$\left.\begin{aligned}
&\frac{\partial u}{\partial x}+\frac{\partial v}{\partial y}+\frac{\partial w}{\partial z}=0\\
&\frac{\partial(\rho u)}{\partial t}+\nabla.(\rho u\mathbf{V})=-\frac{\partial p}{\partial x}+\rho f_x\\
&\frac{\partial(\rho v)}{\partial t}+\nabla.(\rho v\mathbf{V})=-\frac{\partial p}{\partial y}+\rho f_y\\
&\frac{\partial(\rho w)}{\partial t}+\nabla.(\rho w\mathbf{V})=-\frac{\partial p}{\partial z}+\rho f_z
\end{aligned}\right\} \qquad \text{(A.5.2)}$$

Appendix B:
Evaluation of Spray Wetting

Considering a plane AA fixed relative to the earth as shown in Figure B.1, the ship passes through the plane with a constant forward velocity U. Figure B.2 shows the view in the reference plane AA as a freeboard exceedance is occurring and Figure B.3 shows the velocity diagram in the horizontal plane.

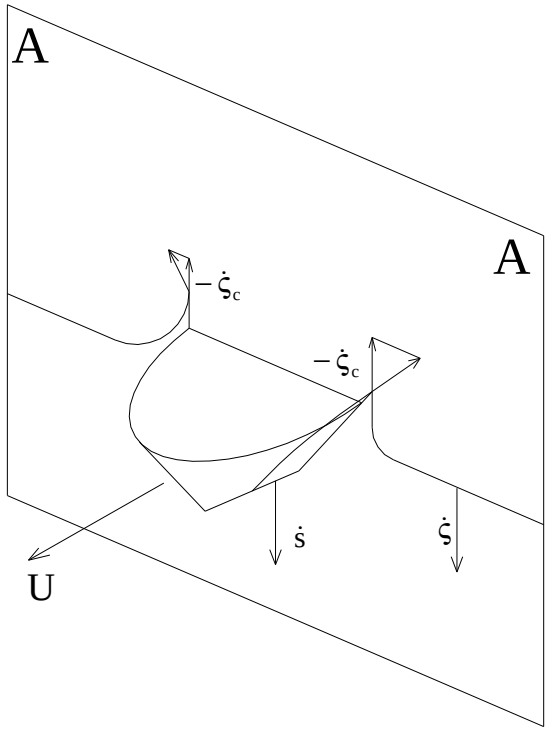

Figure B.1 Ship passing reference plane AA (Lloyd, 1994).

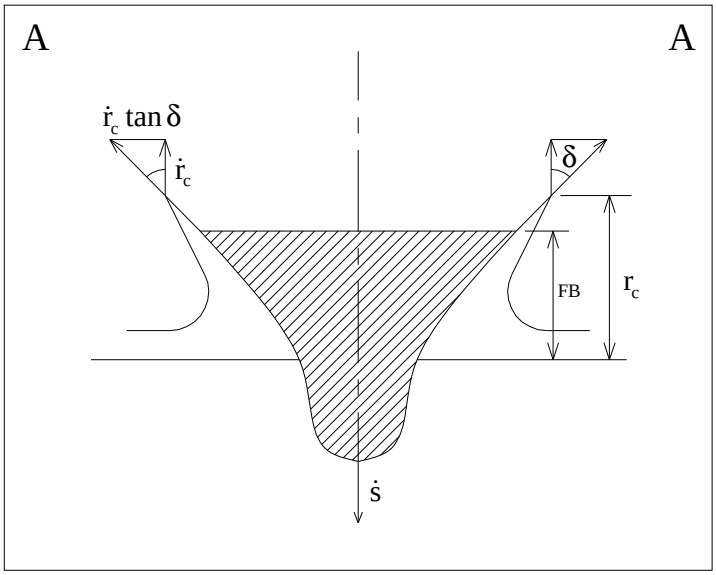

Figure B.2 Vector diagram in reference frame AA (Lloyd, 1994).

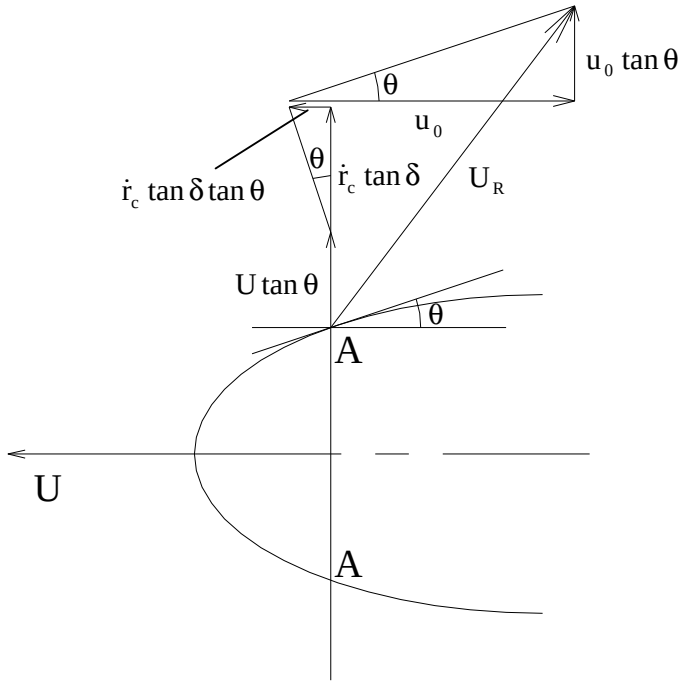

Figure B.3 Top view of horizontal velocity diagram (Lloyd, 1994).

An observer on the ship sees the velocity of the water adjacent to the hull aligned to the hull surface and the horizontal component due to the relative vertical velocity is:

$$\dot{r}_c \tan\delta \tag{B.1}$$

where δ is the flare angle at the deck edge. If there is no forward velocity or waves, the spray sheet would be shed in a direction normal to the deck edge and the forward velocity component of such is:

$$\dot{r}_c \tan\delta \tan\theta \tag{B.2}$$

There is also a transverse component $U\tan\theta$ due to the forward velocity of the expanding hull as it passes through the plane. Finally, there is a longitudinal component velocity u_o due to the orbital velocity of the incident wave at the surface. The expanding hull generates a lateral component velocity $u_o\tan\theta$. Therefore, the total resultant velocity in the horizontal plane is given by:

$$U_R = \sqrt{[(U+u_o)\tan\theta + \dot{r}_c \tan\delta]^2 + (u_o - \dot{r}_c \tan\delta\tan\theta)^2} \tag{B.3}$$

The water surface has an upward vertical velocity $-\dot{\zeta}_c$ relative to the earth. It is assumed that each water particle follows a simple ballistic trajectory and that the vertical motion of the ship between the times of freeboard exceedance and the potential wetting is negligible (i.e. the time of flight of the particle is small). It is also assumed that the freeboard at the exceedance station is the same as the freeboard at the impact station. The range (defined as the horizontal distance travelled when the particle has returned to its original altitude on leaving the edge of the deck) is given by:

$$R = -\frac{2U_R \dot{\zeta}_c}{g} \tag{B.4}$$

and the time of flight is: $$T_F = -\frac{2\dot{\zeta}_c}{g} \tag{B.5}$$

The bearing of the trajectory relative to the axis of the ship is given by:

$$\tan\varepsilon = \frac{(U + u_0)\tan\theta + \dot{r}_c \tan\delta}{u_0 - \dot{r}_c \tan\delta \tan\theta} \tag{B.6}$$

And the particle will return to the deck level at a point x_I metres abaft and y_I metres outboard of the launch point. The impact coordinates are given by:

$$x_I = x_{takeoff} + R\cos\varepsilon \tag{B.7}$$

$$y_I = \frac{B_{takeoff}}{2} + R\sin\varepsilon \tag{B.8}$$

Meanwhile, the ship has moved forward a distance UT_F so that the *x* coordinate of the impact point relative to the ship is extended to:

$$x_I = x_{takeoff} + R\cos\varepsilon + UT_F \tag{B.9}$$

A wetting occurs if $y_I < \frac{B_{local}}{2}$ where B_{local} is the local beam as the deck expands due to forward velocity at impact station x_I.

Appendix C: Investigation of the Sensitivity of CFD Simulation Results to Grid Size

C.1 Introduction

This Section aims to investigate the sensitivity of CFD simulation results to grid file. Three grids of systematically varied sizes were defined and simulated. The results were later compared. The outcome was used as the basis to justify the grid size selected for simulation of green water models in this thesis.

C.2 Sectioning of grid

The control volume was divided into three zones for meshing as in Figure C.2.1. Zone B represented green water and it was filled with water prior to simulation. Zone A was where interaction between water and structure was most active. Zone C made up the rest of the control volume.

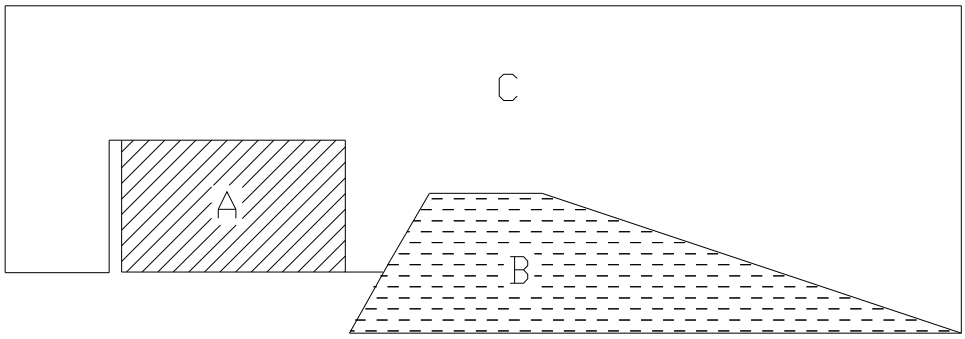

Figure C.2.1 Sectioning of control volume for meshing.

Since most interaction between water and deck structure took place in zone A, the meshing of this zone is critical to output results. The investigation of the sensitivity of simulation results to grid size, therefore, only focused on varying the grid size of zone A. The mesh of zone B was kept unchanged but the mesh of zone C changed slightly with the grid size of zone A because these two zones were attached together.

C.3 Grid variation

At model scale, volume of zone A was 2.903×10^6 mm^3. Three grid sizes were selected. The refinement factor was set to 2.0, i.e. if grid size is denoted by κ, the refinement factor γ is:

$$\gamma = \frac{\kappa_{coarse}}{\kappa_{fine}} = 2.0 \qquad \text{(C.3.1)}$$

For this investigation study, a sample test run was modelled. It corresponded to the case when the ship was without a breakwater and travelled at a velocity equivalent to Fn = 0.25. The corresponding full-scale wave height was 8.0m and wave period 12s. Table C.3.1 summarises the number of elements corresponding to three grid sizes and Figures C.3.1 to C.3.3 show the visualisation of the grids investigated.

Table C.3.1 **Number of elements corresponding to grid sizes of zone A.**

Grid size κ (mm)	**Number of elements in zone A**	**Total number of elements in all zones**
2.5	179,340	813,149
5.0	21,930	460,588
10.0	2.655	391,022

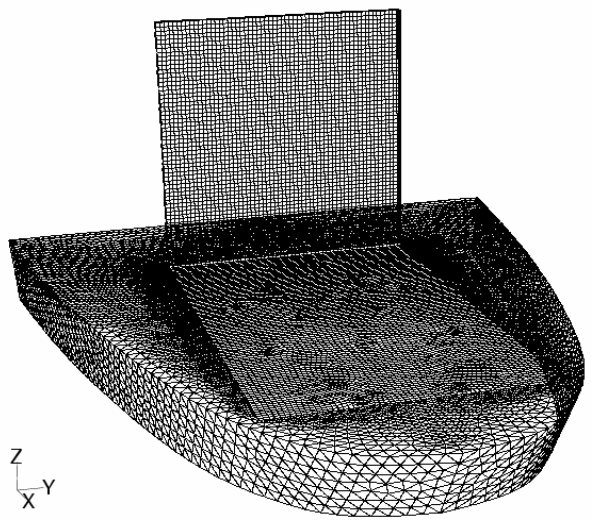

Figure C.3.1 Mesh file of ship body corresponding to grid size of 2.5mm.

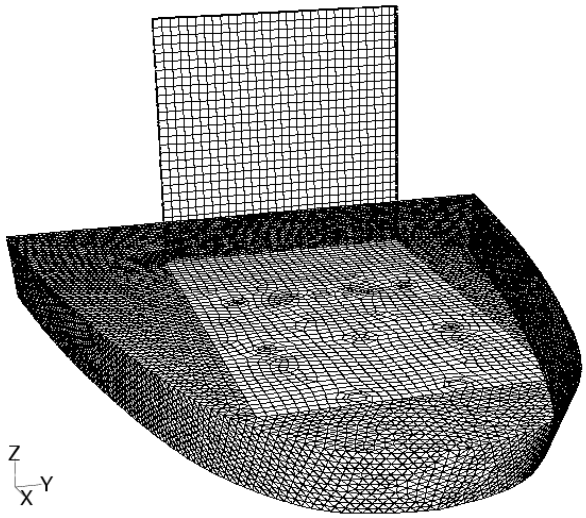

Figure C.3.2 Mesh file of ship body corresponding to grid size of 5.0mm.

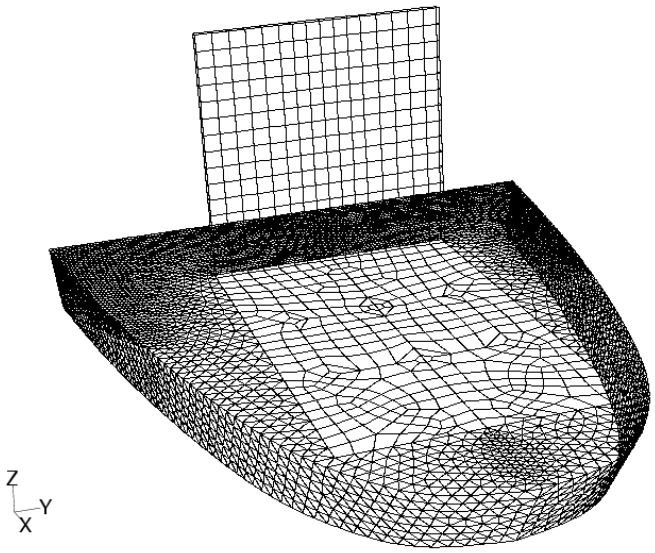

Figure C.3.3 Mesh file of ship body corresponding to grid size of 10.0mm.

C.4 Numerical results

Numerical results were compared in three aspects:

- Green water loads on vertical surfaces or longitudinal deck loads.
- Green water loads on deck plating or vertical deck loads.
- Behaviour of green water flows on deck.

The outcomes are presented in following sub-sections.

C.4.1 Green water loads on vertical surfaces

Figures C.4.1 to C.4.6 compare green water loads on vertical load cells of the load-cell box. In Figure C.4.1, peak impact load corresponding to grid size of 5.0mm was approximately 20 percent higher than those for other grid sizes. However, no significant difference was noticed in any other Figures. The global characteristics of the load curves were relatively consistent. Refinement of the grid did appear to refine the results of loads on vertical surfaces.

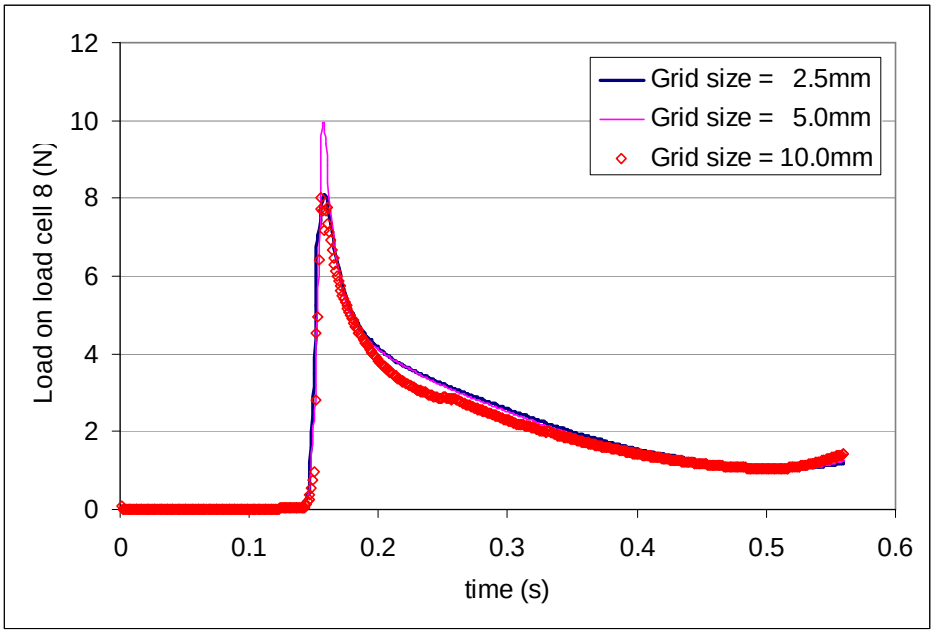

Figure C.4.1 Green water loads on load cell 8.

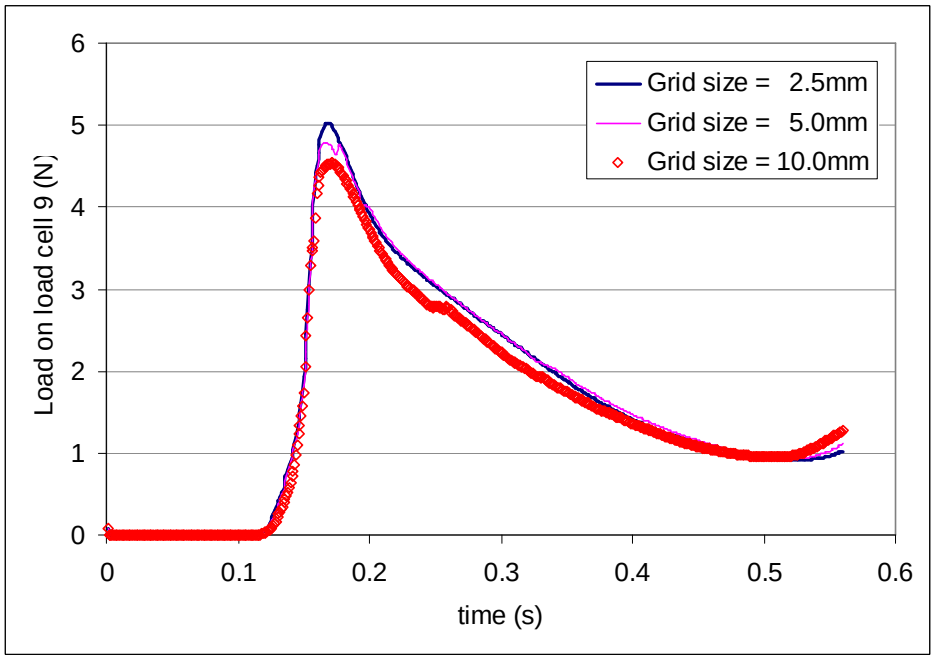

Figure C.4.2 Green water loads on load cell 9.

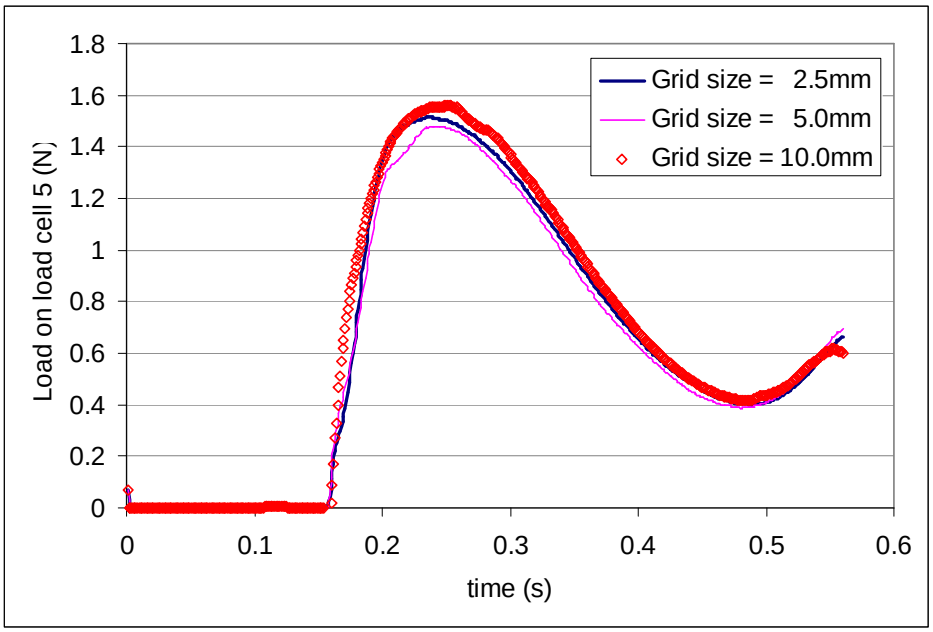

Figure C.4.3 Green water loads on load cell 5.

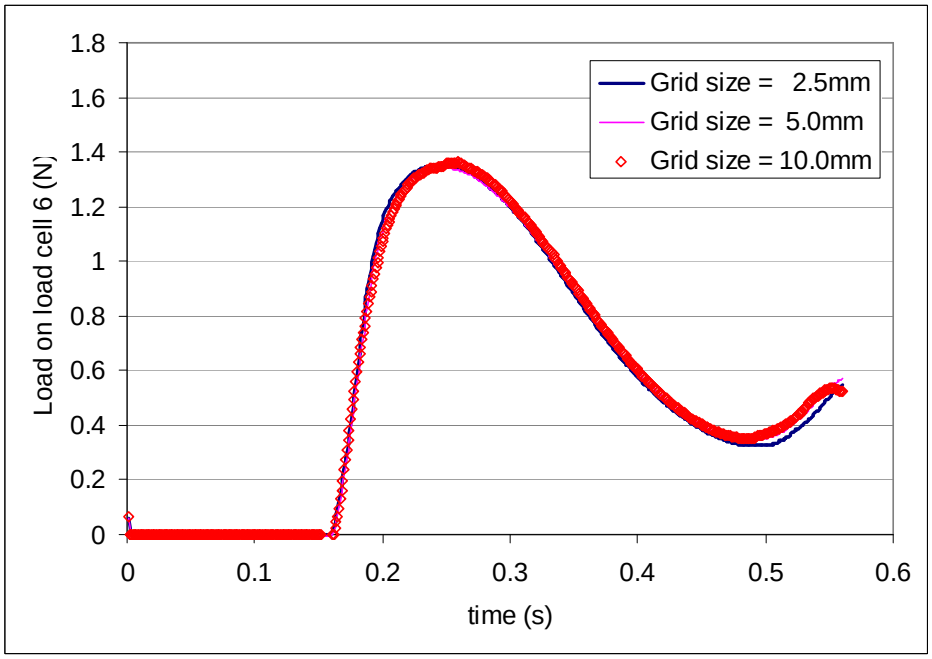

Figure C.4.4 Green water loads on load cell 6.

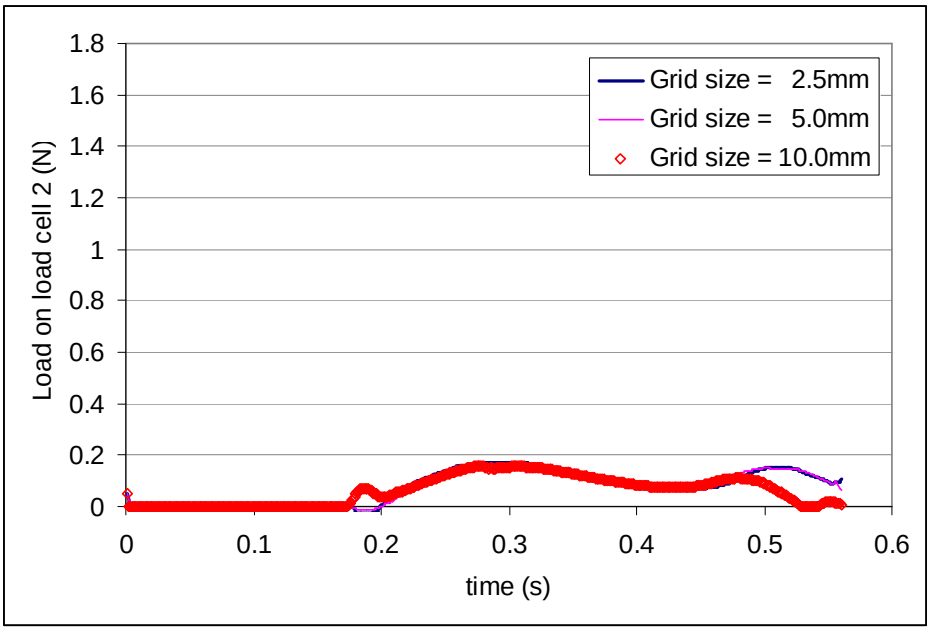

Figure C.4.5 Green water loads on load cell 2.

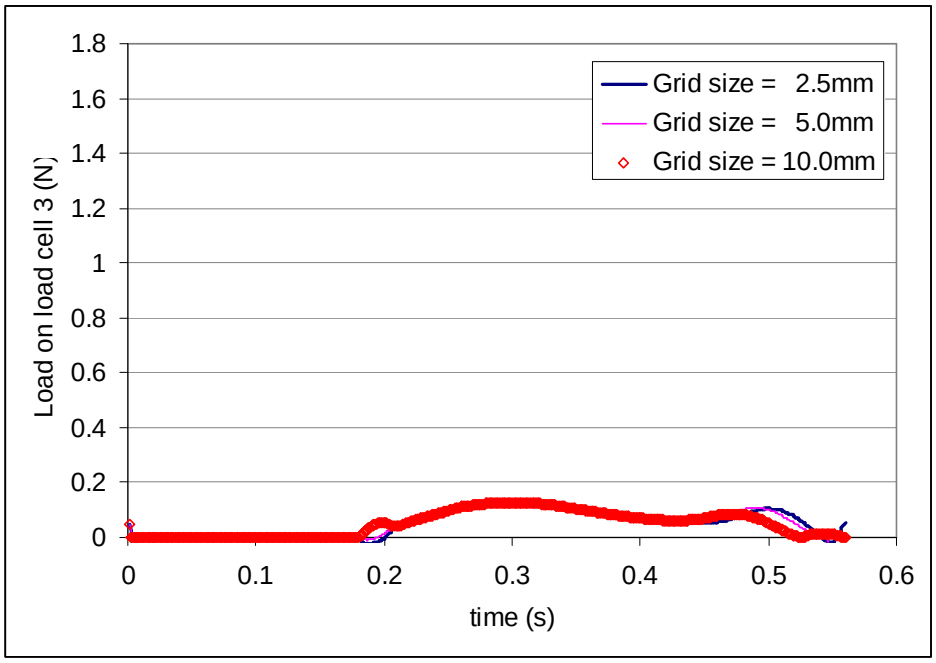

Figure C.4.6 Green water loads on load cell 3.

C.4.2 Green water loads on deck plating

Similar to green water loads on vertical surfaces, load on deck plating shows relatively consistent behaviour (Figure C.4.7). Refinement of the grid also appeared to refine the numerical results. Except for the first impulse in the load curve (which indicates a local effect rather than a global characteristic of the green water load), the difference in results between grid size of 2.5mm and 5.0mm was small. This implies that further refinement of the grid would not have resulted in significant improvement of the output results.

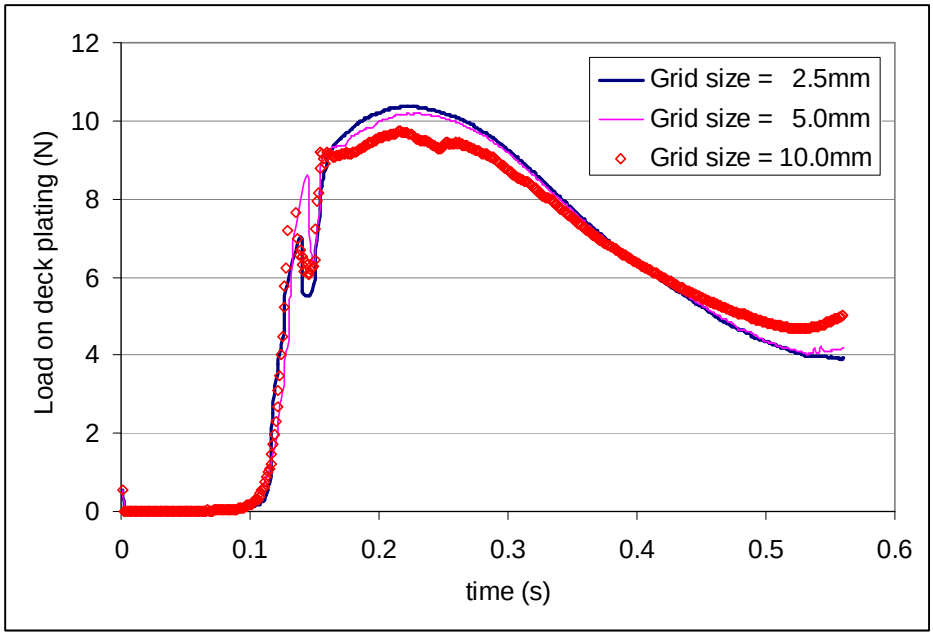

Figure C.4.7 Green water loads on deck plating.

C.4.3 Green water behaviour on deck

Figures C.4.8 and C.4.9 show sample visualisation of green water flow on deck for various grid sizes. It can be seen that finer grid size could reflect better changes in hydro-gradients of the flow. Hence, the output results became more precise. At grid size of 10mm, subtle details of the flow such as air bubbles or cavities could not be reproduced. As the grid size was reduced to 5.0mm, more details in the flow were present. At grid size of 2.5mm, even small air cavities could be reproduced.

C.5 Conclusions

Evaluation of numerical results in Sections C.4.1 to C.4.3 consolidates the fact that finer grid will refine the simulation output results. Some local effects might be present at intermediate grid size but further refinement of the grid can stablise the results. For the simulation in this thesis, grid size of 2.5mm appears to be adequate for achieving reliable results, both in terms of loading and green water behaviour.

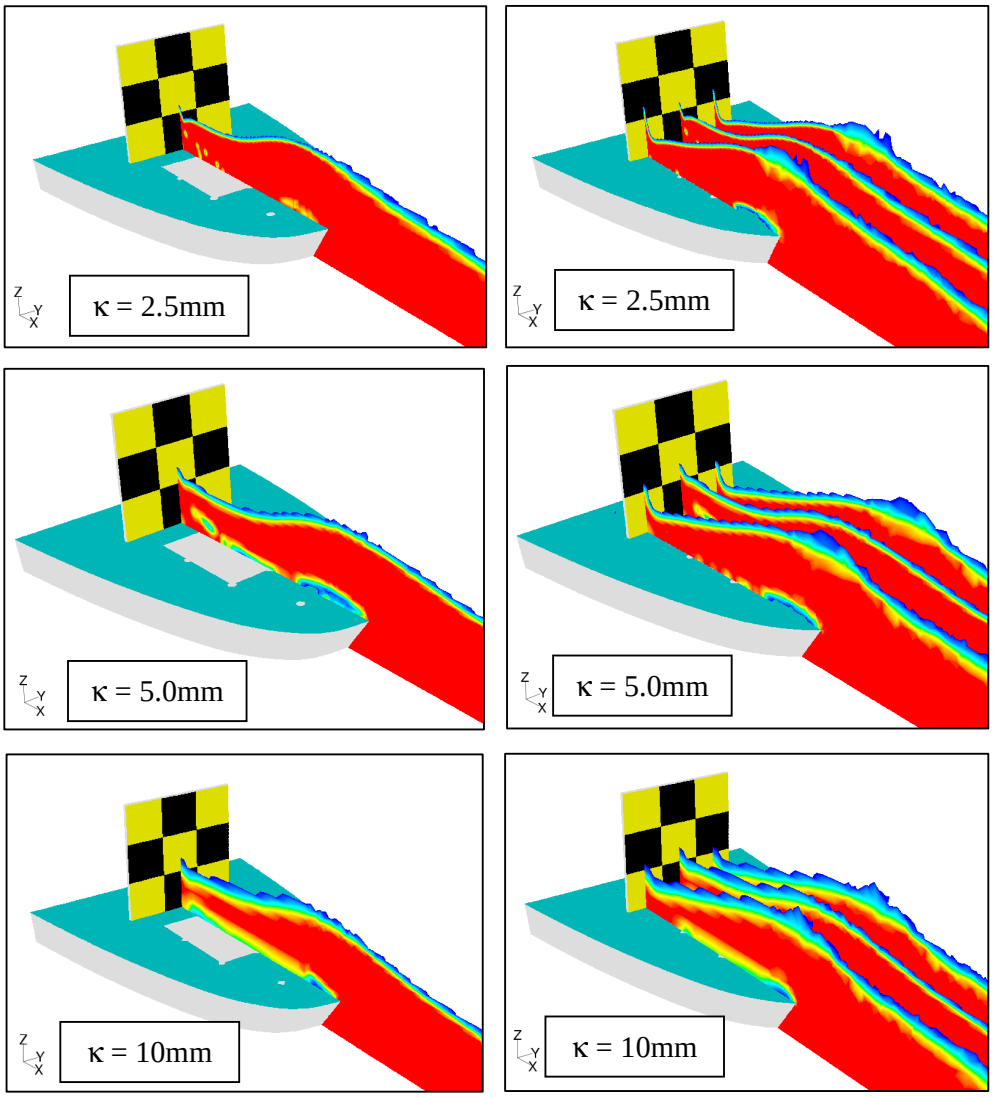

Figure C.4.8 Visualisation of green water flow on deck at the time of peak impact loads on bottom-row load cells (t = 0.16s).

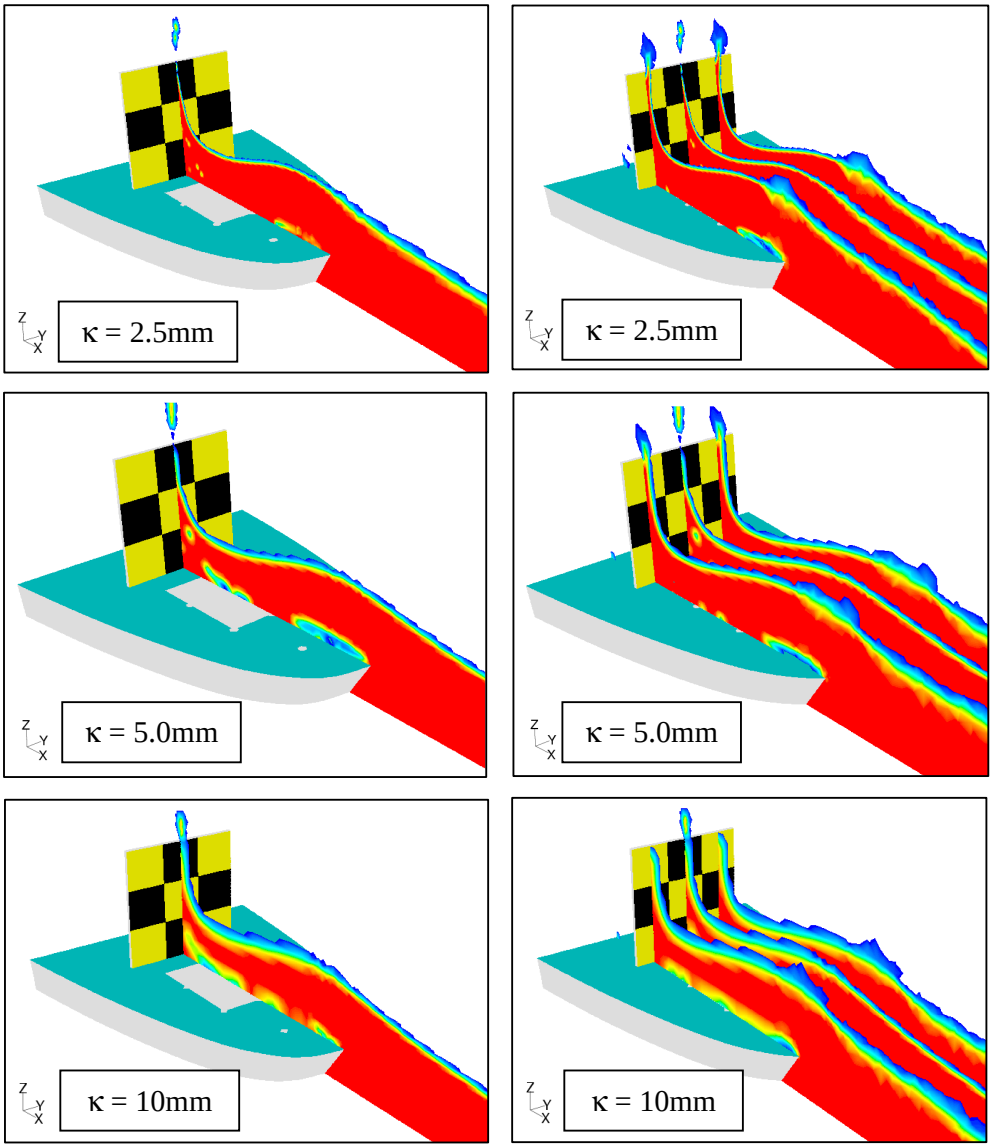

Figure C.4.9 Visualisation of green water flow on deck at t = 0.20s showing run-up of water on vertical surface.